

**Atmospheric Black Carbon: Measurements in the Los
Angeles Atmosphere and Aging by Condensation of Organic
Aerosol**

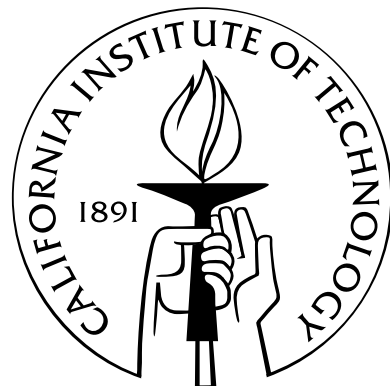
Thesis by

Andrew Richard Metcalf

In Partial Fulfillment of the Requirements

for the Degree of

Doctor of Philosophy



California Institute of Technology

Pasadena, California

2012

(Defended May 17, 2012)

© 2012

Andrew Richard Metcalf

All Rights Reserved

to my parents

Acknowledgements

First and foremost, praise goes to my Lord and Savior Jesus Christ for providing for my every need during graduate school. I am truly blessed to have had my health, financial, emotional, and intellectual needs met at every turn, something no earthly power is capable of. I truly believe that following the example that Jesus set forth for us on this earth has given me the ability to handle whatever life has thrown at me.

My work during these past years was made possible with the support of many people. Special thanks to my advisors John Seinfeld and Richard Flagan. Much of the work I have done at Caltech actually will not end up being presented in this thesis. Clearly, through everything, you both have given me the freedom to explore many things in lab and the patience to let me fail multiple times. Along the way I have gained many valuable skills that I will no doubt call upon for the rest of my career. I also thank the rest of my committee members, past and present, Yuk Yung, Haflidi Jonsson, Geoff Blake, and Paul Wennberg, who have provided valuable feedback, advice, and encouragement. I only wish I had included you all more throughout my studies.

The support staff at Caltech deserve special mention because they truly are second to none. Yvette Grant, Liz Boyd, and many other assistants have handled most of the administrative details over the years so that I could focus on my research and not get bogged down in those details. The machinists and electricians on campus have engaged in many helpful off-the-clock discussions with me as I was building instruments. The cooperative and collaborative nature of this campus has allowed me to knock on several professors' doors and ask very specific questions about modeling techniques and other things that would otherwise take me a long time to figure out. The sharing of tools and ideas across research groups has also been a conduit to accomplishing tasks faster.

I have been blessed to have a great many friends while here at Caltech; too many to name, in fact, lest I omit any in error. A few worth mentioning are Anna Beck and Claire Farnsworth, my fellow ESE classmates. We fought many a battle together our first year here! Arthur Chan was my roommate for most of my time here and is a very dear friend of mine because (or in spite?) of that time together. Arthur, I hope our long, in-depth science discussions continue until we are old men owning and operating a bakery somewhere in our retirement from academics. The many other people of the Seinfeld-Flagan group, both past and present, are a great group of people to be around, even outside of work. Of course, Christine, the love and support you have given me these past 2+ years mean so much to me. I cannot possibly find the words to properly explain what you mean to me, and I hope that in the future I can demonstrate this to you instead.

My entire family has been supportive of my time away from home to pursue the science I am passionate about but can never seem to fully explain. More than anything, I am where I am today because of my parents, Donald and Martha Metcalf. Thank you both for providing for my every need growing up. We (Joe, Micah, and I) are truly blessed to have you as our parents. You both define what it means to put your kids before yourselves. You taught us love, compassion, respect, and showed us the way to Jesus. Any good quality that I have as a person is because of the upbringing I have received by you. I hope the work contained in this thesis and in the career I am about to begin will make you as proud of me and I am to call you my parents.

Abstract

Aerosol particles in the atmosphere scatter and absorb solar radiation; an interaction that yields the largest uncertainty in models of future climate change. While most aerosols scatter light and, therefore, cool the environment, absorbing aerosol warms the environment. In particular, black carbon (BC) aerosol, the largest component of absorbing aerosol, may exhibit the second-largest forcing on climate behind greenhouse gases. In addition, the mixing state of BC aerosol, or the degree to which a BC core is coated with a scattering substance, may significantly increase the absorbing potential of BC. This thesis presents results from field and laboratory studies of BC aerosol, its mixing state in the atmosphere, and how it ages in the presence of condensing secondary organic aerosol.

A major field study, CalNex 2010, was conducted in Southern California to study air quality and climate change issues. Measurements of BC aerosol in and around the Los Angeles (LA) Basin reveal the evolution of BC aerosol from a thinly coated state near sources in the eastern LA Basin to a more thickly coated state in the outflow regions of the Basin. While the majority of BC aerosol emitted in the LA Basin remains near the surface, some BC aerosol is transported to the free troposphere through sea-breeze and mountain-flow coupling. BC aerosol above the inversion layer tends to be thickly coated, indicating that it is more aged than the BC measured near the surface.

To understand how the mixing state of BC evolves with secondary formation of species in the atmosphere, carefully controlled environmental chamber experiments were conducted. Two types of secondary organic aerosol (SOA) precursors, α -pinene and naphthalene, were reacted in the chamber to condense secondary products onto BC seed aerosol. The rate of growth and magnitude of absorption enhancement due to the secondary coating on BC was measured, revealing that growth

of coatings is diffusion-limited. Particle composition measurements reveal that condensed SOA onto BC seed particles is nearly identical to nucleated SOA from the same parent hydrocarbon. Measurements of coating thickness and optical properties provide insight to single-particle SOA growth and volatility.

Contents

Acknowledgements	iv
Abstract	vi
1 Introduction	1
2 Black Carbon Aerosol over the Los Angeles Basin during CalNex	13
2.1 Abstract	14
2.2 Introduction	14
2.3 CalNex 2010	17
2.3.1 Climatology of the Los Angeles Basin	17
2.3.2 FLEXPART Modeling	18
2.3.3 Twin Otter Flights	20
2.4 Refractory Black Carbon Measurement	21
2.4.1 Single Particle Soot Photometer	21
2.4.2 Mixing State Determination	22
2.4.3 Mie Scattering Model	23
2.4.4 rBC Number and Mass Concentrations	24
2.5 Results and Discussion	25
2.5.1 Regional Variability in rBC Aerosol	25
2.5.2 Secondary Aerosol Chemical Composition	27
2.5.3 The rBC Mixing State	30

2.5.4	Variability of rBC Levels with Altitude	31
2.5.5	Case Study: “Weekend Effect” on rBC Aerosol	33
2.6	Summary	34
2.7	Appendix: Calibration of the SP2	35
2.7.1	The rBC Mass Calibration	35
2.7.2	Scattering Calibration	37
2.7.3	LEO Fitting	37
2.8	Acknowledgements	39
3	Secondary Organic Aerosol Coating Formation and Evaporation: Chamber Studies using Black Carbon Seed Aerosol and the Single-Particle Soot Photometer	77
3.1	Abstract	78
3.2	Introduction	78
3.3	Methods	81
3.3.1	Experimental Protocols	81
3.3.2	Instrumentation	83
3.3.3	Mie Scattering Model	86
3.4	Results	87
3.4.1	Fullerene Soot Characteristics	87
3.4.2	General Experimental Results	89
3.4.3	Aerosol Optical Properties	92
3.4.4	AMS Measurements	97
3.5	Conclusions	100
3.6	Appendix: Measurement of Angularly-Resolved Light Scattering from Single Particles	102
3.7	Acknowledgements	103
4	Future Work	132

A The Pasadena Aerosol Characterization Observatory (PACO): Chemical and Physical Analysis of the Western Los Angeles Basin Aerosol	135
B Impact of a Large Wildfire on Water-Soluble Organic Aerosol in a Major Urban Area: The 2009 Station Fire in Los Angeles County	163
C Water-Soluble Organic Aerosol in the Los Angeles Basin and Outflow Regions: Airborne and Ground Measurements during the 2010 CalNex Field Campaign	178
D Inorganic and Black Carbon Aerosols in the Los Angeles Basin during CalNex	194
E Characterization and Airborne Deployment of a New Counterflow Virtual Impactor Inlet	240
F Eastern Pacific Emitted Aerosol Cloud Experiment (E-PEACE)	258
G Ship Impacts on the Marine Atmosphere: Insights into the Contribution of Shipping Emissions to the Properties of Marine Aerosol and Clouds	286

List of Tables

2.1	Urban Black Carbon Measurement Studies.	55
2.2	California Black Carbon Measurement Studies.	56
2.3	Summary of CIRPAS Twin Otter Flights During CalNex 2010.	57
2.4	Summary of SP2 Measurements Broken Down by Region.	58
3.1	Summary of Experiments.	116
3.2	Summary of Non-Sphericity Values.	117
3.3	Optical Properties of Particles in this Study.	118

List of Figures

2.1	All flight paths of the CIRPAS Twin Otter during CalNex.	59
2.2	Regional definitions used for the CalNex study.	60
2.3	The 12-h integrated surface residence times from FLEXPART during two CalNex flights at various locations in the LA Basin.	61
2.4	Surface residence time back-trajectories from FLEXPART for the May 25 flight at various regions sampled during the flight.	62
2.5	Raw spectra of three single particles measured by the SP2.	63
2.6	SP2 mean lag time versus mean coating thickness for all 1-min average measurements during CalNex.	64
2.7	Campaign-average rBC number and mass distributions by region.	65
2.8	rBC mass and number concentrations observed in the LA Basin during CalNex.	66
2.9	The 1-min average SP2 data from Research Flight 16 on May 25, 2010.	67
2.10	The rBC mass-normalized concentration ratios of aerosol chemical compounds broken down by region from west to east in and near the Los Angeles Basin for the May 25 flight.	68
2.11	Positive matrix factorization results for the May 25 flight.	69
2.12	The 2-D histogram of optical diameter versus rBC core diameter of all particles detected in the West LA Basin region.	70
2.13	The 2-D histogram of coating thickness versus rBC core diameter of all particles in the West LA Basin and Banning Outflow regions.	71
2.14	Vertical profile of SP2 measurements during CalNex.	72

2.15	“Weekend Effect” case study results during CalNex.	73
2.16	Calibration data for the SP2 incandescence channels.	74
2.17	Calibration data for the SP2 scattering channels.	75
2.18	Comparison of the leading-edge only (LEO) fit amplitudes to the full Gaussian fit amplitudes for purely scattering particles.	76
3.1	Distributions of non-sphericity values for ammonium sulfate, fullerene soot, and polystyrene latex spheres.	119
3.2	Particle wall deposition rate coefficients of ammonium sulfate and fullerene soot for the two chambers.	120
3.3	Experiment 1, naphthalene photooxidation in the presence of rBC seed particles. . . .	121
3.4	Evolution of coating thickness in Experiment 1.	122
3.5	Experiment 5, high- NO_x α -pinene photooxidation in the presence of rBC seed particles.	123
3.6	Experiment 7, low- NO_x α -pinene photooxidation in the presence of rBC seed particles.	124
3.7	Optical properties as a function of mean coating thickness on the fullerene soot seed during Experiment 1.	125
3.8	Optical properties as a function of mean coating thickness on the fullerene soot seed during Experiment 5.	126
3.9	Optical properties as a function of mean coating thickness on the fullerene soot seed during Experiment 7.	127
3.10	Comparison of Mie-modeled absorption enhancement to measured absorption enhancement.	128
3.11	Normalized unit-mass resolution AMS organic mass fractions for each m/z at peak growth of naphthalene SOA condensed on rBC seed versus nucleated naphthalene SOA.	129
3.12	AMS results from Experiment 5.	130
3.13	AMS results from Experiment 7.	131

Chapter 1

Introduction

Radiative forcing due to aerosols has the largest uncertainty with respect to future climate change (IPCC, 2007). Aerosol particles primarily scatter light, which has a direct cooling effect on the atmosphere by reflecting solar radiation back to space. Aerosols which act as cloud condensation nuclei (CCN, particles onto which water vapor may condense to form clouds) also cool the atmosphere by causing clouds to have more water droplets per volume, resulting in smaller droplets, reduced precipitation, and longer cloud lifetimes. Clouds with a larger number of smaller droplets appear brighter, reflecting more solar radiation back to space than those with a smaller number of larger droplets. Some aerosols also absorb solar energy, which can have a warming effect on Earth's atmosphere. Indeed, the *uncertainty* of total aerosol forcing on Earth's climate is as large in magnitude as the *known* warming effect of greenhouse gases, such as CO₂, which makes the study of these effects critical to improving our understanding of the climate system (IPCC, 2007; Hansen *et al.*, 2011).

Black carbon (BC) aerosol is the dominant component of light-absorbing atmospheric aerosol, and may be second only to CO₂ in terms of contribution to climate warming (Jacobson, 2001; Ramanathan and Carmichael, 2008). BC is emitted from a variety of incomplete combustion sources, including diesel and gasoline-burning vehicles, residential fuel use, ships, and biomass burning. A significant presence of BC in ambient aerosol can lead to heating of the atmosphere, which affects atmospheric transport and cloud dynamics (e.g., Jacobson, 2002; Menon *et al.*, 2002; Chung and Seinfeld, 2005; Ramanathan *et al.*, 2007; Ramanathan and Carmichael, 2008; Bauer *et al.*, 2010; Ramana *et al.*, 2010; Jones *et al.*, 2011). In addition, transport of BC particles to Arctic regions where they deposit onto snow and ice surfaces and can significantly reduce the surface albedo (the proportion of incident light that is reflected), thus reducing the amount of solar radiation reflected back to space, and accelerate melting by absorbing solar energy and heating the snow or ice immediately surrounding the deposited BC particles (e.g., Warren and Wiscombe, 1980, 1985; Conway *et al.*, 1996; Painter *et al.*, 2007; Qian *et al.*, 2011).

After emission, BC particles can become coated by inorganic and organic non-light-absorbing components via coagulation with other particles and condensation of vapors (e.g., Abel *et al.*, 2003; Pósfai *et al.*, 2003; Riemer *et al.*, 2004; Moffet and Prather, 2009). Fresh urban-emitted BC has

been shown to be thinly coated with a light-scattering material, while BC in aged air masses tends to be more thickly coated (e.g., *Johnson et al.*, 2005; *Moteki et al.*, 2007; *Shiraiwa et al.*, 2007, 2008; *Schwarz et al.*, 2008; *Subramanian et al.*, 2010). A coating of non-light-absorbing components onto BC increases the light scattering and absorption cross sections of these particles, meaning that for a given mass of BC in a particle, the coated BC particle will have a larger forcing on climate (e.g., *Fuller et al.*, 1999; *Saathoff et al.*, 2003; *Schnaiter et al.*, 2005; *Bond et al.*, 2006; *Mikhailov et al.*, 2006; *Stier et al.*, 2006; *Slowik et al.*, 2007; *Zhang et al.*, 2008; *Khalizov et al.*, 2009; *Wehner et al.*, 2009; *Cross et al.*, 2010; *Lack and Cappa*, 2010; *Shiraiwa et al.*, 2010). An outstanding question regarding the mixing state of BC particles is whether coated soot is characterized as a soot core coated by a shell of condensed vapors or as a soot particle attached to the side of a scattering particle (e.g., *Fuller et al.*, 1999; *Lack and Cappa*, 2010; *Sedlacek III et al.*, 2012). A core-and-shell Mie model of light scattering describes BC absorption enhancement due to a coating fairly well in some cases, but applicability to atmospheric aerosols remains an open question.

In addition to these climate effects, the mixing state of BC aerosols affects the hygroscopic properties, cloud-formation potential, and atmospheric lifetime by wet deposition, which can affect transport of these particles to remote locations, such as the Arctic, and feed back on the direct radiative effects mentioned above (e.g., *Weingartner et al.*, 1997; *Saathoff et al.*, 2003; *Zuberi et al.*, 2005; *Jacobson*, 2006; *Stier et al.*, 2006). In short, the extent to which BC is mixed with non-light-absorbing aerosol components exerts a strong influence on its interaction with radiation and water and could have profound implications for future climate change (*Stier et al.*, 2007; *Cubison et al.*, 2008).

Until recently, simultaneous detection of BC aerosol and its mixing state was not possible with the most widely used techniques for ambient studies, such as collection of aerosol onto filters for offline analysis (e.g., *Fung*, 1990; *Chow et al.*, 1993; *Birch and Cary*, 1996) and for online analysis (e.g., *Hansen et al.*, 1984; *Petzold and Schönlinner*, 2004). Indirect methods, such as using absorption measurements to calculate the mass of BC based on assumed constants, are prone to artifacts because of the absorption enhancement discussed above (e.g., *Bond et al.*, 1999; *Kirchstetter et al.*,

2001; *Chow et al.*, 2008; *Reche et al.*, 2011). The Single Particle Soot Photometer (SP2, from Droplet Measurement Technologies, Boulder, CO, USA), allows for the simultaneous measurement of refractory black carbon (rBC) mass, from laser-induced incandescence of the rBC, and of the mixing state of those particles, from the light scattering signal (*Stephens et al.*, 2003; *Baumgardner et al.*, 2004; *Schwarz et al.*, 2006; *Moteki and Kondo*, 2007; *Slowik et al.*, 2007). Note that rBC as used here is, strictly speaking, what the SP2 measures, but that other terminology used in aerosol literature, namely BC, light-absorbing carbon, elemental carbon, and sometimes soot, usually mean the same thing.

This thesis presents results from two studies in which an SP2 is used to make rBC measurements. Chapter 2 discusses results from the CalNex field project in May, 2010. During this study, an SP2 was flown onboard a Twin Otter aircraft, which sampled air masses in and around the Los Angeles (LA) Basin. It was found that in the western LA Basin, an area containing many sources of rBC, the rBC aerosol was relatively thinly coated by light-scattering material. Over the desert, to the east of the LA Basin where the daytime sea breeze advects the LA air mass (Section 2.3.2), it was found that these coatings on rBC were thicker, indicating that these particles have aged during transport across the Basin (Section 2.5.3). In addition, rBC aerosol above the inversion layer, which traps most of the freshly emitted pollution near the surface, was found to be much more thickly coated than rBC near the surface, indicating that the air mass above the inversion layer contains more significantly aged aerosol (Section 2.5.4). This finding supports the observation that air masses above the inversion are not well mixed with the surface layer and may, in fact, be transported from far away. An additional finding presented in Chapter 2 was that the “weekend effect” in the LA Basin resulted in more thickly coated rBC particles throughout the Basin. The “weekend effect” is a well-known phenomenon in the Basin that results from lower NO_x emissions due to a decrease in industrial activities and diesel truck traffic on the weekends. All else being equal, lower NO_x results in faster photochemistry, which results in more condensation of secondary organic aerosol (SOA). During a CalNex case study of a Friday and Saturday (Section 2.5.5), it is shown that coatings of light-scattering material onto rBC aerosol were thicker everywhere in the LA Basin on Saturday. Finally, correlations of rBC coating

thicknesses measured with the SP2 to aerosol composition measurements with an Aerodyne Aerosol Mass Spectrometer (AMS, Aerodyne Research, Inc., Billerica, MA USA)) reveal that the coating material likely consists of nitrate and organics (Section 2.5.2).

Chapter 3 presents results from an environmental chamber study that examines SOA formation in the presence of an rBC aerosol seed. These are novel experiments in the sense that an rBC standard, fullerene soot, available from Alfa Aesar (Ward Hill, MA, USA) and used as a calibration material for SP2 instruments, has never been used in an environmental chamber study such as this before. In this study, it is shown that the presence of rBC seed aerosol does not affect the composition of the condensed SOA compared to nucleated SOA from the same parent hydrocarbon (Section 3.4.4). The optical properties of the aerosol studied reveal an enhancement to the absorption due to the organic coatings condensed onto the fullerene soot and comparisons to a Mie scattering model reinforce the assumption of a core-shell morphology for the coated rBC particles (Section 3.4.3). An important result of this study is to demonstrate the usefulness of the SP2 to show particle-by-particle growth of SOA in an environmental chamber. The protocol described in Chapter 3 leads to observations of coating evaporation, reflecting changes in SOA volatility, and of optical property evolution during SOA growth, reflecting chemical aging of the SOA.

Appendix D presents comparisons of the measured rBC levels during CalNex to simulated levels using a regional air quality model. The other appendices present results from three field projects that utilize aerosol size distribution data from custom-built scanning mobility particle sizer (SMPS) instruments. Appendix A and B present findings from the Pasadena Aerosol Characterization Observatory (PACO) study, which sampled ambient aerosol in Pasadena for five months in the summer of 2009. Appendix C presents results of water-soluble organic carbon measurements during CalNex. Appendix E presents characterization of a new counterflow virtual impactor inlet used to sample cloud droplet residuals that was first deployed during the Eastern Pacific Emitted Aerosol Cloud Experiment (E-PEACE) during the summer of 2011. Finally, Appendix F and G present some of the scientific findings from E-PEACE.

Bibliography

Abel, S. J., J. M. Haywood, E. J. Highwood, J. Li, and P. R. Buseck (2003), Evolution of biomass burning aerosol properties from an agricultural fire in southern Africa, *Geophys. Res. Lett.*, *30*(15), 1783, doi:10.1029/2003GL017342. 2

Bauer, S. E., S. Menon, D. Koch, T. C. Bond, and K. Tsigaridis (2010), A global modeling study on carbonaceous aerosol microphysical characteristics and radiative effects, *Atmos. Chem. Phys.*, *10*, 7439–7456, doi:10.5194/acp-10-7439-2010. 2

Baumgardner, D., G. L. Kok, and G. Raga (2004), Warming of the Arctic lower stratosphere by light absorbing particles, *Geophys. Res. Lett.*, *31*, L06117, doi:10.1029/2003GL018883. 4

Birch, M., and R. Cary (1996), Elemental carbon-based method for monitoring occupational exposures to particulate diesel exhaust, *Aerosol Sci. Technol.*, *25*, 221–241, doi:10.1080/02786829608965393. 3

Bond, T. C., T. L. Anderson, and D. Campbell (1999), Calibration and intercomparison of filter-based measurements of visible light absorption by aerosols, *Aerosol Sci. Technol.*, *30*(6), 582–600, doi:10.1080/027868299304435. 3

Bond, T. C., G. Habib, and R. W. Bergstrom (2006), Limitations in the enhancement of visible light absorption due to mixing state, *J. Geophys. Res.*, *111*, D20211, doi:10.1029/2006JD007315. 3

Chow, J. C., J. G. Watson, L. C. Pritchett, W. R. Pierson, C. A. Frazier, and R. G. Purcell (1993), The DRI thermal/optical reflectance carbon analysis system: description, evaluation and applications in U.S. air quality studies, *Atmos. Environ., Part A*, *27*(8), 1185–1201, doi:10.1016/0960-1686(93)90245-T. 3

Chow, J. C., P. Doraiswamy, J. G. Watson, L. W. Antony-Chen, S. S. H. Ho, and D. A. Sodeman (2008), Advances in integrated and continuous measurements for particle mass and chemical composition, *J. Air Waste Manage. Assoc.*, *58*, 141–163, doi:10.3155/1047-3289.58.2.141. 4

Chung, S. H., and J. H. Seinfeld (2005), Climate response of direct radiative forcing of anthropogenic black carbon, *J. Geophys. Res.*, 110, D11102, doi:10.1029/2004JD005441. 2

Conway, H., A. Gades, and C. Raymond (1996), Albedo of dirty snow during conditions of melt, *Water Resour. Res.*, 32(6), 1713–1718, doi:10.1029/96WR00712. 2

Cross, E. S., et al. (2010), Soot particle studies—instrument inter-comparison—project overview, *Aerosol Sci. Technol.*, 44(8), 592–611, doi:10.1080/02786826.2010.482113. 3

Cubison, M. J., B. Ervens, G. Feingold, K. S. Docherty, I. M. Ulbrich, L. Shields, K. A. Prather, S. Hering, and J. L. Jimenez (2008), The influence of chemical composition and mixing state of Los Angeles urban aerosol on CCN number and cloud properties, *Atmos. Chem. Phys.*, 8, 5649–5667, doi:10.5194/acp-8-5649-2008. 3

Fuller, K. A., W. C. Malm, and S. M. Kreidenweis (1999), Effects of mixing on extinction by carbonaceous particles, *J. Geophys. Res.*, 104(D13), 15,941–15,954, doi:10.1029/1998JD100069. 3

Fung, K. (1990), Particulate carbon speciation by MnO₂ oxidation, *Aerosol Sci. Technol.*, 12(1), 122–127, doi:10.1080/02786829008959332. 3

Hansen, A. D. A., H. Rosen, and T. Novakov (1984), The aethalometer—An instrument for the real-time measurement of optical absorption by aerosol particles, *Sci. Total Environ.*, 36, 191–196, doi:10.1016/0048-9697(84)90265-1. 3

Hansen, J., M. Sato, P. Kharecha, and K. von Schuckmann (2011), Earth's energy imbalance and implications, *Atmos. Chem. Phys. Discuss.*, 11(9), 27,031–27,105, doi:10.5194/acpd-11-27031-2011. 2

IPCC (2007), *Climate Change 2007: The Physical Science Basis. Contribution of Working Group I to the Fourth Assessment Report of the Intergovernmental Panel on Climate Change*, Cambridge University Press, Cambridge, United Kingdom and New York, NY, USA. 2

Jacobson, M. Z. (2001), Strong radiative heating due to the mixing state of black carbon in atmospheric aerosols, *Nature*, 409(6821), 695–697. 2

Jacobson, M. Z. (2002), Control of fossil-fuel particulate black carbon and organic matter, possibly the most effective method of slowing global warming, *J. Geophys. Res.*, 107(D19), 4410, doi: 10.1029/2001JD001376. 2

Jacobson, M. Z. (2006), Effects of externally-through-internally-mixed soot inclusions within clouds and precipitation on global climate, *J. Phys. Chem. A*, 110(21), 6860–6873, doi:10.1021/jp056391r. 3

Johnson, K. S., B. Zuberi, L. T. Molina, M. J. Molina, M. J. Iedema, J. P. Cowin, D. J. Gaspar, C. Wang, and A. Laskin (2005), Processing of soot in an urban environment: case study from the Mexico City Metropolitan Area, *Atmos. Chem. Phys.*, 5, 3033–3043, doi:10.5194/acp-5-3033-2005.

3

Jones, G. S., N. Christidis, and P. A. Stott (2011), Detecting the influence of fossil fuel and bio-fuel black carbon aerosols on near surface temperature changes, *Atmos. Chem. Phys.*, 11, 799–816, doi:10.5194/acp-11-799-2011. 2

Khalizov, A. F., H. Xue, L. Wang, J. Zheng, and R. Zhang (2009), Enhanced light absorption and scattering by carbon soot aerosol internally mixed with sulfuric acid, *J. Phys. Chem. A*, 113(6), 1066–1074, doi:10.1021/jp807531n. 3

Kirchstetter, T. W., C. E. Corrigan, and T. Novakov (2001), Laboratory and field investigation of the adsorption of gaseous organic compounds onto quartz filters, *Atmos. Environ.*, 35(9), 1663–1671, doi:10.1016/S1352-2310(00)00448-9. 3

Lack, D. A., and C. D. Cappa (2010), Impact of brown and clear carbon on light absorption enhancement, single scatter albedo and absorption wavelength dependence of black carbon, *Atmos. Chem. Phys.*, 10, 4207–4220, doi:10.5194/acp-10-4207-2010. 3

Menon, S., J. Hansen, L. Nazarenko, and Y. Luo (2002), Climate effects of black carbon aerosols in China and India, *Science*, 297(5590), 2250–2253, doi:10.1126/science.1075159. 2

Mikhailov, E. F., S. S. Vlasenko, I. A. Podgorny, V. Ramanathan, and C. E. Corrigan (2006), Optical properties of soot–water drop agglomerates: An experimental study, *J. Geophys. Res.*, 111, D07209, doi:10.1029/2005JD006389. 3

Moffet, R. C., and K. A. Prather (2009), In-situ measurements of the mixing state and optical properties of soot with implications for radiative forcing estimates, *Proc. Natl. Acad. Sci. U.S.A.*, 106(29), 11,872–11,877, doi:10.1073/pnas.0900040106. 2

Moteki, N., and Y. Kondo (2007), Effects of mixing state on black carbon measurements by laser-induced incandescence, *Aerosol Sci. Technol.*, 41(4), 398–417, doi:10.1080/02786820701199728.

4

Moteki, N., et al. (2007), Evolution of mixing state of black carbon particles: Aircraft measurements over the western Pacific in March 2004, *Geophys. Res. Lett.*, 34, L11803, doi: 10.1029/2006GL028943. 3

Painter, T. H., A. P. Barrett, C. C. Landry, J. C. Neff, M. P. Cassidy, C. R. Lawrence, K. E. McBride, and G. L. Farmer (2007), Impact of disturbed desert soils on duration of mountain snow cover, *Geophys. Res. Lett.*, 34, L12502, doi:10.1029/2007GL030284. 2

Petzold, A., and M. Schönlinner (2004), Multi-angle absorption photometry—a new method for the measurement of aerosol light absorption and atmospheric black carbon, *J. Aerosol Sci.*, 35(4), 421–441, doi:10.1016/j.jaerosci.2003.09.005. 3

Pósfai, M., R. Simonics, J. Li, P. V. Hobbs, and P. R. Buseck (2003), Individual aerosol particles from biomass burning in southern Africa: 1. Compositions and size distributions of carbonaceous particles, *J. Geophys. Res.*, 108(D13), 8483, doi:10.1029/2002JD002291. 2

Qian, Y., M. G. Flanner, L. R. Leung, and W. Wang (2011), Sensitivity studies on the impacts of Tibetan Plateau snowpack pollution on the Asian hydrological cycle and monsoon climate, *Atmos. Chem. Phys.*, 11(5), 1929–1948, doi:10.5194/acp-11-1929-2011. 2

Ramana, M. V., V. Ramanathan, Y. Feng, S.-C. Yoon, S.-W. Kim, G. R. Carmichael, and J. J. Schauer (2010), Warming influenced by the ratio of black carbon to sulphate and the black-carbon source, *Nat. Geosci.*, 3(8), 542–545, doi:10.1038/ngeo918. 2

Ramanathan, V., and G. Carmichael (2008), Global and regional climate changes due to black carbon, *Nat. Geosci.*, 1(4), 221–227, doi:10.1038/ngeo156. 2

Ramanathan, V., M. V. Ramana, G. Roberts, D. Kim, C. Corrigan, C. Chung, and D. Winker (2007), Warming trends in Asia amplified by brown cloud solar absorption, *Nature*, 448(7153), 575–578, doi:10.1038/nature06019. 2

Reche, C., et al. (2011), New considerations for PM, black carbon and particle number concentration for air quality monitoring across different European cities, *Atmos. Chem. Phys.*, 11, 6207–6227, doi:10.5194/acp-11-6207-2011. 4

Riemer, N., H. Vogel, and B. Vogel (2004), Soot aging time scales in polluted regions during day and night, *Atmos. Chem. Phys.*, 4, 1885–1893, doi:10.5194/acp-4-1885-2004. 2

Saathoff, H., K.-H. Naumann, M. Schnaiter, W. Schöck, O. Möhler, U. Schurath, E. Weingartner, M. Gysel, and U. Baltensperger (2003), Coating of soot and NH_4SO_4 particles by ozonolysis products of alpha-pinene, *J. Aerosol Sci.*, 34(10), 1297–1321, doi:10.1016/S0021-8502(03)00364-1.

3

Schnaiter, M., C. Linke, O. Möhler, K.-H. Naumann, H. Saathoff, R. Wagner, U. Schurath, and B. Wehner (2005), Absorption amplification of black carbon internally mixed with secondary organic aerosol, *J. Geophys. Res.*, 110, D19204, doi:10.1029/2005JD006046. 3

Schwarz, J. P., et al. (2006), Single-particle measurements of midlatitude black carbon and light-scattering aerosols from the boundary layer to the lower stratosphere, *J. Geophys. Res.*, 111, D16207, doi:10.1029/2006JD007076. 4

Schwarz, J. P., et al. (2008), Measurement of the mixing state, mass, and optical size of individual

black carbon particles in urban and biomass burning emissions, *Geophys. Res. Lett.*, 35, L13810, doi:10.1029/2008GL033968. 3

Sedlacek III, A. J., E. R. Lewis, L. I. Kleinman, J. Xu, and Q. Zhang (2012), Determination of and evidence for non-core-shell structure of particles containing black carbon using the Single-Particle Soot Photometer (SP2), *Geophys. Res. Lett.*, 39, L06802, doi:10.1029/2012GL050905. 3

Shiraiwa, M., Y. Kondo, N. Moteki, N. Takegawa, Y. Miyazaki, and D. R. Blake (2007), Evolution of mixing state of black carbon in polluted air from Tokyo, *Geophys. Res. Lett.*, 34, L16803, doi:10.1029/2007GL029819. 3

Shiraiwa, M., Y. Kondo, N. Moteki, N. Takegawa, L. K. Sahu, A. Takami, S. Hatakeyama, S. Yonemura, and D. R. Blake (2008), Radiative impact of mixing state of black carbon aerosol in Asian outflow, *J. Geophys. Res.*, 113, D24210, doi:10.1029/2008JD010546. 3

Shiraiwa, M., Y. Kondo, T. Iwamoto, and K. Kita (2010), Amplification of light absorption of black carbon by organic coating, *Aerosol Sci. Technol.*, 44(1), 46–54, doi:10.1080/02786820903357686. 3

Slowik, J. G., et al. (2007), An inter-comparison of instruments measuring black carbon content of soot particles, *Aerosol Sci. Technol.*, 41(3), 295–314, doi:10.1080/02786820701197078. 3, 4

Stephens, M., N. Turner, and J. Sandberg (2003), Particle identification by laser-induced incandescence in a solid-state laser cavity, *Appl. Opt.*, 42(19), 3726–3736, doi:10.1364/AO.42.003726. 4

Stier, P., J. H. Seinfeld, S. Kinne, J. Feichter, and O. Boucher (2006), Impact of nonabsorbing anthropogenic aerosols on clear-sky atmospheric absorption, *J. Geophys. Res.*, 111, D18201, doi:10.1029/2006JD007147. 3

Stier, P., J. H. Seinfeld, S. Kinne, and O. Boucher (2007), Aerosol absorption and radiative forcing, *Atmos. Chem. Phys.*, 7, 5237–5261, doi:10.5194/acp-7-5237-2007. 3

Subramanian, R., et al. (2010), Black carbon over Mexico: the effect of atmospheric transport on mixing state, mass absorption cross-section, and BC/CO ratios, *Atmos. Chem. Phys.*, *10*, 219–237, doi:10.5194/acp-10-219-2010. 3

Warren, S. G., and W. J. Wiscombe (1980), A model for the spectral albedo of snow. II: Snow containing atmospheric aerosols, *J. Atmos. Sci.*, *37*(12), 2734–2745, doi:10.1175/1520-0469(1980)037<2734:AMFTSA>2.0.CO;2. 2

Warren, S. G., and W. J. Wiscombe (1985), Dirty snow after nuclear war, *Nature*, *313*(6002), 467–470, doi:10.1038/313467a0. 2

Wehner, B., et al. (2009), Mixing state of nonvolatile aerosol particle fractions and comparison with light absorption in the polluted Beijing region, *J. Geophys. Res.*, *114*, D00G17, doi:10.1029/2008JD010923. 3

Weingartner, E., H. Burtscher, and U. Baltensperger (1997), Hygroscopic properties of carbon and diesel soot particles, *Atmos. Environ.*, *31*(15), 2311–2327, doi:10.1016/S1352-2310(97)00023-X. 3

Zhang, R., A. F. Khalizov, J. Pagels, D. Zhang, H. Xue, and P. H. McMurry (2008), Variability in morphology, hygroscopicity, and optical properties of soot aerosols during atmospheric processing, *Proc. Natl. Acad. Sci. U.S.A.*, *105*(30), 10,291–10,296, doi:10.1073/pnas.0804860105. 3

Zuberi, B., K. S. Johnson, G. K. Aleks, L. T. Molina, and M. J. Molina (2005), Hydrophilic properties of aged soot, *Geophys. Res. Lett.*, *32*, L01807, doi:10.1029/2004GL021496. 3

Chapter 2

Black Carbon Aerosol over the Los Angeles Basin during CalNex*

*Reproduced with permission from “Black carbon aerosol over the Los Angeles Basin during CalNex” by A. R. Metcalf, J. S. Craven, J. J. Ensberg, J. Brioude, W. Angevine, A. Sorooshian, H. T. Duong, H. H. Jonsson, R. C. Flagan, and J. H. Seinfeld, *Journal of Geophysical Research*, 117, D00V13, doi:10.1029/2011JK017255. Copyright 2012 by the American Geophysical Union.

2.1 Abstract

Refractory black carbon (rBC) mass and number concentrations were quantified by a Single Particle Soot Photometer (SP2) in the CalNex 2010 field study on board the Center for Interdisciplinary Remotely-Piloted Aircraft Studies (CIRPAS) Twin Otter in the Los Angeles (LA) Basin in May, 2010. The mass concentrations of rBC in the LA Basin ranged from 0.002–0.530 $\mu\text{g m}^{-3}$, with an average of 0.172 $\mu\text{g m}^{-3}$. Lower concentrations were measured in the Basin outflow regions and above the inversion layer. The SP2 afforded a quantification of the mixing state of rBC aerosols through modeling the scattering cross-section with a core-and-shell Mie model to determine coating thickness. rBC particles above the inversion layer were more thickly coated by a light-scattering substance than those below, indicating a more aged aerosol in the free troposphere. Near the surface, as the LA plume is advected from west to east with the sea breeze, a coating of scattering material grows on rBC particles, coincident with a clear growth of ammonium nitrate within the LA Basin and the persistence of water-soluble organic compounds as the plume travels through the outflow regions. Detailed analysis of the rBC mixing state reveals two modes of coated rBC particles; a mode with smaller rBC core diameters (~90 nm) but thick (>200 nm) coating diameters and a mode with larger rBC cores (~145 nm) with a thin (<75 nm) coating. The “weekend effect” in the LA Basin results in more thickly coated rBC particles, coinciding with more secondary formation of aerosol.

2.2 Introduction

Black carbon is an important atmospheric constituent owing to its role in both air pollution and climate. Refractory black carbon (rBC), alternatively referred to as elemental carbon, light-absorbing carbon, or simply black carbon, is emitted from a variety of incomplete combustion sources, including diesel and gasoline-burning vehicles, residential fuel use, ships, and biomass burning. rBC refers to the strongly light-absorbing component of soot, which may contain other constituents such as polycyclic aromatic hydrocarbons, aliphatic hydrocarbons, and other volatile compounds. rBC, as defined here, is the quantity reported in emission inventories (*Dentener et al.*, 2006) and simulated

in regional air quality models (*Binkowski and Roselle*, 2003). While the majority of atmospheric particulate chemical constituents primarily scatter sunlight, producing an overall cooling effect on climate, rBC absorbs strongly in visible and ultraviolet wavelengths and is the dominant component of light-absorbing atmospheric aerosol. A significant presence of rBC in ambient aerosol can lead to heating of the atmosphere, with effects on atmospheric transport and cloud dynamics (e.g., *Jacobson*, 2002; *Menon et al.*, 2002; *Chung and Seinfeld*, 2005; *Bond*, 2007; *Ramanathan et al.*, 2007; *Ramanathan and Carmichael*, 2008; *Bauer et al.*, 2010; *Ramana et al.*, 2010; *Jones et al.*, 2011).

After emission, rBC particles generally become coated by inorganic and organic (non-absorbing) components via coagulation with other particles and condensation of vapors (e.g., *Riemer et al.*, 2004). Fresh urban-emitted rBC has typically been shown to be thinly coated with secondary material, while rBC in aged air masses tends to be more thickly coated (*Johnson et al.*, 2005; *Moteki et al.*, 2007; *Shiraiwa et al.*, 2007, 2008; *Schwarz et al.*, 2008a; *Subramanian et al.*, 2010). In addition, rBC at higher altitudes is found to be more thickly coated than that near the ground (*Schwarz et al.*, 2008b). Layers of rBC above reflective clouds have an increased radiative forcing per unit mass relative to those below cloud (*Zarzycki and Bond*, 2010).

Available data indicate that a high fraction of atmospheric rBC particles are mixed with other species (*Pósfai et al.*, 1999; *Park et al.*, 2004; *Seinfeld and Pandis*, 2006; *Schwarz et al.*, 2008a; *Huang et al.*, 2011). A coating of non-absorbing components onto rBC increases the light scattering and absorption cross sections of these mixed-phase particles (*Fuller et al.*, 1999; *Schnaiter et al.*, 2005; *Bond et al.*, 2006; *Mikhailov et al.*, 2006; *Lack and Cappa*, 2010). The overall single scattering albedo (the fraction of total light extinction due to scattering) of an internally mixed rBC and non-absorbing aerosol population (all particles of a given size have the same composition) is smaller than that of an externally mixed aerosol population (no mixing of species in individual particles) of the same overall composition and concentration, resulting in a net increase in light absorption by the internally mixed aerosol population. In addition, the mixing state of atmospheric aerosols affects the hygroscopic properties of those aerosols, cloud formation, and atmospheric lifetime by wet deposition (*Weingartner et al.*, 1997; *Jacobson*, 2006). In short, the extent to which rBC is

mixed with non-absorbing aerosol components, such as sulfate, nitrate, and organics, exerts a strong influence on its interaction with radiation and water (*Stier et al.*, 2007; *Cubison et al.*, 2008).

Extensive measurements of rBC in urban locations around the globe exist (see Table 2.1). Wide variability exists in rBC concentrations owing to proximity to emission sources, the environment into and time of year during which the rBC is emitted, the type of combustion source, and the measurement technique used. The extent to which sulfate, nitrate, organics and other species are co-mixed in rBC particles depends on many factors. Sulfate is the dominant secondary component with rBC in many of the locations in which measurements are available. Mexico City and Riverside, CA are two locations, for example, in which nitrate dominates sulfate as the companion species. Regardless of the total concentrations of rBC and other components, the fraction of rBC particles mixed with some amount of secondary material tends to be appreciable in all regions where data are available.

While California has well-documented air quality problems, the state has also taken a leading role in efforts to address air quality and climate change issues. California has ambitious programs to control emissions of pollutants despite the challenges of increased population and demands for goods and services. Studies of the Los Angeles (LA) area are exemplary in terms of the evolution of our understanding of particulate matter in the atmosphere, from the quantification of the contribution of primary emissions from vehicles (diesel and gasoline) (*Schauer et al.*, 1996), to establishing the importance of secondary aerosol formation (*Turpin and Huntzicker*, 1995; *Zhang et al.*, 2007). Many studies (see Table 2.2) have measured rBC levels at various locations in California. The first 3D modeling study to treat size-resolved internal mixing of rBC suggested that aerosols containing rBC in LA led to a decrease in daytime surface temperatures but increased nighttime temperatures to a greater extent, causing a net warming (*Jacobson*, 1997). In the LA Basin, rBC particles are emitted directly from a variety of sources into a rich background of inorganic and organic airborne gaseous and particulate species. Understanding the evolution of rBC-containing particles as they undergo atmospheric aging in this important region provides a unique window on atmospheric gas and particle phase processes.

2.3 CalNex 2010

The California Research at the Nexus of Air Quality and Climate Change (CalNex) study is a multi-agency collaboration aimed at tackling problems related to both air quality and climate change in California (www.esrl.noaa.gov/csd/calnex/). The CalNex study was conducted May–July 2010 in the Los Angeles Basin and southern San Joaquin Valley, involving the NOAA WP-3D aircraft, the CIRPAS Twin Otter aircraft, the NOAA Twin Otter aircraft, the NOAA R/V Ronald H. Brown ship, and two ground-based super-sites, one in Pasadena (34.1405° N, 118.1225° W) on the campus of the California Institute of Technology and one near Bakersfield (35.3463° N, 118.9654° W) in the southern San Joaquin Valley. We report here comprehensive airborne measurements of rBC-containing aerosols in the Los Angeles Basin during May 2010 on the CIRPAS Twin Otter aircraft. Particular focus is paid to rBC concentrations in the Basin, in its outflow regions, and above the inversion layer, as well as the extent to which rBC-containing particles are coated with other species and how this degree of coating varies with location in the Basin and altitude above the surface. The present work is devoted to the actual rBC measurements; subsequent work will address comparison of model predictions and data.

2.3.1 Climatology of the Los Angeles Basin

The Los Angeles Basin, with a population of about 18 million people, exhibits unique air pollution characteristics and dynamics. Because of the mountainous terrain surrounding the Basin (see Figure 2.1), airborne species occupy an area of about 1300 km², confined near the ground by a relatively shallow day-time mixed layer under 1 km deep (*Robinson*, 1952; *Edinger*, 1959; *Neiburger*, 1969). The typical daytime sea breeze from the southwest advects emissions towards the north and northeast, exiting the Basin through passes in the San Gabriel and San Bernardino mountain ranges to the high desert regions (*Lu and Turco*, 1995). The two main eastern outflows, the El Cajon and Banning (San Gorgonio) Passes, and one less prominent northern outflow, the Tejon (Newhall) Pass, are not sufficient to completely drain the Basin of its atmospheric contents each day, leading to some degree of carry-over from one day to the next (*Harley et al.*, 2005). In addition, mountain-flow circulations

coupled to the sea breeze can produce multiple layers of pollution in and above the temperature inversion; such layers may mix down to the surface on subsequent days as the boundary layer deepens during its diurnal cycle (*Blumenthal et al.*, 1978; *Wakimoto and McElroy*, 1986; *Moore et al.*, 1991; *Lu and Turco*, 1994, 1995; *Collins et al.*, 2000) or may be subject to long-range transport (*Jaffe et al.*, 1999; *Liu et al.*, 2003; *Liang et al.*, 2004). Thus, barring a precipitation event, the atmosphere sampled in the LA Basin on any given day contains a mix of fresh and aged material.

For the analysis presented in this work, we have defined several regions of interest in and around the LA Basin (see Figure 2.2). Given the climatology of the region, we expect the Long Beach and West LA Basin regions to be near major sources of fresh emissions and the Banning Pass and Outflow regions to contain the “LA plume” that has been transported from west to east during the daytime hours.

2.3.2 FLEXPART Modeling

To track the origins of the specific air masses sampled in the Los Angeles basin during CalNex, a modified version of the FLEXPART Lagrangian particle dispersion model (*Stohl et al.*, 2005) is used to calculate back trajectories of air masses based on advection and turbulent mixing processes. FLEXPART has been used extensively to quantify the impacts of meteorological processes on pollution transport (e.g., *de Foy et al.*, 2006; *Palau et al.*, 2006; *Brioude et al.*, 2009; *Ding et al.*, 2009; *Langford et al.*, 2012). The main modification for this work consists of using time-averaged winds from the Weather Research Forecasting (WRF version 3.3) meteorology model instead of snapshot winds to improve mass consistency within the FLEXPART model (*Nehrkorn et al.*, 2010). The WRF output has a spatial grid of 4 km x 4 km, with a temporal resolution of 30 min and 60 vertical levels. In reverse mode, FLEXPART releases virtual tracer particles at receptors, in this case at the instantaneous spatial and temporal location of the Twin Otter aircraft, and integrates their trajectories backward in time using predicted wind fields combined with random turbulent motion. FLEXPART computes the average residence time of the particles in each grid cell (8 km x 8 km) every 2 h over a 24-h period. Surface level contributions to air masses are determined by averaging

the residence times of particles between the surface and 200 m altitude.

Figures 2.3 and 2.4 present FLEXPART back-trajectory analysis results from three representative flights, May 14 and 15 in Figure 2.3, and May 25 in Figure 2.4. In Figure 2.3, the 12-h integrated residence times reveal the surface history of the air masses sampled in the chosen locations within the LA Basin. The model results for locations on both the western side (Figures 2.3a and 2.3b) and the eastern side (Figures 2.3c and 2.3d) of the Basin indicate that the dominant airflow in the Basin is the daytime southwesterly sea breeze that advects air masses from Long Beach and downtown LA towards the northeast side of the Basin. FLEXPART results from other LA Basin flights (not shown) paint a similar picture of airflow throughout the LA Basin during the CalNex flights.

Figure 2.4 displays the FLEXPART results for several locations on the May 25 flight. The left panels are the surface residence times at 4 h prior to sampling and the right panels are the 12-h integrated surface residence times. Figures 2.4a and 2.4b show a location approximately half-way between the El Cajon Pass and the farthest sampling point in the El Cajon Outflow region. The surface contribution clearly tails back towards the El Cajon Pass, showing the connection between the LA Basin and the El Cajon Outflow. Figures 2.4c and 2.4d show the farthest sampling point in the El Cajon Outflow. At this farthest point from the El Cajon Pass, the tail back towards the Pass is faint, showing that, for this particular day, it takes longer than 12 hours for LA Basin air to reach this location. Figures 2.4e and 2.4f show back-trajectories for a location in approximately the center of the Banning Outflow region. The 4-h residence times (Figure 2.4e) clearly show a connection to the Banning Pass and LA Basin. The 12-h integrated residence times (Figure 2.4f) show this connection in addition to a smaller circulation within the Coachella Valley. The FLEXPART results for the Imperial Valley sampling location, in Figures 2.4g and 2.4h, show no connection to the LA Basin, with both the 4 h (Figure 2.4g) and 12-h integrated (Figure 2.4h) back-trajectories indicating flow from the southeast.

2.3.3 Twin Otter Flights

The Center for Interdisciplinary Remotely-Piloted Aircraft Studies (CIRPAS, Naval Postgraduate School, Monterey, CA, USA) Twin Otter conducted a total of 18 research flights during the month of May, 2010 as part of the CalNex field campaign. Figure 2.1 shows all 18 Twin Otter flight tracks during CalNex, and Table 2.3 gives a brief synopsis of each flight. All flights originated from the Ontario International Airport (Ontario, CA, USA). Most sampling was performed at an altitude of about 300 m above ground level at an airspeed of about 50 m s^{-1} . Exceptions were the transits over the San Gabriel and Tehachapi Mountains on the way to the CalNex Bakersfield ground site and the southern San Joaquin Valley. All measurements presented in this work are from instruments inside the unpressurized cabin of the Twin Otter. All instruments are serviced by a two-stage diffusion inlet with a transmission efficiency near unity for particle diameters up to about $3.5 \mu\text{m}$ (*Hegg et al., 2005*). Sampling lines inside the cabin are kept reasonably uniform to all instruments, so further corrections for diffusional losses in these lines have not been made. Owing to a hardware adjustment on the SP2 after the second flight, only data from the final 16 of 18 flights during CalNex are presented here.

A typical flight in the LA Basin consisted of two or three counter-clockwise loops around the Basin, beginning in Ontario and traveling west to Pasadena (passing over the CalNex-LA ground site at Caltech) between the 10 and 210 freeways, then heading south to Long Beach along the 710 freeway to do a loop of missed approaches at the Long Beach and Torrance Airports, then east along the 91 freeway to Riverside, turning west along the 210 freeway just before the San Bernardino mountains. During the first two flights, missed approaches were carried out at additional airports throughout the Basin, including Fullerton, Corona, Riverside, Flabob, Banning, Redlands, San Bernardino, Rialto, Cable, Brackett, and El Monte, but these were deemed unnecessary, as little variation in concentrations between an altitude of 15 m and 300 m above ground level were found. Several flights included north-south tracks in order to sample the interior of the Basin, and several flights probed the two main eastern outflows, the El Cajon Pass and the Banning Pass, into the Mohave Desert and Coachella Valley, respectively (see Figure 2.1).

2.4 Refractory Black Carbon Measurement

2.4.1 Single Particle Soot Photometer

rBC mass measurements were made onboard the Twin Otter aircraft with a Droplet Measurement Technologies (DMT, Boulder, CO, USA) Single Particle Soot Photometer (SP2). The SP2 affords measurements of both the particle-by-particle rBC mass as well as the thickness of non-rBC coating on each particle (*Stephens et al.*, 2003; *Baumgardner et al.*, 2004; *Schwarz et al.*, 2006; *Moteki and Kondo*, 2007; *Slowik et al.*, 2007). The theory of operation and setup of similar SP2 instruments are detailed elsewhere (*Stephens et al.*, 2003; *Schwarz et al.*, 2006, 2010). Briefly, for each particle traversing the optical cavity of the SP2, 36 μ s of signal at 0.2 μ s resolution on four detectors, two incandescence and two scattering, are saved for offline analysis. The two incandescence channels detect refractory black carbon mass by measuring the thermal emission from single rBC-containing particles heated to their boiling point when passing through the intense intra-cavity Nd:YAG laser beam ($\lambda = 1064$ nm). The two scattering channels detect the scattering cross-section of each particle and are used to determine the mixing state of rBC-containing particles, as detailed below. Note that throughout this work, the rBC volume-equivalent diameter (VED) is calculated from the detected rBC mass by assuming this mass is compacted to a spherical particle with a density of 1.8 g cm⁻³ (*Bond and Bergstrom*, 2006).

Appendix 2.7 details the calibration of the Twin Otter SP2. Briefly, the incandescence signals were calibrated with Aquadag (Aqueous Deflocculated Acheson Graphite, Acheson Colloids Company, Port Huron, MI, USA) using the density given by *Gysel et al.* (2011). The detection range of single-particle rBC mass is 0.48–317 fg (80–696 nm VED). We estimate the uncertainty in mass determination to be $\sim 40\%$, based largely on the uncertainty in Aquadag mass during calibration, which translates to a $\sim 12\%$ uncertainty in VED. These uncertainties were determined in a similar fashion to previous SP2 studies (*Schwarz et al.*, 2008b; *Shiraiwa et al.*, 2008). Other rBC standards were tested and the results presented in Appendix 2.7; however, Aquadag is used here because the density is known and samples of Aquadag have been distributed to most SP2 users by DMT, facilitating

the inter-comparison of SP2 instruments. Recent results suggest that the SP2 may be up to 40% more sensitive to Aquadag than to ambient rBC particles (*Moteki and Kondo, 2010; Laborde et al., 2012*), but no attempt has been made to correct for this potential bias because it is not yet known how Aquadag relates to ambient rBC particles in the LA Basin. A three-point inter-comparison of the Twin Otter SP2 with the NOAA SP2, which was calibrated with well-characterized Fullerene soot, found that the Twin Otter SP2 response yielded a 12% smaller mass measurement than the NOAA instrument (A. E. Perring, personal communication, 2012). With this potential bias, the mass concentrations reported in this work may be lower than the true ambient values, but the number concentrations are unaffected by this artifact.

The scattering channels were calibrated with dioctyl sebacate (DOS, refractive index=1.45-0.0*i*), and scattering cross-sections were related to the SP2 signal using Mie theory, as detailed below. For purely scattering ambient particles, we assume a refractive index of 1.5-0.0*i*, in the middle of observed ambient values (*Ensor et al., 1972; Stelson, 1990; Stolzenburg et al., 1998*) and consistent with coating material refractive indices used in this work. The detection range of optical diameter with these assumptions is 169–600 nm. The estimated uncertainty in retrieved scattering amplitude is ~22%, which propagates through Mie theory to an uncertainty of ~5% in optical diameter for purely scattering particles.

2.4.2 Mixing State Determination

Figure 2.5 shows the time traces of signal on the four measurement channels of the SP2 for three single particles: an uncoated rBC particle (Figure 2.5a), a purely scattering particle (Figure 2.5b), and a coated rBC particle (Figure 2.5c). An uncoated rBC particle has little or no discernible signal on the scattering channel and, if present, the scattering peak coincides with the incandescent peak, indicating that the scattering arises from the rBC particle itself. A purely scattering particle has no incandescent signal whatsoever, and the scattering signal has the shape of a Gaussian curve. A coated rBC particle exhibits both scattering and incandescing signals.

Typically, as a coated rBC particle heats up in the laser beam of the SP2, the coating material

will evaporate, causing the scattering signal to peak and decrease before the onset of the incandescent signal. A parameter often used to describe the coating thickness is the lag time between the peak scattering signal and the peak incandescent signal (labeled in Figure 2.5c) (*Schwarz et al.*, 2006; *Moteki and Kondo*, 2007). Previous studies have classified a thickly coated rBC particle as one with a lag time $\geq 2 \mu\text{s}$ (*Moteki et al.*, 2007). In this study, we will classify a thickly coated particle as one with a lag time $\geq 1.8 \mu\text{s}$, a shift of one datapoint, or time-step, in the single-particle data (Figure 2.5). This shift is made to reflect the observation (not shown) that there are two distinct populations of lag time in the single-particle data for CalNex, similar to the two populations shown by *Moteki et al.* (2007, Figure 3). A lag time of $1.8 \mu\text{s}$ is the point that most clearly separates these two populations in our dataset.

Because the coating on rBC particles evaporates before the particle passes through the entire laser beam, the scattering signal is not a true Gaussian shape, as in Figure 2.5b, and is smaller in amplitude than it should be for the full, unperturbed coated rBC diameter (see the difference in Figure 2.5c). To retrieve an accurate scattering cross-section and, therefore, optical size for this particle, we use the leading-edge only (LEO) part of the scattering signal to fit the scattering data to the calibration, as outlined by *Gao et al.* (2007). Figure 2.5c shows a LEO fit compared to the raw signal, which clearly would have under-sized this coated rBC particle had this correction not been made. Appendix 2.7 provides more details of how LEO fitting was calibrated and implemented for the Twin Otter SP2.

2.4.3 Mie Scattering Model

For purely scattering particles detected by the SP2, we calculate scattering cross-section with Mie theory for a given particle diameter and refractive index, for which we have adapted a version of BHMIE (*Bohren and Huffman*, 1998). This adaptation involves integrating the scattering function over the solid angles subtended by the SP2 avalanche photodiodes (APDs) to calculate the differential scattering cross-section specifically detected by those APDs rather than the total scattering cross-section. To calculate scattering cross-section for coated rBC particles, we have replaced the scattering

coefficients with those for stratified spheres from *Toon and Ackerman* (1981) to create a core-and-shell Mie model. Because the rBC mass is detected with the SP2 incandescence channels, the VED from this mass, with assumed rBC refractive index of $1.95-0.79i$ (*Bond and Bergstrom*, 2006) is treated as a known quantity in the core-and-shell Mie model. An assumed coating refractive index of $1.5-0.0i$, consistent with earlier published works (*Schwarz et al.*, 2008a,b), leaves coating thickness diameter as the only unknown when comparing measured scattering cross-sections to core-and-shell Mie model scattering cross-sections. The measurements are then fit to the core-and-shell Mie calculations to determine coating thickness diameters. Given an uncertainty in retrieved scattering amplitude of $\sim 22\%$ and an uncertainty in rBC VED of $\sim 12\%$, uncertainties in coating thicknesses are $\sim 40\%$, with uncertainty decreasing with increasing coating thickness. For the 1-min average SP2 data, in addition to reporting mean coating thicknesses, the Mie model-derived total coated rBC particle diameter is used to calculate the total particle volume, from which we calculate the coating-only volume by subtracting the calculated rBC core volume.

Previous SP2 studies have emphasized lag time as a way of presenting rBC mixing state (e.g., *Subramanian et al.*, 2010). Figure 2.6 relates mean lag times to mean coating thicknesses for all measurements taken during CalNex. The black line is a linear fit of the data ($R^2=0.797$; the actual slope and intercept are unimportant) showing a strong correlation between these two variables, as expected. Both measurements are reported because both suffer from limitations. Interpretations of lag times to infer coating thicknesses rely on the aerosol to follow a core-and-shell physical model and for all coatings to evaporate in the SP2 laser at equal rates such that time is related to thickness only and not to coating material as well. Mean coating thicknesses calculated with Mie theory suffer from limited detection range, additional uncertainties in extracting the true scattering peak signal from an evaporating particle, and, again, relies on the core-and-shell physical model to apply.

2.4.4 rBC Number and Mass Concentrations

Histograms of single-particle rBC mass onto 500 logarithmically-spaced mass bins between 0.48 and 398 fg (80-750 nm VED) were made for every 1-min of single-particle data. Accumulation mode rBC

particle size distributions in the atmosphere have been observed to be single lognormal in nature (*Pueschel et al.*, 1992; *Clarke et al.*, 2004; *Moteki et al.*, 2007; *Schwarz et al.*, 2008a,b); thus, a single lognormal function is fit to each 1-min number distribution to determine the full distribution over the range of 9.4×10^{-7} to 942 fg (1-1000 nm VED). The fitted mass distributions are implied from the fitted number distributions.

Figure 2.7 shows examples of typical number and mass distributions measured and fitted for various regions. At very large rBC masses (>300 nm VED), the measurements deviate from the fitted distribution, because at these large masses a single count becomes a significant differential mass (dM) in the distribution. This potential error illustrates the importance of fitting the number distribution to a log-normal, rather than the mass distribution, in order to avoid biasing the fit of the mass distribution. The rBC mass median diameter (MMD) is the VED at the peak of the mass distribution.

The bulk number and mass concentrations are found by integrating each distribution over all sizes and dividing by the sampled volume of air for that 1-min period. The bulk values reported here are derived from the fitted distributions. Uncertainties in the bulk concentrations are dominated by the single-particle mass uncertainty; thus, additional uncertainties due to flow fluctuations are negligible. Because the fitted range captures a wider diameter range than the detection limits of the SP2, the calculated rBC number and mass concentrations are higher than those corresponding to the strict detection range of the instrument. The number concentration nearly doubles because of this adjustment, while the mass concentration is about 15-20% larger.

2.5 Results and Discussion

2.5.1 Regional Variability in rBC Aerosol

Over the entire monthlong campaign, rBC mass concentrations in the LA Basin varied from 0.002 to $0.530 \mu\text{g m}^{-3}$, with smaller values measured in regions outside of the Basin (see Table 2.4). rBC-containing particle number concentrations ranged from as low as 3 cm^{-3} up to 1180 cm^{-3} .

Figure 2.8 shows rBC mass concentrations for 12 flights in the LA Basin. On the May 28 flight (Figure 2.8l), the spikes in mass concentration on the southeast corner of the sampling pattern are the result of flying through a dense smoke plume from a tanker truck fire on the 91 freeway. These spikes have been removed for the calculated values in Tables 2.2 and 2.4. The anomalously low concentrations on the southern side of the LA Basin on May 6 (Figure 2.8a), in the central Basin on May 15 (Figure 2.8g), and on the northeast corner of the Basin on May 21 (Figure 2.8i) are a result of sampling above the inversion layer; all other measurements were made at ~ 300 m above ground level. Figure 2.9 shows a typical flight contrasting the measurements between the LA Basin and its two eastern outflow regions.

From Figure 2.8, together with Figure 2.9a, a pattern of higher rBC mass concentrations occurring on the north side of the Basin emerges. These larger concentrations to the north are the result of a southwesterly sea breeze during the day (see Figure 2.3) that transports rBC emissions up against the San Gabriel mountains, where the terrain and typically shallow mixed layer collect the air mass prior to exiting the Basin. One might expect enhanced emissions from the Port of Long Beach and the industries (refineries) in the area; however, except for a few spikes in the data near Long Beach, this region is generally characterized by lower concentrations of rBC as compared with the northern side of the LA Basin (see also Table 2.4).

Table 2.4 presents a detailed regional breakdown of the SP2 measurements during CalNex. Except for the free troposphere, all measurements are from below the inversion layer, with region definitions given in Figure 2.2. Within the LA Basin, rBC concentrations are fairly uniform throughout, because the region definitions do not distinguish north and south Basin as discussed above. The rBC mass concentrations in the LA Basin are higher than in the outflow regions (Figure 2.9a). The mean coating thickness and percent thickly coated both increase from west to east, indicating that the rBC particles are becoming more thickly coated. Moving into the outflows, the rBC continues to become more thickly coated, with the thickest coatings (except for the free troposphere) occurring at the farthest points from the LA Basin (see also Figures 2.9c and 2.9d). rBC mass fraction increases in the outflows, despite a decrease in rBC number and mass concentrations, owing to the

evaporation of volatile species from the aerosol as the plume is diluted over the desert regions.

Minor differences exist in the mass median diameter of the rBC core aerosol between regions (see Figures 2.7 and 2.9b). The MMD is the smallest in the LA Basin, at about 122 nm, indicating the rBC in the Basin is characteristic of fresh urban emissions that tend to have smaller rBC cores (e.g., *McMeeking et al.*, 2010; *Schwarz et al.*, 2008a). The MMD is smaller by 30–70 nm than most other urban measurements found in the literature (see *McMeeking et al.*, 2010, Table 5). Most comparable to the Los Angeles values observed are those of fresh rBC emissions at Cranfield airfield in England, which exhibited values near 130 nm (*McMeeking et al.*, 2010), and of the Tokyo, Japan outflow, which exhibited values of 145–150 nm (*Shiraiwa et al.*, 2007). The MMD of rBC in the Imperial Valley is larger than that in the LA Basin and its outflow regions, indicating an airmass of a different origin. Figures 2.4g and 2.4h support this conclusion, showing that the air mass originates from the southeast of its sampling location.

2.5.2 Secondary Aerosol Chemical Composition

Particle mass and composition measurements were made by an Aerodyne compact time-of-flight aerosol mass spectrometer (C-ToF-AMS, Aerodyne Research, Inc., Billerica, MA USA) (*Drewnick et al.*, 2005; *Murphy et al.*, 2009) that was deployed on the final nine Twin Otter flights. The AMS measures sub-micron, non-refractory size-resolved aerosol composition over the diameter range 60 to 600 nm (with unit transmission efficiency) (*Jayne et al.*, 2000). For the purposes of comparison to SP2 measurements, bulk composition AMS data are averaged to 1-min time intervals. Water-soluble organic carbon (WSOC) was quantified by a particle-into-liquid sampler (PILS; Brechtel Manufacturing, Inc., Hayward, CA) coupled to a Total Organic Carbon (TOC) Analyzer (Sievers Model 800) (*Sullivan et al.*, 2006). The major findings on the nature of WSOC in Los Angeles during CalNex have been presented elsewhere (*Duong et al.*, 2011). The WSOC data presented here have been converted to water-soluble organic mass (WSOM) by applying a correction factor of 1.7, which is within range of previous measurements made in Southern California (*Turpin and Lim*, 2001; *Docherty et al.*, 2008; *Wonaschütz et al.*, 2011).

Figure 2.10 presents the region-averaged ratios of the mass concentration of various chemical species to the rBC mass concentration during the May 25 flight. The regions are ordered from west to east, which coincides with the direction of the general LA airflow; thus, for daytime sampling, plume age increases from left to right on Figure 2.10 with the exception of the Imperial Valley, which Figures 2.4g and 2.4h show to be isolated from the LA Basin for at least the 12 hours prior to measurement. Within the LA Basin, the rBC mass concentration decreases slightly from west to east and decreases sharply in the Banning Outflow and Imperial Valley regions, largely due to dilution of the airmass with the cleaner, desert air. In the absence of any major rBC sources over the desert, rBC can be considered a tracer for the LA plume and the mass ratios reveal the occurrence of secondary formation of these chemical species as the LA plume ages.

The overall mass ratio of measured chemical species to rBC increases from west to east within the LA Basin and is at a maximum in the Banning Pass region, reflecting the build-up of secondary aerosol species, particularly nitrate and organics, relative to rBC. The Banning Pass is a relatively narrow mountain pass on the east side of the LA Basin (see Figures 2.1 and 2.2) where the LA plume is advected through this region and out of the Basin by the daytime sea breeze. Figure 2.9c shows the mean coating thicknesses and Figure 2.9d shows the percent thickly coated (defined using single-particle lag times) for this flight. Mean coating thicknesses for this flight do not show much increase within the Basin, much like the campaign-average values in Table 2.4; however, percent thickly coated shows an increase from west to east within the LA Basin with an area of larger percentages in the Banning Pass region. Figure 2.10 indicates that these more thickly coated particles in the Banning Pass region are likely a mix of ammonium nitrate and organics. A previous study found that coating materials on rBC in Nagoya, Japan were likely ammonium sulfate and secondary organic compounds formed during transport away from the urban center (*Moteki et al., 2007*). In the LA Basin, sulfate is a minor constituent of the secondary aerosol relative to nitrate.

In the Banning Outflow region, the overall mass ratio is the smallest, reflecting loss of the volatile species from the aerosol, particularly ammonium nitrate, relative to rBC. For comparison, the Imperial Valley region data are also shown; however, as mentioned above, the timescales over

which LA Basin air may mix into this region are unknown. Figures 2.9c and 2.9d both show that rBC coating thicknesses increase at the farthest sampling points outside of the LA Basin in both the Banning Outflow and El Cajon Outflow regions. The more noticeable increase in coating thicknesses occurring outside the LA Basin may be due to the timescales necessary for the coatings to grow on rBC. *Moteki et al.* (2007) found that rBC particles become internally mixed on a time scale of about 12 h in urban plumes. Figure 2.4f shows a sampling location during the May 25 flight in the Banning Outflow region in which the 12-h integrated surface history of the air mass shows a clear link to the eastern LA Basin. The data in Figure 2.10 show that the water-soluble organics continue to remain high relative to rBC in both the Banning Outflow and Imperial Valley regions and, therefore, likely contribute to any coatings on rBC particles in these regions.

To explain the variation in rBC coating thicknesses, we used Positive Matrix Factorization (PMF) (*Paatero and Tapper*, 1993; *Paterson et al.*, 1999; *Ulbrich et al.*, 2009) with input parameters of mean rBC coating thickness and AMS masses normalized by rBC mass for the May 25 flight. Although Figure 2.10 shows the presence of two dominant species available as coating materials, nitrate and organics, we used a three-factor PMF model in order to compare with similar previous studies (*Shiraiwa et al.*, 2007, 2008). The predicted parameters (ammonium/rBC, nitrate/rBC, organics/rBC, sulfate/rBC, and mean rBC coating thickness) by the PMF model agree well with the measured values ($R^2=0.934$, 0.999, 1.000, 0.625, and 1.000, respectively), indicating that the PMF model sufficiently describes the variance in the data. The three factors are shown in Figures 2.11a–2.11c. The fraction of signal is the contribution of each parameter to the overall signal and is, thus, weighted by the relative abundances of each parameter over the entire May 25 flight. Thus, the ammonium and sulfate fractions are small, because they have small loadings compared to the nitrate, organics, and mean coating thickness signals. If we look at the average fraction of measured signal accounted for by each factor, Factor 1 (Figure 2.11a) describes ~90% of the measured nitrate/rBC signal, ~28% of the organics/rBC, but only ~9% of the mean coating thickness. Factor 2 (Figure 2.11b) describes ~57% of the organics/rBC and ~22% of the mean coating thickness, while Factor 3 (Figure 2.11c) describes ~15% of the organics/rBC and ~69% of the mean coating thickness. Factors 2 and 3 each

only describe \sim 5% of the nitrate/rBC signal. The cumulative explained fraction of measured signal by the PMF model of nitrate/rBC, organics/rBC, and mean coating thickness are 1.008, 0.999, and 1.000, respectively.

Figures 2.11d–2.11f show the spatial pattern of the fraction of total signal contributed by the three factors on the May 25 flight. Factor 1 (Figure 2.11d) has the largest contribution to the signal in the Banning Pass, coincident with the largest loadings of nitrate measured on this flight. Although the overall explained signal of mean coating thickness for the entire flight is small for this factor, the dominance of the total factor signal in this region means that the coatings are likely nitrate and organics within the Banning Pass. Factor 2 (Figure 2.11e) has a more highly variable pattern throughout the flight; however, there are noticeable local maxima in several locations, particularly downwind of the Banning Pass in the Banning Outflow region, where this factor makes up \sim 50% of the total signal. The areas of high Factor 2 signal are characterized by a largely organic rBC coating, consistent with the ammonium nitrate having largely evaporated in this region (Figure 2.10). Factor 3 (Figure 2.11f) is dominant, by far, over most of the flight, with the exception of the two areas mentioned above. Because Factor 3 is essentially mean coating thickness by itself (Figure 2.11c), this factor is, in essence, the residual variation in mean coating thickness not described by Factors 1 and 2. Given its importance over most of the flight, it is clear that the PMF model does not contain enough parameters that vary with mean coating thickness to fully describe, in a physical interpretation, the cause for the variation in coating thickness in most regions. However, in the Banning Pass and Outflow regions, the PMF results support the conclusions from Figure 2.10 that the available coating materials are largely nitrate and organics, especially in regions where these compounds have relatively high loadings.

2.5.3 The rBC Mixing State

Figure 2.12 presents a 2D histogram of all particles measured in the West LA Basin region (see Figure 2.2) during CalNex. rBC core diameters (VED) from 90–260 nm are binned according to their optical diameter (175–410 nm) determined with the LEO method. Optical diameter, calculated

using Mie theory assuming that the particle is purely scattering with a refractive index of $1.5-0.0i$, is used instead of scattering cross-section in this figure for convenience of relating the scattering signal to particle diameter. Given the assumed rBC core sizes of these particles in Figure 2.12, solid lines representing a core-and-shell Mie model have been overlaid with the shell thickness diameters given in nm. Presented this way, the x- and y-axes limits on Figure 2.12 are the limits of detection for coated rBC of the Twin Otter SP2. As shown earlier, the MMD peaks below 130 nm for much of the measurements during CalNex, and Figure 2.12 clearly shows that one cannot determine the mixing state of the majority of these particles unless they have a coating thickness greater than 50 nm in diameter.

Despite these limitations, we can examine how the behavior of coated rBC particles within the detection range of the SP2 change with region. To simplify the presentation of these data, Figure 2.13a is calculated directly from Figure 2.12 by re-binning the 2D histogram in terms of the core-and-shell Mie model scattering cross-sections to put the measurement in terms of coating thickness diameter. Figure 2.13a again shows the limits of detection at small rBC core sizes, as the major mode of coated rBC particles is cut off in the lower-left corner of the plot.

Of particular interest is the evolution of the mixing state of the rBC aerosol as it is transported into the outflow regions. Figures 2.13a and 2.13b demonstrate this evolution from the source-rich area of the western LA Basin to the more aged Banning Outflow region. Figure 2.13 clearly shows that a second mode of particles at small rBC VED's but with thick (≥ 150 nm) coatings become more important relative to the main mode of more thinly-coated, larger rBC in the outflows. In the source-rich region of the western LA Basin, this second mode is barely visible as compared to the main mode of thinly coated rBC, indicating a dominance of thinly coated rBC particles, largely outside the detection range of the SP2.

2.5.4 Variability of rBC Levels with Altitude

Figure 2.14a shows the 1-min resolution rBC mass concentration for all research flights as a function of altitude with single soundings presented in Figures 2.14b and 2.14c. In general, rBC mass

concentration decreases with altitude, with the smallest concentrations measured in the free troposphere. In contrast, the mean coating thickness increases with altitude, with a dramatic increase above the inversion layer. The trend of lower rBC concentrations with increasing coating thickness is also shown in Figure 2.6. That the more thickly coated rBC particles lie in the free troposphere is consistent with a more aged aerosol, on which secondary species have condensed. A dramatic shift in MMD occurs above the inversion layer, indicating the rBC cores themselves are larger in the free troposphere. The characteristic time for coagulation by rBC-containing particles only in the free troposphere is about 82 days, but that of all particles in this region is about 7 days (using a coagulation coefficient $K = 6.41 \times 10^{-9} \text{ cm}^3 \text{ s}^{-1}$ calculated from the measurements) (*Seinfeld and Pandis*, 2006). While this seems excessively long for the rBC particles, it is likely that rBC concentrations were much higher at their source, meaning coagulation would have proceeded much faster initially before being transported above the inversion. Another possible explanation is that the rBC above the inversion layer is from a different combustion source (biogenic vs. anthropogenic) than for the fresh rBC particles in the Basin, which may have caused larger rBC core sizes to begin with (*Schwarz et al.*, 2008a).

Figures 2.14b and 2.14c show single soundings out of and back into the LA Basin on May 20. These soundings are for the same time periods as those presented in Figure 5 of *Duong et al.* (2011). The ascent took place before noon local time on the east side of the LA Basin near the El Cajon Pass, and the temperature profile indicates the presence of a weak inversion layer ($\Delta T = \sim 0.5^\circ\text{C}$ at $\sim 1800 \text{ m}$) and a layer of elevated rBC levels (an increase of $\sim 0.05 \text{ } \mu\text{g m}^{-3}$) around the same level. The decrease in dew point temperature (6.4°C) over this same layer is more dramatic and continues to decrease above this layer, indicating a much drier airmass aloft. Three hours later, on the descent into the LA Basin, again near the El Cajon Pass, rBC levels below the inversion layer are higher overall, especially near the base of the inversion layer ($\Delta T = \sim 1.6^\circ\text{C}$ at $\sim 2400 \text{ m}$). Again, the dew point temperature profile shows a sharp decrease (9.3°C) indicating a much drier airmass aloft. Although *Raga et al.* (2001) argue that the presence of an absorbing aerosol layer just above the temperature inversion helps to strengthen the inversion layer near Mexico City, we do not have

enough soundings at sufficiently high resolution to evaluate this for the LA Basin. In fact, the data show that the rBC mass concentrations on this flight are higher below the inversion, especially later in the afternoon. Figures 2.14b and 2.14c also show the presence of rBC layers with different mean coating thicknesses. On the ascent out of the LA Basin, there is a layer of rBC at \sim 1400 m altitude with a mean coating thickness of \sim 200 nm surrounded above and below by rBC layers with mean coating thicknesses of \sim 115 nm. On the descent into the LA Basin later in the day, just below the inversion layer, at \sim 2350 m altitude, the local maxima in rBC mass concentration (an increase of \sim 0.08 $\mu\text{g m}^{-3}$) coincides with a mean coating thickness of \sim 115 nm with surrounding layers $>$ 160 nm in coating thickness. The descent also records the presence of a second inversion ($\Delta T = \sim$ 2.4°C) much closer to the surface (\sim 600 m altitude) in which a layer of rBC with mean coating thickness \sim 150 nm is surrounded by layers with coating thicknesses of \sim 105 nm. The complicated vertical structure in Figures 2.14b and 2.14c is likely the result of the “mountain-chimney effect” described by *Lu and Turco* (1994, 1995). In both soundings, the rBC just above the inversion layer is dramatically different than below; the rBC is much more thickly coated and the mass median diameters are much larger.

2.5.5 Case Study: “Weekend Effect” on rBC Aerosol

Ozone levels in the LA Basin are subject to the well-documented weekday-weekend effect (e.g., *Marr and Harley*, 2002; *Pollack et al.*, 2012). This so-called “weekend effect” is a result of the dramatically reduced amount of heavy-duty truck traffic (diesel truck emissions decrease by 60–80%), as reflected primarily in NO_x levels (*Harley et al.*, 2005).

To examine the possible effects on rBC in the LA Basin as a result of the weekend effect, Figure 2.15 presents the percent change of several measurements from Friday, May 14 to Saturday, May 15. We define the percent change referenced to the measurements from May 14; thus, positive values denote measurements that are higher on the weekend flight of May 15. The size of the markers is proportional to the measured values on May 14, revealing the weekday pattern of larger values in the Basin. Figure 2.15a shows rBC mass concentration changes in the Basin (see Figures 2.8f and

2.8g for actual measurements). By flight average, there is virtually no change in rBC levels from May 14 to 15 (+0.01%), but there are regions within the Basin of increase and decrease. Figure 2.15b shows change in the WSOC/rBC ratio, which is indicative of secondary organic aerosol (SOA) formation, increasing everywhere in the Basin by a large percent. This observation is consistent with previous observations that the highest levels of SOA formation in the LA Basin occur on weekends (*Turpin and Huntzicker, 1991, 1995*). Figure 2.15c shows that mean coating thicknesses also increase everywhere on May 15 throughout the LA Basin. Finally, Figure 2.15d shows that in the far northeast corner of the LA Basin the coating volume concentration is smaller on May 15, in contrast to the rest of the Basin which has more coating volume on this particular Saturday. While this may seem to conflict with Figure 2.15c, note that mean coating thickness is a particle-by-particle average, which gives the mean state of single rBC particles, whereas coating volume concentration is a bulk measurement that reflects total number concentration as well as average coating thickness. Thus, on Friday, May 14, there were more particles in the LA Basin, and thus more total coating volume on rBC in the northeast corner of the Basin, where pollution accumulates, despite the fact that per rBC particle, there was a thinner coating of material.

2.6 Summary

The present work reports rBC measurements during May 2010 as part of the CalNex 2010 field experiment in California. The measurements were carried out onboard the CIRPAS Twin Otter aircraft during 18 research flights, using the Single Particle Soot Photometer. The dominant feature controlling the regional variability of rBC aerosol in the LA Basin is the daytime southwesterly sea breeze. The sea breeze advects the fresh LA plume inland, where mountain ranges and a shallow inversion layer collect the pollution before exiting the Basin through two narrow mountain passes. While rBC mass concentrations remain fairly uniform west-to-east within the Basin, there is clear growth of secondary organics and ammonium nitrate as the LA plume is advected eastward in the Basin. This secondary growth coincides with an increase in the coating thickness on rBC particles from west to east. In the outflow regions, the volatile ammonium nitrate largely evaporates, leaving

WSOC as the most abundant secondary material available to contribute to the growing mean rBC coating thicknesses. Detailed analysis of the rBC mixing state reveals two modes of coated particles, one with an rBC VED \sim 145 nm with a coating that grows from \sim 50 nm to \sim 70 nm from the western LA Basin to the Banning Outflow region and one with an rBC VED \sim 90 nm, on the edge of the SP2 detection range, with a coating that grows from $<$ 100 nm (out of detection range) to $>$ 200 nm. In general, rBC mass concentrations decrease with altitude, while the coating thickness increases dramatically above the inversion layer, consistent with a more aged aerosol in the free troposphere. The “weekend effect” on rBC resulted in more thickly coated rBC particles on a Saturday vs. the preceding Friday everywhere in the LA Basin, coinciding with higher WSOC/BC ratios, indicating more secondary formation of aerosol on Saturday.

2.7 Appendix: Calibration of the SP2

2.7.1 The rBC Mass Calibration

The SP2 has two incandescence channels, a broadband ($\lambda = 350$ –800 nm) and a narrowband ($\lambda = 630$ –800 nm) channel. The Twin Otter SP2 was additionally configured such that the broadband incandescence channel was set to a higher gain setting than the narrowband channel, to increase the total range of detectable refractory black carbon mass. Figure 2.16 presents the incandescence calibration for the two channels, showing the clear overlap in signal ranges and deviation of the signal from the linear fit at larger particle masses. A comparison is made to other rBC aerosol standards, Fullerene soot (stock #40971, lot #G25N20, Alfa Aesar, Ward Hill, MA, USA) and glassy carbon spheres (GCS, Type II, stock #38008, lot #C14K07, Alfa Aesar). The mass of generated Fullerene particles is calculated using the relation from *Gysel et al.* (2011); however, we note that our batch of Fullerene is different from that used in their study. GCS mobility diameter is converted to mass using the manufacturer-reported density of 1.42 g cm^{-3} . The Fullerene and GCS calibration slopes are both \sim 37% larger than the Aquadag slope, meaning that these calibrations would yield larger rBC masses. When more data becomes available relating these three rBC standards to ambient rBC

in the LA Basin, corrections to the calibration can be made.

The SP2 incandescence channels were calibrated with Aquadag by nebulizing a solution of Aquadag and milliQ water through a differential mobility analyzer (DMA, TSI Model 3081) used to classify the mobility of the generated particles. The mass of those particles was calculated from the mobility diameter using the relation from *Gysel et al.* (2011), who showed that Aquadag mobility density is independent of production batch and specific aerosol generation procedures. We have chosen to use Aquadag as our calibration standard because of this published density and because the different production lots of Aquadag have been distributed to most SP2 users by DMT; thus, providing a means to inter-relate the many SP2 instruments. Recent work by *Laborde et al.* (2012) instead recommend the use of Fullerene soot, as has been recommended previously (*Moteki and Kondo*, 2010). However, the mobility density of Fullerene soot is not consistent across different production lots and may vary by up to 14% between specific batches (*Laborde et al.*, 2012). For this study, we did not have access to a particle mass analyzer and, therefore, could not verify the mobility density of our batch of Fullerene.

It has been previously shown that the incandescence response of the SP2 is linear up to particle masses of 10 fg and independent of particle shape or mixing state (*Moteki and Kondo*, 2007, 2010; *Slowik et al.*, 2007). We have found a linear response over a slightly larger range, up to at least a 50 fg particle (see Figure 2.16), before surface area effects lead to a power law dependence in the signal. The coefficients of determination ($R^2 = 0.993, 0.996$, and 0.997 for Aquadag, Fullerene, and GCS, respectively) clearly demonstrate the linearity in the response of the SP2 to rBC mass. We have chosen to fit both incandescence channels with a linear function and note that errors will be greatest at the extreme large end of the rBC mass spectrum, where few particles were detected in this study. The detection limit of the high-gain broadband incandescence channel was 0.48–11.1 fg rBC per particle (80–227 nm VED) and of the low-gain narrowband incandescence channel was 3.66–317 fg rBC per particle (157–696 nm VED).

2.7.2 Scattering Calibration

The SP2 has two scattering channels, a high-gain and a low-gain channel, which are filtered to detect scattered light at $\lambda = 1064$ nm. The Twin Otter SP2 was configured with a split-detector on the high-gain scatter channel, which is used to obtain particle position information for use in a leading-edge only (LEO) fit of the scattering data on the low-gain channel (*Gao et al.*, 2007). The scattering channels were calibrated with both dioctyl sebacate (DOS, refractive index = 1.45-0.0*i*) and polystyrene latex spheres (PSL, refractive index = 1.59-0.0*i*) size-selected by a DMA. Figure 2.17 shows the results of the calibration for a full Gaussian fit to the scattering signal and for the LEO fits to the scattering signal, detailed below. A Mie scattering model is used to relate diameter and refractive index to the scattering cross-section. In Figure 2.17, each data point represents the median of a sample of about 10,000 particles. The error bars are one standard deviation of the LEO fit amplitude, indicative of the spread in the data for each size. The linear fit was found by forcing a zero intercept, but very little change in slope occurs if this criterion is relaxed. The data used to generate the linear fit were the DOS data only. Both DOS and PSL calibration curves demonstrate the linearity of the scattering response of the SP2 to scattering cross-section ($R^2 = 0.996$ and 0.999, respectively). Uncertainty in the full Gaussian fit amplitude is $\sim 14\%$.

2.7.3 LEO Fitting

We desire to use only the leading-edge of the scattering signal so that coated rBC particles, which have a scattering signal that begins as a Gaussian shape but then is perturbed as the coating evaporates, may be sized according to their full, unperturbed diameter. We have chosen the criterion for determining the last point in the leading-edge signal consistent with *Gao et al.* (2007); that is, an amplification factor of 30, which means signals up to the point where the signal is 3.33% of the maximum observed signal for that particle are used in the LEO fit.

In addition to using only a limited portion of the scattering signal for each particle, we simplify the Gaussian fit based on calibration results. The Gaussian-shaped scatter signal, S , as a function

of time, t , on the low-gain scatter channel is written as

$$S(t) = a \exp \left[-4 \ln 2 \left(\frac{t-b}{c} \right)^2 \right] + d \quad (2.1)$$

where a is the height of the peak, b is the position of the center of the peak, c is the full width at half maximum, and d is the baseline or offset. Owing to the constant flow rate and width of the laser in the instrument, purely scattering particles of all sizes exhibit the same full width at half maximum (c) and peak position (b) relative to the zero-crossing of the split-detector (labeled as “Position Time” on Figure 2.5) (Gao *et al.*, 2007). Thus, equation (2.1) can be simplified to

$$S(t) = aX(t) + d \quad (2.2)$$

where $X = \exp \left(-4 \ln 2 \left(\frac{t-b}{c} \right)^2 \right)$ can be calculated directly from calibration data and S , a , and d are defined above. In fitting equation (2.2), we do not restrict the value of d , the signal baseline, but keep it as a free parameter and compare the fitted d to the baseline value estimated as the minimum average of the first or last 20 signal datapoints on the single-particle time trace (Figure 2.5). This comparison ensures that the fit to the scattering data yields realistic values for a . Due to fluctuations in sample flow and laser profile, LEO fitting increases uncertainty in the retrieved scattering amplitude to $\sim 22\%$.

To validate the LEO method of fitting, we compared the full Gaussian fit amplitude to the leading-edge fits for the DOS and PSL calibration data as well as for a subset of purely scattering particle data from several of the research flights. The results are given in Figure 2.18. For clarity, the fits from a segment of only one of the flights is shown, but all flights gave similar results. Although the slope between the two methods is not ideally unity, the linearity of the plot ($R^2 = 0.998$ and 0.999 for DOS and PSL, respectively) validates this as an effective method for sizing particles.

2.8 Acknowledgements

This work was supported by NOAA grant NA09OAR4310128. The authors wish to thank Greg Kok at DMT and Anne Perring and Joshua (Shuka) Schwarz at NOAA for their guidance on data analysis and calibration. We also acknowledge the entire CIRPAS crew for their professionalism and assistance during the campaign.

Bibliography

Andreae, M., O. Schmid, H. Yang, D. Chand, J. Zhen Yu, L. Zeng, and Y. Zhang (2008), Optical properties and chemical composition of the atmospheric aerosol in urban Guangzhou, China, *Atmos. Environ.*, 42, 6335–6350, doi:10.1016/j.atmosenv.2008.01.030. 55

Babu, S. S., S. K. Satheesh, and K. K. Moorthy (2002), Aerosol radiative forcing due to enhanced black carbon at an urban site in India, *Geophys. Res. Lett.*, 29(18), 1880, doi: 10.1029/2002GL015826. 55

Bauer, S. E., S. Menon, D. Koch, T. C. Bond, and K. Tsigaridis (2010), A global modeling study on carbonaceous aerosol microphysical characteristics and radiative effects, *Atmos. Chem. Phys.*, 10, 7439–7456, doi:10.5194/acp-10-7439-2010. 15

Baumgardner, D., G. L. Kok, and G. B. Raga (2004), Warming of the Arctic lower stratosphere by light absorbing particles, *Geophys. Res. Lett.*, 31, L06117, doi:10.1029/2003GL018883. 21

Baumgardner, D., G. L. Kok, and G. B. Raga (2007), On the diurnal variability of particle properties related to light absorbing carbon in Mexico City, *Atmos. Chem. Phys.*, 7, 2517–2526, doi:10.5194/acp-7-2517-2007. 55

Binkowski, F. S., and S. J. Roselle (2003), Models-3 Community Multiscale Air Quality (CMAQ) model aerosol component 1. Model description, *J. Geophys. Res.*, 108(D6), 4183, doi:10.1029/2001JD001409. 15

Blumenthal, D., W. White, and T. Smith (1978), Anatomy of a Los Angeles smog episode: Pollutant transport in the daytime sea breeze regime, *Atmos. Environ.*, 12(4), 893–907, doi: 10.1016/0004-6981(78)90028-8. 18

Bohren, C. F., and D. R. Huffman (1998), *Absorption and Scattering of Light by Small Particles*, John Wiley, New York. 23

Bond, T. C. (2007), Can warming particles enter global climate discussions?, *Environ. Res. Lett.*, 2(4), 045030, doi:10.1088/1748-9326/2/4/045030. 15

Bond, T. C., and R. W. Bergstrom (2006), Light absorption by carbonaceous particles: An investigative review, *Aerosol Sci. Technol.*, 40(1), 27–67, doi:10.1080/02786820500421521. 21, 24

Bond, T. C., G. Habib, and R. W. Bergstrom (2006), Limitations in the enhancement of visible light absorption due to mixing state, *J. Geophys. Res.*, 111, D20211, doi:10.1029/2006JD007315. 15

Brioude, J., et al. (2009), Effect of biomass burning on marine stratocumulus clouds off the California coast, *Atmos. Chem. Phys.*, 9, 8841–8856, doi:10.5194/acp-9-8841-2009. 18

Brunciak, P. A., J. Dachs, T. P. Franz, C. L. Gigliotti, E. D. Nelson, B. J. Turpin, and S. J. Eisenreich (2001), Polychlorinated biphenyls and particulate organic/elemental carbon in the atmosphere of Chesapeake Bay, USA, *Atmos. Environ.*, 35(32), 5663–5677, doi:10.1016/S1352-2310(01)00222-9.

55

Chazette, P., and C. Liousse (2001), A case study of optical and chemical ground apportionment for urban aerosols in Thessaloniki, *Atmos. Environ.*, 35(14), 2497–2506, doi:10.1016/S1352-2310(00)00425-8. 55

Chow, J. C., J. G. Watson, E. M. Fujita, Z. Lu, D. R. Lawson, and L. L. Ashbaugh (1994), Temporal and spatial variations of PM_{2.5} and PM₁₀ aerosol in the Southern California Air Quality Study, *Atmos. Environ.*, 28(12), 2061–2080, doi:10.1016/1352-2310(94)90474-X. 56

Chow, J. C., J. G. Watson, Z. Lu, D. H. Lowenthal, C. A. Frazier, P. A. Solomon, R. H. Thuillier, and K. Magliano (1996), Descriptive analysis of PM_{2.5} and PM₁₀ at regionally

representative locations during SJVAQS/AUSPEX, *Atmos. Environ.*, *30*(12), 2079–2112, doi: 10.1016/1352-2310(95)00402-5. 56

Chung, S. H., and J. H. Seinfeld (2005), Climate response of direct radiative forcing of anthropogenic black carbon, *J. Geophys. Res.*, *110*, D11102, doi:10.1029/2004JD005441. 15

Clarke, A. D., et al. (2004), Size distributions and mixtures of dust and black carbon aerosol in Asian outflow: Physiochemistry and optical properties, *J. Geophys. Res.*, *109*, D15S09, doi:10.1029/2003JD004378. 25

Collins, D. R., H. H. Jonsson, H. Liao, R. C. Flagan, J. H. Seinfeld, K. J. Noone, and S. Hering (2000), Airborne analysis of the Los Angeles aerosol, *Atmos. Environ.*, *34*(24), 4155–4173, doi: 10.1016/S1352-2310(00)00225-9. 18

Cubison, M. J., B. Ervens, G. Feingold, K. S. Docherty, I. M. Ulbrich, L. Shields, K. Prather, S. Hering, and J. L. Jimenez (2008), The influence of chemical composition and mixing state of Los Angeles urban aerosol on CCN number and cloud properties, *Atmos. Chem. Phys.*, *8*, 5649–5667, doi:10.5194/acp-8-5649-2008. 16

de Foy, B., J. Varela, L. Molina, and M. Molina (2006), Rapid ventilation of the Mexico City basin and regional fate of the urban plume, *Atmos. Chem. Phys.*, *6*, 2321–2335, doi:10.5194/acp-6-2321-2006. 18

Del Delumyea, R., and A. Kalivretenos (1987), Elemental carbon and lead content of fine particles from American and French cities of comparable size and industry, 1985, *Atmos. Environ.*, *21*(7), 1643–1647, doi:10.1016/0004-6981(87)90325-8. 55

Dentener, F., et al. (2006), Emissions of primary aerosol and precursor gases in the years 2000 and 1750 prescribed data-sets for AeroCom, *Atmos. Chem. Phys.*, *6*, 4321–4344, doi:10.5194/acp-6-4321-2006. 14

Didyk, B. M., B. R. T. Simoneit, L. A. Pezoa, M. L. Riveros, and A. A. Flores (2000), Urban aerosol

particles of Santiago, Chile: organic content and molecular characterization, *Atmos. Environ.*, **34**(8), 1167–1179, doi:10.1016/S1352-2310(99)00403-3. 55

Ding, A., et al. (2009), Transport of north China air pollution by midlatitude cyclones: Case study of aircraft measurements in summer 2007, *J. Geophys. Res.*, **114**, D08304, doi:10.1029/2009JD012339. 18

Docherty, K. S., et al. (2008), Apportionment of primary and secondary organic aerosols in Southern California during the 2005 Study of Organic Aerosols in Riverside (SOAR-1), *Environ. Sci. Technol.*, **42**(20), 7655–7662, doi:10.1021/es8008166. 27

Drewnick, F., et al. (2005), A new time-of-flight aerosol mass spectrometer (TOF-AMS)–Instrument description and first field deployment, *Aerosol Sci. Technol.*, **39**(7), 637–658, doi:10.1080/02786820500182040. 27

Duong, H. T., et al. (2011), Water-soluble organic aerosol in the Los Angeles Basin and outflow regions: Airborne and ground measurements during the 2010 CalNex field campaign, *J. Geophys. Res.*, **116**, D00V04, doi:10.1029/2011JD016674. 27, 32

Edinger, J. G. (1959), Changes in the depth of the marine layer over the Los Angeles Basin, *J. Meteorol.*, **16**, 219–226, doi:10.1175/1520-0469(1959)016<0219:CITDOT>2.0.CO;2. 17

Ensor, D. S., R. J. Charlson, N. C. Alhquist, K. T. Whitby, R. B. Husar, and B. Y. H. Liu (1972), Multiwavelength nephelometer measurements in Los Angeles smog aerosol. I. Comparison of calculated and measured light scattering, *J. Colloid Interface Sci.*, **39**(1), 242–251, doi:10.1016/0021-9797(72)90159-2. 22

Fine, P. M., S. Shen, and C. Sioutas (2004), Inferring the sources of fine and ultrafine particulate matter at downwind receptor sites in the Los Angeles Basin using multiple continuous measurements, *Aerosol Sci. Technol.*, **38**(S1), 182–195, doi:10.1080/02786820390229499. 56

Fuller, K. A., W. C. Malm, and S. M. Kreidenweis (1999), Effects of mixing on extinction by

carbonaceous particles, *J. Geophys. Res.*, 104(D13), 15,941–15,954, doi:10.1029/1998JD100069.

15

Gao, R. S., et al. (2007), A novel method for estimating light-scattering properties of soot aerosols using a modified single-particle soot photometer, *Aerosol Sci. Technol.*, 41(2), 125–135, doi:10.1080/02786820601118398. 23, 37, 38

Gray, H. A., G. R. Cass, J. J. Huntzicker, E. K. Heyerdahl, and J. A. Rau (1986), Characteristics of atmospheric organic and elemental carbon particle concentrations in Los Angeles, *Environ. Sci. Technol.*, 20(6), 580–589, doi:10.1021/es00148a006. 56

Gysel, M., M. Laborde, J. S. Olfert, R. Subramanian, and A. J. Gröhn (2011), Effective density of Aquadag and fullerene soot black carbon reference materials used for SP2 calibration, *Atmos. Meas. Tech.*, 4, 2851–2858, doi:10.5194/amt-4-2851-2011. 21, 35, 36, 74

Hansen, A. D. A., V. N. Kapustin, V. M. Kopeikin, D. A. Gillette, and B. A. Bodhaine (1993), Optical absorption by aerosol black carbon and dust in a desert region of Central Asia, *Atmos. Environ., Part A*, 27(16), 2527–2531, doi:10.1016/0960-1686(93)90025-T. 55

Harley, R. A., L. C. Marr, J. K. Lehner, and S. N. Giddings (2005), Changes in motor vehicle emissions on diurnal to decadal time scales and effects on atmospheric composition, *Environ. Sci. Technol.*, 39(14), 5356–5362, doi:10.1021/es048172+. 17, 33

He, K. B., F. M. Yang, Y. L. Ma, Q. Zhang, X. H. Yao, C. K. Chan, S. Cadle, T. Chan, and P. Mulawa (2001), The characteristics of PM_{2.5} in Beijing, China, *Atmos. Environ.*, 35(29), 4959–4970, doi:10.1016/S1352-2310(01)00301-6. 55

Healy, R. M., et al. (2012), Sources and mixing state of size-resolved elemental carbon particles in a European megacity: Paris, *Atmos. Chem. Phys.*, 12, 1681–1700, doi:10.5194/acp-12-1681-2012.

55

Hegg, D., D. Covert, H. Jonsson, and P. Covert (2005), Determination of the transmission

efficiency of an aircraft aerosol inlet, *Aerosol Sci. Technol.*, 39(10), 966–971, doi:10.1080/02786820500377814. 20

Hitzenberger, R., and S. Tohno (2001), Comparison of black carbon (BC) aerosols in two urban areas – concentrations and size distributions, *Atmos. Environ.*, 35(12), 2153–2167, doi:10.1016/S1352-2310(00)00480-5. 55

Huang, X.-F., et al. (2011), Black carbon measurements in the Pearl River Delta region of China, *J. Geophys. Res.*, 116, D12208, doi:10.1029/2010JD014933. 15

Jacobson, M. Z. (1997), Development and application of a new air pollution modeling system — Part III. Aerosol-phase simulations, *Atmos. Environ.*, 31(4), 587–608, doi:10.1016/S1352-2310(96)00201-4. 16

Jacobson, M. Z. (2002), Control of fossil-fuel particulate black carbon and organic matter, possibly the most effective method of slowing global warming, *J. Geophys. Res.*, 107(D19), 4410, doi:10.1029/2001JD001376. 15

Jacobson, M. Z. (2006), Effects of externally-through-internally-mixed soot inclusions within clouds and precipitation on global climate, *J. Phys. Chem. A*, 110(21), 6860–6873, doi:10.1021/jp056391r. 15

Jaffe, D., et al. (1999), Transport of Asian air pollution to North America, *Geophys. Res. Lett.*, 26(6), 711–714, doi:10.1029/1999GL900100. 18

Janssen, N. A. H., D. F. M. Van Mansom, K. Van Der Jagt, H. Harssema, and G. Hoek (1997), Mass concentration and elemental composition of airborne particulate matter at street and background locations, *Atmos. Environ.*, 31(8), 1185–1193, doi:10.1016/S1352-2310(96)00291-9. 55

Jayne, J. T., D. C. Leard, X. Zhang, P. Davidovits, K. A. Smith, C. E. Kolb, and D. R. Worsnop (2000), Development of an aerosol mass spectrometer for size and composition analysis of submicron particles, *Aerosol Sci. Technol.*, 33(1-2), 49–70, doi:10.1080/027868200410840. 27

Johnson, K. S., B. Zuberi, L. T. Molina, M. J. Molina, M. J. Iedema, J. P. Cowin, D. J. Gaspar, C. Wang, and A. Laskin (2005), Processing of soot in an urban environment: case study from the Mexico City Metropolitan Area, *Atmos. Chem. Phys.*, 5, 3033–3043, doi:10.5194/acp-5-3033-2005.

15

Jones, G. S., N. Christidis, and P. A. Stott (2011), Detecting the influence of fossil fuel and bio-fuel black carbon aerosols on near surface temperature changes, *Atmos. Chem. Phys.*, 11, 799–816, doi:10.5194/acp-11-799-2011. 15

Kadowaki, S. (1990), Characterization of carbonaceous aerosols in the Nagoya urban area. 1. Elemental and organic carbon concentrations and the origin of organic aerosols, *Environ. Sci. Technol.*, 24(5), 741–744, doi:10.1021/es00075a020. 55

Kim, B. M., S. Teffera, and M. D. Zeldin (2000), Characterization of PM_{2.5} and PM₁₀ in the South Coast Air Basin of Southern California: Part 1–Spatial variations, *J. Air Waste Manage. Assoc.*, 50(12), 2034–2044. 56

Kim, Y. P., K.-C. Moon, J. H. Lee, and N. J. Baik (1999), Concentrations of carbonaceous species in particles at Seoul and Cheju in Korea, *Atmos. Environ.*, 33(17), 2751–2758, doi: 10.1016/S1352-2310(98)00313-6. 55

Laborde, M., P. Mertes, P. Zieger, J. Dommen, U. Baltensperger, and M. Gysel (2012), Sensitivity of the Single Particle Soot Photometer to different black carbon types, *Atmos. Meas. Tech. Discuss.*, 5, 663–690, doi:10.5194/amt-5-663-2012. 22, 36

Lack, D. A., and C. D. Cappa (2010), Impact of brown and clear carbon on light absorption enhancement, single scatter albedo and absorption wavelength dependence of black carbon, *Atmos. Chem. Phys.*, 10, 4207–4220, doi:10.5194/acp-10-4207-2010. 15

Langford, A. O., J. Brioude, O. R. Cooper, C. J. Senff, R. J. Alvarez II, R. M. Hardesty, B. J. Johnson, and S. J. Oltmans (2012), Stratospheric influence on surface ozone in the Los Angeles

area during late spring and early summer of 2010, *J. Geophys. Res.*, 117, D00V06, doi:10.1029/2011JD016766. 18

Liang, Q., L. Jaeglé, D. A. Jaffe, P. Weiss-Penzias, A. Heckman, and J. A. Snow (2004), Long-range transport of Asian pollution to the northeast Pacific: Seasonal variations and transport pathways of carbon monoxide, *J. Geophys. Res.*, 109, D23S07, doi:10.1029/2003JD004402. 18

Lin, J. J., and H.-S. Tai (2001), Concentrations and distributions of carbonaceous species in ambient particles in Kaohsiung City, Taiwan, *Atmos. Environ.*, 35(15), 2627–2636, doi:10.1016/S1352-2310(00)00444-1. 55

Liu, H., D. J. Jacob, I. Bey, R. M. Yantosca, B. N. Duncan, and G. W. Sachse (2003), Transport pathways for Asian pollution outflow over the Pacific: Interannual and seasonal variations, *J. Geophys. Res.*, 108(D20), 8786, doi:10.1029/2002JD003102. 18

Lu, R., and R. P. Turco (1994), Air pollutant transport in a coastal environment. Part 1: Two-dimensional simulations of sea-breeze and mountain effects, *J. Atmos. Sci.*, 51(15), 2285–2308, doi:10.1175/1520-0469(1994)051\$2285:APTIAC\$2.0.CO;2. 18, 33

Lu, R., and R. P. Turco (1995), Air pollutant transport in a coastal environment-II. Three-dimensional simulations over Los Angeles Basin, *Atmos. Environ.*, 29(13), 1499–1518, doi:10.1016/1352-2310(95)00015-Q. 17, 18, 33

Marr, L. C., and R. A. Harley (2002), Spectral analysis of weekday–weekend differences in ambient ozone, nitrogen oxide, and non-methane hydrocarbon time series in California, *Atmos. Environ.*, 36(14), 2327–2335, doi:10.1016/S1352-2310(02)00188-7. 33

McMeeking, G. R., et al. (2010), Black carbon measurements in the boundary layer over western and northern Europe, *Atmos. Chem. Phys.*, 10, 9393–9414, doi:10.5194/acp-10-9393-2010. 27, 55

Menon, S., J. Hansen, L. Nazarenko, and Y. Luo (2002), Climate effects of black carbon aerosols in China and India, *Science*, 297(5590), 2250–2253, doi:10.1126/science.1075159. 15

Mikhailov, E. F., S. S. Vlasenko, I. A. Podgorny, V. Ramanathan, and C. E. Corrigan (2006), Optical properties of soot–water drop agglomerates: An experimental study, *J. Geophys. Res.*, 111, D07209, doi:10.1029/2005JD006389. 15

Modey, W. K., Y. Pang, N. L. Eatough, and D. J. Eatough (2001), Fine particulate (PM_{2.5}) composition in Atlanta, USA: assessment of the particle concentrator-Brigham Young University organic sampling system, PC-BOSS, during the EPA supersite study, *Atmos. Environ.*, 35(36), 6493–6502, doi:10.1016/S1352-2310(01)00402-2. 55

Moore, G. E., S. G. Douglas, R. C. Kessler, and J. P. Killus (1991), Identification and tracking of polluted air masses in the South-Central Coast Air Basin, *J. Appl. Meteorol.*, 30(5), 715–732, doi:10.1175/1520-0450(1991)030<0715:IATOPA>2.0.CO;2. 18

Moteki, N., and Y. Kondo (2007), Effects of mixing state on black carbon measurements by laser-induced incandescence, *Aerosol Sci. Technol.*, 41(4), 398–417, doi:10.1080/02786820701199728. 21, 23, 36

Moteki, N., and Y. Kondo (2010), Dependence of laser-induced incandescence on physical properties of black carbon aerosols: Measurements and theoretical interpretation, *Aerosol Sci. Technol.*, 44(8), 663–675, doi:10.1080/02786826.2010.484450. 22, 36

Moteki, N., et al. (2007), Evolution of mixing state of black carbon particles: Aircraft measurements over the western Pacific in March 2004, *Geophys. Res. Lett.*, 34, L11803, doi: 10.1029/2006GL028943. 15, 23, 25, 28, 29, 55

Murphy, S. M., et al. (2009), Comprehensive simultaneous shipboard and airborne characterization of exhaust from a modern container ship at sea, *Environ. Sci. Technol.*, 43(13), 4626–4640, doi: 10.1021/es802413j. 27

Nehrkorn, T., J. Eluszkiewicz, S. C. Wofsy, J. C. Lin, C. Gerbig, M. Longo, and S. Freitas (2010), Coupled weather research and forecasting-stochastic time-inverted lagrangian transport (WRF-STILT) model, *Meteorol. Atmos. Phys.*, 107, 51–64, doi:10.1007/s00703-010-0068-x. 18

Neiburger, M. (1969), The role of meteorology in the study and control of air pollution, *Bull. Am. Meteorol. Soc.*, 50(12), 957–965. 17

Offenberg, J., and J. Baker (2000), Aerosol size distributions of elemental and organic carbon in urban and over-water atmospheres, *Atmos. Environ.*, 34(10), 1509–1517, doi:10.1016/S1352-2310(99)00412-4. 55

Ohta, S., and T. Okita (1990), A chemical characterization of atmospheric aerosol in Sapporo, *Atmos. Environ., Part A*, 24(4), 815–822, doi:10.1016/0960-1686(90)90282-R. 55

Ohta, S., M. Hori, S. Yamagata, and N. Murao (1998), Chemical characterization of atmospheric fine particles in Sapporo with determination of water content, *Atmos. Environ.*, 32(6), 1021–1025, doi:10.1016/S1352-2310(97)00347-6. 55

Paatero, P., and U. Tapper (1993), Analysis of different modes of factor analysis as least squares fit problems, *Chemom. Intell. Lab. Syst.*, 18(2), 183–194, doi:10.1016/0169-7439(93)80055-M. 29

Palau, J. L., G. Pérez-Landa, J. Meliá, D. Segarra, and M. M. Millán (2006), A study of dispersion in complex terrain under winter conditions using high-resolution mesoscale and Lagrangian particle models, *Atmos. Chem. Phys.*, 6, 1105–1134, doi:10.5194/acp-6-1105-2006. 18

Park, K., D. B. Kittelson, and P. H. McMurry (2004), Structural properties of diesel exhaust particles measured by transmission electron microscopy (TEM): Relationships to particle mass and mobility, *Aerosol Sci. Technol.*, 38(9), 881–889, doi:10.1080/027868290505189. 15

Park, S. S., Y. J. Kim, and K. Fung (2001), Characteristics of PM_{2.5} carbonaceous aerosol in the Sihwa industrial area, South Korea, *Atmos. Environ.*, 35, 657–665, doi:10.1016/S1352-2310(00)00357-5. 55

Paterson, K. G., J. L. Sagady, D. L. Hooper, S. B. Bertman, M. A. Carroll, and P. B. Shepson (1999), Analysis of air quality data using positive matrix factorization, *Environ. Sci. Technol.*, 33(4), 635–641, doi:10.1021/es980605j. 29

Pollack, I. B., et al. (2012), Airborne and ground-based observations of a weekend effect in ozone, precursors, and oxidation products in the California South Coast Air Basin, *J. Geophys. Res.*, 117, D00V05, doi:10.1029/2011JD016772. 33

Pósfai, M., J. R. Anderson, P. R. Buseck, and H. Sievering (1999), Soot and sulfate aerosol particles in the remote marine troposphere, *J. Geophys. Res.*, 104(D17), 21,685–21,693, doi: 10.1029/1999JD900208. 15

Pratsinis, S. E., M. D. Zeldin, and E. C. Ellis (1988), Source resolution of the fine carbonaceous aerosol by principal component-stepwise regression analysis, *Environ. Sci. Technol.*, 22(2), 212–216, doi:10.1021/es00167a013. 56

Pueschel, R. F., D. F. Blake, K. G. Snetsinger, A. D. A. Hansen, S. Verma, and K. Kato (1992), Black carbon (soot) aerosol in the lower stratosphere and upper troposphere, *Geophys. Res. Lett.*, 19(16), 1659–1662, doi:10.1029/92GL02478. 25

Raga, G., T. Castro, and D. Baumgardner (2001), The impact of megacity pollution on local climate and implications for the regional environment: Mexico City, *Atmos. Environ.*, 35(10), 1805–1811, doi:10.1016/S1352-2310(00)00275-2. 32

Ramana, M. V., V. Ramanathan, Y. Feng, S.-C. Yoon, S.-W. Kim, G. R. Carmichael, and J. J. Schauer (2010), Warming influenced by the ratio of black carbon to sulphate and the black-carbon source, *Nat. Geosci.*, 3(8), 542–545, doi:10.1038/ngeo918. 15

Ramanathan, V., and G. Carmichael (2008), Global and regional climate changes due to black carbon, *Nat. Geosci.*, 1(4), 221–227, doi:10.1038/ngeo156. 15

Ramanathan, V., M. V. Ramana, G. Roberts, D. Kim, C. Corrigan, C. Chung, and D. Winker (2007), Warming trends in Asia amplified by brown cloud solar absorption, *Nature*, 448(7153), 575–578, doi:10.1038/nature06019. 15

Reche, C., et al. (2011), New considerations for PM, Black Carbon and particle number concentration

for air quality monitoring across different European cities, *Atmos. Chem. Phys.*, *11*, 6207–6227, doi:10.5194/acp-11-6207-2011. 55

Riemer, N., H. Vogel, and B. Vogel (2004), Soot aging time scales in polluted regions during day and night, *Atmos. Chem. Phys.*, *4*, 1885–1893, doi:10.5194/acp-4-1885-2004. 15

Robinson, E. (1952), Some air pollution aspects of the Los Angeles temperature inversion, *Bull. Am. Meteorol. Soc.*, *33*(6), 247–250. 17

Ruellan, S., and H. Cachier (2001), Characterisation of fresh particulate vehicular exhausts near a Paris high flow road, *Atmos. Environ.*, *35*(2), 453–468, doi:10.1016/S1352-2310(00)00110-2. 55

Schauer, J. J., W. F. Rogge, L. M. Hildemann, M. A. Masurek, G. R. Cass, and B. R. T. Simoneit (1996), Source apportionment of airborne particulate matter using organic compounds as tracers, *Atmos. Environ.*, *30*(22), 3837–3855, doi:10.1016/1352-2310(96)00085-4. 16

Schnaiter, M., C. Linke, O. Möhler, K. Naumann, H. Saathoff, R. Wagner, U. Schurath, and B. Wehner (2005), Absorption amplification of black carbon internally mixed with secondary organic aerosol, *J. Geophys. Res.*, *110*, D19204, doi:10.1029/2005JD006046. 15

Schwarz, J. P., et al. (2006), Single-particle measurements of midlatitude black carbon and light-scattering aerosols from the boundary layer to the lower stratosphere, *J. Geophys. Res.*, *111*, D16207, doi:10.1029/2006JD007076. 21, 23

Schwarz, J. P., et al. (2008a), Measurement of the mixing state, mass, and optical size of individual black carbon particles in urban and biomass burning emissions, *Geophys. Res. Lett.*, *35*, L13810, doi:10.1029/2008GL033968. 15, 24, 25, 27, 32, 55

Schwarz, J. P., et al. (2008b), Coatings and their enhancement of black carbon light absorption in the tropical atmosphere, *J. Geophys. Res.*, *113*, D03203, doi:10.1029/2007JD009042. 15, 21, 24, 25

Schwarz, J. P., et al. (2010), The detection efficiency of the Single Particle Soot Photometer, *Aerosol Sci. Technol.*, *44*(8), 612–628, doi:10.1080/02786826.2010.481298. 21

Seinfeld, J. H., and S. N. Pandis (2006), *Atmospheric Chemistry and Physics: From Air Pollution to Climate Change*, 2nd ed., John Wiley & Sons, Inc., New York. 15, 32

Shiraiwa, M., Y. Kondo, N. Moteki, N. Takegawa, Y. Miyazaki, and D. R. Blake (2007), Evolution of mixing state of black carbon in polluted air from Tokyo, *Geophys. Res. Lett.*, 34, L16803, doi:10.1029/2007GL029819. 15, 27, 29

Shiraiwa, M., Y. Kondo, N. Moteki, N. Takegawa, L. K. Sahu, A. Takami, S. Hatakeyama, S. Yonemura, and D. R. Blake (2008), Radiative impact of mixing state of black carbon aerosol in Asian outflow, *J. Geophys. Res.*, 113, D24210, doi:10.1029/2008JD010546. 15, 21, 29

Slowik, J. G., et al. (2007), An inter-comparison of instruments measuring black carbon content of soot particles, *Aerosol Sci. Technol.*, 41(3), 295–314, doi:10.1080/02786820701197078. 21, 36

Stelson, A. W. (1990), Urban aerosol refractive index prediction by partial molar refraction approach, *Environ. Sci. Technol.*, 24(11), 1676–1679, doi:10.1021/es00081a008. 22

Stephens, M., N. Turner, and J. Sandberg (2003), Particle identification by laser-induced incandescence in a solid-state laser cavity, *Appl. Opt.*, 42(19), 3726–3736, doi:10.1364/AO.42.003726. 21

Stier, P., J. H. Seinfeld, S. Kinne, and O. Boucher (2007), Aerosol absorption and radiative forcing, *Atmos. Chem. Phys.*, 7, 5237–5261, doi:10.5194/acp-7-5237-2007. 16

Stohl, A., C. Forster, A. Frank, P. Seibert, and G. Wotawa (2005), Technical note: The Lagrangian particle dispersion model FLEXPART version 6.2, *Atmos. Chem. Phys.*, 5, 2461–2474, doi:10.5194/acp-5-2461-2005. 18

Stolzenburg, M., N. Kreisberg, and S. Hering (1998), Atmospheric size distributions measured by differential mobility optical particle size spectrometry, *Aerosol Sci. Technol.*, 29(5), 402–418, doi:10.1080/02786829808965579. 22

Subramanian, R., et al. (2010), Black carbon over Mexico: the effect of atmospheric transport on

mixing state, mass absorption cross-section, and BC/CO ratios, *Atmos. Chem. Phys.*, *10*, 219–237, doi:10.5194/acp-10-219-2010. 15, 24, 55

Sullivan, A. P., R. E. Peltier, C. A. Brock, J. A. de Gouw, J. S. Holloway, C. Warneke, A. G. Wollny, and R. J. Weber (2006), Airborne measurements of carbonaceous aerosol soluble in water over northeastern United States: Method development and an investigation into water-soluble organic carbon sources, *J. Geophys. Res.*, *111*, D23S46, doi:10.1029/2006JD007072. 27

Toon, O. B., and T. P. Ackerman (1981), Algorithms for the calculation of scattering by stratified spheres, *Appl. Opt.*, *20*(20), 3657–3660, doi:10.1364/AO.20.003657. 24

Tripathi, S. N., S. Dey, V. Tare, and S. K. Satheesh (2005), Aerosol black carbon radiative forcing at an industrial city in northern India, *Geophys. Res. Lett.*, *32*, L08802, doi:10.1029/2005GL022515. 55

Turpin, B. J., and J. J. Huntzicker (1991), Secondary formation of organic aerosol in the Los Angeles basin: A descriptive analysis of organic and elemental carbon concentrations, *Atmos. Environ., Part A*, *25*(2), 207–215, doi:10.1016/0960-1686(91)90291-E. 34

Turpin, B. J., and J. J. Huntzicker (1995), Identification of secondary organic aerosol episodes and quantitation of primary and secondary organic aerosol concentrations during SCAQS, *Atmos. Environ.*, *29*(23), 3527–3544, doi:10.1016/1352-2310(94)00276-Q. 16, 34

Turpin, B. J., and H.-J. Lim (2001), Species contributions to PM2.5 mass concentrations: Revisiting common assumptions for estimating organic mass, *Aerosol Sci. Technol.*, *35*(1), 602–610, doi:10.1080/02786820119445. 27

Turpin, B. J., J. J. Huntzicker, S. M. Larson, and G. R. Cass (1991), Los Angeles summer midday particulate carbon: Primary and secondary aerosol, *Environ. Sci. Technol.*, *25*(10), 1788–1793, doi:10.1021/es00022a017. 56

Ulbrich, I. M., M. R. Canagaratna, Q. Zhang, D. R. Worsnop, and J. L. Jimenez (2009), Interpre-

tation of organic components from Positive Matrix Factorization of aerosol mass spectrometric data, *Atmos. Chem. Phys.*, 9, 2891–2918, doi:10.5194/acp-9-2891-2009. 29

Venkataraman, C., C. K. Reddy, S. Josson, and M. S. Reddy (2002), Aerosol size and chemical characteristics at Mumbai, India, during the INDOEX-IPF (1999), *Atmos. Environ.*, 36(12), 1979–1991, doi:10.1016/S1352-2310(02)00167-X. 55

Wakimoto, R. M., and J. L. McElroy (1986), Lidar observation of elevated pollution layers over Los Angeles, *J. Clim. Appl. Meteorol.*, 25(11), 1583–1599, doi:10.1175/1520-0450(1986)025<1583:LOOEPL>2.0.CO;2. 18

Weingartner, E., H. Burtscher, and U. Baltensperger (1997), Hygroscopic properties of carbon and diesel soot particles, *Atmos. Environ.*, 31(15), 2311–2327, doi:10.1016/S1352-2310(97)00023-X. 15

Wonaschütz, A., S. P. Hersey, A. Sorooshian, J. S. Craven, A. R. Metcalf, R. C. Flagan, and J. H. Seinfeld (2011), Impact of a large wildfire on water-soluble organic aerosol in a major urban area: the 2009 Station Fire in Los Angeles County, *Atmos. Chem. Phys.*, 11, 8257–8270, doi:10.5194/acp-11-8257-2011. 27

Zappoli, S., et al. (1999), Inorganic, organic and macromolecular components of fine aerosol in different areas of Europe in relation to their water solubility, *Atmos. Environ.*, 33(17), 2733–2743, doi:10.1016/S1352-2310(98)00362-8. 55

Zarzycki, C. M., and T. C. Bond (2010), How much can the vertical distribution of black carbon affect its global direct radiative forcing?, *Geophys. Res. Lett.*, 37, L20807, doi:10.1029/2010GL044555. 15

Zhang, Q., et al. (2007), Ubiquity and dominance of oxygenated species in organic aerosols in anthropogenically-influenced Northern Hemisphere midlatitudes, *Geophys. Res. Lett.*, 34, L13801, doi:10.1029/2007GL029979. 16

Zier, M. (1991), Mass concentrations of total dust and soot in the near surface air in East Germany,
J. Aerosol Sci., 22(S1), S597–S600, doi:10.1016/S0021-8502(05)80172-7. 55

Table 2.1: Urban Black Carbon Measurement Studies.

Region		Dates	BC Levels ^a [$\mu\text{g m}^{-3}$]	Measurement Method	Reference
<i>Asia</i>					
Sapporo, Japan	1982	5.1 (2.3–8.0) 5.3–34.4	ground, filter	<i>Ohta and Okita</i> (1990)	
Nagoya, Japan	1984–1986	2.6	ground, filter	<i>Kadowaki</i> (1990)	
Uji, Japan	1989–1999	3.9 (2.25–6.93)	ground, filter	<i>Hitzenberger and Tohno</i> (2001)	
Sapporo, Japan	1991–1992	7.6 (4.86–9.86)	ground, filter	<i>Ohta et al.</i> (1998)	
Seoul, Korea	1994	2.2–5.2	ground, filter	<i>Kim et al.</i> (1999)	
Kaohsiung City, Taiwan	1998–1999	7.5–17.5	ground, filter	<i>Lin and Tai</i> (2001)	
Mumbai, India	1999	8.4	ground, filter	<i>Venkataraman et al.</i> (2002)	
Seoul, Korea	1999	6.3–11.1	ground, filter	<i>Park et al.</i> (2001)	
Beijing, China	1999–2000	0.4–10.2	ground, filter	<i>He et al.</i> (2001)	
Bangalore, India	2001	7.1 (3.1–19.4) 6–20	ground, aethalometer	<i>Babu et al.</i> (2002)	
Guangzhou, China	2004	0.5–1.1	ground, filter	<i>Andreae et al.</i> (2008)	
Kaupur, India	2004	0.5–1.1	ground, aethalometer	<i>Tripathi et al.</i> (2005)	
Nagoya, Japan			aircraft, SP2	<i>Moteki et al.</i> (2007)	
<i>Europe</i>					
Orleans, France	1985	2.9	ground, filter	<i>Del Delumyea and Kalivretenos</i> (1987)	
Paris, France	1985	7.9	ground, filter	<i>Del Delumyea and Kalivretenos</i> (1987)	
Clermont, France	1985	2.4	ground, filter	<i>Del Delumyea and Kalivretenos</i> (1987)	
Strasbourg, France	1985	2.9	ground, filter	<i>Del Delumyea and Kalivretenos</i> (1987)	
Görlitz, Germany	1988–1990	1.3–11.8	ground, filter	<i>Zier</i> (1991)	
Halle, Germany	1988–1990	1.6–12.0	ground, filter	<i>Zier</i> (1991)	
Kap Arkona, Germany	1988–1990	0.4–3.5	ground, filter	<i>Zier</i> (1991)	
Neuglobusow, Germany	1988–1990	0.6–5.2	ground, filter	<i>Zier</i> (1991)	
Neuhaus, Germany	1988–1990	0.5–3.5	ground, filter	<i>Zier</i> (1991)	
Potsdam, Germany	1988–1990	1.0–12.3	ground, filter	<i>Zier</i> (1991)	
Radebeul, Germany	1988–1990	1.4–12.6	ground, filter	<i>Zier</i> (1991)	
Dushanbe, Russia	1989	4–20	ground, filter	<i>Hansen et al.</i> (1993)	
Vienna, Austria	1989–1999	2.8	ground, filter	<i>Hitzenberger and Tohno</i> (2001)	
Arnhem, Netherlands	1994	2.95	ground, filter	<i>Janssen et al.</i> (1997)	
Po Valley, Italy	1996	1.0 (0.5–1.5)	ground, filter	<i>Zappoli et al.</i> (1999)	
Paris, France	1997	13.6	ground, filter	<i>Ruellean and Cachier</i> (2001)	
Thessaloniki, Greece	1997	3–3	ground, filter	<i>Chazette and Liousse</i> (2001)	
Thessaloniki, Greece	1997	3.5–8.9	ground, filter	<i>McMeeking et al.</i> (2010)	
Liverpool/Manchester, England	2008	0.3	aircraft, SP2	<i>Reche et al.</i> (2011)	
Barcelona, Spain	2009	1.7 (0.7–3.8)	ground, absorption	<i>Reche et al.</i> (2011)	
Bern, Switzerland	2009	3.5 (1.3–7.1)	ground, absorption	<i>Reche et al.</i> (2011)	
Huelva, Spain	2009	0.7 (0.1–2.3)	ground, absorption	<i>Reche et al.</i> (2011)	
London, England	2009	1.9 (0.8–3.4)	ground, aethalometer	<i>Reche et al.</i> (2011)	
Lugano, Switzerland	2009	1.8 (0.6–3.6)	ground, absorption	<i>Reche et al.</i> (2011)	
Santa Cruz de Tenerife, Spain	2009	0.8 (0.1–2.6)	ground, absorption	<i>Reche et al.</i> (2011)	
Paris, France	2010	1.66	ground, aethalometer	<i>Healy et al.</i> (2012)	
<i>North America</i>					
Akron, Ohio	1985	2.6	ground, filter	<i>Del Delumyea and Kalivretenos</i> (1987)	
Chicago, Illinois	1985	4.6	ground, filter	<i>Del Delumyea and Kalivretenos</i> (1987)	
Norfolk, Virginia	1985	3.0	ground, filter	<i>Offenberg and Baker</i> (2000)	
Chicago, Illinois	1994–1995	0.19–0.45	ground, filter	<i>Bruncik et al.</i> (2001)	
Baltimore, Maryland	1997	0.53–2.60	ground, filter	<i>Modey et al.</i> (2001)	
Atlanta, Georgia	1999	1.5 (0.5–3.0)	ground, filter	<i>Baumgardner et al.</i> (2007)	
Mexico City, Mexico	2003, 2005	0.5–3.0	aircraft, SP2	<i>Schwarz et al.</i> (2008a)	
Dallas/Houston, Texas	2006	0.7 (0.65–0.74)	aircraft, SP2	<i>Subramanian et al.</i> (2010)	
Mexico City, Mexico	2006	0.276–1.100	aircraft, SP2		
<i>South America</i>					
Santiago, Chile	1991	30.6 (11–75)	ground, filters	<i>Didyk et al.</i> (2000)	

^a BC levels are campaign average values (and/or range) depending on availability.

Table 2.2: California Black Carbon Measurement Studies.

Region	Dates	BC Levels ^a [$\mu\text{g m}^{-3}$]	Measurement Method	Reference
<i>Bakersfield area</i>				
Edison	July–September, 1990	2.95	ground, filter	<i>Chow et al. (1996)</i>
Caliente	July–September, 1990	3.33	ground, filter	<i>Chow et al. (1996)</i>
Bakersfield	May, 2010	0.050 (0.040–0.072)	aircraft, SP2	<i>this study</i>
<i>San Joaquin Valley</i>				
Academy	July–September, 1990	1.43	ground, filter	<i>Chow et al. (1996)</i>
Buttonwillow	July–September, 1990	1.86	ground, filter	<i>Chow et al. (1996)</i>
San Joaquin Valley	May, 2010	0.041 (0.014–0.087)	aircraft, SP2	<i>this study</i>
<i>Long Beach area</i>				
Long Beach	Jan–Dec, 1982	3.75	ground, filter	<i>Gray et al. (1986)</i>
Long Beach	Jun–Sep, 1987	0.99	ground, filter	<i>Gray et al. (1986)</i>
Long Beach	May, 2010	0.126 (0.010–0.467)	aircraft, SP2	<i>this study</i>
<i>West Los Angeles Basin</i>				
Lennox	Jan–Dec, 1982	4.51	ground, filter	<i>Gray et al. (1986)</i>
Downtown LA	Jan–Dec, 1982	4.87	ground, filter	<i>Gray et al. (1986)</i>
West Los Angeles	Jan–Dec, 1982	3.61	ground, filter	<i>Gray et al. (1986)</i>
Lennox	Jul–Sep, 1984	1.7	ground, filter	<i>Turpin et al. (1991)</i>
Downtown LA	Jun–Sep, 1987	2.37	ground, filter	<i>Chow et al. (1994)</i>
Hawthorne	Jun–Sep, 1987	0.70	ground, filter	<i>Chow et al. (1994)</i>
Diamond Bar	Jan, 1995–Feb, 1996	3.08	ground, filter	<i>Kim et al. (2000)</i>
Downtown LA	Jan, 1995–Feb, 1996	3.81	ground, filter	<i>Kim et al. (2000)</i>
West LA Basin	May, 2010	0.175 (0.029–0.526)	aircraft, SP2	<i>this study</i>
<i>Pasadena area</i>				
Azusa	Jan–Dec, 1982	3.30	ground, filter	<i>Gray et al. (1986)</i>
Burbank	Jan–Dec, 1982	5.04	ground, filter	<i>Gray et al. (1986)</i>
Pasadena	Jan–Dec, 1982	3.95	ground, filter	<i>Gray et al. (1986)</i>
Duarte	Jan–Dec, 1983	4.35	ground, filter	<i>Prahliris et al. (1988)</i>
Azusa	Jul–Sep, 1984	4.1	ground, filter	<i>Turpin et al. (1991)</i>
Pasadena	Jul–Sep, 1984	2.5	ground, filter	<i>Turpin et al. (1991)</i>
Azusa	Jun–Sep, 1987	2.64	ground, filter	<i>Chow et al. (1994)</i>
Burbank	Jun–Sep, 1987	2.21	ground, filter	<i>Chow et al. (1994)</i>
Pasadena	May, 2010	0.179 (0.097–0.381)	aircraft, SP2	<i>this study</i>
<i>East Los Angeles Basin</i>				
Upland	Jan–Dec, 1982	3.14	ground, filter	<i>Gray et al. (1986)</i>
Rubidoux	Jan–Dec, 1982	3.03	ground, filter	<i>Gray et al. (1986)</i>
Upland	Jul–Sep, 1984	2.8	ground, filter	<i>Turpin et al. (1991)</i>
San Bernardino	Jul–Sep, 1984	1.4	ground, filter	<i>Turpin et al. (1991)</i>
Claremont	Jun–Sep, 1987	1.92	ground, filter	<i>Chow et al. (1994)</i>
Rubidoux	Jun–Sep, 1987	1.73	ground, filter	<i>Chow et al. (1994)</i>
Fontana	Jan, 1995–Feb, 1996	3.49	ground, filter	<i>Kim et al. (2000)</i>
Rubidoux	Feb–May, 2001	3.25	ground, filter	<i>Kim et al. (2000)</i>
Riverside	Jun–Aug, 2001	0.5–2.7	ground, aethalometer	<i>Fine et al. (2004)</i>
Rubidoux	Oct, 2001–Mar, 2002	0.8–3.8	ground, aethalometer	<i>Fine et al. (2004)</i>
Claremont	May, 2010	0.179 (0.047–0.445)	aircraft, SP2	<i>this study</i>
East LA Basin				

^a BC levels are campaign average values (and/or range) depending on availability.

Table 2.3: Summary of CIRPAS Twin Otter Flights During CalNex 2010^a.

Date	Day of Week	Sampling Time (local time ^b)	Region Sampled
May 4	Tues	11:01–14:23	LA Basin, missed approaches ^c
May 5	Wed	11:04–15:10	LA Basin, missed approaches ^c
May 6	Thu	12:06–15:59	LA Basin
May 7	Fri	11:02–14:57	LA Basin
May 10	Mon	12:00–16:05	LA Basin, western edge
May 12	Wed	10:56–15:08	LA Basin, Imperial Valley
May 13	Thu	11:05–14:54	LA Basin, Imperial Valley
May 14	Fri	10:59–15:01	LA Basin
May 15	Sat	11:13–15:13	LA Basin
May 18	Tue	11:59–15:53	San Joaquin Valley
May 19	Wed	11:40–15:45	LA Basin
May 20	Thu	11:33–15:58	San Joaquin Valley
May 21	Fri	10:57–15:05	LA Basin, outflow regions
May 22	Sat	11:01–15:12	San Joaquin Valley
May 24	Mon	11:01–15:03	LA Basin, outflow regions
May 25	Tue	11:27–15:31	LA Basin, outflow regions
May 27	Thu	10:59–14:45	LA Basin
May 28	Fri	10:58–15:03	LA Basin

^aThe month of May, 2010, in particular, was slightly cooler than normal with a relatively strong coastal marine layer present much of the time. The average high temperature in downtown LA for the month was 19 °C, with a maximum high of 24 °C on May 29. The average low was 12 °C, with the lowest minimum of 10 °C on May 25. There were three days (May 17, 18, and 27) with measurable precipitation in downtown LA totaling just 0.11 inches of rain; these days had a particularly strong marine layer leading to measurable drizzle. One day (May 10) had a weak off-shore flow, but all others exhibited the typical day-time sea-breeze from the southwest.

^bLocal time is 7 hours behind UTC time.

^cThe missed approaches on the first two flights took place at various small airports scattered throughout the LA Basin. Beginning with May 6 flight, we performed missed approaches only at the Long Beach and Torrance Airports.

Table 2.4: Summary of SP2 Measurements^a Broken Down by Region.

Region ^b	rBC Number Concentration [cm ⁻³]	rBC Mass Concentration [μg m ⁻³]	Mean Coating Thickness [nm]	Percent Thickly Coated [%]	rBC Mass Fraction [%]	rBC Mass Median Diameter [nm]
LA Basin	267 (288±136)	0.154 (0.167 ±0.0828)	99 (20)	37 (11)	2.4 (1.3)	122 (7)
<i>Long Beach</i>	187 (199±121)	0.112 (0.126 ±0.0777)	99 (23)	38 (13)	2.8 (0.9)	130 (7)
<i>Pasadena</i>	289 (321±109)	0.164 (0.179 ±0.0647)	94 (14)	29 (9)	2.8 (1.2)	120 (3)
<i>West LA Basin</i>	280 (309±149)	0.159 (0.175 ±0.0873)	93 (20)	32 (10)	2.4 (1.0)	123 (7)
<i>East LA Basin</i>	274 (295±119)	0.159 (0.179 ±0.0782)	102 (20)	41 (10)	2.1 (1.2)	122 (4)
Banning Pass	162 (162± 77)	0.0907 (0.0954±0.0445)	135 (29)	55 (13)	2.0 (1.0)	126 (6)
Basin Outflows	136 (165±104)	0.0792 (0.0978±0.0619)	138 (33)	47 (15)	4.5 (2.3)	127 (7)
<i>Banning Outflow</i>	129 (136± 71)	0.0703 (0.0690±0.0265)	144 (28)	54 (15)	4.9 (1.7)	130 (10)
<i>El Cajon Outflow</i>	130 (173±110)	0.0868 (0.105 ±0.0662)	136 (34)	52 (13)	4.4 (2.3)	129 (7)
Imperial Valley	93 (107± 61)	0.0616 (0.0671±0.0293)	156 (17)	65 (8)	5.3 (2.6)	141 (10)
San Joaquin Valley	60 (67± 33)	0.0408 (0.0414±0.0143)	153 (20)	58 (13)	1.0 (0.6)	130 (8)
<i>Bakersfield</i>	86 (82± 19)	0.0472 (0.0502±0.0102)	145 (14)	52 (6)	1.3 (0.5)	127 (5)
Free Troposphere	14 (54± 90)	0.0167 (0.0346±0.0454)	188 (31)	76 (13)	1.7 (2.8)	161 (41)

^aThe concentrations are campaign medians (mean±1 σ); all other values are campaign-average values (±1 σ).

^bRegion definitions are given in Figure 2.2.

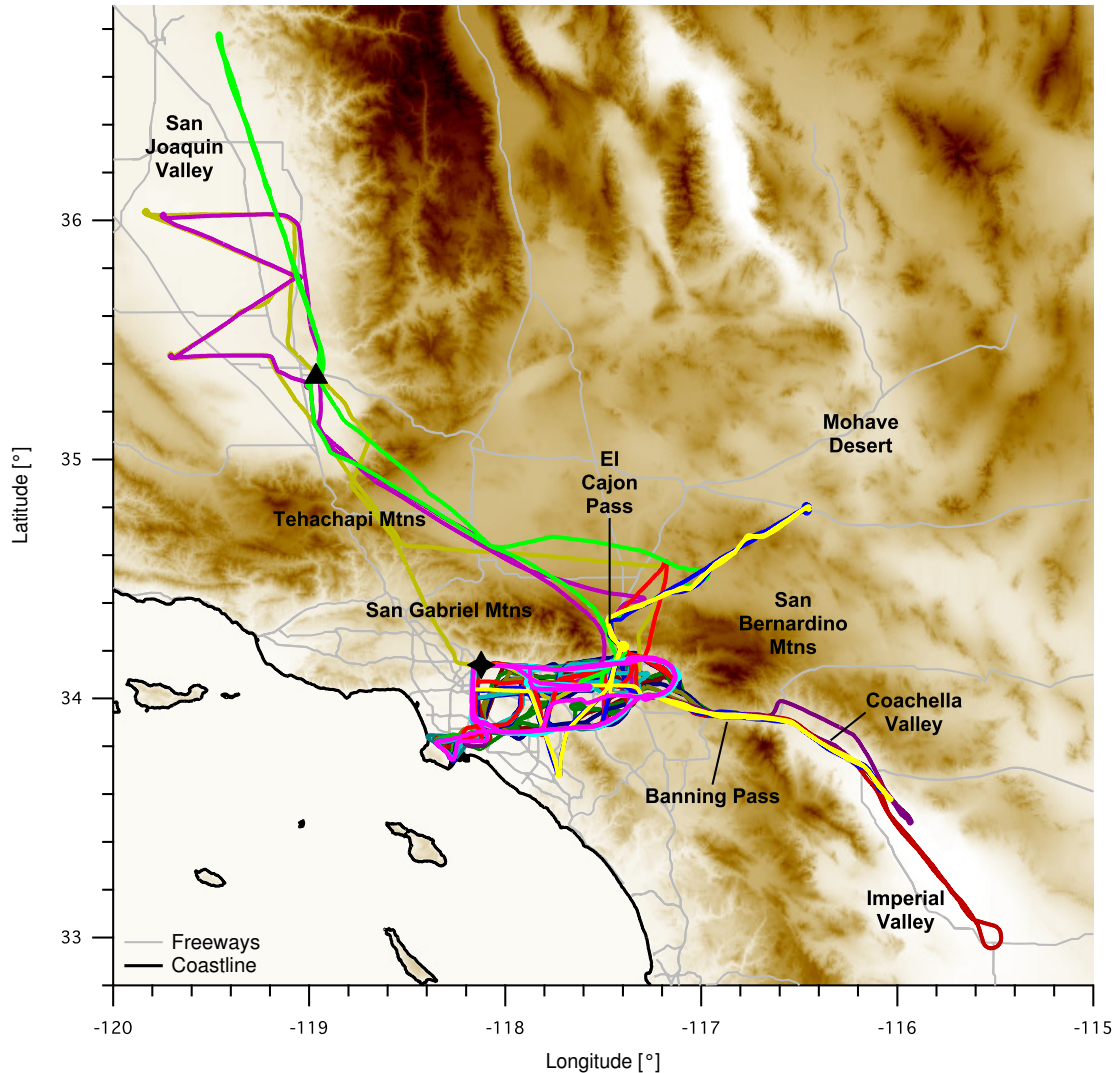


Figure 2.1: All flight paths (colored lines) of the CIRPAS Twin Otter during CalNex. The star denotes the location of the CalNex LA ground site at Caltech and the triangle denotes the CalNex ground site at Bakersfield. Terrain is shaded brown, with darker colors indicating higher elevation.

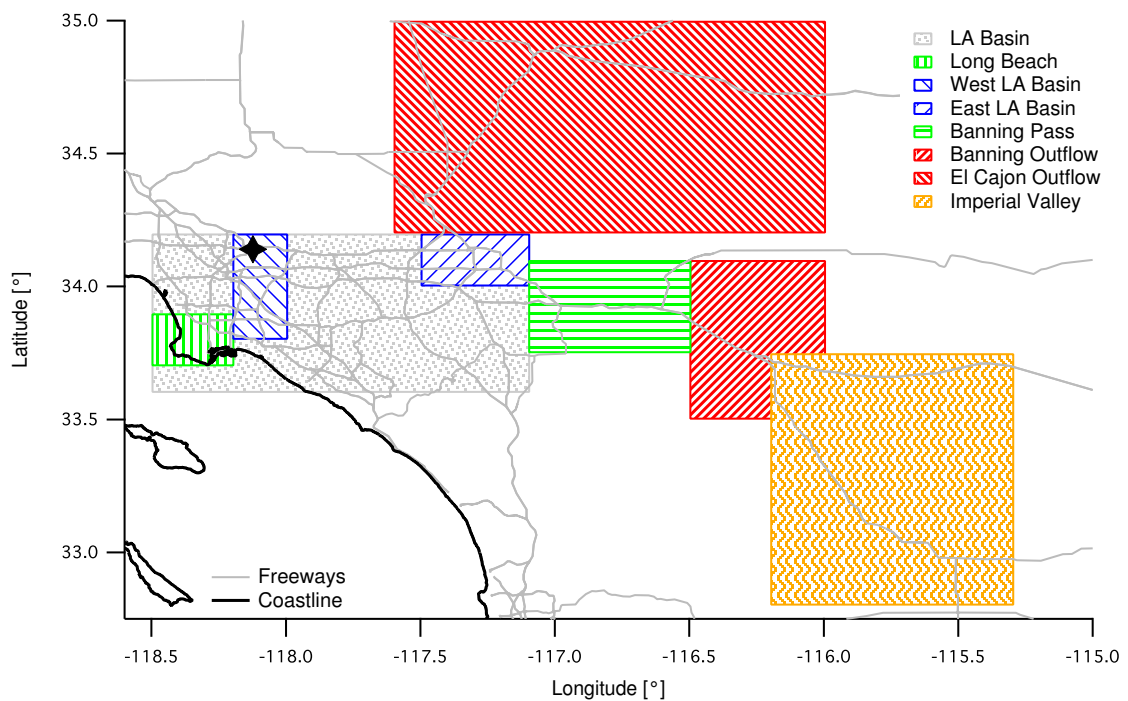


Figure 2.2: Regional definitions used in Table 2.4 and elsewhere in the text. Only measurements below the inversion layer are considered.

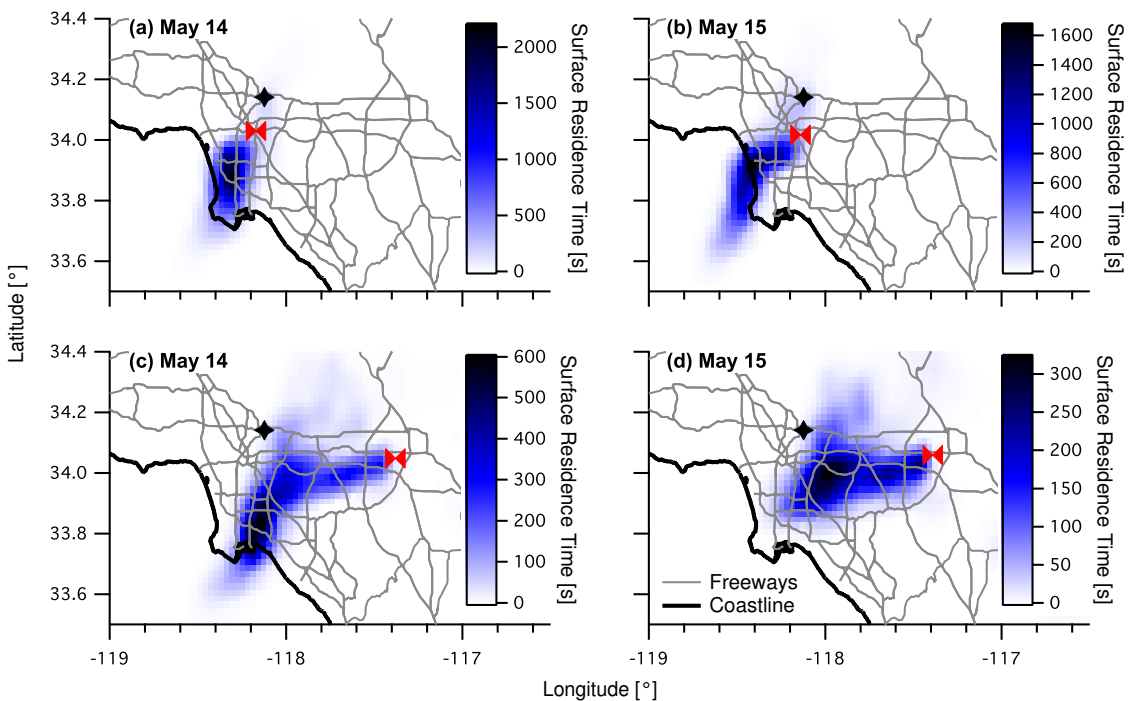


Figure 2.3: The 12-h integrated surface residence times from FLEXPART during (a and c) the Friday, May 14 flight and (b and d) the Saturday, May 15 flight. Figures 2.3a and 2.3b are points on the western side of the LA Basin; Figures 2.3c and 2.3d are points on the eastern side of the LA Basin. The red bow-ties denote the location of the Twin Otter aircraft and the stars denote the CalNex LA ground site at Caltech.

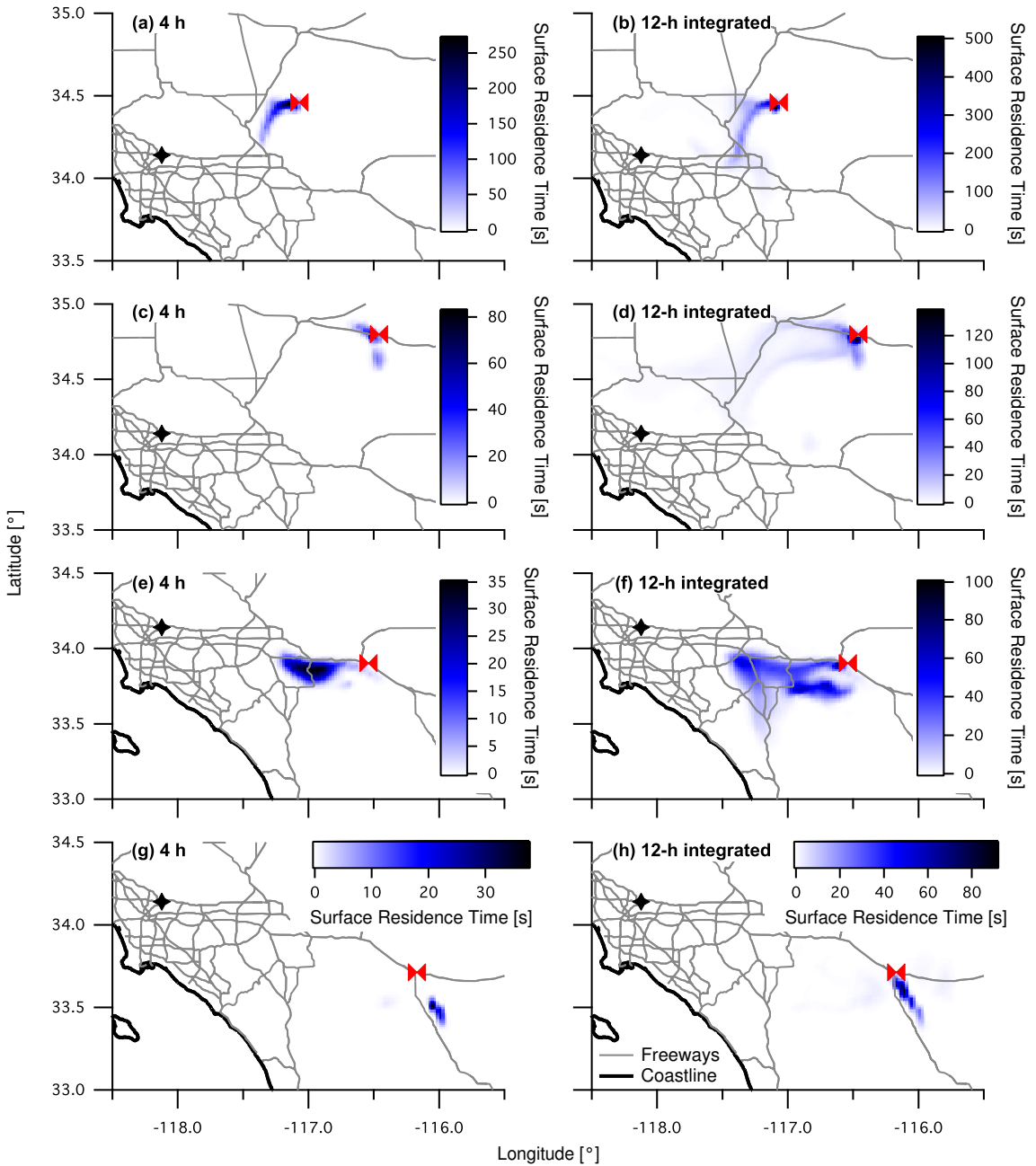


Figure 2.4: Surface residence time back-trajectories from FLEXPART for the May 25 flight at various regions in the flight: (a and b) midway between the El Cajon Pass and the farthest sampling location in the El Cajon outflow, (c and d) the farthest sampling location in the El Cajon Outflow, (e and f) the Banning Outflow, and (g and h) the Imperial Valley. Figures 2.4a, 2.4c, 2.4e, and 2.4g are surface residence times at 4 h, showing where the sampled air mass was 4 h prior to sampling. Figures 2.4b, 2.4d, 2.4f, and 2.4h are 12-h integrated surface residence times, showing the surface contributions for the previous 12 h to the sampled air mass. The red bow-ties denote the location of the Twin Otter aircraft and the stars denote the CalNex LA ground site at Caltech.

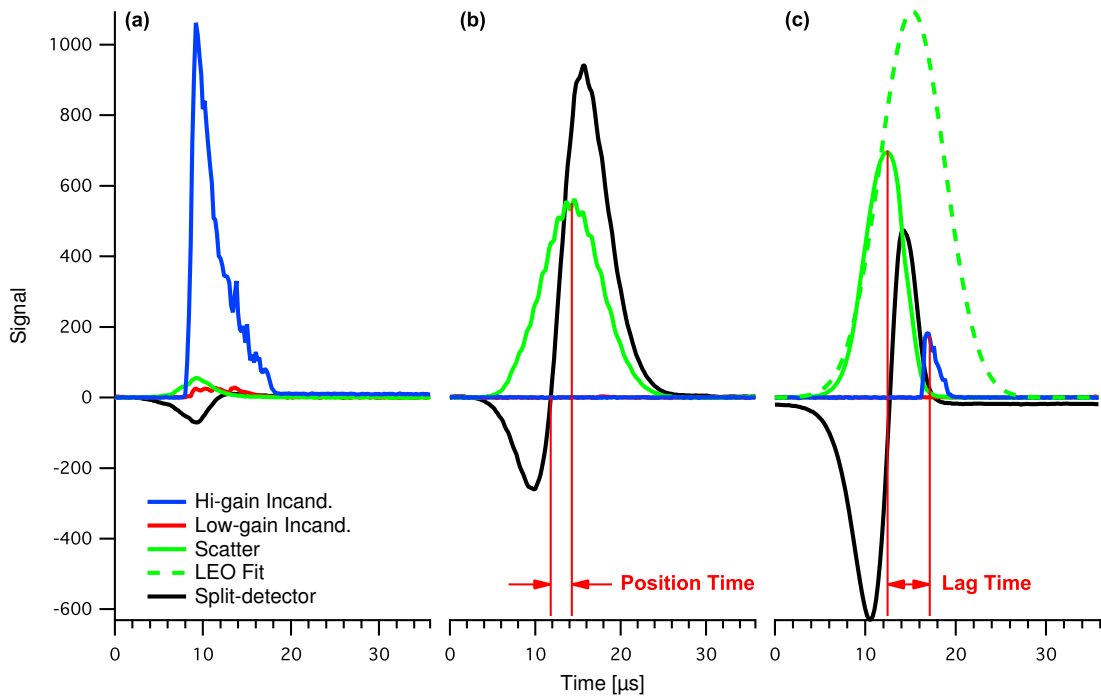


Figure 2.5: Raw spectra of three single particles measured by the SP2: (a) a 149 nm VED uncoated rBC particle, (b) a 286 nm optical diameter purely scattering particle, and (c) an 83 nm VED rBC core coated by a 237 nm thick layer of a purely scattering substance. “Position Time” labeled in Figure 2.5b is the time between the zero-crossing of the split-detector signal and the peak of the scatter signal and is used to determine the position of the scatter peak for particles evaporating in the laser beam. “Lag Time” labeled in Figure 2.5c is the distance between the detected scatter peak and incandescent peak and is used to assess the coating thickness on rBC particles. See the text for a description of the LEO Fit calculation.

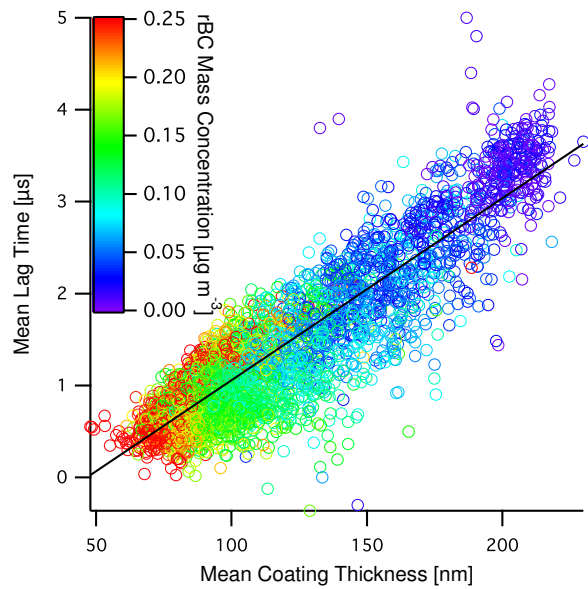


Figure 2.6: Mean lag time versus mean coating thickness for all 1-min average measurements during CalNex. Marker color indicates rBC mass concentration. Coating thickness is the diameter increase from the rBC VED. The solid black line is a linear fit to the data ($R^2 = 0.797$).

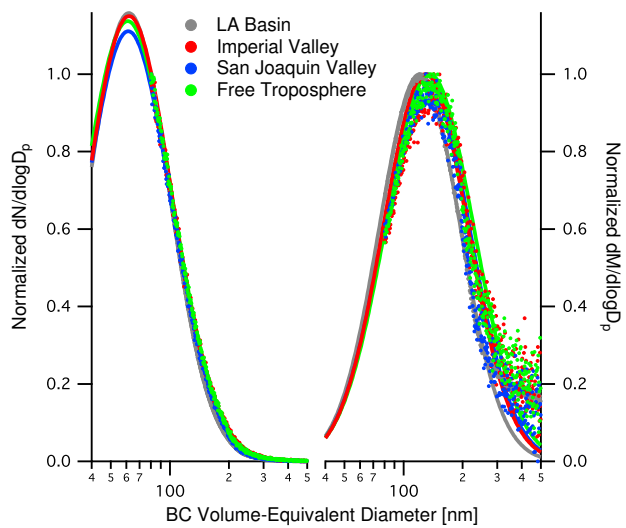


Figure 2.7: Campaign-average rBC number (left trace) and mass (right trace) distributions by region. Solid lines denote single lognormal fits to the data.

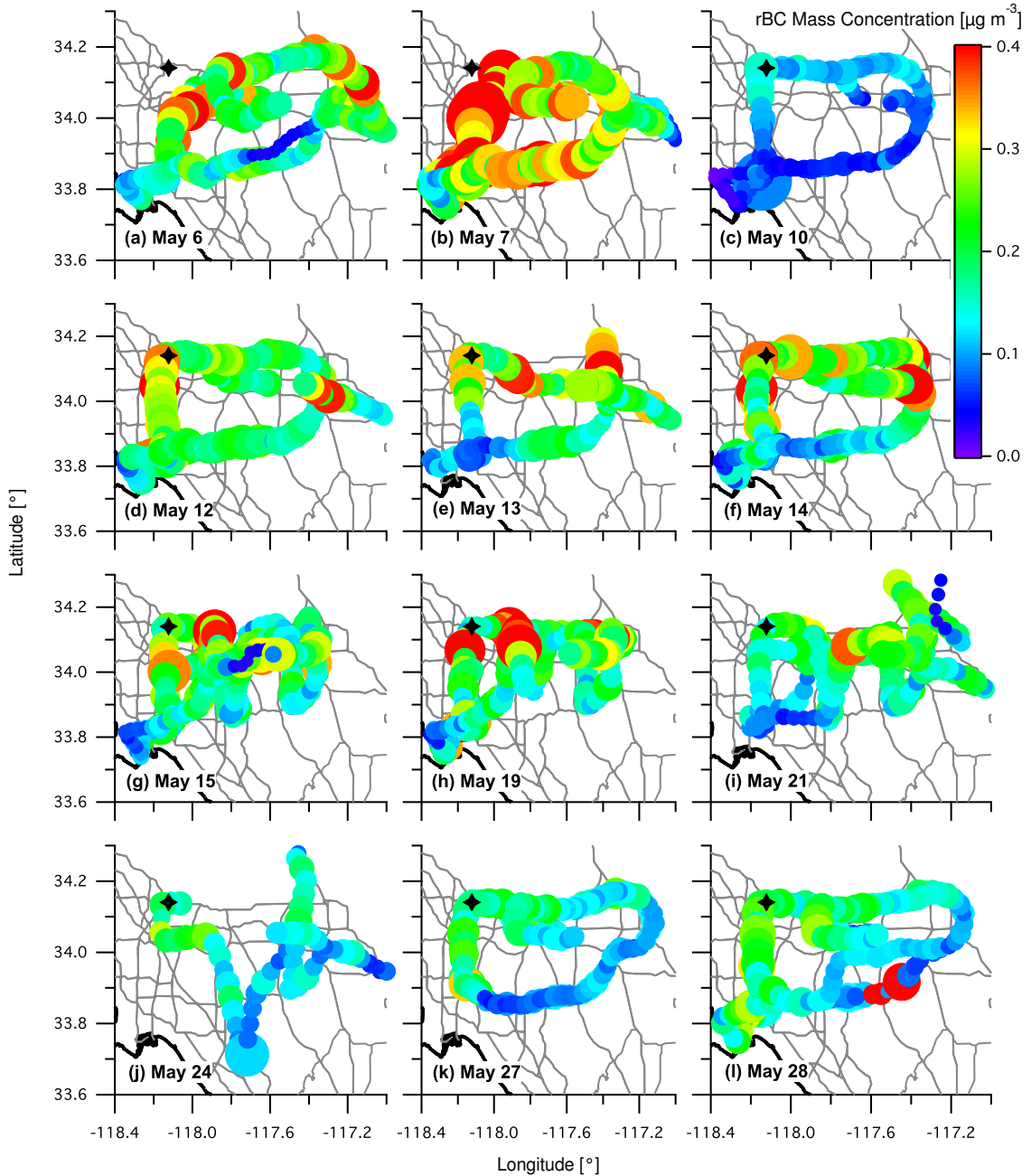


Figure 2.8: All rBC mass (marker color) and number (marker size) concentrations observed in the LA Basin during CalNex, with the exception of the May 25 flight, which can be found in Figure 2.9a. The stars denote the CalNex LA ground site at Caltech.

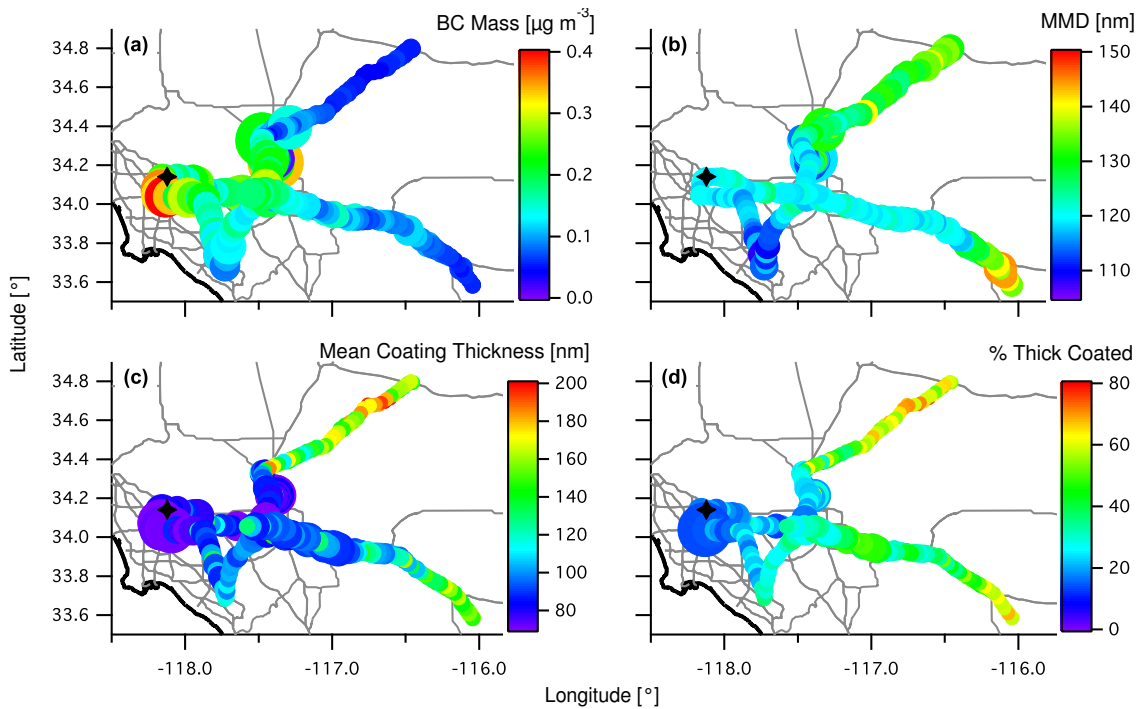


Figure 2.9: The 1-minute average SP2 data from Research Flight 16 on May 25, 2010: (a) rBC mass (marker color) and number (marker size) concentrations, (b) mass-median diameter of rBC cores (marker color) and width of the mass distributions (marker size), (c) mean coating thickness on rBC particles (marker color) and total volume concentration of the coating on rBC particles in SP2 detection range (marker size), and (d) percent of mixed-phase rBC particles thickly coated (marker color) and number concentration of coated rBC particles in SP2 detection range (marker size). The stars denote the CalNex LA ground site at Caltech.

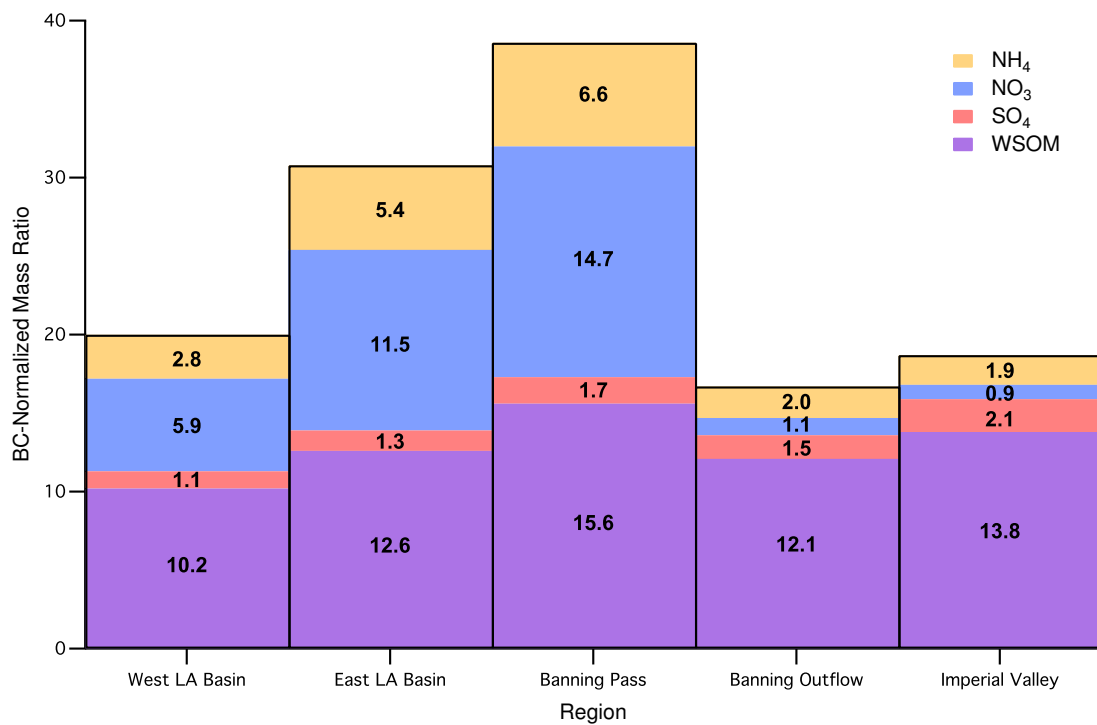


Figure 2.10: The rBC mass-normalized concentration ratios of aerosol chemical compounds broken down by region from west to east in and near the Los Angeles Basin for the May 25 flight. See text for details on the calculation of water-soluble organic mass (WSOM) and Figure 2.2 for region definitions.

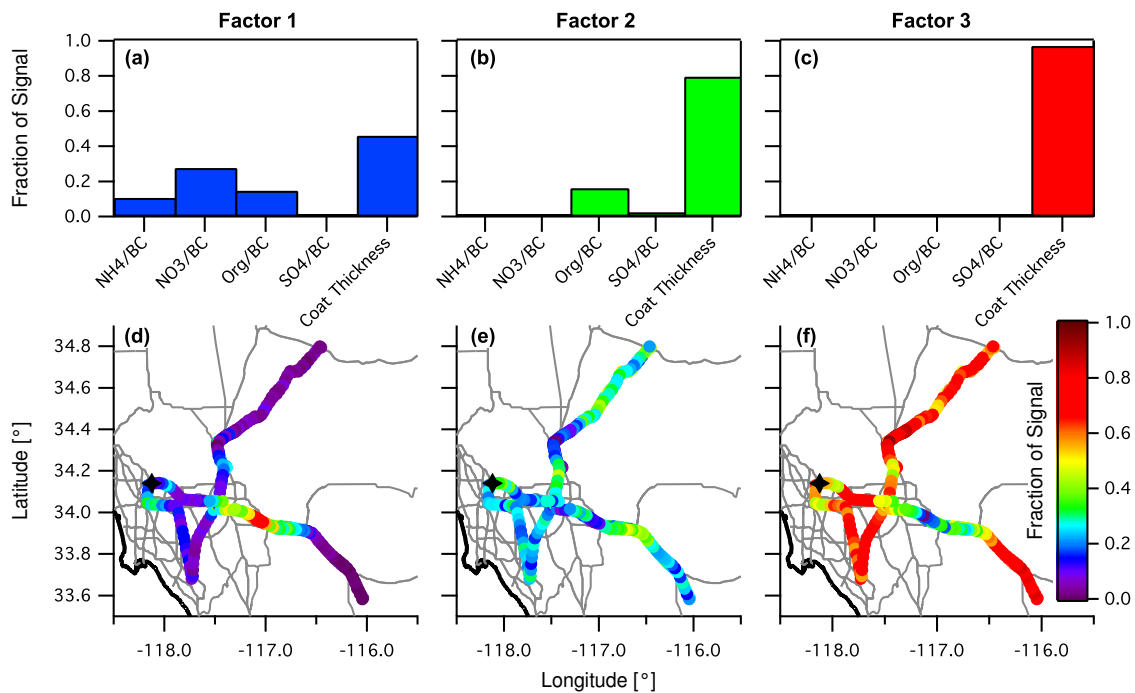


Figure 2.11: (a, b, and c) Fraction of total signal contributions to each PMF input parameter for each factor of the three-factor PMF model and (d, e, and f) fraction of total signal contributions from each factor to the total signal for the May 25 flight.

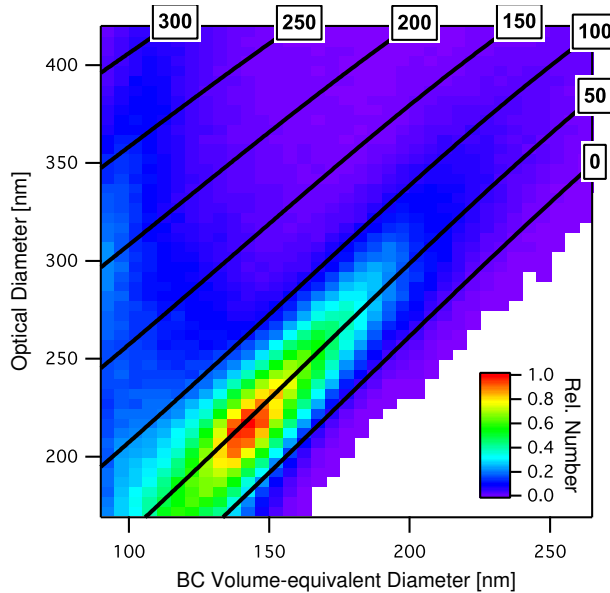


Figure 2.12: The 2-D histogram of all particles detected in the West LA Basin region as defined in Figure 2.2. Optical diameter is calculated with a Mie model (assuming a refractive index of $1.5-0.0i$) fit to the scattering cross-section detected by a LEO fit of these particles' scattering signal. The solid lines denote the results of a core-and-shell Mie model forced with the rBC core diameters on the x axis and fit to the equivalent scattering cross-sections on the y axis. The numbers denote the shell thickness diameters in nm.

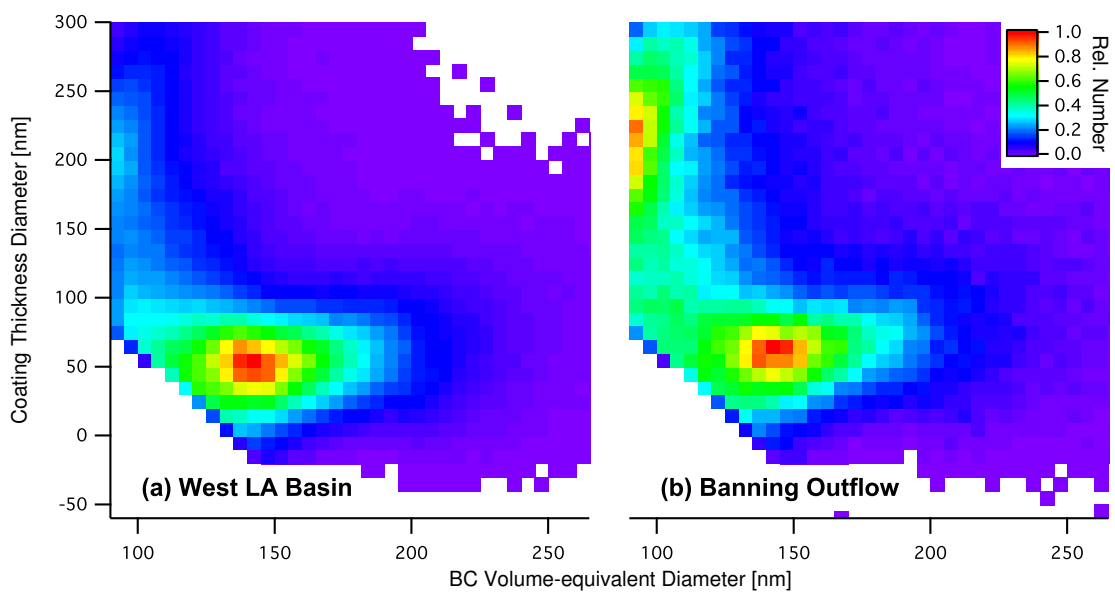


Figure 2.13: The 2-D histogram of all particles detected in (a) the West LA Basin region and (b) the Banning Outflow region, defined in Figure 2.2. Coating thickness is derived from a core-and-shell Mie model fit with the detected scattering cross-section by a LEO fit of the scattering signal.

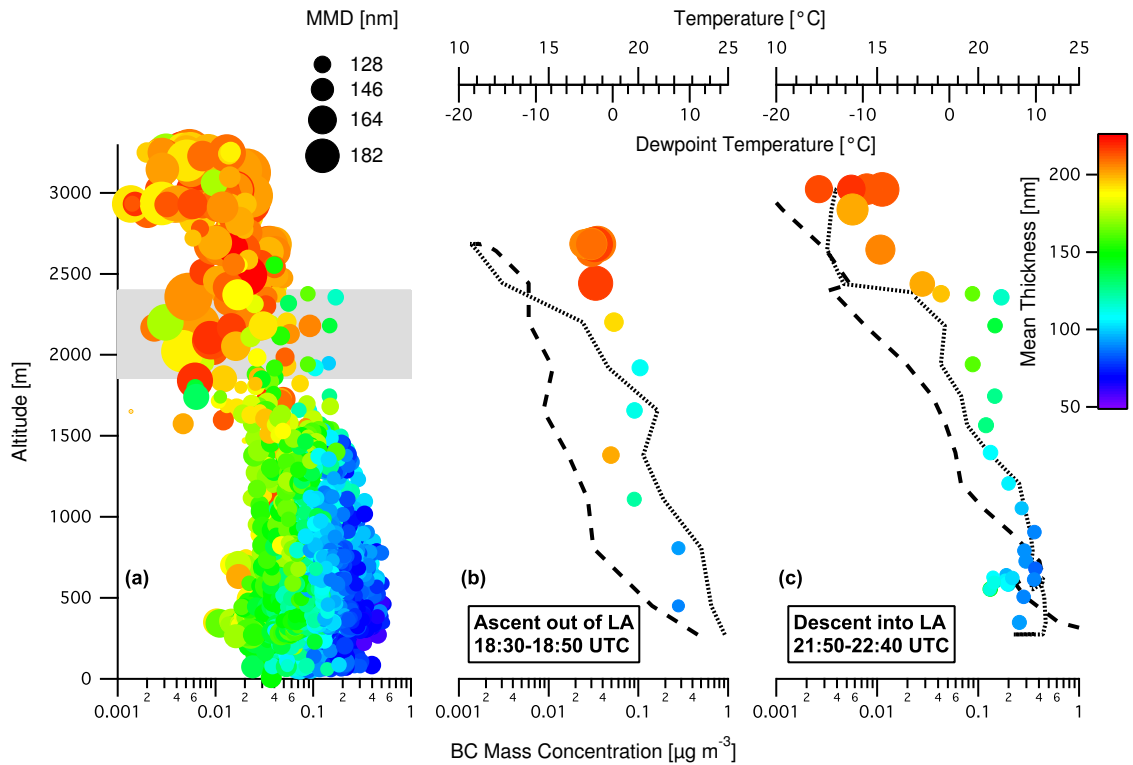


Figure 2.14: Vertical distribution of (a) all SP2 measurements, (b) ascent out of LA on May 20, and (c) descent into LA 3 h later. Each marker is a 1-min average datapoint indicating rBC mass concentration (x axis), mean coating thickness on rBC particles (marker color), and MMD (marker size). The gray shaded region in Figure 2.14a denotes the range of inversion layer altitudes observed during CalNex. The dashed lines in Figures 2.14b and 2.14c are the ambient temperature profiles and the dotted lines are the dew point temperature profiles.

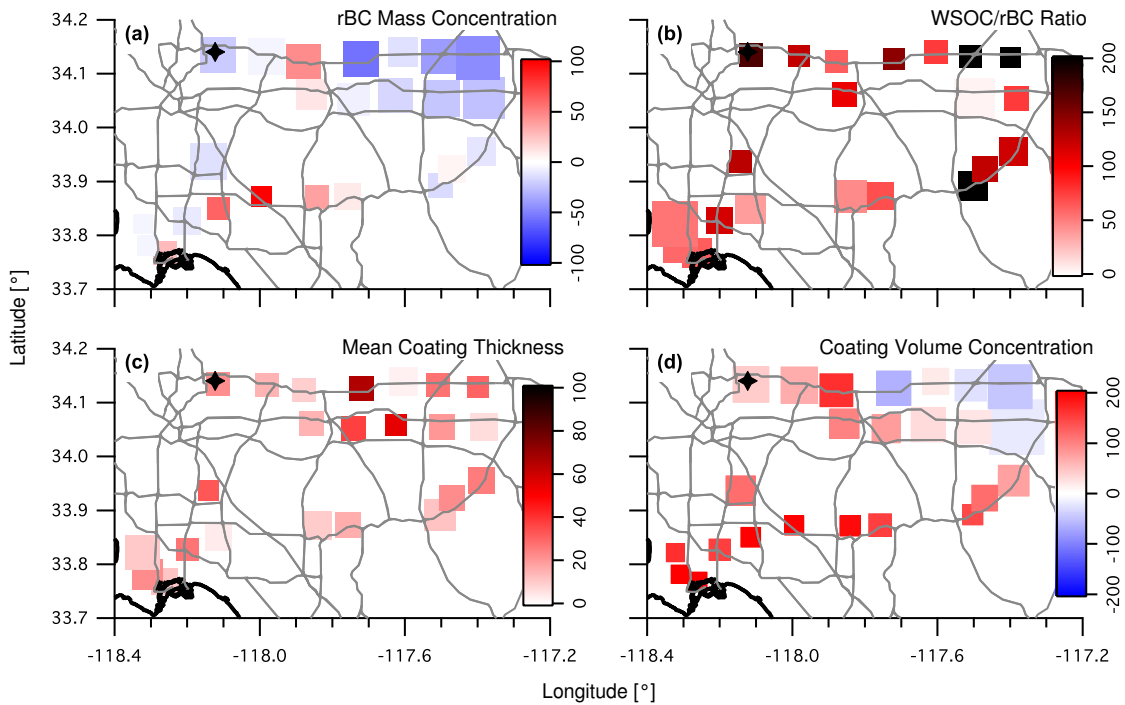


Figure 2.15: Percent change between Friday, May 14 and Saturday, May 15 measurements displayed as percent change from the May 14 values (marker color) for: (a) rBC mass concentration, (b) WSOC/rBC ratio, (c) mean coating thickness, and (d) coating volume concentration. The SP2 measurements are averaged over a grid spacing of 0.12° longitude by 0.1° latitude. The size of the markers in each plot is proportional to the May 14 measurement value. The stars denote the CalNex LA ground site at Caltech.

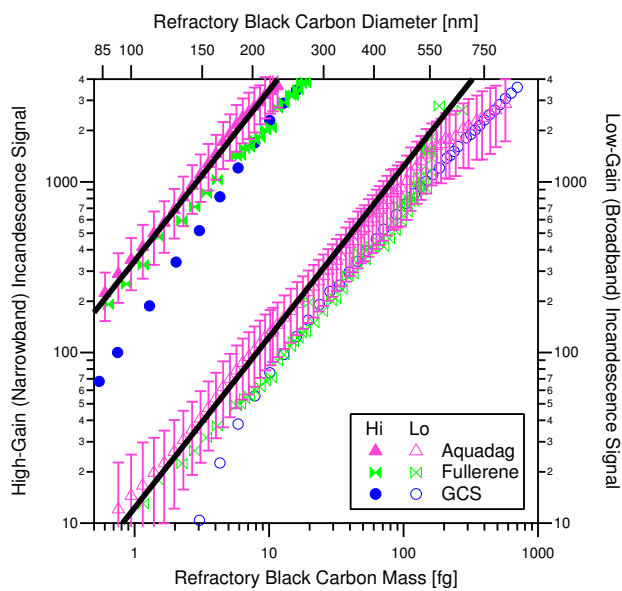


Figure 2.16: Calibration data for the high-gain (upper-left trace) and low-gain (lower-right trace) incandescence channels. The rBC mass (bottom x axis) is calculated from the selected mobility diameter with mobility density for Aquadag and Fullerene from *Gysel et al.* (2011) and density = 1.4 g cm^{-3} for glassy carbon spheres (GCS). rBC diameter (top x axis) is volume-equivalent diameter (VED) calculated as for ambient particles, assuming a spherical particle with a density = 1.8 g cm^{-3} . The solid line is the calibration curve used in this study, calculated from the Aquadag data only.

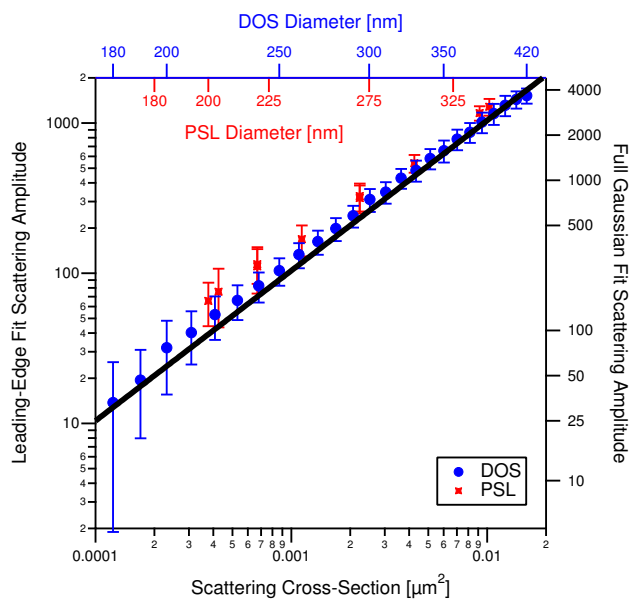


Figure 2.17: PSL and DOS scattering calibration data. Each datapoint is the median of about 10,000 particles, and the error bars indicate one standard deviation. For reference, both the full Gaussian and the leading-edge only fits are shown, but operationally, only the leading edge fits are used to determine an optical diameter.

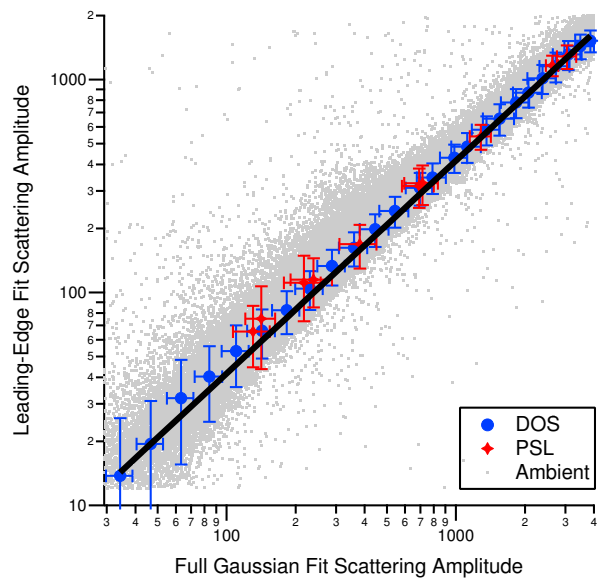


Figure 2.18: Comparison of the leading-edge only (LEO) fit amplitudes to the full Gaussian fit amplitudes for purely scattering particles. DOS ($R^2 = 0.998$) and PSL ($R^2 = 0.999$) calibration data are shown, as well as purely scattering ambient particle data from one of the flights during CalNex.

Chapter 3

Secondary Organic Aerosol Coating Formation and Evaporation: Chamber Studies using Black Carbon Seed Aerosol and the Single-Particle Soot Photometer*

*This chapter is a preprint of “Secondary organic aerosol coating formation and evaporation: Chamber studies using black carbon seed aerosol and the Single-Particle Soot Photometer” by A. R. Metcalf, C. L. Loza, M. M. Coggon, J. S. Craven, H. H. Jonsson, R. C. Flagan, and J. H. Seinfeld, submitted for consideration in *Aerosol Science and Technology*. Copyright 2012 by the American Association for Aerosol Research.

3.1 Abstract

We report a protocol for using black carbon (BC) aerosol as the seed for secondary organic aerosol (SOA) formation in an environmental chamber. We employ a Single-Particle Soot Photometer (SP2) to probe single-particle SOA coating growth dynamics and find that SOA growth on non-spherical BC aerosol is diffusion-limited. Aerosol composition measurements with an Aerodyne High Resolution Time-of-Flight Aerosol Mass Spectrometer (AMS) confirm that the presence of BC seed does not alter the composition of SOA as compared to self-nucleated SOA or condensed SOA on ammonium sulfate seed. We employ a 3-wavelength Photoacoustic Soot Spectrometer (PASS-3) to measure optical properties of the systems studied, including fullerene soot as the surrogate BC seed, nucleated naphthalene SOA from high- NO_x photooxidation, and nucleated α -pinene SOA from low- NO_x photooxidation. A core-and-shell Mie scattering model of the light absorption enhancement is in good agreement with measured enhancements for both the low- and high- NO_x α -pinene photooxidation systems, reinforcing the assumption of a core-shell morphology for coated BC particles. A discrepancy between measured and modeled absorption enhancement factors in the naphthalene photooxidation system is attributed to the wavelength-dependence of refractive index of the naphthalene SOA. The coating of high- NO_x α -pinene SOA decreases after reaching a peak thickness during irradiation, reflecting a volatility change in the aerosol, as confirmed by the relative magnitudes of f_{43} and f_{44} in the AMS spectra. The protocol described here provides a framework by which future studies of SOA optical properties and single-particle growth dynamics may be explored in environmental chambers.

3.2 Introduction

Refractory black carbon (rBC), alternately referred to as elemental carbon, is the dominant component of light-absorbing atmospheric aerosol. While rBC refers to the strongly light-absorbing component of soot, emission sources containing rBC, such as diesel exhaust, may contain other constituents such as polycyclic aromatic hydrocarbons, aliphatic hydrocarbons, and other volatile

compounds (*Schauer et al.*, 1996; *Kleeman et al.*, 2000; *Fruin et al.*, 2004). These organic compounds co-emitted with rBC evaporate substantially upon dilution from the tailpipe to ambient conditions (*Robinson et al.*, 2007).

The traditional understanding is that fresh, urban-emitted rBC is almost entirely composed of hydrophobic rBC and is unlikely to act as cloud condensation nuclei (CCN) (*Weingartner et al.*, 1997). After emission, rBC particles can become coated by inorganic and organic non-light-absorbing components via coagulation with other particles and condensation of vapors (e.g., *Abel et al.*, 2003; *Pósfai et al.*, 2003; *Riemer et al.*, 2004; *Moffet and Prather*, 2009). Recent studies with a Single-Particle Soot Photometer (SP2) have revealed that fresh urban-emitted rBC particles may be thinly coated with light-scattering material, while rBC in aged air masses tends to be more thickly coated (*Moteki et al.*, 2007; *Shiraiwa et al.*, 2007, 2008; *Schwarz et al.*, 2008a; *Subramanian et al.*, 2010; *Metcalf et al.*, 2012). Timescales for the transition from a fresh to a more aged state have been estimated to range from 12 h to a day (e.g., *Johnson et al.*, 2005; *Moteki et al.*, 2007; *Khalizov et al.*, 2009a; *Park et al.*, 2012). Interactions with gas and aerosol species transform rBC into an internally mixed state, where it may eventually serve as a CCN (*Zuberi et al.*, 2005). Hygroscopic coatings also enhance the wet deposition rate of these particles (*Weingartner et al.*, 1997; *Saathoff et al.*, 2003; *Jacobson*, 2006; *Stier et al.*, 2006). A coating of non-light-absorbing components onto rBC increases the light scattering and absorption cross sections of these particles (e.g., *Fuller et al.*, 1999; *Saathoff et al.*, 2003; *Schnaiter et al.*, 2005; *Bond et al.*, 2006; *Mikhailov et al.*, 2006; *Stier et al.*, 2006; *Slowik et al.*, 2007a; *Zhang et al.*, 2008; *Khalizov et al.*, 2009b; *Wehner et al.*, 2009; *Cross et al.*, 2010; *Lack and Cappa*, 2010; *Shiraiwa et al.*, 2010). At least one ambient study, however, found no evidence of an enhancement of light absorption by condensation of secondary material (*Chan et al.*, 2010b). A study of ambient rBC in Toronto showed no detectable change in absorption enhancement between fresh and aged aerosol but attributed this observation to the fact that the fresh rBC had a sufficient coating such that additional coatings did not further enhance absorption (*Knox et al.*, 2009).

While ambient rBC measurements have revealed valuable insights into the aging process, namely coating thicknesses and growth timescales, important questions still remain. What mechanisms

govern the transition from externally to internally mixed rBC aerosol? Does rBC, acting as a site for condensation of secondary organic aerosol (SOA), affect the composition of the SOA as compared to SOA condensed onto other aerosol types or nucleated homogeneous aerosol? To what extent are the coatings on rBC sufficiently volatile to evaporate upon dilution? Of what physical structure is the rBC and its “coating” and how might this affect interpretation of absorption enhancements seen (or not seen) in ambient data?

Controlled laboratory experiments of rBC aging can isolate some of the complexities of the aging process. The absorption enhancement that arises from coating nascent soot particles with a variety of non-light-absorbing materials is readily measured (*Saathoff et al.*, 2003; *Schnaiter et al.*, 2003, 2005; *Mikhailov et al.*, 2006; *Slowik et al.*, 2007a; *Zhang et al.*, 2008; *Khalizov et al.*, 2009b; *Cross et al.*, 2010). Initially fractal soot agglomerates tend to compact substantially after a coating has formed (*Saathoff et al.*, 2003; *Slowik et al.*, 2007b; *Zhang et al.*, 2008; *Khalizov et al.*, 2009b,a; *Cross et al.*, 2010; *Bueno et al.*, 2011). In addition, rBC and polystyrene latex spheres (PSL) of the same mobility are observed to acquire sulfuric acid coatings at the same rate, indicating that the coating mechanism is independent of particle composition and shape (*Khalizov et al.*, 2009a).

Limited laboratory chamber studies of SOA growth in the presence of soot seed particles exist. Studies at the University of North Carolina Ambient Air Research Facility have focused on how the presence of soot affects gas-particle partitioning and found that diffusional mass transfer is the limiting control on gas-particle partitioning (*Strommen and Kamens*, 1997, 1999), and that the polarity of the seed particles, including diesel and wood soot, and the gas-phase organic compounds can affect the equilibrium partitioning (*Leach et al.*, 1999). Studies at the Aerosols, Interactions and Dynamics in the Atmosphere (AIDA) chamber facility report the enhancement of light absorption by soot seed particles coated with α -pinene ozonolysis SOA (*Saathoff et al.*, 2003) and evaluate absorption enhancements by particle coagulation and growth of SOA (*Schnaiter et al.*, 2003, 2005). Studies at the Carnegie Mellon University environmental chamber found that SOA formed by the photooxidation of evaporated diesel exhaust exceeded by a wide margin the SOA mass predicted by oxidation of exhaust hydrocarbons alone (*Weitkamp et al.*, 2007). A study at the Paul Scherrer In-

stitute (PSI) smog chamber characterized the chemical composition and emission factors of primary and secondary organic aerosol from three diesel vehicles with various engine aftertreatment systems (*Chirico et al.*, 2010). Most of these studies used fresh diesel or wood soot, which typically has a thin layer of non-refractory material on the rBC. Uncoated spark-generated soot has also been found to be chemically and optically different than diesel soot and is, therefore, not a good surrogate for atmospheric rBC (*Kirchner et al.*, 2003; *Schnaiter et al.*, 2003).

The principal goal of this study is to demonstrate the utility of chamber experiments that employ refractory black carbon seed aerosol in conjunction with the Single-Particle Soot Photometer, the Photoacoustic Soot Spectrometer, and the Aerosol Mass Spectrometer to probe the dynamics of secondary aerosol formation. The rBC surrogate used in this study is dry, uncoated fullerene soot, and three SOA systems were studied to demonstrate the utility of this experimental protocol on a variety of chemical and optical properties. Particle-by-particle measurements of the coating thickness of SOA on the rBC seed by the SP2 directly reveal dynamic growth and evaporation processes. Once SOA growth has reached a point at which the coating thickness is no longer changing appreciably, chamber dilution can be used to provide a driving force for SOA evaporation and an assessment of SOA volatility through decrease of coating thickness. Simultaneous particle optical property and coating composition measurements provide data that can relate growth and evaporation behavior to SOA chemical composition. A fundamental chemical examination of the composition changes during SOA growth is beyond the scope of this study; however, demonstrating that composition changes occur coincident with changes in rBC coating thicknesses and aerosol optical properties provides a framework by which future mechanistic studies may be carried out.

3.3 Methods

3.3.1 Experimental Protocols

Experiments (see Table 3.1) were conducted in the Caltech dual 28-m³ Teflon chambers. Details of the facilities are given elsewhere (*Cocker et al.*, 2001; *Keywood et al.*, 2004). Before each ex-

periment, the chambers were flushed with dried, purified air for >24 h, until the particle number concentration ($<10 \text{ cm}^{-3}$), mass concentration ($<0.1 \text{ } \mu\text{g m}^{-3}$), and hydrocarbon mixing ratios were below detection limits of the instruments. Seeded experiments were conducted with two types of seeds; fullerene soot (stock #40971, lot #L20W054, Alfa Aesar, Ward Hill, MA, USA) as a fractal, rBC surrogate and ammonium sulfate (AS) as a spherical inorganic particle alternative. Commercially available fullerene soot is a fractal, hydrophobic particle that most resembles ambient BC in the SP2 instrument (*Moteki and Kondo, 2010; Laborde et al., 2012*). Fullerene soot particles were generated by nebulizing a suspension of fullerene soot and milliQ water until the desired particle volume concentration in the chamber was reached. Prior to nebulizing, the fullerene soot suspension was sonicated for ~ 20 min to facilitate the mixing of the hydrophobic soot particles in water and to break up any large agglomerates. Ammonium sulfate, a commonly used seed particle in environmental chambers, was injected into the chamber by atomizing a 0.015 M aqueous ammonium sulfate solution. In the “AS + rBC” experiments denoted in Table 3.1, ammonium sulfate was injected into the chamber and allowed to mix for ~ 30 min while gas-phase species were loaded into the chamber before injection of the fullerene soot. Upon injection of rBC in these dual seed experiments, an attempt was made to match the calculated particle surface areas of the AS and rBC from online scanning mobility particle sizer measurements.

Experiments were run under both low- and high- NO_x conditions using hydrogen peroxide (H_2O_2) and methyl nitrite (CH_3ONO) as the OH sources, respectively. H_2O_2 was injected into the chamber by evaporating 280 μL of 50% wt aqueous solution into the chamber with 5 L min^{-1} of purified air. CH_3ONO was vaporized into an evacuated 500 mL glass bulb and introduced into the chamber with 5 L min^{-1} of purified air. CH_3ONO was synthesized following the method described by *Taylor et al. (1980)* and modified by *Chan et al. (2010a)*.

Two SOA precursors were studied: naphthalene and α -pinene. Naphthalene is an important polycyclic aromatic hydrocarbon (PAH) that, like rBC, is a product of incomplete combustion in diesel engines and biomass burning (*Schauer et al., 1999, 2001; Ravindra et al., 2008*). PAH’s, in general, may account for as much as one-half of SOA from diesel emissions (*Chan et al., 2009*).

Naphthalene (99%, Sigma-Aldrich, St. Louis, MO, USA) was introduced into the chamber by flowing 1 L min⁻¹ purified air through an FEP Teflon tube packed with solid naphthalene (*Chan et al.*, 2009). α -Pinene, the most abundantly emitted monoterpene, is an important biogenic volatile organic compound (VOC), with global emissions of 34–50 Tg C yr⁻¹ (*Guenther et al.*, 1995; *Chung and Seinfeld*, 2002; *Pye et al.*, 2010). α -Pinene was introduced into the chamber by injecting a volume of liquid into a glass bulb, and the vapor was carried into the chamber with 5 L min⁻¹ of purified air. All naphthalene experiments were conducted in the same chamber, while all but one α -pinene experiment (Experiment 8 in Table 3.1) were conducted in the other chamber. In all experiments, the chamber contents, seed particles, parent hydrocarbon, and OH source, were allowed to mix for 1 h before beginning irradiation. In most experiments, after maximum particle growth was obtained, the UV lights were turned off and the chamber was diluted \sim 12–18 h while sampling continued. After irradiation was stopped and before chamber dilution began, cyclohexane, injected by a method similar to α -pinene injection, was introduced to the chamber to be used as a tracer for dilution.

3.3.2 Instrumentation

A suite of instruments was used to study the evolution of the gas and particle phases. The parent hydrocarbons and dilution tracer were measured using a gas chromatograph with flame ionization detector (GC/FID, Model 6890N, Agilent Technologies, Inc., Santa Clara, CA, USA), equipped with an HP-5 column (15 m x 0.53 mm ID x 1.5 μ m thickness, Agilent). The GC/FID response to naphthalene was calibrated by dissolving a known mass of naphthalene in dichloromethane and vaporizing into a 55 L Teflon chamber. The GC/FID response to α -pinene and cyclohexane was calibrated by vaporizing a small volume of liquid into a 50 L chamber and diluting aliquots of that sample into a 55 L chamber. NO and NO_x were measured with a chemiluminescence NO/NO_x analyzer (Model APNA 360, HORIBA Instruments Incorporated, Irvine, CA, USA). Relative humidity (RH), temperature (T), and O₃ were continuously monitored. RH of the chamber was typically $<5\%$ during irradiation periods, rising to $\sim 10\%$ during the overnight chamber dilution. The initial

chamber temperature was typically \sim 20–24°C; however, heating from the UV lights caused a rise in temperature of \sim 4–6°C during irradiation. Initial O₃ concentration was typically <5 ppb. Varying amounts of NO were added from a gas cylinder (Scott-Marrin, Riverside, CA, USA) to ensure high NO_x conditions at the start of most experiments, except where noted in Table 3.1.

Aerosol size distribution and number concentration were measured continuously using a custom-built scanning mobility particle sizer consisting of a differential mobility analyzer (DMA, Model 3081, TSI Incorporated, Shoreview, MN, USA) coupled to a condensation particle counter (CPC, Model 3010, TSI), henceforth referred to as the DMA.

Refractory black carbon (rBC) mass measurements were made with a Droplet Measurement Technologies (DMT, Boulder, CO, USA) Single Particle Soot Photometer (SP2). The SP2 affords measurements of both the particle-by-particle rBC mass as well as the thickness of non-rBC coating on each particle (*Stephens et al.*, 2003; *Baumgardner et al.*, 2004; *Schwarz et al.*, 2006; *Moteki and Kondo*, 2007; *Slowik et al.*, 2007a). This particular SP2 was used in a previous study (*Metcalf et al.*, 2012) and the only difference in configuration was an increase in the gain setting on the narrowband incandescence channel to increase sensitivity to rBC mass. Calibrations, as detailed by *Metcalf et al.* (2012), were repeated just prior to this set of chamber experiments. Aquadag (Aqueous Deflocculated Acheson Graphite, Acheson Colloids Company, Port Huron, MI, USA) was mobility-selected by a DMA and sampled by the SP2. Because the SP2 is known to be more sensitive to Aquadag than to other rBC standards (*Laborde et al.*, 2012), a correction factor of 25% is used to relate the SP2 signals to fullerene soot mass (*Baumgardner et al.*, 2012). Estimated uncertainty in single-particle mass determination is \sim 40%, based largely on the uncertainty in Aquadag mass during calibration and the relationship to fullerene soot mass. To relate rBC mass to particle size, the volume-equivalent diameter (VED) is calculated assuming the rBC is a void-free sphere with an effective mobility density given by *Gysel et al.* (2011). Note that there is additional uncertainty in the fullerene mobility density because not all batches of fullerene soot have the same effective density (*Laborde et al.*, 2012); the batch used in this study differs from that measured by *Gysel et al.* (2011). With propagation of errors through the calculations, estimated uncertainty in VED is \sim 12%.

Aerosol absorption and scattering coefficients (b_{abs} and b_{sca}) were measured with a DMT 3- λ Photoacoustic Soot Spectrometer (PASS-3), which is an instrument based on several previous prototypes (*Lewis et al.*, 2008, and references therein). Briefly, sub-micron aerosol scattering coefficient is determined by an integrating sphere/photodetector at each wavelength, 405 nm, 532 nm, and 781 nm. Aerosol absorption is determined by the photoacoustic method, which uses a microphone to measure sound/pressure waves emanating from heated gas around aerosols absorbing laser light. The PASS-3 scattering signal was calibrated with a concentrated 220 nm polystyrene latex sphere (PSL) solution and the absorption signal with a concentrated Nigrosin dye (product #198285 lot #MKBD9679V, Sigma-Aldrich) solution. Lower detection limit is estimated by three times the standard deviation of signal noise during particle-free sampling. The lower detection limits for b_{abs} are 24.62 ± 0.36 , 68.96 ± 6.51 , and $3.89 \pm 0.65 \text{ Mm}^{-1}$ and for b_{sca} are 10.40 ± 1.42 , 10.28 ± 3.03 , and $8.20 \pm 1.64 \text{ Mm}^{-1}$ for $\lambda = 405$, 532, and 781 nm, respectively.

Real-time particle mass spectra were collected continuously by an Aerodyne High Resolution Time-of-Flight Aerosol Mass Spectrometer (AMS) (*Jayne et al.*, 2000; *DeCarlo et al.*, 2006; *Canagaratna et al.*, 2007). The AMS was operated predominantly in the lower resolution, higher sensitivity “V-mode,” but was manually switched periodically to the high resolution “W-mode.” “V-mode” data were analyzed using a fragmentation table to separate sulfate, ammonium, and organic spectra and to time-trace specific m/z ratios. “W-mode” data were analyzed in IGOR Pro (Wavemetrics, Inc., Lake Oswego, Oregon, USA) using the PIKA 1.10H module to determine the chemical formulas contributing to distinct m/z ratios (*DeCarlo et al.*, 2006). The AMS ionization efficiency was calibrated at the beginning of the study using dried, 350 nm NH_4NO_3 particles. AMS data reported in this work are averaged over 3 min intervals.

A prototype instrument was used to detect particle sphericity by single-particle laser light scattering (see Appendix). Briefly, single particles are brought into a circularly-polarized laser beam ($\lambda = 532 \text{ nm}$) and the angular pattern of light scattered off the particle is detected with a photomultiplier tube (PMT) assembly. Eight detectors positioned at a polar angle of 50° in the forward scattering direction measure light scattered onto lenses at one end of fiber optic cables, the other

ends of which are mounted in front of a PMT assembly that has a single channel devoted to each cable.

According to Mie theory, homogeneous spherical particles scatter circularly-polarized light uniformly around the azimuth of a given polar angle. Particle sphericity, the degree to which a given particle acts like a sphere when scattering light, has been measured and analyzed previously with instruments similar to that used here (*Dick et al.*, 1994, 1998; *Sachweh et al.*, 1995). Our analysis follows the same logic as that of previous authors, although our mathematical formulation of sphericity is different (see Appendix). To determine the degree of sphericity, we quantify the deviation among eight sensors at a fixed polar angle, which we call “non-sphericity” (Φ). Little deviation and smaller non-sphericity values are indicative of a spherical particle, while a large deviation and larger non-sphericity values indicate a non-spherical particle. Because the optical fibers differ in length and in radii of curvature between the lenses and the PMT, these artifacts are accounted for in the non-sphericity calculation by quantifying the extent to which each channel has the same deviation from its respective median signal.

3.3.3 Mie Scattering Model

For determination of single-particle coating thicknesses from SP2 light-scattering measurements and for comparison to bulk optical properties measured by the PASS-3, the Mie scattering model is used to calculate scattering and absorption cross sections for single particles. The Mie scattering model (*Metcalf et al.*, 2012) was adapted from a version of BHMIE (*Bohren and Huffman*, 1998) to compute scattering coefficients for a stratified sphere (*Toon and Ackerman*, 1981). For interpretation of SP2 scattering signals, the scattering function is integrated over the solid angles subtended by the SP2 detectors for comparison of measured to modeled signals to derive coating thickness on an rBC core. The measured scattering signal is derived from a leading edge-only (LEO) fit of the scattering signal in order to correct for evaporating coatings as particles traverse the laser in the SP2 (*Gao et al.*, 2007). The rBC refractive index is assumed to be $1.95 - 0.79i$ (*Bond and Bergstrom*, 2006), and a coating refractive index of $1.5 - 0.0i$ is used, matching previous studies (*Schwarz et al.*,

2008a,b; *Metcalf et al.*, 2012). Uncertainty in retrieved coating thickness from the SP2 scattering signal is $\sim 40\%$ (*Metcalf et al.*, 2012). The Mie scattering model is also used to determine the size of purely scattering particles. Again, a refractive index of $1.5-0.0i$ and the LEO fitting method on the measured scattering signal are used, and the optical size range of detection is 169–600 nm. Estimated uncertainty in retrieved optical diameter is $\sim 5\%$ for purely scattering particles.

For comparison to bulk optical properties, an enhancement factor is calculated as the ratio of absorption cross section at any given time to that of initially uncoated fullerene soot particles. Because total scattering and absorption is considered, integration over the SP2 detection angles is not carried out in this calculation. The rBC core and coating thickness used in the model are derived from averaged SP2 measurements. To simplify the calculation, an rBC core size of 170 nm VED is used with the coating thickness diameter measured by the SP2 for 160–180 nm VED rBC to calculate modeled absorption enhancement.

3.4 Results

3.4.1 Fullerene Soot Characteristics

3.4.1.1 Sphericity

Figure 3.1 presents distributions of non-sphericity values calculated for dry, uncoated fullerene soot (BC), ammonium sulfate (AS), and polystyrene latex spheres (PSL). Lognormal fits to each histogram were calculated to determine the mean non-sphericity values for these populations of particle types (see Table 3.2). PSL exhibits the smallest mean non-sphericity value (0.070), while dry, uncoated rBC has the largest (0.353) indicating non-sphericity. The AS sample in Figure 3.1 was taken from a chamber wall-deposition experiment in which AS seed was injected into a dry (<10% RH) chamber. AS mean non-sphericity is slightly larger than that for PSL, likely indicating that some AS particles do not retain water in the dry chamber. Calibrations with oxalic acid particles (data not shown in Figure 3.1, but statistics reported in Table 3.2) generated with a collision atomizer and sampled directly into the prototype instrument yield a mean non-sphericity similar to

that of AS. Dried, cubic salt particles (statistics reported in Table 3.2), generated by atomizing a solution of NaCl and water and sampling through a nafion dryer directly into the instrument, yield a non-sphericity similar to that for rBC. Like the AS sample, the fullerene soot sample was measured during wall-deposition experiments in which only rBC was present in the chamber. These measurements confirm that the fullerene soot, as we have prepared and loaded into the chamber as seed particles, is non-spherical.

3.4.1.2 Particle Wall Deposition

In environmental chamber studies, wall deposition rates must be known in order to calculate SOA yields from a parent hydrocarbon (e.g., *Keywood et al.*, 2004; *Ng et al.*, 2007; *Loza et al.*, 2012). Wall deposition processes have been well-described in the literature (e.g., *Crump and Seinfeld*, 1981; *McMurry and Rader*, 1985; *Park et al.*, 2001; *Pierce et al.*, 2008). Particles in the bulk of the chamber can diffuse or settle through a boundary layer near the chamber wall and deposit on the wall. Electrostatic effects can enhance deposition rates, especially for intermediate-sized particles (50–1000 nm diameter) (*McMurry and Rader*, 1985).

Typically, wall deposition rates are determined by atomizing seed aerosol into a clean chamber and measuring the decay of particle concentration over \sim 24 h. From these data, size-dependent, first-order loss coefficients, β , are obtained. Measured wall deposition rates for both AS seed and fullerene soot seed exhibit differences, as shown in Figure 3.2. The wall deposition rates presented in Figure 3.2, calculated from DMA size distribution data, are presented with respect to particle mass rather than mobility diameter in order to better relate the nearly spherical AS with the fractal rBC. The different range of masses for the two particle types in Figure 3.2 is the result of the smaller effective density ($0.6\text{--}0.35\text{ g cm}^{-3}$ for mobility diameters $300\text{--}800\text{ nm}$ (*Gysel et al.*, 2011)) for fullerene soot than for AS (1.77 g cm^{-3}) over all mobility diameters displayed.

The characteristic “V”-shape of the wall deposition rate curves in Figure 3.2 arises because of two competing processes: diffusion dominates wall deposition at smaller-size particles and gravitational settling dominates wall deposition at larger-size particles. The fact that the rBC deposition rate

achieves a minimum at the same size as that for AS particles indicates a similar balance between these effects. At larger masses, where gravitational settling dominates, AS and rBC have similar values of β , indicating reduced effect of particle shape in this range. At smaller masses, however, the significant difference in β reflects differences in diffusion rates to the chamber walls or an invalid assumption of a first-order wall deposition rate with unit sticking probability.

Because effective density measurements from a coupled DMA-SP2 system are used (*Gysel et al., 2011*), any artifacts in the DMA data used to calculate β in these experiments due to particle non-sphericity should be consistent during the entire wall-deposition experiment. Therefore, the differences in wall deposition rates between AS and fullerene soot are likely not the product of measurement artifacts. The diffusion rate of the fullerene soot could be less than that for AS particles of the same mass owing to the larger size of the fullerene soot particles. Sticking probabilities may also be smaller for the dry fullerene soot than for the AS particles, which likely retain some water, even in a dry chamber. The implication for the current chamber experiments is that the rate of wall deposition can be expected to change over the course of an experiment as initially pure rBC particles become coated. For this reason, SOA yields are not calculated in this study.

3.4.2 General Experimental Results

Figure 3.3 shows the reaction profile during naphthalene photooxidation, Experiment 1 (Table 3.1), in the presence of rBC seed particles. The rapidly formed SOA deposits onto the fullerene soot, as indicated by the immediate increase in mean coating thickness. A modest amount (~30% by number in the SP2 detection range) of purely scattering particles, presumably from nucleation, are present after growth initiates, indicated by an increase in total number concentration just after the start of irradiation (Figure 3.3a). Despite the temperature increase that occurs once the UV lights are turned on (Figure 3.3b), the coating thickness rapidly increases early in the irradiation. Temperature decreases once the lights are turned off, accompanied by only a small increase in mean coating thickness. Single-particle mean coating thickness does not decrease at any point during Experiment 1, indicating that the decrease of aerosol mass during dilution of the chamber is the

result of flushing the particles out of the chamber and wall deposition within the chamber and is not due to evaporation of the aerosol itself. The temperature decrease during dilution favors condensation and could influence mean coating thickness; however, the rate of temperature decrease varies during Experiment 1 while the rate of mean coating thickness increase does not vary in the same manner. Thus, it is unlikely that temperature alone is the dominant control of condensation of SOA in this system.

The evolution of coating thickness as a function of rBC core diameter is presented in Figure 3.4. About 30 min after the start of irradiation (Figure 3.4a), rBC particles of all core sizes already have an organic coating growing. As organic growth progresses (Figures 3.4b and 3.4c), the smaller rBC cores have markedly thicker coatings than the larger rBC cores. After ~ 7.5 h of chamber dilution (Figure 3.4d), there is no clear, systematic evidence of evaporation of these coatings.

In Figure 3.4, gray lines representing a diffusion-controlled growth law (*Seinfeld and Pandis, 2006*) are shown,

$$\frac{dD_p}{dt} = \frac{A}{D_p} \quad (3.1)$$

where D_p is the rBC VED. The parameter A varies with time and was determined as a function of time by matching the value of $\frac{dD_p}{dt}$ to the coating thickness of 160 nm VED rBC cores (thicknesses of 35, 120, 130, and 150 nm for Figures 3.4a–3.4d, respectively). The agreement between the model and measurement indicate that the coating thickness diameters follow a diffusion-controlled growth rate. During chamber dilution (Figure 3.4d), there is some deviation from the diffusion-controlled growth law for particles with rBC core VED < 100 nm, but this deviation is likely due to a faster wall deposition rate of larger particles (see Figure 3.2). These rBC size-dependent results are consistent with ambient measurements by *Moteki et al. (2007)* over the western Pacific and with a recent modeling study of the aging of rBC by condensation of hygroscopic layers (*Park et al., 2012*). That this simple, one-hydrocarbon system produces results that resemble ambient rBC aging by condensation of SOA supports this experimental protocol to study rBC aging dynamics in more detail with controlled environmental chambers.

Figure 3.5 presents results from Experiment 5 (Table 3.1), high- NO_x α -pinene photooxidation in

the presence of fullerene seed particles. Growth of SOA is rapid, indicated by immediate increase of organic mass (Figure 3.5a), coating thickness (Figure 3.5b), and change in optical properties (Figure 3.5c). What differentiates this experiment from the others is that mean coating thickness reaches a peak and then decreases during the irradiation period. Throughout the irradiation period, temperature in the chamber increases, but there is no distinct change in temperature near the peak in coating thickness that would indicate that the aerosol should suddenly start evaporating. Thus, it is likely that the evaporation of coating material is indicative of a chemical change causing particle-phase loss of higher-volatility species. The coating evaporation continues after irradiation is stopped, and mean coating thickness does not level off until ~4.25 h into the dilution period. Examination of the evolution of coating thickness for this system (not shown) reveals that a diffusion-limited growth law continues to be valid, and all rBC core sizes exhibit evaporation of coatings. At the very end of the dilution period, a temperature increase of ~2°C over the final 2 h of the experiment leads to a coating thickness decrease of ~5 nm, highlighting the role of temperature in SOA volatility. SOA evaporation during chamber irradiation in this system will be further discussed in Section 3.4.4.2.

Figure 3.6 presents the results from Experiment 7 (Table 3.1), low- NO_x α -pinene photooxidation in the presence of fullerene seed particles. In this system, SOA growth proceeds more slowly than in the high- NO_x photooxidation systems as a result of a lower OH concentration produced by H_2O_2 versus CH_3ONO . Total particle number concentration (Figure 3.6a) gives no evidence of SOA nucleation and shows a steady decline during irradiation, owing to wall-deposition and particle coagulation. Wall deposition rates are slightly faster in the α -pinene chamber versus the naphthalene chamber (Figure 3.2) and characteristic time for coagulation is shorter (~1.8 d versus ~3.4 d, respectively) (*Seinfeld and Pandis*, 2006) owing to higher initial particle number concentration. Despite a temperature decrease, which favors condensation of SOA (Figure 3.6b), there is a slight decrease in mean coating thickness during chamber dilution (~8 nm in ~10 h). The flushing rate of the chamber does not change during dilution (see cyclohexane curve in Figure 3.6a), and the rate of decline in mean coating thickness remains constant as well (Figure 3.6b) despite the change in temperature trend from the first 5 h of flushing (-6.2°C) to the second 5 h of flushing (-0.2°C). A distinguishing

feature of this SOA system is the change in SOA growth rate (see organic mass trace in Figure 3.6a) coincident with a change in optical properties (see the change in slope of the curves in Figure 3.6c) ~ 4 h into the chamber irradiation. The change in particle composition during SOA growth in this system will be discussed in Section 3.4.4.3.

In this work, we focus on results from these three SOA systems in the presence of rBC seed aerosol. For completeness, Table 3.1 lists all experiments performed for this study. Although not shown in this work, each experiment in Table 3.1 was characterized by growth of organic layers on the rBC aerosol. In Experiment 3, the growth of coating by coagulation is estimated to be small (~ 20 nm coating diameter in ~ 16 h), owing to the modest particle number concentration ($\sim 11,000$ cm^{-3}) and coagulation timescale (~ 1.3 d). In the dual seed experiments with rBC and AS (Experiments 2, 6, and 8) and with rBC and nucleated SOA (Experiments 4 and 9), growth of coatings occurred during irradiation of the chamber at a faster rate than during the period of mixing prior to irradiation, indicative that growth by condensation of SOA was dominant.

3.4.3 Aerosol Optical Properties

Table 3.3 presents optical properties of the seed particles and nucleated SOA in this study, including the mass scattering cross section (MSC), mass absorption cross section (MAC), and single-scatter albedo (ω_0). The fullerene soot and ammonium sulfate values are averages of measurements taken during the hour of chamber mixing prior to the start of irradiation on Experiments 1, 5, and 7 for fullerene soot and Experiments 2, 6, and 8 for ammonium sulfate (before injection of fullerene soot). The nucleated naphthalene and α -pinene SOA values are taken before rBC was injected into the chamber on Experiments 3, 4, and 9. The mass absorption cross section of uncoated fullerene soot (12.57 ± 0.30 $\text{m}^2 \text{ g}^{-1}$ at $\lambda = 532$ nm) is considerably higher than reported values for uncoated ambient rBC (7.5 ± 1.2 $\text{m}^2 \text{ g}^{-1}$ at $\lambda = 550$ nm, *Bond and Bergstrom*, 2006). This is consistent with a previous observation that the fullerene soot standard popular for calibration of the SP2 is more than 6 times more efficient at absorbing light than flame-generated soot (A. J. Sedlacek III, personal communication, 2012). In addition, the absorption Ångström exponent (\AA_{abs}), defined in this work

as

$$\text{Å}_{\text{abs}} = -\frac{\ln \frac{b_{\text{abs}, 405 \text{ nm}}}{b_{\text{abs}, 781 \text{ nm}}}}{\ln \frac{405}{781}} \quad (3.2)$$

where b_{abs} is the observed absorption coefficient at the specified wavelengths, is 1.37 ± 0.03 for our sample of fullerene soot. This value of Å_{abs} is slightly higher than $\text{Å}_{\text{abs}} = 1$ recommended for uncoated rBC (*Bond and Bergstrom, 2006*) but lies within the range of modeled conditions (*Lack and Cappa, 2010*) and ambient measurements of rBC (e.g., *Gyawali et al., 2009*).

Nucleated naphthalene SOA exhibits a small absorption signal at $\lambda = 405$ nm; these particles may be classified as “brown carbon,” a mildly absorbing carbonaceous aerosol that is distinct from black carbon but has progressively stronger absorption at UV wavelengths as compared to visible wavelengths (*Andreae and Gelencsér, 2006*; *Wonaschütz et al., 2012*). Some authors have detected absorption from gaseous PAH’s (e.g., *Weiner and Harris, 1989*; *Schoemaecker Moreau et al., 2004*), but in the present experiments the initial concentration of naphthalene gave no measurable absorption signal in the PASS-3. The measured value of the MAC of $2.66 \text{ m}^2 \text{ g}^{-1}$ at $\lambda = 405$ nm for naphthalene SOA can be compared to that of $2.9 \text{ m}^2 \text{ g}^{-1}$ at $\lambda = 400$ nm reported by *Kirchstetter et al. (2004)* for organic carbon from biomass burning aerosols.

3.4.3.1 Evolution of Aerosol Optical Properties during SOA Growth on rBC Seed

Figures 3.3c, 3.5c, and 3.6c show the absorption and scattering coefficients of the rBC-coated SOA during Experiments 1, 5, and 7, respectively. For all experiments, after UV lights are turned on, a clear increase in absorption coefficients at all wavelengths occurs, while rBC mass remains constant or slightly decreases due to wall deposition. Figures 3.7, 3.8, and 3.9 display absorption coefficient (b_{abs}), measured absorption enhancement, and single-scatter albedo (ω_0) as a function of mean coating thickness for Experiments 1, 5, and 7, respectively. Time is shown by marker shading on each figure, generally increasing from left to right because the coating thickness grows during irradiation. For the α -pinene systems (Figures 3.8 and 3.9), the coating thickness eventually decreases, slightly during dilution of the low- NO_x system (Figure 3.9) and more dramatically during irradiation of the high- NO_x system (Figure 3.8).

As noted above, there is a small absorption signal from the naphthalene SOA at $\lambda = 405$ nm, but not at the other wavelengths. We expect that naphthalene SOA condensed onto seed particles will exhibit optical properties similar to nucleated naphthalene SOA, and, therefore, that the absorption enhancement in Experiment 1 (Figure 3.7b) at $\lambda = 781$ nm is a result of the lensing effect of the coatings on the rBC seed particles, while at $\lambda = 405$ nm there is additional absorption from the coating itself (Fuller *et al.*, 1999; Lack and Cappa, 2010). In Experiment 1, \AA_{abs} increased from 1.37 ± 0.029 to 1.76 ± 0.026 during irradiation, indicating that the aerosol absorption at peak growth is more sensitive to wavelength than the uncoated fullerene soot seed. This is consistent with a small absorption coefficient at $\lambda = 405$ nm of the condensed naphthalene SOA (Table 3.3) and exceeds the threshold (1.6) for which attribution of brown carbon to observed absorption can be made (Lack and Cappa, 2010). The sharp decrease in b_{abs} (Figure 3.7a) occurs simultaneously with the start of chamber dilution. The apparent gap in data between ~ 25 and 75 nm thickness is a result of the rapid growth of the coatings during irradiation and the timing of an automatic background signal correction on the PASS-3.

In Experiment 5 (high- NO_x α -pinene photooxidation, Figure 3.5), absorption and scattering coefficients increase rapidly with formation of SOA, then decrease during irradiation as the SOA evaporates. Figure 3.8 shows the rather dramatic decrease in coating thicknesses by the end of the experiment. Note that after reaching the peak in coating thicknesses, b_{abs} and ω_0 decrease along the same trajectory as the coatings evaporate. The sharp decreases in b_{abs} that deviate from this trajectory occur when dilution is initiated, because the decrease in total particle concentration has a larger influence on b_{abs} in this experiment than the single-particle coatings evaporating. Single-scatter albedo continues its decline along the same trajectory because ω_0 is a property of the single particles rather than of the bulk population of particles.

In Experiment 7 (low- NO_x α -pinene photooxidation, Figure 3.6), absorption and scattering coefficients increase steadily with the slowly forming SOA. During irradiation, there is a clear change in the rate of increase of these properties, coincident with a change in rate of growth of organic mass (Figure 3.6a). This change in growth is not seen in the mean coating thickness of 160–180 nm

VED rBC cores (Figure 3.6b). In the absorption coefficient and absorption enhancement especially (Figures 3.9a and 3.9b), this change indicates that additional absorption enhancement has nearly stopped despite continued growth of organic mass and coating thicknesses. Because the coatings are still relatively thin as compared to measurements in Experiment 1 (Figure 3.7), it is unlikely that further absorption enhancement is being thwarted by the scattering shell shielding the absorbing core, as is seen by coatings >300 nm in diameter (Cross *et al.*, 2010).

In all experiments presented, coatings on the rBC cores enhance the light absorption of these particles. Single-scatter albedo increased in all systems as the organic coating thicknesses on the fullerene soot grew. In the naphthalene system, there is clear wavelength dependence of the absorption enhancements (Figure 3.7), owing to the wavelength dependence of refractive index of naphthalene SOA. In the α -pinene systems, evaporation of the coatings leads to a decline of ω_0 from its peak value, indicating that the changes in optical properties can be considered reversible as the coating material is removed from the rBC cores. The absorption enhancements reported here provide further evidence that the mixing state of rBC in the atmosphere is an important consideration for the radiative forcing by these particles.

3.4.3.2 Comparison of Measured and Modeled Absorption Enhancements

Figure 3.10 presents a comparison of a core-and-shell Mie model of absorption enhancement to measured absorption enhancement for Experiments 1 (Figure 3.10a), 5 (Figure 3.10b), and 7 (Figure 3.10c). The PASS-3 measurements at $\lambda = 532$ nm are omitted from the analysis due to larger noise on this channel. The size of rBC core used in the Mie model was chosen because most of the bulk aerosol absorption signal comes from the larger particle sizes, and the chosen core size is within the range for which the SP2 can detect both coated and uncoated rBC.

The rapid increase in absorption enhancement and large enhancement factor (~ 1.8) at $\lambda = 405$ nm in Experiment 1 (Figure 3.10a) are represented by the single-particle Mie model, despite the fact that all rBC particles do not exhibit uniform coating thicknesses (Figure 3.4) and that the refractive index used in the Mie scattering model does not include an absorbing or imaginary part. Modeled absorp-

tion enhancement at $\lambda = 781$ nm does not match the measured enhancement well. This discrepancy indicates a wavelength-dependence of the real part of the refractive index of the naphthalene SOA, which we have not captured with our Mie scattering model. *Lack and Cappa* (2010) found that coatings on rBC by mildly absorbing material reduces the absorption enhancement relative to rBC coated by non-absorbing material. Our results at $\lambda = 781$ nm support this finding, as the measured enhancement is significantly smaller than modeled enhancement using a purely-scattering refractive index. Despite the fact that no absorption at this wavelength was detected during the naphthalene nucleation experiment, it is possible that absorption signals were below detection limits on PASS-3. A more detailed Mie model with proper refractive indices for naphthalene SOA is needed to reconcile these differences.

In Experiment 5 (Figure 3.10b), the measured increase and decrease in absorption enhancement due to the increase and decrease of coating thickness during irradiation are captured by the model. We expect fairly good agreement using a coating refractive index of $1.5-0.0i$ based on a recent finding of no significant absorption for α -pinene SOA (*Nakayama et al.*, 2010) and on recent measurements of α -pinene SOA refractive index in the range of 1.42–1.56 for $\lambda = 450$ –700 nm (*Barkey et al.*, 2007; *Yu et al.*, 2008). The small wavelength-dependence of refractive index (increasing refractive index with decreasing wavelength) reported by *Yu et al.* (2008) explains the small difference in the measured enhancement factors in this system.

In Experiment 7 (Figure 3.10c), there was a change in optical properties during the irradiation period (see Figures 3.6c and 3.9b). This change, in which the measured absorption enhancement ceases to increase, is not reflected by the Mie model because organic coatings are continuing to grow (Figure 3.6b). To reconcile the differences between the measurements and model, a change in refractive index of the coating material at the time of this deviation needs to be considered. In addition, a more complete Mie model representation that includes the full range of rBC core sizes and coatings may be needed to properly simulate the contribution from all sizes of particles to the bulk absorption.

The results presented here, of a core-and-shell Mie scattering model of absorption enhancement

during these single-hydrocarbon SOA systems, suggest that a careful treatment of SOA refractive index is needed to fully model aerosol optical properties. SOA from the photooxidation of naphthalene under dry, high- NO_x conditions has a refractive index with a strong wavelength-dependence. In the α -pinene system, for which measured refractive indices from previous studies exist, a change in optical properties during photooxidation causes discrepancies between the modeled and measured light absorption.

3.4.4 AMS Measurements

3.4.4.1 Naphthalene SOA

Figure 3.11 presents normalized (signal at each m/z is divided by the total organic signal) unit-mass resolution AMS organic mass fractions for each m/z of SOA formed by the photooxidation of naphthalene in the presence of rBC seed particles (Experiment 1) versus nucleated naphthalene SOA (Experiment 3). The data are taken at the “peak growth” periods of each experiment, defined as the time after the parent hydrocarbon has either been consumed or has ceased to decrease (presumably due to OH being fully consumed) and when growth of suspended particle volume concentration has leveled off through reaching a balance with wall deposition. The oxidation lifetime is defined as $k_i[\text{OH}]\Delta t$, where k_i is the second-order rate constant of species i reaction with OH, $[\text{OH}]$ is the gas-phase concentration of OH, and Δt is the exposure time (Kroll *et al.*, 2009). In Figure 3.11, the data were taken at an oxidation lifetime of about 2.5 in both cases, and there was about 1.3 (7.8% of initial) and 2.1 ppb (9.6% of initial) naphthalene remaining in the chamber at peak growth for Experiments 1 and 3, respectively.

All AMS mass fractions are shown in Figure 3.11; masses larger than about m/z 275 from the nucleation experiment and masses larger than about m/z 200 from the fullerene soot-seeded experiment are generally at or near the detection limit of the AMS for those individual masses. A notable exception is m/z 360 for Experiment 1, which is well above the detection limit of this mass. The detection limits at each m/z are calculated as three times the standard deviation of the measured signal during sampling with a particle filter in front of the inlet before the start of the

experiment.

There is negligible difference in the SOA composition formed by nucleation or condensation onto fullerene soot for this system; the largest change in mass fraction at any given m/z is about $\pm 1\%$ of total organic mass. It cannot be ruled out that the discrepancies in the particular m/z 's between the two experiments may arise owing to a different organic loading at the times of interest; for Experiment 1, organic mass was $6.5 \pm 0.08 \text{ } \mu\text{g m}^{-3}$, while for Experiment 3, organic mass was $18.2 \pm 0.22 \text{ } \mu\text{g m}^{-3}$. The most noticeable differences between condensed and nucleated SOA in Figure 3.11 are in m/z 360 and 361, which we propose are $^{12}\text{C}_{30}^+$ and $^{13}\text{C}_1 \text{ } ^{12}\text{C}_{29}^+$ ions, following similar analysis by *Onasch et al.* (2012). High-resolution analysis of W-mode AMS mass spectra (not shown) confirm that only one ion is present each at m/z 360 and 361. It has been shown that the smallest stable fullerene structure may be C_{30} (*von Heden et al.*, 1993), while below this m/z there is a shift to different carbon clusters (*Onasch et al.*, 2012). Despite previous assumptions that the AMS cannot detect rBC (*Slowik et al.*, 2004), our data suggest that these small fullerenes are able to be ionized in the high-resolution AMS at detectable levels.

Although not shown in this work, similar AMS mass spectra comparisons were made at peak growth for the AS + rBC seeded experiment (Experiment 2 on Table 3.1) compared to the two experiments presented above. The only noticeable difference in the mass spectra arises from interferences from sulfate at m/z 48 and 64, which is remedied by properly adjusting the AMS fragmentation table. One concludes that the fullerene soot seed does not affect the composition of the naphthalene SOA as compared to nucleated SOA or to condensed SOA onto the more conventional AS seed.

3.4.4.2 High- NO_x α -pinene SOA

During high- NO_x α -pinene photooxidation (Experiment 5), the mean coating thickness initially increases rapidly, achieves a maximum, then decreases for the remainder of the irradiation period (Figure 3.5b). Figure 3.12a and 3.12b present normalized AMS mass spectra at two times during irradiation in Experiment 5, at oxidation lifetimes of 9, near the end of the irradiation period, and 1, during the early rapid growth of SOA, respectively. Figure 3.12c presents the difference

between these two mass spectra, relative to the earlier mass spectra, where positive values denote mass fragments enriched at the end of irradiation. Typically, the dominant mass fragments in AMS organic mass spectra of ambient aerosol are at m/z 44, which represents highly oxygenated organic species with low volatility, and at m/z 43, which represents less oxygenated semi-volatile species (Ng *et al.*, 2010). f_{43} is initially $\sim 15\%$ of the total organic mass (Figure 3.12b) and decreases to $\sim 13\%$ (Figure 3.12a) near the end of the irradiation period. Simultaneously, f_{44} increases from $\sim 8\%$ (Figure 3.12b) to $\sim 12\%$ (Figure 3.12a) of total organic mass during the irradiation period. These results indicate that the aerosol is transitioning from a semi-volatile to a lower volatility state, as is commonly observed during chemical aging of aerosol (Ng *et al.*, 2010).

From the time series traces (Figure 3.12d) of AMS m/z 43 and 44, the ratio of m/z 43/44, and mean coating thickness on rBC as measured by the SP2, AMS m/z 43 clearly traces the mean coating thickness ($R^2=0.97$), capturing the decrease in thickness with time quite well, deviating only after chamber dilution has begun. AMS m/z 44 lags behind m/z 43 in formation, and, therefore, does not trace coating thickness as well ($R^2=0.89$). After the initial rapid growth, the m/z 43/44 ratio continuously decreases due to f_{44} continuously increasing throughout the experiment. The combination of single-particle coating thickness measured by the SP2 and the bulk organic mass spectra measured by the AMS suggest that the more semi-volatile species are actually evaporating from the aerosol even as aerosol-phase chemical aging may be occurring. The SP2 unambiguously shows changes in single particles, whereas AMS measurements of small decreases in organic mass alone may have been attributed to other processes, such as wall deposition.

3.4.4.3 Low- NO_x α -pinene SOA

In the evolution of various measured parameters during the low- NO_x α -pinene photooxidation (Experiment 7), mean coating thickness steadily increased as SOA was formed (Figure 3.6b). About halfway through the irradiation period, a decrease in the rate of change of the absorption and scattering coefficients occurred (Figure 3.6c), coincident with a decrease in the growth rate of total organic mass concentration measured by the AMS (Figure 3.6a). This change during irradiation

occurred at an oxidation lifetime of ~ 2 (~ 4 h after the onset of irradiation).

Figures 3.13a and 3.13b present normalized AMS mass spectra at oxidation lifetimes of 1 and 3, respectively, on either side of the change in aerosol growth rate. Figure 3.13c presents the difference spectrum relative to the earlier spectrum and shows a decrease in f_{43} . Figure 3.13d shows the evolution of various AMS mass fractions with oxidation lifetime in addition to the absorption and scattering coefficients at $\lambda = 405$ nm measured by the PASS-3. A shift in optical properties is evident at an oxidation lifetime of 2, while f_{43} and f_{44} continually change during the experiment and show no clear shift. Other mass fractions, namely f_{1-50} and f_{50-100} , do exhibit a change near an oxidation lifetime of 2; these mass fractions reach a constant value after evolving throughout the first part of the organic growth period. Throughout the entire period displayed in Figure 3.13d, organic mass is growing and the raw m/z 's are increasing; thus, the shifts in mass fractions reflect the fact that different mass fragments are growing at different rates relative to each other.

While m/z 43 and 44 are important individual mass fragments in the AMS mass spectra, they fail to capture the change in aerosol behavior that occurs at an oxidation lifetime of 2 in this system. The mass fractions f_{1-50} and f_{50-100} do exhibit a change coincident with the change in optical properties during SOA growth, indicating a change in SOA composition. This change in composition is likely accompanied by a change in refractive index, explaining the shift in optical properties despite steady growth of rBC coating thicknesses. This experiment demonstrates that measurement of aerosol optical properties can help guide the analysis of data from other instruments, namely the AMS. In the low- NO_x α -pinene photooxidation system, the SOA optical properties change with time, and could help in understanding the evolution of atmospheric SOA optical properties.

3.5 Conclusions

In this work we demonstrate the utility of employing refractory black carbon (rBC) as a seed aerosol in chamber studies of secondary organic aerosol formation, when done in conjunction with the Single-Particle Soot Photometer. Particle-by-particle measurement of the dynamics of the organic coating thickness on the rBC seed over the course of SOA formation allows evaluation of the rate of

growth as a function of particle size. An experimental strategy is implemented in which a period of VOC oxidation and SOA growth is followed by one in which growth is quenched while the chamber undergoes dilution. The dilution phase is used as a means to assess SOA volatility by measuring the possible evaporation of coatings on the rBC seed. In the experiments presented here, a 3- λ Photoacoustic Soot Spectrometer is used to measure the optical properties of the uncoated rBC seed, initially, and the coated rBC seed during the course of SOA formation. These measurements, coupled with the application of a core-and-shell Mie scattering model, allow one to infer the optical properties of the SOA. Application of a prototype single-particle angularly-resolved light scattering instrument confirms that the uncoated rBC particles are non-spherical. Important to understanding the effect rBC has on SOA formation is whether or not SOA condensed onto rBC seed is chemically and optically similar to nucleated SOA under dry conditions. High-resolution Aerodyne Aerosol Mass Spectrometer measurements for the three systems considered here, naphthalene photooxidation and photooxidation of α -pinene under both high- and low- NO_x conditions, confirm that the composition of SOA coating rBC seed particles is essentially identical to that generated by homogeneous nucleation in the absence of seed particles, so that the use of rBC as a seed is not expected to alter the basic chemistry of SOA formation under dry conditions. Both SP2 and PASS-3 measurements reveal a change in the SOA coating and particle optical properties during SOA growth in the high- NO_x α -pinene system, which is mirrored by a corresponding change in the AMS mass spectra. The combination of SP2 and AMS measurements in this system suggest that semi-volatile species are evaporating from the aerosol during chemical aging. A change in optical properties during SOA growth in the low- NO_x α -pinene system is mirrored by a change in organic growth rate and AMS mass spectra, but not in single-particle coating thicknesses. Exploration of a fundamental explanation of the chemistry leading to these changes lies beyond the scope of the present work. We have provided a framework by which future studies of SOA optical properties and single-particle growth dynamics may be explored in environmental chambers.

3.6 Appendix: Measurement of Angularly-Resolved Light Scattering from Single Particles

The prototype instrument used in this study to measure particle sphericity was designed by MSP Corporation (Shoreview, MN, USA) to measure angularly-resolved light scattering from single particles. Air with particles enters the instrument and is guided towards the detection block by filtered sheath air and a focusing nozzle. The stream of particles is focused to align with the center of the laser beam in the detection block. The sheath and aerosol flows are feedback-controlled to maintain constant operating conditions throughout a sampling period. The laser is a 100 mW Diode Pumped Green CrystaLaser (Reno, NV, USA) at a peak wavelength of 532 nm. Lenses tightly focus the laser beam into the detection block, and a quarter-wave plate transforms the linearly polarized laser light into circular polarization inside the detection block. At its intersection with the particle stream, the Gaussian laser beam profile is approximately 440 μm in diameter. The sphericity signal is detected with lenses placed on the end of 16 fiber optic cables attached to the detection block. Eight of the lenses are placed axisymmetrically about a polar angle of 50° in the forward scattering direction, and the other eight are placed axisymmetrically about a polar angle of 130°. The other ends of all the fiber optic cables are mounted in front of a Hamamatsu H8711 4x4 multianode photomultiplier tube (PMT) assembly. Each of the fiber optic cables is focused toward one of the 16 channels in this PMT assembly. In this study, only the eight signals from a polar angle of 50° are used to determine particle sphericity.

Particle sphericity is determined by quantifying the degree to which the light scattered onto the eight detectors at a fixed polar angle is uniform. Owing to artifacts introduced by the different optical fiber characteristics on each of these channels, the signal must be adjusted on each channel independently of the other channels. This adjustment is done by normalizing the signal, Ψ , on each detector by the median response of that detector for a fixed amount of time before and after each

individual measurement by

$$\hat{\Psi}_{i,j} = \frac{\Psi_{i,j}}{\mu_{1/2}(\Psi_i)} \quad (3.3)$$

where i is the detector number (1–8), j is the particle number for a given experiment, and $\mu_{1/2}(\Psi_i)$ is the median of all measurements on a single channel for the given time period. In this study, we used a time period of 5 min, as little variation in instrument conditions occurred over this time period.

After all signals have been normalized, the particle non-sphericity can be calculated by finding, for each particle, the median absolute deviation of the signal among the eight detectors by

$$\Phi_j = \mu_{1/2} \left(\left| \hat{\Psi}_{i,j} - \mu_{1/2}(\hat{\Psi}_j) \right| \right) \quad (3.4)$$

where $\mu_{1/2}(\hat{\Psi}_j)$ here is the median of the normalized signal across the eight detectors for a single particle.

In an ideal case, the non-sphericity of a spherical particle is zero; that is, there is no variation in the light intensity scattered onto the eight shape detectors. Given that no instrument or particle is absolutely ideal, non-sphericity values close to zero are taken to indicate a spherical particle and values somewhat greater than zero indicate a non-spherical particle, with larger values indicating larger degrees of non-sphericity.

3.7 Acknowledgements

This work was supported by U.S. Department of Energy grant DE-SC0006626.

Bibliography

Abel, S. J., J. M. Haywood, E. J. Highwood, J. Li, and P. R. Buseck (2003), Evolution of biomass burning aerosol properties from an agricultural fire in southern Africa, *Geophys. Res. Lett.*, 30(15),

1783, doi:10.1029/2003GL017342. 79

Andreae, M. O., and A. Gelencsér (2006), Black carbon or brown carbon? The nature of light-absorbing carbonaceous aerosols, *Atmos. Chem. Phys.*, 6, 3131–3148, doi:10.5194/acp-6-3131-2006. 93

Barkey, B., S. E. Paulson, and A. Chung (2007), Genetic Algorithm Inversion of Dual Polarization Polar Nephelometer Data to Determine Aerosol Refractive Index, *Aerosol Sci. Technol.*, 41(8), 751–760, doi:10.1080/02786820701432640. 96

Baumgardner, D., G. L. Kok, and G. Raga (2004), Warming of the Arctic lower stratosphere by light absorbing particles, *Geophys. Res. Lett.*, 31, L06117, doi:10.1029/2003GL018883. 84

Baumgardner, D., et al. (2012), Soot reference materials for instrument calibration and intercomparisons: a workshop summary with recommendations, *Atmos. Meas. Tech. Discuss.*, 5, 2315–2362, doi:10.5194/amtd-5-2315-2012. 84

Bohren, C. F., and D. R. Huffman (1998), *Absorption and Scattering of Light by Small Particles*, John Wiley & Sons, Inc., New York. 86

Bond, T. C., and R. W. Bergstrom (2006), Light absorption by carbonaceous particles: An investigative review, *Aerosol Sci. Technol.*, 40(1), 27–67, doi:10.1080/02786820500421521. 86, 92, 93

Bond, T. C., G. Habib, and R. W. Bergstrom (2006), Limitations in the enhancement of visible light absorption due to mixing state, *J. Geophys. Res.*, 111, D20211, doi:10.1029/2006JD007315. 79

Bueno, P. A., D. K. Havey, G. W. Mulholland, J. T. Hodges, K. A. Gillis, R. R. Dickerson, and M. R. Zachariah (2011), Photoacoustic measurements of amplification of the absorption cross section for coated soot aerosols, *Aerosol Sci. Technol.*, 45(10), 1217–1230, doi:10.1080/02786826.2011.587477.

80

Canagaratna, M. R., et al. (2007), Chemical and microphysical characterization of ambient aerosols

with the Aerodyne Aerosol Mass Spectrometer, *Mass Spectrom. Rev.*, 26(2), 185–222, doi:10.1002/mas.20115. 85

Chan, A. W. H., et al. (2009), Secondary organic aerosol formation from photooxidation of naphthalene and alkylnaphthalenes: implications for oxidation of intermediate volatility organic compounds (IVOCs), *Atmos. Chem. Phys.*, 9, 3049–3060, doi:10.5194/acp-9-3049-2009. 82, 83

Chan, A. W. H., et al. (2010a), Role of aldehyde chemistry and NO_x concentrations in secondary organic aerosol formation, *Atmos. Chem. Phys.*, 10, 7169–7188, doi:10.5194/acp-10-7169-2010. 82

Chan, T. W., et al. (2010b), Observations of OM/OC and specific attenuation coefficients (SAC) in ambient fine PM at a rural site in central Ontario, Canada, *Atmos. Chem. Phys.*, 10, 2393–2411, doi:10.5194/acp-10-2393-2010. 79

Chirico, R., et al. (2010), Impact of aftertreatment devices on primary emissions and secondary organic aerosol formation potential from in-use diesel vehicles: results from smog chamber experiments, *Atmos. Chem. Phys.*, 10, 11,545–11,563, doi:10.5194/acp-10-11545-2010. 81

Chung, S. H., and J. H. Seinfeld (2002), Global distribution and climate forcing of carbonaceous aerosols, *J. Geophys. Res.*, 107(D19), 4407, doi:10.1029/2001JD001397. 83

Cocker, D. R., R. C. Flagan, and J. H. Seinfeld (2001), State-of-the-art chamber facility for studying atmospheric aerosol chemistry, *Environ. Sci. Technol.*, 35(12), 2594–2601, doi:10.1021/es0019169. 81

Cross, E. S., et al. (2010), Soot particle studies—Instrument Inter-comparison—Project overview, *Aerosol Sci. Technol.*, 44(8), 592–611, doi:10.1080/02786826.2010.482113. 79, 80, 95

Crump, J. G., and J. H. Seinfeld (1981), Turbulent deposition and gravitational sedimentation of an aerosol in a vessel of arbitrary shape, *J. Aerosol Sci.*, 12(5), 405–415, doi:10.1016/0021-8502(81)90036-7. 88

DeCarlo, P. F., et al. (2006), Field-deployable, high-resolution, time-of-flight aerosol mass spectrometer, *Anal. Chem.*, 78(24), 8281–8289, doi:10.1021/ac061249n. 85

Dick, W. D., P. H. McMurry, and J. R. Bottiger (1994), Size- and composition-dependent response of the DAWN-A multiangle single-particle optical detector, *Aerosol Sci. Technol.*, 20(4), 345–362, doi:10.1080/02786829408959690. 86

Dick, W. D., P. J. Ziemann, P.-F. Huang, and P. H. McMurry (1998), Optical shape fraction measurements of submicrometre laboratory and atmospheric aerosols, *Meas. Sci. Technol.*, 9(2), 183–196, doi:10.1088/0957-0233/9/2/006. 86

Fruin, S. A., A. M. Winer, and C. E. Rodes (2004), Black carbon concentrations in California vehicles and estimation of in-vehicle diesel exhaust particulate matter exposures, *Atmos. Environ.*, 38(25), 4123–4133, doi:10.1016/j.atmosenv.2004.04.026. 79

Fuller, K. A., W. C. Malm, and S. M. Kreidenweis (1999), Effects of mixing on extinction by carbonaceous particles, *J. Geophys. Res.*, 104(D13), 15,941–15,954, doi:10.1029/1998JD100069. 79, 94

Gao, R. S., et al. (2007), A novel method for estimating light-scattering properties of soot aerosols using a modified single-particle soot photometer, *Aerosol Sci. Technol.*, 41(2), 125–135, doi:10.1080/02786820601118398. 86

Guenther, A., et al. (1995), A global model of natural volatile organic compound emissions, *J. Geophys. Res.*, 100(D5), 8873–8892. 83

Gyawali, M., W. Arnott, K. Lewis, and H. Moosmüller (2009), In situ aerosol optics in Reno, NV, USA during and after the summer 2008 California wildfires and the influence of absorbing and non-absorbing organic coatings on spectral light absorption, *Atmos. Chem. Phys.*, 9, 8007–8015, doi:10.5194/acp-9-8007-2009. 93

Gysel, M., M. Laborde, J. S. Olfert, R. Subramanian, and A. J. Gröhn (2011), Effective density of Aquadag and fullerene soot black carbon reference materials used for SP2 calibration, *Atmos. Meas. Tech.*, 4, 2851–2858, doi:10.5194/amt-4-2851-2011. 84, 88, 89, 120

Jacobson, M. Z. (2006), Effects of externally-through-internally-mixed soot inclusions within clouds and precipitation on global climate, *J. Phys. Chem. A*, 110(21), 6860–6873, doi:10.1021/jp056391r. 79

Jayne, J. T., D. C. Leard, X. Zhang, P. Davidovits, K. A. Smith, C. E. Kolb, and D. R. Worsnop (2000), Development of an aerosol mass spectrometer for size and composition analysis of submicron particles, *Aerosol Sci. Technol.*, 33(1-2), 49–70, doi:10.1080/027868200410840. 85

Johnson, K. S., B. Zuberi, L. T. Molina, M. J. Molina, M. J. Iedema, J. P. Cowin, D. J. Gaspar, C. Wang, and A. Laskin (2005), Processing of soot in an urban environment: case study from the Mexico City Metropolitan Area, *Atmos. Chem. Phys.*, 5, 3033–3043, doi:10.5194/acp-5-3033-2005. 79

Keywood, M. D., V. Varutbangkul, R. Bahreini, R. C. Flagan, and J. H. Seinfeld (2004), Secondary organic aerosol formation from the ozonolysis of cycloalkenes and related compounds, *Environ. Sci. Technol.*, 38(15), 4157–4164, doi:10.1021/es035363o. 81, 88

Khalizov, A. F., R. Zhang, D. Zhang, H. Xue, J. Pagels, and P. H. McMurry (2009a), Formation of highly hygroscopic soot aerosols upon internal mixing with sulfuric acid vapor, *J. Geophys. Res.*, 114, D05208, doi:10.1029/2008JD010595. 79, 80

Khalizov, A. F., H. Xue, L. Wang, J. Zheng, and R. Zhang (2009b), Enhanced light absorption and scattering by carbon soot aerosol internally mixed with sulfuric acid, *J. Phys. Chem. A*, 113(6), 1066–1074, doi:10.1021/jp807531n. 79, 80

Kirchner, U., R. Vogt, C. Natzeck, and J. Goschnick (2003), Single particle MS, SNMS, SIMS, XPS, and FTIR spectroscopic analysis of soot particles during the AIDA campaign, *J. Aerosol Sci.*, 34(10), 1323–1346, doi:10.1016/S0021-8502(03)00362-8. 81

Kirchstetter, T. W., T. Novakov, and P. V. Hobbs (2004), Evidence that the spectral dependence of light absorption by aerosols is affected by organic carbon, *J. Geophys. Res.*, 109, D21208, doi:10.1029/2004JD004999. 93

Kleeman, M. J., J. J. Schauer, and G. R. Cass (2000), Size and composition distribution of fine particulate matter emitted from motor vehicles, *Environ. Sci. Technol.*, 34(7), 1132–1142, doi: doi:10.1021/es981276y. 79

Knox, A., G. J. Evans, J. R. Brook, X. Yao, C.-H. Jeong, K. J. Godri, K. Sabaliauskas, and J. G. Slowik (2009), Mass absorption cross-section of ambient black carbon aerosol in relation to chemical age, *Aerosol Sci. Technol.*, 43(6), 522–532, doi:10.1080/02786820902777207. 79

Kroll, J. H., J. D. Smith, D. L. Che, S. H. Kessler, D. R. Worsnop, and K. R. Wilson (2009), Measurement of fragmentation and functionalization pathways in the heterogeneous oxidation of oxidized organic aerosol, *Phys. Chem. Chem. Phys.*, 11(36), 8005–8014, doi:10.1039/b905289e. 97

Laborde, M., P. Mertes, P. Zieger, J. Dommen, U. Baltensperger, and M. Gysel (2012), Sensitivity of the Single Particle Soot Photometer to different black carbon types, *Atmos. Meas. Tech.*, 5, 1031–1043, doi:10.5194/amt-5-1031-2012. 82, 84

Lack, D. A., and C. D. Cappa (2010), Impact of brown and clear carbon on light absorption enhancement, single scatter albedo and absorption wavelength dependence of black carbon, *Atmos. Chem. Phys.*, 10, 4207–4220, doi:10.5194/acp-10-4207-2010. 79, 93, 94, 96

Leach, K. B., R. M. Kamens, M. R. Strommen, and M. Jang (1999), Partitioning of semivolatile organic compounds in the presence of a secondary organic aerosol in a controlled atmosphere, *J. Atmos. Chem.*, 33(3), 241–264, doi:10.1023/A:1006108430033. 80

Lewis, K., W. P. Arnott, H. Moosmüller, and C. E. Wold (2008), Strong spectral variation of biomass smoke light absorption and single scattering albedo observed with a novel dual-wavelength photoacoustic instrument, *J. Geophys. Res.*, 113, D16203, doi:10.1029/2007JD009699. 85

Loza, C. L., P. S. Chhabra, L. D. Yee, J. S. Craven, R. C. Flagan, and J. H. Seinfeld (2012), Chemical aging of *m*-xylene secondary organic aerosol: laboratory chamber study, *Atmos. Chem. Phys.*, 12, 151–167, doi:10.5194/acp-12-151-2012. 88

McMurry, P. H., and D. J. Rader (1985), Aerosol wall losses in electrically charged chambers, *Aerosol Sci. Technol.*, 4(3), 249–268, doi:10.1080/02786828508959054. 88

Metcalf, A. R., et al. (2012), Black carbon aerosol over the Los Angeles Basin during CalNex, *J. Geophys. Res.*, 117, D00V13, doi:10.1029/2011JD017255. 79, 84, 86, 87

Mikhailov, E. F., S. S. Vlasenko, I. A. Podgorny, V. Ramanathan, and C. E. Corrigan (2006), Optical properties of soot–water drop agglomerates: An experimental study, *J. Geophys. Res.*, 111, D07209, doi:10.1029/2005JD006389. 79, 80

Moffet, R. C., and K. A. Prather (2009), In-situ measurements of the mixing state and optical properties of soot with implications for radiative forcing estimates, *Proc. Natl. Acad. Sci. U.S.A.*, 106(29), 11,872–11,877, doi:10.1073/pnas.0900040106. 79

Moteki, N., and Y. Kondo (2007), Effects of mixing state on black carbon measurements by laser-induced incandescence, *Aerosol Sci. Technol.*, 41(4), 398–417, doi:10.1080/02786820701199728. 84

Moteki, N., and Y. Kondo (2010), Dependence of laser-induced incandescence on physical properties of black carbon aerosols: Measurements and theoretical interpretation, *Aerosol Sci. Technol.*, 44(8), 663–675, doi:10.1080/02786826.2010.484450. 82

Moteki, N., et al. (2007), Evolution of mixing state of black carbon particles: Aircraft measurements over the western Pacific in March 2004, *Geophys. Res. Lett.*, 34, L11803, doi:10.1029/2006GL028943. 79, 90

Nakayama, T., Y. Matsumi, K. Sato, T. Imamura, A. Yamazaki, and A. Uchiyama (2010), Laboratory studies on optical properties of secondary organic aerosols generated during the photooxidation of toluene and the ozonolysis of alpha-pinene, *J. Geophys. Res.*, 115, D24203, doi:10.1029/2010JD014387. 96

Ng, N. L., J. H. Kroll, A. W. H. Chan, P. S. Chhabra, R. C. Flagan, and J. H. Seinfeld (2007),

Secondary organic aerosol formation from *m*-xylene, toluene, and benzene, *Atmos. Chem. Phys.*, 7, 3909–3922, doi:10.5194/acp-7-3909-2007. 88

Ng, N. L., et al. (2010), Organic aerosol components observed in Northern Hemispheric datasets from aerosol mass spectrometry, *Atmos. Chem. Phys.*, 10, 4625–4641, doi:10.5194/acp-10-4625-2010. 99

Onasch, T. B., A. Trimborn, E. C. Fortner, J. T. Jayne, G. L. Kok, L. Williams, P. Davidovits, and D. R. Worsnop (2012), Soot Particle Aerosol Mass Spectrometer: development, validation, and initial application, *Aerosol Sci. Technol.*, 46(7), 804–817, doi:10.1080/02786826.2012.663948. 98

Park, S. H., H. O. Kim, Y. T. Han, S. B. Kwon, and K. W. Lee (2001), Wall loss rate of polydispersed aerosols, *Aerosol Sci. Technol.*, 35(3), 710–717, doi:10.1080/02786820152546752. 88

Park, Y.-K., S. H. Park, and G.-N. Bae (2012), Analytical expression on characteristic time scale of black carbon aging due to condensation of hygroscopic species, *Aerosol Sci. Technol.*, 46(6), 601–609, doi:10.1080/02786826.2011.647119. 79, 90

Pierce, J. R., G. J. Engelhart, L. Hildebrandt, E. A. Weitkamp, R. K. Pathak, N. M. Donahue, A. L. Robinson, P. J. Adams, and S. N. Pandis (2008), Constraining particle evolution from wall losses, coagulation, and condensation-evaporation in smog-chamber experiments: optimal estimation based on size distribution measurements, *Aerosol Sci. Technol.*, 42(12), 1001–1015, doi:10.1080/02786820802389251. 88

Pósfai, M., R. Simonics, J. Li, P. V. Hobbs, and P. R. Buseck (2003), Individual aerosol particles from biomass burning in southern Africa: 1. Compositions and size distributions of carbonaceous particles, *J. Geophys. Res.*, 108(D13), 8483, doi:10.1029/2002JD002291. 79

Pye, H. O. T., A. W. H. Chan, M. P. Barkley, and J. H. Seinfeld (2010), Global modeling of organic aerosol: the importance of reactive nitrogen (NO_x and NO_3), *Atmos. Chem. Phys.*, 10, 11,261–11,276, doi:10.5194/acp-10-11261-2010. 83

Ravindra, K., R. Sokhi, and R. Van Grieken (2008), Atmospheric polycyclic aromatic hydrocarbons: Source attribution, emission factors and regulation, *Atmos. Environ.*, 42(13), 2895–2921, doi: 10.1016/j.atmosenv.2007.12.010. 82

Riemer, N., H. Vogel, and B. Vogel (2004), Soot aging time scales in polluted regions during day and night, *Atmos. Chem. Phys.*, 4, 1885–1893, doi:10.5194/acp-4-1885-2004. 79

Robinson, A. L., N. M. Donahue, M. K. Shrivastava, E. A. Weitkamp, A. M. Sage, A. P. Grieshop, T. E. Lane, J. R. Pierce, and S. N. Pandis (2007), Rethinking organic aerosols: semivolatile emissions and photochemical aging, *Science*, 315(5816), 1259–1262, doi:10.1126/science.1133061.

79

Saathoff, H., K.-H. Naumann, M. Schnaiter, W. Schöck, O. Möhler, U. Schurath, E. Weingartner, M. Gysel, and U. Baltensperger (2003), Coating of soot and $(\text{NH}_4)_2\text{SO}_4$ particles by ozonolysis products of α -pinene, *J. Aerosol Sci.*, 34(10), 1297–1321, doi:10.1016/S0021-8502(03)00364-1. 79, 80

Sachweh, B. A., W. D. Dick, and P. H. McMurry (1995), Distinguishing between spherical and nonspherical particles by measuring the variability in azimuthal light scattering, *Aerosol Sci. Technol.*, 23(3), 373–391, doi:10.1080/02786829508965321. 86

Schauer, J. J., W. F. Rogge, L. M. Hildemann, M. A. Masurek, G. R. Cass, and B. R. T. Simoneit (1996), Source apportionment of airborne particulate matter using organic compounds as tracers, *Atmos. Environ.*, 30(22), 3837–3855, doi:10.1016/1352-2310(96)00085-4. 79

Schauer, J. J., M. J. Kleeman, G. R. Cass, and B. R. T. Simoneit (1999), Measurement of emissions from air pollution sources. 2. C_1 through C_{30} organic compounds from medium duty diesel trucks, *Environ. Sci. Technol.*, 33(10), 1578–1587, doi:10.1021/es980081n. 82

Schauer, J. J., M. J. Kleeman, G. R. Cass, and B. R. T. Simoneit (2001), Measurement of Emissions from air pollution sources. 3. C_1 – C_{29} organic compounds from fireplace combustion of wood, *Environ. Sci. Technol.*, 35(9), 1716–1728, doi:10.1021/es001331e. 82

Schnaiter, M., H. Horvath, O. Möhler, K.-H. Naumann, H. Saathoff, and O. W. Schöck (2003), UV-VIS-NIR spectral optical properties of soot and soot-containing aerosols, *J. Aerosol Sci.*, 34(10), 1421–1444, doi:10.1016/S0021-8502(03)00361-6. 80, 81

Schnaiter, M., C. Linke, O. Möhler, K.-H. Naumann, H. Saathoff, R. Wagner, U. Schurath, and B. Wehner (2005), Absorption amplification of black carbon internally mixed with secondary organic aerosol, *J. Geophys. Res.*, 110, D19204, doi:10.1029/2005JD006046. 79, 80

Schoemaecker Moreau, C., E. Therssen, X. Mercier, J. F. Pauwels, and P. Desgroux (2004), Two-color laser-induced incandescence and cavity ring-down spectroscopy for sensitive and quantitative imaging of soot and PAHs in flames, *Appl. Phys. B: Lasers Opt.*, 78(3-4), 485–492, doi:10.1007/s00340-003-1370-9. 93

Schwarz, J. P., et al. (2006), Single-particle measurements of midlatitude black carbon and light-scattering aerosols from the boundary layer to the lower stratosphere, *J. Geophys. Res.*, 111, D16207, doi:10.1029/2006JD007076. 84

Schwarz, J. P., et al. (2008a), Measurement of the mixing state, mass, and optical size of individual black carbon particles in urban and biomass burning emissions, *Geophys. Res. Lett.*, 35, L13810, doi:10.1029/2008GL033968. 79, 86

Schwarz, J. P., et al. (2008b), Coatings and their enhancement of black carbon light absorption in the tropical atmosphere, *J. Geophys. Res.*, 113, D03203, doi:10.1029/2007JD009042. 87

Seinfeld, J. H., and S. N. Pandis (2006), *Atmospheric Chemistry and Physics: From Air Pollution to Climate Change*, 2nd ed., John Wiley & Sons, Inc., New York. 90, 91

Shiraiwa, M., Y. Kondo, N. Moteki, N. Takegawa, Y. Miyazaki, and D. R. Blake (2007), Evolution of mixing state of black carbon in polluted air from Tokyo, *Geophys. Res. Lett.*, 34, L16803, doi:10.1029/2007GL029819. 79

Shiraiwa, M., Y. Kondo, N. Moteki, N. Takegawa, L. K. Sahu, A. Takami, S. Hatakeyama, S. Yone-

mura, and D. R. Blake (2008), Radiative impact of mixing state of black carbon aerosol in Asian outflow, *J. Geophys. Res.*, 113, D24210, doi:10.1029/2008JD010546. 79

Shiraiwa, M., Y. Kondo, T. Iwamoto, and K. Kita (2010), Amplification of light absorption of black carbon by organic coating, *Aerosol Sci. Technol.*, 44(1), 46–54, doi:10.1080/02786820903357686.

79

Slowik, J., et al. (2004), Particle morphology and density characterization by combined mobility and aerodynamic diameter measurements. Part 2: Application to combustion-generated soot aerosols as a function of fuel equivalence ratio, *Aerosol Sci. Technol.*, 38(12), 1206–1222, doi:10.1080/027868290903916. 98

Slowik, J. G., et al. (2007a), An inter-comparison of instruments measuring black carbon content of soot particles, *Aerosol Sci. Technol.*, 41(3), 295–314, doi:10.1080/02786820701197078. 79, 80, 84

Slowik, J. G., et al. (2007b), Measurements of morphology changes of fractal soot particles using coating and denuding experiments: Implications for optical absorption and atmospheric lifetime, *Aerosol Sci. Technol.*, 41(8), 734–750, doi:10.1080/02786820701432632. 80

Stephens, M., N. Turner, and J. Sandberg (2003), Particle identification by laser-induced incandescence in a solid-state laser cavity, *Appl. Opt.*, 42(19), 3726–3736, doi:10.1364/AO.42.003726. 84

Stier, P., J. H. Seinfeld, S. Kinne, J. Feichter, and O. Boucher (2006), Impact of nonabsorbing anthropogenic aerosols on clear-sky atmospheric absorption, *J. Geophys. Res.*, 111, D18201, doi:10.1029/2006JD007147. 79

Strommen, M. R., and R. M. Kamens (1997), Development and application of a dual-impedance radial diffusion model to simulate the partitioning of semivolatile organic compounds in combustion aerosols, *Environ. Sci. Technol.*, 31(10), 2983–2990, doi:10.1021/es970079g. 80

Strommen, M. R., and R. M. Kamens (1999), Simulation of semivolatile organic compound micro-

transport at different time scales in airborne diesel soot particles, *Environ. Sci. Technol.*, 33(10), 1738–1746, doi:10.1021/es981035q. 80

Subramanian, R., et al. (2010), Black carbon over Mexico: the effect of atmospheric transport on mixing state, mass absorption cross-section, and BC/CO ratios, *Atmos. Chem. Phys.*, 10, 219–237, doi:10.5194/acp-10-219-2010. 79

Taylor, W. D., T. D. Allston, M. J. Moscato, G. B. Fazekas, R. Kozlowski, and G. A. Takacs (1980), Atmospheric photodissociation lifetimes for nitromethane, methyl nitrite, and methyl nitrate, *Int. J. Chem. Kinet.*, 12(4), 231–240, doi:10.1002/kin.550120404. 82

Toon, O. B., and T. P. Ackerman (1981), Algorithms for the calculation of scattering by stratified spheres, *Appl. Opt.*, 20(20), 3657–3660, doi:10.1364/AO.20.003657. 86

von Helden, G., M. T. Hsu, N. Gotts, and M. T. Bowers (1993), Carbon cluster cations with up to 84 atoms: structures, formation mechanism, and reactivity, *J. Phys. Chem.*, 97(31), 8182–8192, doi:10.1021/j100133a011. 98

Wehner, B., et al. (2009), Mixing state of nonvolatile aerosol particle fractions and comparison with light absorption in the polluted Beijing region, *J. Geophys. Res.*, 114, D00G17, doi:10.1029/2008JD010923. 79

Weiner, A. M., and S. J. Harris (1989), Optical detection of large soot precursors, *Combust. Flame*, 77(3–4), 261–266, doi:10.1016/0010-2180(89)90133-8. 93

Weingartner, E., H. Burtscher, and U. Baltensperger (1997), Hygroscopic properties of carbon and diesel soot particles, *Atmos. Environ.*, 31(15), 2311–2327, doi:10.1016/S1352-2310(97)00023-X. 79

Weitkamp, E. A., A. M. Sage, J. R. Pierce, N. M. Donahue, and A. L. Robinson (2007), Organic aerosol formation from photochemical oxidation of diesel exhaust in a smog chamber, *Environ. Sci. Technol.*, 41(20), 6969–6975, doi:10.1021/es070193r. 80

Wonaschütz, A., R. Hitzenberger, H. Bauer, P. Pouresmaeil, B. Klatzer, A. Caseiro, and H. Puxbaum (2012), Application of the integrating sphere method to separate the contributions of brown and black carbon in atmospheric aerosols, *Environ. Sci. Technol.*, 43(4), 1141–1146, doi:doi:10.1021/es8008503. 93

Yu, Y., et al. (2008), Photooxidation of α -pinene at high relative humidity in the presence of increasing concentrations of NO_x , *Atmos. Environ.*, 42(20), 5044–5060, doi:10.1016/j.atmosenv.2008.02.026. 96

Zhang, R., A. F. Khalizov, J. Pagels, D. Zhang, H. Xue, and P. H. McMurry (2008), Variability in morphology, hygroscopicity, and optical properties of soot aerosols during atmospheric processing, *Proc. Natl. Acad. Sci. U.S.A.*, 105(30), 10,291–10,296, doi:10.1073/pnas.0804860105. 79, 80

Zuberi, B., K. S. Johnson, G. K. Aleks, L. T. Molina, and M. J. Molina (2005), Hydrophilic properties of aged soot, *Geophys. Res. Lett.*, 32, L01807, doi:10.1029/2004GL021496. 79

Table 3.1: Summary of Experiments.

Experiment Number	[HC] _o [ppb]	OH source	Seed	Seed Volume ^a [μm ³ cm ⁻³]	SOA Mass [μg m ⁻³]	Description
<i>naphthalene</i>						
1	16.6 ± 0.1	CH ₃ ONO ^b	rBC ^c	10.1 ± 0.7	6.5 ± 0.10	SOA condensation followed by chamber dilution
2	10.7 ± 0.1	CH ₃ ONO	AS ^d + rBC	34.4 ± 2.8	7.1 ± 0.07	SOA condensation with seed competition followed by chamber dilution
3	21.9 ± 0.1	CH ₃ ONO	SOA ^d	43.6 ± 0.5	—	SOA nucleation with rBC injection and coagulation
4	27.5 ± 0.1	CH ₃ ONO	SOA + rBC	62.3 ± 1.5	11.0 ± 0.17 ^f	SOA nucleation followed by rBC injection and SOA growth then chamber dilution
<i>α-pinene</i>						
5	27.0 ± 0.1	CH ₃ ONO	rBC	14.4 ± 0.5	14.6 ± 0.35 ^g	SOA condensation followed by chamber dilution
6	24.1 ± 0.1	CH ₃ ONO	AS + rBC	28.9 ± 1.1	4.7 ± 0.18	SOA condensation with seed competition followed by chamber dilution
7	10.8 ± 0.2	H ₂ O ₂ ^h	rBC	18.2 ± 1.0	11.5 ± 0.06	SOA condensation followed by chamber dilution
8	11.6 ± 0.2	H ₂ O ₂	AS + rBC	32.6 ± 1.5	8.1 ± 0.07	SOA condensation with seed competition followed by chamber dilution
9	18.0 ± 0.1	H ₂ O ₂	SOA + rBC	28.2 ± 1.0	24.9 ± 0.33 ^f	SOA nucleation followed by rBC injection and SOA growth then chamber dilution

^a Calculated from DMA data assuming spherical particles.^b CH₃ONO was used for high-NO_x experiments, to which extra NO was added prior to irradiation to bring [NO]_o to 369–416 ppb.^c rBC = fullerene soot aerosol.^d AS = ammonium sulfate aerosol.^e SOA = nucleated SOA prior to rBC injection.^f SOA mass after the second growth period with SOA mass from the first period subtracted.^g Measurement taken after some evaporation of SOA had occurred.^h H₂O₂ was used for low-NO_x experiments, to which no extra NO was added prior to irradiation and [NO]_o was 1.5–2.6 ppb prior to irradiation.

Table 3.2: Summary of Non-Sphericity Values.

Particle Type	Mean Non-sphericity ($\pm 1\sigma$)
BC	0.353 ± 0.042
NaCl	0.303 ± 0.057
AS	0.173 ± 0.091
Oxalic Acid	0.150 ± 0.030
PSL	0.070 ± 0.029

Table 3.3: Optical Properties of Particles in this Study (mean $\pm 1\sigma$).

	λ	Fullerene soot	Ammonium sulfate	naphthalene SOA	α -pinene SOA ^a
MSC ^b [m ² g ⁻¹]	405 nm	11.49 \pm 0.42	35.63 \pm 2.38	27.50 \pm 1.50 ^c	13.43 \pm 0.19 ^c
	532 nm	6.64 \pm 0.45	29.79 \pm 0.57		
	781 nm	5.68 \pm 0.34	14.75 \pm 1.02	3.18 \pm 0.68	1.28 \pm 0.074
MAC ^e [m ² g ⁻¹]	405 nm	27.67 \pm 1.39	< 3.03 ^d	2.66 \pm 0.13 ^c	< 2.65 ^d ^c
	532 nm	12.57 \pm 0.30	< 8.48 ^d		
	781 nm	10.77 \pm 0.32	< 0.49 ^d	< 0.22 ^d	< 0.42 ^d
ω_0 ^f	405 nm	0.29 \pm 0.0041	1.00 \pm 0.0065	0.91 \pm 0.012 ^c	1.00 \pm 0.012 ^c
	532 nm	0.34 \pm 0.018	0.98 \pm 0.027		
	781 nm	0.35 \pm 0.0087	0.99 \pm 0.0018	0.99 \pm 0.0018	0.94 \pm 0.026

^a Low-NO_x experiment.^b MSC = mass scattering cross section.^c 532 nm laser malfunction in the PASS-3 instrument; data on this channel are unusable.^d Absorption coefficient (b_{abs}) measurements are at or below detection limit on PASS-3.^e MAC = mass absorption cross section.^f ω_0 = single-scatter albedo.

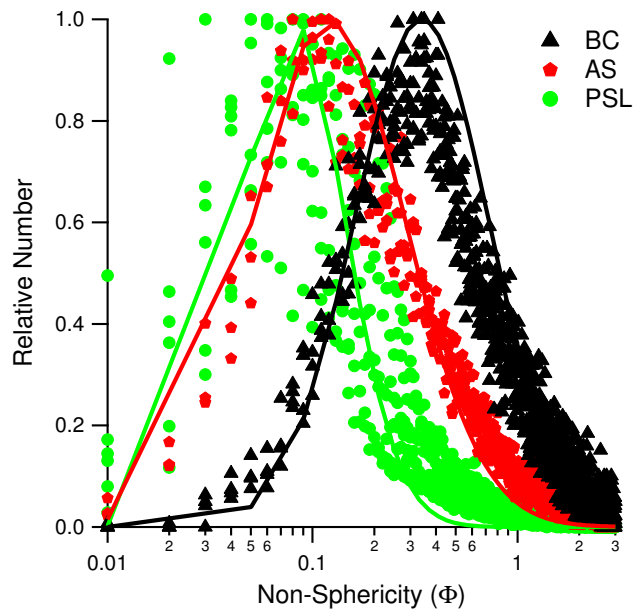


Figure 3.1: Distributions of non-sphericity values for ammonium sulfate (AS), fullerene soot (BC) particles, and polystyrene latex spheres (PSL). Each distribution represents $\sim 10,000$ particles sampled at various times throughout the respective experiments. “Relative number” is the number of particles in each bin divided by the maximum number in any bin for the given distribution. Solid lines denote a lognormal fit to a single distribution; only one fit per particle type is shown. Mean non-sphericity values corresponding to lognormal fits to all distributions are given in Table 3.2.

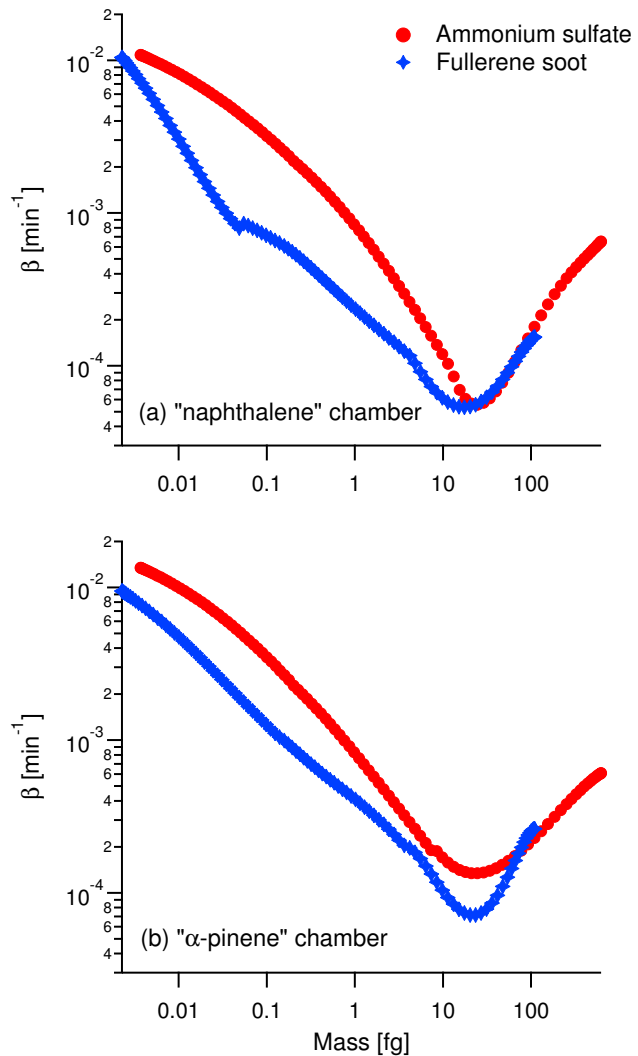


Figure 3.2: Particle wall deposition rate coefficients, β , for the two chambers with ammonium sulfate and fullerene soot as the seed particles. Data are displayed by single-particle mass rather than mobility diameter to directly compare AS and BC. Ammonium sulfate mass is calculated from mobility diameter assuming a spherical particle and a density of 1.77 g cm^{-3} . Fullerene soot mass is calculated from mobility diameter using the relation reported by *Gysel et al. (2011)*.

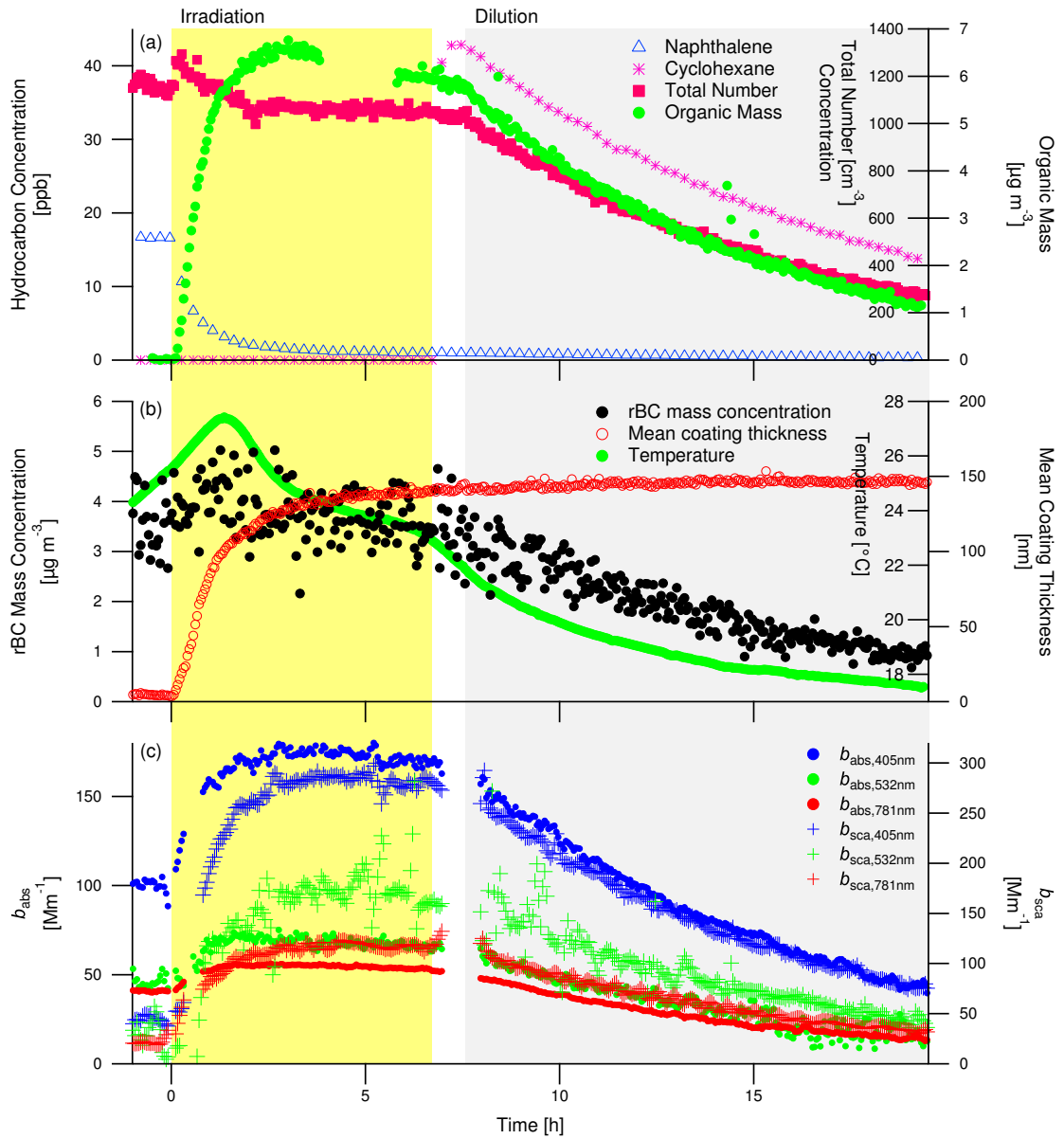


Figure 3.3: Experiment 1, naphthalene photooxidation in the presence of rBC seed particles. The yellow shaded region denotes the irradiation of the chamber; the gray shading denotes chamber dilution. Mean coating thickness reported in Figure 3.3b is for 160–180 nm rBC VED core particles.

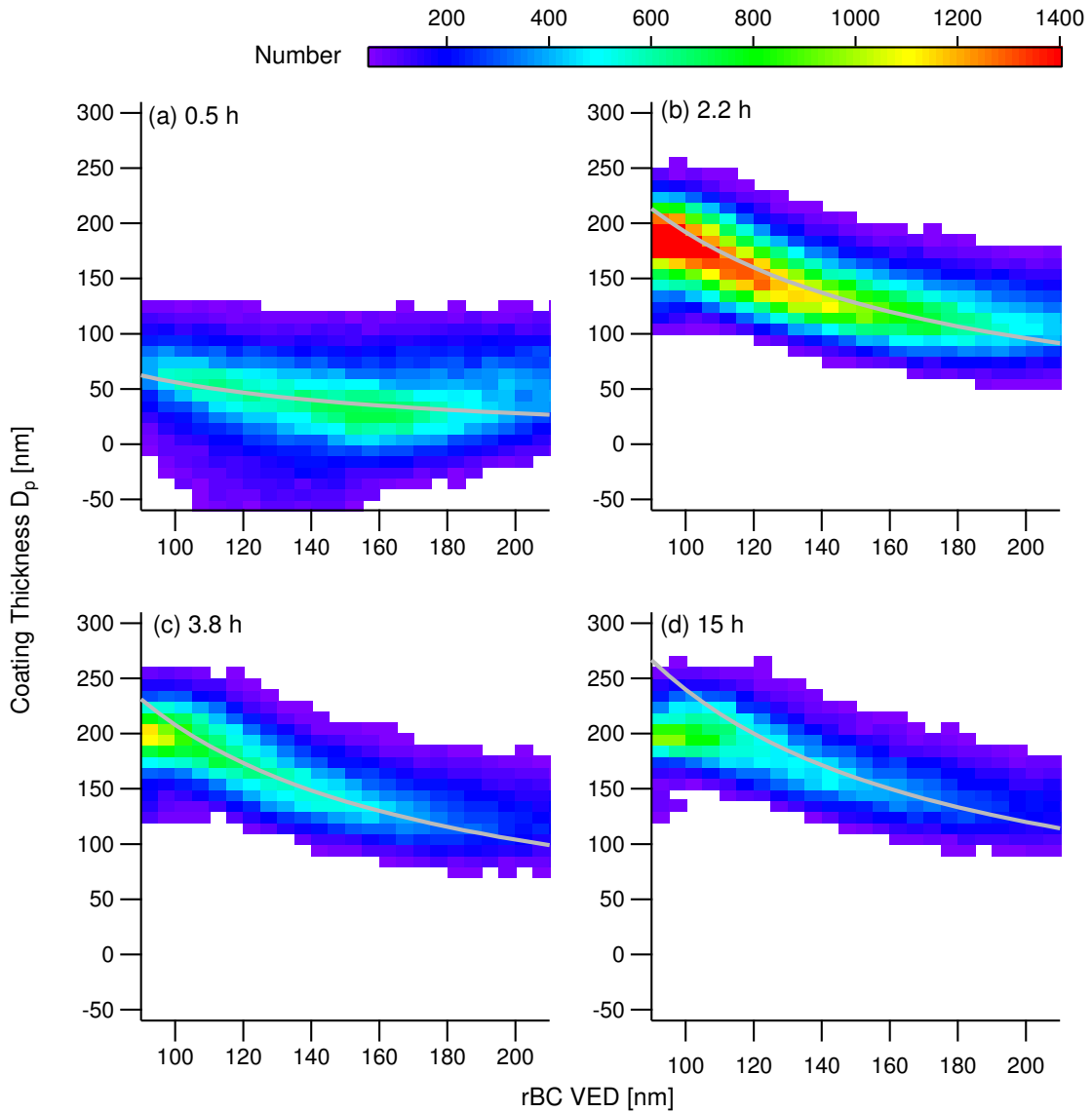


Figure 3.4: Evolution of coating thickness in Experiment 1 presented as 2-D histograms of coating thickness, detected by fitting the SP2 scattering signal to a core-and-shell Mie model, versus rBC volume-equivalent diameter. The times are in hours after the onset of irradiation. The gray lines are diffusion-controlled growth laws matched to the coating thickness diameter at an rBC VED of 160 nm.

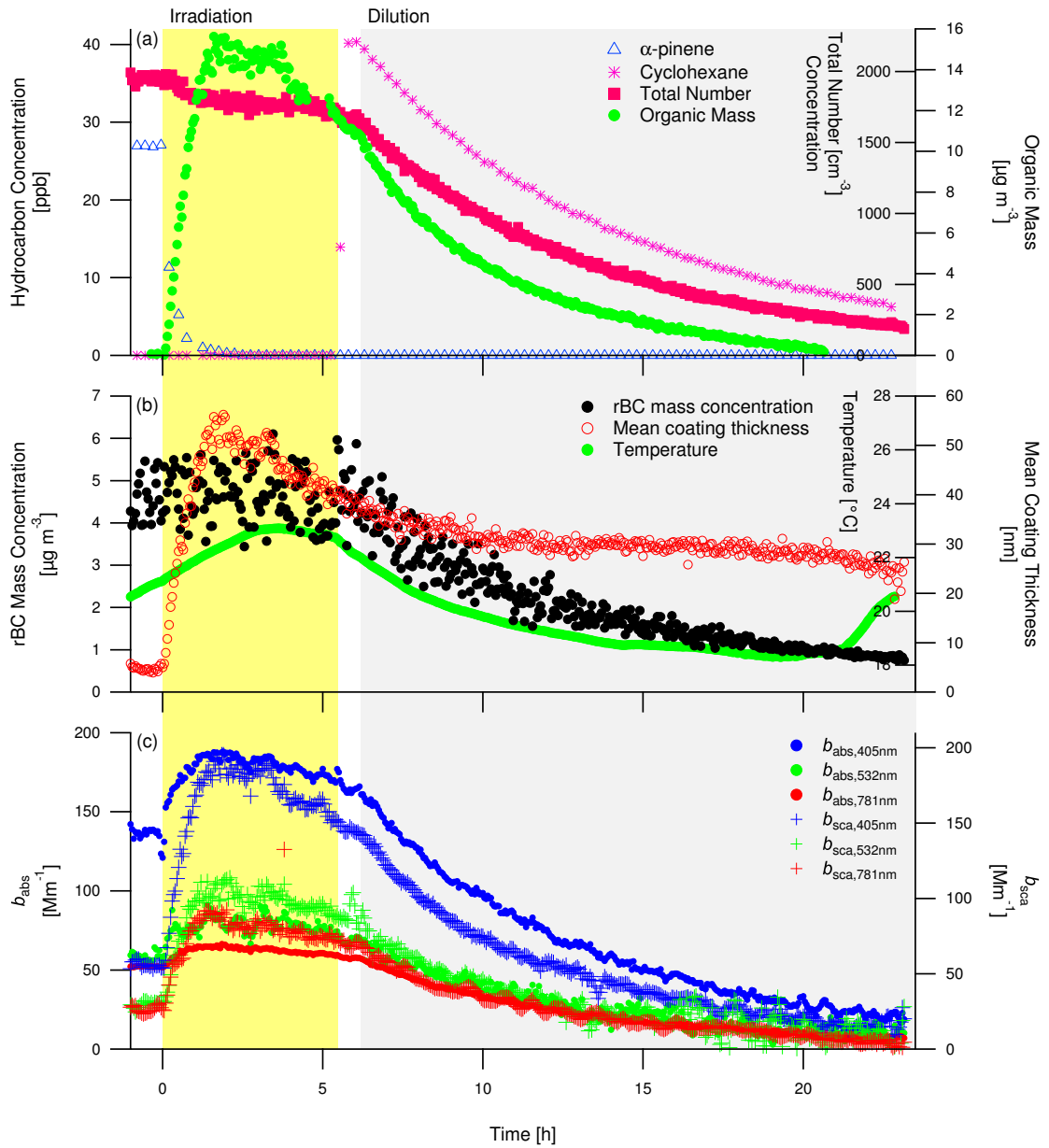


Figure 3.5: Experiment 5, high- NO_x α -pinene photooxidation in the presence of rBC seed particles. The yellow shaded region denotes the irradiation of the chamber; the gray shading denotes chamber dilution. Mean coating thickness reported in Figure 3.5b is for 160–180 nm rBC VED core particles.

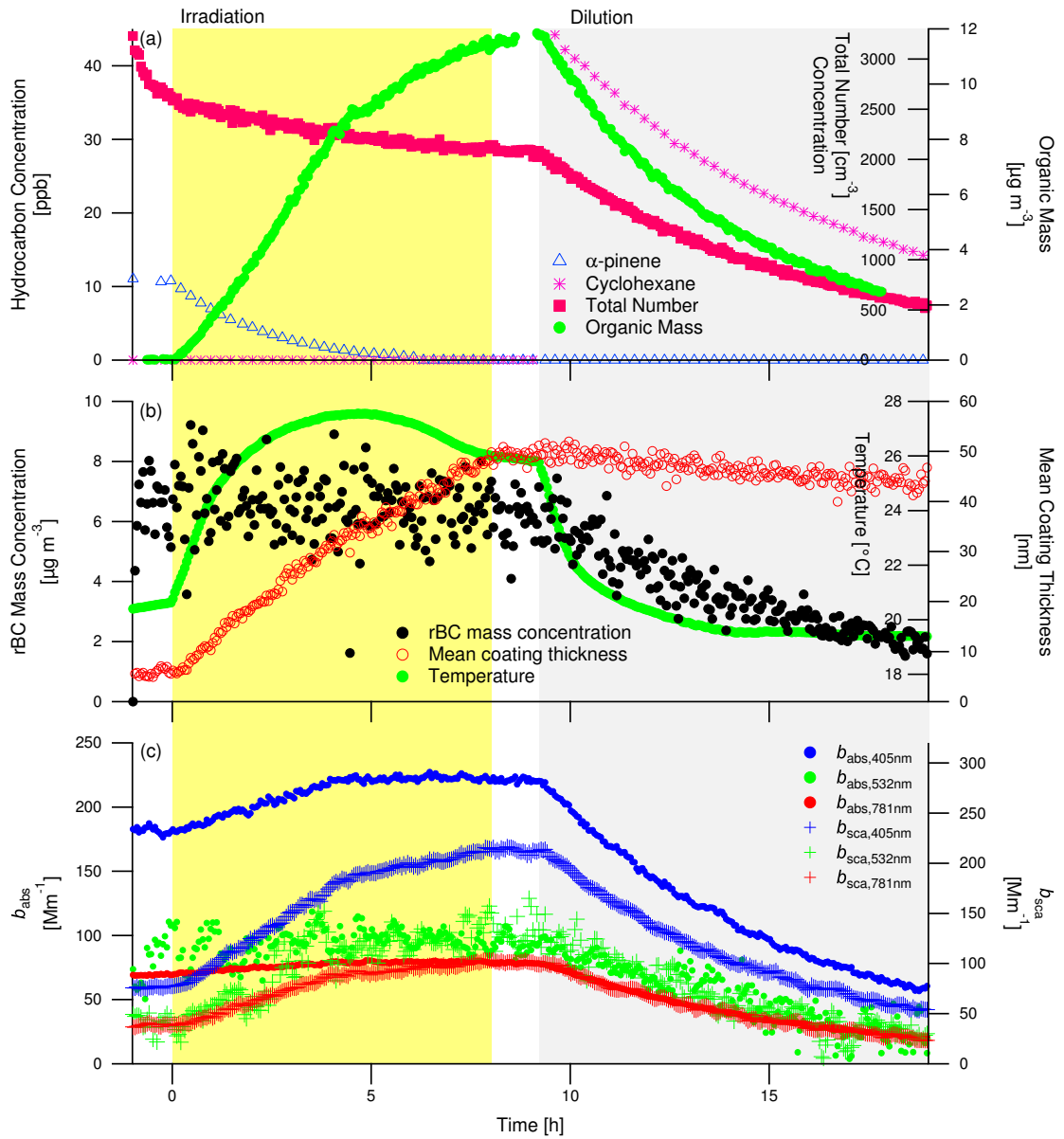


Figure 3.6: Experiment 7, low- NO_x α -pinene photooxidation in the presence of rBC seed particles. The yellow shaded region denotes the irradiation of the chamber; the gray shading denotes chamber dilution. Mean coating thickness reported in Figure 3.6b is for 160–180 nm rBC VED core particles.

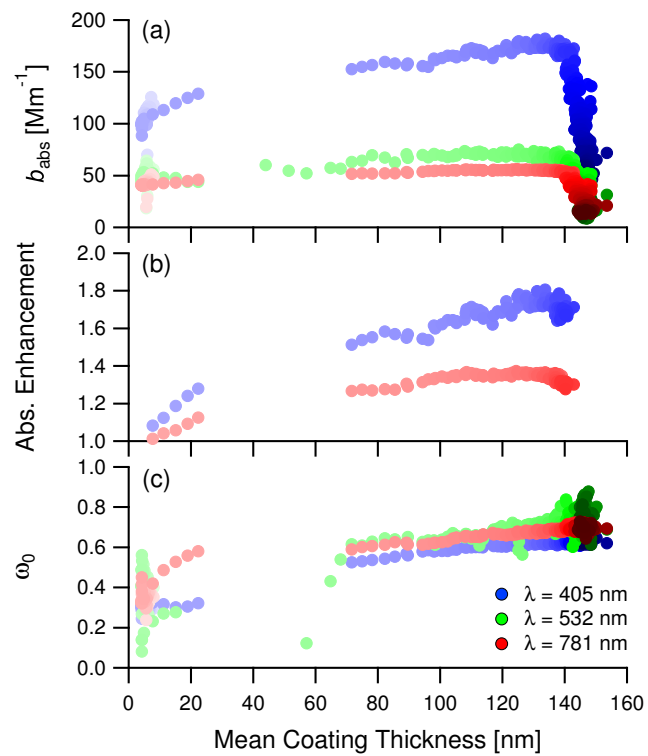


Figure 3.7: Optical properties as a function of mean coating thickness on the fullerene soot seed during Experiment 1, naphthalene photooxidation. Marker shading is a function of time after onset of irradiation, with later times indicated by darker colors. Absorption enhancement (Figure 3.7b) is presented for the irradiation time period only.

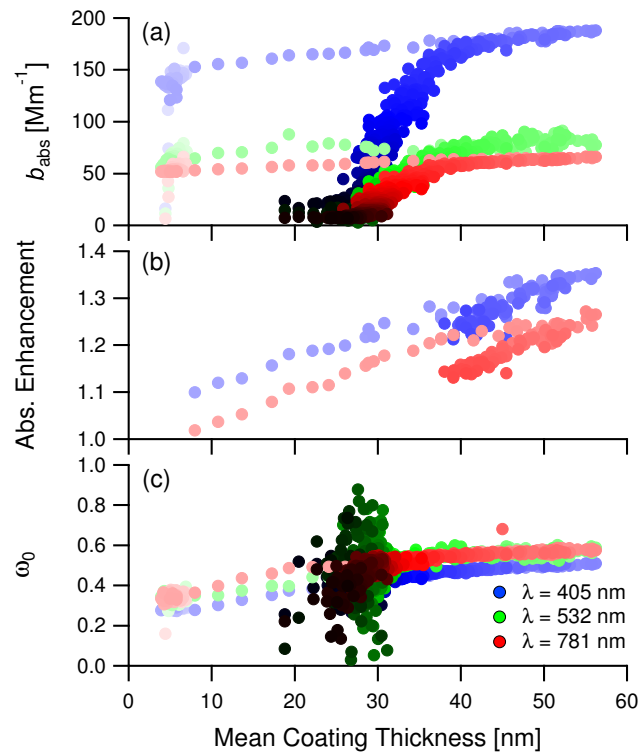


Figure 3.8: Optical properties as a function of mean coating thickness on the fullerene soot seed during Experiment 5, high- NO_x α -pinene photooxidation. Marker shading is a function of time after onset of irradiation, with later times indicated by darker colors. Absorption enhancement (Figure 3.8b) is presented for the irradiation time period only.

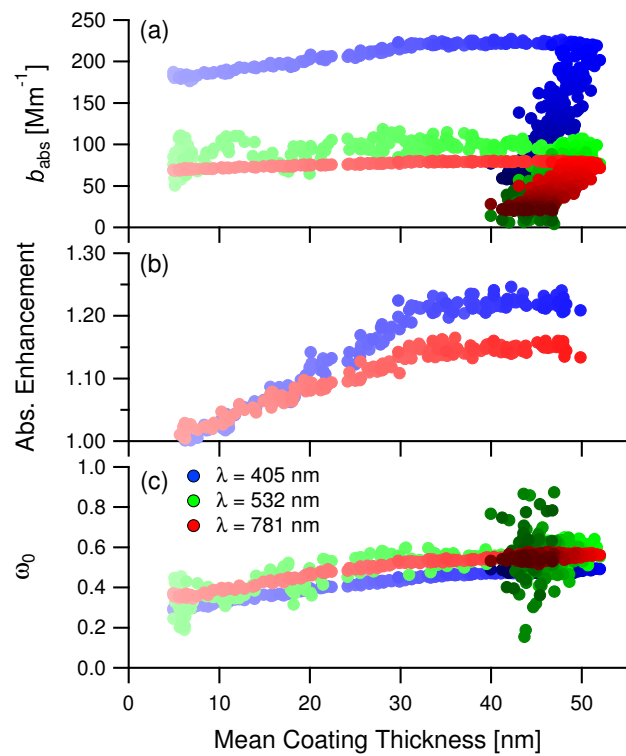


Figure 3.9: Optical properties as a function of mean coating thickness on the fullerene soot seed during Experiment 7, low- NO_x α -pinene photooxidation. Marker shading is a function of time after onset of irradiation, with later times indicated by darker colors. Absorption enhancement (Figure 3.9b) is presented for the irradiation time period only.

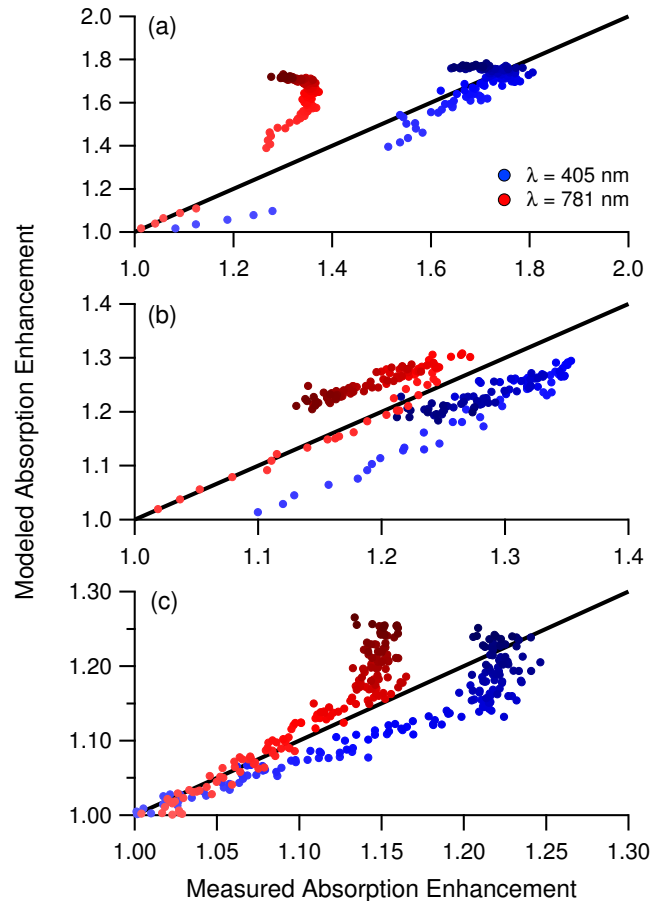
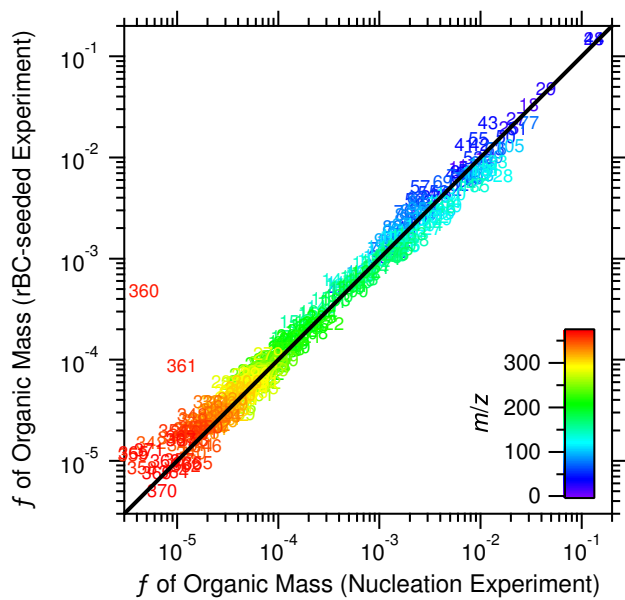


Figure 3.10: Comparison of Mie-modeled absorption enhancement to measured absorption enhancement. Enhancements are calculated relative to the values measured for the fullerene soot seed particles prior to irradiation. The measurements are enhancements of b_{abs} at $\lambda = 405$ nm and $\lambda = 781$ nm measured by the PASS-3. The Mie model enhancements are calculated by the increase in absorption cross section using a 170 nm rBC core with the mean coating thickness on 160–180 nm rBC cores measured by the SP2. Results for (a) Experiment 1, naphthalene photooxidation, (b) Experiment 5, high- NO_x α -pinene photooxidation, and (c) Experiment 7, low- NO_x α -pinene photooxidation are presented. Marker shading is a function of time after onset of irradiation, with later times indicated by darker colors. Data during chamber irradiation only are shown. The solid line is a 1-to-1 line.



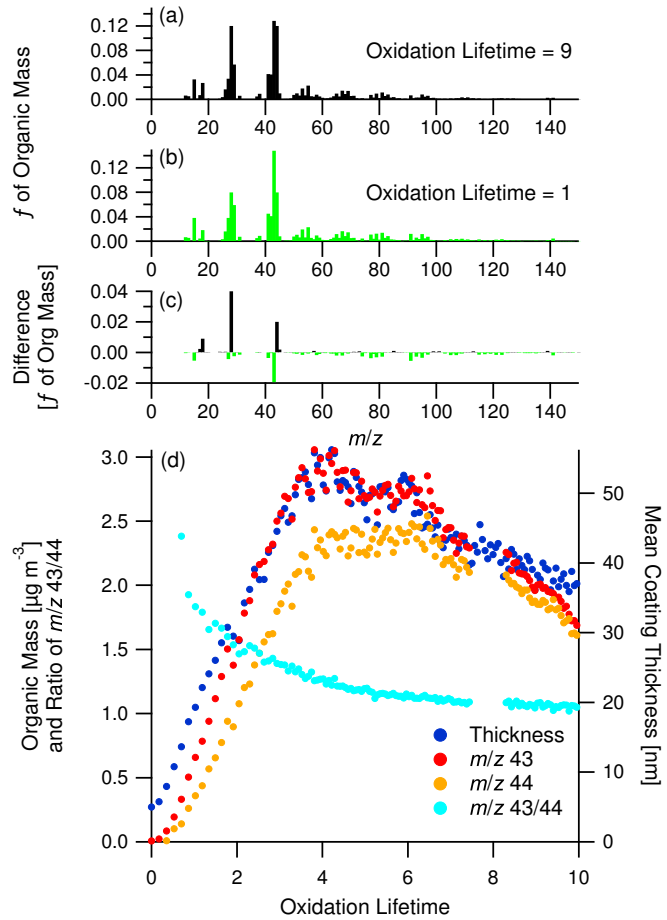


Figure 3.12: Normalized unit-mass resolution AMS organic mass spectra from Experiment 5, high- NO_x α -pinene photooxidation in the presence of fullerene soot, at (a) oxidation lifetime = 9 (after peak growth has been reached) and (b) oxidation lifetime = 1 (during rapid growth), (c) the difference spectrum, calculated relative to the earlier mass spectrum, and (d) comparison of AMS m/z 43 and 44 and ratio of m/z 43/44 with mean coating thickness measured by the SP2. On the difference spectrum, positive values (in black) denote m/z 's enriched in the later condensed SOA and negative values (in green) denote m/z 's enriched in the earliest condensed SOA. Note that dilution of the chamber began at an oxidation lifetime of approximately 9.5.

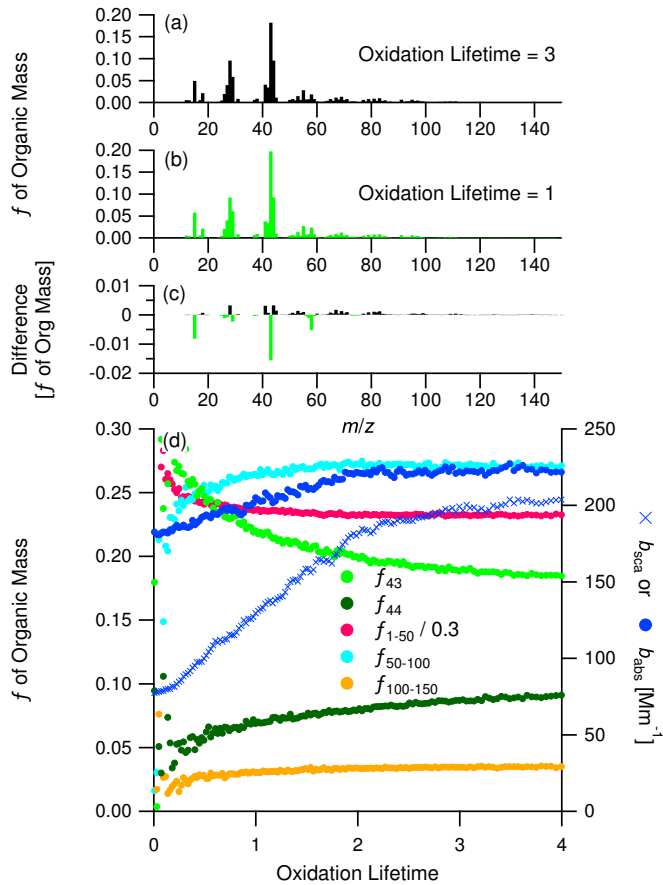


Figure 3.13: Normalized unit-mass resolution AMS organic mass spectra from Experiment 7, low- NO_x α -pinene photooxidation in the presence of fullerene soot, at (a) an oxidation lifetime = 3 (during the slower growth rate after the shift in optical properties) and (b) an oxidation lifetime = 1 (during the more rapid growth rate before the change in optical properties), (c) the difference spectrum, calculated relative to the earlier mass spectrum, and (d) comparison of f_{43} , f_{44} , f_{1-50} , f_{50-100} , and $f_{100-150}$ from the AMS with the scattering and absorption coefficients at $\lambda = 405$ nm measured by the PASS-3. On the difference spectrum, positive values (in black) denote m/z 's enriched in the later condensed SOA and negative values (in green) denote m/z 's enriched in the earliest condensed SOA.

Chapter 4

Future Work

Black carbon aerosol is an important contribution to climate warming, the magnitude of which depends on the mixing state of the BC with other species in the atmosphere. The thesis presents measurements of BC mixing state in the Los Angeles atmosphere and shows the evolution during transport through the LA Basin (see Chapter 2). BC aerosol above the inversion layer was found to be distinctly different than the BC aerosol near the surface. The LA “weekend effect” had a profound influence on the coatings on BC aerosol while having a minimal effect on the mass of BC present in the atmosphere. The LA outflow regions were characterized by having two distinct modes of coated BC aerosol, one of smaller BC cores with thicker coatings and one of larger BC cores with much thinner coatings. A remaining question from this ambient study is; What is the mechanism causing these two modes of coated BC cores observed in the outflows?

A controlled study of SOA growth onto BC particles is presented in Chapter 3. In this study, it was shown that SOA growth onto fractal BC particles is diffusion-limited, which was clearly not seen in the ambient BC in the LA outflows (or else there would have been just one mode of coated BC cores). Clearly, future work must be done to identify the mechanisms governing coated BC behavior in Los Angeles.

Chapter 3 laid the groundwork for future environmental chamber studies using BC seed particles. Because the BC seed does not effect SOA composition or the diffusion-limited growth, BC seed aerosol may be used for a wide variety of parent hydrocarbons where direct measurements of coating thickness by an SP2 instrument can provide valuable information on SOA volatility. The additional measurements afforded by the SP2 and PASS-3 instruments during this chamber study provided evidence of multiple generations of photooxidation products that may have been missed with the more traditional suite of instruments commonly used in these studies. The enhancement of absorption and scattering properties of the BC seed particles due to the growth of organic layers provide further evidence that the mixing state of BC aerosols in the atmosphere will have a profound impact on the climate forcing potential of these particles.

Despite these findings, there are a number of important inquiries regarding BC aerosol in the atmosphere left to be made. As stated above, the exact mechanism causing the two modes of

coated BC aerosol in the LA Basin Outflows is still unknown. Direct measurement of coated BC aerosol is a relatively recent development, and, thus, more ambient measurements are needed to better constrain global models of BC aerosol behavior. Additional environmental chamber studies or controlled experiments in a flow reactor are needed to elucidate BC aerosol interactions with different organic and inorganic compounds commonly found in the atmosphere. There is still a question of applicability of the core-and-shell model for coated BC to all atmospheric conditions where BC is mixed with other species. And finally, despite the fact that the SP2 is able to provide the first direct, *in situ* measurements of coating thickness on single BC particles, the detection limits on the instrument are still rather restrictive. The lower detection limit of the SP2 in usual configurations does not permit detection of particles smaller than \sim 180 nm in optical diameter, which approximately translates to a 100 nm diameter BC core surrounded by a 50 nm thick shell of a light-scattering material. This limitation restricts measurements of the full mixing state of BC particles, that is, of coated and uncoated BC, to those with BC cores larger than \sim 150 nm. SP2 data reveals that the majority of BC particles, by number, have cores smaller than \sim 150 nm in diameter. It is not yet known how representative the coatings on larger BC cores are of the entire population of BC in the atmosphere.

Appendix A

The Pasadena Aerosol Characterization Observatory (PACO): Chemical and Physical Analysis of the Western Los Angeles Basin Aerosol*

*Reproduced with permission from “The Pasadena Aerosol Characterization Observatory (PACO): chemical and physical analysis of the Western Los Angeles basin aerosol” by S. P. Hersey, J. S. Craven, K. A. Schilling, A. R. Metcalf, A. Sorooshian, M. N. Chan, R. C. Flagan, and J. H. Seinfeld, *Atmospheric Chemistry and Physics*, 11, 7417–7443, doi:10.5194/acp-11-7417-2011. Copyright 2011 by the Authors. This work is distributed under the Creative Commons Attribution 3.0 License.

The Pasadena Aerosol Characterization Observatory (PACO): chemical and physical analysis of the Western Los Angeles basin aerosol

S. P. Hersey¹, J. S. Craven², K. A. Schilling², A. R. Metcalf¹, A. Sorooshian³, M. N. Chan¹, R. C. Flagan^{1,2}, and J. H. Seinfeld^{1,2}

¹Division of Engineering and Applied Science, California Institute of Technology, Pasadena, CA, USA

²Division of Chemistry and Chemical Engineering, California Institute of Technology, Pasadena, CA, USA

³Department of Chemical and Environmental Engineering, University of Arizona, Tucson, AZ, USA

Received: 3 February 2011 – Published in Atmos. Chem. Phys. Discuss.: 18 February 2011

Revised: 16 June 2011 – Accepted: 25 June 2011 – Published: 1 August 2011

Abstract. The Pasadena Aerosol Characterization Observatory (PACO) represents the first major aerosol characterization experiment centered in the Western/Central Los Angeles Basin. The sampling site, located on the campus of the California Institute of Technology in Pasadena, was positioned to sample a continuous afternoon influx of transported urban aerosol with a photochemical age of 1–2 h and generally free from major local contributions. Sampling spanned 5 months during the summer of 2009, which were broken into 3 regimes on the basis of distinct meteorological conditions. Regime I was characterized by a series of low pressure systems, resulting in high humidity and rainy periods with clean conditions. Regime II typified early summer meteorology, with significant morning marine layers and warm, sunny afternoons. Regime III was characterized by hot, dry conditions with little marine layer influence. Regardless of regime, organic aerosol (OA) is the most significant constituent of nonrefractory submicron Los Angeles aerosol (42, 43, and 55 % of total submicron mass in regimes I, II, and III, respectively). The overall oxidation state remains relatively constant on timescales of days to weeks (O:C = 0.44 ± 0.08, 0.55 ± 0.05, and 0.48 ± 0.08 during regimes I, II, and III, respectively), with no difference in O:C between morning and afternoon periods. Periods characterized by significant morning marine layer influence followed by photochemically favorable afternoons displayed significantly higher aerosol mass and O:C ratio, suggesting that aqueous processes may

be important in the generation of secondary aerosol and oxidized organic aerosol (OOA) in Los Angeles. Online analysis of water soluble organic carbon (WSOC) indicates that water soluble organic mass (WSOM) reaches maxima near 14:00–15:00 local time (LT), but the percentage of AMS organic mass contributed by WSOM remains relatively constant throughout the day. Sulfate and nitrate reside predominantly in accumulation mode aerosol, while afternoon SOA production coincides with the appearance of a distinct fine mode dominated by organics. Particulate NH_4NO_3 and $(\text{NH}_4)_2\text{SO}_4$ appear to be NH_3 -limited in regimes I and II, but a significant excess of particulate NH_4^+ in the hot, dry regime III suggests less SO_4^{2-} and the presence of either organic amines or NH_4^+ -associated organic acids. C-ToF-AMS data were analyzed by Positive Matrix Factorization (PMF), which resolved three factors, corresponding to a hydrocarbon-like OA (HOA), semivolatile OOA (SV-OOA), and low-volatility OOA (LV-OOA). HOA appears to be a periodic plume source, while SV-OOA exhibits a strong diurnal pattern correlating with ozone. Peaks in SV-OOA concentration correspond to peaks in DMA number concentration and the appearance of a fine organic mode. LV-OOA appears to be an aged accumulation mode constituent that may be associated with aqueous-phase processing, correlating strongly with sulfate and representing the dominant background organic component. Periods characterized by high SV-OOA and LV-OOA were analyzed by filter analysis, revealing a complex mixture of species during periods dominated by SV-OOA and LV-OOA, with LV-OOA periods characterized by shorter-chain dicarboxylic acids (higher O:C ratio), as well as appreciable amounts of nitrate- and



Correspondence to: J. H. Seinfeld
(jseinfeld@caltech.edu)

sulfate-substituted organics. Phthalic acid was ubiquitous in filter samples, suggesting that PAH photochemistry may be an important SOA pathway in Los Angeles. Aerosol composition was related to water uptake characteristics, and it is concluded that hygroscopicity is largely controlled by organic mass fraction (OMF). The hygroscopicity parameter κ averaged 0.31 ± 0.08 , approaching 0.5 at low OMF and 0.1 at high OMF, with increasing OMF suppressing hygroscopic growth and increasing critical dry diameter for CCN activation (D_d). An experiment-averaged κ_{org} of 0.14 was calculated, indicating that the highly-oxidized organic fraction of aerosol in Los Angeles is appreciably more hygroscopic than previously reported in urban areas. Finally, PACO will provide context for results forthcoming from the CalNex field campaign, which involved ground sampling in Pasadena during the spring and summer of 2010.

1 Introduction

Over half the world's population lives in urban areas, and that fraction is expected to increase in coming decades (Bremner et al., 2009). There have been a number of recent coordinated studies focused on characterizing particulate air quality in major urban areas, such as Pittsburgh, PA (Pittsburgh Air Quality Study, PAQS; e.g., Pekney et al., 2006; Bein et al., 2006; Wittig et al., 2004; Cabada et al., 2004; Modey et al., 2004), Los Angeles, CA (Southern California Air Quality Study, SCAQS; e.g., Eldering et al., 1994; Watson et al., 1994; Chow et al., 1994; Turpin and Huntzicker, 1991; Southern California Ozone Study 1997, SCOS97-NARSTO; e.g., Croes and Fujita, 2003; Liu et al., 2000; Pastor et al., 2003; Hughes et al., 2002; Secondary Organic Aerosol in Riverside, SOAR; e.g., Docherty et al., 2008; Eatough et al., 2008; Denkenberger et al., 2007), Mexico City, Mexico (Megacity Initiative: Local and Global Research Observations, MILAGRO; e.g., DeCarlo et al., 2008; Stone et al., 2008; Aiken et al., 2009), and Beijing, China (Campaign of Air Quality Research in Beijing, CAREBEIJING; e.g., Matsui et al., 2009; Yue et al., 2009; van Pinxteren et al., 2009).

The Los Angeles metropolitan area, with a population of over 17 million people, has long been considered a laboratory for air quality. Once the quintessential example of classic photochemical smog, the Los Angeles area has, as a result of decades of aggressive emission controls, reached a point where 8-h US National Ambient Air Quality Standard ozone exceedances have decreased from over 200 days/year in the 1980s to 120 in 2008 (AQMD, 2010). Nonetheless, this area remains one in which particulate matter levels continue to regularly exceed air quality standards, with annual PM_{2.5} averages exceeding the national standard every year from 2000–2008 in Los Angeles County (CARB, 2010).

The Los Angeles Basin is generally characterized as source-rich in its western area, with prevailing west and

southwest winds transporting emissions downwind toward the east and northeast (Lu and Turco, 1995). Three major coordinated studies have been undertaken to characterize Los Angeles air quality, in addition to ongoing work to describe facets of Los Angeles aerosol (Table 1). The majority of previous studies in the Los Angeles Basin have been centered in the downwind, eastern part of the basin, roughly 60 km east of downtown Los Angeles. The aerosol in this region is predominantly aged, with local contributions as well.

A major source of gaseous and particulate pollution in the Los Angeles area is mobile source emissions. The Los Angeles aerosol undergoes dramatic evolution from night-time/morning periods to the photochemically active afternoon, characterized by changes in both its microphysical properties and composition. Overall, the submicron aerosol is dominated by organic aerosol (OA), which is predominantly secondary in origin (SOA), and nitrate (Docherty et al., 2008), with smaller amounts of sulfate and a minor chloride contribution. Primary marine and secondary sulfate aerosol are expected to contribute a relatively uniform loading of sulfate across the Los Angeles Basin (Watson et al., 1994). Marine sulfate is expected to be contributed by natural primary processes (biological, sea spray, bubble bursting), with anthropogenic shipping-related emissions contributing a varied and often significant loading of sulfate (Ault et al., 2010).

The Pasadena Aerosol Characterization Observatory experiment (PACO) was conducted from May–August 2009 in Pasadena, CA, in the north-central/north-western portion of the Los Angeles Basin, 16 km NE of downtown Los Angeles. Aerosol physics, composition, and hygroscopicity were measured during 54 days that spanned three distinct regimes of the annual meteorological cycle. A major forest fire occurred at the end of the sampling period, starting on 26 August and consuming over 160 000 acres of the Angeles National Forest before containment on 16 October. Named the "Station Fire", its southernmost extent was roughly 8 km from the sampling site, and emissions from the fire impacted the sampling site with periodic heavy smoke, soot, and ash. Results from PACO sampling during the Station Fire will be presented in subsequent work.

PACO represents the first prolonged experiment aimed at characterizing the aerosol near the source-rich western/central part of the Los Angeles basin; comparisons with previous studies in downwind areas will help determine the rate of aerosol generation from Los Angeles sources, as well as the nature of aerosol transformations with downwind transport. Further, the PACO study was well-timed to precede the 2010 CalNex field campaign (<http://www.esrl.noaa.gov/csd/calnex/>).

This paper presents an overview of the PACO experiment. Aerosol number and volume distributions measured by a differential mobility analyzer (DMA) exhibit distinct diurnal patterns, and composition data from an Aerodyne Compact-Time-of-Flight Aerosol Mass Spectrometer (C-ToF AMS)

Table 1. Previous Los Angeles air quality studies and major findings relative to particulate matter.

Study	Date	Major aerosol findings
Southern California Air Quality Study (SCAQS)	Summer/ fall 1987	- SOA/OA ~ 40 % in summer afternoon (Turpin and Huntzicker, 1991) - Primary vehicle exhaust is the major aerosol component near PACO sampling site (Watson et al., 1994) - 20- 32 % of PM ₁₀ is SO ₄ ²⁻ and NO ₃ ⁻ (Watson et al., 1994)
Southern California Ozone Study (SCOS97-NARSTO)	Summer 1997	- Submicron organic mode evolves during periods of intense photochemistry, coincident with maximum O ₃ (Pastor et al., 2003) - NH ₄ NO ₃ and organics added to submicron aerosol with photochemical age (Pastor et al., 2003) - NH ₃ sources in eastern basin enhance particulate NH ₄ NO ₃ (Hughes et al., 2002)
Secondary Organic Aerosol in River-side (SOAR-1, 2)	Aug, Nov 2005	- Significant diurnal changes in organic aerosol, with species more reduced in the morning and more oxidized in the afternoon (DeCarlo et al., 2006) - Oligomers detected in aged, acidic particles (Denkenberger et al., 2007) - SOA/OA = 70- 90 % at midday and ~ 45 % during morning commute; SOAR average = 74 % (Docherty et al., 2008)
Individual studies	1999, 2001- 2002	- Complex, multi-modal GF data in Pasadena (Cocker et al., 2001) - SOA > 50 % of total PM _{2.5} in eastern basin (Sawant et al., 2004; Na et al., 2004)

indicate that these patterns are associated largely with the production of semivolatile oxidized organic species during photochemically active daytime periods. AMS-based Positive Matrix Factorization (PMF) results indicate that the character of OA in Los Angeles is overwhelmingly oxidized and secondary, and the high time resolution data allow for investigation of the daily evolution of OA components. Ultra Performance Liquid Chromatography/Electrospray Ionization Time-of-Flight High-Resolution Mass Spectrometry (UPLC/ESI-TOFMS) analysis of high-volume filter samples provides further evidence for diurnal changes in the character of OA, while thermal-optical analysis of low-volume, denuded filter samples reveals the magnitude of organic and elemental carbon in morning versus afternoon sampling periods. A particle-into-liquid sampler with offline ion chromatography analysis (PILS-IC) provides quantitative water-soluble inorganic ion composition during PACO, while a PILS coupled with online total organic carbon analysis (PILS-TOC) measured total water soluble organic carbon measurements during the third regime. Finally, trends in aerosol hygroscopicity indicate the degree to which changes in the magnitude and character of OA affect particle water uptake. PACO results are compared with previous aerosol characterization experiments in the Los Angeles Basin, with major differences attributed to regional variations in both source profiles and degree of aging.

2 Methods

Sampling was conducted on the Caltech campus in Pasadena, at 34.138° N, 118.124° W. Caltech is located in the west-

ern/central portion of the Los Angeles Basin, 8 km south of the San Gabriel Mountains and 16 km NE of downtown Los Angeles in the San Gabriel Valley. The 210 freeway is located 1.5 km north of the site, with heavy traffic between the hours of 08:00 and 09:00 LT, and then again between 15:00 and 19:00 LT. Prevailing daytime winds are from the W or SW, minimizing the impact of primary emissions from the 210 freeway at the sampling site, but overnight NW winds occasionally bring freeway emissions to Caltech. Other than this periodic impact from local primary emissions, the Pasadena aerosol is representative of transported urban particulate pollution from near the source-rich downtown area of the Los Angeles Basin.

PACO sampling took place between May and August of 2009, spanning the transition from spring to summer meteorological regimes. PACO was separated into three distinct analysis periods on the basis of meteorology, as summarized in Table 2.

2.1 Meteorology

Hourly meteorological data were downloaded from the Remote Automatic Weather Stations (RAWS) archive from the Western Regional Climate Center at the Desert Research Institute (DRI, Reno, Nevada). Data are from the Santa Fe Dam station, approximately 16 km east of the sampling site in the San Gabriel Valley, and are available online: <http://www.raws.dri.edu/cgi-bin/rawMAIN.pl?caCSFD>.

Table 2. PACO sampling regimes (2009).

Regime	Dates	Characteristics
Springtime meteorology	22 May to 12 Jun	<ul style="list-style-type: none"> - Basin impacted by a series of low pressure systems - Cutoff low brought rare springtime precipitation and cleaner atmosphere - Persistent cloudcover, unstable atmosphere - Low daytime temperatures, high RH, and limited photochemistry - High visibility with low O₃
Early summer/ marine influence	18 Jun to 7 Jul	<ul style="list-style-type: none"> - Limited impact from low pressure systems - Morning marine layer eroded several hours after sunrise - Higher daytime temperatures, slightly lower RH, and photochemically active afternoons - Hazy afternoons with increased O₃
Photo-chemically active	10 Jul to 4 Aug	<ul style="list-style-type: none"> - Semi-permanent high pressure over Southern California - Little marine moisture and infrequent, quickly-eroded marine layer - High daytime temp. (often exceeding 35 °C), very low daytime RH ($\leq 15\%$), photochemically active days - Decreased visibility, high afternoon O₃

2.2 Gas-phase data

Hourly O₃, NO_x, and CO data were obtained from the California Air Resources Board's Pasadena (South Wilson) monitoring site located on the Caltech campus. Data are available online at <http://www.arb.ca.gov/adam/hourly/hourly1.php>.

2.3 Differential mobility analyzer

Particle size distribution measurements were performed with a cylindrical scanning differential mobility analyzer (TSI Model 3081) upstream from a condensation particle counter (TSI Model 3760). A logarithmic scan from a mobility diameter of 15 nm to 815 nm was completed every 237 s. The sheath and excess flows of 2.51 min⁻¹ were used, with a 10 : 1 flow rate ratio of sheath-to-aerosol.

2.4 Aerosol mass spectrometer

An Aerodyne compact time-of-flight aerosol mass spectrometer (C-ToF-AMS; Drewnick et al., 2005; Canagaratna et al., 2007) measured aerosol composition and size information for 54 days during PACO. The AMS collects sub-micron particles via an aerodynamic lens into a particle sizing chamber, after which particles are vaporized and ionized by a heater and filament assembly. Aerosol fragments are then orthogonally extracted into an ion time-of-flight chamber where they are detected and interpreted as mass spectra. Adjustments to the AMS fragmentation table were made regularly, based on 21 filter sample periods over the course of PACO (Allan et al., 2004b). Additionally, thirteen ionization efficiency calibrations were made using ammonium nitrate solutions. The AMS sulfate measurement was compared to sulfate concentrations from the PILS-IC, resulting in an AMS collection

efficiency (CE) of 0.5. This CE is in agreement with previous ambient studies (Huffman et al., 2005; Drewnick et al., 2003; Allan et al., 2004a). AMS data were processed with the ToF-AMS Analysis Toolkit in Igor Pro 6 (Wavemetrics, Lake Oswego, OR).

2.5 Positive matrix factorization analysis

The dominant fraction of submicron nonrefractory aerosol is organic in most urban areas (Zhang et al., 2007). OA comprises a multitude of compounds, such that characterization by identification of each component is not currently possible (Schauer et al., 1996). Positive Matrix Factorization (PMF) has been used to deconvolve AMS mass spectra in order to identify classes of organic compounds that constitute OA (Paatero and Tapper, 1994; Paatero, 1997; Ulbrich et al., 2009). PMF solutions represent linear, positive combinations of mass spectra that describe variability in data, and AMS-based PMF results from most sites resolve factors whose mass spectra have characteristics of hydrocarbon-like OA (HOA) and oxygenated OA (OOA), with other factors such as biomass burning OA (BBOA) occurring in some areas (Zhang et al., 2007). OOA can often be further deconvolved into low-volatility OOA (LV-OOA) and semivolatile OOA (SV-OOA), broadly representing aged, transported, and highly oxidized OA and fresher, local, and less oxidized OA, respectively (Ng et al., 2010). AMS measurements, in conjunction with PMF analysis, allow for investigation of the diurnal evolution of OA and rapid changes in OA occurring during photochemically intense periods. Further, the combination of PMF solutions with analysis of the relative abundance of mass-to-charge (*m/z*) ratios 43 and 44 can be used as an aerosol aging diagnostic that allows comparison between locations (Ng et al., 2010).

For the PACO dataset, bulk AMS organic aerosol was prepared and then processed using the PMF2.exe algorithm (Paatero and Tapper, 1994). Solutions from the PMF algorithm were compared to meteorological variables and chemical tracers, as well as previously published mass spectra, using the PMF Evaluation Tool (PET Ulbrich et al., 2009). The strategic procedure for probing the PMF solution space is provided in Appendix A.

2.6 PILS-IC

A particle-into-liquid sampler coupled with off-line ion chromatography (PILS-IC, Sorooshian et al., 2006) sampled during 4-h periods (07:00–11:00 and 15:00–19:00 LT), providing quantitative measurements of inorganic and organic ions. The PILS samples ambient air through a 1 μm cut size impactor and three denuders (URG and Sunset Laboratory) designed to remove inorganic and organic gases that might bias aerosol measurements. Sampled air is then exposed to high water supersaturation in a steam chamber, where particles grow sufficiently large to be collected by inertial impaction before being delivered to vials held on a rotating carousel. Samples were collected every 30 min, and were stored at 2 $^{\circ}\text{C}$ until analysis by a dual IC system (Dionex ICS-2000). PILS-IC data from PACO are used primarily to determine collection efficiency corrections for the AMS and are not presented in detail here.

2.7 PILS-TOC

Water-soluble organic carbon (WSOC) was quantified during 12-h periods (07:00–19:00 LT) using a PILS (Brechtel Manufacturing Inc.) coupled to a Sievers Model 800 Total Organic Carbon (TOC) Analyzer (PILS-TOC). Details of this technique are described in detail by (Sullivan et al., 2004, 2006). Briefly, particles smaller than 2.5 μm in diameter are sampled by the PILS and passed immediately through an organic carbon denuder (Sunset Laboratory Inc.) to remove organic vapors. Particles are grown into droplets, collected by inertial impaction, and delivered to a TOC analyzer for quantification of WSOC, with data reported every 6 min. To account for dilution of the PILS liquid wash flow to the TOC analyzer owing to collected drops and condensation on the PILS droplet impactor, a constant dilution factor of 1.15 is assumed. This factor is based on measurements with an independent PILS system coupled to ion chromatography, a technique that can more precisely quantify the dilution factor. The reported WSOC levels are the difference between the measured and background concentrations. Contamination in the MQ water was the main component of the background levels, which were assumed to be constant between periodic background measurements. The overall measurement uncertainty is estimated to be approximately 10 %. The PILS-TOC was employed during the final, photochemically active regime of PACO, from 10 July to 4 August.

2.8 Filter sampling

Both high- and low-volume filter samples were collected during 4-h sampling periods (07:00–11:00 and 15:00–19:00 LT). High-volume (1250 l min^{-1}) samples were collected with a Tisch TE-6001 sampler fitted with a $\text{PM}_{2.5}$ fractionator, using Whatman Quartz Microfibre Filters (cat. #1851-865). Low volume (15.9 l min^{-1}) samples were collected on 47 mm PALL Life Sciences Pallflex membrane filters, downstream from a Sunset Laboratory parallel-plate carbon filter denuder. Sampling was carried out according to the IMPROVE_A protocol, except that oven limitations forced filters to be pre-baked at 300 $^{\circ}\text{C}$ before sampling. Despite the lower pre-baking temperature, subsequent analysis of pre-baked filters revealed $\leq 0.01 \mu\text{g}$ of organic carbon (OC) and elemental carbon (EC). After sampling, filters were wrapped in two layers of aluminum foil and stored at -20°C until analysis.

Low- and high- volume samples were analyzed for OC and EC via thermal-optical analysis (TOA) with a Sunset OC-EC TOA analyzer, following the IMPROVE_A temperature and calibration protocols. High volume quartz filters were also analyzed by Ultra Performance Liquid Chromatography/Electrospray Ionization Time-of-Flight High-Resolution Mass Spectrometry (UPLC/ESI-TOFMS). One-eighth of each filter was extracted with high-purity methanol under ultrasonication for 45 min. Filter extracts were filtered through a PALL Life Sciences Acrodisc CR 25-mm syringe filter (PTFE membrane, 0.2-mm pore size) into a scintillation vial. The filtered extracts were blown dry under a gentle nitrogen stream at ambient temperature. The residue was reconstituted with 50 : 50 v/v methanol with 0.1 % acetic acid and water. Blank filters were extracted and treated in the same manner as the field samples. Extracts were analyzed by a Waters ACQUITY ultra performance liquid chromatography (UPLC) system, coupled with a Waters LCT Premier TOF mass spectrometer equipped with an electrospray ionization (ESI) source, allowing for accurate mass measurements (i.e., determination of molecular formulas) to be obtained for each observed ion. Extracts were analyzed by UPLC/ESI TOFMS operated in both negative and positive ion modes. Details of operation protocols, including column information and chromatographic method for the UPLC/ESI-TOFMS are given by Surratt et al. (2008).

2.9 Hygroscopicity

Hygroscopicity measurements were carried out with the Differential Aerosol Sizing and Hygroscopicity Spectrometer Probe (DASH-SP, Brechtel Mfg), which is described by Sorooshian et al. (2008). Briefly, ambient particles pass through a nafion dryer before size-selection by a cylindrical, single-classification differential mobility analyzer (DMA). The resulting monodisperse aerosol is split into five separate flows – one providing a redundant measurement of total

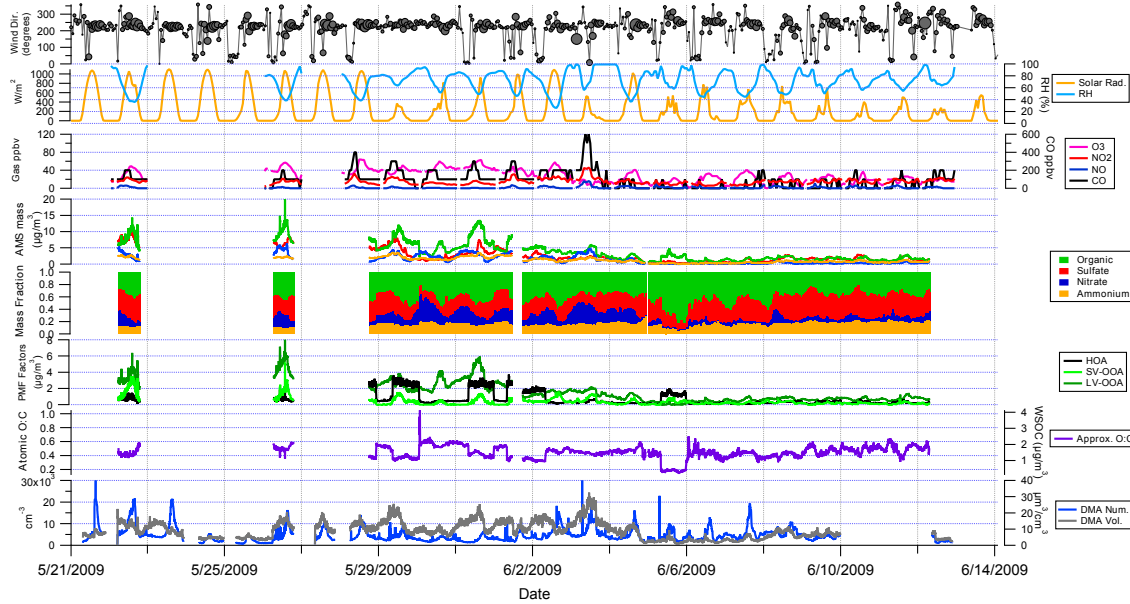


Fig. 1a. Regime I (wind direction marker size proportional to wind speed; max size = 20 km h^{-1}).

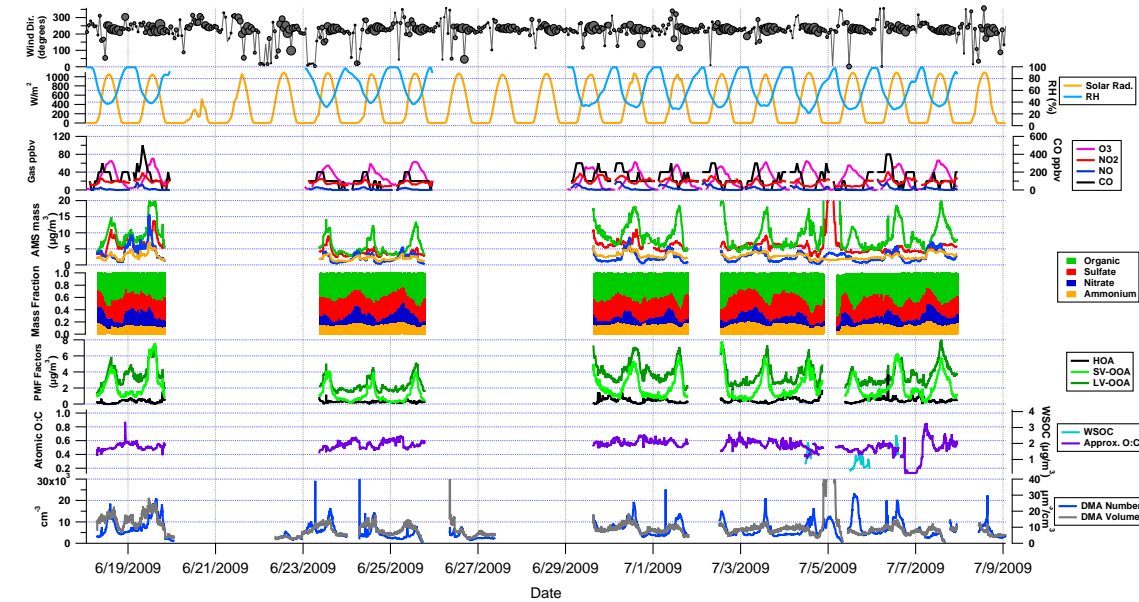


Fig. 1b. Regime II (wind direction marker size proportional to wind speed; max size = 20 km h^{-1}).

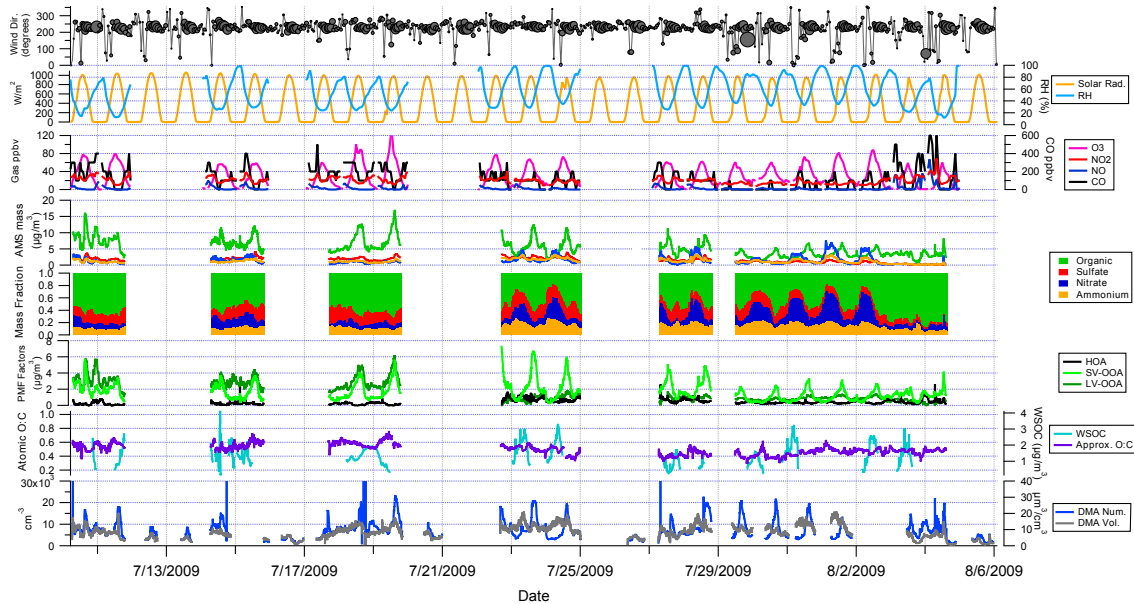


Fig. 1c. Regime III (wind direction marker size proportional to wind speed; max size = 20 km h^{-1}).

particle concentration at the DMA-selected size with a water condensation particle counter (TSI Model 3831), and the remaining four channels consisting of parallel nafton humidification chambers (Perma Pure, LLP, Model MD-070-24FS-4), followed by correspondingly humidified custom optical particle counters (OPCs). In the OPC sample volume, particles pass through a focused laser beam ($\lambda = 532 \text{ nm}$, World Star Technologies, Model TECGL-30) and scatter light in proportion to size (D_p) and refractive index (RI). Forward-scattered light is collected and focused on a photomultiplier tube, and the resulting electrical pulse is recorded by a high-speed data acquisition computer. An iterative data processing algorithm, based on laboratory calibrations with salts of known refractive indices, is used to determine the best fit on a solution surface relating electrical pulse height, size, and refractive index. The hygroscopic growth factor ($\text{GF} = D_{p,\text{wet}}/D_{p,\text{dry}}$) is corrected for the RI change caused by particulate liquid water at elevated RH.

In the current study, the DASH-SP sampled for 4-h periods (07:00–11:00 and 15:00–19:00 LT). Hygroscopicity was measured at dry sizes corresponding to $D_{p,\text{em}}$ of 150, 175, 200, and 225 nm. Multiple RH sensors in the nafton tubes and OPCs controlled RHs to dry ($\leq 8\%$), 74%, 85%, and 92%, with RH uncertainty of 1.5%. Because calculated RI varied little during sampling periods, GF calculations were made with a single RI for each sampling period, representing the average RI calculated for the entire period. The error introduced by this assumption is small, as light scattering in

the DASH is far more sensitive to size than RI. Overall uncertainty in GF calculations is calculated to be 4.5%.

3 Results and discussion

3.1 Atmospheric conditions

Figure 1a–c is a compilation of meteorological data, as well as gas- and aerosol-phase composition for regimes I, II, and III, respectively. Wind speed and direction display distinct diurnal patterns, with stagnant or very light winds from the N/NE in the overnight to early morning hours (20:00–06:00 LT) changing direction to come from the W/SW shortly after sunrise (06:00–07:00 LT). Between 06:00 and 16:00 LT, wind speed increases from $3\text{--}4 \text{ km h}^{-1}$ to $13\text{--}15 \text{ km h}^{-1}$ out of the W/SW before decreasing back to very light or stagnant out of the N/NE by 20:00 LT. One effect of these wind patterns is to allow local emissions to build up in the Los Angeles Basin during the nighttime and early morning hours, leading to significant carryover of aged aerosol in the background Los Angeles air, as proposed by (Blumenthal et al., 1978). When sea breezes develop, fresh emissions in source-rich areas are gradually transported from the Western Los Angeles Basin toward downwind areas in the E/NE. Situated 16 km from downtown Los Angeles, Pasadena can be considered as a receptor site that first receives transported pollution between 10:00 and 11:00 LT, after roughly 4–5 h of transport. During the afternoon hours

(13:00–18:00 LT), the sampling site receives a steady influx of air from the W/SW with photochemical age of 1–2 h. There are no significant freeways or point sources of particulate pollution in close W/SW proximity to the sampling site, and so it is expected that air sampled during PACO is representative of transported urban air in Los Angeles. A major freeway with significant diesel and gasoline mobile sources is located 1.5 km to the north of the sampling site, and so overnight N/NE winds may have periodically impacted the site with primary particulate emissions. Daytime variation in gas- and aerosol-phase composition is expected to result from three sources: (1) temporal changes in emissions from source-rich areas, (2) diurnal variations in the intensity of photochemistry, and (3) the age of transported pollution.

A clear diurnal trend is observed in RH and solar radiation, with RH increasing to near 100 % on most nights and remaining at or near saturation until sunrise. The incidence of nighttime and morning marine cloudcover was common during regimes I and II, while regime III was typically drier, with clear nighttime skies more common. Periods of more significant marine layer influence are indicated by longer periods of saturated RH and more gradual decrease in RH (and slower increase in solar radiation) after sunrise. Regime I has been classified as “springtime meteorology” due to the impact of several low pressure systems in Southern California, bringing periodic drizzle and leading to several days of cloudcover and significantly diminished solar radiation (i.e. 6 to 12 June). Daytime RH rarely fell below 50 % during regime I. Regime II exhibited the strongest summertime marine layer influence, with heavy cloudcover persisting until late morning (10:00 to 12:00 LT) nearly every day before making way for sunny, hazy afternoons with daytime RH between 25 and 40 %. Regime III observed the least marine layer influence, with many mornings of clear skies and daytime RH typically between 10 and 30 %. Despite differences in meteorology, the diurnal wind patterns described above were robust, with stagnant morning winds giving way to afternoon sea breezes and pollutant transport from the W/SW.

Gas-phase data give a sense of the atmospheric chemical environment during sampling. O_3 exhibits a strong diurnal pattern correlated with solar radiation and serves as a tracer for photochemical activity. During periods of relatively dry atmospheric conditions, the O_3 concentration peak increases in magnitude over subsequent days (see 17 to 19 July and 27 July to 2 August in regime III), suggesting that either pollutants accumulate or photochemical activity increases during periods of consistent, stable atmospheric conditions, resulting in photochemical episodes. CO and NO_x display more random behavior, exhibiting periodic peaks in concentration indicative of plumes of fresher emissions.

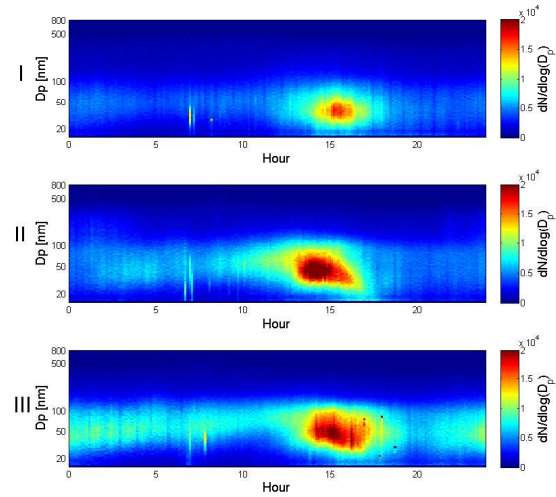


Fig. 2. Average diurnal DMA number concentrations (cm^{-3}) for regimes I, II, and III.

3.2 Aerosol composition

OC and EC mass concentrations, in addition to OC:EC ratios from representative days in each regime, are presented in Table 3. OC is higher in afternoon periods when compared with mornings in each regime (27, 18, and 4 % higher in regimes I, II, and III, respectively), while EC is lower during afternoons (7, 35, and 22 % lower in regimes I, II, and III, respectively). Further, OC:EC ratios are significantly higher during afternoon periods. These diurnal trends in OC are expected, given the importance of photochemical SOA production, and the percentage increase in OC mass between morning and afternoon periods is similar to that observed by the AMS (15, 17, and 10 % higher in regime I, II, and III, respectively). Discrepancies may arise due to the different size ranges measured by the AMS and filter sampling (upper limits of measurement are 1.0 and $2.5 \mu\text{m}$ for the AMS and filters, respectively), in addition to potential volatilization of semivolatile organics relating to the thermo-optical OC/EC analysis technique. The modest increase in OC between morning and afternoon periods during the photochemically intense regime III may indicate that significant OC existed in the background aerosol during this period. The decrease in EC observed between morning and afternoon periods suggests that primary organics are a more significant portion of the Los Angeles aerosol in the mornings, and the relatively low concentrations of EC suggest that the dominant source of organic aerosol in Los Angeles is secondary.

DMA data are presented in panel 8 of Fig. 1a–c. Diurnal patterns are evident in both DMA volume and number in all regimes. DMA volume tends to reach a maximum in the mid-to-late morning (10:00, 11:00, 08:00 LT in regime I, II, and

Table 3. OC/EC concentrations ($\mu\text{g m}^{-3}$) for representative days from each regime.

Regime	OC		EC		OC:EC	
	AM	PM	AM	PM	AM	PM
I	3.88 ± 0.32	4.92 ± 1.18	0.43 ± 0.02	0.40 ± 0.27	9.1	12.4
II	4.24 ± 0.46	5.01 ± 1.62	0.80 ± 0.31	0.52 ± 0.40	5.3	9.6
III	6.16 ± 1.40	6.41 ± 1.44	0.83 ± 0.47	0.65 ± 0.22	7.4	9.9

III, respectively), when RH is still high and particles have presumably undergone cloud processing. The early maxima in regime III underscore the absence of significant marine layer influence persisting into the late morning. On average, DMA number concentration reaches a maximum between 14:00 and 15:00 LT during each regime, roughly 3 h after transported pollution is expected to first arrive at the sampling site (Fig. 2). This indicates that increases in fine particle mass at the PACO sampling site are not the result of transport alone, but also affected by photochemical production in transported, polluted air from source-rich areas. There was no significant difference in wind patterns between regimes, so the slightly earlier peak in DMA number in regime II suggests that marine moisture and aqueous-phase processes (most prevalent in regime II) may hasten secondary aerosol production. Figure 2 indicates that appreciable concentrations of fine particles (< 100 nm) are present in late nights and early mornings (particularly in regimes II and III), possibly comprised of fresh emissions, nighttime-generated NO_3^- , or fine particle carryover residing in a shallow mixed layer.

With the exception of a high-volume filter sampler located outdoors on the roof, instruments sampled from inlets connected to a main sampling line drawing in ambient air at a 161 per minute (1 min^{-1}) laminar flow rate. Sample flow to each instrument was supplemented with pumps to be isokinetic with flow in the main sampling line, and sample lines were designed to draw from the center of flow through the main line. Ambient air was dried by nafion driers upstream of each instrument.

The third and fourth panels of Fig. 1a–c show time traces of bulk AMS aerosol mass concentration and mass fraction, respectively, while the sixth panel shows a time trace of approximate O:C ratio, based on Aiken et al. (2008), as well as WSOC concentration from the PILS-TOC (regime III). Organics dominated the aerosol sampled during PACO, and except for short episodes in regime I, the approximate O:C ratio remained relatively constant during each regime (0.44 ± 0.08 , 0.55 ± 0.05 , and 0.48 ± 0.08 during regimes I, II, and III, respectively). Organic aerosol in regime II appears to be more oxidized than I and III, suggesting that the marine moisture and presumed aqueous processing may enhance the rate of organic oxidation in Los Angeles. From bulk AMS time traces it is evident that organics increase in

both magnitude and mass fraction each afternoon, particularly during the more photochemically active regimes II and III. It is noteworthy that there are no distinct trends in approximate O:C between mornings and afternoons (morning approximate O:C = 0.44 ± 0.08 , 0.54 ± 0.08 , and 0.49 ± 0.07 for regimes I, II, and III, respectively, while afternoon approximate O:C = 0.44 ± 0.08 , 0.53 ± 0.06 , 0.50 ± 0.08 for regimes I, II, and III, respectively). This suggests that there is little change in overall oxidation state of Los Angeles aerosol, even on timescales of weeks. It is unlikely that all organics are uniformly oxidized at all times in Los Angeles, but rather that there exists a continuum of OA oxidation, with more reduced and more oxidized ends of that continuum maintaining a relatively constant ratio for extended periods of time.

Trends in aerosol mass fraction are presented in Fig. 4. Organics dominate the Los Angeles submicron aerosol, contributing 42, 43, and 55 % of aerosol mass in regimes I, II, and III, respectively. Diurnal trends are evident in Fig. 4, with organic mass fraction increasing significantly from morning (07:00–11:00 LT) to midday (11:00–15:00 LT) to afternoon (15:00–19:00 LT) in each regime. Sulfate is a significant component in marine/moisture-influenced regimes I and II, and is a more minor component in regime III, suggesting that cloud processing and marine influence may be an important source of sulfate aerosol in Los Angeles. Nitrate contributes equal mass fractions in each regime, with a minimum in the afternoon and a maximum in the morning. Ammonium contributes a remarkably constant mass fraction to the aerosol, despite significantly less inorganic sulfate in regime III, suggesting an ammonium surplus for aerosol sampled in regime III. The significant peak in AMS masses during the early morning of 5 July (regime II) corresponds to a total submicron mass of over $200 \mu\text{g m}^{-3}$, and resulted from a myriad of fireworks displays in the area surrounding the sampling site. This plume has been removed from further analysis. Diurnal trends in bulk composition are highlighted in the top panel of Fig. 3. It is noteworthy that during the significantly marine-layer-impacted regime II, bulk organic, sulfate, nitrate, and ammonium masses are all enhanced. This is further evidence that aqueous processing associated with marine layer influence may be an important factor in generating aerosol mass in Los Angeles. Typically, organics increase in magnitude to a maximum near 14:00–15:00 LT in each

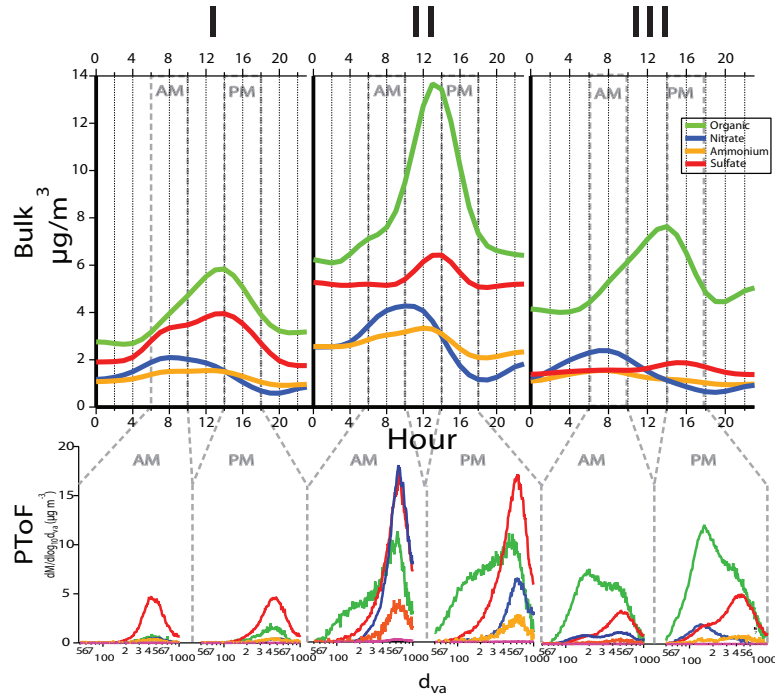


Fig. 3. Bulk AMS diurnal mass averages for regimes I, II, and III. Bottom panel shows size-resolved PToF AMS data for a representative morning and afternoon period in each regime, where morning = 07:00–11:00 LT and afternoon = 15:00–19:00 LT.

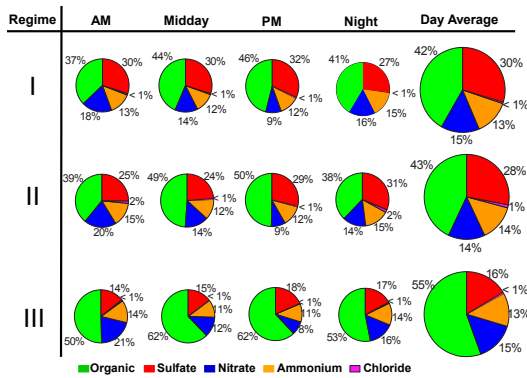


Fig. 4. AMS bulk mass fractions for AM (07:00–11:00 LT), midday (11:00–15:00 LT), PM (15:00–19:00 LT), and night (19:00–07:00 LT) for regimes I, II, and III.

regime, corresponding to a maximum in ozone, solar radiation, and DMA number – evidence of photochemical SOA production. Sulfate exhibits slight enhancements during periods of peak photochemical activity in all three regimes, but as

suggested by Kleeman et al. (1999), it appears to be predominantly a background marine species. Nitrate mass is highest in the nighttime and morning periods, likely resulting from ozone- NO_x production of HNO_3 at night and $\text{HO}_x\text{-NO}_x$ production of HNO_3 after rush hour in the mornings. As mentioned in Sect. 3.1, there were periods of high O_3 observed during PACO, and during several of these periods there also appeared to be significantly elevated levels of aerosol nitrate during nighttime sampling (e.g. 30 July to 3 August). Further, morning peaks in aerosol nitrate varied significantly in magnitude, suggesting that there may be significant variation in the amount of gas-phase HNO_3 production from day to day.

Ammonium mass generally follows the combined trends of SO_4^{2-} and NO_3^- , but appears to be in excess in regime III. Defining an ammonium ratio as:

$$\frac{(\text{moles of } \text{NH}_4^+ \text{ measured by AMS})}{(\text{moles of } \text{NH}_4^+ \text{ required to neutralize } \text{SO}_4^{2-} \text{ and } \text{NO}_3^-)} \quad (1)$$

aerosol sampled in regimes I and II was found to be generally neutralized (average ammonium ratio = 0.96 ± 0.21 and 0.94 ± 0.17 for regimes I and II, respectively), while aerosol from regime III was characterized by significant ammonium excess (ammonium ratio = 1.28 ± 0.30). These

results suggest that aerosol phase NH_4NO_3 was ammonia-limited during regimes I and II, but ammonia may have been in excess during regime III. Investigating molar ratios of inorganic species, it is apparent that the role of SO_4^{2-} is significantly diminished in regime III, corresponding to the absence of marine layer influence. The ratio of NO_3^- to NH_4^+ remains relatively constant across regimes (0.32, 0.29, and 0.34 in regimes I, II, and III, respectively), while the ratio of SO_4^{2-} to NH_4^+ exhibits a marked decrease in regime III (0.42, 0.41, and 0.24 in regimes I, II, and III, respectively). The AMS has difficulty distinguishing whether NH_3 , NH_2 , and NH_3^+ (m/z 15, 16, and 17, respectively) are contributed by inorganics or organic amines. One explanation for these trends is that ammonium may be chiefly inorganic during the moister, marine-layer-influenced regimes I and II, serving primarily to neutralize SO_4^{2-} and NO_3^- , while there may be an influence from organic amines in the absence of marine layer influence during regime III. While particulate amines have been observed in the particle phase, it is unclear why they would appear to be more prevalent in regime III, as amines are typically associated with cooler, moister environments. Another explanation is that the “excess” NH_4^+ may be associated with organic anions. An enhancement in acidic organic species, which would not be unexpected in a hot, dry, photochemically active regime, may lead to a corresponding enhancement in neutralizing NH_4^+ . Since the AMS does not specifically quantify organic anions, such an enhancement in both organic acids and associated NH_4^+ would lead to an increased ammonium ratio.

The bottom panel of Fig. 3 shows size-resolved PToF-AMS composition for a representative morning and afternoon period in each regime, with 9 June, 19 June, and 19 July representing regimes I, II, and III, respectively. Size-resolved data indicate that aerosol in regime I is typically internally-mixed, with the mode centered at ~ 400 –500 nm. Afternoon PToF data from regime I indicate that photochemical organic production typically results in organics condensing on existing accumulation mode aerosol. Regime II is characterized by significantly higher aerosol mass and more complex size distributions. While there is a significant internally-mixed accumulation mode present and centered at ~ 600 –700 nm, there is also significant aerosol mass at sizes smaller than 300 nm in both morning and afternoon sampling periods, though the mass at smaller sizes does not comprise a distinct mode. Afternoon PToF data from regime II indicate that a fine mode appears coincident with photochemistry, suggesting that fine mode aerosol is predominately comprised of secondary species. Nitrate, sulfate, and ammonium are generally confined to accumulation mode aerosol in regime II. Regime III PToF data reveal an aerosol that is dominated by organics at all sizes and is distinctly bimodal. In addition to an internally mixed accumulation mode centered at ~ 500 –600 nm, distributions from regime III also reveal a significant fine mode centered at ~ 100 –200 nm. The accumulation mode tends to be comprised of sulfate, nitrate,

and ammonium (in addition to organics) in the morning periods, with less nitrate in afternoons. Afternoon PToF data from regime III, like those from regime II, reveal fine-mode aerosol growth resulting from production of secondary organic species. Numerous studies have shown that the critical species for new particle formation in the atmosphere is H_2SO_4 . The extent to which the observed fine mode aerosol might have originated from the nucleation of gas-phase species during PACO is unclear. However, given the relatively large amount of pre-existing aerosol surface area, as well as the relatively low concentration of SO_2 , the precursor to H_2SO_4 , it is unlikely that new particle formation by nucleation is an important process in Los Angeles. Instead, the growth of fine-mode organics is proposed to occur by condensation of SOA on existing ultrafine primary aerosol. This tentative conclusion is contrasted with results from Pittsburgh, in which Stanier et al. (2004) found new particle formation to be an important process, strongly correlated with SO_2 concentrations. Whether condensing on nucleated sulfate or existing ultrafine primary aerosol, growth of fine mode particles in Los Angeles is predominantly due to SOA.

Figure 5 shows the hourly average for WSOC mass (top panel, representing WSOC organic mass) and % of AMS organic accounted for by WSOC (bottom panel) for regime III. A factor of 1.8 was used to convert water soluble carbon (WSOC) mass to water soluble organic mass (WSOM), within the range of factors presented by Turpin and Lim (2001), and matching the factor used by Docherty et al. (2008) for aerosol in the Los Angeles Basin. Averaged hourly data reveal a trend in WSOM, increasing from a minimum in the late evening and early morning to a maximum at 15:00 LT, corresponding to maxima in O_3 concentration, solar radiation, AMS organic, and DMA number concentration. This suggests that photochemical production of SOA in air transported from source-rich areas is a significant source of WSOM in the Los Angeles Basin. While there is a diurnal trend in WSOM, the fraction of AMS organic accounted for by WSOM is relatively constant at 0.44 ± 0.16 during regime III, with a slight enhancement between 15:00 and 19:00 LT. This suggests that while significant WSOM is photochemically generated during the course of a day, water soluble organics comprise a relatively constant percentage of organic aerosol in Los Angeles. WSOC has been found to correlate well with oxidation state of organic aerosol (e.g., Kondo et al., 2007). Given the relatively constant approximate O:C ratio observed in regime III and steady afternoon influx of polluted air on the order of 1–2 h old, the constant WSOM:AMS organic ratio is not unexpected.

3.3 PMF results

AMS data from PACO were combined into a single continuous dataset for analysis by the PMF method. PMF produced several non-unique solutions that were compared with known

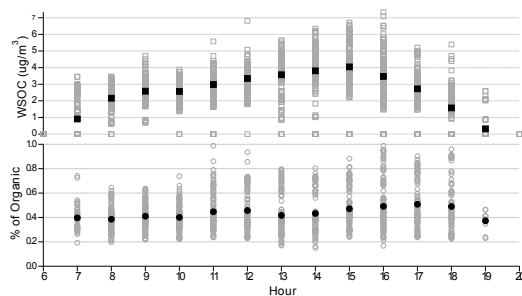


Fig. 5. WSOC magnitude (squares) and % of AMS organic (circles). Black markers represent the average over regime III.

mass spectra and external time traces in order to choose final solutions. Figure 6 presents a summary of PMF factors, while panel 6 of Fig. 1a–c represents time traces for PMF factors for regimes I, II, and III, respectively. Details of the PMF method and solution selection are presented in Appendix A.

Three factors were resolved from the PMF method, and comparisons with previously published spectra indicate that they correspond to a hydrocarbon-like organic aerosol (HOA) and semivolatile- and low-volatility-oxygenated organic aerosol (SV-OOA and LV-OOA, respectively). PMF analysis was also performed on each regime separately, to determine the sensitivity of solutions to the assumption that OA is comprised of factors with constant mass spectra. In each case (HOA, SV-OOA, and LV-OOA), the factors resolved in the bulk analysis displayed a high degree of correlation (Pearson's R generally on the order of 0.94–0.99 for LV-OOA, SV-OOA, and HOA) with those resolved in analysis of individual regimes. The HOA factor is closely correlated with previously published spectra from periods dominated by reduced, primary organics (Zhang et al., 2005; Lanz et al., 2007; Ulbrich et al., 2009), and has significant signal at m/z 41 and 57. The LV-OOA factor is closely correlated with previously-published OOA-1 factors and OOA-like factors observed in highly oxidizing environments (Zhang et al., 2005; Lanz et al., 2007; Ulbrich et al., 2009; Alfarra et al., 2004). The SV-OOA factor is also correlated with previously-published OOA factors, but has a higher degree of correlation with previously-published factors expected to represent less-aged, less-oxidized, semivolatile oxygenated organic aerosol, or SV-OOA (Zhang et al., 2005; Lanz et al., 2007; Ulbrich et al., 2009; Bahreini et al., 2005; Alfarra et al., 2004). The LV-OOA factor has a larger ratio of m/z 44 to m/z 43, an indication of a more aged, oxidized organic component (Ng et al., 2010). The SV-OOA factor, on the other hand, has a smaller m/z 44 to m/z 43 ratio. PACO PMF factors correlated closely with “standard” HOA, SV-OOA, and LV-OOA factors reported by Ng et al. (2011), based on an average of results from 15 sites.

As seen in Fig. 1a–c, the HOA factor has the character of a periodic plume source, with low background concentrations punctuated by sudden, significant increases in concentration that remain high for several hours at a time. These increases in HOA concentration occurred primarily during regime I and are typically correlated with or just following peaks in CO concentration (panel 3 in Fig. 1a–c), though the low time- and concentration-resolution of CO measurements made statistical analysis difficult. HOA is typically associated with primary organic aerosol (POA) (e.g., Ulbrich et al., 2009; Ng et al., 2010), and the only significant local source of POA is expected to be the 210 freeway, 1.5 km north of the sampling site. There appears to be a trend of HOA plumes coinciding with or immediately following periods of light winds out of the N, which suggests that the HOA-like factor may represent primary freeway emissions. It is unclear why this HOA factor does not appear during every period of light winds out of the N. Low correlation between the HOA factor and ozone ($Pr = 0.39$) suggests that HOA production is not a photochemical process, and low correlations with inorganic AMS traces ($Pr = 0.18, 0.15, 0.21$, and 0.02 for sulfate, nitrate, ammonium, and chloride, respectively) suggest that HOA production is independent of formation of inorganic aerosol, and that HOA may comprise an externally mixed mode, separate from the accumulation mode aerosol that is typically comprised of inorganic constituents.

The more dominant LV-OOA factor is most significantly correlated with inorganic AMS traces ($Pr = 0.75, 0.46, 0.65$, and 0.46 for sulfate, nitrate, ammonium, and chloride, respectively). As discussed in Sect. 3.2, inorganics are most prevalent in accumulation mode aerosol (rather than fine mode), and their loadings appear to be associated with significant marine layer influence in the Los Angeles Basin (e.g., regimes I and II). The high degree of correlation between LV-OOA and inorganic constituents suggests that the LV-OOA factor represents an organic component that typically resides in accumulation mode aerosol and may be associated with marine layer/cloud processing influence. The correlation between LV-OOA and ozone is relatively low ($Pr = 0.39$), indicative of an aged background organic species, as opposed to a rapidly-produced photochemical product that exhibits a distinct diurnal trend. Examining time traces for LV-OOA in Fig. 1a–c reveals that the LV-OOA factor exhibits relatively high background levels in the mornings and at night, while periodically showing moderate increases in magnitude during midday periods of photochemistry. These periodic photochemical trends in LV-OOA correspond to periods of intense photochemistry (e.g., 18–19 July), characterized by midday ozone concentrations near 80–100 ppb. This suggests that while LV-OOA appears to be the major constituent of the aged background aerosol discussed in Sect. 3.2, it can be photochemically produced on relatively short timescales during periods of intense photochemical activity. Its strong correlation with SO_4^{2-} , consistent presence during humid overnight and morning hours, coincidence

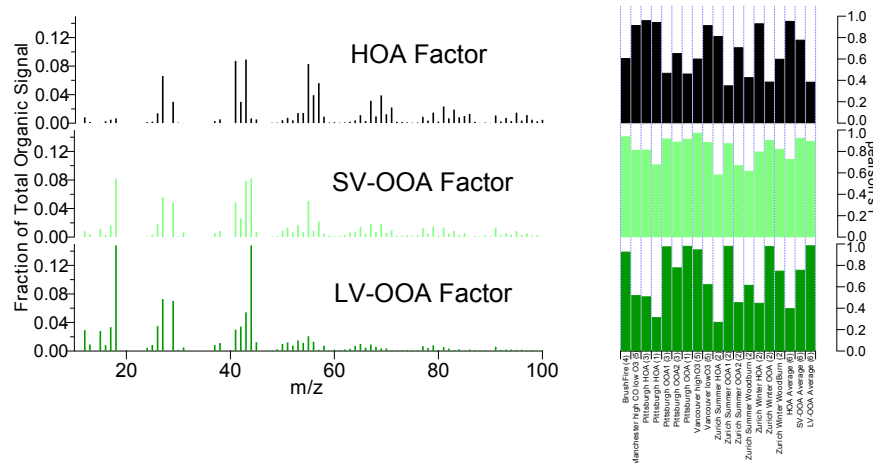


Fig. 6. Mass spectra for the three factors identified in PMF analysis (HOA, SV-OOA, and LV-OOA; left) and Pearson's R correlations of those solution mass spectra with previously reported mass spectra (1, 2, 3, 4, 5, 6: Zhang et al., 2005; Lanz et al., 2007; Ulbrich et al., 2009; Bahrneini et al., 2005; Alfarra et al., 2004; Ng et al., 2011, respectively).

with accumulation mode aerosol, and greater prevalence in moisture-impacted regimes I and II suggest that there may be significant aqueous processing sources for LV-OOA in Los Angeles.

Figure 1a–c show a regular diurnal trend in SV-OOA, with overnight minima increasing to maximum concentrations daily at approximately 14:00–15:00 LT, correlating with maxima in solar radiation, AMS organic, and DMA number concentration. The SV-OOA factor exhibits a reasonable degree of correlation with ozone ($Pr = 0.53$), suggesting that semivolatile organics are products of short-timescale photochemical oxidation of VOCs. Correlations with inorganic traces are lower than those for LV-OOA ($Pr = 0.42$, 0.31, 0.45, and 0.19 for sulfate, nitrate, ammonium, and chloride, respectively). As discussed in Sect. 3.2, aerosol size distributions exhibit significant enhancements in fine mode aerosol in afternoon periods, with the fine mode comprised almost entirely of organics (particularly in regimes II and III). Further, SV-OOA correlates strongly with DMA number concentration ($Pr = 0.62$, vs. 0.00 and 0.33 for HOA and LV-OOA, respectively). The regular, significant enhancements in SV-OOA during peak photochemical periods, high correlation with DMA number concentration combined with lower correlations with inorganics (which typically comprise accumulation mode aerosol), and the regular appearance of fine organic modes during afternoons suggests that the SV-OOA factor is comprised of early-generation photochemical products that are chiefly responsible for the growth of fine-mode aerosol in the afternoons. Based on wind patterns discussed in Sect. 3.1, SV-OOA is proposed to consist of secondary organic products on the order of 1–2 h old, based on

the transport time from source-rich areas near downtown to the sampling site.

Traditional PMF analysis correlates LV-OOA with sulfate, since SO_4^{2-} is essentially nonvolatile, and SV-OOA with nitrate since NO_3^- is more volatile. These correlations are not necessarily based on mechanistic chemistry, but rather a similarity in volatilities. So there is no reason, on a fundamental chemical basis, that NO_3^- should correlate better with SV-OOA than with LV-OOA. That is, the routes by which semivolatile organics and NO_3^- reach the particle phase are distinctly different chemically. In the Los Angeles aerosol, these distinct pathways result in a relatively poor correlation between SV-OOA and NO_3^- . A better correlation between inorganics and LV-OOA suggests that the pathways by which they reach the aerosol phase are more similar than for SV-OOA in transported Los Angeles Aerosol.

Ng et al. (2011) applied a simple method for making real-time estimates of OA components, based on an empirical scaling factor that relates HOA and OOA (further segregated as SV-OOA and LV-OOA) to signal at fragments m/z 57 and m/z 44. HOA is estimated by $b \times (C_{57} - 0.1 \times C_{44})$, where b for PACO was found to be 14.0, compared with 13.4 (range = 8.5–19.2) for Ng et al. (2011). PACO OOA (combined SV-OOA and LV-OOA) is estimated by $c \times C_{44}$, where c was found to be 8.1 for PACO, compared with 6.6 (range = 2.9–9.0) by Ng et al. (2011). The PACO SV-OOA and LV-OOA factors are estimated by $3.3 \times C_{44}$ and $4.8 \times C_{44}$, respectively.

Figure 7 shows the mass fraction of organic accounted for by each organic component during each regime. OA in Los Angeles is overwhelmingly oxidized in nature, with LV- and

SV-OOA combined contributing 77, 92, and 86 % of OA during regimes I, II, and III, respectively. HOA contributed the largest fraction to OA during regime I, in large part due to episodically high HOA concentrations during May and early June. HOA is a minor factor during regimes II and III. SV-OOA is a major constituent of OA during periods of photochemistry, with the hot, dry, photochemically intense regime III seeing the most significant contribution of SV-OOA to OA. LV-OOA dominates in regimes I and II, which were both periods of significant marine/moisture influence and cloud processing.

3.4 Filter analysis

PMF factors are mathematical solutions that return constant mass spectra that are combined linearly to describe variability in AMS data, and it is important to compare PMF results to physical, independent characterizations of OA. For PACO, UPLC-ESI-(+ and -)-MS analysis of high-volume filter samples was performed on 9 selected filters representing periods of high HOA, SV-OOA, and LV-OOA concentrations, in order to distinguish chemical profiles associated with the PMF factors. Periods distinguished as “high SV- and LV-OOA” were chosen such that those species were the single, dominant component of OA. PACO filter sampling did not include any periods in which HOA was the isolated, dominant species, as periods distinguished as “high HOA” were also impacted by high background levels of LV-OOA.

Functional groups of interest in UPLC-ESI-(+)-TOF-MS analysis were basic nitrogen groups (i.e. amines, imines) as well as oxygen-containing moieties (i.e. carbonyls, alcohols, ethers). The complexity of the samples made complete speciation by this technique difficult, but it was possible to identify the majority of the base peaks. Non-oxygenated nitrogenous compounds likely to be amines were detected in significant concentrations and with some variety of carbon chain-length (C8–C16) in the high HOA + LV-OOA periods, as well as during morning periods in which background LV-OOA dominated the organic fraction. This suggests that amines may be an important class of organic compounds in aged, background Los Angeles aerosol. The most prominent class of compounds in all filters was oxygenated organic species, with increased variety of oxygenated species during periods of significant photochemical organic production.

UPLC-ESI-(−)-TOF-MS offered better mass spectral resolution and more complete identification of base peaks than (+)-mode, allowing for more complete chemical profiles. Phthalic acid is ubiquitous in appreciable quantities in the extractable fraction of Los Angeles OA. Phthalic acid has been identified as a significant product of poly-aromatic hydrocarbon (PAH) photochemistry (Kautzman et al., 2010), so this result suggests that PAHs may be a significant class of precursor VOCs to OA in Los Angeles. The high HOA + LV-OOA samples were characterized by appreciable quantities of nitrogen- and sulfur-containing organics (> 10 % of the

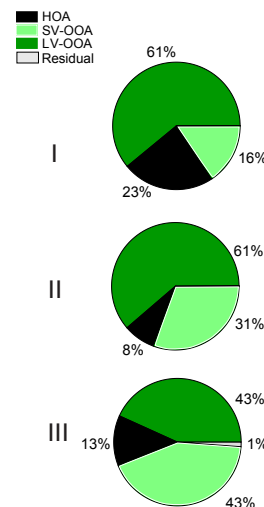


Fig. 7. Mass fraction of total organic accounted for by each PMF factor during regimes I, II, and III.

extractable, identifiable fraction), which is unique to periods in which both HOA and LV-OOA were high in magnitude. Carboxylic acids were significant during both SV- and LV-OOA periods (> 15 % of extractable, identifiable fraction), though the carboxylic acids identified during SV-OOA periods tended to be longer-chain (C7–C10, as opposed to C4–C9 for LV-OOA periods). Additionally, aerosol in LV-OOA periods tended to have a more complex chemical profile, with no single class of compounds dominating the extractable fraction identified by UPLC. This suggests that while the SV- and LV-OOA periods contain many of the same chemical compounds, LV-OOA tends to be characterized by smaller organic acids (higher O:C ratio), as well as a more complex profile of organonitrates, organosulfates, and oxidized acids. As explained in Ulbrich et al. (2009), aerosol partitioning with a bilinear PMF model is inherently limited in fitting a dynamic organic component. With a dataset as large as that represented by PACO, it is not unexpected that the organic component undergoes numerous and significant changes over the course of a single regime. Thus, two unique, constant mass spectra used to describe variability in a bilinear model may be more accurately viewed as two points on a continuum of volatility, rather than two distinct components of differing volatility. This hypothesis is supported by the commonality of compound classes identified by UPLC analysis for SV- and LV-OOA periods. The continuum of oxygenation is further illustrated in Fig. 8, a plot of m/z 44 (CO_2^+) vs. m/z 43 (mostly $\text{C}_2\text{H}_3\text{O}^+$) proposed by Ng et al. (2010) as a mass spectral diagnostic for the age of organic aerosol. It is hypothesized that LV-OOA components tend to have a higher ratio of m/z 44 to m/z 43 and represent a lower-

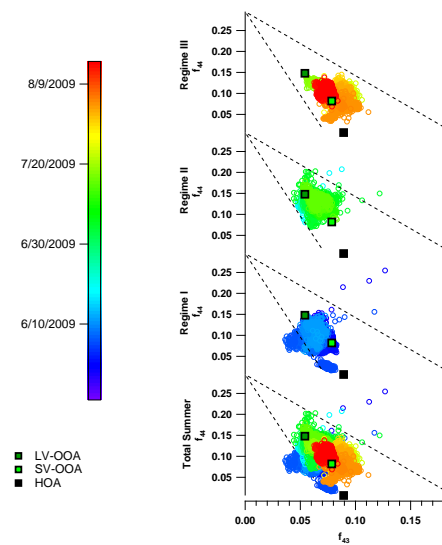


Fig. 8. f_{44} vs. f_{43} for PACO, with color scale corresponding to date. Square markers represent values for HOA, SV-OOA, and LV-OOA factors identified in PACO.

volatility, more-aged organic component with a higher degree of oxidation. Results from PACO indicate that the organic component of Los Angeles aerosol produces a continuum of f_{44} values during each regime and that the most aged organic fraction may actually be characterized by a predominance of longer-chain, oxidized monoacids, complex amines, and nitrate- and sulfate- containing organics. It is concluded that for the Los Angeles aerosol, a bilinear PMF model, with mass spectra assumed to be constant over an entire regime, is helpful in qualitatively assessing the degree of aging of the organic component, but represents a broad simplification of a dynamic organic fraction of aerosol.

3.5 Hygroscopicity

The intensity of scattered light is a strong function of particle diameter (D_p), and since aerosol water uptake largely determines particle size, it is a major variable determining the interaction of particles with radiation. Urban aerosol tends to be dominated by organic material, which is often hydrophobic, leading to overall growth factors (GFs, $D_{p,wet}/D_{p,dry}$) that are smaller than those for pure inorganic aerosol. At RH above the deliquescence RH of common inorganic aerosol constituents, the comparatively low hygroscopicity of organics tends to result in an inverse correlation between organic mass fraction and overall aerosol hygroscopicity (Shinozuka et al., 2009; Quinn et al., 2005; Hersey et al., 2009).

Because urban aerosol is, in part, an external mixture of organic and inorganic components, hygroscopic behavior is of-

ten complex, with several GF modes observed (e.g., Cocker et al., 2001; Massling et al., 2005, 2009; Swietlicki et al., 2008; Meier et al., 2009; Tiitta et al., 2010; Rose et al., 2010). The optical sizing method utilized by the DASH-SP provides rapid measurements on timescales suitable for aircraft studies, but does not allow resolution of more than two modes (a nonhygroscopic and hygroscopic mode). During PACO, two modes were typically distinguishable: a nonhygroscopic mode ($1 < GF < 1.15$ at 92 % RH) identified during morning sampling (≤ 30 % of aerosol), decreasing to very minor significance in the afternoon, in addition to a dominant hygroscopic mode that will be the focus of the rest of this section. This suggests that aerosol sampled in the morning included an appreciable fraction of nonhygroscopic particles, with afternoon photochemistry and SOA production resulting in an aerosol of more uniform, unimodal hygroscopicity. Since it was not possible to resolve multiple growth modes, GF data represent the overall subsaturated water uptake behavior for hygroscopic particles.

The DASH-SP measured GF at dry particle sizes of 150, 175, 200, and 225 nm. There was no statistically significant difference between GF at these dry sizes, and so data were averaged to give GFs representative for particles between 150 and 225 nm dry diameter. Particles sampled during morning periods (07:00–11:00 LT) were significantly more hygroscopic at 74 and 92 % than those sampled during afternoon periods (15:00–19:00 LT); morning GF averaged 1.14 ± 0.13 , 1.37 ± 0.10 , and 1.97 ± 0.45 at 74, 85, and 92 % RH, respectively, while afternoon GF averaged 1.06 ± 0.04 , 1.37 ± 0.07 , and 1.74 ± 0.20 at 74, 85, and 92 % RH, respectively. Suppressed GF at 74 and 92 % during afternoon sampling but constant GF at 85 % suggests that the hygroscopic growth curve (GF vs. RH) for morning-sampled aerosol is one with a higher GF at lower RHs, combined with a steep ascending section at $RH > 85$ %, suggestive of a predominantly inorganic aerosol with a small hygroscopic organic component and little nonhygroscopic aerosol.

These GF values are significantly higher than those measured during the 1987 SCAQS study in the eastern Los Angeles Basin (1.23 ± 0.08 for 200 nm particles at 90 ± 3 % RH; Zhang and McMurray, 1993), and are more consistent with the most hygroscopic mode measured in Pasadena in 1999 (1.6 at 89 % RH; Cocker et al., 2001).

Figure 9 shows GF at 74, 85, and 92 % plotted against organic mass fraction (OMF), with markers colored by sampling date and time. PACO data show a clear trend of suppressed GF with increasing organic mass fraction ($Pr = -0.56, -0.78, -0.71$ for 74, 85, and 92 %, respectively). The lowest GFs and highest values of organic mass fraction occur late in PACO, during the dry and photochemically intense regime III characterized by significant photochemical production of SV-OOA.

An increasingly popular representation of aerosol hygroscopicity is the κ parameter, developed by Petters and Kreidenweis (2007). As outlined in Shinozuka et al. (2009), one

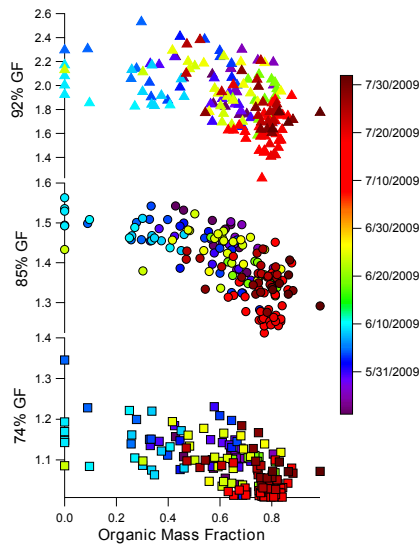


Fig. 9. GF at 74, 85, and 92 % RH plotted against organic mass fraction, with color scale corresponding to date.

can use size-resolved GF data at sub-saturated RH to solve the equation:

$$S(D) = \frac{D^3 - D_d^3}{D^3 - D_d^3(1 - \kappa)} \exp \left[\frac{4\sigma M_w}{RT\rho_w D} \right] \quad (2)$$

for κ , where S is the saturation ratio over an aqueous droplet (0.74, 0.85, or 0.92), D and D_d are the humidified and dry diameters, respectively, σ is the surface tension at the interface of air and pure water (0.072 J m^{-2}), M_w is the molecular weight of water (18 g mol^{-1}), R is the gas constant ($8.3 \text{ J mol}^{-1} \text{ K}^{-1}$), T is the temperature (298 K), and ρ_w is the density of water (1 g cm^{-3}). Because the effect of organics on surface tension is not explicitly accounted for in this model, the κ here may be regarded an “effective hygroscopicity parameter”, which includes both solute-induced water activity changes and surface tension effects (Petters and Kreidenweis, 2007; Rose et al., 2010).

Using the calculated κ values, one may estimate critical dry diameter (D_d), or the diameter above which aerosol particles activate as cloud condensation nuclei (CCN) at a given saturation ratio (S), using the following equations:

$$\kappa = \frac{4A^3}{27D_d^3 \ln^2 S} \quad (3)$$

where:

$$A = \frac{4\sigma M_w}{RT\rho_w} \quad (4)$$

Following Shinozuka et al. (2009) and assuming a supersaturation (S_c) of 0.2 %, the relationship between κ and D_d becomes:

$$D_d = \kappa^{(-1/3)} \cdot 70 \text{ nm} \quad (5)$$

Values of κ and critical dry diameter at 0.2 % supersaturation were calculated based on GFs at 85 % RH and dry particle diameter of 200 nm. Uncertainties are estimated to be 25 %, based on sizing uncertainties in the DASH-SP and RH variation in the instrument (Sorooshian et al., 2008). Figure 10 shows κ (left axis) and critical dry diameter (right axis; D_d) plotted against organic mass fraction (OMF), colored by time and date. Kappa values range from 0.15 to 0.51, with an average of 0.31 ± 0.08 , while critical diameters ranged from 87 to 131 nm, with an average of 105 ± 10 nm. As with GF data, there is a clear trend of decreasing κ and increasing critical dry diameter with increasing organic mass fraction, with the lowest hygroscopicity and CCN activity occurring during regime III. Earlier periods characterized by more marine influence and higher RH exhibited more hygroscopic behavior. At low values of organic mass fraction, κ approaches that of nitrate and sulfate salts (0.53–0.67), while approaching 0.1 at high organic fraction. Cubison et al. (2008) found that CCN concentrations in eastern Los Angeles were best modeled by treating organics (including the oxidized fraction) as nonhygroscopic. GF- and CCN- derived κ values for hygroscopic organics range from 0.01 to 0.5 (Petters and Kreidenweis, 2007), with only the most hygroscopic organics (i.e. malonic acid) approaching the high end of that range. Results from PACO suggest that organics are moderately hygroscopic, with κ values on the lower end of the range cited by Petters and Kreidenweis (2007).

Shinozuka et al. (2009) presented parameterizations for calculating as a function of organic mass fraction for 100 nm D_p , dry aerosol in Central Mexico and the North American West Coast ($\kappa = 0.34 - 0.20 \cdot \text{OMF}$ and $\kappa = 0.47 - 0.43 \cdot \text{OMF}$, respectively), and these parameterizations are shown in Fig. 10. Overall, aerosol sampled during PACO are more hygroscopic at a given OMF than those presented in Shinozuka et al. (2009), and are parameterized as $\kappa = 0.50 - 0.29 \cdot \text{OMF}$. This suggests that the organic fraction measured by Shinozuka et al. (2009) inhibits hygroscopicity significantly more than in Los Angeles. It is possible that the organics measured in Central Mexico and off the N. American West Coast exhibit more surface-active behavior, inhibiting hygroscopic activity, or that those organics are predominantly non-hygroscopic. In order to further investigate the hygroscopicity of organics, κ calculations were combined with AMS data giving mass fractions of individual aerosol species in order to estimate a κ value for organics, κ_{org} . If the overall hygroscopicity parameter, κ is given by:

$$\kappa = \sum_{i=1}^n \kappa_i \cdot \chi_i, \quad (6)$$

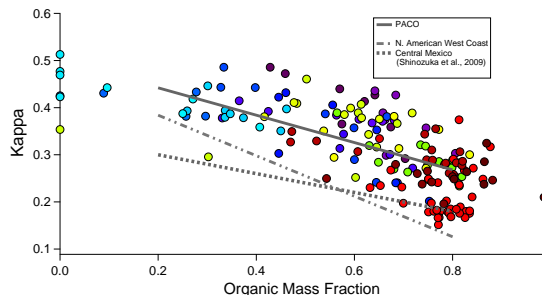


Fig. 10. κ and critical dry diameter plotted against mass fraction organic, with color scale corresponding to date; lines represent empirical parameterizations from PACO, Central Mexico, and N. American West Coast.

where n is the number of chemical constituents, i , with mole fraction χ_i and hygroscopicity parameter κ_i , then the organic hygroscopicity parameter, κ_{org} can be estimated by:

$$\kappa_{\text{org}} = \frac{\kappa - \sum_{i=1}^{n_{\text{inorg}}} \kappa_i \cdot \chi_i}{\chi_{\text{org}}}, \quad (7)$$

where n_{inorg} is the number of inorganic constituents, i , with hygroscopicity parameter κ_i and mole fraction χ_i , and χ_{org} is the mole fraction of organics in the aerosol. Previous publications have assumed κ_{org} of 0.1 for “hygroscopic” organics, and 0 for “nonhygroscopic” organics (Dusek et al., 2010; Wang et al., 2010; Wex et al., 2010). Assuming κ_i for inorganics to be 0.6 and κ_i for sea salt to be 1.3 (Wex et al., 2010), Eq. (7) gives κ_{org} of 0.16 for urban background aerosol transported to the PACO sampling site. Assuming κ_i for inorganics to be 0.7 (Dusek et al., 2010) gives κ_{org} of 0.12. Taking a median κ_{org} of 0.14, it is clear that the organics measured during PACO are significantly more hygroscopic than those previously measured in urban areas. This is not unexpected, given the consistently high O:C ratios of organics and the dominance of SV-OOA and LV-OOA during all three regimes of PACO. Further, the PACO sampling site is relatively free from the influence of local sources of primary aerosol, which would have the effect of reducing κ_{org} . Given that organics dominate aerosol in most urban areas, it is potentially significant to find that organics in an important urban center such as Los Angeles would have a value of κ_{org} appreciably higher than previously calculated for urban aerosol.

4 Conclusions

A major ambient sampling experiment was conducted at a site in Pasadena, CA positioned to sample a constant afternoon influx of transported Los Angeles pollution with a photochemical age of roughly 1–2 h and generally free from the influence of local point sources. Sampling spanned 4 months during the summer of 2009, and was characterized by three distinct meteorological regimes: a “springtime” period characterized by clean conditions coincident with low pressure systems (regime I), a typical early-summer period characterized by significant morning marine layer followed by warm, photochemically active afternoons (regime II), and a late-summer period characterized by little marine layer influence, hot and dry conditions, and elevated photochemical activity (regime III).

Chemical analysis of aerosol revealed that OC dominates particulate carbon in Los Angeles (OC:EC average of 8.04), and is enhanced relative to EC by an average of 47 % in the afternoon, suggesting significant SOA production. High RH during marine-layer-influenced morning sampling periods resulted in aqueous processing of aerosol particles and high aerosol volume, while drier afternoon periods saw increased aerosol number and volume due to SOA production. Maxima in aerosol volume occurred in the mid-late morning, reflecting a balance between RH-induced hygroscopic growth and SOA production. Maxima in aerosol number tended to occur near 14:00–15:00 LT, indicating that daytime photochemistry tended to generate a fine aerosol mode.

Organics are the most significant constituent of transported Los Angeles aerosol, contributing an average of 42, 43, and 55 % of total submicron mass in regimes I, II, and III, respectively. Interestingly, there was no significant difference between morning and afternoon O:C ratios, suggesting that the constant influx of 1–2 h old aerosol results in an overall organic oxidation state at the sampling site varying little despite significant SOA production. Regime II, characterized by significant morning marine layer influence followed by photochemically active afternoons, displayed significantly higher aerosol mass and 15–25 % higher average O:C ratio, suggesting that aqueous processes may be important in the generation of secondary aerosol and OOA in Los Angeles. Afternoons during regime II and III are characterized by the appearance of a fine organic mode, suggesting that SOA contributes significantly to growth of fine particles. It is unclear whether these fine particles are the result of sulfate nucleation and subsequent SOA growth or SOA condensation on existing primary aerosol.

Water soluble organic mass (WSOM) reaches maxima near 14:00–15:00 LT, coincident with markers for photochemistry and suggesting significant SOA contribution to WSOM. Sulfate is predominantly an accumulation mode constituent, and its magnitude appears to depend on the degree of marine influence. Nitrate is similarly a predominantly accumulation mode species, reaching maxima after morning

rush hour periods. Nighttime nitrate production is observed during periods in which maximum ozone levels indicated significant photochemical events. An ammonium ratio, defined as the moles of ammonium measured divided by the moles of ammonium required to neutralize sulfate and nitrate as $(\text{NH}_4)_2\text{SO}_4$ and NH_4NO_3 , respectively, revealed that ammonia limits particulate $(\text{NH}_4)_2\text{SO}_4$ and NH_4NO_3 in regimes I and II. An ammonium ratio of 1.28 ± 0.30 in regime III suggests that ammonium was in excess and that organic amines may have been an important constituent of submicron aerosol during this hot, dry, photochemically intense sampling period with reduced marine sulfate influence.

PMF analysis of C-ToF-AMS data resolved three factors, corresponding to HOA, SV-OOA, and LV-OOA, and correlating well with the "standard" factors presented in Ng et al. (2011). The HOA factor appears to be a periodic plume source, generally appearing during or shortly after peaks in CO concentration. SV-OOA displays a strong diurnal pattern, correlating strongly with ozone and the appearance of a fine mode (< 100 nm) in the aerosol size distribution, suggesting that these SOA products are generated on timescales of 1–2 h and tend to comprise a fine aerosol mode. LV-OOA is correlated with inorganic nitrate and sulfate and appears to be an aged carryover organic component that resides in accumulation mode aerosol, but may be generated on short timescales (1–2 h) under extremely oxidizing conditions. Its prevalence during humid overnight and morning hours and enhanced importance in moisture-influenced regimes I and II suggest that there may be significant aqueous-phase sources for LV-OOA. Overall the organic fraction of Los Angeles aerosol is overwhelmingly oxidized, with LV- and SV-OOA contributing 77, 92, and 86 % of OA in regimes I, II, and III, respectively.

Filter analysis by both (+) and (–) mode UPLC-ESI-TOF-MS reveals a complex mixture of organic compounds dominated by oxygenated species. Long (C8–C16), non-oxygenated nitrogenous compounds likely to be amines are detected during periods impacted by high concentrations of background LV-OOA, suggesting that amines may be an important constituent of aged organic aerosol in Los Angeles. Phthalic acid represents a ubiquitous, appreciable fraction of extractable OA, suggesting that PAH photochemistry may be an important pathway for SOA production in Los Angeles. Organo-nitro-sulfate species are observed during periods when aerosol appears to be a mixture of aged background species and freshly emitted particles. Carboxylic acids appear to be major contributors to both SV- and LV-OOA, with LV-OOA tending to be associated with shorter (C4–C9) carboxylic acids and thereby higher O:C ratio.

The organic fraction of transported Los Angeles aerosol is dynamic and undergoes numerous and significant changes on timescales of days to weeks, despite exhibiting consistency in the overall degree of oxidation. Many compounds are common to periods identified as distinct by PMF analysis, and PACO data suggest that Los Angeles OA is best

described as a complex, dynamic mixture of compounds that represent a continuum of oxidation. Thus, a bilinear PMF model that assumes constant mass spectra representative of classes of OA is a useful tool in qualitatively assessing the degree of OA aging and oxidation, but is a dramatic simplification of a complex organic fraction.

Finally, aerosol water uptake characteristics measured by the DASH-SP indicate that a bimodal distribution becomes more unimodal during periods of photochemical SOA production. The degree of hygroscopicity of the main hygroscopic mode is highly anti-correlated with organic mass fraction, as indicated by decreasing GF and κ , as well as increasing critical diameter with increased organic fraction. Values for κ averaged 0.31 ± 0.08 , approaching 0.5 at low OMF and 0.1 at high OMF. It appears that organics in Los Angeles inhibit hygroscopicity less than those measured in Central Mexico and off the N. American West Coast, potentially owing to less surface-active behavior or an organic fraction comprised of more water soluble species.

PACO represents the first major aerosol characterization in the Western Los Angeles Basin, and comparison with SOAR will help identify spatial variation in Los Angeles aerosol and determine the nature of aerosol evolution as it is transported from source-rich (western) to downwind (eastern) parts of Los Angeles. Further, its timing will serve to contextualize and compare forthcoming results from the CalNex field campaign, part of which involved ground sampling at the PACO site.

Appendix A

PMF analysis

PMF was initiated using 50 seed values, and then again using a range of fpeak values from –1 to 1 varying by 0.1. Figures A1 and A2 show the Q/Q_{expected} values for the different solutions. The PMF results were sorted by regime, number of factors, and seed (only where it caused the solution to vary) and compared to previously published mass spectra in the AMS online Spectral Database explained in Ulbrich et al. (2009). Table A1 shows Pearson's r values comparing the PMF mass spectral profile solutions to existing mass spectra. Table A2 shows Pearson's r values comparing the PMF time series solutions to gas phase tracers, AMS inorganic tracers, PILS tracers, and WSOC. Figure A3 shows total residuals of all masses over time for solutions with different factor numbers. Figure A4 shows the scaled residuals at each mass for the presented 3 factor solution. The 2 and 4 factor solution profiles and time series contributions are shown in Figs. A5a, b.

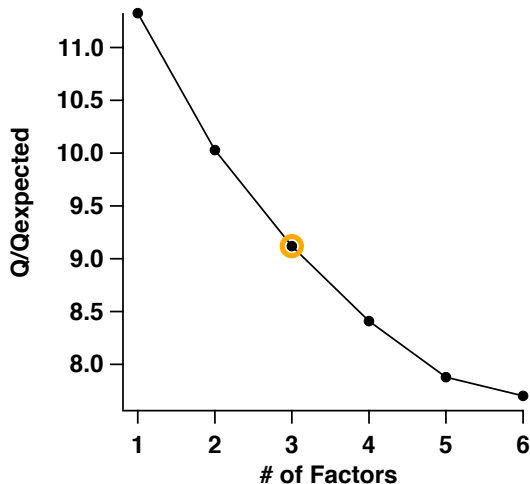


Fig. A1. Q/Q_{exp} values for varying number of factors (p values). The circled marker is the presented solution.

The difference in the total residuals was noticeable between the 1 and 2 factor solution and the 2 and 3 factor solution, but negligible between the 3 and 4 factor solution. In the 2 factor solution there is evidence of an HOA-like factor and OOA-like factor from the mass spectral comparison, but when compared to the 3 factor solution, the time series correlations with AMS inorganic and certain gas phase tracers is improved. In the 3 factor case, 3 solutions were explored, and were representative of the 50 possible solutions from the PMF results. Regarding the mass spectral profile, the seed = 6 solution was chosen since it has very strong correlations with the real mass spectra, and each of the profiles are least similar to one another (see the right hand side of Table A2) when compared to the two other 3 factor solutions. When considering the time series comparison, the seed = 6 LV-OOA like factor (factor 1) has the highest correlation with the AMS inorganic species. The p-ToF data suggests the organic profile of LV-OOA has similar particle size distributions to the AMS inorganic species (this was investigated in areas of known LV-OOA like factor and low SV-OOA like factor, since PMF was not performed on pToF data). When the afternoon sun reaches a maximum, there is another, smaller mode that is believed to be SV-OOA, without the strong inorganic signal. Also, the seed = 6 SV-OOA

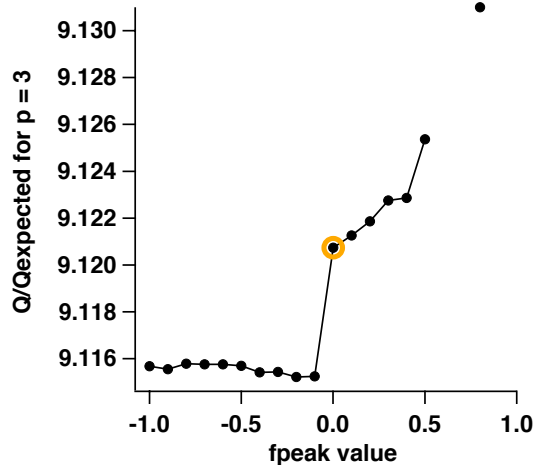


Fig. A2. Q/Q_{exp} for varying peak values for $p = 3$. The circled marker is the presented solution.

factor correlates best with ozone when compared to the two other solutions. The tracers for HOA were limited in this study since the resolution for the CO and NO_x were poor and the r values are very low. However, when comparing the seed = 6 and seed = 1 solutions, the correlations of the HOA-like factor to CO and NO_x are slightly larger. Additionally, the HOA-like factor was compared to *m/z* 57, which is higher for the seed = 6 solutions. The HOA correlations for the seed = 4 solutions are slightly higher than in the seed = 1 and seed = 6 solutions, but this solution is not as strong mass spectrally, and when comparing the tracers for the two other factors. The four factor situation provided two different solutions, representative of the 50 seeds. In addition to the residuals not changing dramatically, in the mass spectral comparison, for both solutions, two of the factors have very similar r values (factor 1 and 4 for seed 1 and factor 2 and 4 for seed 4). Also, the time series correlations are worse in the four factor solutions, when compared to the presented 3 factor solution.

Table A1. Mass spectral comparison of several PMF solutions.

Mass Spectra Comparison																		
Factor Number (p)		Mass Spectra Comparison																
Seed	Brushfire (4)																	
Manchester high CO low O ₃ (5)	Pittsburgh HOA (3)	Pittsburgh HOA (1)	Pittsburgh OOA I (3)	Pittsburgh OOA II (3)	Pittsburgh OOA (1)	Urban Vancouver high O ₃ (5)	Urban Vancouver low O ₃ (5)	Zurich Summer HOA (2)	Zurich Summer OOA I (2)	Zurich Summer OOA II (2)	Zurich Summer Wood burning (2)	Zurich Winter HOA (2)	Zurich Winter OOA (2)	Zurich Winter Wood burning (2)	Factor 1	Factor 2	Factor 3	Factor 4
1 1 0.96 0.68 0.68 0.51 0.97 0.85 0.97 0.99 0.77 0.44 0.95 0.58 0.64 0.66 0.97 0.81	1 1 0.94 0.55 0.54 0.35 0.98 0.80 0.98 0.96 0.65 0.30 0.98 0.47 0.62 0.50 0.98 0.76	2 1 0.77 0.94 0.97 0.91 0.67 0.78 0.66 0.78 0.96 0.78 0.57 0.76 0.51 0.90 0.61 0.73													0.64			
1 1 0.92 0.50 0.49 0.29 0.98 0.77 0.98 0.94 0.60 0.25 0.98 0.44 0.61 0.42 0.98 0.74	2 1 0.74 0.91 0.95 0.88 0.63 0.73 0.62 0.74 0.93 0.76 0.53 0.71 0.51 0.88 0.56 0.69	3 1 0.74 0.95 0.97 0.93 0.63 0.79 0.63 0.76 0.97 0.79 0.54 0.75 0.48 0.92 0.58 0.70													0.56	0.56	0.94	
1 4 0.93 0.66 0.66 0.49 0.93 0.79 0.93 0.93 0.73 0.42 0.89 0.56 0.64 0.55 0.92 0.81	2 4 0.92 0.51 0.50 0.30 0.98 0.78 0.98 0.95 0.61 0.26 0.99 0.45 0.61 0.44 0.98 0.74	3 4 0.59 0.93 0.97 0.96 0.46 0.67 0.45 0.61 0.93 0.83 0.35 0.72 0.39 0.95 0.58 0.57													0.92	0.57	0.92	0.39
1 6 0.93 0.52 0.51 0.32 0.98 0.78 0.98 0.95 0.62 0.27 0.98 0.46 0.62 0.45 0.98 0.75	2 6 0.61 0.92 0.96 0.95 0.47 0.65 0.46 0.60 0.92 0.81 0.35 0.71 0.43 0.93 0.39 0.60	3 6 0.94 0.81 0.82 0.68 0.92 0.89 0.92 0.97 0.89 0.58 0.88 0.67 0.62 0.80 0.91 0.82													0.41	0.90	0.73	
1 1 0.94 0.57 0.56 0.37 0.98 0.81 0.98 0.97 0.67 0.32 0.98 0.49 0.63 0.54 0.98 0.76	2 1 0.90 0.60 0.59 0.43 0.89 0.74 0.89 0.87 0.66 0.37 0.84 0.54 0.65 0.43 0.87 0.80	3 1 0.61 0.92 0.96 0.94 0.48 0.67 0.48 0.63 0.93 0.81 0.38 0.68 0.41 0.94 0.41 0.58	4 1 0.93 0.69 0.66 0.51 0.95 0.86 0.94 0.96 0.75 0.46 0.92 0.62 0.58 0.60 0.95 0.82												0.89	0.49	0.93	0.56
1 4 0.90 0.60 0.59 0.43 0.89 0.74 0.89 0.87 0.66 0.37 0.85 0.54 0.65 0.43 0.88 0.80	2 4 0.94 0.57 0.56 0.37 0.98 0.81 0.98 0.97 0.67 0.32 0.98 0.49 0.63 0.54 0.98 0.76	3 4 0.61 0.92 0.96 0.94 0.48 0.67 0.48 0.63 0.93 0.81 0.38 0.68 0.41 0.94 0.41 0.58	4 4 0.93 0.69 0.66 0.51 0.95 0.87 0.94 0.96 0.76 0.46 0.92 0.63 0.58 0.60 0.95 0.82												0.89	0.53	0.87	0.56

(1) Zhang, et al., 2005; (2) Lanz et al., 2007; (3) Ulbrich, et al., 2009; (4) Bahreini et al., 2005; (5) Alfarra et al., 2004

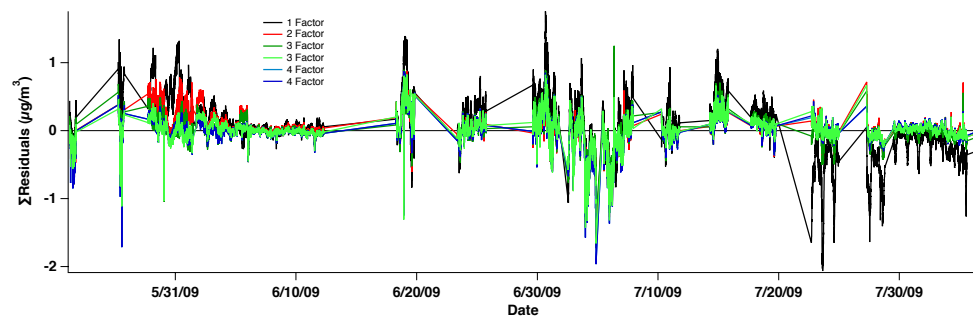
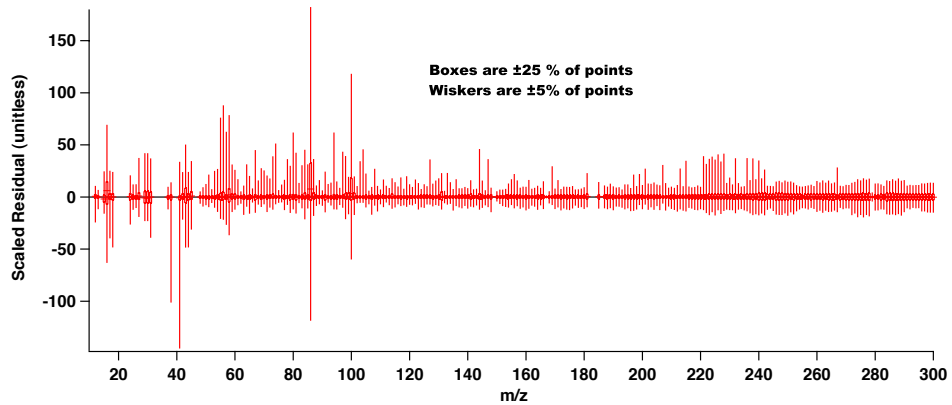
**Fig. A3.** Sum of the residuals for 1, 2, 3, and 4 factor solutions.

Table A2. Time series comparison of several PMF solutions.

		Gas Phase Tracers				AMS Inorganic Tracers				Organic Tracers				PILS Tracers					
Factor Number (<i>p</i>)	Seed	Ozone	CO	NO _x	SO ₄	NO ₃	NH ₄	Chl	WSOC	org ⁵⁷	NH ₄	NO ₃	SO ₄	Factor 1	Factor 2	Factor 3	Factor 4		
1	1	0.51	0.38	0.24	0.66	0.45	0.63	0.35	0.58	0.79	0.70	0.67	0.76						
1	1	0.46	0.33	0.14	0.73	0.45	0.64	0.43	0.53	0.54	0.74	0.69	0.79		0.51				
2	1	0.41	0.34	0.30	0.37	0.31	0.44	0.12	0.30	0.91	0.56	0.56	0.63	0.51					
1	1	0.47	0.33	0.16	0.71	0.44	0.63	0.42	0.56	0.53	0.73	0.68	0.79		-0.02	0.73			
2	1	-0.06	0.15	-0.03	0.23	0.18	0.24	0.06	-0.39	0.61	0.22	0.22	0.20	-0.02	0.00				
3	1	0.51	0.34	0.30	0.43	0.32	0.47	0.18	0.50	0.77	0.60	0.59	0.67	0.73	0.00				
1	4	0.07	0.12	-0.14	0.22	0.29	0.30	0.02	-0.19	0.22	0.10	0.25	0.14		-0.19	-0.02			
2	4	0.47	0.32	0.19	0.66	0.39	0.58	0.40	0.58	0.54	0.71	0.66	0.77	-0.19	0.64				
3	4	0.42	0.35	0.30	0.42	0.31	0.45	0.15	0.36	0.93	0.59	0.58	0.65	-0.02	0.64				
1	6	0.39	0.31	0.09	0.75	0.46	0.65	0.46	0.47	0.49	0.76	0.73	0.81		0.05	0.60			
2	6	0.39	0.17	0.04	0.18	0.15	0.21	0.02	-0.29	0.70	0.16	0.17	0.14	0.05	-0.08				
3	6	0.53	0.31	0.28	0.42	0.31	0.45	0.19	0.56	0.62	0.60	0.58	0.67	0.60	-0.08				
1	1	0.43	0.30	0.15	0.71	0.39	0.58	0.43	0.53	0.52	0.73	0.66	0.79		-0.14	0.26	0.56		
2	1	0.01	0.15	-0.07	0.16	0.29	0.26	0.01	-0.22	0.07	0.03	0.20	0.04	-0.14	0.06	-0.18			
3	1	0.24	0.29	0.22	0.28	0.19	0.30	0.04	0.16	0.94	0.43	0.43	0.46	0.26	0.06	0.44			
4	1	0.51	0.28	0.27	0.31	0.34	0.44	0.13	0.39	0.58	0.57	0.58	0.66	0.56	-0.18	0.44			
1	4	0.01	0.15	-0.07	0.16	0.29	0.26	0.01	-0.23	0.07	0.02	0.20	0.04		-0.15	0.06	-0.18		
2	4	0.43	0.30	0.15	0.70	0.39	0.58	0.43	0.54	0.52	0.73	0.66	0.79	-0.15	0.26	0.56			
3	4	0.24	0.29	0.22	0.27	0.19	0.30	0.04	0.16	0.94	0.43	0.43	0.46	0.06	0.26	0.43			
4	4	0.51	0.28	0.27	0.31	0.34	0.44	0.13	0.39	0.58	0.57	0.58	0.66	-0.18	0.56	0.43			

**Fig. A4.** Scaled residuals for the 3 factor solution (seed = 6).

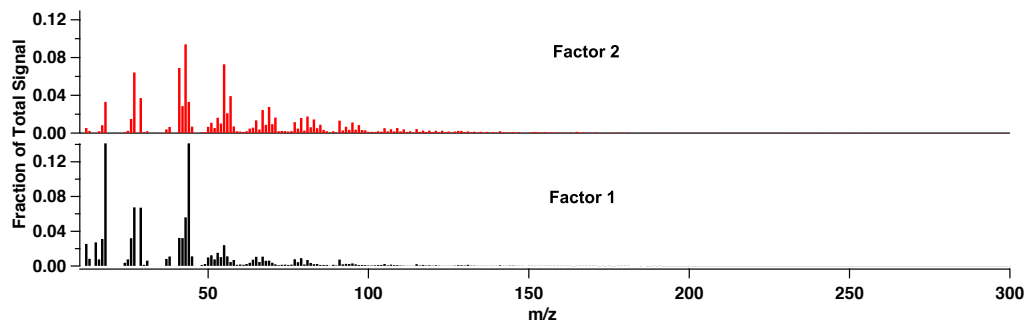


Fig. A5a. Mass spectral profiles for the 2 factor solution.

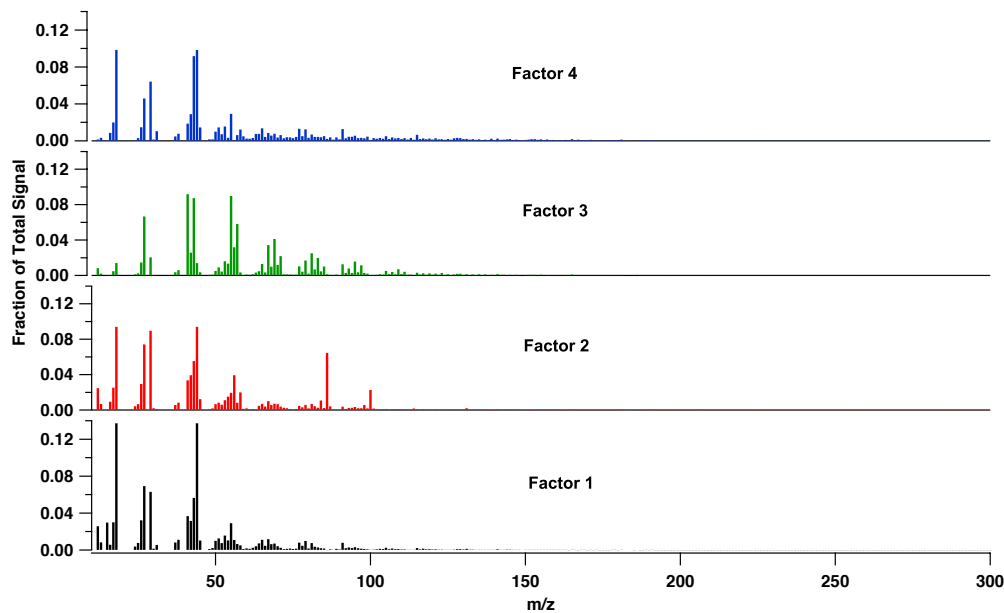


Fig. A5b. Mass spectral profiles for the 4 factor solution.

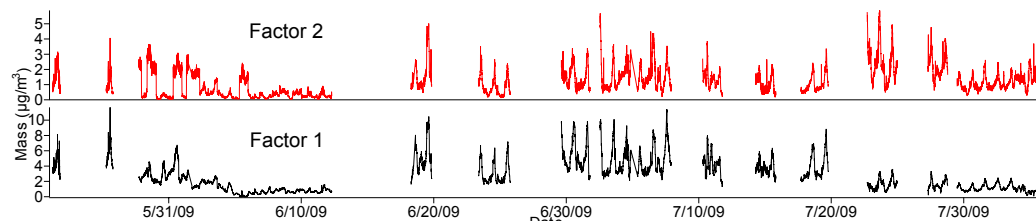


Fig. A6. Time series contributions for the 2-factor solution.

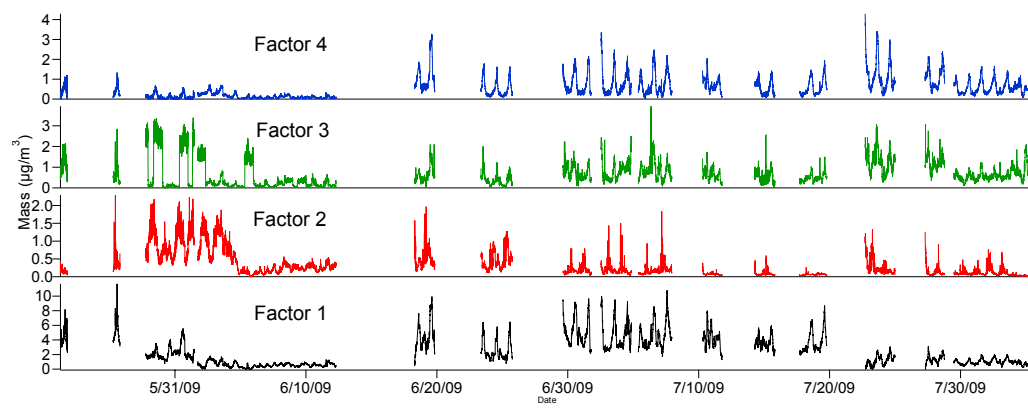


Fig. A7. Time series contributions for the 4-factor solution.

Acknowledgements. Funding was provided by the Electric Power Research Institute. The authors would like to thank Jason Surratt for his helpful comments and direction. We would also like to thank Eric Edgerton and the SEARCH network for guidance on high-volume filter sampling and for the use of a sampler during PACO.

Edited by: M. C. Facchini

References

Aiken, A. C., DeCarlo, P. F., Kroll, J. H., Worsnop, D. R., Huffman, J. A., Docherty, K. S., Ulbrich, I. M., Mohr, C., Kimmel, J. R., Sueper, D., Sun, Y., Zhang, Q., Trimborn, A., Northway, M., Ziemann, P. J., Canagaratna, M. R., Onasch, T. B., Alfarra, M. R., Prevot, A. S. H., Dommen, J., Duplissy, J., Metzger, A., Baltensperger, U., and Jimenez, J. L.: O/C and OM/OC ratios of primary, secondary, and ambient organic aerosols with high-resolution time-of-flight aerosol mass spectrometry, *Environ. Sci. Technol.*, 42, 4478–4485, 2008.

Aiken, A. C., Salcedo, D., Cubison, M. J., Huffman, J. A., DeCarlo, P. F., Ulbrich, I. M., Docherty, K. S., Sueper, D., Kimmel, J. R., Worsnop, D. R., Trimborn, A., Northway, M., Stone, E. A., Schauer, J. J., Volkamer, R. M., Fortner, E., de Foy, B., Wang, J., Laskin, A., Shutthanandan, V., Zheng, J., Zhang, R., Gaffney, J., Marley, N. A., Paredes-Miranda, G., Arnott, W. P., Molina, L. T., Sosa, G., and Jimenez, J. L.: Mexico City aerosol analysis during MILAGRO using high resolution aerosol mass spectrometry at the urban supersite (T0) – Part 1: Fine particle composition and organic source apportionment, *Atmos. Chem. Phys.*, 9, 6633–6653, doi:10.5194/acp-9-6633-2009, 2009.

Alfarra, M., Coe, H., Allan, J., Bower, K., Boudries, H., Canagaratna, M., Jimenez, J., Jayne, J., Garforth, A., Li, S., and Worsnop, D. R.: Characterization of urban and rural organic particulate in the Lower Fraser Valley using two aerodyne aerosol mass spectrometers, *Atmos. Environ.*, 38, 5745–5758, 2004.

Allan, J., Bower, K., Coe, H., Boudries, H., Jayne, J., Canagaratna, M., Millet, D., Goldstein, A., Quinn, P., Weber, R., and Worsnop, D.: Submicron aerosol composition at Trinidad Head, California, during ITCT 2K2: its relationship with gas phase volatile organic carbon and assessment of instrument performance, *J. Geophys. Res. Atmos.*, 109, D23S24, doi:10.1029/2003JD004208, 2004a.

Allan, J., Delia, A., Coe, H., Bower, K., Alfarra, M., Jimenez, J., Middlebrook, A., Drewnick, F., Onasch, T., Canagaratna, M., Jayne, J., and Worsnop, D.: A generalised method for the extraction of chemically resolved mass spectra from aerodyne aerosol mass spectrometer data, *J. Aerosol Sci.*, 35, 909–922, doi:10.1016/j.jaerosci.2004.02.007, 2004b.

Ault, A. P., Gaston, C. J., Wang, Y., Dominguez, G., Thiemens, M. H., and Prather, K. A.: Characterization of the single particle mixing state of individual ship plume events measured at the port of Los Angeles, *Environ. Sci. Technol.*, 44(6), 1954–1961, 2010.

AQMD: Historic ozone air quality trends, available at: <http://www.aqmd.gov/smog/o3trend.html>, last access: August 2010, 2010.

Bahreini, R., Keywood, M., Ng, N., Varutbangkul, V., Gao, S., Flagan, R., Seinfeld, J., Worsnop, D., and Jimenez, J.: Measurements of secondary organic aerosol from oxidation of cycloalkenes, terpenes, and m-xylene using an Aerodyne aerosol mass spectrometer, *Environ. Sci. Technol.*, 39, 5674–5688, 2005.

Bein, K. J., Zhao, Y. J., Pekney, N. J., Davidson, C. I., Johnston, M. V., and Wexler, A. S.: Identification of sources of atmospheric PM at the Pittsburgh Supersite – Part II: Quantitative comparisons of single particle, particle number, and particle mass measurements, *Atmos. Environ.*, 40, S424–S444, 2006.

Blumenthal, D., White, W., and Smith, T.: Anatomy of a Los Angeles smog episode: pollutant transport in the daytime sea breeze regime, *Atmos. Environ.*, 12, 893–907, 1978.

Bremner, J., Haub, C., Lee, M., Mather, M., and Zuehlke, E.: World Population Highlights: Key Findings From PRB's 2009 World Population Data Sheet, Population Reference Bureau, available at: www.prb.org, 2009.

Cabada, J. C., Rees, S., Takahama, S., Khlystov, A., Pandis, S. N., Davidson, C. I., and Robinson, A. L.: Mass size distributions and size resolved chemical composition of fine particulate matter at the Pittsburgh supersite, *Atmos. Environ.*, 38, 3127–3141, 2004.

Canagaratna, M., Jayne, J., Jimenez, J., Allan, J., Alfarra, M., Zhang, Q., Onasch, T., Drewnick, F., Coe, H., Middlebrook, A., Worsnop, D. R., and Jimenez, J. L.: Chemical and microphysical characterization of ambient aerosols with the aerodyne aerosol mass spectrometer, *Mass Spectrom. Rev.*, 26, 185–222, 2007.

CARB: iADAM Air Quality Data Statistics, California Air Resources Board, available at: <http://www.arb.ca.gov/adam/>, 2010.

Chow, J. C., Fujita, E. M., Watson, J. G., Lu, Z. Q., Lawson, D. R., and Asbaugh, L. L.: Evaluation of filter-based aerosol measurements during the 1987 Southern California-Quality Study, *Environ. Monit. Assess.*, 30, 49–80, 1994.

Cocker, D. R., Whitlock, N. E., Flagan, R. C., and Seinfeld, J. H.: Hygroscopic properties of Pasadena, California aerosol, *Aerosol Sci. Technol.*, 35, 637–647, 2001.

Croes, B. E. and Fujita, E. M.: Overview of the 1997 Southern California Ozone Study (SCOS97-NARSTO), *Atmos. Environ.*, 37, S3–S26, 2003.

Cubison, M. J., Ervens, B., Feingold, G., Docherty, K. S., Ulbrich, I. M., Shields, L., Prather, K., Hering, S., and Jimenez, J. L.: The influence of chemical composition and mixing state of Los Angeles urban aerosol on CCN number and cloud properties, *Atmos. Chem. Phys.*, 8, 5649–5667, doi:10.5194/acp-8-5649-2008, 2008.

DeCarlo, P. F., Kimmel, J. R., Trimborn, A., Northway, M. J., Jayne, J. T., Aiken, A. C., Gonin, M., Fuhrer, K., Horvath, T., Docherty, K. S., Worsnop, D. R., and Jimenez, J. L.: Field-deployable, high-resolution, time-of-flight aerosol mass spectrometer, *Anal. Chem.*, 78, 8281–8289, 2006.

DeCarlo, P. F., Dunlea, E. J., Kimmel, J. R., Aiken, A. C., Sueper, D., Crounse, J., Wennberg, P. O., Emmons, L., Shinozuka, Y., Clarke, A., Zhou, J., Tomlinson, J., Collins, D. R., Knapp, D., Weinheimer, A. J., Montzka, D. D., Campos, T., and Jimenez, J. L.: Fast airborne aerosol size and chemistry measurements above Mexico City and Central Mexico during the MILAGRO campaign, *Atmos. Chem. Phys.*, 8, 4027–4048, doi:10.5194/acp-8-4027-2008, 2008.

Denkenberger, K. A., Moffet, R. C., Holecek, J. C., Rebotier, T. P., and Prather, K. A.: Real-time, single-particle measurements of oligomers in aged ambient aerosol particles, *Environ. Sci. Technol.*, 41, 5439–5446, 2007.

Dusek, U., Frank, G. P., Curtius, J., Drewnick, F., Schneider,

J., Kürten, A., Rose, D., Andreae, M. O., Borrmann, S., and Pöschl, U.: Enhanced organic mass fraction and decreased hygroscopicity of cloud condensation nuclei (CCN) during new particle formation events, *Geophys. Res. Lett.*, 37, L03804, doi:10.1029/2009GL040930, 2010.

Docherty, K. S., Stone, E. A., Ulbrich, I. M., DeCarlo, P. F., Snyder, D. C., Schauer, J. J., Peltier, R. E., Weber, R. J., Murphy, S. M., Seinfeld, J. H., Grover, B. D., Eatough, D. J., and Jimenez, J. L.: Apportionment of primary and secondary organic aerosols in Southern California during the 2005 Study of Organic Aerosols in Riverside (SOAR-1), *Environ. Sci. Technol.*, 42, 7655–7662, 2008.

Drewnick, F., Schwab, J., Hogrefe, O., Peters, S., Husain, L., Diamond, D., Weber, R., and Demerjian, K.: Intercomparison and evaluation of four semi-continuous PM_{2.5} sulfate instruments, *Atmos. Environ.*, 37, 3335–3350, doi:10.1016/S1352-2310(03)00351-0, 2003.

Drewnick, F., Hings, S., DeCarlo, P., Jayne, J., Gonin, M., Fuhrer, K., Weimer, S., Jimenez, J., Demerjian, K., Borrmann, S., and Worsnop, D.: A new time-of-flight aerosol mass spectrometer (TOF-AMS) – instrument description and first field deployment, *Aerosol Sci. Tech.*, 39, 637–658, doi:10.1080/02786820500182040, 2005.

Eatough, D. J., Grover, B. D., Woolwine, W. R., Eatough, N. L., Long, R., and Farber, R.: Source apportionment of 1 h semi-continuous data during the 2005 Study of Organic Aerosols in Riverside (SOAR) using positive matrix factorization, *Atmos. Environ.*, 42, 2706–2719, 2008.

Elderling, A., Cass, G. R., and Moon, K. C.: An Air monitoring network using continuous particle-size distribution monitors – connecting pollutant properties to visibility via mie scattering calculations, *Atmos. Environ.*, 28, 2733–2749, 1994.

Hersey, S. P., Sorooshian, A., Murphy, S. M., Flagan, R. C., and Seinfeld, J. H.: Aerosol hygroscopicity in the marine atmosphere: a closure study using high-time-resolution, multiple-RH DASH-SP and size-resolved C-ToF-AMS data, *Atmos. Chem. Phys.*, 9, 2543–2554, doi:10.5194/acp-9-2543-2009, 2009.

Huffman, J., Jayne, J., Drewnick, F., Aiken, A., Onasch, T., Worsnop, D., and Jimenez, J.: Design, modeling, optimization, and experimental tests of a particle beam width probe for the aerodyne aerosol mass spectrometer, *Aerosol Sci. Tech.*, 39, 1143–1163, doi:10.1080/02786820500423782, 2005.

Hughes, L. S., Allen, J. O., Salmon, L. G., Mayo, P. R., Johnson, R. J., and Cass, G. R.: Evolution of nitrogen species air pollutants along trajectories crossing the Los Angeles area, *Environ. Sci. Technol.*, 36, 3928–3935, 2002.

Kautzman, K. E., Surratt, J. D., Chan, M. N., Chan, A. W. H., Hersey, S. P., Chhabra, P. S., Dalleska, N. F., Wennberg, P. O., Flagan, R. C., and Seinfeld, J. H.: Chemical composition of gas- and aerosol-phase products from the photooxidation of naphthalene, *J. Phys. Chem. A*, 114, 913–934, 2010.

Kleeman, M., Hughes, L., Allen, J., and Cass, G.: Source contributions to the size and composition distribution of atmospheric particles: Southern California in September 1996, *Environ. Sci. Technol.*, 33, 4331–4341, 1999.

Kondo, Y., Miyazaki, Y., Takegawa, N., Miyakawa, T., Weber, R. J., Jimenez, J. L., Zhang, Q., and Worsnop, D. R.: Oxygenated and water-soluble organic aerosols in Tokyo, *J. Geophys. Res.*, 112, D01203, doi:10.1029/2006JD007056, 2007.

Lanz, V. A., Alfarra, M. R., Baltensperger, U., Buchmann, B., Hueglin, C., and Prévôt, A. S. H.: Source apportionment of submicron organic aerosols at an urban site by factor analytical modelling of aerosol mass spectra, *Atmos. Chem. Phys.*, 7, 1503–1522, doi:10.5194/acp-7-1503-2007, 2007.

Liu, D. Y., Prather, K. A., and Hering, S. V.: Variations in the size and chemical composition of nitrate-containing particles in Riverside, CA, *Aerosol Sci. Technol.*, 33, 71–86, 2000.

Lu, R. and Turco, R.: Air pollutant transport in a coastal environment – II. Three-dimensional simulations over Los Angeles Basin, *Atmos. Environ.*, 29, 1499–1518, 1995.

Massling, A., Stock, M., and Wiedensohler, A.: Diurnal, weekly, and seasonal variation of hygroscopic properties of submicrometer urban aerosol particles, *Atmos. Environ.*, 39, 3911–3922, 2005.

Massling, A., Stock, M., Wehner, B., Wu, Z. J., Hu, M., Bruggemann, E., Gnauk, T., Herrmann, H., and Wiedensohler, A.: Size segregated water uptake of the urban submicrometer aerosol in Beijing, *Atmos. Environ.*, 43, 1578–1589, 2009.

Matsui, H., Koike, M., Kondo, Y., Takegawa, N., Kita, K., Miyazaki, Y., Hu, M., Chang, S. Y., Blake, D. R., Fast, J. D., Zaveri, R. A., Streets, D. G., Zhang, Q., and Zhu, T.: Spatial and temporal variations of aerosols around Beijing in summer 2006: model evaluation and source apportionment, *J. Geophys. Res. Atmos.*, 114, D00G13, 2009.

Meier, J., Wehner, B., Massling, A., Birmili, W., Nowak, A., Gnauk, T., Brüggemann, E., Herrmann, H., Min, H., and Wiedensohler, A.: Hygroscopic growth of urban aerosol particles in Beijing (China) during wintertime: a comparison of three experimental methods, *Atmos. Chem. Phys.*, 9, 6865–6880, doi:10.5194/acp-9-6865-2009, 2009.

Modey, W. K., Eatough, D. J., Anderson, R. R., Martello, D. V., Takahama, S., Lucas, L. J., and Davidson, C. I.: Ambient fine particulate concentrations and chemical composition at two sampling sites in metropolitan Pittsburgh: a 2001 intensive summer study, *Atmos. Environ.*, 38, 3165–3178, 2004.

Na, K., Sawant, A. A., Song, C., and Cocker, D. R.: Primary and secondary carbonaceous species in the atmosphere of Western Riverside County, California *Atmos. Environ.*, 38, 1345–1355, 2004.

Ng, N. L., Canagaratna, M. R., Zhang, Q., Jimenez, J. L., Tian, J., Ulbrich, I. M., Kroll, J. H., Docherty, K. S., Chhabra, P. S., Bahreini, R., Murphy, S. M., Seinfeld, J. H., Hildebrandt, L., Donahue, N. M., DeCarlo, P. F., Lanz, V. A., Prévôt, A. S. H., Dinar, E., Rudich, Y., and Worsnop, D. R.: Organic aerosol components observed in Northern Hemispheric datasets from Aerosol Mass Spectrometry, *Atmos. Chem. Phys.*, 10, 4625–4641, doi:10.5194/acp-10-4625-2010, 2010.

Ng, N. L., Canagaratna, M. R., Jimenez, J. L., Zhang, Q., Ulbrich, I. M., and Worsnop, D. R.: Real-time methods for estimating organic component mass concentrations from aerosol mass spectrometer data, *Environ. Sci. Technol.*, 45, 910–916, doi:10.1021/es102951k, 2011.

Paatero, P.: A weighted non-negative least squares algorithm for three-way “PARAFAC” factor analysis, *Chemom. Intell. Lab. Syst.*, 38, 223–242, 1997.

Paatero, P. and Tapper, U.: Positive matrix factorization – a nonnegative factor model with optimal utilization of error-estimates of data values, *Environmetrics*, 5, 111–126, 1994.

Pastor, S. H., Allen, J. O., Hughes, L. S., Bhawe, P., Cass, G. R., and Prather, K. A.: Ambient single particle analysis in Riverside, California by aerosol time-of-flight mass spectrometry during the SCOS97-NARSTO, *Atmos. Environ.*, 37, S239–S258, 2003.

Pekney, N. J., Davidson, C. I., Bein, K. J., Wexler, A. S., and Johnston, M. V.: Identification of sources of atmospheric PM at the Pittsburgh Supersite, Part I: single particle analysis and filter-based positive matrix factorization, *Atmos. Environ.*, 40, S411–S423, 2006.

Petters, M. D. and Kreidenweis, S. M.: A single parameter representation of hygroscopic growth and cloud condensation nucleus activity, *Atmos. Chem. Phys.*, 7, 1961–1971, doi:10.5194/acp-7-1961-2007, 2007.

van Pinxteren, D., Bruggemann, E., Gnauk, T., Iinuma, Y., Muller, K., Nowak, A., Achtert, P., Wiedensohler, A., and Herrmann, H.: Size- and time-resolved chemical particle characterization during CAREBeijing-2006: different pollution regimes and diurnal profiles, *J. Geophys. Res. Atmos.*, 114, D00G09, doi:10.1029/2008JD010890, 2009.

Quinn, P., Bates, T., Baynard, T., Clarke, A., Onasch, T., Wang, W., Rood, M., Andrews, E., Allan, J., Carrico, C., Coffman, D., and Worsnop, D. R.: Impact of particulate organic matter on the relative humidity dependence of light scattering: a simplified parameterization, *Geophys. Res. Lett.*, 32(22), L22809, doi:10.1029/2005GL024322, 2005.

Rose, D., Nowak, A., Achtert, P., Wiedensohler, A., Hu, M., Shao, M., Zhang, Y., Andreae, M. O., and Pöschl, U.: Cloud condensation nuclei in polluted air and biomass burning smoke near the mega-city Guangzhou, China – Part 1: Size-resolved measurements and implications for the modeling of aerosol particle hygroscopicity and CCN activity, *Atmos. Chem. Phys.*, 10, 3365–3383, doi:10.5194/acp-10-3365-2010, 2010.

Sawant, A. A., Na, K., Zhu, X., Cocker, K., Butt, S., Song, C., and Cocker III, D. R.: Characterization of $PM_{2.5}$ and selected gas-phase compounds at multiple indoor and outdoor sites in Mira Loma, California, *Atmos. Environ.*, 38, 6269–6278, 2004.

Schauer, J. J., Rogge, W. F., Hildemann, L. M., Masurek, M. A., and Cass, G. R.: Source apportionment of airborne particulate matter using organic compounds as tracers, *Atmos. Environ.*, 30, 3837–3855, 1996.

Shinozuka, Y., Clarke, A. D., DeCarlo, P. F., Jimenez, J. L., Dunlea, E. J., Roberts, G. C., Tomlinson, J. M., Collins, D. R., Howell, S. G., Kapustin, V. N., McNaughton, C. S., and Zhou, J.: Aerosol optical properties relevant to regional remote sensing of CCN activity and links to their organic mass fraction: airborne observations over Central Mexico and the US West Coast during MILAGRO/INTEX-B, *Atmos. Chem. Phys.*, 9, 6727–6742, doi:10.5194/acp-9-6727-2009, 2009.

Sorooshian, A., Brechtel, F., Weber, R., Corless, A., Flagan, R., and Seinfeld, J.: Modeling and characterization of a particle-into-liquid sampler (PILS), *Aerosol Sci. Technol.*, 40, 396–409, 2006.

Sorooshian, A., Hersey, S., Brechtel, F., Corless, A., Flagan, R., and Seinfeld, J.: Rapid, size-resolved aerosol hygroscopic growth measurements: differential aerosol sizing and hygroscopicity spectrometer probe (DASH-SP), *Aerosol Sci. Technol.*, 42, 445–464, 2008.

Stanier, C., Khlystov, A., and Pandis, S.: Nucleation events during the Pittsburgh Air Quality Study: description and relation to key meteorological, gas phase, and aerosol parameters special issue of aerosol science and technology on findings from the fine particulate matter supersites program, *Aerosol Sci. Technol.*, 38, 253–264, 2004.

Stone, E. A., Snyder, D. C., Sheesley, R. J., Sullivan, A. P., Weber, R. J., and Schauer, J. J.: Source apportionment of fine organic aerosol in Mexico City during the MILAGRO experiment 2006, *Atmos. Chem. Phys.*, 8, 1249–1259, doi:10.5194/acp-8-1249-2008, 2008.

Sullivan, A., Weber, R., Clements, A., Turner, J., Bae, M., and Schauer, J.: A method for on-line measurement of water-soluble organic carbon in ambient aerosol particles: results from an urban site, *Geophys. Res. Lett.*, 31, L13105, doi:10.1029/2004GL019681, 2004.

Sullivan, A., Peltier, R., Brock, C., De Gouw, J., Holloway, J., Warneke, C., Wollny, A., and Weber, R.: Airborne measurements of carbonaceous aerosol soluble in water over Northeastern United States: method development and an investigation into water-soluble organic carbon sources, *J. Geophys. Res.*, 111, 1–14, 2006.

Surratt, J., Gomez-Gonzalez, Y., Chan, A., Vermeulen, R., Shahgholi, M., Kleindienst, T., Edney, E., Offenberg, J., Lewandowski, M., Jaoui, M., Maenhaut, W., Claeys, M., Flagan, R. C., and Seinfeld, J. H.: Organosulfate formation in biogenic secondary organic aerosol, *J. Phys. Chem. A*, 112, 8345–8378, 2008.

Swietlicki, E., Hansson, H., Hameri, K., Svenningsson, B., Massling, A., McFiggans, G., McMurry, P., Petaja, T., Tunved, P., Gysel, M., Topping, D., Weingartner, E., Baltensperger, U., Rissler, J., Wiedensohler, A., and Kulmala, M.: Hygroscopic properties of submicrometer atmospheric aerosol particles measured with H-TDMA instruments in various environments – a review, *Tellus B*, 60, 432–469, 2008.

Tiitta, P., Miettinen, P., Vaattovaara, P., Joutsensaari, J., Pet, T., Virtanen, A., Raatikainen, T., Aalto, P., Portin, H., Romakkaniemi, S., Kokkolab, H., Lehtinen, E. J., Markku, K., and Laaksonen, A.: Roadside aerosol study using hygroscopic, organic and volatility TDMA: characterization and mixing state, *Atmos. Environ.*, 44, 976–986, 2010.

Turpin, B. J. and Huntzicker, J. J.: Secondary formation of organic aerosol in the Los-Angeles Basin – a descriptive analysis of organic and elemental carbon concentrations, *Atmos. Environ. A*, 25, 207–215, 1991.

Turpin, B. J. and Lim, H.-J.: Species contributions to $PM_{2.5}$ mass concentrations: revisiting common assumptions for estimating organic mass, *Aerosol Sci. Technol.*, 35, 602–610, 2001.

Ulbrich, I. M., Canagaratna, M. R., Zhang, Q., Worsnop, D. R., and Jimenez, J. L.: Interpretation of organic components from Positive Matrix Factorization of aerosol mass spectrometric data, *Atmos. Chem. Phys.*, 9, 2891–2918, doi:10.5194/acp-9-2891-2009, 2009.

Ulbrich, I. M., Lechner, M., and Jimenez, J. L.: AMS Spectral Database, available at: <http://cires.colorado.edu/jimenez-group/AMSSd/>, 2009.

Wang, J., Cubison, M. J., Aiken, A. C., Jimenez, J. L., and Collins, D. R.: The importance of aerosol mixing state and size-resolved composition on CCN concentration and the variation of the importance with atmospheric aging of aerosols, *Atmos. Chem. Phys.*, 10, 7267–7283, doi:10.5194/acp-10-7267-2010, 2010.

Watson, J. G., Chow, J. C., Lu, Z. Q., Fujita, E. M., Lowenthal, D. H., Lawson, D. R., and Ashbaugh, L. L.: Chemical mass-balance source apportionment of PM₍₁₀₎ during the Southern California Air-Quality Study, *Aerosol Sci. Technol.*, 21, 1–36, 1994.

Wex, H., McFiggans, G., Henning, S., and Stratmann, F.: Influence of the external mixing state of atmospheric aerosol on derived CCN number concentrations, *Geophys. Res. Lett.*, 37, L10805, doi:10.1029/2010GL043337, 2010.

Wittig, A. E., Anderson, N., Khlystov, A. Y., Pandis, S. N., Davidson, C., and Robinson, A. L.: Pittsburgh air quality study overview, *Atmos. Environ.*, 38, 3107–3125, 2004.

Yue, D. L., Hu, M., Wu, Z. J., Wang, Z. B., Guo, S., Wehner, B., Nowak, A., Achtert, P., Wiedensohler, A., Jung, J., Kim, Y. J., and Liu, S.: Characteristics of aerosol size distributions and new particle formation in the summer in Beijing, *J. Geophys. Res. Atmos.*, 114, D00G12, doi:10.1029/2008JD010894, 2009.

Zhang, X. and McMurray, S.: Mixing characteristics and water content of submicron aerosols measured in Los Angeles and at the Grand Canyon, *Atmos. Environ. A*, 27, 1593–1607, 1993.

Zhang, Q., Alfarra, M., Worsnop, D., Allan, J., Coe, H., Canagaratna, M., and Jimenez, J.: Deconvolution and quantification of hydrocarbon-like and oxygenated organic aerosols based on aerosol mass spectrometry, *Environ. Sci. Technol.*, 39, 4938–4952, 2005.

Zhang, Q., Jimenez, J. L., Canagaratna, M. R., Allan, J. D., Coe, H., Ulbrich, I., Alfarra, M. R., Takami, A., Middlebrook, A. M., Sun, Y. L., Dzepina, K., Dunlea, E., Docherty, K., DeCarlo, P. F., Salcedo, D., Onasch, T., Jayne, J. T., Miyoshi, T., Shimono, A., Hatakeyama, S., Takegawa, N., Kondo, Y., Schneider, J., Drewnick, F., Borrmann, S., Weimer, S., Demerjian, K., Williams, P., Bower, K., Bahreini, R., Cottrell, L., Griffin, R. J., Rautiainen, J., Sun, J. Y., Zhang, Y. M., and Worsnop, D. R.: Ubiquity and dominance of oxygenated species in organic aerosols in anthropogenically-influenced Northern Hemisphere midlatitudes, *Geophys. Res. Lett.*, 34, L13801, doi:10.1029/2007GL029979, 2007.

Appendix B

Impact of a Large Wildfire on Water-Soluble Organic Aerosol in a Major Urban Area: The 2009 Station Fire in Los Angeles County*

*Reproduced with permission from “Impact of a large wildfire on water-soluble organic aerosol in a major urban area: the 2009 Station Fire in Los Angeles County” by A. Wonaschütz, S. P. Hersey, A. Sorooshian, J. S. Craven, A. R. Metcalf, R. C. Flagan, and J. H. Seinfeld, *Atmospheric Chemistry and Physics*, 11, 8257–8270, doi:10.5194/acp-11-8257-2011. Copyright 2011 by the Authors. This work is distributed under the Creative Commons Attribution 3.0 License.

Impact of a large wildfire on water-soluble organic aerosol in a major urban area: the 2009 Station Fire in Los Angeles County

A. Wonaschütz¹, S. P. Hersey², A. Sorooshian^{1,3}, J. S. Craven², A. R. Metcalf², R. C. Flagan², and J. H. Seinfeld²

¹Department of Atmospheric Sciences, University of Arizona, P.O. Box 210081, Tucson, Arizona, 85721, USA

²Departments of Environmental Science and Engineering and Chemical Engineering, California Institute of Technology, 1200 E. California Blvd., Pasadena, California 91125, USA

³Department of Chemical and Environmental Engineering, Univ. of Arizona, P.O. Box 210011, Tucson, Arizona, 85721, USA

Received: 13 April 2011 – Published in Atmos. Chem. Phys. Discuss.: 27 April 2011

Revised: 24 June 2011 – Accepted: 2 August 2011 – Published: 15 August 2011

Abstract. This study examines the nature of water-soluble organic aerosol measured in Pasadena, CA, under typical conditions and under the influence of a large wildfire (the 2009 Station Fire). During non-fire periods, water-soluble organic carbon (WSOC) variability was driven by photochemical production processes and sea breeze transport, resulting in an average diurnal cycle with a maximum at 15:00 local time (up to $4.9 \mu\text{g C m}^{-3}$). During the Station Fire, primary production was a key formation mechanism for WSOC. High concentrations of WSOC (up to $41 \mu\text{g C m}^{-3}$) in smoke plumes advected to the site in the morning hours were tightly correlated with nitrate and chloride, numerous aerosol mass spectrometer (AMS) organic mass spectral markers, and total non-refractory organic mass. Processed residual smoke was transported to the measurement site by the sea breeze later in the day, leading to higher afternoon WSOC levels than on non-fire days. Parameters representing higher degrees of oxidation of organics, including the ratios of the organic metrics $m/z 44:m/z 57$ and $m/z 44:m/z 43$, were elevated in those air masses. Intercomparisons of relative amounts of WSOC, organics, $m/z 44$, and $m/z 43$ show that the fraction of WSOC comprising acid-oxygenates increased as a function of photochemical aging owing to the conversion of aliphatic and non-acid oxygenated organics to more acid-like organics. The contribution of water-soluble organic species to the organic mass budget (10th–90th percentile values) ranged between 27%–72% and 27%–68% during fire and non-fire periods, respectively. The seasonal incidence of wildfires in the Los Angeles Basin greatly enhances the importance of water-soluble organics, which has implications for the radiative and hygroscopic properties of the regional aerosol.

1 Introduction

Organic compounds constitute roughly one half of atmospheric aerosol mass globally; this fraction can be even higher in urban areas. Between 40–85% of organic carbon measured in different locations worldwide has been shown to be water-soluble (Ruellan et al., 1999; Graham et al., 2002; Mayol-Bracero et al., 2002; Gao et al., 2003; Jaffrezo et al., 2005; Decesari et al., 2006). Water-soluble organic carbon (WSOC) species are directly emitted in primary particles, especially during biomass combustion, and produced as a result of reactions in the gas and aqueous phases (Miyazaki et al., 2006; Sullivan et al., 2006; Kondo et al., 2007; Weber et al., 2007; Ervens and Volkamer, 2010; Sorooshian et al., 2010; Timonen et al., 2010). WSOC has been suggested as a marker for secondary organic aerosol (SOA) in the absence of biomass burning (e.g. Docherty et al., 2008).

The Los Angeles Basin has been the subject of many studies examining the transport and chemical evolution of atmospheric aerosols. In Pasadena, the setting of this work, particulate pollutant concentrations are governed by numerous production and transport processes. The meteorology in the basin is characterized by early morning inversions, which, through increasing surface heating over the course of the day, give way to a robust midday-afternoon sea breeze. Elevated pollution layers can form by horizontal and vertical displacement of the morning inversion layer and orographic uplift (Lu and Turco, 1995), allowing for aerosol processing in air masses separated from surface pollution sources during the day. These pollution layers can remain aloft during the night and re-entrain the next day through turbulent mixing in a deepening boundary layer, contributing to surface concentrations of aerosols (Husar et al., 1977; Blumenthal et al., 1978).



Correspondence to: A. Sorooshian
(armin@email.arizona.edu)

Organic compounds are a major constituent of the local pollution and are emitted directly as well as produced via secondary processes. Hughes et al. (2000) found increasing relative contributions of organic compounds to increasing mass concentrations of total suspended particulates and fine particles due to chemical processing along a sea breeze trajectory in the Los Angeles Basin. More recent summertime measurements in the area showed that SOA is a major contributor to organic aerosol (Docherty et al., 2008), of which WSOC is an important component (Peltier et al., 2007). Owing to transport processes and spatial gradients in the oxidative capacity of the atmosphere, SOA is expected to contribute more to organic aerosol concentrations at inland areas than at the pollution source regions near the coast (Lu and Turco, 1995; Vutukuru et al., 2006).

In the late summer to fall months (August–November), following hot and dry summers, smoke from wildfires can be an additional component of the organic aerosol budget in the Los Angeles Basin (Phuleria et al., 2005). The impact of wildfires on urban aerosol physicochemical properties has been examined in other locations (Lee et al., 2008) but aerosol studies examining the superposition of biomass burning emissions and typical Los Angeles atmospheric conditions are limited. The issue is especially of interest as wildfires in the southwestern United States have been shown to occur more frequently and to last longer than only a few decades ago and are thus expected to be a major concern in a future drier and warmer climate (Westerling et al., 2006).

An opportunity to study the nature of WSOC in the Los Angeles Basin in both the presence and absence of a major fire presented itself during the 2009 Pasadena Aerosol Characterization Observatory (PACO) field campaign. The Station Fire, which began on 26 August 2009 in the Angeles National Forest and came as close as 10 km to the PACO field site, was the tenth largest wildfire in modern California history and the largest ever in Los Angeles County, burning an area of more than 600 km² (California Department of Forestry and Fire Protection; http://bof.fire.ca.gov/incidents/incidents_archived). The overall PACO campaign is described in detail by Hersey et al. (2011). Here we report an analysis of the nature of particulate WSOC in Pasadena during a three-month period with an aim towards characterizing time-dependent concentrations, relationships with other organic aerosol metrics, sensitivity to meteorology and transport, and the impact of the Station Fire. This work also provides a valuable database for comparison with subsequent field datasets collected from surface and airborne platforms during the 2010 CalNex field campaign (<http://www.esrl.noaa.gov/csd/calnex/>).

2 Methods

2.1 Data

During the PACO field study (May–September 2009), ground-based aerosol measurements were conducted on the roof of the Keck Building on the campus of the California Institute of Technology (Caltech). The focus of this work is the period from 6 July 2009 to 16 September 2009. WSOC in PM_{2.5} was measured every six minutes with a particle-into-liquid sampler (PILS; Brechtel Mfg. Inc.) coupled to a total organic carbon (TOC) analyzer (Sievers Model 800 Turbo, Boulder, CO). The instrument design and operational details are discussed extensively elsewhere (Sullivan et al., 2004). Briefly, the PILS samples particles smaller than 2.5 µm in diameter and passes them through an organic carbon denuder (Sunset Laboratory Inc.) to remove organic vapors. The particles are grown into droplets, which are collected by inertial impaction. The liquid then passes through a 0.5 µm PEEK (polyetheretherketone) liquid filter and is transported to a TOC analyzer for quantification of WSOC. The reported WSOC levels are the difference between the measured and background concentrations. The overall measurement uncertainty is estimated to be approximately 10 %.

Inorganic and non-refractory organic sub-micrometer aerosol measurements were carried out with an Aerodyne Compact Time of Flight Aerosol Mass Spectrometer (C-ToF-AMS) (Drewnick et al., 2005; Murphy et al., 2009) during the non-fire portion of the study and a High-Resolution AMS (HR-AMS) during the Station Fire. AMS data used here include organic markers at specific mass-to-charge ratios (*m/z*) that serve as proxies for organics with a range of oxidation states: acid-like oxygenated organics (*m/z* 44 = COO⁺), aliphatic and non-acid oxygenated organics (*m/z* 43 = C₃H₇⁺ and C₂H₅O⁺; *m/z* 55 = C₃H₃O⁺), aliphatic organics (*m/z* 57 = C₄H₉⁺), and a biomass burning tracer (*m/z* 60) (McLafferty and Turecek, 1993; Zhang et al., 2005; Aiken et al., 2008; Ng et al., 2010; Alfarra et al., 2007). The PILS and AMS chemical measurements were time synchronized, accounting for sampling time delays in the PILS relative to the AMS (Sorooshian et al., 2006). Since the PILS sampled sub-2.5 µm particles while the AMS measured sub-micrometer particles, ratios of WSOC to AMS data represent an upper limit.

Particle size distributions were measured with a cylindrical Scanning Differential Mobility Analyzer (DMA; TSI Model 3081) coupled to a Condensation Particle Counter (CPC, TSI Model 3760). Thirty-two days of hourly CO, O₃ and PM_{2.5} measurements from ground sites in Pasadena (South Wilson Avenue), Upland, Burbank, and downtown Los Angeles (North Main Street) (<http://www.arb.ca.gov>) are used to help interpret the WSOC data. Additionally, hourly meteorological data were obtained from the Mesowest database (<http://mesowest.utah.edu/index.html>). The stations used include the South Wilson Avenue station on the

Caltech campus, the North Main Street station near downtown Los Angeles (~ 12.5 km southwest of measurement site), and the Santa Fe Dam station located ~ 15 km east of the measurement site.

2.2 Fire development and influence on the measurement site

The Station Fire burned over several weeks. Its spatial extent and exact location, and thus the influence it exerted on the measurement site, changed over that time period. Figure 1 shows the progression of the fire over several days. The fire perimeter was estimated from Moderate Resolution Imaging Spectroradiometer (MODIS) fire maps (<http://firefly.geog.umd.edu/firemap/>; Justice et al., 2002; Davies et al., 2009). The fire started on 26 August less than 10 km north of the sampling site and grew in areal extent over the next four days. It split into an eastern and a western part on 31 August. The western part quickly decreased in size while moving northward, was reduced to a relatively small remnant ~ 25 km northwest of the site by 2 September, and became unidentifiable by MODIS by 4 September. The eastern part remained sizeable, but moved farther eastward. Notable easterly wind patterns did not occur during the measurement period, making the eastern part of the fire an unlikely direct influence on the measurement site.

The dataset was split into a “fire period” and a “non-fire period” by examining the MODIS fire maps and using the AMS m/z 60 concentration as a tracer for biomass burning. The “fire period”, consisting of the eight days between 26 August and 2 September, was marked by frequent high spikes in the measured m/z 60 concentration, reaching values of up to $1.4 \mu\text{g m}^{-3}$. The mean m/z 60 concentration during the fire period was $0.065 \pm 0.122 \mu\text{g m}^{-3}$. During the remaining measurement days (“non-fire period”) the mean m/z 60 concentration was $0.013 \pm 0.005 \mu\text{g m}^{-3}$. While m/z 60 (and levoglucosan) have been shown to decay with exposure to the hydroxyl radical (Hennigan et al., 2010), the systematically higher levels of this mass spectral marker during the Station Fire make it a robust tool to identify periods with fire influence. CO similarly exhibited contrasting behavior during non-fire and fire periods, with mean concentrations of $0.13 \pm 0.12 \text{ ppmv}$ and $0.45 \pm 0.50 \text{ ppmv}$, respectively.

3 Results and discussion

3.1 PACO study background

Hersey et al. (2011) provide a comprehensive summary of the physical and chemical properties of aerosols sampled at the PACO measurement site over the time period between 10 July and 4 August, which overlaps with the beginning of the period examined in this work. We briefly describe

results from that study that are relevant to the interpretation of WSOC measurements during non-fire periods. Organic mass accounted for approximately 55 % of the submicrometer AMS aerosol mass. Average organic carbon (OC) concentrations were greater by approximately 4 % in the afternoons (15:00–19:00 LT) than in the mornings (07:00–11:00 LT). Conversely, elemental carbon (EC) decreased by approximately 22 % from the mornings to the afternoons. Both trends lead to an enhanced afternoon OC:EC ratio. It was concluded that production of primary organic carbon was more important in the mornings while secondary production of organic carbon was more dominant in the afternoons. Size-resolved measurements showed that the afternoon submicrometer organic mass distribution was bimodal with one modal vacuum aerodynamic diameter centered around 100–200 nm and another around 500–600 nm. Positive matrix factorization analysis showed that low-volatility and semi-volatile oxidized organic aerosol (LV-OOA and SV-OOA) accounted for 86 % of organic aerosol, suggestive of a large oxidized organic fraction. This work will examine the nature and character of the water-soluble fraction of the organic aerosol.

3.2 Meteorological setting and origin of air masses

Weather conditions were warm and dry during the entire WSOC measurement period (Fig. 2). Ambient temperatures ranged approximately from 15° to 40°C . Relative humidity (RH) usually dropped below 40 % during the day but reached 100 % in the early morning hours of many days. Temperatures averaged several degrees higher during the Station Fire period, while RH was around 20 % lower, helping to sustain the duration and spread of the fire. Air mass back-trajectories calculated with the NOAA HYSPLIT model (Draxler and Rolph, 2003) showed that sampled air masses were generally of marine origin with brief continental exposure prior to reaching the sampling site.

Since the western edge of the Los Angeles Basin is a major source region for pollutants (Lu and Turco, 1995), it is important to identify dominant wind patterns and transport times to Pasadena. Figure 3 shows the local wind characteristics at South Wilson Avenue (next to measurement site) and at several surrounding stations. The most common wind directions at all stations are southerly to westerly, a manifestation of the sea breeze. The diurnal development of wind at South Wilson Avenue starts with very calm air in the early mornings (and late evenings). During the late morning hours the wind tends to turn clockwise from the NE through S to the predominant afternoon sea breeze direction from the SW. Wind speeds increase during the development of the sea breeze. The stagnant air in the early morning is expected to be influenced by local sources and by accumulated residual pollution from the previous day. Over the course of the late morning, air masses from more polluted urban areas are transported to Pasadena and ultimately replaced by air masses of largely

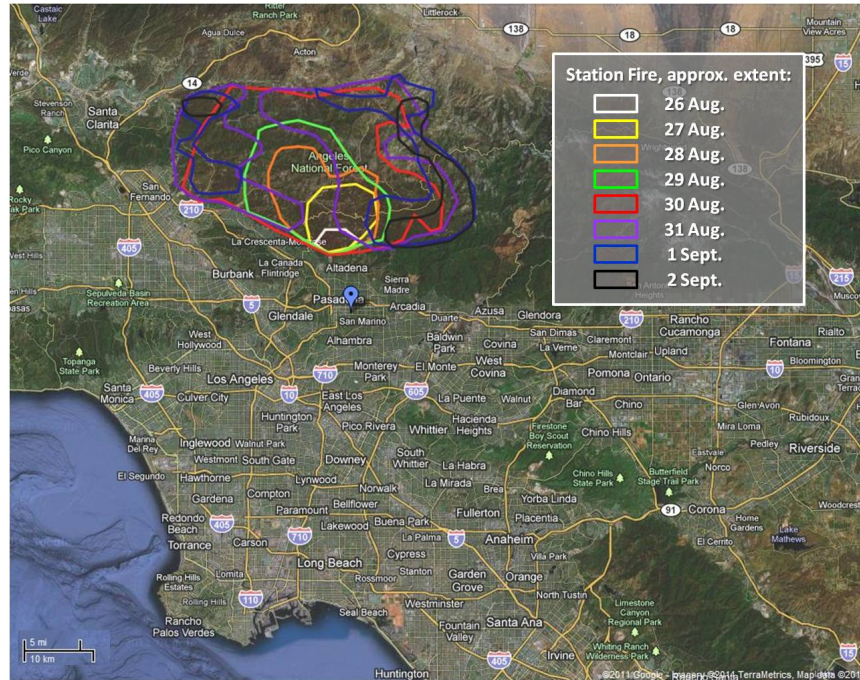


Fig. 1. Approximate spatial extent of the Station Fire by date (bordered areas). The fire area was estimated using fire maps by “Firefly” (University of Maryland; <http://firefly.geog.umd.edu/firemap/>). The blue marker in Pasadena represents the measurement site.

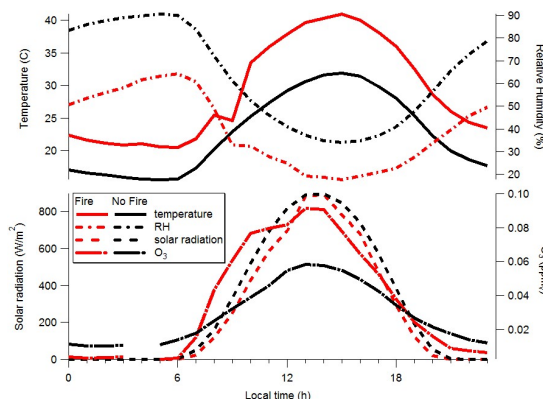


Fig. 2. Diurnal averages of meteorological parameters (Santa Fe Dam station) and O₃ concentrations during the fire- and non-fire periods.

marine origin with anthropogenic influence, carrying particles with a mix of fresh and aged components. The South Wilson Avenue Station measures systematically lower wind speeds than the surrounding stations, which is likely a local effect caused by buildings and trees in the immediate

surroundings of the station. Wind speeds measured at that site are therefore assumed to represent a lower limit of the areal wind speed. A statistical analysis of wind speeds and directions between 13:00–18:00 LT showed that the most common wind speeds were 4.5 m s^{-1} at North Main Street and 1.3 m s^{-1} at South Wilson Avenue. The most common wind directions were 270° and 225° , respectively. The afternoon (13:00–18:00 LT) transport time of urban pollution from downtown Los Angeles to Pasadena is thus on the order of 1–2 h, consistent with the estimate by Hersey et al. (2011) for the period between May and August 2009. Based on the most common afternoon wind speed at North Main Street, the transport time of anthropogenically-influenced marine air from the coast to Pasadena from a southwesterly direction is approximately two hours.

3.3 WSOC production pathways and relationship with ozone

Identifying the relative importance of primary and secondary production mechanisms of WSOC is difficult given the large variety of aerosol and precursor sources, the diurnal transport patterns and the dynamic vertical structure of the boundary layer in the basin (Blumenthal et al., 1978; Vutukuru et al., 2006). WSOC concentrations measured on non-fire days

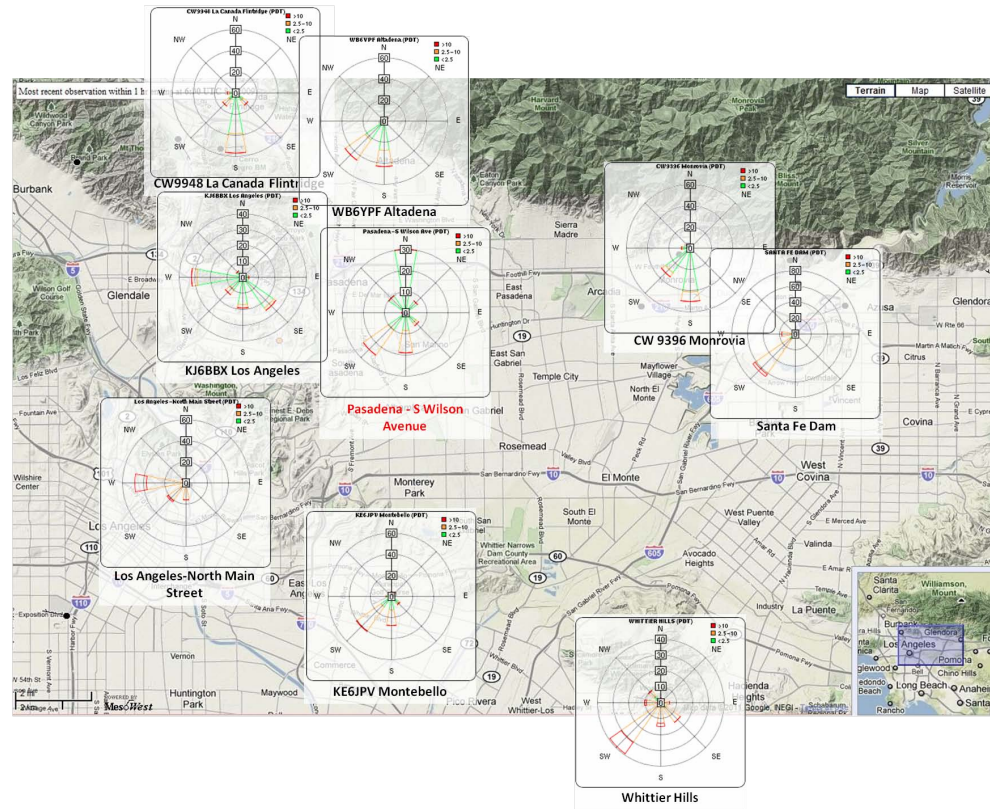


Fig. 3. Wind roses for the month of July for South Wilson Avenue and surrounding stations (data from Mesowest, <http://mesowest.utah.edu/index.html>).

may be governed by all or a subset of the following mechanisms: (1) local primary production of WSOC; (2) local secondary production; (3) advection of existing WSOC that was either primarily or secondarily produced; (4) advection of precursor volatile organic compounds (VOCs), with WSOC production occurring during transport; (5) volatilization of semivolatile primary organic aerosol (POA) and subsequent oxidation into SOA (Robinson et al., 2007); and (6) re-entrainment of pollution layers aloft. The Station Fire adds another level of complexity by introducing additional sources of WSOC: direct emission and secondary production from precursors emitted in the fire.

Previous work within the PACO campaign has shown that the temporal behavior of organic aerosol is closely related to that of O_3 , indicative of photochemical production of SOA (Hersey et al., 2011). In this study, this relationship is explored by examining the relative temporal behavior of O_3 and WSOC on 20 days. WSOC peaked after O_3 on 16 of those days with a typical time lag of 1.5–2.5 h. WSOC peaks occurred simultaneously or slightly before O_3 peaks (0.5 h) on three days, and only on one day did the WSOC peak precede

an unusually late O_3 peak by hours. This points to a strong link between overall WSOC concentrations and photochemical processes.

The variability of O_3 concentrations at different ground sites in the Los Angeles Basin provides insight into the spatiotemporal behavior of photochemical processes and the photochemical potential at the Pasadena site. O_3 concentrations measured at ground stations in Pasadena (South Wilson Avenue), Burbank, Upland and downtown Los Angeles (North Main Street) were examined for a period of 24 days in July (Fig. S1, Supplement). In the prevailing sea breeze regime, transport of precursors from downtown Los Angeles (a classic pollutant source location) is expected to influence O_3 concentrations at the measurement site. On 10 out of the examined 24 non-fire days, O_3 peaked in downtown Los Angeles approximately an hour before it did in Pasadena, consistent with the transport times of 1–2 h, given most common mid-afternoon (13:00 to 16:00 LT) wind speeds of 1.3 m s^{-1} in Pasadena and 3.6 m s^{-1} at downtown Los Angeles. Peak O_3 concentrations in Pasadena were consistently higher (22 out of 24 days) than in downtown Los Angeles, owing to

advection of O_3 from upwind locations and additional time for photochemical processing of O_3 precursors during transport. The farther downwind site of Upland is characterized by even higher and more delayed O_3 peaks. This observed spatial O_3 behavior and its implications for SOA production are consistent with the findings of Vutukuru et al. (2006) who showed that SOA levels in the basin are higher at inland sites (e.g. Azusa, Riverside) than at coastal sites. However, on six days O_3 reached peak concentrations in Pasadena before it did in downtown Los Angeles (an average of 1.5 h earlier) and on six other days, it peaked within the same hour as in downtown Los Angeles. These days were not associated with unusual wind directions or increased wind speeds. Local sources, downward mixing of elevated pollution layers from previous days in a deepening mixed layer, and/or unusually vigorous photochemical activity (as described by Hersey et al., 2011) could explain these “early” O_3 peaks. Therefore, on any given day, advection of oxidants from downtown Los Angeles is not necessarily a requirement for photochemical activity in Pasadena.

3.4 Cumulative WSOC statistics

During the non-fire period, the highest WSOC concentration measured was $4.9 \mu\text{g C m}^{-3}$. The observed concentration range is consistent with that of independent measurements in other urban areas (Jaffrezo et al., 2005; Sullivan et al., 2004, 2006; Kondo et al., 2007), including those in nearby Riverside during the summer of 2005 (Peltier et al., 2007). WSOC exhibits a weak correlation with solar radiation ($r^2 = 0.28$) and somewhat higher correlations with O_3 ($r^2 = 0.35$) and T ($r^2 = 0.44$) (Table 1). The highest correlations between WSOC and AMS aerosol components were found for the following organic markers: m/z 43 ($r^2 = 0.49$), total AMS organic mass ($r^2 = 0.47$), and m/z 55 and 60 ($r^2 = 0.45$). The correlation of WSOC with m/z 57 ($r^2 = 0.20$) is the lowest among the correlations with AMS organic markers. Although m/z 55 and m/z 43 are prominent components in traffic emissions, they are more related to oxygenated organics than the primary hydrocarbon-like organic aerosol (HOA) marker m/z 57 (e.g. Zhang et al., 2005); for example, they are in general less correlated with NO_x and CO. WSOC exhibits little to no correlation with the inorganic compounds nitrate (NO_3^-), sulfate (SO_4^{2-}), chloride (Cl^-), and ammonium (NH_4^+) ($r^2 \leq 0.08$).

During the fire period, the range of measured WSOC levels (0.8 – $40.6 \mu\text{g C m}^{-3}$) was consistent with that observed in other measurements with major biomass burning influence: 11 – $46 \mu\text{g C m}^{-3}$ (Mayol-Bracero et al., 2002), 2.2 – $39.6 \mu\text{g C m}^{-3}$ (Graham et al., 2002), 4.4 – $52.6 \mu\text{g C m}^{-3}$ (Decesari et al., 2006), and 0.57 – $18.45 \mu\text{g C m}^{-3}$ (Sullivan et al., 2006). The highest WSOC concentration, $40.6 \mu\text{g C m}^{-3}$, was measured in the morning of 30 August. WSOC correlations (r^2) with most organic metrics (i.e. total AMS organic mass and m/z 44, 60, 43, and 55, but not m/z 57) ranged

between 0.80 and 0.92 (cf. 0.35 and 0.49 during non-fire periods). The systematically higher correlations during the fire period indicate that there was a dominant factor governing the variability of both organic and WSOC levels; since WSOC was highly correlated with m/z 60 ($r^2 = 0.90$), the fire emissions were clearly influential. The correlation of WSOC with O_3 is absent during the fire period, even though O_3 concentrations are influenced by the fire (peak concentrations in the diurnal average of 91.5 ppbv during the fire vs. 58.5 ppbv for the non-fire diurnal average; Fig. 2). This suggests that photochemical production is not the dominant process governing the large variability of WSOC concentrations during the fire. A high correlation was observed between WSOC and both NO_3^- ($r^2 = 0.79$) and Cl^- ($r^2 = 0.57$). Correlations with NH_4^+ and SO_4^{2-} ($r^2 \leq 0.18$) were poor. Fresh biomass burning emissions consist mainly of organic carbonaceous components and have been reported to have only minor contributions from inorganic species (Reid et al., 2005; Fuzzi et al., 2007; Grieshop et al., 2009); however, enhanced NO_3^- concentrations have been observed in smoke plumes (Gao et al., 2003; Reid et al., 2005; Peltier et al., 2007). Potassium chloride is also thought to be a common constituent in biomass burning emissions (Posfai et al., 2003; Reid et al., 2005), which can explain the enhanced correlation of WSOC and Cl^- and provides support for a primary WSOC production mechanism. Reid et al. (2005) note that while SO_4^{2-} is a secondary product of biomass burning, its production requires high RH. Enhanced RH also increases WSOC partitioning to the aerosol phase (Hennigan et al., 2008, 2009). However, ambient RH was low during the majority of the PACO study and especially low during the fire (Fig. 2). Liquid-phase production of SO_4^{2-} and organics could conceivably have taken place in pyrocumulus clouds formed by the fire, but given the lack of observed SO_4^{2-} at the sampling site during smoke events and the low RH, it is unlikely that multi-phase processes played a key role in influencing surface WSOC levels.

During the fire period, the ratio of WSOC to organic mass ranged from 0.11 to $0.53 \mu\text{g C} \mu\text{g}^{-1}$, with a 10th percentile of 0.15 and a 90th percentile of $0.40 \mu\text{g C} \mu\text{g}^{-1}$. After converting the 10th and 90th percentile values to an equivalent organic mass concentration using a factor of 1.8 (Docherty et al., 2008), water soluble organics are estimated to account for between 27 % and 72 % (with an average of $47\% \pm 15\%$) of the organic mass. The WSOC:organic ratio range during the non-fire period is similar ($10\text{th}/90\text{th} = 0.15/0.38 \mu\text{g C} \mu\text{g}^{-1}$). After applying the 1.8 conversion factor to WSOC the 10th–90th percentile range is 27 %–68 % (average of $45\% \pm 16\%$).

Table 1. Summary of the statistical relationships between WSOC ($\mu\text{g C m}^{-3}$) and other chemical and meteorological parameters (meteorological data from the Santa Fe Dam station).

		Station Fire				No Fire			
		r^2	Slope	Intercept	<i>n</i>	r^2	Slope	Intercept	<i>n</i>
AMS ($\mu\text{g m}^{-3}$)	Total organic	0.92	-1.05	0.34	1298	0.47	0.14	0.69	1557
	<i>m/z</i> 60	0.90	40.16	1.88	1298	0.45	94.46	0.48	1557
	<i>m/z</i> 44	0.84	3.04	-1.15	1298	0.35	0.95	0.94	1557
	<i>m/z</i> 43	0.84	5.22	-1.45	1298	0.49	2.25	0.51	1557
	<i>m/z</i> 55	0.80	9.47	-1.43	1298	0.45	3.79	0.61	1557
	NO_3^-	0.79	4.30	-1.09	1298	0.00	-0.02	1.75	1557
	Cl^-	0.57	77.39	0.99	1296	0.03	-1.28	1.82	1557
	<i>m/z</i> 57	0.47	1.24	0.60	1298	0.20	6.58	0.96	1557
	NH_4^+	0.18	7.06	0.54	1298	0.00	0.04	1.64	1557
	SO_4^{2-}	0.14	-2.67	7.41	1298	0.08	0.14	1.40	1557
Gas	CO (ppmv)	0.18	3.66	2.78	151	0.00	0.26	1.69	212
	O_3 (ppbv)	0.05	0.03	3.35	151	0.35	0.02	0.83	212
	NO_x (ppbv)	-0.01	-0.01	4.77	151	0.03	-0.01	1.94	212
Meteorology	Wind speed (m s^{-1})	0.07	-	-	144	0.11	-	-	210
	Solar radiation (W m^{-2})	0.00	-	-	148	0.28	-	-	209
	<i>T</i> (C)	0.01	-	-	144	0.44	-	-	209
	RH (%)	0.00	-	-	147	0.14	-	-	209

3.5 Diurnal WSOC behavior

3.5.1 Non-fire period

During the non-fire period, the daytime diurnal average concentration of WSOC (Fig. 4) exhibits a maximum at 15:00 LT, around the same time as maxima in AMS organic mass, *m/z* 44 and *m/z* 43, but after O_3 (13:00 LT) and solar radiation (14:00 LT) (Fig. 2). Since wind direction has a pronounced diurnal cycle, too, the afternoon peak in WSOC can be explained plausibly by both photochemical production and/or transport from downtown Los Angeles via the afternoon sea breeze (a complication in explaining diurnal variability of pollutants noted specifically for Pasadena by Blumenthal et al., 1978). The behavior of the HOA marker *m/z* 57 provides some insight: while it does show an increase starting at 06:00 and a local peak at 09:00, consistent with local rush hour traffic, its maximum concentration occurs at 13:00, when local primary emissions are expected to be lower than in the morning. Since all other organic metrics and total AMS mass also reach their highest concentrations with high temporal coincidence in the early afternoon, it is likely that transport from more polluted areas, including downtown Los Angeles, plays the dominant role. From the peak at 15:00 until the evening hours, WSOC concentrations decrease, as do other organic metrics and total AMS mass. While dilution as a result of a deepening boundary layer can

be a mechanism for daytime concentration decreases, the late onset of the decrease suggests that it is caused by the sea breeze: After initially transporting pollutants from source areas to Pasadena, the continuing onshore winds advect cleaner marine air. This advancing sea breeze front has been shown to produce strong gradients in pollutant concentrations in the Los Angeles Basin (Lu and Turco, 1995).

Transport does not explain all features of diurnal WSOC behavior. Even when it dominates the observed concentration variability at the measurement site, it is possible that the WSOC was secondarily produced upwind or during transport. In the diurnal average, WSOC concentrations (and *m/z* 44) do not show as steep of a decrease as organics and total AMS mass (Fig. 4). The ratio WSOC:organic (Fig. 5) is relatively constant until 14:00, but then begins to increase. A likely scenario for the relative increase of WSOC during the decrease of absolute concentrations of most every organic marker is the superposition of secondary production of WSOC by photochemical processing and transport. Adveected marine air may exhibit enhanced WSOC:organic ratios and, in addition, the organic aerosol advected by the sea breeze ages and oxidizes while moving inland.

Examples for these mechanisms governing WSOC concentrations on individual days can be seen in the time series in Fig. 6. On 7 July, sea breeze transport was dominant: there is strong covariance between WSOC, AMS organic mass and numerous *m/z* markers (43, 44, 55, 57, 60). All exhibit a

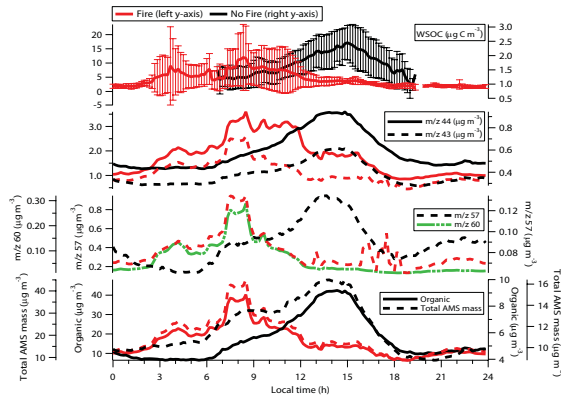


Fig. 4. Diurnal averages of aerosol chemistry (m/z 60 shown for the fire period only).

smooth morning increase followed by an equally smooth afternoon decrease which coincides with increasing afternoon wind speeds and southerly to southwesterly wind direction. The ratio of WSOC:total AMS mass shows the same behavior, likely due to photochemical processing of the transported air. The afternoon increase in SO_4^{2-} coupled with the decrease of organics can be attributed to the influx of marine air. On 11 and 15 July, in contrast, WSOC concentrations began to increase before the sea breeze was fully established, indicating that local photochemical production may have played a more important role.

3.5.2 Station Fire period

During the fire period, organic mass fractions (organics:total AMS mass) were substantially higher than in the non-fire period (Fig. 5). The contribution of WSOC to organic mass was systematically elevated from the early morning hours through the late afternoon, with higher WSOC:organic ratios between 04:00–12:00 than at other times. Absolute WSOC concentrations peaked in the mornings. For 08:30 in the morning, the average WSOC concentration (Fig. 4) is higher by a factor of 10 than the non-fire average for the same time of day. The diurnal behavior of the biomass burning tracer m/z 60 matches that of WSOC (with the exception of a sharper decrease from 08:00 to 12:00), providing evidence for the presence of biomass burning aerosols at the measurement site when WSOC increased in concentration. Boundary layer deepening over the course of the late morning and the onset of the sea breeze with its southwesterly winds directing smoke plumes away from the measurement site lead to a decrease in measured WSOC concentrations during the rest of the day. The afternoon peak of diurnally-averaged WSOC at 15:00 that was evident during the non-fire period is barely visible given the high WSOC concentrations during earlier parts of the days; nonetheless, the diurnally-averaged WSOC

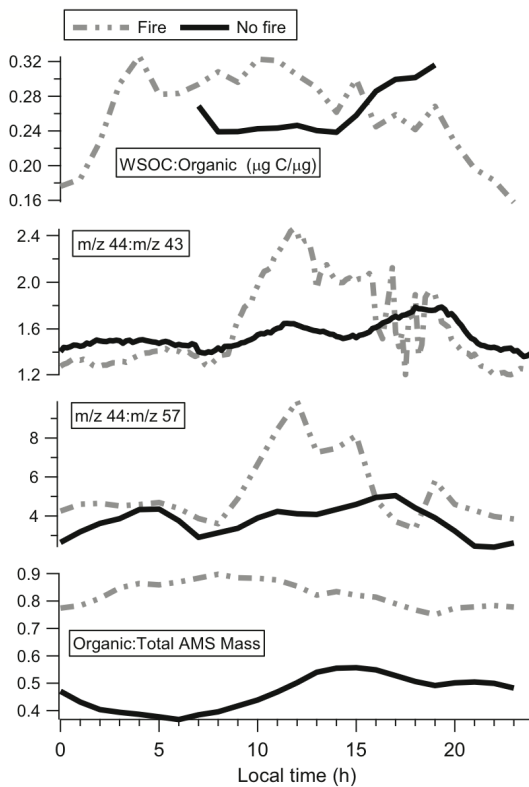


Fig. 5. Diurnally averaged ratios of different organic aerosol measurements during the fire and non-fire periods.

concentration at this time of day exceeds that of the non-fire period by a factor of 1.5. As organic precursors emitted in the fire were likely present in the entire Los Angeles Basin after several days of burning, residual and processed smoke are thought to have played an additional role in the usual transport of pollutants by the afternoon sea breeze.

Day-to-day variability of WSOC concentrations and other aerosol constituents was high during the fire period (Fig. 7). The impact of the fire on the measurement site ranged from large increases of every measured quantity on 29, 30 and 31 August, to much reduced fire influence on 29 August and 1 September. This can be attributed to the dynamic development of the fire itself, as well as effects associated with wind and boundary layer depth. The connection between wind and smoke influence on aerosol composition is clearly visible in Fig. 7: using m/z 60 as a tracer for the smoke plume, it is evident that periods with low wind speeds and wind directions with a northerly component feature the highest smoke concentrations. Concentrations are higher in the morning hours than in the evenings (when wind speeds are equally low) because the boundary layer is shallowest in the morning and

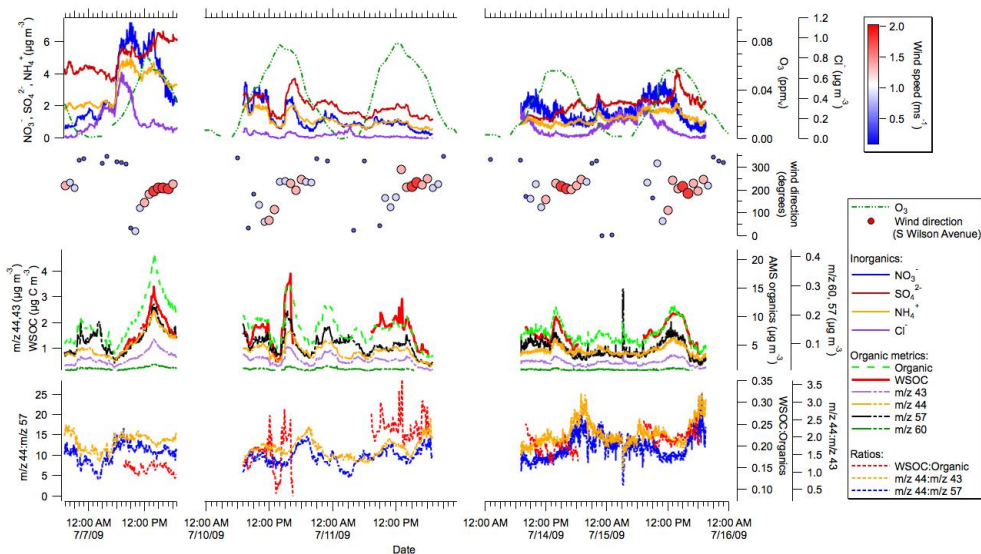


Fig. 6. Time series of various measured and derived parameters during selected days outside the fire period. The symbol size for wind direction is proportional to measured wind speed (South Wilson Avenue station).

the smoke has had time to accumulate in stagnant conditions. Concentrations of m/z 60 decrease immediately as the wind direction shifts and the wind speed picks up in the developing sea breeze. During the heavily smoke-impacted mornings of 28, 30 and 31 August, WSOC shows a very tight correlation with m/z 60, NO_3^- , and Cl^- , suggestive of primary production of WSOC in the fire. Most other AMS measurements also vary in lockstep with WSOC, with the notable exception of SO_4^{2-} , which exhibited a poor correlation with WSOC and lower levels in the diurnal average than on non-fire days.

In the afternoons of 28, 30 and 31 August, WSOC concentrations were about a factor of two higher than the non-fire average. Concentrations of m/z 60, while having dropped since the morning, were still elevated by a factor of two to three above average non-fire concentrations, an indicator that smoke distributed all over the Los Angeles Basin. CO Measurements from ground stations (Fig. S1, Supplement) were used to confirm this wider impact of the fire: on 30 and 31 August, CO levels in downtown Los Angeles exceeded typical rush hour values by a factor of two to three showing that the fire had a direct influence on locations farther south and southwest of Pasadena. Thus, even when the afternoon sea breeze directed the smoke plume away from the site, it still transported residual smoke to the site. This residual smoke was subject to photochemical processing: Fig. 5 shows large systematic increases in the ratios m/z 44:43 and m/z 44:57 between 09:00–15:00 while the absolute values of all organic measurements decreased (cf. Fig. 4). The larger increases of these ratios during the fire compared to

non-fire conditions point to a more vigorous conversion of organics towards a more oxidized state at a relatively stable WSOC:organic ratio. Diurnal average O_3 concentrations (Fig. 2) exhibit an earlier rise and a higher maximum than during the non-fire period, underlining the impact of the fire on the timing and magnitude of photochemical activity. The afternoon increases of m/z 44:57 and m/z 44:43 and the unusually high O_3 concentrations (176 ppbv at 14:00 on 30 August and 124 ppbv at 10:00 on 31 August) are also clearly visible in the time series for individual days (Fig. 7). Size distribution data (Fig. S2, Supplement) show that the smoke events in the morning hours are associated with larger particles (modal diameter of about 150 nm) than typically observed during that time on non-fire days (modal diameter of 80 nm). In the afternoon, there is a distinct shift to smaller particles (around 40 nm) with a maximum concentration at approximately 15:00, coinciding with an increase in WSOC concentrations owing most likely to photochemical production.

3.6 Relationships between WSOC, AMS organic, m/z 44, and m/z 43

Primary emission in a fire is a very different source of WSOC than photochemical processing of precursor pollutants. The chemical nature of the WSOC measured in the morning smoke-plumes is therefore expected to differ from that measured in the afternoons. Since WSOC contains both hydrophobic and hydrophilic fractions (e.g. Sullivan and Weber, 2006), it is of interest to investigate the relative behavior

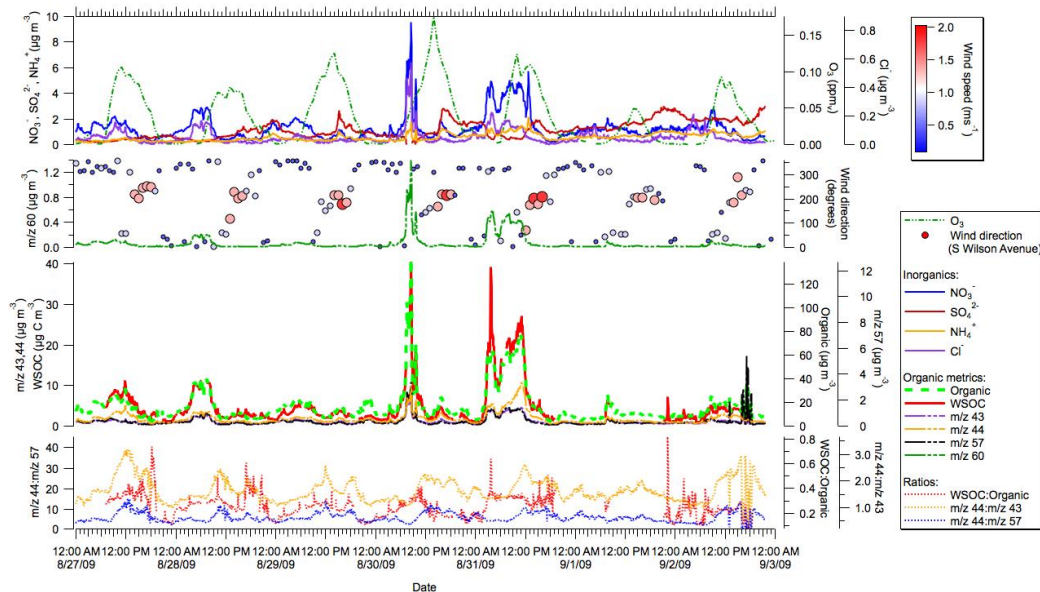


Fig. 7. Time series of various measured and derived parameters during the Station Fire period. The symbol size for wind direction is proportional to measured wind speed (South Wilson Avenue station).

of m/z 44, m/z 43, total AMS organic, and WSOC. Fire period morning-to-afternoon ratios (i.e. concentrations at 08:00 versus 14:00) of diurnally-averaged m/z 44, 43, 60, organic, and WSOC concentrations (shown in Fig. 4) were examined. The smallest morning-to-afternoon ratio for any of these organic metrics was found for m/z 44 (1.9), followed by AMS organic (2.4), m/z 43 (2.7), and WSOC (3.3). The morning-to-afternoon ratio for m/z 60 was 9.6, confirming the much larger direct influence of the fire in the morning. Given the different morning-to-afternoon ratios of m/z 44 and 43, it is plausible that the afternoon WSOC contained constituents produced as a result of photochemical processing of smoke, with more of the non-acid oxygenates having been converted to acid-like oxygenates.

Recent studies have utilized m/z 44 and m/z 43 (Ng et al., 2010; Chhabra et al., 2011) to track the aging of organic aerosols in the atmosphere. For the PACO campaign, Hersey et al. (2011) conducted an analysis of f_{44} (m/z 44:total organic signal) versus f_{43} (m/z 43:total organic signal), where higher levels of f_{44} relative to f_{43} are thought to indicate a greater degree of organic oxygenation and lower volatility. Over the span of four months, they observed a high level of consistency in the overall degree of oxidation of the aerosol over a span of several months. Ng et al. (2010) conduct a related type of analysis (see their Fig. 5), suitable for incorporating measurements from instruments other than the AMS: plotting f_{44} and the O:C ratio versus m/z 44:43, they observed that both f_{44} and the O:C ratio increase sharply

at the beginning of oxidation and then plateau at larger m/z 44:43 ratios, suggesting the existence of a maximum oxidation state of the aerosol. Following a similar approach, we examine the ratio of m/z 44:WSOC as a function of the m/z 44:43 ratio for both the fire- and non-fire period (Fig. 8). The m/z 44:43 ratios range between 0.6–2.7 (non-fire period) and 1.1–3.1 (fire period). In the mentioned plot in Ng et al. (2010, Fig. 5), this is a range in which the O:C ratio and f_{44} are increasing rapidly prior to reaching a plateau. During both the fire-and the non-fire period, the ratio m/z 44:WSOC grows as a function of m/z 44:43, indicating that the contribution of acid-like oxygenates to WSOC increases as the chemical functionality of the species contributing to m/z 44 and 43 moves towards a more oxidized state. This is most clearly illustrated by the data representing the greatest influence by the fire (larger symbols in Fig. 8). The early morning smoke plumes advected to the measurement site exhibit relatively low values of m/z 44:43. The m/z 44:WSOC ratio increases gradually as a function of m/z 44:43 and time of day, suggesting that conditions associated with transitioning from morning to afternoon hours (higher temperatures, O_3 , solar radiation) promoted processing of organics to contain more oxidized species and of WSOC to contain more acid-like oxygenates.

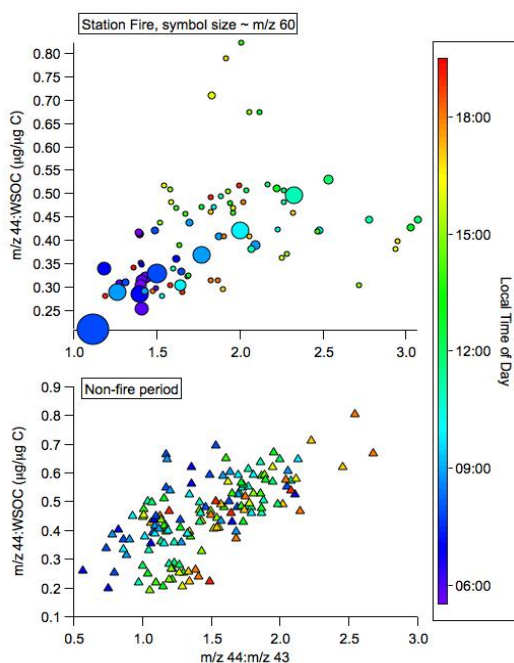


Fig. 8. Summary of the ratio m/z 44:WSOC as a function of m/z 44:43 during (top panel) and outside (bottom panel) the Station Fire period. Symbols are color-coded by time of day, and in the Station Fire panel the symbol size is proportional to the tracer for biomass burning, m/z 60 (range = 0.03–0.9 $\mu\text{g m}^{-3}$).

4 Conclusions

This work examines a ground-based field dataset of WSOC in conjunction with numerous other aerosol, gas, and meteorological measurements. Two periods governed by the presence and absence of a major wildfire are separately examined with respect to WSOC and the processes governing its temporal variability at a fixed site in Pasadena, California. The PACO study showed that in the absence of biomass burning, changes in WSOC concentrations in Pasadena are largely driven by the diurnal sea breeze circulation and concurrent photooxidation of the transported airmasses. Initially, in the early afternoon, the sea breeze transports pollutants from the direction of the source-rich western Los Angeles area to Pasadena. Chemical processing of those air masses likely occurs while they are on their way and contributes to the temporal WSOC concentration gradient observed at the measurement site, in addition to the influx of WSOC that was already produced at upwind locations. Later in the afternoons, the continuing sea breeze brings in cleaner air masses. These processes cause a marked decrease in WSOC, but enhanced WSOC:organic ratios. Given our observations, photochemical processes are important for overall WSOC forma-

tion in the Los Angeles Basin, but cannot be assumed to dominate the observed variability at a single site. That variability is determined by a combination of transport and secondary formation processes, as well as factors we were unable to quantify, such as the magnitude of residual WSOC levels in upwind areas and in layers aloft that may be re-entrained into a deepening boundary layer over the course of the day.

During the Station Fire, WSOC concentrations and their contributions to total organic mass were substantially higher than on typical non-fire days. WSOC was produced via both primary and secondary pathways. Close covariance of WSOC with many other measured species (nitrate, chloride, total AMS organic aerosol mass) in smoke events (defined by unusually high m/z 60 concentrations in stagnant/northerly wind conditions) is a good indicator for primary (and potentially sufficiently fast secondary) production of WSOC in the fire emissions. Secondary production of WSOC becomes detectable after the initial morning smoke plumes are directed away from the sampling site and aged smoke from farther upwind makes its way back to the measurement site with the afternoon sea breeze. Increasing m/z 44:57 and m/z 44:43 ratios show the ongoing oxidation of the smoke-influenced air masses once they arrive back at the measurement site. Unusually high and early O_3 concentration maxima indicate high photochemical activity, which may contribute to the increased WSOC concentrations observed outside of the direct smoke plume. Multiphase processes were not a dominant source of WSOC owing to low relative humidities during the majority of the observation period.

A close examination of the relationship between WSOC, m/z 44, and m/z 43 provided insight into the contribution of various classes of oxygenated species to WSOC as a result of aerosol aging. The ratio of m/z 44:WSOC increased as a function of m/z 44:43 both during the fire- and the non-fire period, suggesting that non-acid oxygenates were being converted to more acidic oxygenates, thereby enhancing the contribution of the latter to WSOC.

This work has illustrated the complexity of factors governing WSOC levels at a fixed point in the Los Angeles Basin. A follow-up study using aircraft observations in the same region during the 2010 CalNex field campaign will extend the discussion of the relative importance of various factors (e.g. transport, meteorology, diverse sources) in governing concentrations and spatiotemporal variability in WSOC in this metropolitan center and outflow regions (Duong et al., 2011).

Supplementary material related to this article is available online at:

<http://www.atmos-chem-phys.net/11/8257/2011/acp-11-8257-2011-supplement.pdf>.

Acknowledgements. This work was supported by the Electric Power Research Institute. The authors gratefully acknowledge the NOAA Air Resources Laboratory (ARL) for provision of the HYSPLIT transport and dispersion model. We thank the governmental agencies, commercial firms, and educational institutions participating in MesoWest for providing the meteorological station data and the California EPA Air Resources Board for the access to the measurements of gaseous pollutants. We also acknowledge NASA for the production of the data used in this research effort.

Edited by: A. Nenes

References

Aiken, A. C., Decarlo, P. F., Kroll, J. H., Worsnop, D. R., Huffman, J. A., Docherty, K. S., Ulbrich, I. M., Mohr, C., Kimmel, J. R., Sueper, D., Sun, Y., Zhang, Q., Trimborn, A., Northway, M., Ziemann, P. J., Canagaratna, M. R., Onasch, T. B., Alfarra, M. R., Prevot, A. S. H., Dommen, J., Duplissy, J., Metzger, A., Baltensperger, U., and Jimenez, J. L.: O/C and OM/OC ratios of primary, secondary, and ambient organic aerosols with high-resolution time-of-flight aerosol mass spectrometry, *Environ. Sci. Technol.*, 42, 4478–4485, doi:10.1021/Es703009q, 2008.

Alfarra, M. R., Prevot, A. S. H., Szidat, S., Sandradewi, J., Weimer, S., Lanz, V. A., Schreiber, D., Mohr, M., and Baltensperger, U.: Identification of the mass spectral signature of organic aerosols from wood burning emissions, *Environ. Sci. Technol.*, 41, 5770–5777, doi:10.1021/Es062289b, 2007.

Blumenthal, D. L., White, W. H., and Smith, T. B.: Anatomy of a Los-Angeles Smog Episode - Pollutant Transport in Daytime Sea Breeze Regime, *Atmos. Environ.*, 12, 893–907, 1978.

Chhabra, P. S., Ng, N. L., Canagaratna, M. R., Corrigan, A. L., Russell, L. M., Worsnop, D. R., Flagan, R. C., and Seinfeld, J. H.: Elemental composition and oxidation of chamber organic aerosol, *Atmos. Chem. Phys. Discuss.*, 11, 10305–10342, doi:10.5194/acpd-11-10305-2011, 2011.

Davies, D. K., Ilavajhala, S., Wong, M. M., and Justice, C. O.: Fire information for resource management system: Archiving and distributing MODIS active fire data, *IEEE T. Geosci. Remote*, 47, 72–79, 2009.

Decesari, S., Fuzzi, S., Facchini, M. C., Mircea, M., Emblico, L., Cavalli, F., Maenhaut, W., Chi, X., Schkolnik, G., Falkovich, A., Rudich, Y., Claeys, M., Pashynska, V., Vas, G., Kourtchev, I., Vermeylen, R., Hoffer, A., Andreae, M. O., Tagliavini, E., Moretti, F., and Artaxo, P.: Characterization of the organic composition of aerosols from Rondonia, Brazil, during the LBA-SMOC 2002 experiment and its representation through model compounds, *Atmos. Chem. Phys.*, 6, 375–402, doi:10.5194/acp-6-375-2006, 2006.

Docherty, K. S., Stone, E. A., Ulbrich, I. M., DeCarlo, P. F., Snyder, D. C., Schauer, J. J., Peltier, R. E., Weber, R. J., Murphy, S. M., Seinfeld, J. H., Eatough, D. J., Grover, B. D., and Jimenez, J. L.: Apportionment of primary and secondary organic aerosols in Southern California during the 2005 study of organic aerosols in riverside (SOAR), *Environ. Sci. Technol.*, 42, 7655–7662, 2008.

Draxler, R. R. and Rolph, G. D.: HYSPLIT (HYbrid Single-Particle Lagrangian Integrated Trajectory) Model access via NOAA ARL READY Website (<http://www.arl.noaa.gov/ready/hysplit4.html>), NOAA Air Resources Laboratory, Silver Spring (last access: August 2010), 2003.

Drewnick, F., Hings, S. S., DeCarlo, P., Jayne, J. T., Gonin, M., Fuhrer, K., Weimer, S., Jimenez, J. L., Demerjian, K. L., Borrmann, S., and Worsnop, D. R.: A new time-of-flight aerosol mass spectrometer (TOF-AMS) – Instrument description and first field deployment, *Aerosol Sci. Tech.*, 39, 637–658, doi:10.1080/02786820500182040, 2005.

Duong, H. T., Sorooshian, A., Craven, J. S., Hersey, S. P., Metcalf, A. R., Zhang, X., Weber, R. J., Jonsson, H., Flagan, R. C., and Seinfeld, J. H.: Water-Soluble Organic Aerosol in the Los Angeles Basin and Outflow Regions: Airborne and Ground Measurements During the 2010 CalNex Field Campaign, *J. Geophys. Res.*, in review, 2011.

Ervens, B. and Volkamer, R.: Glyoxal processing by aerosol multi-phase chemistry: towards a kinetic modeling framework of secondary organic aerosol formation in aqueous particles, *Atmos. Chem. Phys.*, 10, 8219–8244, doi:10.5194/acp-10-8219-2010, 2010.

Fuzzi, S., Decesari, S., Facchini, M. C., Cavalli, F., Emblico, L., Mircea, M., Andreae, M. O., Trebs, I., Hoffer, A., Guyon, P., Artaxo, P., Rizzo, L. V., Lara, L. L., Pauliquevis, T., Maenhaut, W., Raes, N., Chi, X. G., Mayol-Bracero, O. L., Soto-Garcia, L. L., Claeys, M., Kourtchev, I., Rissler, J., Swietlicki, E., Tagliavini, E., Schkolnik, G., Falkovich, A. H., Rudich, Y., Fisch, G., and Gatti, L. V.: Overview of the inorganic and organic composition of size-segregated aerosol in Rondonia, Brazil, from the biomass-burning period to the onset of the wet season, *J. Geophys. Res.*, 112, D01201, doi:10.1029/2005jd006741, 2007.

Gao, S., Hegg, D. A., Hobbs, P. V., Kirchstetter, T. W., Magi, B. I., and Sadilek, M.: Water-soluble organic components in aerosols associated with savanna fires in southern Africa: Identification, evolution, and distribution, *J. Geophys. Res.*, 108(D13), 8491, doi:10.1029/2002JD002324, 2003.

Graham, B., Mayol-Bracero, O. L., Guyon, P., Roberts, G. C., Decesari, S., Facchini, M. C., Artaxo, P., Maenhaut, W., Koll, P., and Andreae, M. O.: Water-soluble organic compounds in biomass burning aerosols over Amazonia – 1. Characterization by NMR and GC-MS, *J. Geophys. Res.*, 107(D20), 8047, doi:10.1029/2001jd000336, 2002.

Grieshop, A. P., Logue, J. M., Donahue, N. M., and Robinson, A. L.: Laboratory investigation of photochemical oxidation of organic aerosol from wood fires 1: measurement and simulation of organic aerosol evolution, *Atmos. Chem. Phys.*, 9, 1263–1277, doi:10.5194/acp-9-1263-2009, 2009.

Hennigan, C. J., Bergin, M. H., Dibb, J. E., and Weber, R. J.: Enhanced secondary organic aerosol formation due to water uptake by fine particles, *Geophys. Res. Lett.*, 35, L18801, doi:10.1029/2008gl035046, 2008.

Hennigan, C. J., Bergin, M. H., Russell, A. G., Nenes, A., and Weber, R. J.: Gas/particle partitioning of water-soluble organic aerosol in Atlanta, *Atmos. Chem. Phys.*, 9, 3613–3628, doi:10.5194/acp-9-3613-2009, 2009.

Hennigan, C. J., Sullivan, A. P., Collett Jr., J. L., and Robinson, A. L.: Levoglucosan stability in biomass burning particles exposed to hydroxyl radicals, *Geophys. Res. Lett.*, 37, L09806, doi:10.1029/2010GL043088, 2010.

Hersey, S. P., Craven, J. S., Schilling, K. A., Metcalf, A. R., Sorooshian, A., Chan, M. N., Flagan, R. C., and Seinfeld, J. H.:

The Pasadena Aerosol Characterization Observatory (PACO): chemical and physical analysis of the Western Los Angeles basin aerosol, *Atmos. Chem. Phys.*, 11, 7417–7443, doi:10.5194/acp-11-7417-2011, 2011.

Hughes, L. S., Allen, J. O., Bhave, P., Kleeman, M. J., Cass, G. R., Liu, D.-Y., Fergenson, D. P., Morrical, B. D., and Prather, K. A.: Evolution of atmospheric particles along trajectories crossing the Los Angeles Basin, *Environ. Sci. Technol.*, 34, 3058–3068, 2000.

Husar, R. B., Patterson, D. E., Blumenthal, D. L., White, W. H., and Smith, T. B.: 3-dimensional distribution of air-pollutants in Los-Angeles Basin, *J. Appl. Meteorol.*, 16, 1089–1096, 1977.

Jaffrezo, J.-L., Aymoz, G., Delaval, C., and Cozic, J.: Seasonal variations of the water soluble organic carbon mass fraction of aerosol in two valleys of the French Alps, *Atmos. Chem. Phys.*, 5, 2809–2821, doi:10.5194/acp-5-2809-2005, 2005.

Justice, C. O., Giglio, L., Korontzi, S., Owens, J., Morisette, J. T., Roy, D., Descloitres, J., Alleaume, S., Petitcolin, F., and Kaufman, F.: The MODIS fire products, *Remote Sens. Environ.*, 83, 244–262, 2002.

Kondo, Y., Miyazaki, Y., Takegawa, N., Miyakawa, T., Weber, R. J., Jimenez, J. L., Zhang, Q., and Worsnop, D. R.: Oxygenated and water-soluble organic aerosols in Tokyo, *J. Geophys. Res.*, 112, D01203, doi:10.1029/2006jd007056, 2007.

Lee, S., Kim, H. K., Yan, B., Cobb, C. E., Hennigan, C., Nichols, S., Chamber, M., Edgerton, E. S., Jansen, J. J., Hu, Y. T., Zheng, M., Weber, R. J., and Russell, A. G.: Diagnosis of aged prescribed burning plumes impacting an urban area, *Environ. Sci. Technol.*, 42, 1438–1444, doi:10.1021/Es7023059, 2008.

Lu, R. and Turco, R. P.: Air Pollutant Transport in a Coastal Environment .2. 3-Dimensional Simulations over Los-Angeles Basin, *Atmos. Environ.*, 29, 1499–1518, 1995.

Mayol-Bracero, O. L., Guyon, P., Graham, B., Roberts, G., Andreae, M. O., Decesari, S., Facchini, M. C., Fuzzi, S., and Artaxo, P.: Water-soluble organic compounds in biomass burning aerosols over Amazonia – 2. Apportionment of the chemical composition and importance of the polyacidic fraction, *J. Geophys. Res.*, 107(D20), 8091, doi:10.1029/2001jd000522, 2002.

McLafferty, F. W. and Turecek, F.: Interpretation of Mass Spectra, Fourth Edition, University Science Books, Mill Valley, California, 1993.

Miyazaki, Y., Kondo, Y., Takegawa, N., Komazaki, Y., Fukuda, M., Kawamura, K., Mochida, M., Okuzawa, K., and Weber, R. J.: Time-resolved measurements of water-soluble organic carbon in Tokyo, *J. Geophys. Res.*, 111, D23206, doi:10.1029/2006jd007125, 2006.

Murphy, S. M., Agrawal, H., Sorooshian, A., Padro, L. T., Gates, H., Hersey, S., Welch, W. A., Jung, H., Miller, J. W., Cocker, D. R., Nenes, A., Jonsson, H. H., Flagan, R. C., and Seinfeld, J. H.: Comprehensive Simultaneous Shipboard and Airborne Characterization of Exhaust from a Modern Container Ship at Sea, *Environ. Sci. Technol.*, 43, 4626–4640, doi:10.1021/Es802413j, 2009.

Ng, N. L., Canagaratna, M. R., Zhang, Q., Jimenez, J. L., Tian, J., Ulbrich, I. M., Kroll, J. H., Docherty, K. S., Chhabra, P. S., Bahreini, R., Murphy, S. M., Seinfeld, J. H., Hildebrandt, L., Donahue, N. M., DeCarlo, P. F., Lanz, V. A., Prévôt, A. S. H., Dinar, E., Rudich, Y., and Worsnop, D. R.: Organic aerosol components observed in Northern Hemispheric datasets from Aerosol Mass Spectrometry, *Atmos. Chem. Phys.*, 10, 4625–4641, doi:10.5194/acp-10-4625-2010, 2010.

Peltier, R. E., Weber, R. J., and Sullivan, A. P.: Investigating a liquid-based method for online organic carbon detection in atmospheric particles, *Aerosol Sci. Tech.*, 41, 1117–1127, doi:10.1080/02786820701777465, 2007.

Phuleria, H. C., Fine, P. M., Zhu, Y. F., and Sioutas, C.: Air quality impacts of the October 2003 Southern California wildfires, *J. Geophys. Res.*, 110, D07S20, doi:10.1029/2004jd004626, 2005.

Posfai, M., Simonics, R., Li, J., Hobbs, P. V., and Buseck, P. R.: Individual aerosol particles from biomass burning in southern Africa: 1. Composition and size distributions of carbonaceous particles, *J. Geophys. Res.*, 108(D13), 8483, doi:10.1029/2002JD002291, 2003.

Reid, J. S., Koppmann, R., Eck, T. F., and Eleuterio, D. P.: A review of biomass burning emissions part II: intensive physical properties of biomass burning particles, *Atmos. Chem. Phys.*, 5, 799–825, doi:10.5194/acp-5-799-2005, 2005.

Robinson, A. L., Donahue, N. M., Shrivastava, M. K., Weitkamp, E. A., Sage, A. M., Grieshop, A. P., Lane, T. E., Pierce, J. R., and Pandis, S. N.: Rethinking organic aerosols: Semivolatile emissions and photochemical aging, *Science*, 315, 1259–1262, doi:10.1126/science.1133061, 2007.

Ruellan, S., Cachier, H., Gaudichet, A., Masclet, P., and Lacaux, J. P.: Airborne aerosols over central Africa during the experiment for regional sources and sinks of oxidants (EXPRESSO), *J. Geophys. Res.*, 104, 30673–30690, 1999.

Sorooshian, A., Brechtel, F. J., Ma, Y. L., Weber, R. J., Corless, A., Flagan, R. C., and Seinfeld, J. H.: Modeling and characterization of a particle-into-liquid sampler (PILS), *Aerosol Sci. Tech.*, 40, 396–409, doi:10.1080/02786820600632282, 2006.

Sorooshian, A., Murphy, S. M., Hersey, S., Bahreini, R., Jonsson, H., Flagan, R. C., and Seinfeld, J. H.: Constraining the contribution of organic acids and AMS m/z 44 to the organic aerosol budget: on the importance of meteorology, aerosol hygroscopicity, and region, *Geophys. Res. Lett.*, 37, L21807, doi:10.1029/2010GL044951, 2010.

Sullivan, A. P. and Weber, R. J.: Chemical characterization of the ambient organic aerosol soluble in water: 1. Isolation of hydrophobic and hydrophilic fractions with a XAD-8 resin, *J. Geophys. Res.*, 111, D05314, doi:10.1029/2005jd006485, 2006.

Sullivan, A. P., Weber, R. J., Clements, A. L., Turner, J. R., Bae, M. S., and Schauer, J. J.: A method for on-line measurement of water-soluble organic carbon in ambient aerosol particles: Results from an urban site, *Geophys. Res. Lett.*, 31, L13105, doi:10.1029/2004gl019681, 2004.

Sullivan, A. P., Peltier, R. E., Brock, C. A., de Gouw, J. A., Holloway, J. S., Warneke, C., Wollny, A. G., and Weber, R. J.: Airborne measurements of carbonaceous aerosol soluble in water over northeastern United States: Method development and an investigation into water-soluble organic carbon sources, *J. Geophys. Res.*, 111, D23S46, doi:10.1029/2006jd007072, 2006.

Timonen, H., Aurela, M., Carbone, S., Saarnio, K., Saarikoski, S., Mäkelä, T., Kulmala, M., Kerminen, V.-M., Worsnop, D. R., and Hillamo, R.: High time-resolution chemical characterization of the water-soluble fraction of ambient aerosols with PILS-TOC-IC and AMS, *Atmos. Meas. Tech.*, 3, 1063–1074, doi:10.5194/amt-3-1063-2010, 2010.

Vutukuru, S., Griffin, R. J., and Dabdub, D.: Simulation and

analysis of secondary organic aerosol dynamics in the South Coast Air Basin of California, *J. Geophys. Res.*, 111, D10S12, doi:10.1029/2005jd006139, 2006.

Weber, R. J., Sullivan, A. P., Peltier, R. E., Russell, A., Yan, B., Zheng, M., de Gouw, J., Warneke, C., Brock, C., Holloway, J. S., Atlas, E. L., and Edgerton, E.: A study of secondary organic aerosol formation in the anthropogenic-influenced southeastern United States, *J. Geophys. Res.*, 112, D13302, doi:10.1029/2007jd008408, 2007.

Westerling, A. L., Hidalgo, H. G., Cayan, D. R., and Swetnam, T. W.: Warming and earlier spring increase western US forest wildfire activity, *Science*, 313, 940–943, doi:10.1126/science.1128834, 2006.

Zhang, Q., Alfarra, M. R., Worsnop, D. R., Allan, J. D., Coe, H., Canagaratna, M. R., and Jimenez, J. L.: Deconvolution and quantification of hydrocarbon-like and oxygenated organic aerosols based on aerosol mass spectrometry, *Environ. Sci. Technol.*, 39, 4938–4952, doi:10.1021/es048568l, 2005.

Appendix C

Water-Soluble Organic Aerosol in the Los Angeles Basin and Outflow Regions: Airborne and Ground Measurements during the 2010 CalNex Field Campaign*

*Reproduced with permission from “Water-soluble organic aerosol in the Los Angeles Basin and outflow regions: Airborne and ground measurements during the 2010 CalNex field campaign” by H. T. Duong, A. Sorooshian, J. S. Craven, S. P. Hersey, A. R. Metcalf, X. Zhang, R. J. Weber, H. Jonsson, R. C. Flagan, and J. H. Seinfeld, *Journal of Geophysical Research*, 116, D00V04, doi:10.1029/2011JD016674. Copyright 2011 by the American Geophysical Union.

Water-soluble organic aerosol in the Los Angeles Basin and outflow regions: Airborne and ground measurements during the 2010 CalNex field campaign

Hanh T. Duong,¹ Armin Sorooshian,^{1,2} Jill S. Craven,³ Scott P. Hersey,³ Andrew R. Metcalf,³ Xiaolu Zhang,⁴ Rodney J. Weber,⁴ Hafliði Jonsson,⁵ Richard C. Flagan,³ and John H. Seinfeld³

Received 3 August 2011; revised 21 September 2011; accepted 25 September 2011; published 18 November 2011.

[1] A particle-into-liquid sampler coupled to a total organic carbon analyzer (PILS-TOC) quantified particulate water-soluble organic carbon (WSOC) mass concentrations during the May 2010 deployment of the Center for Interdisciplinary Remotely Piloted Aircraft Studies (CIRPAS) Twin Otter in the CalNex field study. WSOC data collected during 16 flights provide the first spatiotemporal maps of WSOC in the San Joaquin Valley, Los Angeles Basin, and outflow regions of the Basin. WSOC was consistently higher in concentration within the Los Angeles Basin, where sea breeze transport and Basin topography strongly influence the spatial distribution of WSOC. The highest WSOC levels were associated with fire plumes, highlighting the importance of both primary and secondary sources for WSOC in the region. Residual pollution layers enriched with WSOC are observed aloft up to an altitude of 3.2 km and the highest WSOC levels for each flight were typically observed above 500 m. Simultaneous ground WSOC measurements during aircraft overpasses in Pasadena and Riverside typically exhibit lower levels, especially when relative humidity (RH) was higher aloft suggestive of the influence of aerosol-phase water. This points to the underestimation of the radiative effects of WSOC when using only surface measurements. Reduced aerosol-phase water in the eastern desert outflow region likely promotes the re-partitioning of WSOC to the gas phase and suppression of processes to produce these species (partitioning, multiphase chemistry, photolytic production); as a result, WSOC is reduced relative to sulfate (but not as much as nitrate) as aerosol is advected from the Basin to the outflows.

Citation: Duong, H. T., A. Sorooshian, J. S. Craven, S. P. Hersey, A. R. Metcalf, X. Zhang, R. J. Weber, H. Jonsson, R. C. Flagan, and J. H. Seinfeld (2011), Water-soluble organic aerosol in the Los Angeles Basin and outflow regions: Airborne and ground measurements during the 2010 CalNex field campaign, *J. Geophys. Res.*, 116, D00V04, doi:10.1029/2011JD016674.

1. Introduction

[2] The spatiotemporal distribution of aerosol chemical composition is influential in aerosol interactions with water vapor and radiation. Organics are of major importance in this regard as they typically represent between 20 and 90% of fine aerosol mass [Kanakidou *et al.*, 2005]. As it is vir-

tually impossible to speciate and quantify the entire spectrum of particulate organic compounds, it is useful to examine classes of organic species. A key category of particulate organics is water-soluble organic species, where water-soluble organic carbon (WSOC) has been shown to account for between 40 and 85% of the global organic carbon (OC) budget [Ruellan *et al.*, 1999; Graham *et al.*, 2002; Mayol-Bracero *et al.*, 2002; Jaffrezo *et al.*, 2005; Decesari *et al.*, 2006]. In the absence of biomass burning, WSOC is often considered a proxy for secondary organic aerosol (SOA) due to the oxidized nature of these species as compared to other organics.

[3] Two widely studied areas in the United States with regard to atmospheric aerosol properties and composition include the Los Angeles Basin [Hidy *et al.*, 1974; Grosjean and Friedlander, 1975; Husar *et al.*, 1976, 1977; Blumenthal *et al.*, 1978; Russell *et al.*, 1983; McElroy and Smith, 1986; Russell and Cass, 1984, 1986; Kawamura and Kaplan, 1987; Wall *et al.*, 1988; Pandis *et al.*, 1992a, 1992b; Zhang *et al.*,

¹Department of Chemical and Environmental Engineering, University of Arizona, Tucson, Arizona, USA.

²Department of Atmospheric Sciences, University of Arizona, Tucson, Arizona, USA.

³Departments of Environmental Science and Engineering and Chemical Engineering, California Institute of Technology, Pasadena, California, USA.

⁴School of Earth and Atmospheric Sciences, Georgia Institute of Technology, Atlanta, Georgia, USA.

⁵Center for Interdisciplinary Remotely-Piloted Aircraft Studies, Naval Postgraduate School, Monterey, California, USA.

Table 1. Summary of CIRPAS Twin Otter Research Flights (RF)^a

RF	Flight Date	Day of Week	Flight Time (UTC)	Mission Type
1	5/4/2010	Tuesday	18:01–21:23	LA Basin
2	5/5/2010	Wednesday	18:04–22:10	LA Basin
3	5/6/2010	Thursday	19:06–22:59	LA Basin
4	5/7/2010	Friday	18:02–21:57	LA Basin
5	5/10/2010	Monday	19:00–23:05	LA Basin
6	5/12/2010	Wednesday	17:56–22:08	LA Basin + Salton Sea
7	5/13/2010	Thursday	18:05–21:54	LA Basin + Salton Sea
8	5/14/2010	Friday	17:59–22:01	LA Basin
9	5/15/2010	Saturday	18:13–22:13	LA Basin
10	5/18/2010	Tuesday	18:59–22:53	San Joaquin Valley
11	5/19/2010	Wednesday	18:40–22:45	LA Basin
12	5/20/2010	Thursday	18:53–22:58	San Joaquin Valley + Cajon Pass
13	5/21/2010	Friday	17:57–22:05	LA Basin + Cajon/Banning Passes
14 ^b	5/22/2010	Saturday	18:01–22:12	San Joaquin Valley
15 ^b	5/24/2010	Monday	18:01–22:03	LA Basin + Cajon Pass + Salton Sea
16	5/25/2010	Tuesday	18:27–22:31	LA Basin + Cajon Pass + Salton Sea
17	5/27/2010	Thursday	17:59–21:45	LA Basin
18	5/28/2010	Friday	17:58–22:03	LA Basin

^aLocal time = UTC – seven hours.^bWSOC measurements are not available.

1993; Chow *et al.*, 1994; Hildemann *et al.*, 1994a, 1994b, 1996; Eldering and Cass, 1996; Kleeman *et al.*, 1999; Collins *et al.*, 2000; Hughes *et al.*, 2000; Neuman *et al.*, 2003; Sardar *et al.*, 2005; Vutukuru *et al.*, 2006; Docherty *et al.*, 2008; Hersey *et al.*, 2011] and the San Joaquin Valley of California [Magliano *et al.*, 1999; Schauer and Cass, 2000; Chow *et al.*, 1992, 1993, 1996, 2006; Neuman *et al.*, 2003; Sorooshian *et al.*, 2008a]. While these studies have provided significant knowledge of regional aerosol characteristics, there remain important uncertainties with regard to organic aerosol composition and properties. There are particularly limited airborne measurements that have attempted to characterize the organic composition of aerosol in the Los Angeles Basin and downwind regions.

[4] Recent ground-based measurements in Pasadena, CA between May and September 2009 indicate that organics account for on average between 40 and 60% of the western Los Angeles Basin sub-micrometer aerosol mass [Hersey *et al.*, 2011]. The oxidation state of the Pasadena organic aerosol, as expressed by the atomic oxygen:carbon ratio (O:C) was relatively stable (~0.5) for periods of weeks with little difference at different times of the day. Water-soluble organics were estimated to account for between ~30–70% of the organic mass [Wonaschütz *et al.*, 2011]. Measurements by Peltier *et al.* [2007a] during the SOAR-1 campaign at Riverside, CA (summer 2005) showed that WSOC accounted for an approximate average of 52% of OC mass. Understanding the main sources and production mechanisms of WSOC in the Los Angeles Basin based on measurements at a fixed site has limitations owing to the meteorology of the Basin and the spatial distribution of the sources that lead to organic aerosol. For example, Wonaschütz *et al.* [2011] showed that the diurnal WSOC profile at Pasadena is governed by a combination of sea breeze winds, boundary layer height, and secondary production along the trajectory of air parcels in the Basin. Constraining the spatiotemporal nature of the amount, composition, and vertical distribution of particulate organic matter is critical as aerosol hygroscopicity in the region is largely governed by the organic mass fraction.

[5] In this work, detailed measurements of the nature and character of WSOC in the Los Angeles Basin and outflow regions were performed using both airborne and ground-based sampling during the California Research at the Nexus of Air Quality and Climate Change (CalNex) study in May 2010. Ground-based measurements of WSOC were carried out at two CalNex ground sites. Aircraft overpasses of the ground sites enabled a simultaneous comparison of WSOC in the same vertical column. We address the temporal and spatial variation of WSOC, with an aim to understand the factors that influence WSOC concentrations such as sources, transport and aging, topography, and meteorology. The structure of this paper is as follows: (i) overview of experimental methods; (ii) cumulative summary of WSOC measurements (e.g., vertical profiles, spatial maps, and relationships with other chemical and meteorological variables); (iii) detailed case studies of specific flights; (iv) conceptual model of the nature of WSOC in the study region; and (v) conclusions.

2. Experimental Methods

[6] A total of 18 flights were carried out with the Center for Interdisciplinary Remotely Piloted Aircraft Studies (CIRPAS) Twin Otter during the 2010 CalNex study between 4 May 2010 and 28 May 2010 (Table 1). WSOC was quantified during 16 flights, using a particle-into-liquid sampler (PILS; Brechtel Manufacturing Inc.) coupled to a Total Organic Carbon (TOC) Analyzer (Sievers Model 800) [Sullivan *et al.*, 2006]. Briefly, particles smaller than 2.5 μm in diameter are sampled by the PILS and passed immediately through an organic carbon denuder (Sunset Laboratory Inc.) to remove organic vapors. Particles are grown into droplets, collected by inertial impaction, and delivered through a 0.5 μm PEEK (polyetheretherketone) liquid filter prior to entering a TOC analyzer for quantification of WSOC every ~4 s. Reported WSOC levels represent the difference between the measured and background concentrations, which were obtained by passing sampled air through a high efficiency particulate air (HEPA) filter. The overall measurement uncertainty is estimated to be approximately 10%, with a minimum detection limit of 0.1 $\mu\text{g C m}^{-3}$. Synchronization

Table 2. Summary of Measurements in the Vicinity of Banning Pass (33.89°N, 33.98°N; -116.77°W, -116.99°W)^a

RF of Day	Local Time	WSOC ($\mu\text{g C m}^{-3}$)	PCASP Volume ($\mu\text{m}^3 \text{cm}^{-3}$)	PCASP (Number per cm^3)	DMA Volume ($\mu\text{m}^3 \text{cm}^{-3}$)	DMA (Number per cm^3)	Alt (m)	T (°C)	RH (%)	Wind Speed (m s^{-1})	Wind Direction (deg)
1	12:20	0.41 (0.12)	3.66 (1.38)	952 (227)	2.51 (0.39)	8031 (941)	1036 (158)	20.8 (1.8)	23.9 (2.4)	5.5 (1.8)	256 (17)
2	12:30	0.94 (0.14)			3.33 (0.73)	6942 (2019)	992 (156)	19.2 (1.6)	36.3 (3.1)	7.5 (2.3)	252 (14)
2	14:30	1.21 (0.17)			4.19 (0.46)	7345 (961)	976 (139)	21.0 (1.5)	30.6 (2.6)	8.2 (1.9)	261 (14)
3	1:30	1.46 (0.15)	8.19 (2.04)	1367 (125)	4.31 (0.60)	5063 (650)	985 (149)	17.6 (1.7)	41.2 (5.7)	6.9 (2.4)	256 (14)
3	3:10	1.15 (0.13)	8.23 (2.70)	1443 (181)	4.72 (1.49)	6469 (99)	1114 (23)	18.3 (0.3)	40.6 (4.6)	7.4 (1.9)	264 (12)
4	12:30	0.37 (0.03)	1.54 (1.04)	269 (39)	1.34 (0.46)	2480 (130)	1065 (24)	21.1 (0.2)	11.4 (0.6)	7.1 (1.2)	94 (13)
4	2:20	0.50 (0.05)			1.49 (0.30)	7720 (1439)	1068 (36)	22.8 (0.3)	14.3 (1.3)	2.8 (1.6)	217 (79)
6	2:20	0.41 (0.07)			3.27 (1.83)	6029 (1194)	1102 (69)	17.6 (0.8)	25.7 (2.5)	5.6 (1.5)	258 (24)
7	1:30	0.48 (0.19)	4.48 (2.70)	1037 (393)	4.38 (2.97)	4967 (1341)	1088 (49)	19.3 (0.8)	25.3 (3.5)	5.1 (2.3)	177(79)
13	2:40	2.12 (0.14)	15.11 (2.83)	2437 (213)	9.38 (1.86)	5416 (352)	1170 (19)	17.2 (0.3)	54.5 (1.8)	8.7 (2.6)	264 (16)
16	2:40	0.89 (0.08)	6.35 (2.04)	1604 (385)	4.38 (0.31)	5186 (396)	1058 (81)	16.0 (1.0)	39.2 (3.1)	7.3 (1.9)	267 (14)

^aDMA data are reported since PCASP data are not available from Flights 2, 4, and 6.

of WSOC measurements with the other aircraft instrument data described below takes into account well-documented liquid transport delays in the PILS instrument [Sorooshian *et al.*, 2006].

[7] Contemporaneous with the airborne measurements, online $\text{PM}_{2.5}$ WSOC measurements were carried out at two ground sites (Pasadena and Riverside) with the same instrument set-up as on the aircraft. The Pasadena CalNex ground site was located on the California Institute of Technology campus (34.1406°N, -118.1225°W). The Riverside site was located on the University of California-Riverside campus (33.9719°N, -117.3227°W). The sample inlet was 7 m above ground level at the Pasadena ground site, and 4.5 m above ground level at Riverside.

[8] Measurements of sub-micrometer inorganic and non-refractory organic mass were obtained with an Aerodyne compact Time of Flight Aerosol Mass Spectrometer (C-ToF-AMS) [Drewnick *et al.*, 2005; Murphy *et al.*, 2009]. AMS data used here include organic markers at specific mass-to-charge ratios (m/z) that serve as proxies for organics with a range of oxidation states: acid-like oxygenated organics (m/z 44 = COO^+), aliphatic and non-acid oxygenated organics (m/z 43 = C_3H_7^+ and $\text{C}_2\text{H}_3\text{O}^+$), and aliphatic organics (m/z 57 = C_4H_9^+) [McLafferty and Turecek, 1993; Zhang *et al.*, 2005; Aiken *et al.*, 2008; Ng *et al.*, 2010]. Owing to the size cutoff of the AMS being smaller than the PILS (1 μm versus 2.5 μm), any mass ratios between WSOC and AMS measurements represent an upper limit.

[9] Particle size distribution measurements ($D_p = 10 \text{ nm}$ –800 nm) on the aircraft were carried out with a cylindrical scanning differential mobility analyzer (DMA; TSI Model 3081) coupled to a condensation particle counter (CPC; TSI Model 3760), in addition to a passive cavity aerosol spectrometer probe (PCASP; $D_p = 100 \text{ nm}$ –2.6 μm). WSOC data are usually compared only to PCASP data in this study owing to similar size bins, while DMA data are used only when PCASP data were not available (Table 2). Sub-saturated aerosol hygroscopicity measurements were provided by a differential aerosol sizing and hygroscopicity spectrometer probe at relative humidities of 74% and 92% and for dry diameters ranging between 150–225 nm (DASH-SP; Brechtel Mfg Inc. [Sorooshian *et al.*, 2008b]). Black carbon (BC) measurements were obtained using a single particle soot photometer instrument (SP2; Droplet Measurement Technologies).

[10] Ground-based gas (CO, O₃) and aerosol (PM_{2.5}) measurements were obtained from existing monitoring stations throughout the Los Angeles Basin and outflow areas (see Figure 1) (<http://www.arb.ca.gov/aqmis2/aqmis2.php>; CARB IADAM Air Quality Data Statistics, 2010, <http://www.arb.ca.gov/adam>). Additional hourly meteorological data were obtained from regional surface sites using the Mesowest Database [<http://mesowest.utah.edu/index.html>]. Solar radiation data were obtained from a ground site at Tonner Canyon (33.948°N, -117.822°W, ~410 m altitude; Mesowest), which is centrally located within the Basin.

3. Los Angeles Basin and Outflow Area Description

[11] The metropolitan Los Angeles population exceeds 17 million and the Basin contains a complete spectrum of air pollution sources, including vehicular emissions, cooking, biomass burning, industrial activity, agricultural activity, and marine shipping. The Los Angeles Basin is bordered on three sides by mountainous terrain and by the Pacific Ocean on the southwestern side (Figure 1). Transport of pollutants in the Los Angeles Basin is governed largely by sea breeze and mountain flows [Lu and Turco, 1995]. Average monthly wind roses are shown in auxiliary material Figure S1 for the month of May across the study region and representative wind directions are shown in Figure 1.¹ The general wind pattern in the region during the period of time that flights occurred was as follows: westerly and southwesterly winds transporting air from the western edge of the Basin toward the eastern edge, where air is funneled out of narrow passes into desert regions. The two main passes are to the north through the Cajon Pass toward Victorville and Barstow and to the east via the Banning Pass.

[12] During CalNex, fine particle number concentrations were typically highest ($>10,000 \text{ cm}^{-3}$) at the western side of the Los Angeles Basin (longitude: 118.05°W–118.3°W), especially in the Long Beach area owing to major point sources. Fine particle number concentrations generally decreased as a function of distance eastward, while PCASP particle number and volume concentrations exhibited the opposite behavior and typically reached peak levels near the northern and eastern edges of the Basin. This can be explained by aging processes along the typical sea breeze

¹Auxiliary materials are available in the HTML. doi:10.1029/2011JD016674.

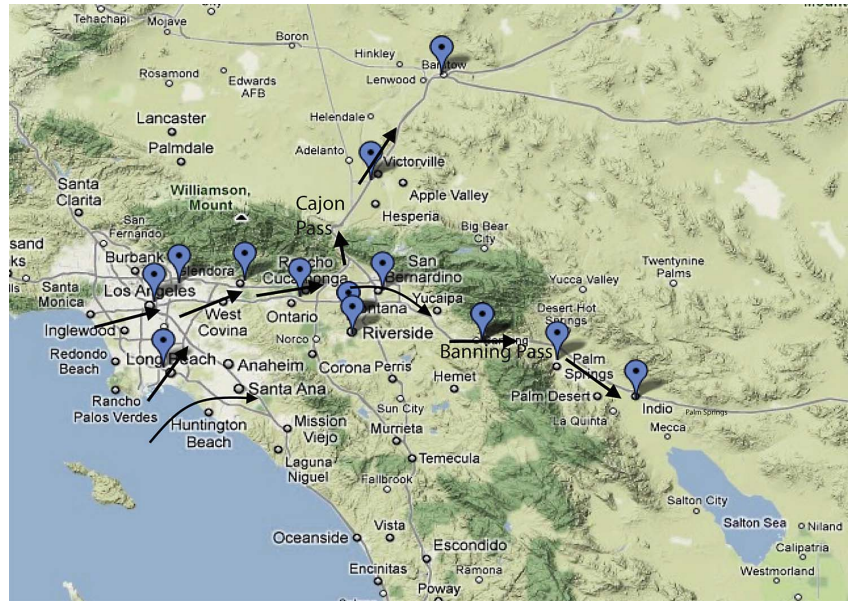


Figure 1. Terrain map of the Los Angeles Basin and outflow regions including Banning Pass, which funnels air out toward areas including Indio and the Salton Sea, and the Cajon Pass, which transports air toward Victorville and Barstow. Blue markers correspond to ground stations (<http://www.arb.ca.gov/aqmis2/aqmis2.php>) at which gas and PM_{2.5} data were obtained. Black arrows correspond to the typical wind directions during the durations of the flights; specific monthly averaged wind roses across the study region are shown in auxiliary material Figure S1.

trajectory leading to the growth of particles into the size range of the PCASP ($D_p > 100$ nm).

4. WSOC Distributions

4.1. Spatial WSOC Distribution

[13] Figure 2 shows the cumulative spatial distribution of WSOC concentration measured on the Twin Otter during

May 2010. Average levels in specific portions of the region are shown in Figure 3a. WSOC was fairly well-correlated with particle number concentration ($r^2 = 0.49$; slope = $0.85 \text{ ng C m}^{-3}/\text{cm}^{-3}$; $n = 34655$) and volume concentration ($r^2 = 0.53$; slope = $0.12 \mu\text{g C m}^{-3}/(\mu\text{m}^3 \text{ cm}^{-3})$; $n = 33975$), as measured by the PCASP. The highest WSOC concentrations were consistently observed in the Los Angeles Basin, as compared to desert outflow regions and the San

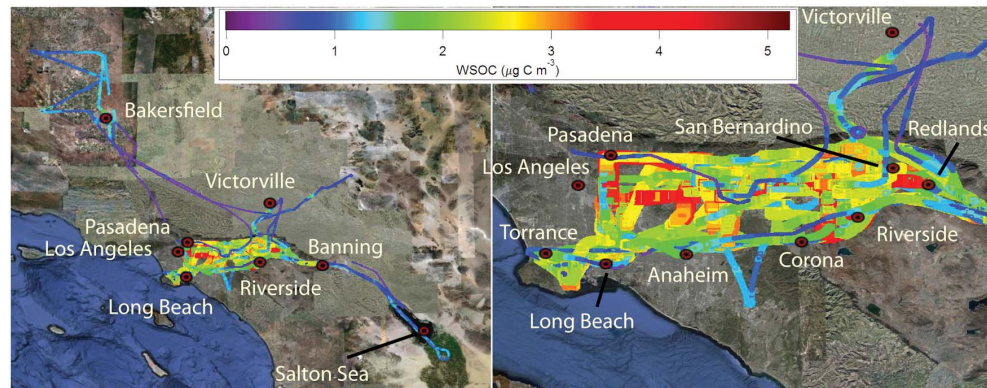


Figure 2. (left) Spatial distribution of WSOC concentrations during the CalNex campaign in the San Joaquin Valley, the Los Angeles Basin, and outflow regions extending north through the Cajon Pass and east through the Banning Pass toward Indio and the Salton Sea. (right) Close-up of WSOC in the Los Angeles Basin.

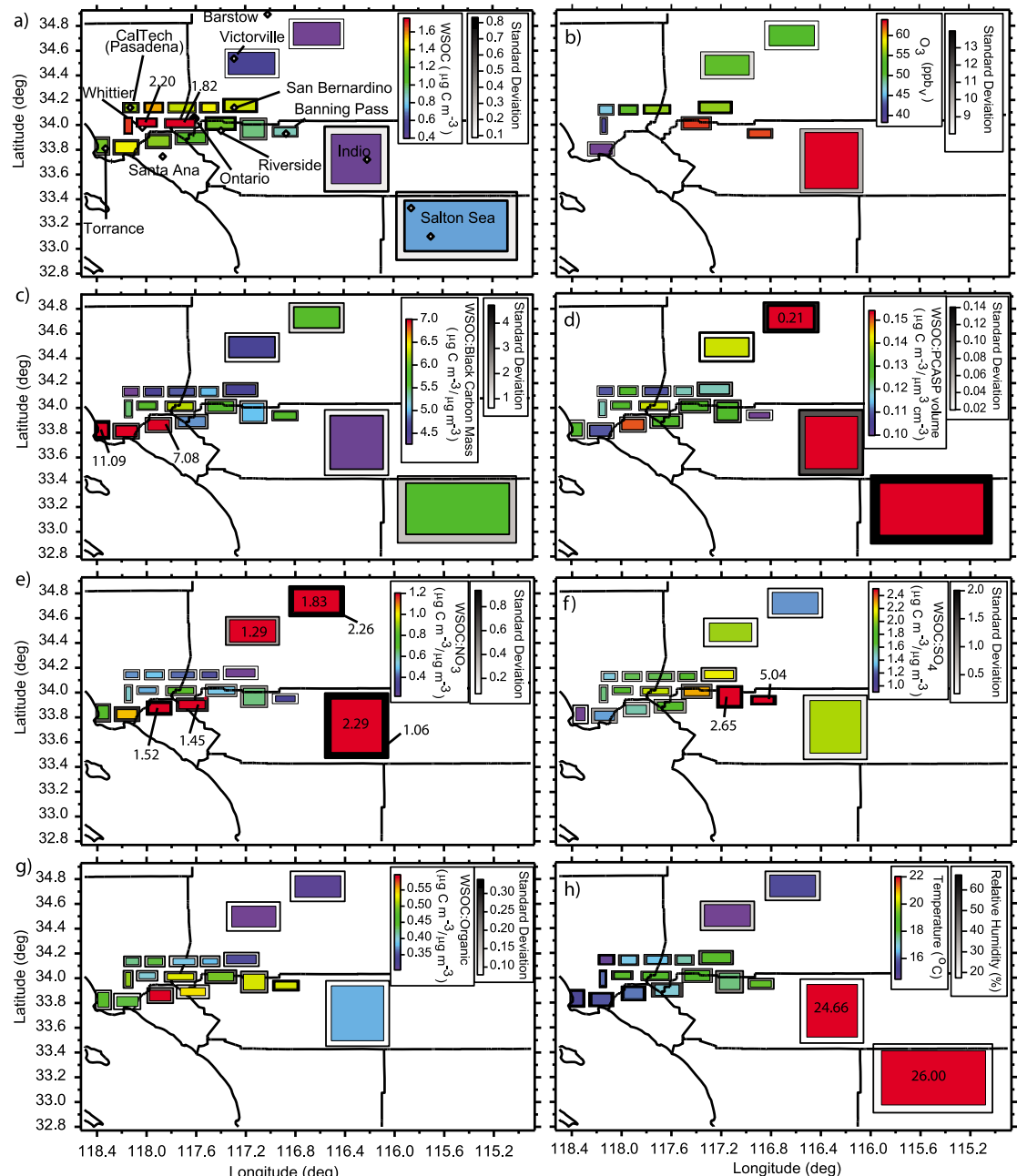


Figure 3. Cumulative spatial averages of (a) WSOC, (b) surface O₃ concentration, (c) WSOC:BC, (d) WSOC:PCASP volume concentration, (e) WSOC:nitrate, (f) WSOC:sulfate, (g) WSOC:organic, and (h) ambient temperature and RH. Numbers in boxes correspond to true values that exceed the range shown in color bars. Sizes of the boxes correspond to the geographic area within which the data were averaged. City labels are included in Figure 3a.

Joaquin Valley, reaching values as high as $5.3 \mu\text{g C m}^{-3}$. High concentrations were often observed along the north-south corridor extending between Pasadena and the downtown Los Angeles area, coincident with the highest levels

of BC, CO, and $m/z 57$ ($>0.3 \mu\text{g m}^{-3}$, $>0.35 \text{ ppm}_v$, $>80 \text{ ng m}^{-3}$, respectively). Comparable or higher concentrations were also observed during some flights on the eastern side of the Basin near San Bernardino and Redlands. The lowest concentrations

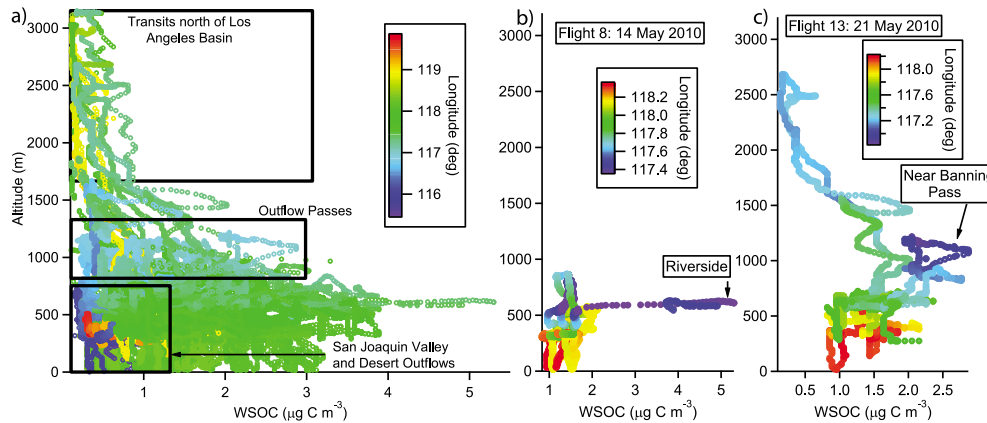


Figure 4. (a) Vertical profile of WSOC mass concentrations during 16 flights over the spatial domain shown in Figure 1. The majority of the data collected below 1 km are from the Los Angeles Basin, with the minority of the yellow-red and blue markers corresponding to San Joaquin Valley and outflow areas to the east of the Basin, respectively. The majority of the markers near 1 km correspond to transits through outflow-passes (i.e., Banning Pass and Cajon Pass), while higher altitudes correspond to transits north of the Los Angeles Basin. (b and c) Examples of vertical profiles during two flights in the Los Angeles Basin showing that the highest WSOC levels were observed above the first few hundred meters. The maximum WSOC level during Flight 8 corresponded to a local fire plume, while the peak WSOC level in Flight 13 was observed over the eastern edge of the Basin near Banning Pass.

of WSOC in the Los Angeles Basin were usually observed near Torrance when the dominant wind direction was westerly from the ocean (i.e., upwind of major emissions sources in Long Beach), and to the southeast/east of the Puente and Chino Hills, which serve as a barrier to the transport of pollution from the western side of the Basin. Outflow regions were characterized by lower WSOC levels than those observed in the Basin mainly owing to dilution during urban plume transport and a lack of significant WSOC sources in the desert. The general west-to-east transect of highest WSOC levels coincided with the average westerly/southwesterly wind patterns during the period of flights, with increases from the western side of the Basin near downtown Los Angeles toward maximum levels near Whittier, then decreasing to the northeast near San Bernardino. Smoke plumes were occasionally intercepted in the Los Angeles Basin, usually near the eastern side in the vicinity of Riverside, owing to small-scale fires. These plumes resulted in the highest WSOC concentrations during the respective flights, with one being the highest of the campaign (maximum levels observed in separate fire plumes: $1.7 \mu\text{g C m}^{-3}$, Flight 6; $5.3 \mu\text{g C m}^{-3}$, Flight 8; $1.8 \mu\text{g C m}^{-3}$, Flight 12; $1.6 \mu\text{g C m}^{-3}$, Flight 18). Chemical ratios that can be used to trace secondary production (e.g., WSOC:CO; WSOC:BC) become perturbed in these cases owing to primary production (i.e., direct emission) of WSOC in these fresh plumes.

[14] A number of flights focused on Banning Pass, owing to the role of this area as an exit for the Basin pollution. Table 2 shows a summary of all the WSOC measurements in this area with relevant meteorological information. Out of eleven flight legs through this outflow-pass, nine were characterized by westerly winds and higher WSOC levels than periods with easterly winds. For example, during Flight 4 the first transect was characterized by easterly winds and lower concentrations of WSOC and particle concentration.

Approximately two hours later, winds shifted to be westerly resulting in enhancements in WSOC (0.37 to $0.50 \mu\text{g C m}^{-3}$) and fine particle number concentration (2480 to 7720 cm^{-3}). Of the other parameters shown in Table 2, WSOC was best correlated with RH and PCASP particle volume concentration ($r^2 = 0.79$ for both).

4.2. Vertical WSOC Distribution

[15] The airborne measurements were usually conducted below an altitude of 1 km in the Los Angeles Basin and San Joaquin Valley and at higher altitudes through the outflow-passes (Figure 4a). On 11 of the 16 flights, WSOC exhibited its highest concentration above 500 m, usually near the eastern end of the Basin by Riverside, San Bernardino, and Banning Pass. Two representative flights demonstrating this behavior are shown in Figures 4b and 4c, where WSOC peaks between 600 and 1100 m in altitude near Banning Pass and Riverside. The maximum concentration during Flight 8 ($5.3 \mu\text{g C m}^{-3}$, 14 May 2010) corresponded to a Riverside fire plume and was the highest Twin Otter WSOC measurement of the entire CalNex field study. A cluster of points in Figure 4a (color-coded as blue and yellow-orange) are relatively lower in WSOC concentration than the rest below 1 km as they are from the San Joaquin Valley and outflow areas.

[16] Multiple pollution layers have been observed aloft in this region in past airborne measurements [Blumenthal *et al.*, 1978; McElroy and Smith, 1986; Collins *et al.*, 2000]. These layers arise by horizontal and vertical displacement of the morning inversion layer and orographic uplift [Lu and Turco, 1995]. It is possible that such layers, which can undergo continued chemical processing while separated from the mixing layer, contribute to surface concentrations through turbulent mixing as the boundary layer deepens [Husar *et al.*,

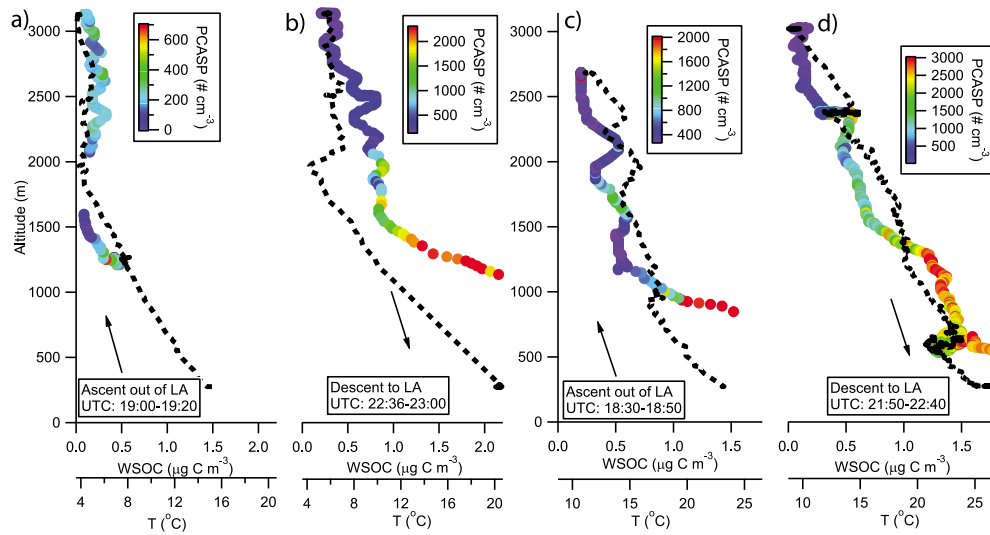


Figure 5. Vertical profiles of WSOC during two flights: (a and b) Flight 10 on 18 May 2010 and (c and d) Flight 12 on 20 May 2010. Colored markers correspond to WSOC and dashed black lines represent ambient temperature. Local time = UTC – seven hours.

1977; Blumenthal *et al.*, 1978]. Vertical profiles of WSOC were obtained during two flights up to an altitude of approximately 3.2 km (Figure 5). The ascents and descents occurred at the northern edge of the Basin. These profiles offer a direct comparison of WSOC separated by 2–4 h of aging time. The ascents out of Los Angeles at the beginning of the flights (Figures 5a and 5c) were characterized by a decrease in WSOC with altitude until a point where a series of vertical layers became evident with enhanced WSOC levels and PCASP particle number concentrations. The descents into the Basin (Figures 5b and 5d) more than two hours later exhibited systematically larger WSOC and PCASP number concentrations in the bottom 1.5 km above the surface with similar layers of WSOC enrichment at higher altitudes. This is likely due to continuous emissions during the daytime and higher photochemical activity occurring to generate more WSOC.

[17] To identify the level of vertical WSOC variation in the mixing layer, simultaneous ground and airborne measurements in the same vertical column are compared at Pasadena (Figure 6a) and Riverside (Figure 6b). A total of 13 and 12 simultaneous measurements were conducted in Pasadena and Riverside, respectively, between 11:00–15:30 (LT). The airborne measurements during the overpasses were conducted within the mixing layer at altitudes between 500–800 m. At both sites, WSOC levels were generally higher aloft, and the difference is more evident in Pasadena. The greatest enhancements aloft relative to ground measurements at both sites were coincident with the highest ratios of RH aloft relative to at the surface, which is most evident at Riverside. The average RHs during the overpasses at Pasadena and Riverside were $67 \pm 10\%$ (max = 78%) and $52 \pm 9\%$ (max = 65%), respectively. This may be indicative of production of WSOC by processes that are more efficient as a function of increasing aerosol-phase water. High RHs (>70%) have been shown to coincide with enhanced partic-

ulate WSOC and organic acid concentrations owing to more effective partitioning of these species to the aerosol phase and multiphase chemistry [e.g., Hennigan *et al.*, 2008b, 2009; Ervens and Volkamer, 2010; Sorooshian *et al.*, 2010]. In addition, direct photolytic processing has also been suggested to be an important mechanism to generate SOA in particles residing in humid air [Bateman *et al.*, 2011].

[18] Vertical profiles of ratios of WSOC to PCASP particle volume concentration and AMS organic mass are shown in Figure 7. The range of the average WSOC:particle volume concentration ratio (Figure 7a) was between 0.11 and 0.19 between the surface and 3.2 km, while the WSOC:organic ratio (Figure 7b) ranged widely between 0.26 and 0.63. Both ratios exhibit variable behavior as a function of altitude, with an average reduction from the surface to ~800 m, and with maximum values occurring at altitudes exceeding 1500 m. The large variability in these ratios is largely a result of day-to-day variability; however, the absolute range of the ratios is indicative of WSOC being a significant component of the aerosol from the surface up to 3.2 km.

4.3. WSOC Ratios to Other Aerosol Mass and Volume Measurements

[19] To gain more insight into the relative importance of WSOC to the total aerosol budget and the sources and sinks of WSOC, the ratios of WSOC to other aerosol parameters are examined in Figures 3 and 8. Despite the existence of vertical gradients in aerosol composition and mass, it is useful to constrain airborne-measured WSOC with simultaneous ground-based PM_{2.5} measurements (PM_{2.5} was not quantified on the Twin Otter). For the limited sites at which PM_{2.5} measurements were available within the Basin, WSOC contributed typically between 6 and 11% to PM_{2.5} mass. Note that converting WSOC to an organic mass equivalent concentration requires a conversion factor, which was previously assumed to be ~1.8 for the region [Docherty

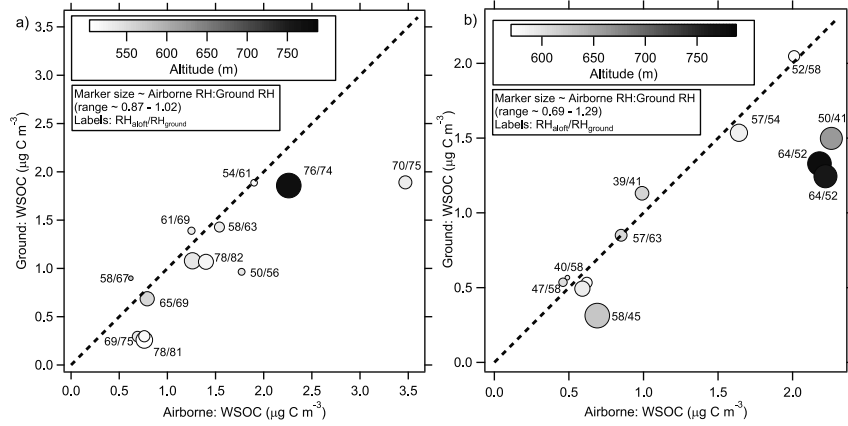


Figure 6. Comparison of simultaneous ground and airborne WSOC measurements in the same vertical column at (a) Pasadena and (b) Riverside.

et al., 2008]. The ratio of WSOC to $\text{PM}_{2.5}$ was highest in the western portion of the Los Angeles Basin near Long Beach, downtown Los Angeles, and Glendora (0.10–0.11) and was lowest near Banning Pass (~0.06) owing partly to the major enhancement in ammonium nitrate levels near the eastern side of the Basin. The closest measure of how WSOC contributes to total $\text{PM}_{2.5}$ using aircraft measurements is the comparison to PCASP volume concentration, where the PCASP measures particles in a similar size range as the PILSTOC (<2.5 μm). The WSOC:PCASP volume ratio (Figure 3d) was typically between ~ 0.1 – $0.15 \mu\text{g C m}^{-3}/(\mu\text{m}^3 \text{cm}^{-3})$ in the Los Angeles Basin, while higher average values were observed in the outflow regions. Ratios reached an average of 0.30 ± 0.14 near the Salton Sea to the east of the Basin and

0.21 ± 0.12 near Barstow to the northeast of the Basin. As a basis for comparison, the ratio of WSOC to fine particle volume concentration was 0.12 and 0.10–0.22 $\mu\text{g C m}^{-3}/(\mu\text{m}^3 \text{cm}^{-3})$ in non-biomass and biomass burning plumes, respectively, in the northeastern United States [Sullivan et al., 2006; Peltier et al., 2007b]. An increase in this ratio can be due to a variety of reasons including losses in other aerosol components (e.g., nitrate volatilization), increased production of WSOC during transport, local sources such as fires, or entrained air masses from aloft that are enriched with WSOC relative to other aerosol components.

[20] Examining the variation of relative concentrations of WSOC and other particle and gas-phase constituents along the sea breeze trajectory from west to east provides insight

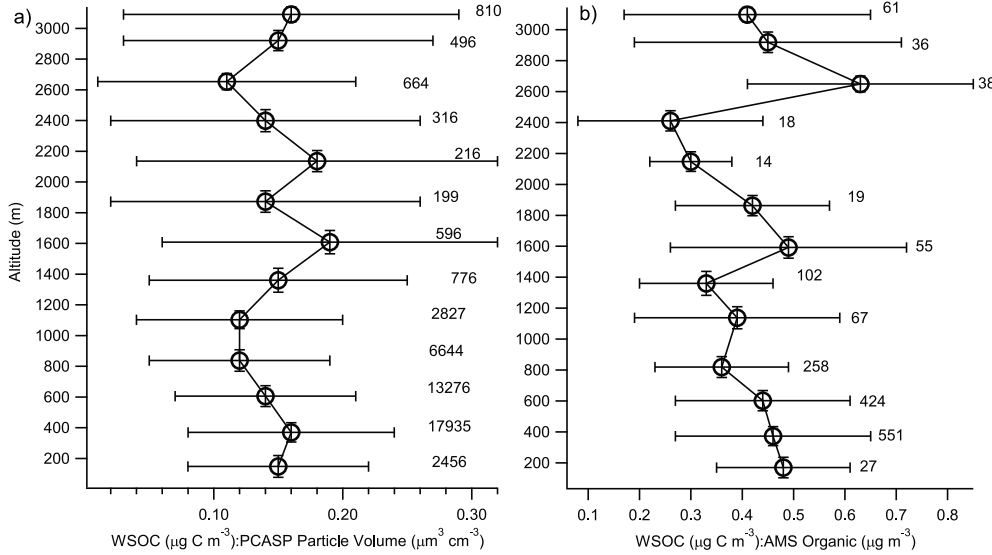


Figure 7. Vertical distribution of (a) the ratio of WSOC to PCASP particle volume concentration (data from all flights) and (b) the ratio of WSOC to total AMS non-refractory organic aerosol mass (Flight 11, 13, 16–18). Numbers beside each point in each panel correspond to the sample size.

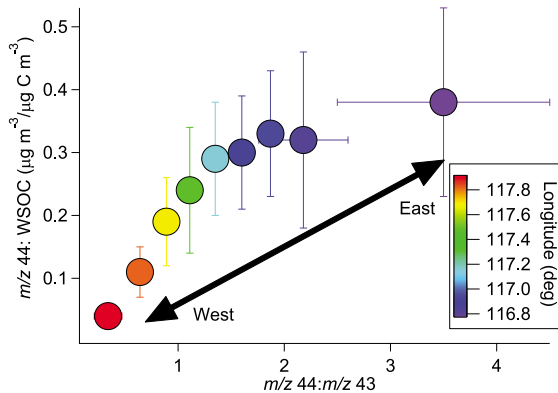


Figure 8. Ratio of m/z 44:WSOC as a function of m/z 44:43. Markers are color-coded with longitude where red corresponds to western side of the Los Angeles Basin and purple corresponds to outflow desert regions to the east of the Basin.

into the relative importance of volatilization and secondary formation of WSOC (Figure 3). The highest O_3 levels were observed farther inland and were highest in the outflows to the east of the Basin (Figure 3b). This is indicative of increased photochemical processing during sea breeze transport of air masses from the coast to the desert. This would likewise favor secondary production of WSOC. Black carbon is a primary species and thus an increase in the WSOC:BC ratio is a tracer for secondary production. This ratio was highest near the southwestern portion of the study region, presumably owing to the low levels of BC in marine air and upwind of major BC sources in the Basin (Figure 3c). This ratio did not show any clear trend as a function of downwind distance, likely a result of the abundance of BC and organic aerosol sources in the Basin, including the fires observed on the eastern side of the Basin. Unlike the majority of the Basin, there are fewer BC sources along trajectories to the east of the outflow channels; WSOC:BC initially decreases and then increases owing possibly to a combination of WSOC volatilization initially and secondary production afterwards.

[21] The contribution of WSOC to total non-refractory organic mass was highest near the southwestern portion of the Los Angeles Basin (up to $\sim 60\%$ just north of Santa Ana) and lowest in the desert outflow regions ($< 40\%$) (Figure 3g). Along the sea breeze trajectory on the northern side of the Basin, the WSOC:Organic ratio tended to increase toward Banning Pass reaching an average value of $53 \pm 34\%$. Recent studies have utilized m/z 44 and m/z 43 [e.g., Ng *et al.*, 2010] to track the aging of organic aerosol in the atmosphere. The ratio of m/z 44:43 provides information about the chemical functionality of oxygenated organic aerosol (OOA), with higher values indicative of a higher state of oxidation. Wonaschütz *et al.* [2011] examined the ratio of m/z 44:WSOC as a function of m/z 44:43 during the PACO campaign as a way of understanding how the composition of the WSOC fraction of the aerosol changed with photochemical age. Aircraft measurements in Figure 8 show that the ratio of m/z 44:WSOC increased as a function

of m/z 44:43, with increases in both ratios as a function of longitude (higher values to the east). This is consistent with a shift from semi-volatile OOA components to more low-volatility OOA components as a function of photochemical aging. The immediate sharp increase in m/z 44:WSOC followed by a plateau is consistent with the findings of Ng *et al.* [2010] and previous measurements during PACO [Wonaschütz *et al.*, 2011]. It is noted that m/z 44 levels reached as high as $\sim 1.8 \mu\text{g m}^{-3}$, which is roughly similar to peak levels observed in Pittsburgh during September (up to $\sim 1.2 \mu\text{g m}^{-3}$ [Zhang *et al.*, 2005]), Tokyo in August (up to $\sim 2.29 \mu\text{g m}^{-3}$ [Takegawa *et al.*, 2007]), but less than that in Tokyo during the summer (up to $\sim 3.5 \mu\text{g m}^{-3}$ [Kondo *et al.*, 2007]).

[22] More insight into the secondary production of organics arises from the ratio of WSOC: SO_4^{2-} (Figure 3f) as a function of distance eastward from the western end of the Basin where the highest SO_4^{2-} levels were observed, owing to marine shipping sources and other major point sources near the coast. The WSOC: SO_4^{2-} ratio ranged between 0.9 and 5.0 in the study region, which is greater than the cumulative average ratio (~ 0.55) observed by Peltier *et al.* [2007b] in the northeastern United States. The peak WSOC: SO_4^{2-} ratios between Riverside and Banning are coincident with an area with intense ammonium nitrate production owing largely to the influence of agricultural activity as a source of NH_3 , including animal husbandry operations. Ammonium nitrate production results in enhanced aerosol hygroscopicity and aerosol-phase water, which would promote more partitioning of WSOC to the aerosol phase and both multi-phase chemistry and photolytic processing to produce WSOC [Hennigan *et al.*, 2008a; Ervens and Volkamer, 2010; Sorooshian *et al.*, 2010; Bateman *et al.*, 2011]. In addition, WSOC may have been produced in the emissions from the agricultural activity. The WSOC: SO_4^{2-} ratio decreased immediately downwind of Banning by an average factor of nearly 2.5 and this may be due to volatilization of WSOC (note that SO_4^{2-} is not volatile), which is consistent with the reduction in the WSOC:BC ratio (by an average factor of ~ 2) in the same area. Production of SO_4^{2-} in this area can likely be ruled out owing to the low RHs, high temperatures, and lack of aqueous-phase chemistry to produce SO_4^{2-} during afternoons (Table 2). The average RH during traverses through Banning Pass ranged between 11 and 55%.

[23] Reductions in aerosol-phase water, such as what happens when air is advected from the Basin to the desert outflows, promotes re-partitioning of WSOC to the gas phase [Hennigan *et al.*, 2008b; 2009]. Lower amounts of the aerosol-phase water are associated with reduced RH and aerosol hygroscopicity. As shown in Figure 3h, the average temperature generally increases from west to east, and vice versa for average RH. The sub-saturated hygroscopicity of the regional aerosol decreased in the outflows, largely owing to ammonium nitrate volatilization. The average hygroscopic growth factor ($D_{p,wet}/D_{p,dry}$) at an RH of 92% for fine aerosol was 1.72 ± 0.25 in the Basin and 1.57 ± 0.19 in the desert outflows. To further examine the likelihood that volatilization is a sink for WSOC downwind of the Los Angeles Basin, the ratio of WSOC: NO_3^- is also examined (Figure 3e), as NO_3^- is vulnerable to evaporation. The range of this ratio was 0.2–2.3, within which are values observed in Mexico City (~ 0.2 –1.0)

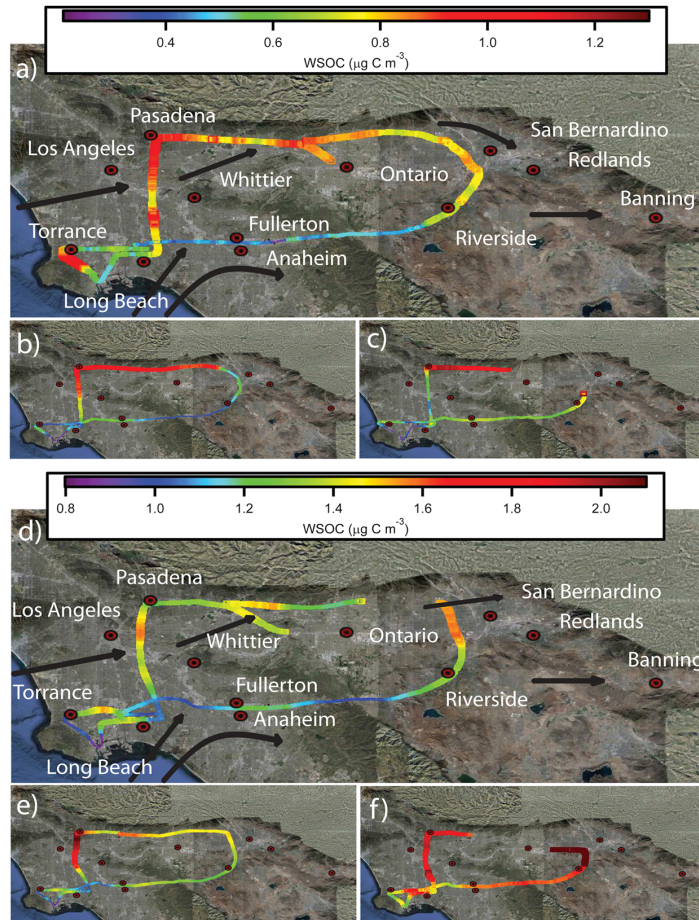


Figure 9. Spatial maps of WSOC during three successive Basin loops in Flight 5 on 10 May 2010 ((a) UTC = 19:00–20:30, (b) 20:30–21:50, and (c) 21:50–23:00) and in Flight 8 on 14 May 2010 ((d) UTC = 18:00–19:30, (e) 19:30–20:50, and (f) 20:50–22:00). Black arrows in Figures 10a and 10d correspond to the typical wind directions during the duration of the two flights as determined by wind roses obtained from the Mesowest Database [<http://mesowest.utah.edu/index.html>]. Local time = UTC – seven hours.

[Hennigan *et al.*, 2008a] but much less than the cumulative average ratio (>30) observed in the northeastern United States [Peltier *et al.*, 2007b]. AMS NO_3^- mass concentrations are typically highest at San Bernardino ($6.08 \pm 5.87 \mu\text{g m}^{-3}$ for the box labeled with this city in Figure 3) and they decrease significantly immediately downwind of the outflow-passes. As a result, the WSOC: NO_3^- ratio increased sharply in the outflows (greater than a factor of six), in contrast to the WSOC: SO_4^{2-} ratio. This indicates that WSOC is less sensitive to volatilization as compared to ammonium nitrate. Such results are consistent with observations in Mexico City [Hennigan *et al.*, 2008a].

[24] The general picture drawn in Figure 3 involves the following: (i) the western Basin is an important anthropogenic source for WSOC and precursors; and (ii) pollutants are transported to the eastern side of the Basin and through outflow-passes with the sea breeze, with aerosol aging processes during this time including dilution, secondary formation of WSOC, and volatilization of some fraction of

WSOC. The increasing temperatures (decreasing RH) and reduction of aerosol hygroscopicity and aerosol-phase water in the outflows is likely responsible for the loss of some WSOC mass.

5. Case Studies in the Los Angeles Basin

5.1. Basin Loops

[25] Two weekdays characterized by different meteorological conditions and nearly identical flight paths in the Los Angeles Basin are examined to study the sensitivity of the spatiotemporal distribution of WSOC to meteorology (Figure 9). Flight 5 on 10 May 2010 was characterized by higher wind speeds, higher ambient temperature, and lower incident solar radiation as compared to Flight 8 on 14 May 2010 during the duration of the flights (Table 3). Flight 5 was characterized by cloudy conditions in the Basin during the time span of the flight, unlike Flight 8. The aircraft flew at an altitude of approximately ~300–600 m both

Table 3. Average Values of Meteorological and Aerosol Parameters During Los Angeles Basin Loops During Five Flights^a

	UTC Time	T (°C)	RH (%)	Wind (m s ⁻¹)	CPC (Number per cm ³)	PCASP (Number per cm ³)	WSOC (µg C m ⁻³)	O ₃ (ppb)	WSOC:BC (µg C m ⁻³ /µg m ⁻³)	Solar Radiation (W m ⁻²)
Flight 5	Loop 1 (19:00–20:30)	13.3 (1.1)	62.5 (6.5)	4.8 (1.8)	9583 (4649)	754 (312)	0.72 (0.19)	52.3 (8.4)	5.6 (0.8)	896 (173)
	Loop 2 (20:30–21:50)	13.7 (1.1)	61.2 (5.7)	5.8 (1.5)	11025 (4466)	774 (393)	0.66 (0.28)	53.7 (9.7)	6.2 (1.8)	816 (71)
	Loop 3 (21:50–23:00)	13.8 (1.0)	60.3 (6.1)	6.3 (1.8)	10747 (4386)	642 (354)	0.67 (0.25)	53.9 (9.6)	8.8 (5.4)	728 (185)
Flight 8	Loop 1 (18:00–19:30)	14.8 (0.5)	70.4 (3.0)	2.6 (1.0)	9664 (2517)	1372 (264)	1.33 (0.12)	50.8 (11.9)	5.0 (1.1)	1066 (40)
	Loop 2 (19:30–20:50)	16.7 (0.7)	62.8 (4.6)	3.3 (1.0)	12299 (3574)	1575 (294)	1.57 (0.27)	53.3 (11.6)	4.5 (2.4)	1064 (43)
	Loop 3 (20:50–22:00)	17.7 (1.26)	60.8 (6.4)	3.8 (1.0)	14723 (3514)	1641 (301)	1.75 (0.15)	55.8 (11.8)	6.9 (3.9)	985 (85)
Flight 9	Loop 1 (18:20–20:05)	18.1 (2.7)	61.2 (14.5)	3.2 (1.5)	9953 (3706)	1751 (422)	2.61 (0.55)	61.1 (12.2)	9.6 (1.9)	1083 (41)
	Loop 2 (20:05–22:15)	20.2 (3.3)	53.2 (17.1)	5.0 (1.9)	11635 (4155)	1654 (436)	2.89 (0.68)	72.4 (10.1)	10.2 (4.3)	1003 (112)
Flight 11	Loop 1 (18:50–21:05)	17.2 (1.9)	65.6 (10.2)	3.4 (1.5)	10328 (3665)	1580 (1987)	2.11 (0.33)	46.8 (12.8)	6.4 (1.6)	1087 (32)
	Loop 2 (21:05–22:50)	18.4 (2.5)	63.2 (11.2)	5.3 (2.0)	13331 (4383)	1521 (401)	2.23 (0.34)	53.3 (11.6)	8.1 (3.3)	999 (114)
Flight 13	Loop 1 (18:10–20:25)	14.4 (2.0)	65.0 (22.1)	5.0 (3.2)	6815 (2501)	1460 (654)	1.41 (0.53)	56.4 (10.5)	4.7 (1.0)	829 (372)
	Loop 2 (20:25–22:10)	17.7 (1.8)	60.0 (8.8)	4.8 (2.1)	10671 (4535)	1644 (556)	2.27 (0.43)	62.0 (11.3)	6.4 (3.2)	1004 (98)

^aRefer to Figures 9 and 10. Numbers in parentheses represent standard deviations.

flights. There was no significant difference in wind patterns between these two days. Fine particle concentrations were on average similar, but PCASP particle number concentrations were almost twice as large during Flight 8, indicative of more abundant larger particles.

[26] During Flight 5, three identical loops were carried out as shown in Figures 9a–9c: first loop (19:00–20:30, UTC), second loop (20:30–21:50), and third loop (21:50–23:00). When the sea breeze started to develop around 18:00 UTC, wind speeds gradually increased up to >10 m s⁻¹ and changed direction to westerly/southwesterly, resulting in the usual transport from west to east. In the southwestern portion of the Basin, WSOC concentrations were highest during the first loop, presumably owing to the influence of residual aged aerosol from the previous day and anthropogenic emissions near Long Beach. In the first loop, the highest WSOC and PCASP particle number concentrations were observed along the north-south axis between Pasadena and downtown Los Angeles. As a result of the westerly/southwesterly flow later during the day, the highest WSOC levels occurred at the base of the San Gabriel Mountains at the northern edge of the Basin. The southern half of the Basin loops extending from Fullerton/Anaheim to San Bernardino were characterized by significantly lower WSOC levels during all three loops, most likely a result of the Basin topography (i.e., Puente and Chino Hills). The data from Flight 5 indicate that the significant factors governing WSOC levels were likely residual aerosol in the Basin from the previous day, pollution near the western edge of the Basin, and the prevailing west-to-east winds with potential production during the transport. These data do not allow one to discern a clear connection between WSOC measurements and the influence of boundary layer deepening and potential entrainment of aerosol aloft.

[27] Flight 8 was conducted almost identically to Flight 5, as shown in Figures 9d–9f. In contrast to Flight 5, the aerosol number concentrations and WSOC increased with each successive loop during Flight 8 (similar to ambient temperature and O₃). The spatial WSOC distribution during the first loop was similar to that of Flight 5, both of which were likely influenced by residual pollutants from the previous day and

sources near the western side of the Basin. WSOC increased significantly in concentration over the western side of the Basin during the second and third loops. Unlike Flight 5, the entire north-south axis between Pasadena and downtown Los Angeles exhibited high WSOC levels later in the day owing likely to a combination of secondary WSOC production and lower wind speeds. The third loop of Flight 8 was characterized by systematically higher WSOC levels across the entire Basin. WSOC levels were especially high between Ontario and Riverside owing to a fire that began immediately prior to the third loop.

[28] The data from both flights indicate that, with higher incident solar radiation and relatively low wind speeds, it is likely that secondary production mechanisms contribute to sustained levels of WSOC throughout the daytime periods (especially in Flight 8) even though the mixing layer progressively deepened. While entrainment of polluted air aloft may have contributed to WSOC levels during these flights, this process was not a dominant influence on WSOC in the mixing layer as there were large spatial differences in WSOC across the Basin that are largely controlled by transport and topography.

5.2. Basin North-South Transects

[29] To examine the spatial gradients of WSOC within the regions outlined by the loops in Figure 9, a series of north-south zig zag patterns were flown within the Los Angeles Basin. The paths during Flights 9, 11, and 13 are shown in Figure 10. The flights were conducted approximately during the same time on different days at a similar altitude (~300–700 m). Flight 9 was conducted on a Saturday, whereas the other two are from weekdays (Table 1). Meteorological conditions were relatively similar on these three days (Table 3), with the exception of reduced temperature and incident solar radiation values during the early part of Flight 13 due to cloudy conditions. Particle number concentrations were similar during these flights. WSOC concentrations were enhanced during the second loops, coincident with higher O₃ concentrations, ambient temperatures, and WSOC:BC ratios than the first loop within each flight. This is most evident during Flight 13 presumably due to the shift

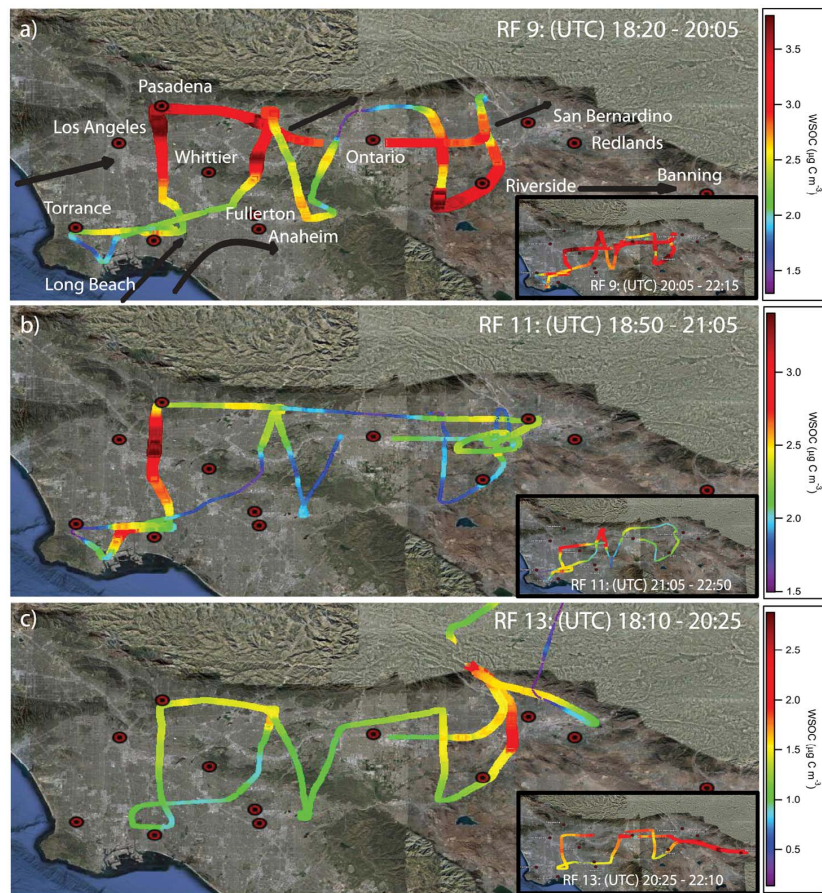


Figure 10. Spatial maps of WSOC during Flights (a) 9 (15 May 2010), (b) 11 (19 May 2010), and (c) 13 (21 May 2010) with black arrows in Figure 10a corresponding to the typical wind directions during the duration of all three flights as determined by wind roses obtained from the Mesowest Database [<http://mesowest.utah.edu/index.html>]. Local time = UTC – seven hours.

from cloudy to clear conditions (and increase in incident solar radiation) between the two loops. The absolute increases in WSOC later in the daytime most likely were influenced by secondary production.

[30] These three flights demonstrate the influence of the Basin topography on WSOC levels. The Puente and Chino Hills extending from Whittier to the east create a gradient of low WSOC from south of these hills to higher levels on the north side. Sea breeze winds (westerly/southwesterly) near the coast transport air enriched with WSOC to the north side of these hills, which then gets redistributed across a larger area on the eastern end of the Basin extending from San Bernardino down south to Riverside. In addition to the transport of existing WSOC, there is likely production of these species over inland areas that are characterized by enhanced O_3 concentrations (Figure 3b).

6. Conceptual Model of WSOC in the Study Region

[31] Figure 11 shows a conceptual model of the mechanisms describing the sources, transformation, and fate of

WSOC during CalNex. Industrial and marine sources of pollution near the western side of the Basin result in enhanced levels of sulfate and carbonaceous components including WSOC. As aerosol is advected with the sea breeze from the west to the east through the outflows, the overall aerosol composition changes owing to numerous point sources, increasing (decreasing) temperature (RH), amount of aerosol-phase water, and secondary formation processes. For example, VOC emissions lead to SOA formation and primary emissions from episodic fires significantly lead to enhanced levels in organics, especially WSOC. The components comprising WSOC become increasingly oxidized as a function of photochemical age from west-to-east. Near the eastern half of the Basin, NH_3 emissions contribute to significant ammonium nitrate formation, leading to more hygroscopic aerosol and increased aerosol-phase water depending on the ambient RH. A number of processes can lead to higher levels of particulate WSOC with increasing aerosol-phase water: partitioning of WSOC to the aerosol phase [Hennigan *et al.*, 2008b, 2009], multiphase chemistry [Ervens and Volkamer, 2010; Sorooshian *et al.*, 2010], and

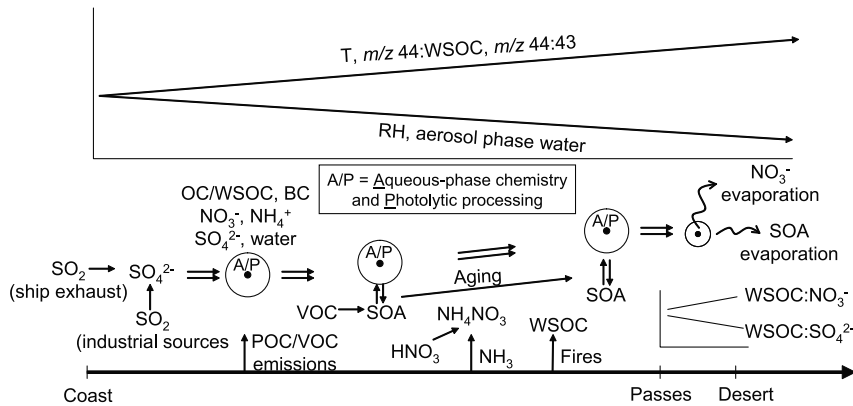


Figure 11. Conceptual model of WSOC in the Los Angeles Basin and desert outflows. The x axis represents longitude and extends from the coast to the desert outflows to the east of the Los Angeles Basin.

photolytic processing [Bateman *et al.*, 2011]. As aerosol is transported through the outflows to desert regions, the enhanced temperatures and reduced RH result in NO_3^- evaporation and consequently, reductions in aerosol-phase water. This may promote re-partitioning of WSOC to the gas phase while suppressing humidity-dependent processes that increase particulate WSOC levels.

7. Conclusions

[32] During the May 2010 deployment of the CIRPAS Twin Otter in the CalNex field study, a PILS-TOC instrument was employed to rapidly quantify particulate water-soluble organic carbon (WSOC) during 16 flights covering the Los Angeles Basin, outflow regions, and the San Joaquin Valley. The WSOC measurements were focused on building a spatial map of concentrations across this region in the lateral and vertical directions, on constraining the contribution of these species to the overall aerosol mass budget, and on examining the nature and evolution of this important class of organics due to the prevailing meteorology and daytime air transport patterns.

[33] The highest absolute WSOC concentrations were observed in the Basin (up to $5.3 \mu\text{g C m}^{-3}$) and the lowest WSOC levels were in the San Joaquin Valley and in Basin outflow regions owing to plume dilution. The highest WSOC levels during individual flights and for the entire campaign occurred in biomass burning plumes from small-scale fires on the eastern side of the Basin. WSOC contributes approximately 6–11% by mass to $\text{PM}_{2.5}$ within the Basin. WSOC was highest relative to both $\text{PM}_{2.5}$ near the western Basin sites of Torrance and Long Beach, likely owing to these sites being upwind of major pollution sources and influenced by aged marine aerosol and residual pollutants from the previous day. WSOC levels were typically higher above 500 m in the study region, and layers of enhanced WSOC were identified aloft up to an altitude of 3.2 km. The ratio of WSOC to PCASP particle volume concentration and organic non-refractory mass ranged between 0.11–0.19 and 0.26–0.63, respectively, between the surface and 3.2 km.

[34] Simultaneous ground-based measurements of WSOC during aircraft overpasses in Riverside and Pasadena indicate that higher levels occur more frequently aloft within the mixing layer. This was most evident when the ratio of RH measured on the aircraft versus the surface was also higher, suggestive of an important role for processes that increase particulate WSOC levels as a function of increasing aerosol-phase water such as more efficient partitioning to the aerosol phase. Furthermore, WSOC was highly correlated with RH within the Banning Pass area where pollution is funneled out of the Basin to the east. Since aerosol hygroscopicity and ambient RH generally decreased from the Basin to the eastern desert outflows, there was a reduction in aerosol-phase water that likely influenced WSOC levels; WSOC levels dropped more relative to both BC and SO_4^{2-} , both of which are non-volatile, downwind of the outflows indicative of partitioning of WSOC to the gas phase and suppression of multiphase processes (i.e., partitioning of WSOC to the aerosol phase, multiphase chemistry, photolytic processing) to produce these species. However, WSOC increased relative to NO_3^- , suggesting that although both have a semi-volatile character, NO_3^- was more volatile. Farther downwind in the deserts (e.g., near Salton Sea), WSOC begins to increase relative to BC indicative of secondary production, especially as O_3 levels were enhanced in these areas.

[35] The contribution of acid-like oxygenated organics ($m/z 44$) to WSOC increases from west to east as a result of photochemical aging. Comparisons of nearly identical flight paths on different days show that with higher incident solar radiation and relatively low wind speeds, secondary production mechanisms more clearly contribute to sustained levels of WSOC throughout the daytime periods even though the mixing layer progressively deepens. Entrainment of air aloft may have contributed to WSOC levels within the mixing layer; however, this process was not the key regulator of WSOC in the mixing layer as there were large spatial differences in WSOC across the Basin that are largely controlled by sea breeze transport, topography, secondary production during transport, and presence of fires.

[36] This work adds to the inventory of WSOC data in major mega-cities such as Beijing [Feng *et al.*, 2006], New

Delhi [Miyazaki *et al.*, 2009], and Mexico City [Hennigan *et al.*, 2008a] showing that WSOC contributes significantly to urban aerosol mass concentrations. The aircraft measurements in CalNex highlight the importance of considering the vertical structure of WSOC in the atmosphere. Surface measurements of WSOC are shown to not be entirely representative of the radiative impact of this class of species. This work also emphasizes the importance of considering spatial gradients in aerosol-phase water. For example, the Los Angeles Basin and outflow regions exhibit large variations in RH and have a variety of sources including shipping and agricultural emissions that can create gradients in aerosol hygroscopicity. The resulting spatial variations in aerosol-phase water influence WSOC levels via production processes with efficiencies dependent on this amount of water. Episodic fires and potential volatilization of WSOC point to the use of caution in using ratios of WSOC to other species (e.g., CO and BC) in quantifying the magnitude of SOA production.

[37] **Acknowledgments.** This work was supported by NOAA grant NA 09 OAR 4310128. Surface WSOC measurements were supported by the NSF under grants ATM-0931492 and ATM-0802237.

References

Aiken, A. C., *et al.* (2008), O/C and OM/OC ratios of primary, secondary, and ambient organic aerosols with high-resolution time-of-flight aerosol mass spectrometry, *Environ. Sci. Technol.*, 42(12), 4478–4485, doi:10.1021/es703009q.

Bateman, A. P., S. A. Nizkorodov, J. Laskin, and A. Laskin (2011), Photolytic processing of secondary organic aerosols dissolved in cloud droplets, *Phys. Chem. Chem. Phys.*, 13, 12,199–12,212, doi:10.1039/c1cp20526a.

Blumenthal, D. L., W. H. White, and T. B. Smith (1978), Anatomy of a Los Angeles smog episode: Pollutant transport in daytime sea breeze regime, *Atmos. Environ.*, 12(4), 893–907, doi:10.1016/0004-6981(78)90028-8.

Chow, J. C., J. G. Watson, D. H. Lowenthal, P. A. Solomon, K. L. Magliano, S. D. Ziman, and L. W. Richards (1992), PM₁₀ source apportionment in California San Joaquin Valley, *Atmos. Environ.*, 26(18), 3335–3354.

Chow, J. C., J. G. Watson, D. H. Lowenthal, P. A. Solomon, K. L. Magliano, S. D. Ziman, and L. W. Richards (1993), PM₁₀ and PM_{2.5} compositions in California San Joaquin Valley, *Aerosol Sci. Technol.*, 18(2), 105–128, doi:10.1080/02786829308959588.

Chow, J. C., J. G. Watson, E. M. Fujita, Z. Q. Lu, D. R. Lawson, and L. L. Ashbaugh (1994), Temporal and spatial variations of PM_{2.5} and PM₁₀ aerosol in the Southern California air quality study, *Atmos. Environ.*, 28(12), 2061–2080, doi:10.1016/1352-2310(94)90474-X.

Chow, J. C., J. G. Watson, Z. Q. Lu, D. H. Lowenthal, C. A. Frazier, P. A. Solomon, R. H. Thuillier, and K. Magliano (1996), Descriptive analysis of PM_{2.5} and PM₁₀ at regionally representative locations during SJVAQS/AUSPEX, *Atmos. Environ.*, 30(12), 2079–2112, doi:10.1016/1352-2310(95)00402-5.

Chow, J. C., L. W. A. Chen, J. G. Watson, D. H. Lowenthal, K. A. Magliano, K. Turkiewicz, and D. E. Lehrman (2006), PM_{2.5} chemical composition and spatiotemporal variability during the California Regional PM₁₀/PM_{2.5} Air Quality Study (CRPAQS), *J. Geophys. Res.*, 111, D10S04, doi:10.1029/2005JD006457.

Collins, D. R., H. H. Jonsson, H. Liao, R. C. Flagan, J. H. Seinfeld, K. J. Noone, and S. V. Hering (2000), Airborne analysis of the Los Angeles aerosol, *Atmos. Environ.*, 34(24), 4155–4173, doi:10.1016/S1352-2310(00)00225-9.

Decesari, S., *et al.* (2006), Characterization of the organic composition of aerosols from Rondonia, Brazil, during the LBA-SMOCC 2002 experiment and its representation through model compounds, *Atmos. Chem. Phys.*, 6, 375–402, doi:10.5194/acp-6-375-2006.

Docherty, K. S., *et al.* (2008), Apportionment of primary and secondary organic aerosols in southern California during the 2005 study of organic aerosols in Riverside (SOAR-1), *Environ. Sci. Technol.*, 42(20), 7655–7662, doi:10.1021/es08008166.

Drewnick, F., *et al.* (2005), A new time-of-flight aerosol mass spectrometer (TOF-AMS)—Instrument description and first field deployment, *Aerosol Sci. Technol.*, 39(7), 637–658, doi:10.1080/02786820500182040.

Eldering, A., and G. R. Cass (1996), Source-oriented model for air pollutant effects on visibility, *J. Geophys. Res.*, 101(D14), 19,343–19,369, doi:10.1029/95JD02928.

Ervens, B., and R. Volkamer (2010), Glyoxal processing by aerosol multi-phase chemistry: Towards a kinetic modeling framework of secondary organic aerosol formation in aqueous particles, *Atmos. Chem. Phys.*, 10(17), 8219–8244, doi:10.5194/acp-10-8219-2010.

Feng, J. L., M. Hu, C. K. Chan, P. S. Lau, L. Y. He, and X. Y. Tang (2006), A comparative study of the organic matter in PM_{2.5} from three Chinese megacities in three different climatic zones, *Atmos. Environ.*, 40, 3983–3994, doi:10.1016/j.atmosenv.2006.02.017.

Graham, B., O. L. Mayol-Bracero, P. Guyon, G. C. Roberts, S. Decesari, M. C. Facchini, P. Ártaxo, W. Maenhaut, P. Koll, and M. O. Andreae (2002), Water-soluble organic compounds in biomass burning aerosols over Amazonia: 1. Characterization by NMR and GC-MS, *J. Geophys. Res.*, 107(D20), 8047, doi:10.1029/2001JD000336.

Grosjean, D., and S. K. Friedlander (1975), Gas-particle distribution factors for organic and other pollutants in Los Angeles atmosphere, *J. Air Pollut. Control Assoc.*, 25(10), 1038–1044.

Hennigan, C. J., *et al.* (2008a), On the volatility and production mechanisms of newly formed nitrate and water soluble organic aerosol in Mexico City, *Atmos. Chem. Phys.*, 8(14), 3761–3768, doi:10.5194/acp-8-3761-2008.

Hennigan, C. J., M. H. Bergin, J. E. Dibb, and R. J. Weber (2008b), Enhanced secondary organic aerosol formation due to water uptake by fine particles, *Geophys. Res. Lett.*, 35, L18801, doi:10.1029/2008GL035046.

Hennigan, C. J., M. H. Bergin, A. G. Russell, A. Nenes, and R. J. Weber (2009), Gas/particle partitioning of water-soluble organic aerosol in Atlanta, *Atmos. Chem. Phys.*, 9(11), 3613–3628, doi:10.5194/acp-9-3613-2009.

Hersey, S. P., J. S. Craven, K. A. Schilling, A. R. Metcalf, A. Sorooshian, M. N. Chan, R. C. Flagan, and J. H. Seinfeld (2011), The Pasadena aerosol characterization observatory (PACO): Chemical and physical analysis of the western Los Angeles Basin aerosol, *Atmos. Chem. Phys.*, 11, 7417–7443, doi:10.5194/acp-11-7417-2011.

Hidy, G. M., *et al.* (1974), Characterization of aerosols in California (ACHEX): Final report, *NTIS PB 247*, 947 pp., Calif. Air Resour. Board, Sacramento, Calif.

Hildemann, L. M., D. B. Klinedinst, G. A. Kluuda, L. A. Currie, and G. R. Cass (1994a), Sources of urban contemporary carbon aerosol, *Environ. Sci. Technol.*, 28(9), 1565–1576, doi:10.1021/es00058a006.

Hildemann, L. M., M. A. Mazurek, G. R. Cass, and B. R. T. Simoneit (1994b), Seasonal trends in Los Angeles ambient organic aerosol observed by high-resolution gas chromatography, *Aerosol Sci. Technol.*, 20(4), 303–317, doi:10.1080/02786829408959687.

Hildemann, L. M., W. F. Rogge, G. R. Cass, M. A. Mazurek, and B. R. T. Simoneit (1996), Contribution of primary aerosol emissions from vegetation-derived sources to fine particle concentrations in Los Angeles, *J. Geophys. Res.*, 101(D14), 19,541–19,549, doi:10.1029/95JD02136.

Hughes, L. S., J. O. Allen, P. Bhawe, M. J. Kleeman, G. R. Cass, D. Y. Liu, D. F. Ferguson, B. D. Morrical, and K. A. Prather (2000), Evolution of atmospheric particles along trajectories crossing the Los Angeles Basin, *Environ. Sci. Technol.*, 34(15), 3058–3068, doi:10.1021/es9908671.

Husar, R. B., W. H. White, and D. L. Blumenthal (1976), Direct evidence of heterogeneous aerosol formation in Los Angeles smog, *Environ. Sci. Technol.*, 10(5), 490–491, doi:10.1021/es60116a008.

Husar, R. B., D. E. Patterson, D. L. Blumenthal, W. H. White, and T. B. Smith (1977), 3-dimensional distribution of air-pollutants in Los Angeles Basin, *J. Appl. Meteorol.*, 16(10), 1089–1096, doi:10.1175/1520-0450-16.10.1089.

Jaffrezo, J. L., G. Aymoz, C. Delaval, and J. Cozic (2005), Seasonal variations of the water soluble organic carbon mass fraction of aerosol in two valleys of the French Alps, *Atmos. Chem. Phys.*, 5, 2809–2821, doi:10.5194/acp-5-2809-2005.

Kanakidou, M., *et al.* (2005), Organic aerosol and global climate modeling: A review, *Atmos. Chem. Phys.*, 5, 1053–1123, doi:10.5194/acp-5-1053-2005.

Kawamura, K., and I. R. Kaplan (1987), Motor exhaust emissions as a primary source for dicarboxylic acids in Los Angeles ambient air, *Environ. Sci. Technol.*, 21(1), 105–110, doi:10.1021/es00155a014.

Kleeman, M. J., L. S. Hughes, J. O. Allen, and G. R. Cass (1999), Source contributions to the size and composition distribution of atmospheric particles: Southern California in September 1996, *Environ. Sci. Technol.*, 33(23), 4331–4341, doi:10.1021/es990632p.

Kondo, Y., Y. Miyazaki, N. Takegawa, T. Miyakawa, R. J. Weber, J. L. Jimenez, Q. Zhang, and D. R. Worsnop (2007), Oxygenated and

water-soluble organic aerosols in Tokyo, *J. Geophys. Res.*, **112**, D01203, doi:10.1029/2006JD007056.

Lu, R., and R. P. Turco (1995), Air pollutant transport in a coastal environment—II. Three-dimensional simulations over Los Angeles Basin, *Atmos. Environ.*, **29**(13), 1499–1518, doi:10.1016/1352-2310(95)00015-Q.

Magliano, K. L., V. M. Hughes, L. R. Chinkin, D. L. Coe, T. L. Haste, N. Kumar, and F. W. Lurmann (1999), Spatial and temporal variations in PM₁₀ and PM_{2.5} source contributions and comparison to emissions during the 1995 integrated monitoring study, *Atmos. Environ.*, **33**(29), 4757–4773, doi:10.1016/S1352-2310(99)00265-4.

Mayol-Bracero, O. L., P. Guyon, B. Graham, G. Roberts, M. O. Andreae, S. Decesari, M. C. Facchini, S. Fuzzi, and P. Artaxo (2002), Water-soluble organic compounds in biomass burning aerosols over Amazonia: 2. Apportionment of the chemical composition and importance of the polyacidic fraction, *J. Geophys. Res.*, **107**(D20), 8091, doi:10.1029/2001JD000522.

McElroy, J. L., and T. B. Smith (1986), Vertical pollutant distributions and boundary layer structure observed by airborne lidar near the complex southern California coastline, *Atmos. Environ.*, **20**(8), 1555–1566, doi:10.1016/0004-6981(86)90244-1.

McLafferty, F. W., and F. Turecek (1993), *Interpretation of Mass Spectra*, 4th ed., Univ. Sci., Mill Valley, Calif.

Miyazaki, Y., S. G. Aggarwal, K. Singh, P. K. Gupta, and K. Kawamura (2009), Dicarboxylic acids and water-soluble organic carbon in aerosols in New Delhi, India, in winter: Characteristics and formation processes, *J. Geophys. Res.*, **114**, D19206, doi:10.1029/2009JD011790.

Murphy, S. M., et al. (2009), Comprehensive simultaneous shipboard and airborne characterization of exhaust from a modern container ship at sea, *Environ. Sci. Technol.*, **43**(13), 4626–4640, doi:10.1021/es802413j.

Neuman, J. A., et al. (2003), Variability in ammonium nitrate formation and nitric acid depletion with altitude and location over California, *J. Geophys. Res.*, **108**(D17), 4557, doi:10.1029/2003JD003616.

Ng, N. L., et al. (2010), Organic aerosol components observed in Northern Hemispheric datasets from aerosol mass spectrometry, *Atmos. Chem. Phys.*, **10**, 4625–4641, doi:10.5194/acp-10-4625-2010.

Pandis, S. N., J. H. Seinfeld, and C. Pilinis (1992a), Heterogeneous sulfate production in an urban fog, *Atmos. Environ.*, **26**(14), 2509–2522.

Pandis, S. N., R. A. Harley, G. R. Cass, and J. H. Seinfeld (1992b), Secondary organic aerosol formation and transport, *Atmos. Environ.*, **26**(13), 2269–2282.

Peltier, R. E., R. J. Weber, and A. P. Sullivan (2007a), Investigating a liquid-based method for online organic carbon detection in atmospheric particles, *Aerosol Sci. Technol.*, **41**(12), 1117–1127, doi:10.1080/02786820701777465.

Peltier, R. E., A. P. Sullivan, R. J. Weber, C. A. Brock, A. G. Wollny, J. S. Holloway, J. A. de Gouw, and C. Warneke (2007b), Fine aerosol bulk composition measured on WP-3D research aircraft in vicinity of the Northeastern United States—Results from NEAQS, *Atmos. Chem. Phys.*, **7**, 3231–3247, doi:10.5194/acp-7-3231-2007.

Ruellan, S., H. Cachier, A. Gaudichet, P. Masclet, and J. P. Lacaux (1999), Airborne aerosols over central Africa during the experiment for regional sources and sinks of oxidants (EXPRESSO), *J. Geophys. Res.*, **104**(D23), 30,673–30,690, doi:10.1029/1999JD900804.

Russell, A. G., and G. R. Cass (1984), Acquisition of regional air quality model validation data for nitrate, sulfate, ammonium ion and their precursors, *Atmos. Environ.*, **18**(9), 1815–1827, doi:10.1016/0004-6981(84)90357-3.

Russell, A. G., and G. R. Cass (1986), Verification of a mathematical model for aerosol nitrate and nitric acid formation and its use for control measure evaluation, *Atmos. Environ.*, **20**(10), 2011–2025, doi:10.1016/0004-6981(86)90342-2.

Russell, A. G., G. J. McRae, and G. R. Cass (1983), Mathematical modeling of the formation and transport of ammonium-nitrate aerosol, *Atmos. Environ.*, **17**(5), 949–964, doi:10.1016/0004-6981(83)90247-0.

Sardar, S. B., P. M. Fine, and C. Sioutas (2005), Seasonal and spatial variability of the size-resolved chemical composition of particulate matter (PM₁₀) in the Los Angeles Basin, *J. Geophys. Res.*, **110**, D07S08, doi:10.1029/2004JD004627.

Schauer, J. J., and G. R. Cass (2000), Source apportionment of wintertime gas-phase and particle-phase air pollutants using organic compounds as tracers, *Environ. Sci. Technol.*, **34**(9), 1821–1832, doi:10.1021/es981312t.

Sorooshian, A., F. J. Brechtel, Y. L. Ma, R. J. Weber, A. Corless, R. C. Flagan, and J. H. Seinfeld (2006), Modeling and characterization of a particle-into-liquid sampler (PILS), *Aerosol Sci. Technol.*, **40**(6), 396–409, doi:10.1080/02786820600632282.

Sorooshian, A., S. N. Murphy, S. Hersey, H. Gates, L. T. Padro, A. Nenes, F. J. Brechtel, H. Jonsson, R. C. Flagan, and J. H. Seinfeld (2008a), Comprehensive airborne characterization of aerosol from a major bovine source, *Atmos. Chem. Phys.*, **8**(17), 5489–5520, doi:10.5194/acp-8-5489-2008.

Sorooshian, A., S. Hersey, F. J. Brechtel, A. Corless, R. C. Flagan, and J. H. Seinfeld (2008b), Rapid, size-resolved aerosol hygroscopic growth measurements: Differential aerosol sizing and hygroscopicity spectrometer probe (DASH-SP), *Aerosol Sci. Technol.*, **42**(6), 445–464, doi:10.1080/02786820802178506.

Sorooshian, A., S. M. Murphy, S. Hersey, R. Bahreini, H. Jonsson, R. C. Flagan, and J. H. Seinfeld (2010), Constraining the contribution of organic acids and AMS m/z 44 to the organic aerosol budget: On the importance of meteorology, aerosol hygroscopicity, and region, *Geophys. Res. Lett.*, **37**, L21807, doi:10.1029/2010GL044951.

Sullivan, A. P., R. E. Peltier, C. A. Brock, J. A. de Gouw, J. S. Holloway, C. Warneke, A. G. Wollny, and R. J. Weber (2006), Airborne measurements of carbonaceous aerosol soluble in water over northeastern United States: Method development and an investigation into water-soluble organic carbon sources, *J. Geophys. Res.*, **111**, D23S46, doi:10.1029/2006JD007072.

Takegawa, N., T. Miyakawa, K. Kawamura, and Y. Kondo (2007), Contribution of selected dicarboxylic and ω -oxocarboxylic acids in ambient aerosol to the m/z 44 signal of an Aerodyne aerosol mass spectrometer, *Aerosol Sci. Technol.*, **41**, 418–437, doi:10.1080/02786820701203215.

Vutukuru, S., R. J. Griffin, and D. Dabdub (2006), Simulation and analysis of secondary organic aerosol dynamics in the South Coast Air Basin of California, *J. Geophys. Res.*, **111**, D10S12, doi:10.1029/2005JD006139.

Wall, S. M., W. John, and J. L. Ondo (1988), Measurement of aerosol size distributions for nitrate and major ionic species, *Atmos. Environ.*, **22**(8), 1649–1656, doi:10.1016/0004-6981(88)90392-7.

Wonaschütz, A., S. Hersey, A. Sorooshian, J. Craven, A. R. Metcalf, R. C. Flagan, and J. H. Seinfeld (2011), Impact of a large wildfire on water-soluble organic aerosol in a major urban setting: The 2009 station fire in Los Angeles County, *Atmos. Chem. Phys.*, **11**, 8257–8270, doi:10.5194/acp-11-8257-2011.

Zhang, Q., M. R. Alfarra, D. R. Worsnop, J. D. Allan, H. Coe, M. R. Canagaratna, and J. L. Jimenez (2005), Deconvolution and quantification of hydrocarbon-like and oxygenated organic aerosols based on aerosol mass spectrometry, *Environ. Sci. Technol.*, **39**(13), 4938–4952, doi:10.1021/es0485681.

Zhang, X. Q., P. H. McMurry, S. V. Hering, and G. S. Casuccio (1993), Mixing characteristics and water-content of submicron aerosols measured in Los Angeles and at the Grand Canyon, *Atmos. Environ.*, **27**(10), 1593–1607.

J. S. Craven, R. C. Flagan, S. P. Hersey, A. R. Metcalf, and J. H. Seinfeld, Department of Environmental Science and Engineering, California Institute of Technology, 1200 E. California Blvd., Pasadena, CA 91125, USA.

H. T. Duong and A. Sorooshian, Department of Chemical and Environmental Engineering, University of Arizona, PO Box 210011, Tucson, AZ 85721, USA. (armin@email.arizona.edu)

H. Jonsson, Center for Interdisciplinary Remotely-Piloted Aircraft Studies, Naval Postgraduate School, Monterey, CA 93943, USA.

R. J. Weber and X. Zhang, School of Earth and Atmospheric Sciences, Georgia Institute of Technology, Atlanta, GA 30332, USA.

Appendix D

Inorganic and Black Carbon Aerosols in the Los Angeles Basin during CalNex*

*Submitted as “Inorganic and black carbon aerosols in the Los Angeles Basin during CalNex” by J. J. Ensberg, J. S. Craven, A. R. Metcalf, W. M. Angevine, R. Bahreini, J. Brioude, C. Cai, J. A. de Gouw, R. A. Ellis, J. H. Flynn, C. L. Haman, P. L. Hayes, J. L. Jimenez, B. L. Lefer, A. M. Middlebrook, J. G. Murphy, J. B. Nowak, J. A. Neuman, J. M. Roberts, J. Stutz, P. Veres, J. M. Walker, and J. H. Seinfeld to *Journal of Geophysical Research*. Copyright 2012 by the American Geophysical Union.

Inorganic and black carbon aerosols in the Los Angeles Basin during CalNex

J. J. Ensberg¹, J. S. Craven¹, A. R. Metcalf², W. M. Angevine^{3,4}, R. Bahreini^{3,4}, J. Brioude^{3,4}, C. Cai⁹, J. A. de Gouw^{3,4}, R. A. Ellis⁸, J. H. Flynn⁷, C. L. Haman⁷, P. L. Hayes^{3,5}, J. L. Jimenez^{3,5}, B. L. Lefer⁷, A. M. Middlebrook⁴, J. G. Murphy⁸, J. A. Neuman^{3,4}, J. B. Nowak^{3,4}, J. M. Roberts⁴, J. Stutz⁶, P. R. Veres^{3,4}, J. M. Walker², and J. H. Seinfeld^{1,2}

Abstract. We report comprehensive ground-based and airborne inorganic and black carbon (BC) aerosol measurements over Southern California during the California Research at the Nexus of Air Quality and Climate Change (CalNex) study in May 2010. The Community Multiscale Air Quality (CMAQ version 4.7.1) model is employed to simulate May 2010 over the region using emission inventories and meteorological fields provided by the California Air Resources Board (CARB) and boundary conditions from the GEOS-Chem global chemical transport model. Gas-phase and aerosol-phase measurements from the CalNex Pasadena ground site, as well as five CIRPAS Twin Otter flights and five NOAA WP-3D flights within the L.A. Basin are compared to CMAQ predictions. The BC concentration is consistently over-predicted throughout the L.A. Basin. SO₂ mixing ratios are over-predicted at all ground-site locations within the L.A. Basin. The degree of agreement between predicted and observed sulfate levels varies depending on the location or aircraft platform. NH₃ mixing ratios are severely under-predicted in the eastern part of the L.A. Basin. These under-predictions serve to artificially shift predicted nitrate from the particle phase to the gas phase. Despite potentially overstated NO_x emissions, predicted total nitrate (HNO₃ + NO₃⁻) concentrations are generally lower than P3 measurements. This is likely due to retarded HNO₃ formation or accelerated total nitrate removal in CMAQ, and not to inaccurate distributions of predicted nitrate between the accumulation and coarse aerosol mode.

1. Introduction

The Los Angeles mega-city has consistently experienced the among the highest particulate matter levels in the United States and the highest ozone levels (<http://www.stateoftheair.org/2012/city-rankings/most-polluted-cities.html>). Several recent measurement campaigns have focused on characterizing particulate air

quality in the Los Angeles Basin (e.g. *Appel et al. [1982]; Turpin and Huntzicker [1991]; Chow et al. [1994]; Watson et al. [1994]; Eldering et al. [1994]; Liu et al. [2000]; Hughes et al. [2002]; Pastor et al. [2003]; Croes and Fujita [2003]; Neuman et al. [2003]; Jacob et al. [2010]; Docherty et al. [2011]*), and in other urban areas, such as Pittsburgh, PA (Pittsburgh Air Quality Study, PAQS; e.g. *Wittig et al. [2004]; Cabada et al. [2004]; Modey et al. [2004]; Pekney et al. [2006]; Bein et al. [2006]*), Mexico City, Mexico (Mega-city Initiative: Local and Global Research Observations, MILAGRO; e.g. *Salcedo et al. [2006]; DeCarlo et al. [2008]; Querol et al. [2008]; Molina et al. [2010]*), Houston, Texas (2006 Texas Air Quality Study, TexAQS; e.g. *Parish et al. [2009]; Nowak et al. [2010]; Washenfelder et al. [2010]*), and Beijing, China (Campaign of Air Quality Research in Beijing, CAREBEIJING; e.g. *van Pinxteren et al. [2009]; Yue et al. [2009, 2010]; Ianniello et al. [2011]; Zheng et al. [2011]*). Many studies have used data gathered during these field campaigns to evaluate and improve the fidelity of three-dimensional atmospheric chemical transport models (CTMs) (e.g. *Sarwar and Bhave [2007]; Fountoukis and Nenes [2007]; Nolte et al. [2008]; Matsui et al. [2009]; Fountoukis et al. [2009]; McKeen et al. [2009]; Fast et al. [2009]; Foley et al. [2010]; Renner and Wolke [2010]; Zhang and Ying [2010]; Karydis et al. [2010]; Kelly et al. [2010]; Lee et al. [2011]; Huang et al. [2011]; Pfister et al. [2011]*).

The California Research at the Nexus of Air Quality and Climate Change (CalNex) study was conducted during May–June 2010 to address both air quality and climate change through coordination and collaboration between several government agencies, such as the California Air Resources Board (CARB), the National Oceanic and Atmospheric Administration (NOAA), and academic institutions

¹Division of Chemistry and Chemical Engineering, California Institute of Technology, Pasadena, California, USA

²Division of Engineering and Applied Science, California Institute of Technology, Pasadena, California, USA

³Cooperative Institute for Research in Environmental Sciences, University of Colorado Boulder, Boulder, Colorado, USA

⁴Chemical Sciences Division, Earth System Research Laboratory, NOAA, Boulder, Colorado, USA

⁵Department of Chemistry and Biochemistry, University of Colorado, Boulder, Colorado, USA

⁶Department of Atmospheric Sciences, University of California, Los Angeles, California, USA

⁷Department of Earth and Atmospheric Sciences, University of Houston, Houston, Texas, USA

⁸Department of Chemistry, University of Toronto, Toronto, Ontario, Canada

⁹Planning and Technical Support Division, Air Resources Board, California Environmental Protection Agency, Sacramento, California, USA

(www.esrl.noaa.gov/csd/calnex/). During CalNex, state-of-the-art airborne, ship-based, and ground-based measurements of atmospheric species, and of their transport over and off the coast of California, were conducted with the goal of understanding the impact of airborne pollutants on air quality and climate.

We focus here on comprehensive ground-based and airborne gas- and aerosol-phase inorganic measurements over Southern California during the CalNex field campaign. Airborne measurements took place onboard the Center for Interdisciplinary Remotely-Piloted Aircraft Studies (CIRPAS) Navy Twin Otter aircraft (hereafter known as the Twin Otter) and the NOAA WP-3D (hereafter known as the P3) aircraft during May and June 2010. Black carbon (BC) is also a focus, owing to its importance in direct radiative absorption [Ramanathan and Carmichael, 2008], and because the radiative properties of BC particles are strongly affected by coatings that can result from the rich background of inorganic and organic airborne gaseous and particulate species [Schwarz *et al.*, 2008b]. Our goal is to provide an up-to-date assessment of inorganic and BC aerosol distributions within the Los Angeles Basin. To evaluate the extent to which predictions of a state-of-the-science CTM, driven by current emission inventories and resolved meteorological fields, agree with measured concentrations, we employ the Community Multiscale Air Quality (CMAQ) model version 4.7.1 (<http://www.cmaq-model.org/>, Foley *et al.* [2010]) to simulate the three-dimensional distribution of aerosols and gases over Southern California during the CalNex field campaign. In addition, a Lagrangian particle dispersion model, FLEXPART (<http://transport.nilu.no/flexpart>, Stohl *et al.* [2005]), is used to track the origins of measured and predicted species in the Los Angeles Basin during CalNex by calculating back trajectories based on advection and turbulent mixing processes.

Application of chemical transport models to a complex region rarely produces consistently close agreement between predictions and observations. This discrepancy serves as a stimulus to explore whether model inputs, such as emissions, are inaccurate, whether the chemistry and physics in the model are not appropriately up to date, or whether systematic biases exist within the measurement techniques. The present study serves, in some respects, as a roadmap to future work aimed at better characterizing air quality in the Los Angeles airshed.

We carry out direct comparisons of meteorological, gas-phase, and aerosol-phase measurements from the CalNex Pasadena ground site, as well as gas-phase measurements taken from the Air Quality and Meteorological Information System (AQMIS, <http://www.arb.ca.gov/aqmis2/aqmis2.php>) to CMAQ predictions. We also carry out direct comparisons of airborne meteorological and gas- and aerosol-phase measurements during CalNex to CMAQ predictions. The organic component of the particulate matter will be addressed in a future study.

2. Model description and application

2.1. CMAQ

In this study, we use CMAQ version 4.7.1 [Foley *et al.*, 2010] on a domain that includes a large portion of Southern California as well as parts of Mexico (Figure 1), covering the area from (31.83°N, 121.43°W) to (35.69°N, 114.43°W) with 4 km by 4 km horizontal grid cells (102 x 156 grid points). Simulations cover the time period of May 2010. All simulations include a minimum spin-up period of four days to mitigate the influence of initial conditions. The meteorological fields used to drive the model were generated by the 5th generation Penn State/National Center for Atmospheric Research Meso-scale Model (MM5 version 3.7.4; Grell *et al.*

[1995]). CMAQ-compatible meteorological fields were generated by processing MM5 output using the Meteorology-Chemistry Interface Program (MCIP) version 3.6. Vertically, the meteorological fields extend from the surface to 100 mb using 30 layers. All meteorological fields and gridded emission inventories were prepared and provided by the California Air Resources Board (CARB). California emission inventories from June 2008 were averaged to produce emissions for one representative week-day and one representative weekend-day, which are used for every week-day and weekend-day, respectively, during May 2010. It is implicitly assumed that emissions did not change appreciably from 2008 to 2010. This assumption may be in question due to the recent emissions control programs such as the diesel truck rules and ocean going vessel (OGV) fuel regulations (<http://www.arb.ca.gov/msprog/operators.htm>), such that emissions of BC and sulfur containing compounds may have decreased significantly from 2008 to 2010. The CARB recognizes this limitation and is working toward releasing a newer version of emission inventory. In this study, the limitations of the current CARB inventory are expected to impact agreement between observations and predictions of anthropogenic BC and sulfur containing compounds, but not sea-salt emissions of SO_4^{2-} which are modeled interactively in CMAQ [Sarwar and Bhave, 2007; Kelly *et al.*, 2010].

Gas-phase predictions are based on a modified version of the Statewide Air Pollution Research Center (SAPRC) chemical mechanism (version SAPRC07TC, Carter [2010]) implemented in CMAQ with the Rosenbrock numerical solver. The main modification consists of using an updated isoprene photooxidation mechanism based on Paulot *et al.* [2009a, b]. Atmospheric mass distributions of particulate matter by size are represented in CMAQ as the superposition of three log-normal distributions, referred to as modes. These are the Aitken mode (typical D_p range is 20 nm to 90 nm), the accumulation mode (typical D_p range is 90 nm to 1-2.5 μm), and the coarse aerosol mode (typical D_p range is 1-2.5 to 10 μm) [Binkowski and Roselle, 2003]. Each mode is defined by its geometric standard deviation, geometric mean diameter, and the magnitude of mass within the mode. All particles are assumed to be spherical and each mode is assumed to be internally mixed chemically. Aerosol processes such as evaporation, condensation, coagulation, nucleation, advection, and wet and dry deposition affect the total number of particles, total surface area, and total mass within each mode. The majority of primary $\text{PM}_{2.5}$ emissions (99.9% by mass), including BC, are assigned to the accumulation mode, and a small fraction (0.1% by mass) is assigned to the Aitken mode according to section 1.3 of Binkowski and Roselle [2003].

The thermodynamic model ISORROPIA-II [Fountoukis and Nenes, 2007] is used in CMAQ to compute the thermodynamic equilibrium of the $\text{NH}_4^+ \text{-Na}^+ \text{-SO}_4^{2-} \text{-NO}_3^- \text{-Cl}^- \text{-H}_2\text{O}$ aerosol system. The assumption of thermodynamic equilibrium between fine inorganic particulate nitrate and ammonium with gas-phase nitric acid and ammonia is commonly invoked in atmospheric CTMs. The validity of this assumption for fine particles (D_p typically $< 2.5 \mu\text{m}$) was confirmed on the basis of data obtained during the 1999 Atlanta Supersite Experiment [Zhang *et al.*, 2002]. Karydis *et al.* [2010] used the PMCAMx model with ISORROPIA-II to model inorganic aerosol measured during the Mexico City MILAGRO campaign. They concluded that explicitly treating mass transfer to and from coarse aerosol as a dynamic process is essential for capturing the competition between small and large particles for condensable inorganic vapors. Consequently, in the present study, the inorganic aerosol module of CMAQ was configured to partition mass between the gas- and aerosol-phases according to the hybrid method [Capaldo *et al.*, 2000], in which instantaneous equilibrium

is assumed between the gas and aerosol-phases in the two fine modes, and dynamic mass transfer governs the coarse aerosol mode. Although ISORROPIA-II is capable of simulating aerosol systems that include K^+ - Ca^{2+} - Mg^{2+} , we do not consider these species as the lack of inclusion of these crustal species is not deemed a significant source of error in this study.

2.2. GEOS-Chem

Dynamic chemical boundary conditions (1-h temporal resolution) used in the CMAQ simulations were generated from the GEOS-Chem global chemical transport model (version 9-01-01, <http://acmg.seas.harvard.edu/geos/>). GEOS-Chem was used to simulate global gas- and aerosol-phase concentrations at 2° latitude $\times 2.5^\circ$ longitude horizontal resolution, with 47 vertical levels. Boundary conditions were extracted from the global simulation and used to drive a nested GEOS-Chem simulation over North America at 0.5° latitude $\times 0.667^\circ$ longitude horizontal resolution, with 47 vertical levels. Finally, CMAQ-consistent boundary conditions were then extracted from the nested GEOS-Chem simulations for the domain shown in Figure 1. The coarse GEOS-Chem parent grid simulation spin-up period was 1 year, and the spin-up period for the nested grid simulation was 4 months (Jan-Apr 2010). Goddard Earth Observing System (GEOS-5) assimilated meteorological data from the NASA Global Modeling and Assimilation Office (GMAO) were used for all GEOS-Chem model simulations, which included ozone- NO_x -hydrocarbon chemistry [Bey *et al.*, 2001] coupled with sulfate-nitrate-ammonium aerosol chemistry [Park *et al.*, 2004]. Outside North America, global emissions used in the coarse simulations are from the Emissions Database for Global Atmospheric Research (EDGAR) inventory [Olivier and Berdowski, 2001]. Anthropogenic emissions data for the United States, used in GEOS-Chem, were from the EPA National Emissions Inventory (NEI) 2005, scaled to the simulation period according to trends in the EPA Acid Rain Program (<http://camdataandmaps.epa.gov/gdm/>) and the NEI Air Pollutant Emissions Trends Data (<http://www.epa.gov/ttn/chief/trends/>). The nested GEOS-Chem simulation also includes aircraft, biofuel and natural emissions of inorganic aerosol precursors, as described by Park *et al.* [2004].

Since the nested GEOS-Chem horizontal grid resolution of 0.5° latitude $\times 0.667^\circ$ longitude (~ 55 km $\times \sim 60$ km at latitude $33^\circ N$) is considerably coarser than the 4 km \times 4 km resolution of CMAQ, and the domain shown in Figure 1 is relatively small compared to the North American continent, the potential double-counting of species in the L.A. Basin was taken into consideration. Coarse resolution acts to smooth concentration gradients via dilution, thereby reducing peak values within the region and increasing species concentrations at the boundaries. These species can then partially reenter the L.A. Basin as boundary conditions, while simultaneously being emitted within the L.A. Basin via the ARCTAS-CARB emission inventory. To avoid this double-counting, all emissions within the domain shown in Figure 1 were set to zero during the nested GEOS-Chem simulation. Therefore, the CMAQ boundary conditions contain only information from emissions that occur outside of the domain (red box) shown in Figure 1.

2.3. FLEXPART

To trace the origins of measured and predicted species during CalNex, a modified version of the FLEXPART Lagrangian particle dispersion model [Stohl *et al.*, 2005] is used to calculate back trajectories of air masses. FLEXPART has been used extensively to quantify the impacts of meteorological processes on pollution transport (e.g., de Foy *et al.* [2006]; Palau *et al.* [2006]; Ding *et al.* [2009]; Brioude

et al. [2009]). The main modification consists in using time-averaged winds from the Weather Research Forecasting (WRF version 3.3) meteorology model instead of instantaneous winds to reduce uncertainties within the FLEXPART model [Nehrkorn *et al.*, 2010]. The WRF output has a horizontal grid of 4 km \times 4 km, with a temporal resolution of 30 min and 60 vertical levels. In reverse mode, FLEXPART releases virtual tracer particles at receptors (in this study, a receptor is the instantaneous spatial and temporal location of the Pasadena ground site, the Twin Otter aircraft, or the P3 aircraft) and integrates their trajectories backward in time using predicted wind fields combined with random turbulent motion. FLEXPART then maps the individual particles to a grid (8 km \times 8 km horizontal resolution) every 2 h over a 24-h period and calculates the average particle residence times in each grid box. Surface-level contributions to air masses are determined by averaging the residence times of particles between the surface and 200 m altitude. The species contributions from air masses aloft may be estimated based on mean column residence times, but are not included in this study because surface emissions are expected to influence measurements most strongly at low altitudes (~ 300 m above ground).

3. Observations

3.1. Pasadena Ground-Site Data

Planetary boundary layer (PBL) heights were measured at the Pasadena ground site using a Vaisala CL31 ceilometer and are compared to predicted PBL heights in Figure 2 (see Münkel *et al.* [2006] for an in depth description of the Vaisala CL31 ceilometer). Inorganic aerosol measurements were made by the University of Colorado-Boulder Aerodyne high-resolution time-of-flight aerosol mass spectrometer (Aerodyne HR-ToF-AMS, Aerodyne Research, Inc., Billerica, MA USA, [DeCarlo *et al.*, 2008]) at the CalNex Pasadena ground site. The inlet is designed to transmit particles with aerodynamic diameters (D_{va}) of 60 to 600 nm with unit transmission efficiency, although particles with D_{va} above 600 nm are also detected [Canagaratna *et al.*, 2007; DeCarlo *et al.*, 2004]. A composition-dependent collection efficiency was applied to the AMS data based on recent work [Middlebrook *et al.*, 2012]. The ground-site AMS measurements are reported as 5-min averages and have an uncertainty $<30\%$. NH_3 was measured at 1 Hz by quantum cascade tunable infrared laser differential absorption spectroscopy (QC-TILDAS from Aerodyne Inc.) with an overall uncertainty during the CalNex campaign of $10\% + 0.42$ ppb. [Ellis *et al.*, 2010]. HNO_3 measurements were made with the acetate ion CIMS described by Roberts *et al.* [2010]. Data were acquired every 10 seconds, and were averaged to one minute. The calibrations were performed with permeation tubes calibrated as described by Neuman *et al.* [2002]. The time constant for transmission of HNO_3 through the inlet was found to be several minutes. The overall uncertainty of the HNO_3 measurement was $34\% + 0.05$ ppbv. SO_2 mixing ratios were measured at the Pasadena site with a commercial pulsed fluorescence detector (Model 43i-TL, Thermo Electron Corp) operated as described in Luke [1997]. All inorganic species measurements from the Pasadena ground site are shown in Figure 3. Hourly measurements of NO_x and SO_2 at various ground sites in the L.A. Basin are also reported by the CARB ground network (<http://www.arb.ca.gov/aqmis2/aqmis2.php>) and shown in Figure 4.

3.2. CIRPAS Twin Otter

Refractory black carbon (BC) aerosol mass was measured onboard the Twin Otter aircraft with a Droplet Measurement Technologies (DMT, Boulder, CO, USA) Single Particle Soot Photometer (SP2). The major findings from this

SP2 during CalNex, including calibration of the instrument, are detailed elsewhere [Metcalf *et al.*, 2012]. Briefly, the SP2 detects refractory BC mass by measuring the incandescence signal emitted from single BC-containing particles heated to their boiling point when passing through an intense Nd:YAG laser beam ($\lambda = 1064$ nm). BC volume-equivalent diameter (VED) is calculated from the detected mass assuming a spherical particle with density of 1.8 g cm^{-3} [Bond and Bergstrom, 2006]. Histograms of single-particle BC mass between 0.48 and 290 fg ($80\text{--}675 \text{ nm VED}$) were made and integrated to give bulk BC mass concentrations. In Metcalf *et al.* [2012], 1-min average data are reported, but in this study, we have re-sampled the dataset at 1 Hz to take advantage of the highest time-resolution available. Uncertainty in single-particle BC mass determination and bulk mass concentrations is estimated to be $\sim 40\%$, based largely on the calibration standards available.

Non-refractory particle mass and composition measurements were made by an Aerodyne compact time-of-flight aerosol mass spectrometer (C-ToF-AMS, Aerodyne Research, Inc., Billerica, MA USA) [Drewnick *et al.*, 2005; Murphy *et al.*, 2009]. The AMS onboard the Twin Otter measures sub-micron, non-refractory, size-resolved aerosol composition. The inlet and collection efficiency of the AMS onboard the Twin Otter were similar to those of the AMS at the Pasadena ground site. In an effort to measure aerosol mass distributions, the AMS onboard the Twin Otter was periodically run in particle-time-of-flight (PToF) mode. Due to relatively low aerosol loadings, the signal-to-noise ratio was not of sufficient quality for a meaningful comparison to size distributions predicted by CMAQ. Instead, we focus on bulk particulate ammonium (NH_4^+), particulate nitrate (NO_3^-), and particulate sulfate (SO_4^{2-}) mass concentrations reported as 10-s averages. We note that due to the attempted size-resolved measurements, narrow plumes may have been missed by the AMS onboard the Twin Otter.

All Twin Otter measurements reported here are from instruments inside an unpressurized cabin. All instruments sampled downstream of a two-stage diffusion inlet with a transmission efficiency near unity for particle diameters up to about $3.5 \mu\text{m}$ [Hegg *et al.*, 2005]. Sampling lines inside the cabin are kept reasonably uniform to all instruments, so further corrections for diffusional losses in these lines have not been made. The Twin Otter conducted 18 research flights from Ontario, CA between 4 May and 28 May 2010 during CalNex. The AMS was onboard during 8 of the flights, three of which were to San Joaquin Valley, which is outside the domain (red box) shown in Figure 1. Therefore, this analysis makes use of 5 Twin Otter flights during which inorganic aerosol concentrations were measured within the L.A. Basin.

3.3. NOAA P3

The P3 aircraft conducted 18 research flights from Ontario, CA between 4 May and 20 June 2010 during CalNex 2010 (esrl.noaa.gov/csd/calnex/). This study uses daytime measurements from 5 P3 flights that focused on sampling L.A. Basin emissions and the resulting photochemical products. NH_3 , HNO_3 , NH_4^+ , NO_3^- , and SO_4^{2-} , and various meteorological parameters were measured onboard the P3 aircraft. NH_3 was measured at 1 Hz (equivalent to 100 m spatial resolution) by chemical ionization mass spectrometry (CIMS) with typical uncertainties of $(30\% \pm 0.2 \text{ ppbv})$ and a 1σ imprecision of 0.08 ppbv [Nowak *et al.*, 2010]. HNO_3 was measured at 1 Hz by a separate CIMS instrument with an uncertainty of $(15\% \pm 0.040 \text{ ppbv})$ and a 1σ imprecision of 0.012 ppbv [Neuman *et al.*, 2012]. SO_4^{2-} , NH_4^+ , and NO_3^- were measured from a pressure-controlled region downstream of a low turbulence inlet using a compact time-of-flight aerosol mass spectrometer (Aerodyne, Billerica, Massachusetts) [Bahreini *et al.*, 2009]. The AMS data are reported as 10-s averages with 2σ uncertainty (1σ imprecision) of 34% ($0.06 \mu\text{g m}^{-3}$), 34% ($0.01 \mu\text{g m}^{-3}$), and

36% ($0.01 \mu\text{g m}^{-3}$) for ammonium, nitrate, and sulfate, respectively. BC measurements in the size range of 95–720 nm VED (still assuming a BC void-free density of 1.8 g cm^{-3}) were made by an SP2 similar to that used onboard the Twin Otter [Schwarz *et al.*, 2006]. As described in detail in Metcalf *et al.* [2012], due to differences in calibration, measurements from the SP2 onboard the Twin Otter are biased low by up to 12%, as compared to those from the SP2 onboard the P3.

The AMSs used in this study, both ground-based and airborne, measured only particles with vacuum aerodynamic diameters between 60 nm and 600 nm diameter with 100% efficiency. Particles with aerodynamic diameters above 600 nm were also measured, but with reduced collection efficiency. However, since the predicted Aitken, accumulation, and coarse aerosol modes are expressed in CMAQ in terms of log-normal functions, each mode is defined for particle diameters ranging from zero to infinity. Therefore, all aerosol predictions are adjusted to match the transmission efficiency of the AMS based on the following piece-wise defined transmission function:

1. 0% transmission below $D_{va} = 40 \text{ nm}$;
2. linear increase in transmission vs $\ln(D_{va})$, from 0% at $D_{va} = 40 \text{ nm}$ to 100% at $D_{va} = 100 \text{ nm}$;
3. 100% transmission from $D_{va} = 100 \text{ nm}$ up to $D_{va} = 550 \text{ nm}$;
4. linear decrease in transmission vs $\ln(D_{va})$, from 100% at $D_{va} = 550 \text{ nm}$ to 0% at $D_{va} = 2 \mu\text{m}$.
5. 0% transmission above $D_{va} = 2 \mu\text{m}$;

This transmission function is an average of the transmission curves used in several AMS studies as described in Knotek *et al.* [2011] and references therein, and is applied to all inorganic aerosol predictions (CMAQ) that are compared to AMS measurements from the Pasadena site, the Twin Otter aircraft, and the P3 aircraft. We note that due to variation between specific aerodynamic lenses in different instruments, the exact transmission efficiencies of the AMS at the Pasadena site, onboard the Twin Otter, and onboard the P3 will be slightly different than the one used in this study. BC concentration predictions are restricted to particles with $95 \text{ nm} < D_p < 720 \text{ nm}$ when comparing to P3 measurements and $80 \text{ nm} < D_p < 675 \text{ nm}$ when comparing to the Twin Otter measurements based on the transmissions windows of the respective SP2s. Appendix A presents the equations used to modify CMAQ predictions based on instrumentation transmission windows and efficiencies.

4. Results and discussion

The Aerosol Modeling Testbed analysis toolkit [Fast *et al.*, 2011] was used to map three-dimensional CMAQ meteorological parameters, predicted gas-phase concentrations, and predicted aerosol-phase concentrations onto each flight path (as well as for various ground sites). The temporal resolution of the CARB emission inventory and MM5 meteorology is 1-h. However, CMAQ predictions can be output with any temporal resolution via linear interpolation. In this work, one predicted concentration field, averaged over one hour, is output every hour and observations are compared to these concentration fields according to observational time-stamps (i.e. observational points with time-stamps of 12:20 and 12:40 would both be compared to predictions averaged between the hours of 12:00–13:00). The discrepancy between measured and simulated species concentration fields and meteorological parameters is quantitatively assessed using the following four statistical metrics:

$$ME = \frac{1}{N} \sum_{i=1}^N |P_i - M_i| \quad (\text{mean error}) \quad (1)$$

$$MB = \frac{1}{N} \sum_{i=1}^N (P_i - M_i) \quad (\text{mean bias}) \quad (2)$$

$$NME = \frac{\sum_{i=1}^N |P_i - M_i|}{\sum_{i=1}^N M_i} \quad (\text{normalized mean error}) \quad (3)$$

$$NMB = \frac{\sum_{i=1}^N (P_i - M_i)}{\sum_{i=1}^N M_i} \quad (\text{normalized mean bias}) \quad (4)$$

where N, P, and M stand for the number of data points, predicted quantity, and measured quantity, respectively.

4.1. Meteorological variables

4.1.1. Ground Site

Observed and predicted temperature, relative humidity (RH), and planetary boundary layer (PBL) height from the Pasadena ground site are shown in Figure 2 and statistical metrics are given in Table 1. Overall, the agreement between observed and predicted PBL height in Pasadena has a 15-day average bias of 43 m (~8%). Agreement between observed and predicted temperature has a 15-day average bias of 4°C. The agreement between observed and predicted RH has a 15-day average bias of -19.4%. The precise reason for the discrepancy in RH cannot be pinpointed at this time, but is most likely due to the saturation-vapor pressure being exponentially dependent on errors in temperature (1°C temperature error leads to approximately 5% RH error).

4.1.2. Twin Otter and P3

The Twin Otter and P3 flight paths and altitudes are shown in Figures 5 and 6, and Figures 7 and 8, respectively. Temperature and relative humidity (RH) measurements from the Twin Otter and P3 flights are compared to MM5 predictions in Table 2. Observed and predicted temperatures (averaged over each flight) typically agree to within 4°C, while observed and predicted RH (averaged over each flight) typically agree to within 15%. The most notable exceptions are the 21 May Twin Otter flight and the 14 May P3 flight, during which predicted RH was biased low by 26.6% and 22.1%, respectively. Wind speed and wind directions measurements onboard the Twin Otter and the P3 are shown in Table 3. Predicted and observed wind speeds generally agree to within ~50% when averaged over each flight. Although the mean discrepancy between predicted and observed wind direction ranges between 22-65°, the average predicted and observed wind direction is that of the daytime southwesterly sea breeze which advects emissions towards the north and northeast, exiting the Basin through passes in the San Gabriel and San Bernardino mountain ranges [Lu and Turco, 1995]. However, it is difficult to quantify errors in species concentrations attributable to discrepancies between measured and observed wind vectors.

4.2. Black carbon (Twin Otter and P3)

Measured and predicted BC concentrations from the Twin Otter flights and the P3 flights during May 2010 are shown in Figure 9. A statistical comparison between BC predictions and observations is given in Table 4. Although the extent of agreement between observations and predictions varies from flight to flight, the overall agreement between predicted BC concentrations and those measured by the P3 and Twin Otter are comparable. Visual inspection of Figures 5, 6, and 9 suggests that the CMAQ predictions capture the spatial distribution of BC during many flights, although the predicted concentration range is biased by 80 to 111% as compared to Twin Otter measurements, and biased by -8%

to 135% as compared to P3 measurements. Over-predictions in BC could be the result of any (or all) of several factors: (1) the BC emission rates in the emission inventory are overestimated, (2) the meteorological inversion layer depth and/or the planetary boundary layer (PBL) depth is underpredicted in this area, (3) dry-deposition rates of BC are overpredicted, (4) the SP2 instruments onboard the Twin Otter and the P3 during CalNex were biased low, and (5) the predicted BC mass-distributions do not match the actual BC mass-distributions, which could cause biases after the SP2 transmission window is applied to predictions.

As mentioned previously, the calibration of the SP2 onboard the Twin Otter biased BC measurements low by 12% as compared to those of the SP2 onboard the P3 [Metcalf *et al.*, 2012]. Since the normalized statistical metrics used in this study are nonlinear functions of observed concentrations, the 12% measurement bias will cause higher than 12% bias when compared to predictions. As an example, in a 1-point data set, if the predicted BC concentration is $1 \mu\text{g m}^{-3}$ and the observed BC concentration is $0.56 \mu\text{g m}^{-3}$, the NMB will be 78.6%. However, if the measured concentration is reduced to $0.5 \mu\text{g m}^{-3}$ due to the 12% instrument bias, the NMB becomes 100%. This must be taken into consideration when comparing BC statistics from both aircraft (Table 4). In addition, the P3 aircraft sampled high and low altitudes much more frequently than the Twin Otter did. This could influence the level of agreement as CMAQ is more likely to predict low BC concentrations accurately at high altitudes. In contrast, the Twin Otter altitude with respect to the ground was relatively constant (~300 m) on most flights. The agreement between observed and predicted PBL heights at the Pasadena ground site establishes confidence that meteorology is not the source of discrepancy in BC. Due to recent retrofitting programs and accelerated diesel truck replacement [Dallmann *et al.*, 2011], overpredictions of BC levels are most likely associated with overstated BC emissions in the Long Beach and downtown L.A. area.

A comparison of aircraft locations in Figures 5, 6, 7, and 8 with BC concentrations shown in Figure 9 suggests that the highest BC concentrations exist in air masses strongly influenced by emissions in the Long Beach industrial area. Back trajectory analyses provide a tool to evaluate this hypothesis as it relates to the history of air masses sampled by the aircraft. The distributions of the mean residence times for virtual surface particles, predicted by FLEXPART, arriving in the vicinity of the Twin Otter during the 24 May flight are shown in Figure 10. Two 24-h integrated trajectories from the 24 May flight are used to elucidate the history of the observed and predicted air masses at different parts of the L.A. Basin. For example, the trajectory paths shown in Figure 10 suggest that during the 24 May flight, both observed and predicted concentrations of BC, at 11:21 (downtown Los Angeles) and 14:59 (Fontana), occurred in air masses that were influenced by emissions near Long Beach and downtown Los Angeles. The extent of agreement between observed and predicted BC concentrations from both aircraft suggests that the locations of the BC sources are well accounted for in the CARB BC inventory used in this study. However, owing to possible reductions in PM emissions from ships and diesel trucks between 2008 and 2010, the emission rates are likely overstated by a factor of ~1.5-2 throughout the L.A. Basin [Dallmann *et al.*, 2011].

4.3. Sulfate

To characterize the sources of the predicted sulfate, the CMAQ sulfate tracking system was employed, in which separate tracers are used to keep track of the sulfate contributions from the formation pathways listed in Table S1. Due to the transmission window of the AMS, the mass contributions

from the Aitken mode and the coarse mode sulfate are a negligible fraction of the total predicted sulfate aerosol mass (< 1%) in the applicable size range and are not shown in Figure 3. Sulfate predicted to be formed by aqueous-phase oxidation by methylhydrogenperoxide (MHP) and peroxyacetic acid (PAA) is also negligible. Although Fe^{3+} and Mn^{2+} are not model-predicted species, CMAQ prescribed background concentrations of $0.01 \mu\text{g m}^{-3}$ Fe^{3+} and $0.005 \mu\text{g m}^{-3}$ Mn^{2+} still lead to a small, but non-negligible, portion (up to 5%) of accumulation mode sulfate forming via these routes [Walcek and Taylor, 1986; Chang *et al.*, 1987]. The predominant predicted accumulation mode sulfate comes from four sources: the inflow of sulfate from the boundaries (e.g. Asian inflow [Lin *et al.*, 2012]), aqueous-phase oxidation of S(IV) by H_2O_2 and O_3 , gas-phase photooxidation of SO_2 , and direct sulfate emission.

4.3.1. Pasadena Ground Site

Observed and predicted sulfate and sulfur dioxide concentrations from the CalNex Pasadena ground site are shown in Figure 3, and statistical metrics are given in Table 1. In addition, ground-site SO_2 measurements from several locations within the L.A. Basin, taken from the CARB Air Quality and Meteorological Information System (AQMS, <http://www.arb.ca.gov/aqmis2/aqmis2.php>), are compared to CMAQ predictions in Figure 4. As at the Pasadena ground site, SO_2 mixing ratios are over-predicted at all locations within the L.A. Basin.

Despite over-predictions in SO_2 , predicted sulfate concentrations are actually biased low compared to sulfate measurements at the Pasadena ground site, mostly due to underestimations during the first few days of comparison. The relative sulfate contributions are listed in Table 5. Few clouds are present during daylight hours, but an MM5 predicted nighttime coastal marine layer facilitates aqueous-phase conversion of S(IV) to S(VI) in CMAQ. The predicted marine layer evaporates during the day, but the cloud-processed sulfate remains airborne. At the Pasadena ground-site, enhancements in the relative sulfate contributions from aqueous-phase oxidation of SO_2 are not directly proportional to over-predictions in SO_2 emissions owing partially to the nonlinear pH dependence of the rate of S(IV) oxidation by O_3 . More specifically, the second-order reaction rate constant for the S(IV)- O_3 reaction varies by up to four orders of magnitude for aerosol pH ranging from 1 to 6 [Seinfeld and Pandis, 2006]. Production of sulfate via this reaction lowers the pH and slows down the reaction. In addition, if the oxidants H_2O_2 and O_3 are the limiting reactants, the impacts of overestimated SO_2 emissions will also be lessened. Sulfate formation via gas-phase oxidation of SO_2 should respond more linearly to increases in SO_2 concentrations. However, the lifetime of SO_2 against the hydroxyl radical is relatively long (~ 1 week, Seinfeld and Pandis [2006]) and only represents 7% of the average predicted sulfate at the Pasadena ground site.

4.3.2. Twin Otter and P3

Observed and predicted sulfate concentrations from the Twin Otter and P3 flights are shown in Figure 11. A statistical comparison between sulfate predictions and observations is given in Table 6. The average predicted sulfate concentration is biased high by 55% to 268% as compared to Twin Otter measurements, and biased by 0% to 71% as compared to P3 measurements (Table 6). Moreover, the relative contributions predicted from each sulfate source vary considerably for both aircraft depending on the individual flight path (Figures 12 and 13).

A significant fraction of the predicted sulfate (airborne and ground-based) comes from direct sulfate emission and boundary inflow of sulfate, both of which are independent of SO_2 concentrations (Table 5 and Figures 12 and 13). That

direct sulfate emission contributes a significant fraction of the predicted sulfate in the L.A. Basin can be understood via analysis of the CARB sulfur emission inventory. The CARB sulfur emission inventory includes gas-phase SO_2 emissions, gas-phase H_2SO_4 emissions, and particle-phase SO_4^{2-} emissions (i.e. direct sulfate emission). Since, sulfuric acid is highly water-soluble and has an extremely low vapor pressure, it is assumed to enter the particle-phase immediately upon emission. Therefore, direct sulfate emissions include both direct emission of sulfate and direct emission of sulfuric acid. The ratio (by mass) of the different sulfur emissions in the CARB inventory, $(\text{H}_2\text{SO}_4 + \text{SO}_4^{2-}) / (\text{H}_2\text{SO}_4 + \text{SO}_4^{2-} + \text{SO}_2)$ within the Basin is $\sim 5\%$. However, since only a fraction of the SO_2 emitted is converted to sulfate, the sulfate from primary emissions will account for more than 5% of the total sulfate measured at the ground site and by the aircraft [Dominguez *et al.*, 2008]. FLEXPART back trajectories suggest that during the 21 May flight (at 11:23 and 13:57, specifically), high predicted concentrations of primary sulfate occurred in air masses that were influenced by emissions near Long Beach (Figure 14). These hot spots of predicted primary sulfate near Long Beach were generally not observed by the Twin Otter (Figure 12). Similarly, as shown in Figure 11, sharp increases in predicted sulfate were predicted but not measured by the P3 near Long Beach (e.g. 8 May just before 13:00 and 14 May just after 13:00).

Sulfate concentrations measured onboard the Twin Otter were below $1 \mu\text{g m}^{-3}$ on 21, 24, and 25 May and showed little spatial variation. For these three flights, the predicted sulfate attributable to the GEOS-Chem boundary conditions represents 43-58% of the total predicted sulfate and accounts for almost the entire measured sulfate. Boundary inflow of sulfate affects predicted sulfate concentrations along P3 flight paths in a similar manner. That the sulfate boundary conditions exert a noticeable impact on sulfate concentrations within the basin is not totally unexpected. For instance, Huang *et al.* [2011] evaluated the inflow of sulfur oxides ($\text{SO}_x = \text{SO}_2 + \text{SO}_4^{2-}$) to the South Coast (SC) of California by comparing predictions from the STEM atmospheric chemical transport model against aircraft measurements during the ARCTAS-CARB campaign [Jacob *et al.*, 2010] in June 2008. They estimated that elevated SO_x levels at altitudes between 1-4 km enhanced SO_4^{2-} surface levels by a maximum of $\sim 0.13 \text{ ppb}$ ($0.13 \text{ ppb} \text{ } \text{SO}_4^{2-} \simeq 0.5 \mu\text{g m}^{-3}$ at 1 atmosphere and 300 K) during this time period. Despite the influence of long-range SO_x transport, Huang *et al.* [2011] found that near-surface SO_x concentrations were mostly influenced by local emissions and estimated that the 2005 CARB sulfur emissions were low by about a factor of two. This is in contrast to our findings which suggest that the 2008 CARB SO_2 emissions are overestimated (Figure 4). Since the sulfur emission inventory used in Huang *et al.* [2011] is similar to that used in this study, the most likely explanation is that SO_2 emissions have decreased from 2008 to 2010, which is consistent with sulfur emission regulations that went into effect during those two years. The sharp increases in measured sulfate during the P3 8 May flight, measured outside the boundary layer (e.g. just before 14:00 and 15:00 and after 16:00), were not captured by CMAQ. These sharp increases in measured sulfate are believed to be due to Asian transport [Lin *et al.*, 2012]. Future work should continue to quantify the impact of foreign and domestic emissions on Southern California air quality as this is crucial for determining the potential efficacy of emission control strategies.

4.4. Ammonium and Nitrate

Ammonium nitrate aerosol is semivolatile and continuously partitions between the gas- and aerosol-phase. The distributions of total ammonium ($\text{NH}_3 + \text{NH}_4^+$) and total nitrate ($\text{NO}_3^- + \text{HNO}_3$) between the gas- and aerosol-phases

are sensitive to the relative concentrations of other ions such as sulfate, sodium, and chloride, as well as meteorological factors such as temperature and relative humidity.

4.4.1. Pasadena Ground Site

Particulate ammonium and nitrate predictions are generally biased low at the Pasadena ground site (Table 1). Aside from the large over-prediction on 24 May, NH_3 concentrations are well predicted (average bias of 22%), and predicted HNO_3 concentrations have a 15-day average bias of -38%. Nowak *et al.* [2012] used observations from the P3 aircraft during CalNex to show that the NH_3 emissions from automobiles in the CARB inventory are fairly accurate and contribute ~ 60 metric tons day $^{-1}$ to the NH_3 budget within the L.A. Basin. Nowak *et al.* [2012] also found the NH_3 emissions from dairy facilities in the eastern part of the L.A. Basin are likely understated by up to a factor of 20. Since, strictly during the daytime, the Pasadena ground site is downwind of downtown L.A. but upwind of the dairy facilities, the predicted and observed NH_3 at this location is represented well within CMAQ.

Ground-site NO_x ($\text{NO} + \text{NO}_2$) measurements taken from the CARB Air Quality and Meteorological Information System (AQMS, <http://www.arb.ca.gov/aqmis2/aqmis2.php>) are compared to CMAQ predictions in Figure 4. NO_x mixing ratios are over-predicted by a factor of ~ 2 at the three locations (North Long Beach, L.A. Westchester, and L.A. North Main Street location). Although over-predictions of temperature and under-predictions of RH artificially shift particulate ammonium and nitrate to the gas-phase, both particulate nitrate and nitric acid are over underpredicted from 15-20 May. Since SO_4^{2-} , HNO_3 , NO_3^- , and NH_4^+ are underpredicted during the first week of comparison, but are represented accurately by CMAQ during the second week, and since these species have different upwind sources, it is likely that errors in predicted wind fields, as opposed to uncertainties in the CARB emission inventory, are responsible for disagreement during the first week of comparison. Uncertainties/inaccuracies in predicted sea-salt emissions may also influence the agreement between predictions and observations at the Pasadena ground site, as will be discussed in the next section.

4.4.2. Twin Otter and P3

Observed and predicted particulate nitrate and ammonium concentrations from the Twin Otter and P3 flights are shown in Figures 15 and Figure 16, respectively. Statistical metrics for inorganic aerosol species from both aircraft are given in Table 6. Gas-phase measurements of HNO_3 and NH_3 were not conducted on the Twin Otter, so one cannot determine based on that data set alone if discrepancies between particulate ammonium and nitrate observations and predictions are the result of errors in the NO_x ($\text{NO} + \text{NO}_2$) emissions, NH_3 emissions, or predictions of HNO_3 within the SAPRC07TC chemical mechanism. However, HNO_3 and NH_3 measurements were conducted onboard the P3 aircraft (Figure 17 and Table 7). As stated previously, Nowak *et al.* [2012] found that the NH_3 emissions from automobiles in the CARB inventory are consistent with their measurements (~ 60 metric tons day $^{-1}$), but that the CARB inventory underestimates NH_3 emissions from dairy facilities by a factor of 3-20. The observed and predicted ammonia concentrations in the eastern part of the L.A. Basin are consistent with the conclusions of Nowak *et al.* [2012] and indicate that NH_3 mixing ratios, based on the prevailing emissions inventory, can be under-predicted by factors as high as 10^2 - 10^3 (Figure 17). Other than immediately downwind of dairies, predicted NH_3 mixing ratios are in better agreement with observations (see “no dairy” metrics in Table 7). Similarly, HNO_3 mixing ratios are generally predicted well during the

P3 flights (NME typically ~ 0.5) with the most notable exception being 14 May between 11:00 and 12:00 when the aircraft flew off the coast. HNO_3 and NO_x contour maps (not shown) suggest that the over-predictions on 14 May are caused by overstated coastal NO_x emissions (Figure 4).

Total nitrate ($\text{NO}_3^- + \text{HNO}_3$ [ppbv]) mixing ratios and nitrate partitioning fractions ($\text{NO}_3^- / (\text{NO}_3^- + \text{HNO}_3)$) are shown in Figure 18. Nitrate mass concentrations are converted to mixing ratios using predicted and observed temperatures and pressures (this is equivalent to multiplying measurements reported in $\mu\text{g sm}^{-3}$ by $22.41/\text{MW ppbv}$ $\mu\text{g}^{-1} \text{sm}^3$, where sm^{-3} refers to concentrations at 1 atm and 273 K and MW is the molecular weight of the species). Predicted particulate nitrate concentrations used in Figure 18 are still adjusted to match the transmissions efficiency of the AMS. As shown in Figure 18, the agreement between predicted and observed total nitrate mixing ratios is typically better than between particulate nitrate fractions. While inaccuracies in predicted temperature and RH (Table 2), as well as sulfate overpredictions (Table 6), each contribute to inaccuracies in the predicted particulate nitrate fraction, NH_3 underpredictions in the eastern part of the L.A. Basin, seen very clearly during most P3 flights, are the dominant factor. For instance, during the 4 May flight, sharp increases in measured particulate nitrate fraction (Figure 18) coincide with large NH_3 underpredictions just before 13:00 and 15:00. Similar behavior is visible just before and after 14:00 on the 14 May flight, and at 17:00 on the 16 May flight.

Given that surface-level NO_x concentrations are generally over-predicted (Figure 4), one would expect the total nitrate mixing ratios to be over-predicted. However, as shown in Figure 18 and given in Table S2, the predicted total nitrate mixing ratios (within the AMS transmission window) agree with observations to within 50% NME, but tend to be underpredicted. There are several potential explanations for this. (1) Since the daytime production of HNO_3 occurs via gas-phase oxidation of NO_2 ($\text{OH} + \text{NO}_2 \rightarrow \text{HNO}_3$), the predicted OH concentration, which is highly dependent on the concentrations of hydrocarbons and other oxidants, may be too low. (2) The rate of conversion of NO to NO_2 , which is also highly dependent on the concentrations of hydrocarbons and other oxidants, may be limiting. (3) The nighttime heterogeneous reaction of N_2O_5 ($\text{N}_2\text{O}_5(\text{g}) + \text{H}_2\text{O}(\text{s}) \rightarrow 2\text{HNO}_3$) may be understated. (4) If the predicted particulate nitrate mass concentrations are correct, but the size distributions predicted by CMAQ are inaccurate, the amount of predicted particulate nitrate could be biased low once predictions are adjusted to match the size-dependent transmission efficiency of the AMS. (5) Inaccurate shifting of total nitrate from the particle phase to the gas phase for various potential reasons (e.g. over-predicted temperature, under-predicted RH, overpredicted SO_4^{2-} concentrations, under-predicted NH_3 emissions) may artificially enhance the removal of total nitrate from the system due to faster dry deposition rates for gas-phase HNO_3 [Dzepina *et al.*, 2009]. (6) If a coastal environment (e.g. the L.A. Basin) is ammonia-limited, coarse sea-salt particles can significantly reduce the amount of HNO_3 , via formation of NaNO_3 , available to form ammonium nitrate in the accumulation mode [Hsu *et al.*, 2007].

Positive temperature biases and negative RH biases (Table 2), as well as positive sulfate biases (Table 6) and negative ammonia biases (Table 7), suggest that several of these possible factors contribute to shifting of predicted particulate nitrate to the gas-phase. Due to the coastal location of the L.A. Basin, we focus on the possibility (6) regarding total nitrate underpredictions and defer a detailed analysis regarding the extent to which the other five sources of inaccuracy/uncertainty impact the amount of total nitrate predicted, as well as what fraction of the total nitrate partitions to the particle-phase, as the subject of future work. As shown in Figures S1, S2, and S3, the AMS transmission efficiency results in the removal of $\sim 35\%$ of the total predicted

particulate sulfate and ammonium, and 20-100% (higher removal at low altitudes where sea-salt is present) of the total predicted nitrate during all flights. Since all predicted inorganic components are assumed to be in a metastable state (i.e. an aqueous electrolyte solution), predicted coarse mode particulate nitrate forms when HNO_3 reversibly condenses onto coarse NaCl particles via solution thermodynamics [Kelly *et al.*, 2010]. This causes a significant fraction of the predicted particulate nitrate to reside in the coarse aerosol mode, while ammonium and sulfate reside primarily within the accumulation mode.

To examine the hypothesis that total nitrate concentrations remain underpredicted during most flights because HNO_3 is inaccurately distributed between the accumulation and coarse aerosol modes, we present statistical metrics for all five P3 flights (Table S2) with and without the AMS transmission curve applied to predictions. When the AMS transmission efficiency is taken into consideration, total nitrate concentrations are underpredicted during four of the five P3 flights by 0-42% (S2). However, when full transmission (i.e. all predicted particulate nitrate and gas-phase nitric acid) is assumed, total nitrate concentrations are still underpredicted by up to 33% during the 4, 16, and 19 May flights. Since coarse particles were not measured onboard the Twin Otter or P3, the accuracy of the coarse mode nitrate predictions cannot be assessed. The statistics given in Table S2 strongly suggest that total nitrate is underpredicted due to predicted HNO_3 formation occurring too slowly or accelerated removal of predicted total nitrate. This does not occur because nitrate mass distributions are predicted to be outside the AMS transmission window; however, it should be noted that inaccurately predicted mass distributions may artificially enhance dry deposition rates.

Even though gas-phase measurements were not taken onboard the Twin Otter, the impact of understated ammonia emissions and underpredicted total nitrate concentrations can be seen in the particulate ammonium and nitrate measurements (Figures 15). For instance, as shown in Figure 15, particulate ammonium and nitrate concentrations are significantly under-predicted in the eastern part of the L.A. Basin before the Twin Otter flew into the outflow regions at 12:30 and 14:30 during the 21 May flight. These under-predictions are exacerbated by an under-prediction of RH by 26.6% (flight average, Table 2). Particulate ammonium and nitrate concentrations are also under-predicted in the eastern part of the L.A. Basin during the 24 (between 13:00 and 15:00), 25 (between 13:30 and 15:30), and 27 (just after every hour) flights (Figure 15). Both predicted and observed nitrate concentrations are ~ 2 times higher in the eastern part of the L.A. Basin on 25 May as compared to 24 May. The differences in nitrate concentrations are potentially attributable to warmer temperatures and lower RHs (predicted and observed) that shift both predicted and observed particulate nitrate to the gas-phase during the 24 May flight. However, the differences may also be attributable to variations in wind speed leading to fluctuating sea-salt emissions, and therefore different distributions of nitrate between the accumulation mode and the coarse mode. This is suggested by the differences in the fraction of nitrate removed by the AMS transmission curve along somewhat similar flight paths (Figure S3).

Twin Otter flight paths are also very similar during the 27 and 28 May flights. However, the amount of predicted nitrate removed as a result of the AMS transmission efficiency curve is $\sim 60\%$ on the 27 May flight and $\sim 45\%$ on the 28 May flight. This indicates that coarse mode chloride depletion via HNO_3 condensation is more pronounced on the 28 May flight as compared to the 27 May. The differences in measured ammonium and nitrate loadings on the 27 and 28 May flights, as well as the differences in agreement between predictions and observations, may be attributable to uncertainties in meteorology directly influencing both sea-salt emissions, as well as transport and dilution. However, as a result of the sub-micron AMS transmission window, it is difficult to determine conclusively the impact of sea-salt emissions on nitrate levels in the L.A. Basin.

5. Conclusions

A detailed three-dimensional chemical transport model (CMAQ version 4.7.1), which contains state-of-the-science gas-phase chemistry and aerosol thermodynamics, was applied during the May 2010 CalNex campaign in the Los Angeles Basin. Boundary conditions were extracted from a nested global-scale GEOS-Chem model (version 9.1.1) simulation. Input meteorology and emission inventories were provided by the CARB. Inorganic and BC aerosol predictions were compared against the suite of ground-based and airborne measurements taken from various CIRPAS Twin Otter and WP-3D flights. The FLEXPART Lagrangian particle dispersion model is used to determine the trajectories of air parcels that reached the aircraft.

Predicted BC concentrations are compared to BC SP2 measurements onboard the Twin Otter and P3 for 10 flights during May 2010 (Figure 9). FLEXPART back-trajectories indicate that high concentrations of BC generally occurred in air-masses that had passed over the Long Beach and downtown L.A. areas within the previous 24 h. Comparisons of predictions and observations onboard both aircraft indicate that the spatial distribution of BC emissions in the CARB emission inventory used in this study are reasonable, but emission magnitudes are generally over-predicted by a factor of 1.5 to 2. Measurements by the SP2 onboard the Twin Otter were systematically biased only 12% lower than those onboard the P3, so measurement uncertainty cannot be considered a cause of the discrepancy.

Predicted SO_2 mixing ratios and sulfate concentrations are compared to measurements from the CARB Air Quality and Meteorological Information System (AQMSIS, <http://www.arb.ca.gov/aqmis2/aqmis2.php>), the CalNex Pasadena ground site, the Twin Otter aircraft, and the P3 aircraft. All SO_2 measurements indicate that the SO_2 emissions in the CARB inventory used in this study are too high. However, the impact of SO_2 over-predictions on predicted sulfate concentrations is variable. Sulfate is over-predicted by 55%-268% as compared to Twin Otter measurements, 0%-71% as compared to P3 measurements, and is actually under-predicted by 17% as compared to observations at the Pasadena ground site. Sulfate from gas-phase oxidation should respond linearly to SO_2 mixing ratios, but due to the relatively long lifetime SO_2 against OH reaction (~ 1 week), this pathway represents only 4-16% of the predicted sulfate budget during CalNex. Similarly to BC, FLEXPART back trajectories suggest that sharp increases in predicted primary sulfate (direct emission of SO_4^{2-} and H_2SO_4) concentrations occur in air masses that pass over the Long Beach industrial area. These sharp increases were generally not evident in P3 or Twin Otter measurements owing potentially to recent ocean-going vessel (OGV) emission reductions (<http://www.arb.ca.gov/msprog/operators.htm>). The boundary inflow of sulfate from large-scale GEOS-Chem simulations represents 26% of that predicted at the Pasadena site, 23%-58% of that predicted along the Twin Otter flight paths, and 44%-82% of that predicted along the P3 flight paths. Boundary inflow of sulfate represents a larger fraction of sulfate predicted along P3 flight paths because the P3 sampled the free-troposphere, where Asian inflow of sulfate is frequently a primary contribution [Lin *et al.*, 2012].

Ammonia mixing ratios are severely under-predicted in the eastern part of the L.A. Basin due to understated dairy

emissions. These under-predictions cause an artificial shift of nitrate from the particle-phase to the gas-phase. Over-predictions in SO_4^{2-} , under-predictions in RH, and over-predictions in temperature all also contribute to particulate nitrate under-predictions. Total predicted nitrate ($\text{NO}_3^- + \text{HNO}_3$) mixing ratios and nitrate partitioning fractions ($\text{NO}_3^-/(\text{NO}_3^- + \text{HNO}_3)$) are compared to those measured along several P3 flights. Despite over-predicted NO_x concentrations at most CARB sites within the L.A. Basin, total nitrate mixing ratios are under-predicted along most P3 flight paths. This may be a result of retarded day-time and night-time HNO_3 formation, or accelerated total nitrate removal via dry deposition. Comparison of total nitrate predictions considering the AMS transmission efficiency curve indicate that, although a considerable amount of the predicted nitrate resides in the coarse aerosol mode, due to sea-salt emissions and subsequent chloride displacement, uncertainties in predicted nitrate mass distributions outside the AMS transmission window are not responsible for total nitrate underpredictions. However, inaccurate distribution of predicted nitrate between the fine and coarse aerosol modes may artificially enhance or retard dry deposition rates. The largest under-predictions in particulate ammonium and nitrate generally occurred along Twin Otter flight paths in the eastern part of the L.A. Basin where concentrated dairy facilities are located. In addition, the differences in the fraction of nitrate removed as a result of the AMS transmission curve along somewhat similar flight paths (e.g. Twin Otter 27 May and 28 May flights) suggest that day-to-day variations in sea-salt emissions may lead to different distributions of nitrate between the accumulation and the coarse modes.

This work, as part of the CalNex campaign, provides an up-to-date characterization of the inorganic and black carbon fraction of the Los Angeles Basin particulate matter and a roadmap for what to address regarding potential causes of disagreement between predictions and observations. Future work will focus on characterizing the nature of organic aerosol formation and evolution in the Los Angeles Basin as well as the aforementioned topics.

Appendix A: Instrument Transmission Windows and Efficiencies

A1. SP2 Transmission Windows

SP2 measurements from the Twin Otter were used to generate histograms of single-particle BC mass between 80–675 nm (VED), which were then integrated to give bulk BC mass concentrations. Similarly, SP2 measurements from the P3 were used to generate histograms of single-particle BC mass between 95–720 nm (VED), which were then integrated to give bulk BC mass concentrations. Since aerosol mass-distributions in CMAQ are assumed to be log-normal, the following equation was used to modify the total predicted BC concentrations to match the transmission windows of the SP2:

$$\text{BC}(\text{D}_{p,min} < \text{D}_p < \text{D}_{p,max}) = \quad (\text{A1})$$

$$\begin{aligned} & \frac{\text{BC}_I}{2} \times \left[\text{erf} \left(\frac{\ln \left(\text{D}_{p,max}/\bar{D}_{pgV}^{I,dry} \right)}{\sqrt{2} \times \ln (\sigma_{I,dry})} \right) - \right. \\ & \quad \left. \text{erf} \left(\frac{\ln \left(\text{D}_{p,min}/\bar{D}_{pgV}^{I,dry} \right)}{\sqrt{2} \times \ln (\sigma_{I,dry})} \right) \right] \\ & + \frac{\text{BC}_J}{2} \times \left[\text{erf} \left(\frac{\ln \left(\text{D}_{p,max}/\bar{D}_{pgV}^{J,dry} \right)}{\sqrt{2} \times \ln (\sigma_{J,dry})} \right) - \right. \\ & \quad \left. \text{erf} \left(\frac{\ln \left(\text{D}_{p,min}/\bar{D}_{pgV}^{J,dry} \right)}{\sqrt{2} \times \ln (\sigma_{J,dry})} \right) \right] \end{aligned}$$

where $I, J, \text{D}_{p,min}, \text{D}_{p,max}, \bar{D}_{pgV}^{dry}, \sigma_{dry}$, and $\text{BC}, \text{BC}_I, \text{BC}_J$, and $\text{erf}()$ are the Aitken mode, the accumulation mode, the minimum SP2 detection limit, the maximum SP2 detection limit, the geometric mean diameter of the mass-distribution mode (not including water), the geometric standard deviation of the mass-distribution mode, the total BC mass comparable to SP2 measurements, the total BC mass in the Aitken mode, the total BC mass in the accumulation mode, and the error-function, respectively.

A2. AMS Transmission Efficiencies

The AMS transmission curve used in this study is piecewise defined for three diameter ranges: (a) linear increase in transmission vs $\ln(\text{D}_{va})$, from 0% at $\text{D}_{va} = 40$ nm to 100% at $\text{D}_{va} = 100$ nm, (b) 100% transmission from $\text{D}_{va} = 100$ nm up to $\text{D}_{va} = 550$ nm, (c) linear decrease in transmission vs $\ln(\text{D}_{va})$, from 100% at $\text{D}_{va} = 550$ nm to 0% at $\text{D}_{va} = 2 \mu\text{m}$, and zero elsewhere. This transmission curve can be applied analytically to any log-normal mass distribution:

40 nm < $\text{D}_{va} < 100$ nm:

$$f(\text{D}_{va}) = \frac{\ln(\text{D}_{va}/40\text{nm})}{\ln(100\text{nm}/40\text{nm})} \quad (\text{A2})$$

$$M(40\text{nm} < \text{D}_{va} < 100\text{nm}) = \quad (\text{A3})$$

$$\begin{aligned} & \frac{M_{\text{tot}}}{2} \times \frac{\ln(\bar{D}_{pgV}^{dry}/40\text{nm})}{\ln(100\text{nm}/40\text{nm})} \times \\ & \left[\text{erf} \left(\frac{\ln \left(100\text{nm}/\bar{D}_{pgV}^{dry} \right)}{\sqrt{2} \times \ln (\sigma_{dry})} \right) - \right. \\ & \quad \left. \text{erf} \left(\frac{\ln \left(40\text{nm}/\bar{D}_{pgV}^{dry} \right)}{\sqrt{2} \times \ln (\sigma_{dry})} \right) \right] + \\ & \frac{M_{\text{tot}}}{2} \times \frac{\ln(\sigma_{dry})}{\ln(100\text{nm}/40\text{nm}) \times \sqrt{\frac{\pi}{2}}} \times \\ & \left\{ \exp \left[- \left(\frac{\ln \left(40\text{nm}/\bar{D}_{pgV}^{dry} \right)}{\sqrt{2} \times \ln (\sigma_{dry})} \right)^2 \right] - \right. \\ & \quad \left. \exp \left[- \left(\frac{\ln \left(100\text{nm}/\bar{D}_{pgV}^{dry} \right)}{\sqrt{2} \times \ln (\sigma_{dry})} \right)^2 \right] \right\} \end{aligned}$$

100 nm < $\text{D}_{va} < 550$ nm:

$$f(\text{D}_{va}) = \frac{1}{\text{D}_{va} < 550\text{nm}} \quad (\text{A4})$$

$$M(100\text{nm} < \text{D}_{va} < 550\text{nm}) = \quad (\text{A5})$$

$$\begin{aligned} & \frac{M}{2} \times \left[\text{erf} \left(\frac{\ln \left(550\text{nm}/\bar{D}_{pgV}^{dry} \right)}{\sqrt{2} \times \ln (\sigma_{dry})} \right) - \right. \\ & \quad \left. \text{erf} \left(\frac{\ln \left(100\text{nm}/\bar{D}_{pgV}^{dry} \right)}{\sqrt{2} \times \ln (\sigma_{dry})} \right) \right] \end{aligned}$$

X - 10

550 nm < D_{va} < 2000 nm:

$$f(D_{va}) = \frac{\ln(D_{va}/550\text{nm})}{\ln(2000\text{nm}/550\text{nm})} \quad (\text{A6})$$

$$M(550\text{nm} < D_{va} < 2000\text{nm}) = \quad (\text{A7})$$

$$\begin{aligned} \frac{M_{\text{tot}}}{2} \times & \frac{\ln(\bar{D}_{pgV}^{dry}/2000\text{nm})}{\ln(550\text{nm}/2000\text{nm})} \times \\ & \left[\text{erf} \left(\frac{\ln(2000\text{nm}/\bar{D}_{pgV}^{dry})}{\sqrt{2} \times \ln(\sigma_{dry})} \right) - \right. \\ & \left. \text{erf} \left(\frac{\ln(550\text{nm}/\bar{D}_{pgV}^{dry})}{\sqrt{2} \times \ln(\sigma_{dry})} \right) \right] + \\ \frac{M_{\text{tot}}}{2} \times & \frac{\ln(\sigma_{dry})}{\ln(550\text{nm}/2000\text{nm}) \times \sqrt{\frac{\pi}{2}}} \times \\ & \left\{ \exp \left[- \left(\frac{\ln(550\text{nm}/\bar{D}_{pgV}^{dry})}{\sqrt{2} \times \ln(\sigma_{dry})} \right)^2 \right] - \right. \\ & \left. \exp \left[- \left(\frac{\ln(2000\text{nm}/\bar{D}_{pgV}^{dry})}{\sqrt{2} \times \ln(\sigma_{dry})} \right)^2 \right] \right\} \end{aligned}$$

where f is the transmission efficiency as a function of D_{va} , M_{tot} is the unmodified, total amount of predicted species mass (e.g. nitrate, sulfate, ammonium) in the mode, and $M(D_{va,min} < D_{va} < D_{va,max})$ is the modified amount of species mass, within the mode, in the given vacuum-aerodynamic diameter range. The vacuum-aerodynamic diameter limits of the AMS transmission curve are converted to particle (Stokes) diameters for each data point by using $D_p = (\frac{\rho_o}{\rho_{dry}})D_{va}$ [DeCarlo *et al.*, 2004], where D_p is the physical (Stokes) diameter of the particle, D_{va} is the vacuum-aerodynamic diameter, ρ_o is the standard density (1 g cm^{-3}), and ρ_{dry} is the density of the particle predicted by CMAQ not including water. The total mass from each mode (using this specific AMS transmission efficiency curve) is then:

$$\begin{aligned} M_{\text{mode}}^{\text{AMS}} = & M(40\text{nm} < D_{va} < 100\text{nm}) + \quad (\text{A8}) \\ & M(100\text{nm} < D_{va} < 550\text{nm}) + \\ & M(550\text{nm} < D_{va} < 2000\text{nm}) \end{aligned}$$

where $M_{\text{mode}}^{\text{AMS}}$ is the total amount of predicted species mass in the mode that has been adjusted to match the transmission curve of the AMS. The total amount of predicted species mass that should be compared to the AMS is then the sum of all three adjusted modes ($M = M_I^{\text{AMS}} + M_J^{\text{AMS}} + M_K^{\text{AMS}}$), where I, J, and K are the Aitken mode, the accumulation mode, and the coarse mode, respectively.

Acknowledgments. This work was funded by NOAA grant NA09OAR4310128 and by the State of California Air Resources Board (CARB) Agreement 10-328. NOAA's Climate and Air Quality programs supported the NOAA-P3 deployment. The authors would like to thank Nehzat Motallebi, Havaala O. T. Pye, and Andreas Zuent for useful discussions. The authors would also like to thank Ying Xie and Rob Pinder at the Environmental Protection Agency (EPA) for providing the SAPRC07TC chemical mechanism, and Anne Perring, Joshua Schwartz, and David Fahey for the use of their SP2 measurements from the NOAA P3 aircraft and for useful discussion. PLH and JLJ were supported

by CARB-319 and DOE (BER, ASR program) DE-SC0006035, and PLH acknowledges a CIRES Visiting Postdoctoral Fellowship. This work was supported in part by the NOAA Health of the Atmosphere Program and the NOAA Climate Goal. The statements and conclusions in this paper are those of the researchers (contractor) and not necessarily those of CARB. The mention of commercial products, their source, or their use in connection with material reported herein is not to be construed as actual or implied endorsement of such products.

References

Appel, B., Hoffer, E., Tokiwa, Y., and Kothny, E. (1982), Measurement of sulfuric-acid and particulate strong acidity in the Los-Angeles basin, *Atmos. Environ.*, **16**, 589–593, doi: 10.1016/0004-6981(82)90168-8.

Bahreini, R., Ervens, B., Middlebrook, A. M., Warneke, C., de Gouw, J. A., DeCarlo, P. F., Jimenez, J. L., Brock, C. A., Neuman, J. A., Ryerson, T. B., Stark, H., Atlas, E., Brioude, J., Fried, A., Holloway, J. S., Peischl, J., Richter, D., Walega, J., Weibring, P., Wollny, A. G., and Fehsenfeld, F. C. (2009), Organic aerosol formation in urban and industrial plumes near Houston and Dallas, Texas, *J. Geophys. Res.-Atmos.*, **114**, doi: 10.1029/2008JD011493.

Bein, K. J., Zhao, Y., Pekney, N. J., Davidson, C. I., Johnston, M. V., and Wexler, A. S.: Identification of sources of atmospheric PM at the Pittsburgh Supersite - Part II (2006), Quantitative comparisons of single particle, particle number, and particle mass measurements, *Atmos. Environ.*, **40**, S424–S444, doi:10.1016/j.atmosenv.2006.01.064.

Bein, I., Jacob, D., Yantosca, R., Logan, J., Field, B., Fiore, A., Li, Q., Liu, H., Mickley, L., and Schultz, M.: Global modeling of tropospheric chemistry with assimilated meteorology (2001), Model description and evaluation, *J. Geophys. Res.-Atmos.*, **106**, 23 073–23 095, doi:10.1029/2001JD000807.

Binkowski, F. and Roselle, S. (2003), Models-3 community multiscale air quality (CMAQ) model aerosol component - 1. Model description, *J. Geophys. Res.-Atmos.*, **108**, doi: 10.1029/2001JD001409.

Bond, T. and Bergstrom, R. (2006), Light absorption by carbonaceous particles: An investigative review, *Aerosol. Sci. Tech.*, **40**, 27–67, doi:10.1080/02786820500421521.

Brioude, J., Cooper, O. R., Feingold, G., Trainer, M., Freitas, S. R., Kowal, D., Ayers, J. K., Prins, E., Minnis, P., McKeen, S. A., Frost, G. J., and Hsie, E. Y. (2009), Effect of biomass burning on marine stratocumulus clouds off the California coast, *Atmos. Chem. Phys.*, **9**, 8841–8856.

Cabada, J., Rees, S., Takahama, S., Khlystov, A., Pandis, S., Davidson, C., and Robinson, A. (2004), Mass size distributions and size resolved chemical composition of fine particulate matter at the Pittsburgh supersite, *Atmos. Environ.*, **38**, 3127–3141, doi:10.1016/j.atmosenv.2004.03.004.

Canagaratna, M. R., Jayne, J. T., Jimenez, J. L., Allan, J. D., Alfarra, M. R., Zhang, Q., Onasch, T. B., Drewnick, F., Coe, H., Middlebrook, A., Delia, A., Williams, L. R., Trimborn, A. M., Northway, M. J., DeCarlo, P. F., Kolb, C. E., Davidovits, P., and Worsnop, D. R. (2007), Chemical and microphysical characterization of ambient aerosols with the aerodynamic aerosol mass spectrometer, *Mass Spectrom. Rev.*, **26**, 185–222, doi: 10.1002/mas.20115.

Capaldo, K., Pilinis, C., and Pandis, S. (2000), A computationally efficient hybrid approach for dynamic gas/aerosol transfer in air quality models, *Atmos. Environ.*, **34**, 3617–3627.

Carter, W. P. L. (2010), Development of a condensed SAPRC-07 chemical mechanism, *Atmos. Environ.*, **44**, 5336–5345, doi: 10.1016/j.atmosenv.2010.01.024, 2nd Biennial Conference on Atmospheric Chemistry Mechanisms, Air Quality Res Ctr, Davis, CA, DEC, 2008.

Chang, J., Brost, R., Isaksen, I., Madronich, S., Middleton, P., Stockwell, W., and Walcek, C. (1987), A 3-dimensional eulerian acid deposition model - physics concepts and formulation, *J. Geophys. Res.-Atmos.*, **92**, 14 681–14 700, doi: 10.1029/JD092iD12p14681.

Chow, J., Fujita, E., Watson, J., Lu, Z., Lawson, D., and Asbaugh, L. (1994), Evaluation of filter-based aerosol measurements during the 1987 Southern California Air-Quality Study, *Env. Monit. Assess.*, **30**, 49–80, doi:10.1007/BF00546199.

Clarke, A., Shinozuka, Y., Kapustin, V., Howell, S., Huebert, B., Doherty, S., Anderson, T., Covert, D., Anderson, J., Hua, X., Moore, K., McNaughton, C., Carmichael, G., and Weber, R. (2004), Size distributions and mixtures of dust and black carbon aerosol in Asian outflow: Physiochemistry and optical properties, *J. Geophys. Res.-Atmos.*, 109, doi: 10.1029/2003JD004378.

Croes, B. and Fujita, E. (2003), Overview of the 1997 Southern California Ozone Study (SCOS97-NARSTO), *Atmos. Environ.*, 37, S3–S26, doi:10.1016/S1352-2310(03)00379-0.

Dallmann, T., Harley, R., and Kirchstetter, T. (2011), Effects of Diesel Particle Filter Retrofits and Accelerated Fleet Turnover on Drayage Truck Emissions at the Port of Oakland, *Environ. Sci. Technol.*, 45,10773-10779, doi:10.1021/es202609q.

de Foy, B., Varela, J., Molina, L., and Molina, M. (2006), Rapid ventilation of the Mexico City basin and regional fate of the urban plume, *Atmos. Chem. Phys.*, 6, 2321–2335.

de Leeuw, G., Neele, F., Hill, M., Smith, M., and Vignali, E. (2000), Production of sea spray aerosol in the surf zone, *J. Geophys. Res.-Atmos.*, 105, 29 397–29 409, doi: 10.1029/2000JD900549.

DeCarlo, P., Slowik, J., Worsnop, D., Davidovits, P., and Jimenez, J. (2004), Particle morphology and density characterization by combined mobility and aerodynamic diameter measurements. Part 1: Theory, *Aerosol. Sci. Tech.*, 38, 1185–1205, doi:10.1080/027868290903907.

DeCarlo, P. F., Dunlea, E. J., Kimmel, J. R., Aiken, A. C., Sueper, D., Crounse, J., Wennberg, P. O., Emmons, L., Shinozuka, Y., Clarke, A., Zhou, J., Tomlinson, J., Collins, D. R., Knapp, D., Weinheimer, A. J., Montzka, D. D., Campos, T., and Jimenez, J. L. (2008), Fast airborne aerosol size and chemistry measurements above Mexico City and Central Mexico during the MILAGRO campaign, *Atmos. Chem. Phys.*, 8, 4027–4048.

Ding, A., Wang, T., Xue, L., Gao, J., Stohl, A., Lei, H., Jin, D., Ren, Y., Wang, X., Wei, X., Qi, Y., Liu, J., and Zhang, X. (2009), Transport of north China air pollution by midlatitude cyclones: Case study of aircraft measurements in summer 2007, *J. Geophys. Res.-Atmos.*, 114, doi: 10.1029/2008JD011023.

Docherty, K. S., Aiken, A. C., Huffman, J. A., Ulbrich, I. M., DeCarlo, P. F., Sueper, D., Worsnop, D. R., Snyder, D. C., Peltier, R. E., Weber, R. J., Grover, B. D., Eatough, D. J., Williams, B. J., Goldstein, A. H., Ziemann, P. J., and Jimenez, J. L. (2011), The 2005 Study of Organic Aerosols at Riverside (SOAR-1): instrumental intercomparisons and fine particle composition, *Atmos. Chem. Phys.*, 11, 12387–12420, doi: 10.5194/acp-11-12387-2011, 2011.

Dominguez, G., Jackson, T., Brothers, L., Barnett, B., Nguyen, B., and Thiemen, M. H. (2008), Discovery and measurement of an isotopically distinct source of sulfate in Earth's atmosphere, *Proc. Nat. Acad. Sci. USA*, 105, 12 769–12 773, doi: 10.1073/pnas.0805255105.

Drewnick, F., Hines, S., DeCarlo, P., Jayne, J., Gomis, M., Fuhrer, K., Weimer, S., Jimenez, J., Demerjian, K., Borrmann, S., and Worsnop, D. (2005), A new time-of-flight aerosol mass spectrometer (TOF-AMS) - Instrument description and first field deployment, *Aerosol. Sci. Tech.*, 39, 637–658, doi:10.1080/02786820500182040.

Dzepina, K., Volkamer, R. M., Madronich, S., Tulet, P., Ulbrich, I. M., Zhang, Q., Cappa, C. D., Ziemann, P. J., and Jimenez, J. L. (2009), Evaluation of recently-proposed secondary organic aerosol models for a case study in Mexico City, *Atmos. Chem. Phys.*, 9, 5681–5709, doi:10.5194/acp-9-5681-2009.

Elderding, A., Cass, G., and Moon, K. (1994), An air monitoring network using continuous particle-size distribution monitors - connecting pollutant properties to visibility via mie scattering calculations, *Atmos. Environ.*, 28, 2733–2749, doi: 10.1016/1352-2310(94)90445-6.

Ellis, R. A., Murphy, J. G., Pattie, E., van Haarlem, R., O'Brien, J. M., and Herndon, S. C. (2010), Characterizing a Quantum Cascade Tunable Infrared Laser Differential Absorption Spectrometer (QC-TILDAS) for measurements of atmospheric ammonia, *Atmos. Meas. Tech.*, 3, 397–406, doi:10.5194/amt-3-397-2010.

Fast, J., Aiken, A. C., Allan, J., Alexander, L., Campos, T., Canagaratna, M. R., Chapman, E., DeCarlo, P. F., de Foy, B., Gaffney, J., de Gouw, J., Doran, J. C., Emmons, L., Hodzic, A., Herndon, S. C., Huey, G., Jayne, J. T., Jimenez, J. L., Kleinman, L., Kuster, W., Marley, N., Russell, L., Ochoa, C., Onasch, T. B., Pekour, M., Song, C., Ulbrich, I. M., Warneke, C., Welsh-Bon, D., Wiedinmyer, C., Worsnop, D. R., Yu, X.-Y., and Zaveri, R. (2009), Evaluating simulated primary anthropogenic and biomass burning organic aerosols during MILAGRO: implications for assessing treatments of secondary organic aerosols, *Atmos. Chem. Phys.*, 9, 6191–6215, doi: 10.5194/acp-9-6191-2009.

Fast, J. D., Gustafson, Jr., W. I., Chapman, E. G., Easter, R. C., Rishel, J. P., Zaveri, R. A., Grell, G. A., and Barth, M. C. (2011), The Aerosol Modeling Testbed: A Community Tool to Objectively Evaluate Aerosol Process Modules, *Bull. Amer. Meteor. Soc.*, 92, 343–360, doi:10.1175/2010BAMS2868.1.

Foley, K. M., Roselle, S. J., Appel, K. W., Bhave, P. V., Pleim, J. E., Otte, T. L., Mathur, R., Sarwar, G., Young, J. O., Gilliam, R. C., Nolte, C. G., Kelly, J. T., Gilliland, A. B., and Bash, J. O. (2010), Incremental testing of the Community Multiscale Air Quality (CMAQ) modeling system version 4.7, *Geosci. Mod. Devel.*, 3, 205–226.

Fountoukis, C. and Nenes, A. (2007), ISORROPIA II: a computationally efficient thermodynamic equilibrium model for $K^+ + Ca^{2+} + Mg^{2+} + NH_4^+ + Na^+ + SO_4^{2-} + NO_3^- + Cl^- + H_2O$ aerosols, *Atmos. Chem. Phys.*, 7, 4639–4659.

Fountoukis, C., Nenes, A., Sullivan, A., Weber, R., Van Reken, T., Fischer, M., Matias, E., Moya, M., Farmer, D., and Cohen, R. C. (2009), Thermodynamic characterization of Mexico City aerosol during MILAGRO 2006, *Atmos. Chem. Phys.*, 9, 2141–2156.

Gong, S. (2003), A parameterization of sea-salt aerosol source function for sub- and super-micron particles, *Glo. Biogeochem. Cycles*, 17, doi:10.1029/2003GB002079.

Grell, G. A., Dudhia, J., and Stauffer, D. R. (1995), A description of the fifth-generation Penn State/NCAR mesoscale model (MM5). NCAR Technical Note NCAR/TN-398+STR, Note TN398 STR, p. 138.

Hegg, D., D. Covert, H. Jonsson, and P. Covert (2005), Determination of the transmission efficiency of an aircraft aerosol inlet, *Aerosol. Sci. Technol.*, 39(10), 966–971, doi: 10.1080/02786820500377814.

Hsu, S.-C., Liu, S. C., Kao, S.-J., Jeng, W.-L., Huang, Y.-T., Tseng, C.-M., Tsai, F., Tu, J.-Y., and Yang, Y. (2007), Water-soluble species in the marine aerosol from the northern South China Sea: High chloride depletion related to air pollution, *J. Geophys. Res.*, 112, D19304, doi:10.1029/2007JD008844.

Huang, M., Carmichael, G. R., Spak, S. N., Adhikary, B., Kulikarni, S., Cheng, Y., Wei, C., Tang, Y., D'Allura, A., Wennberg, P. O., Huey, G. L., Dibb, J. E., Jimenez, J. L., Cubison, M. J., Weinheimer, A. J., Kaduwela, A., Cai, C., Wong, M., Pierce, R. B., Al-Saadi, J. A., Streets, D. G., and Zhang, Q. (2011), Multi-scale modeling study of the source contributions to near-surface ozone and sulfur oxides levels over California during the ARCTAS-CARB period, *Atmos. Chem. Phys.*, 11, 3173–3194, doi:10.5194/acp-11-3173-2011.

Hughes, L., Allen, J., Salmon, L., Mayo, P., Johnson, R., and Cass, G. (2002), Evolution of nitrogen species air pollutants along trajectories crossing the Los Angeles area, *Environ. Sci. Technol.*, 36, 3928–3935, doi:10.1021/es0110630.

Ianniello, A., Spataro, F., Esposito, G., Allegrini, I., Hu, M., and Zhu, T. (2011), Chemical characteristics of inorganic ammonium salts in PM(2.5) in the atmosphere of Beijing (China), *Atmos. Chem. Phys.*, 11, 10 803–10 822, doi:10.5194/acp-11-10803-2011.

Jacob, D. J., Crawford, J. H., Maring, H., Clarke, A. D., Dibb, J. E., Emmons, L. K., Ferrare, R. A., Hostetler, C. A., Russell, P. B., Singh, H. B., Thompson, A. M., Shaw, G. E., McCauley, E., Pederson, J. R., and Fisher, J. A. (2010), The Arctic Research of the Composition of the Troposphere from Aircraft and Satellites (ARCTAS) mission: design, execution, and first results, *Atmos. Chem. Phys.*, 10, 5191–5212, doi:10.5194/acp-10-5191-2010.

Jayne, J., Leard, D., Zhang, X., Davidovits, P., Smith, K., Kolb, C., and Worsnop, D. (2000), Development of an aerosol mass spectrometer for size and composition analysis of submicron particles, *Aerosol. Sci. Tech.*, 33, 49–70, doi: 10.1080/027868200410840.

Jiang, W., Smyth, S., Giroux, E., Roth, H., and Yin, D. (2006), Differences between CMAQ fine mode particle and PM2.5 concentrations and their impact on model performance evaluation in the lower Fraser valley, *Atmos. Env.*, **40**, 4973–4985, doi: 10.1016/j.atmosenv.2005.10.069

Karydis, V. A., Tsimpidi, A. P., Fountoukis, C., Nenes, A., Zavalas, M., Lei, W., Molina, L. T., and Pandis, S. N. (2010), Simulating the fine and coarse inorganic particulate matter concentrations in a polluted megacity, *Atmos. Environ.*, **44**, 608–620, doi:10.1016/j.atmosenv.2009.11.023.

Kelly, J. T., Bhave, P. V., Nolte, C. G., Shankar, U., and Foley, K. M. (2010), Simulating emission and chemical evolution of coarse sea-salt particles in the Community Multiscale Air Quality (CMAQ) model, *Geosci. Mod. Devel.*, **3**, 257–273, doi: 10.5194/gmd-3-257-2010.

Knote, C., Brunner, D., Vogel, H., Allan, J., Asmi, A., Äijälä, M., Carbone, S., van der Gon, H. D., Jimenez, J. L., Kiendler-Scharr, A., Mohr, C., Poulain, L., Prévôt, A. S. H., Swietlicki, E., and Vogel, C. (2011), Towards an online-coupled chemistry-climate model: evaluation of trace gases and aerosols in COSMO-ART, *Geosci. Model Dev.*, **4**, 1077–1102, doi:10.5194/gmd-4-1077-2011.

Lee, S. H., Kim, S. W., Angevine, W. M., Bianco, L., McKeen, S. A., Senff, C. J., Trainer, M., Tucker, S. C., and Zamora, R. J. (2011), Evaluation of urban surface parameterizations in the WRF model using measurements during the Texas Air Quality Study 2006 field campaign, *Atmos. Chem. Phys.*, **11**, 2127–2143, doi:10.5194/acp-11-2127-2011.

Lin, M., Fiore, A. M., Horowitz, L. W., Cooper, O. R., Naik, V., Holloway, J., Johnson, B. J., Middlebrook, A. M., Oltmans, S. J., Pollack, I. B., Ryerson, T. B., Warner, J. X., Wiedinmyer, C., Wilson, J., and Wyman, B. (2012), Transport of Asian ozone pollution into surface air over the western United States in spring, *J. Geophys. Res.-Atmos.*, **117**, doi: 10.1029/2011JD016961.

Liu, D., Prather, K., and Hering, S. (2000), Variations in the size and chemical composition of nitrate-containing particles in Riverside, CA, *Aerosol. Sci. Tech.*, **33**, 71–86, doi: 10.1080/027868200410859.

Lu, R. and Turco, R. (1995), Air Pollutant Transport in a Coastal Environment -II. 3-Dimensional Simulations Over Los-Angeles Basin, *Atmos. Environ.*, **29**, 14991518, doi:10.1016/1352-2310(95)00015-Q.

Luke, W. T. (1997), Evaluation of a commercial pulsed fluorescence detector for the measurement of low-level SO₂ concentrations during GASIE. *J. Geophys. Res.* **102**, 16, 25516, doi: 10.1029/96JD03347.

Matsui, H., Koike, M., Kondo, Y., Takegawa, N., Kita, K., Miyazaki, Y., Hu, M., Chang, S. Y., Blake, D. R., Fast, J. D., Zaveri, R. A., Streets, D. G., Zhang, Q., and Zhu, T. (2009), Spatial and temporal variations of aerosols around Beijing in summer 2006: Model evaluation and source apportionment, *J. Geophys. Res.-Atmos.*, **114**, doi:10.1029/2008JD010906.

McKeen, S., Grell, G., Peckham, S., Wilczak, J., Djalalova, I., Hsie, E. Y., Frost, G., Peischl, J., Schwar, J., Spackman, R., Holloway, J., de Gouw, J., Warneke, C., Gong, W., Bouchet, V., Gaudreault, S., Racine, J., McHenry, J., McQueen, J., Lee, P., Tang, Y., Carmichael, G. R., and Mathur, R. (2009), An evaluation of real-time air quality forecasts and their urban emissions over eastern Texas during the summer of 2006 Second Texas Air Quality Study field study, *J. Geophys. Res.-Atmos.*, **114**, doi:10.1029/2008JD011697.

Metcalf, A. R., J. S. Craven, J. J. Ensberg, J. Brioude, W. M. M. Angevine, A. Sorooshian, H. T. Duong, H. H. Jonsson, R. C. Flagan, and J. H. Seinfeld (2012), Black carbon aerosol over the Los Angeles Basin during CalNex, *J. Geophys. Res.*, **117**, doi:10.1029/2011JD017255.

Middlebrook, A. M., Bahreini, R., Jimenez, J. L., and Canagaratna, M. R. (2012), Evaluation of Composition-Dependent Collection Efficiencies for the Aerodyne Aerosol Mass Spectrometer using Field Data, *Aerosol. Sci. Tech.*, **46**, 258–271, doi:10.1080/02786826.2011.620041.

Modey, W., Eatough, D., Anderson, R., Martello, D., Takahama, S., Lucas, L., and Davidson, C. (2004), Ambient fine particulate concentrations and chemical composition at two sampling sites in metropolitan Pittsburgh: a 2001 intensive summer study, *Atmos. Environ.*, **38**, 3165–3178, doi: 10.1016/j.atmosenv.2004.03.005.

Molina, L. T., Madronich, S., Gaffney, J. S., Apel, E., de Foy, B., Fast, J., Ferrare, R., Herndon, S., Jimenez, J. L., Lamb, B., Osornio-Vargas, A. R., Russell, P., Schauer, J. J., Stevens, P. S., and Zavala, M. (2010), An overview of the MILAGRO 2006 Campaign: Mexico City emissions and their transport and transformation, *Atmos. Chem. Phys.*, **10**, 8697–8760, doi: 10.5194/acp-10-8697-2010.

Moteki, N., Kondo, Y., Miyazaki, Y., Takegawa, N., Komazaki, Y., Kurata, G., Shirai, T., Blake, D. R., Miyakawa, T., and Koike, M. (2007), Evolution of mixing state of black carbon particles: Aircraft measurements over the western Pacific in March 2004, *Geophys. Res. Lett.*, **34**, doi: 10.1029/2006GL028943.

Münkel, C., E. Noora, J. Räsänen, and A. Karppinen (2006), Retrieval of mixing height and dust concentration with lidar ceilometer, *Bound.-Lay. Meteorol.*, doi:10.1007/s10546-006-9103-3.

Murphy, S. M., Agrawal, H., Sorooshian, A., Padro, L. T., Gates, H., Hersey, S., Welch, W. A., Jung, H., Miller, J. W., Cocker, III, D. R., Nenes, A., Jonsson, H. H., Flagan, R. C., and Seinfeld, J. H. (2009), Comprehensive Simultaneous Shipboard and Airborne Characterization of Exhaust from a Modern Container Ship at Sea, *Environ. Sci. Technol.*, **43**, 4626–4640, doi: 10.1021/es802413j.

Nehrkorn, T., Eluszkiewicz, J., Wofsy, S. C., Lin, J. C., Gerbig, C., Longo, M., and Freitas, S. (2010): Coupled weather research and forecasting-stochastic time-inverted lagrangian transport (WRF-STILT) model, *Met. Atmos. Phys.*, **107**, 51–64, doi:10.1007/s00703-010-0068-x.

Neuman, J., Huey, L., Dissly, R., Fehsenfeld, F., Flocke, F., Holecek, J., Holloway, J., Hubler, G., Jakoubek, R., Nicks, D., Parrish, D., Ryerson, T., Sueper, D., and Weinheimer, A. (2002), Fast-response airborne in situ measurements of HNO₃ during the Texas 2000 Air Quality Study, *J. Geophys. Res.-Atmos.*, **107**, doi:10.1029/2001JD001437.

Neuman, J., Nowak, J., Brock, C., Trainer, M., Fehsenfeld, F., Holloway, J., Hubler, G., Hudson, P., Murphy, D., Nicks, D., Orsini, D., Parrish, D., Ryerson, T., Sueper, D., Sullivan, A., and Weber, R. (2003), Variability in ammonium nitrate formation and nitric acid depletion with altitude and location over California, *J. Geophys. Res.-Atmos.*, **108**, doi: 10.1029/2003JD003616.

Neuman, J. A., Trainer, M., Aikin, K. C., Angevine, W. M., Brioude, J., Brown, S. S., de Gouw, J. A., Dube, W. P., Flynn, J. H., Graus, M., Holloway, J. S., Lefer, B. L., Nedelec, P., Nowak, J. B., Parrish, D. D., Pollack, I. B., Roberts, J. M., Ryerson, T. B., Smit, H., Thouret, V., and Wagner, N. L. (2012), Observations of ozone transport from the free troposphere to the Los Angeles basin, *J. Geophys. Res.-Atmos.*, **117**, doi:10.1029/2011JD016919.

Nolte, C. G., Bhave, P. V., Arnold, J. R., Dennis, R. L., Zhang, K. M., and Wexler, A. S. (2008), Modeling urban and regional aerosols - Application of the CMAQ-UCD Aerosol Model to Tampa, a coastal urban site, *Atmos. Environ.*, **42**, 3179–3191, doi:10.1016/j.atmosenv.2007.12.059.

Nowak, J. B., Neuman, J. A., Bahreini, R., Brock, C. A., Middlebrook, A. M., Wollny, A. G., Holloway, J. S., Peischl, J., Ryerson, T. B., and Fehsenfeld, F. C. (2010), Airborne observations of ammonia and ammonium nitrate formation over Houston, Texas, *J. Geophys. Res.-Atmos.*, **115**, doi:10.1029/2010JD014195.

Nowak, J. B., J. A. Neuman, R. Bahreini, A. M. Middlebrook, J. S. Holloway, S. A. McKeen, D. D. Parrish, T. B. Ryerson, and M. K. Trainer (2012), Ammonia sources in the California South Coast Air Basin and their impact on ammonium nitrate formation, *J. Geophys. Res.-Lett.*, **39**, doi: 10.1029/2012GL051197.

Olivier, J.G.J. and J.J.M. Berdowski (2001), Global emissions sources and sinks. In: Berdowski, J., Guicherit, R. and B.J. Heij (eds.) The Climate System, pp. 33–78. A. A. Balkema Publishers/Swets and Zeitlinger Publishers, Lisse, The Netherlands, 2001.

Palau, J., Perez-Landa, G., Melia, J., Segarra, D., and Millan, M. (2006), A study of dispersion in complex terrain under winter conditions using high-resolution mesoscale and Lagrangian particle models, *Atmos. Chem. Phys.*, **6**, 1105–1134.

Park, R., Jacob, D., Field, B., Yantosca, R., and Chin, M.: Natural and transboundary pollution influences on sulfate-nitrate-ammonium aerosols in the United States (2004), Implications for policy, *J. Geophys. Res.-Atmos.*, **109**, doi:10.1029/2003JD004473.

Parrish, D. D., Allen, D. T., Bates, T. S., Estes, M., Fehsenfeld, F. C., Feingold, G., Ferrare, R., Hardesty, R. M., Meagher, J. F., Nielsen-Gammon, J. W., Pierce, R. B., Ryerson, T. B., Seinfeld, J. H., and Williams, E. J. (2009), Overview of the Second Texas Air Quality Study (TexAQS II) and the Gulf of Mexico Atmospheric Composition and Climate Study (GoMACCS), *J. Geophys. Res.-Atmos.*, **114**, doi:10.1029/2009JD011842.

Pastor, S., Allen, J., Hughes, L., Bhave, P., Cass, G., and Prather, K. (2003), Ambient single particle analysis in Riverside, California by aerosol time-of-flight mass spectrometry during the SCOS97-NARSTO, *Atmos. Environ.*, **37**, S239–S258, doi:10.1016/S1352-2310(03)00393-5.

Paulot, F., Crounse, J. D., Kjaergaard, H. G., Kroll, J. H., Seinfeld, J. H., and Wennberg, P. O. (2009a), Isoprene photooxidation: new insights into the production of acids and organic nitrates, *Atmos. Chem. Phys.*, **9**, 1479–1501.

Paulot, F., Crounse, J. D., Kjaergaard, H. G., Kuerten, A., St Clair, J. M., Seinfeld, J. H., and Wennberg, P. O. (2009b), Unexpected Epoxide Formation in the Gas-Phase Photooxidation of Isoprene, *Science*, **325**, 730–733, doi:10.1126/science.1172910.

Pekney, N. J., Davidson, C. I., Bein, K. J., Wexler, A. S., and Johnston, M. V.: Identification of sources of atmospheric PM at the Pittsburgh Supersite, Part I (2006), Single particle analysis and filter-based positive matrix factorization, *Atmos. Environ.*, **40**, S411–S423, doi:10.1016/j.atmosenv.2005.12.072.

Pfister, G. G., Parrish, D. D., Worden, H., Emmons, L. K., Edwards, D. P., Wiedinmyer, C., Diskin, G. S., Huey, G., Oltmans, S. J., Thouret, V., Weinheimer, A., and Wisthaler, A. (2011), Characterizing summertime chemical boundary conditions for airmasses entering the US West Coast, *Atmos. Chem. Phys.*, **11**, 1769–1790, doi:10.5194/acp-11-1769-2011.

Pueschel, R. F., D. F. Blake, K. G. Snetsinger, A. D. A. Hansen, S. Verma, and K. Kato (1992), Black carbon (soot) aerosol in the lower stratosphere and upper troposphere, *Geophys. Res. Lett.*, **19**(16), 1659–1662, doi:10.1029/92GL02478.

Pun, B. K., Seigneur, C., Bailey, E. M., Gautney, L. L., Douglas, S. G., Haney, J. L., and Kumar, N. (2008), Response of atmospheric particulate matter to changes in precursor emissions: A comparison of three air quality models, *Environ. Sci. Technol.*, **42**, 831–837, doi:10.1021/es702333d.

Querol, X., Pey, J., Minguillon, M. C., Perez, N., Alastuey, A., Viana, M., Moreno, T., Bernabe, R. M., Blanco, S., Cardenas, B., Vega, E., Sosa, G., Escalona, S., Ruiz, H., and Artinano, B. (2008), PM speciation and sources in Mexico during the MILAGRO-2006 Campaign, *Atmos. Chem. Phys.*, **8**, 111–128.

Ramanathan, V., and Carmichael, G. (2008), Global and regional climate changes due to black carbon, *Nat. Geosci.*, **1**, 221–227, doi:10.1038/ngeo156.

Renner, E. and Wolke, R. (2010), Modelling the formation and atmospheric transport of secondary inorganic aerosols with special attention to regions with high ammonia emissions, *Atmos. Environ.*, **44**, 1904–1912, doi:10.1016/j.atmosenv.2010.02.018.

Roberts, J. M., Veres, P., Warneke, C., Neuman, J. A., Washenfelder, R. A., Brown, S. S., Baasandorj, M., Burkholder, J. B., Burling, I. R., Johnson, T. J., Yokelson, R. J., de Gouw, J. (2010), Measurement of HONO, HNCO, and other inorganic acids by negative-ion proton-transfer chemical-ionization mass spectrometry (NI-PT-CIMS): Application to biomass burning emissions, *Atmos. Meas. Tech.*, **3**, 981–990, doi:10.5194/amt-3-981-2010.

Salcedo, D., Onasch, T., Dzepina, K., Canagaratna, M., Zhang, Q., Huffman, J., DeCarlo, P., Jayne, J., Mortimer, P., Worsnop, D., Kolb, C., Johnson, K., Zuberi, B., Marr, L., Volkamer, R., Molina, L., Molina, M., Cardenas, B., Bernabe, R., Marquez, C., Gaffney, J., Marley, N., Laskin, A., Shutthanandan, V., Xie, Y., Brune, W., Leshner, R., Shirley, T., and Jimenez, J. (2006), Characterization of ambient aerosols in Mexico City during the MCMA-2003 campaign with Aerosol Mass Spectrometry: results from the CENICA Supersite, *Atmos. Chem. Phys.*, **6**, 925–946.

Sarwar, G. and Bhave, P. V. (2007), Modeling the effect of chlorine emissions on ozone levels over the eastern United States, *J. Appl. Met. Clim.*, **46**, 1009–1019, doi:10.1175/JAM2519.1.

Schwarz, J. P., Gao, R. S., Fahey, D. W., Thomson, D. S., Watts, L. A., Wilson, J. C., Reeves, J. M., Darbeheshti, M., Baumgardner, D. G., Kok, G. L., Chung, S. H., Schulz, M., Hendricks, J., Lauer, A., Kaercher, B., Slowik, J. G., Rosenlof, K. H., Thompson, T. L., Langford, A. O., Loewenstein, M., and Aikin, K. C. (2006), Single-particle measurements of mid-latitude black carbon and light-scattering aerosols from the boundary layer to the lower stratosphere, *J. Geophys. Res.-Atmos.*, **111**, doi:10.1029/2006JD007076.

Schwarz, J. P., Spackman, J. R., Fahey, D. W., Gao, R. S., Lohmann, U., Stier, P., Watts, L. A., Thomson, D. S., Lack, D. A., Pfister, L., Mahoney, M. J., Baumgardner, D., Wilson, J. C., and Reeves, J. M. (2008), Coatings and their enhancement of black carbon light absorption in the tropical atmosphere, *J. Geophys. Res.-Atmos.*, **113**, doi:10.1029/2007JD009042.

Seinfeld, J. and Pandis, S. (2006), *Atmospheric chemistry and physics: from air pollution to climate change* (Second Edition), John Wiley and Sons, Inc.

Stephens, M., Turner, N., and Sandberg, J. (2003), Particle identification by laser-induced incandescence in a solid-state laser cavity, *Appl. Optics.*, **42**, 3726–3736, doi:10.1364/AO.42.003726.

Stohl, A., Forster, C., Frank, A., Seibert, P., and Wotawa, G. (2005), Technical note: The Lagrangian particle dispersion model FLEXPART version 6.2, *Atmos. Chem. Phys.*, **5**, 2461–2474.

Turpin, B. and Huntzicker, J. (1991), Secondary formation of organic aerosol in the Los Angeles Basin - A descriptive analysis of organic and elemental carbon concentrations, *Atmos. Environ.*, **25**, 207–215, doi:10.1016/0960-1686(91)90291-E.

van Pinxteren, D., Brueggemann, E., Gnauk, T., Iinuma, Y., Mueller, K., Nowak, A., Achtert, P., Wiedensohler, A., and Herrmann, H. (2009), Size- and time-resolved chemical particle characterization during CAREBeijing-2006: Different pollution regimes and diurnal profiles, *J. Geophys. Res.-Atmos.*, **114**, doi:10.1029/2008JD010890.

Walcek, C. and Taylor, G. (1986), A theoretical method for computing vertical distributions of acidity and sulfate production within cumulus clouds, *J. Atmos. Sci.*, **43**, 339–355, doi:10.1175/1520-0469(1986)043<0339:ATMFCA>2.0.CO;2.

Washenfelder, R. A., Trainer, M., Frost, G. J., Ryerson, T. B., Atlas, E. L., de Gouw, J. A., Flocke, F. M., Fried, A., Holloway, J. S., Parrish, D. D., Peischl, J., Richter, D., Schauffler, S. M., Walega, J. G., Warneke, C., Weibring, P., and Zheng, W. (2010), Characterization of NO(x), SO(2), ethene, and propene from industrial emission sources in Houston, Texas, *J. Geophys. Res.-Atmos.*, **115**, doi:10.1029/2009JD013645.

Watson, J., Chow, J., LU, Z., Fujita, E., Lowenthal, D., Lawson, D., and Ashbaugh, L. (1994), Chemical mass-balance source apportionment of pm(10) during the Southern California air-quality study, *Aerosol. Sci. Tech.*, **21**, 1–36, doi:10.1080/02786829408959693.

Wittig, A., Anderson, N., Khlystov, A., Pandis, S., Davidson, C., and Robinson, A. (2004), Pittsburgh air quality study overview, *Atmos. Environ.*, **38**, 3107–3125, doi:10.1016/j.atmosenv.2004.03.003.

Yue, D., Hu, M., Wu, Z., Wang, Z., Guo, S., Wehner, B., Nowak, A., Achtert, P., Wiedensohler, A., Jung, J., Kim, Y. J., and Liu, S. (2009), Characteristics of aerosol size distributions and new particle formation in the summer in Beijing, *J. Geophys. Res.-Atmos.*, **114**, doi:10.1029/2008JD010894.

Yue, D. L., Hu, M., Zhang, R. Y., Wang, Z. B., Zheng, J., Wu, Z. J., Wiedensohler, A., He, L. Y., Huang, X. F., and Zhu, T. (2010), The roles of sulfuric acid in new particle formation and growth in the mega-city of Beijing, *Atmos. Chem. Phys.*, **10**, 4953–4960, doi:10.5194/acp-10-4953-2010.

Zhang, H. and Ying, Q. (2010), Source apportionment of airborne particulate matter in Southeast Texas using a source-oriented 3D air quality model, *Atmos. Environ.*, **44**, 3547–3557, doi:10.1016/j.atmosenv.2010.06.004.

Zhang, J., Chameides, W., Weber, R., Cass, G., Orsini, D., Edgerton, E., Jongejan, P., and Slanina, J.: An evaluation of the thermodynamic equilibrium assumption for fine particulate composition (2002), Nitrate and ammonium during the 1999 Atlanta Supersite Experiment, *J. Geophys. Res.-Atmos.*, **108**, doi:10.1029/2001JD001592.

X - 14

Zheng, J., Hu, M., Zhang, R., Yue, D., Wang, Z., Guo, S., Li, X., Bohn, B., Shao, M., He, L., Huang, X., Wiedensohler, A., and Zhu, T. (2011), Measurements of gaseous H₂SO₄(4) by AP-ID-CIMS during CAREBeijing 2008 Campaign, *Atmos. Chem. Phys.*, 11, 7755–7765, doi:10.5194/acp-11-7755-2011.

Table 1. Statistical metrics based on measurements and predictions at the Pasadena ground site during May 2010.

Parameter	N	ME	MB	NME	NMB
PBL Height (m)	1179	210.39	16.69	0.37	0.08
Temperature (k)	24697	4.43	4.01		
RH (%)	24697	21.24	-19.40		
SO_4^{2-} ($\mu\text{g m}^{-3}$)	1860	0.93	-0.36	0.44	-0.17
NO_3^- ($\mu\text{g m}^{-3}$)	1860	2.15	-1.50	0.72	-0.50
NH_4^+ ($\mu\text{g m}^{-3}$)	1860	1.07	-0.76	0.35	-0.25
SO_2 (ppbv)	22491	0.72	0.64	2.50	2.01
HNO_3 (ppbv)	22761	0.98	-0.38	0.85	-0.38
NH_3 (ppbv)	366	1.51	0.45	0.74	0.22

ME = Mean Error, MB = Mean Bias, NME = Normalized Mean Error, NMB = Normalized Mean Bias. N is the number of data points collected during May 2010.

Table 2. Statistical metrics based on measured and predicted temperature and relative humidity for Twin Otter and P3 flights during May 2010.

Flight Date	N	ME [°C]	MB [°C]
Temperature (Twin Otter)			
21	189	3.89	3.88
24	167	3.33	3.32
25	334	2.21	2.21
27	219	1.55	-1.23
28	239	0.75	-0.23
Temperature (P3)			
4	17219	2.12	0.60
8	25439	2.10	1.60
14	22258	3.77	3.33
16	27899	2.17	0.92
19	24239	1.67	0.71
Flight Date	N	ME [%]	MB [%]
Relative Humidity (Twin Otter)			
21	189	26.65	-26.60
24	167	9.99	-9.13
25	334	5.76	-5.12
27	219	10.52	5.67
28	239	7.16	-0.33
Relative Humidity (P3)			
4	17219	12.28	-0.47
8	25439	14.58	-1.00
14	22258	24.85	-22.13
16	27899	16.11	-7.91
19	24239	8.89	-2.49

ME = Mean Error, MB = Mean Bias. N is the number of data points collected during a given flight.

Table 3. Statistical metrics based on measured and predicted wind magnitudes and directions for Twin Otter and P3 flights during May 2010.

Flight Date	N	ME [m/s]	MB [m/s]	NME	NMB
Wind Magnitudes (Twin Otter)					
21	180	1.89	1.19	0.38	0.23
24	167	1.79	-0.61	0.36	-0.12
25	334	1.89	0.49	0.37	0.10
27	219	2.04	0.98	0.56	0.27
28	239	2.00	2.11	0.55	0.52
Wind Magnitudes (P3)					
4	17219	2.33	-0.48	0.48	-0.10
8	25439	2.15	1.06	0.27	0.14
14	22258	1.69	0.57	0.55	0.19
16	27899	2.10	-0.26	0.41	-0.05
19	24239	4.03	-2.63	0.48	-0.31
Flight Date	N	ME [deg]	$\bar{\theta}_{obs}$ [deg]	$\bar{\theta}_{mod}$ [deg]	
Wind Directions (Twin Otter)					
21	180	23.79	241.51	254.01	
24	167	40.68	228.16	252.86	
25	334	28.75	209.34	222.78	
27	219	36.94	225.17	242.22	
28	239	22.53	240.49	245.71	
Wind Directions (P3)					
4	17219	64.02	263.26	238.74	
8	25439	24.24	263.21	275.67	
14	22258	65.09	203.37	205.56	
16	27899	54.46	223.77	229.74	
19	24239	25.16	277.69	267.41	

ME = Mean Error, MB = Mean Bias, NME = Normalized Mean Error, NMB = Normalized Mean Bias, and $\bar{\theta}$ = average wind direction. N is the number of data points collected during a given flight. The wind directions θ_{obs} and θ_{mod} are the observed and modeled wind directions, respectively, in units of degrees ($0^\circ \leq \theta \leq 360^\circ$). Wind direction, θ , is defined as the direction from which the wind is blowing, and is measured in degrees clockwise from true north.

Table 4. Statistical metrics based on measured and predicted black carbon concentrations for Twin Otter flights and P3 flights during May 2010.

Flight Date	N	ME [$\mu\text{g m}^{-3}$]	MB [$\mu\text{g m}^{-3}$]	NME	NMB
Black Carbon (Twin Otter)					
21	14631	0.189	0.168	1.268	1.113
24	13640	0.080	0.074	1.178	1.097
25	14620	0.090	0.081	0.889	0.804
27	13434	0.107	0.096	0.953	0.859
28	14160	0.102	0.090	0.835	0.743
Black Carbon (P3)					
4	17219	0.056	0.031	0.759	0.410
8	25439	0.082	0.063	1.083	0.835
14	22258	0.121	0.079	0.980	0.635
16	27899	0.103	0.098	1.417	1.356
19	24239	0.068	-0.011	0.500	-0.083

ME = Mean Error, MB = Mean Bias, NME = Normalized Mean Error, NMB = Normalized Mean Bias. N is the number of data points collected during a given flight.

Table 5. Relative contributions to predicted sulfate concentrations at the Pasadena ground site averaged over 15-30 May 2010.

Sulfate Pathway	Predicted contribution (%)
Boundary inflow	26
Aq, O ₃	6
Aq, H ₂ O ₂	29
Aq, O ₂ (FEMN)	4
Gas, OH	7
Primary SO ₄ ²⁻	28

“Boundary inflow” refers to sulfate attributable to boundary conditions, “(Aq, Gas), OX” refers to secondary sulfate produced by aqueous-phase (Aq) or gas-phase (Gas) oxidation of SO₂ by oxidant OX. “Primary SO₄²⁻” refers to sulfate emitted within the basin. “FEMN” refers to catalysts Fe³⁺ and Mn²⁺

Table 6. Statistical metrics based on measured and predicted particulate sulfate, ammonium, and nitrate concentrations for Twin Otter and P3 flights during May 2010.

Twin Otter		P3									
		Flight Date	N	ME [$\mu\text{g m}^{-3}$]	MB [$\mu\text{g m}^{-3}$]	NME	NMB	Flight Data	N	ME [$\mu\text{g m}^{-3}$]	MB [$\mu\text{g m}^{-3}$]
Sulfate											
21	185	1.30	1.30	2.68	2.68	4	1722	0.26	0.24	0.79	0.71
24	172	0.28	0.27	0.84	0.82	8	2544	0.41	0.20	0.65	0.32
25	337	0.39	0.39	1.11	1.11	14	2226	0.47	0.16	0.59	0.20
27	224	0.50	0.44	0.62	0.55	16	2790	0.33	0.00	0.33	0.00
28	244	0.53	0.46	0.77	0.65	19	2424	0.20	0.02	0.33	0.02
Ammonium											
21	185	0.92	-0.77	0.62	-0.52	4	1722	0.23	-0.11	0.77	-0.36
24	172	0.29	-0.14	0.68	-0.33	8	2544	0.27	-0.17	0.65	-0.42
25	337	0.54	-0.51	0.60	-0.56	14	2226	0.33	-0.15	0.64	-0.28
27	224	0.59	-0.47	0.46	-0.36	16	2790	0.47	-0.38	0.65	-0.52
28	244	0.42	-0.20	0.46	-0.22	19	2424	0.70	-0.65	0.71	-0.65
Nitrate											
21	185	1.64	-1.47	0.73	-0.65	4	1722	0.50	-0.31	0.99	-0.62
24	172	0.80	-0.50	0.84	-0.52	8	2544	0.51	-0.38	0.93	-0.68
25	337	1.17	-0.94	0.72	-0.58	14	2226	0.62	-0.37	0.91	-0.55
27	224	1.24	-0.85	0.52	-0.35	16	2790	0.94	-0.77	0.94	-0.76
28	244	0.93	-0.37	0.61	-0.24	19	2424	2.03	-1.99	0.80	-0.78

Table 7. Statistical metrics based on measured and predicted ammonia and nitric acid mixing ratios for P3 flights during May 2010.

P3						
Flight Date	N	ME [ppbv]	MB [ppbv]	NME	NMB	
Nitric Acid						
4	17219	0.92	-0.54	0.46	-0.27	
8	25439	0.86	0.15	0.56	0.09	
14	22258	2.50	2.32	1.96	1.82	
16	27899	0.60	0.09	0.41	0.06	
19	24239	0.96	-0.31	0.46	-0.15	
Ammonia						
4	17219	2.96	-2.00	0.81	-0.55	
8	25439	3.37	-3.00	0.98	-0.60	
14	22258	3.80	-3.11	0.72	-0.59	
16	27899	2.78	-2.05	0.86	-0.63	
19	24239	12.38	-12.31	0.91	-0.90	
Ammonia (no dairy)						
4	17219	1.39	-0.15	0.78	-0.09	
8	25439	2.17	-1.98	0.60	-0.55	
14	22258	1.25	-0.83	0.47	-0.31	
16	27899	0.82	-0.34	0.77	-0.32	
19	24239	2.80	-2.73	0.67	-0.68	

Statistical metrics based on ammonia measurements in the “no dairy” column are calculated excluding all data points east of longitude 117.7°W.

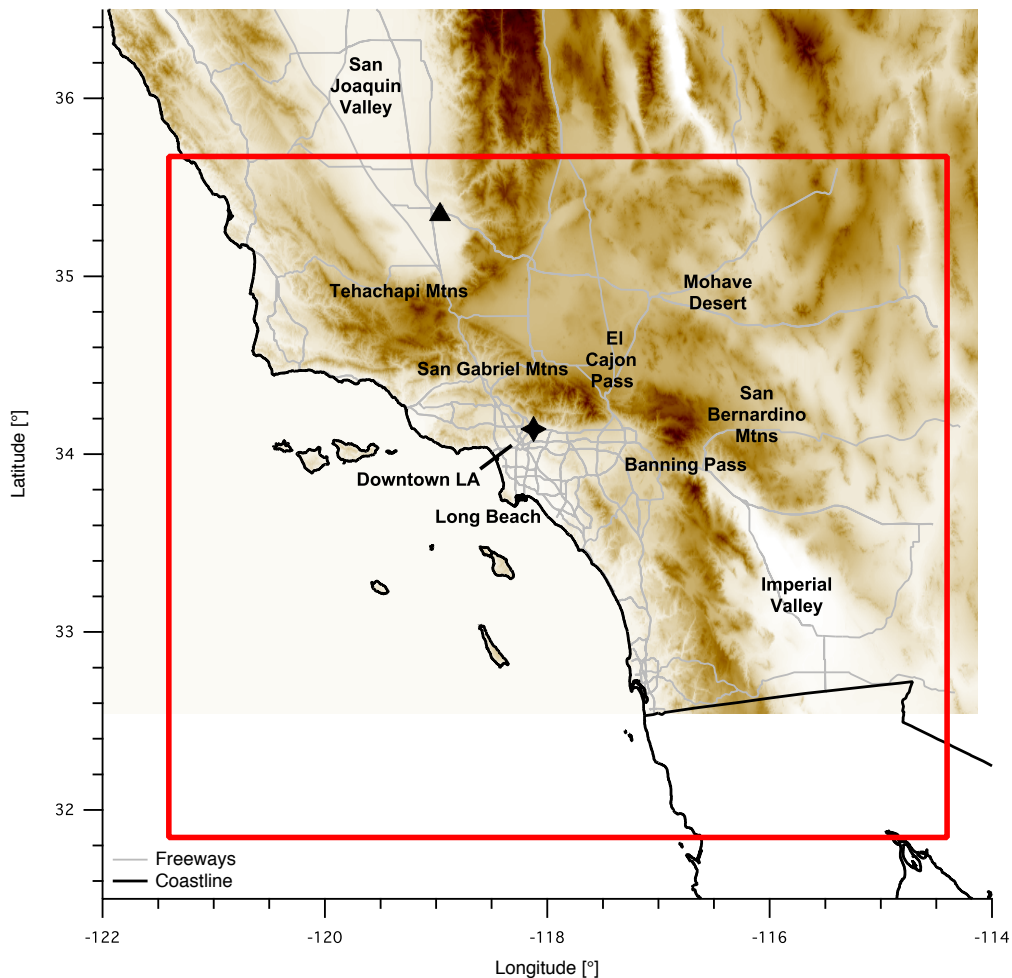


Figure 1. CMAQ modeling domain (red line) used for simulations during the CalNex Field Campaign. The domain covers the area from (31.83°N, 121.43°W) to (35.69°N, 114.43°W) with 4 km x 4 km horizontal grid cells (102 x 156 grid points). The star represents the Pasadena ground site and the triangle represents Bakersfield.

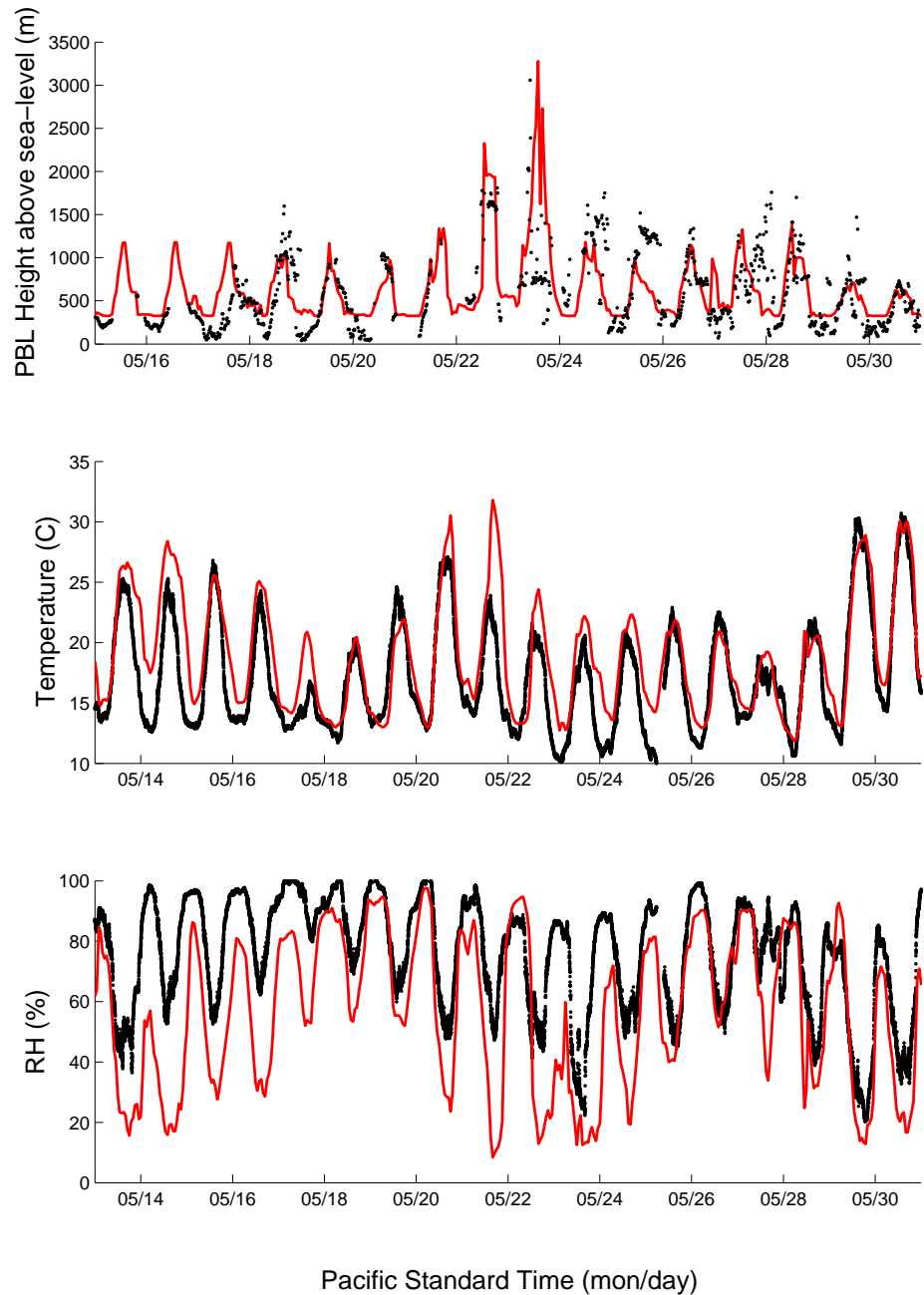


Figure 2. Observed (black) and predicted (red) planetary boundary layer (PBL) heights, temperature, and relative humidity (RH) from the Pasadena ground site.

X - 24

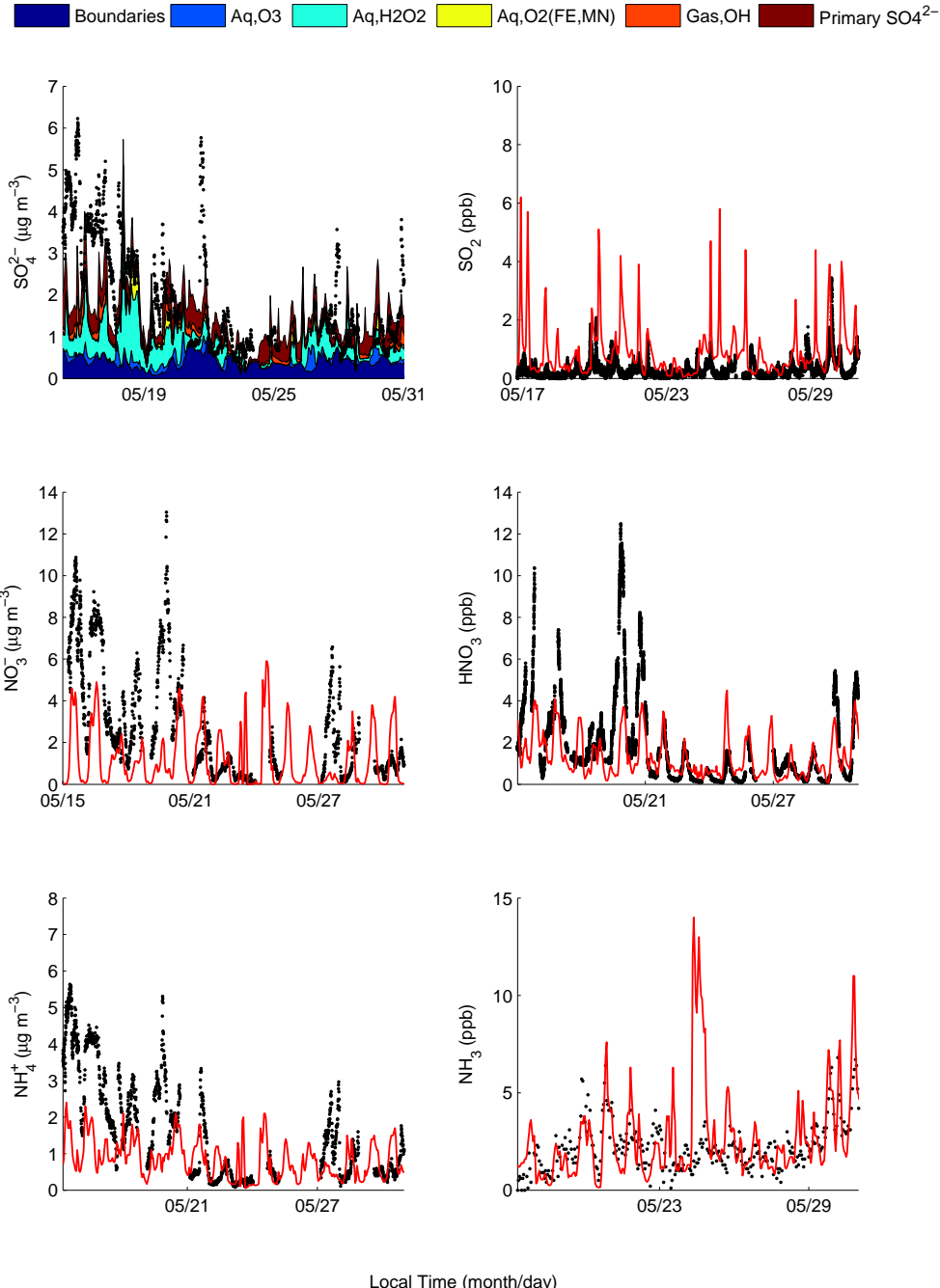


Figure 3. Observed (black) and predicted (red) particulate sulfate, nitrate, ammonium, sulfur dioxide, nitric acid, and ammonia concentrations from the CalNex Pasadena ground site. In the legend, “Boundaries” refers to sulfate attributable to boundary conditions, “(Aq, Gas), OX” refers to secondary sulfate produced by aqueous-phase (Aq) or gas-phase (Gas) oxidation of SO_2 by oxidant OX. “Primary SO_4^{2-} ” refers to sulfate emitted within the basin.

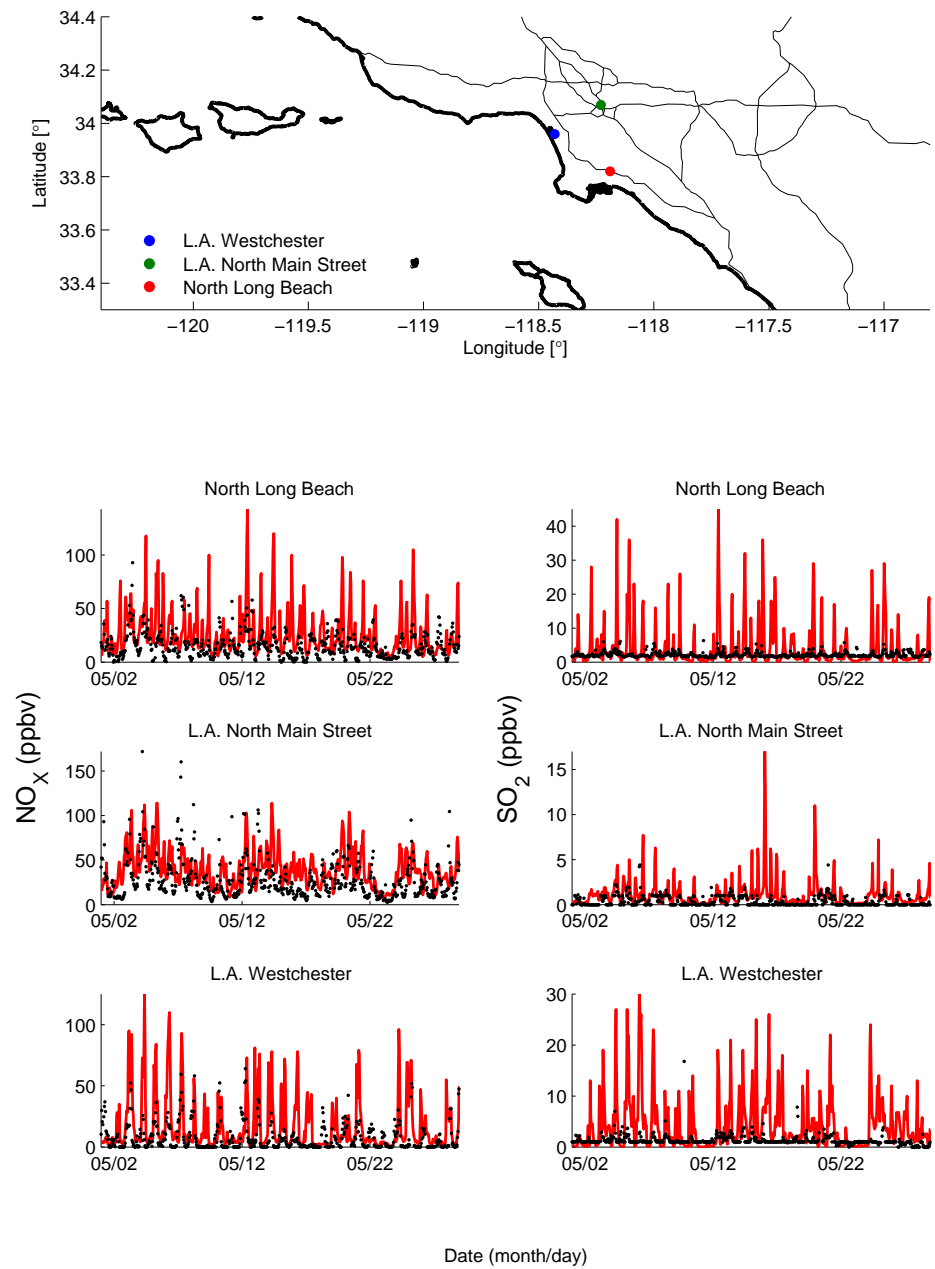


Figure 4. Measured (black) and predicted (red) NO_x and SO₂ mixing ratios for May 2010 at five locations in the Los Angeles Basin. Gaseous measurements were taken from the Air Quality and Meteorological Information System (AQMIS, <http://www.arb.ca.gov/aqmis2/aqmis2.php>).

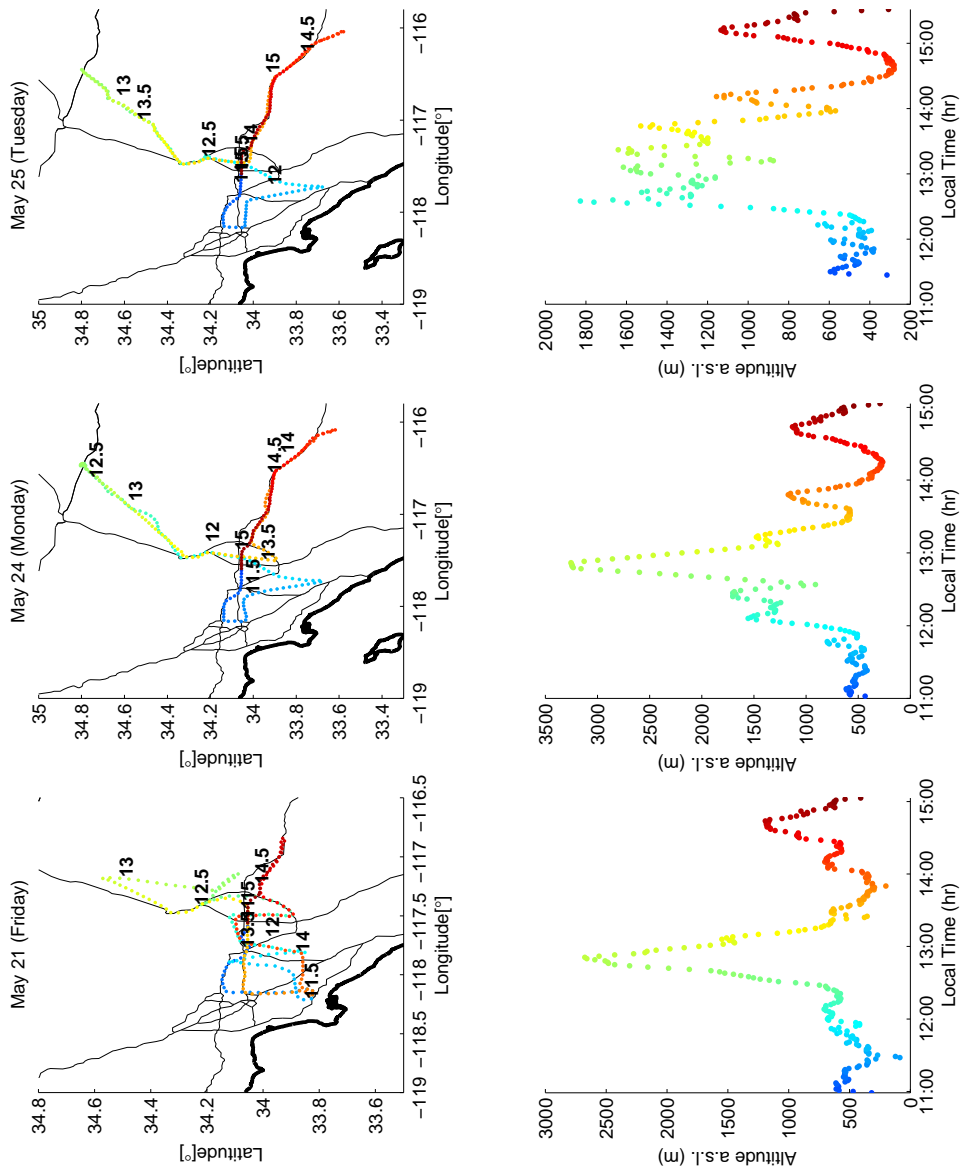


Figure 5. Twin Otter aircraft flight paths and altitudes (with respect to sea level) for May 2010. The flight track and altitude trace are colored by the time (Pacific Standard Time) of day. Time-stamps are also printed along each flight path in 30 min increments.

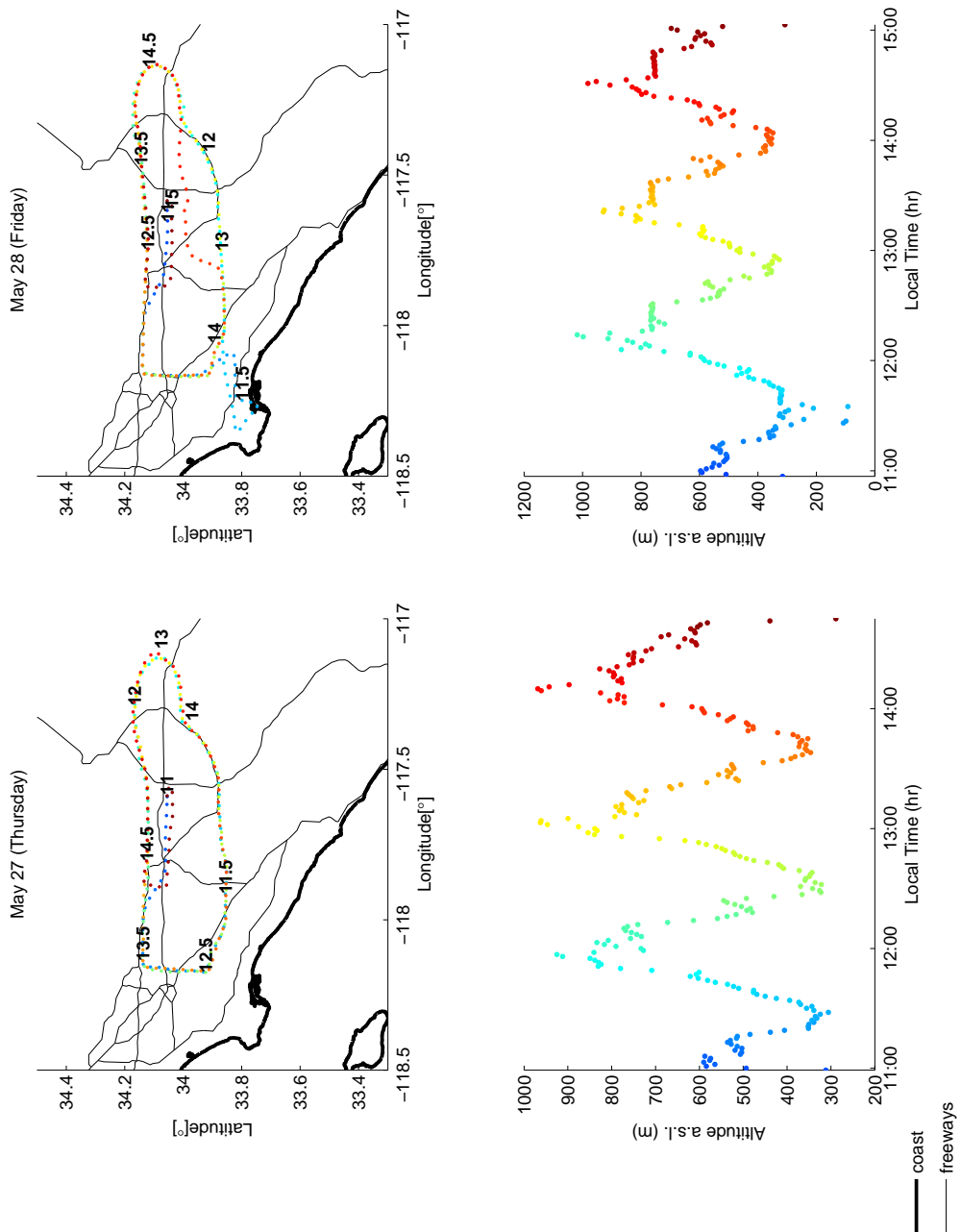


Figure 6. Twin Otter aircraft flight paths and altitudes (with respect to sea level) for May 2010. The flight track and altitude trace are colored by the time (Pacific Standard Time) of day. Time-stamps are also printed along each flight path in 30 min increments.

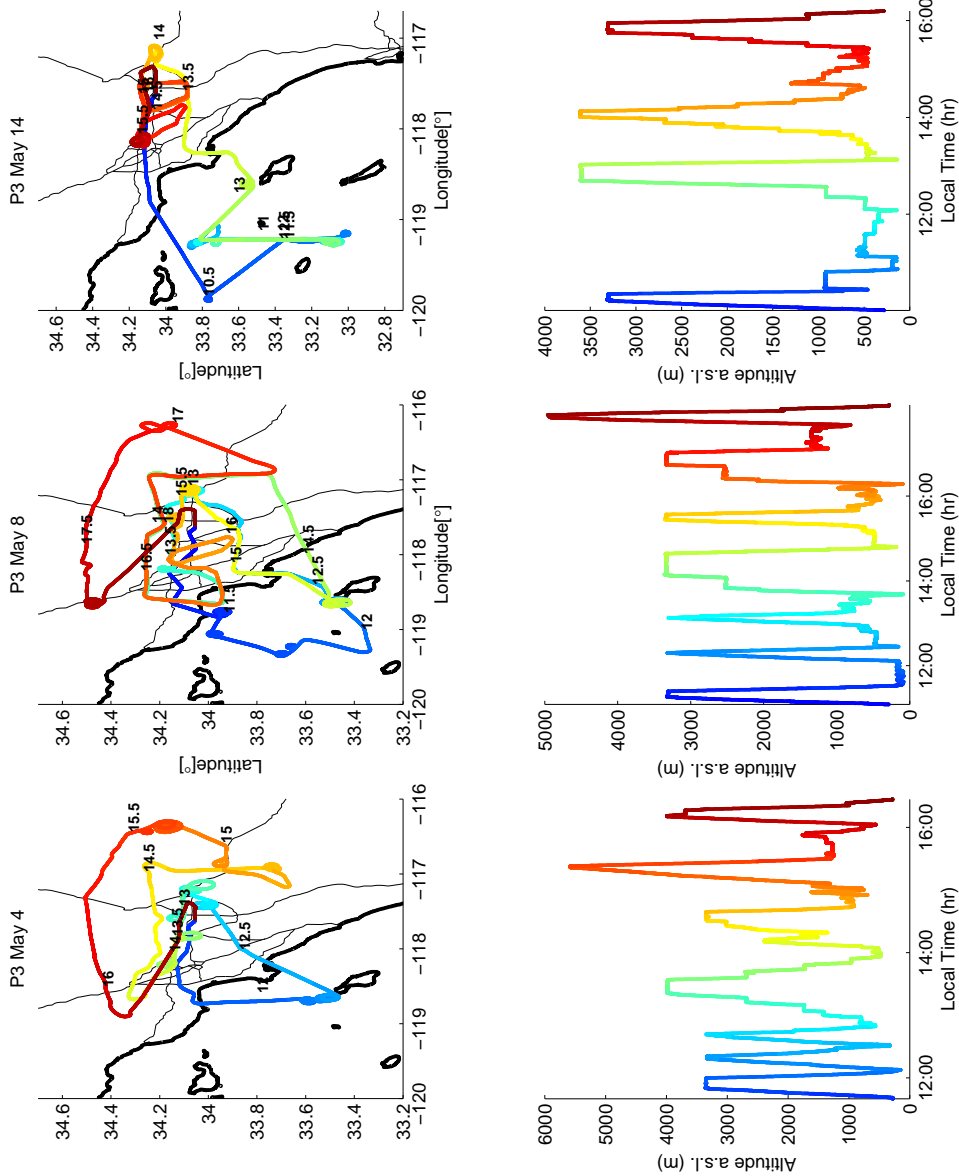


Figure 7. P3 aircraft flight paths and altitudes (with respect to sea level) for May 2010. The flight track and altitude trace are colored by the time (Pacific Standard Time) of day. Time-stamps are also printed along each flight path in 30 min increments.

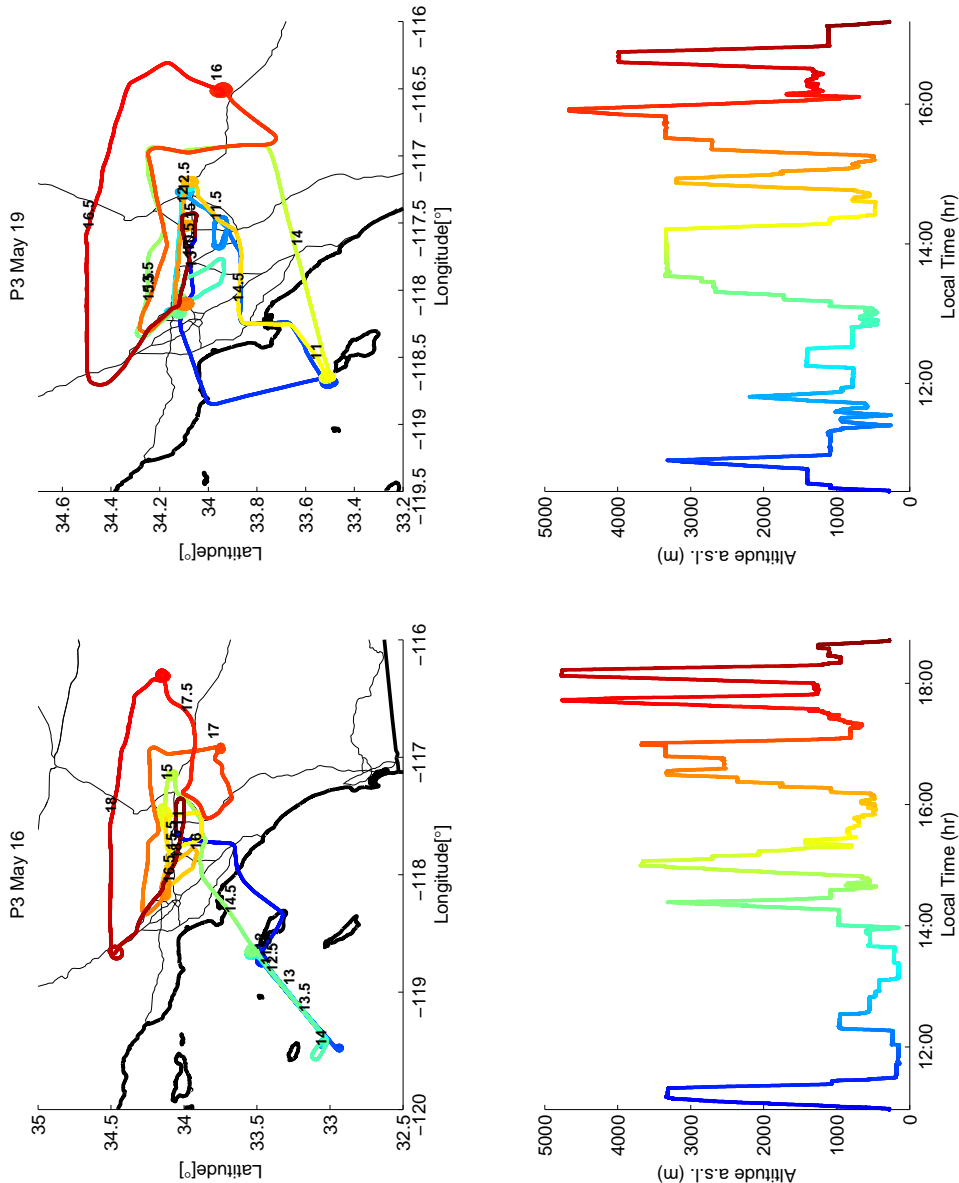


Figure 8. P3 aircraft flight paths and altitudes (with respect to sea level) for May 2010. The flight track and altitude trace are colored by the time (Pacific Standard Time) of day. Time-stamps are also printed along each flight path in 30 min increments.

X - 30

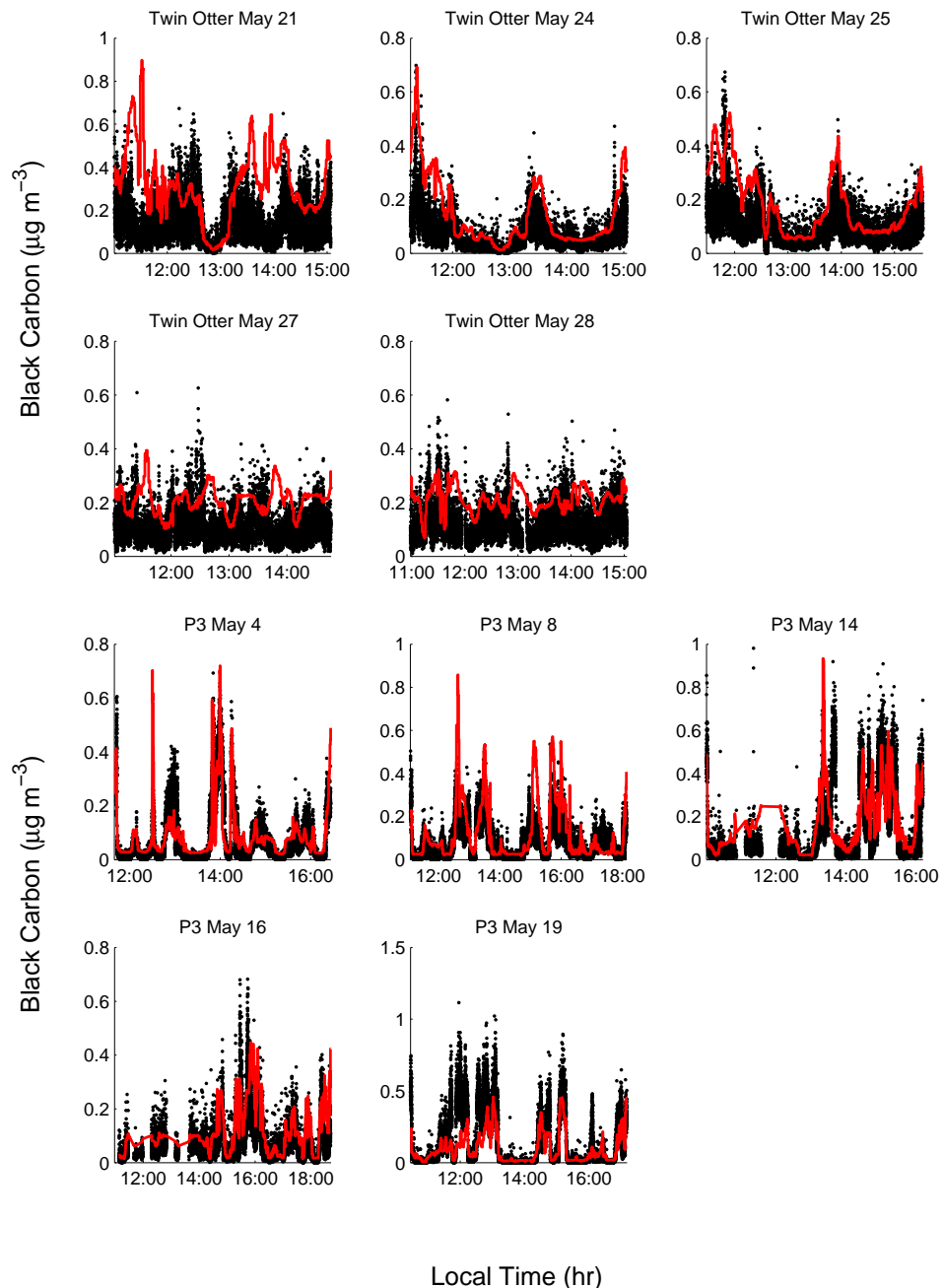


Figure 9. Measured (black) and predicted (red) black carbon concentrations for CalNex Twin Otter and P3 flights during May 2010. Several high concentration data points have been removed from the May 28 Twin Otter data set because the aircraft flew through smoke caused by a major traffic accident involving a gasoline tanker truck.

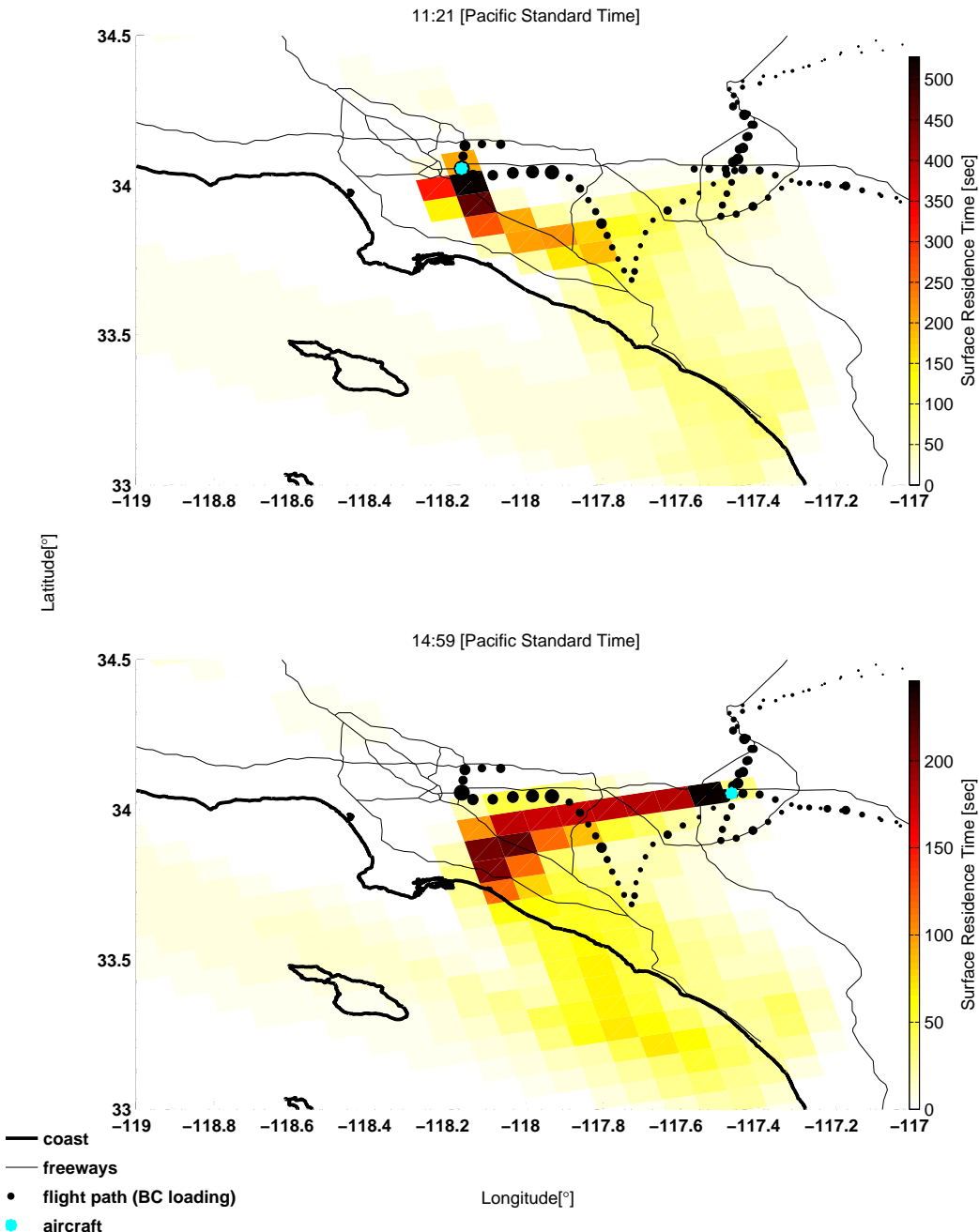


Figure 10. Map of mean residence times based on integrated 24-h back trajectories for the surface level particles (particles at < 200 m altitude) arriving in the vicinity of the Twin Otter for flights on May 24. Flight path marker (black dots) sizes are proportional to 1-min average measured BC concentrations (maximum concentration is $0.29 \mu\text{g m}^{-3}$)

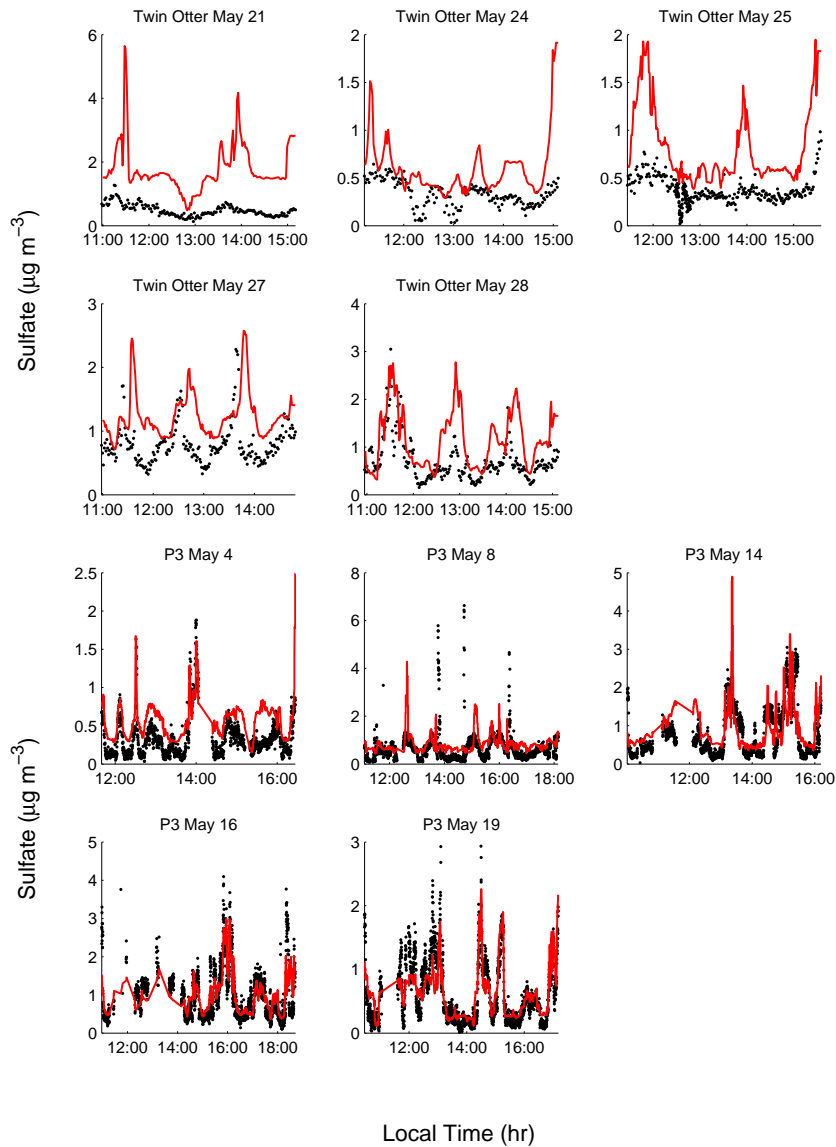


Figure 11. Measured (black) and predicted (red) sulfate concentrations for Twin Otter and P3 flights.

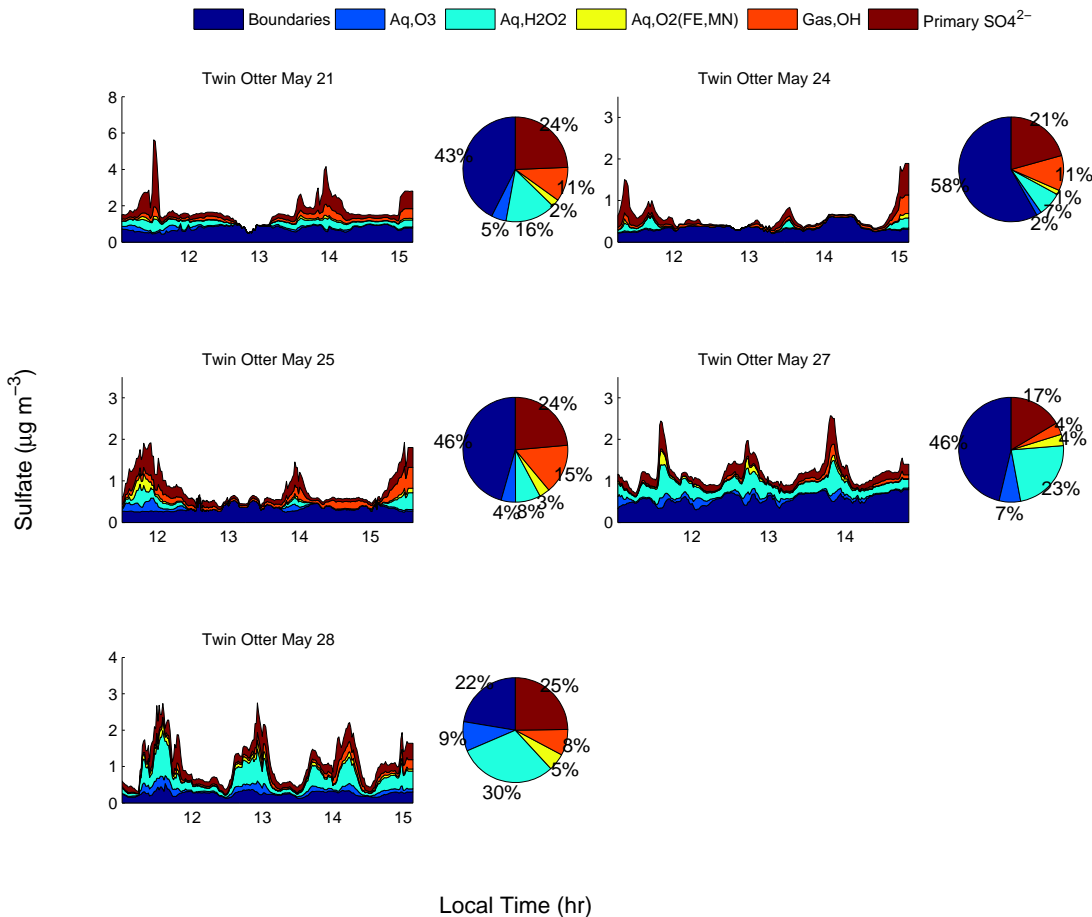


Figure 12. Predicted sulfate concentrations for Twin Otter flights. Pie charts indicate the relative contribution from routes to sulfate averaged over a given flight. In the legend, “Boundaries” refers to sulfate attributable to boundary conditions, “(Aq, Gas), OX” refers to secondary sulfate produced by aqueous-phase (Aq) or gas-phase (Gas) oxidation of SO_2 by oxidant OX. “Primary SO_4^{2-} ” refers to sulfate emitted within the basin.

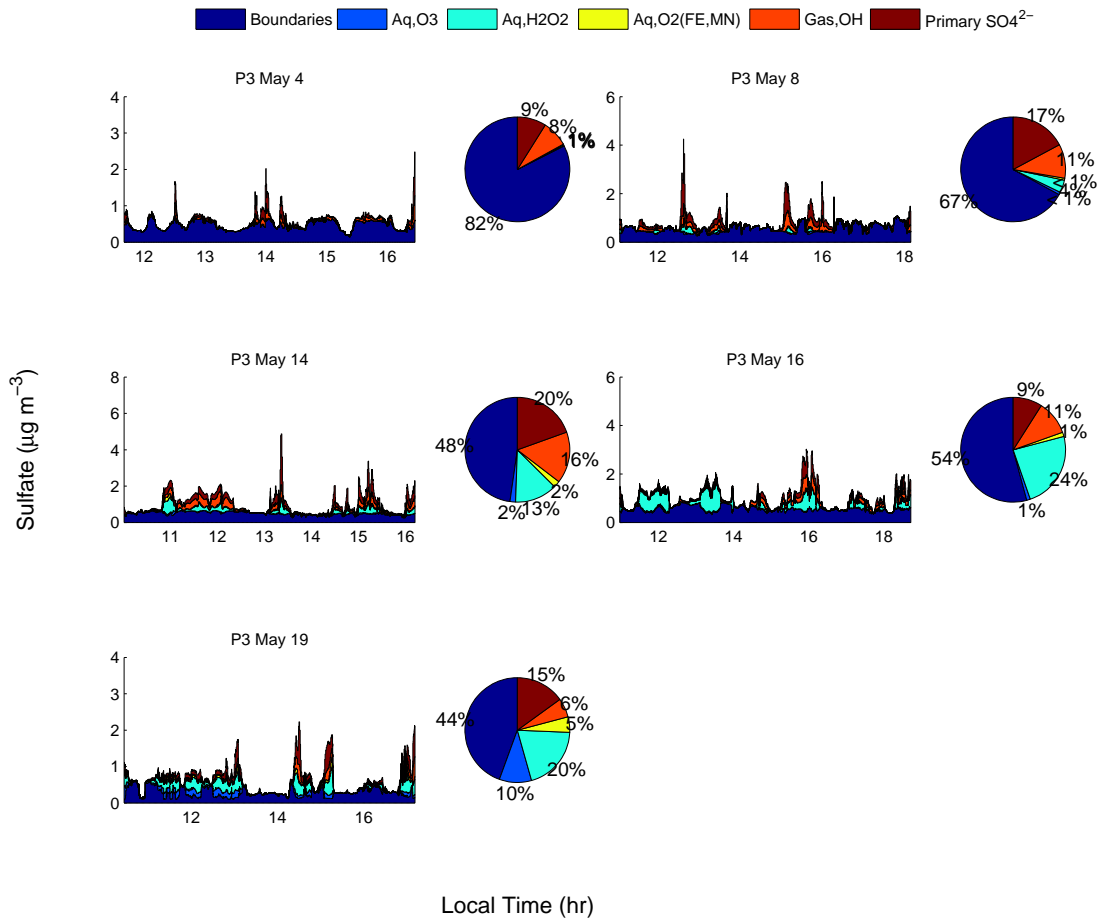


Figure 13. Predicted sulfate concentrations for P3 flights. Pie charts indicate the relative contribution from various routes to sulfate averaged over a given flight. In the legend, “Boundaries” refers to sulfate attributable to boundary conditions, “(Aq, Gas), OX” refers to secondary sulfate produced by aqueous-phase (Aq) or gas-phase (Gas) oxidation of SO_2 by oxidant OX. “Primary SO_4^{2-} ” refers to sulfate emitted within the basin.

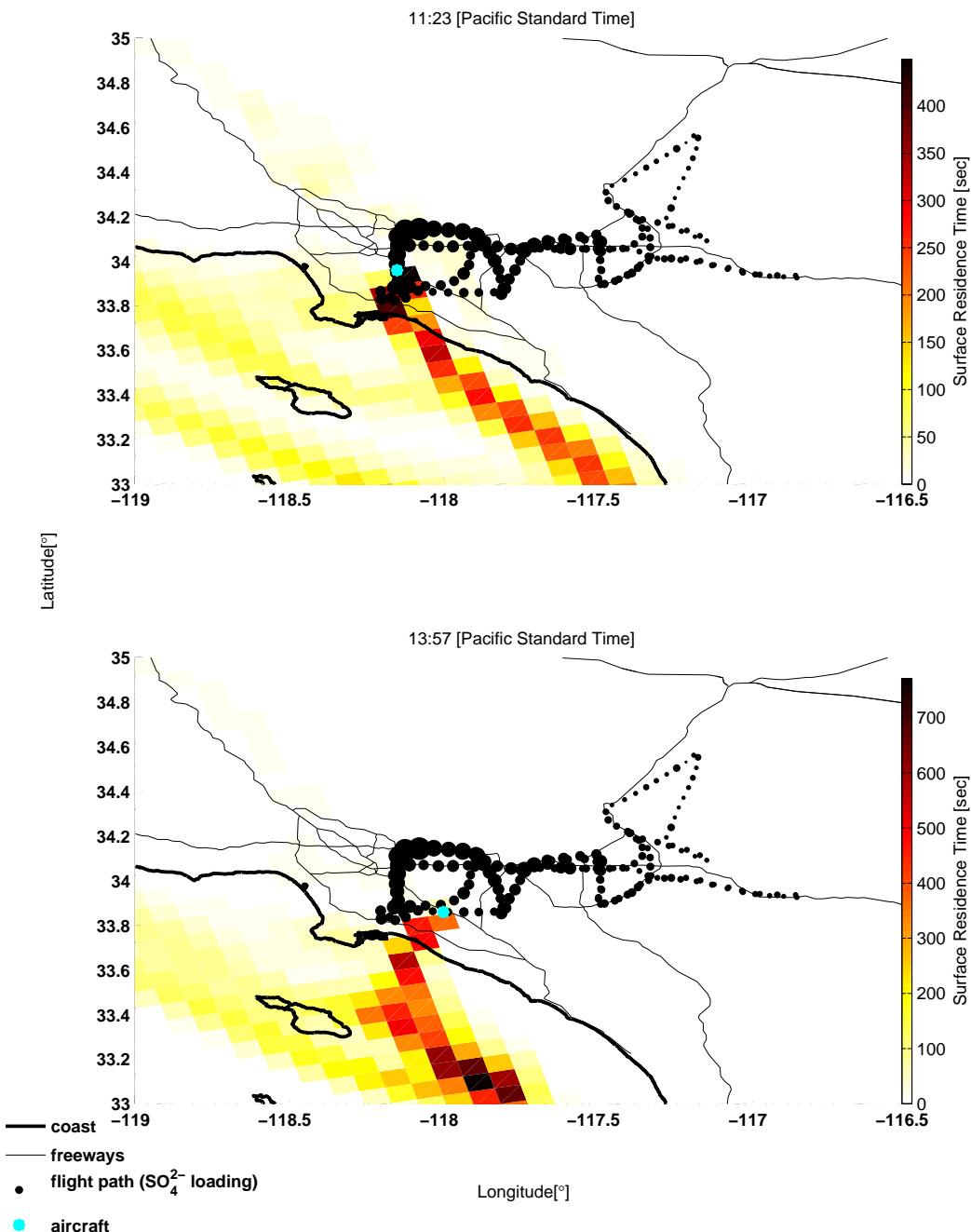


Figure 14. Map of mean residence times based on integrated 24-h back trajectories for the surface level particles (particles at < 200 m altitude) arriving in the vicinity of the Twin Otter for flights on May 21. Flight path marker (black dots) sizes are proportional to 10-sec average measured sulfate concentrations (maximum concentration is $1.26 \mu\text{g m}^{-3}$)

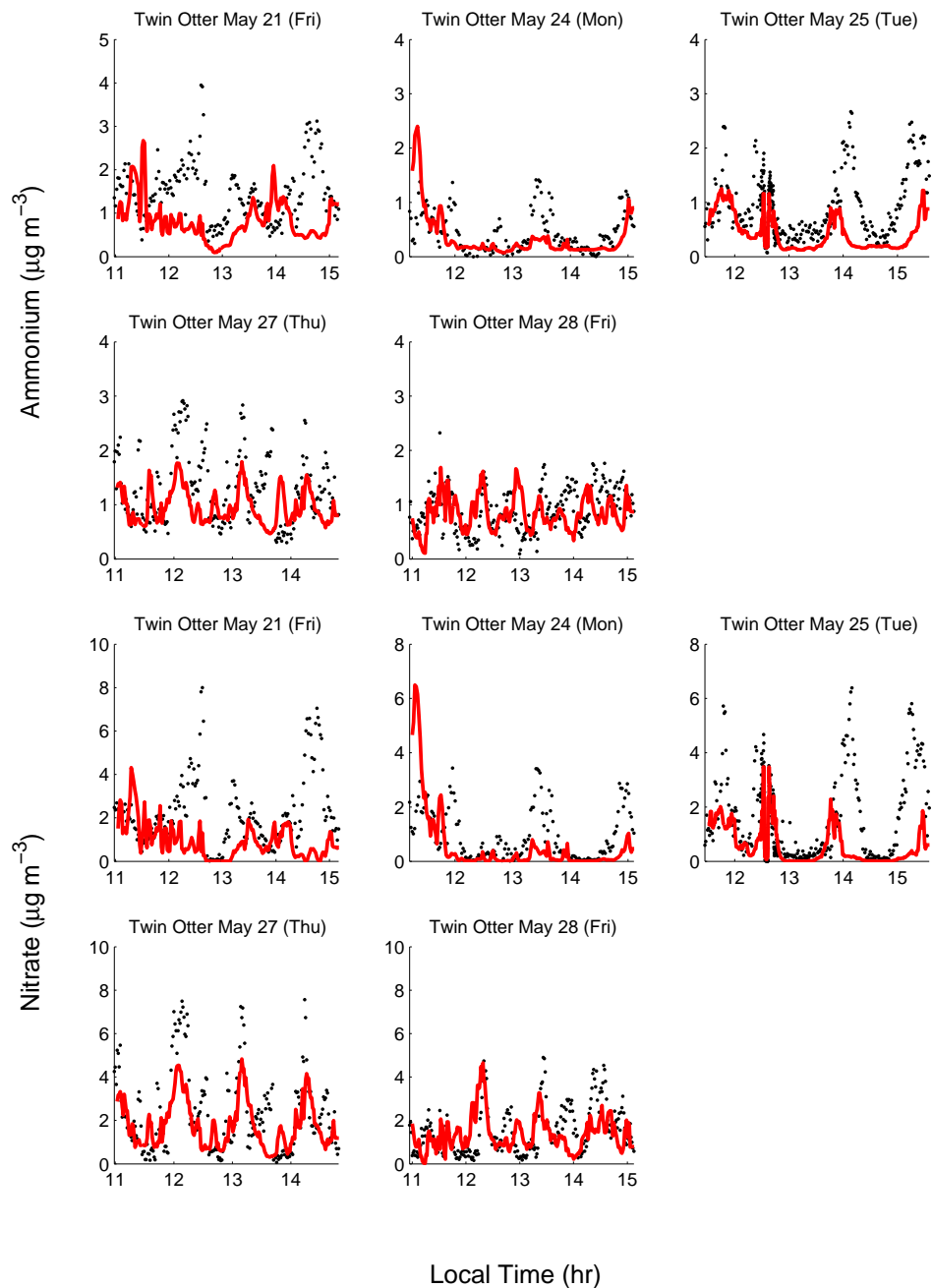


Figure 15. Measured (black) and predicted (red) particulate ammonium and nitrate concentrations for Twin Otter flights during May 2010.

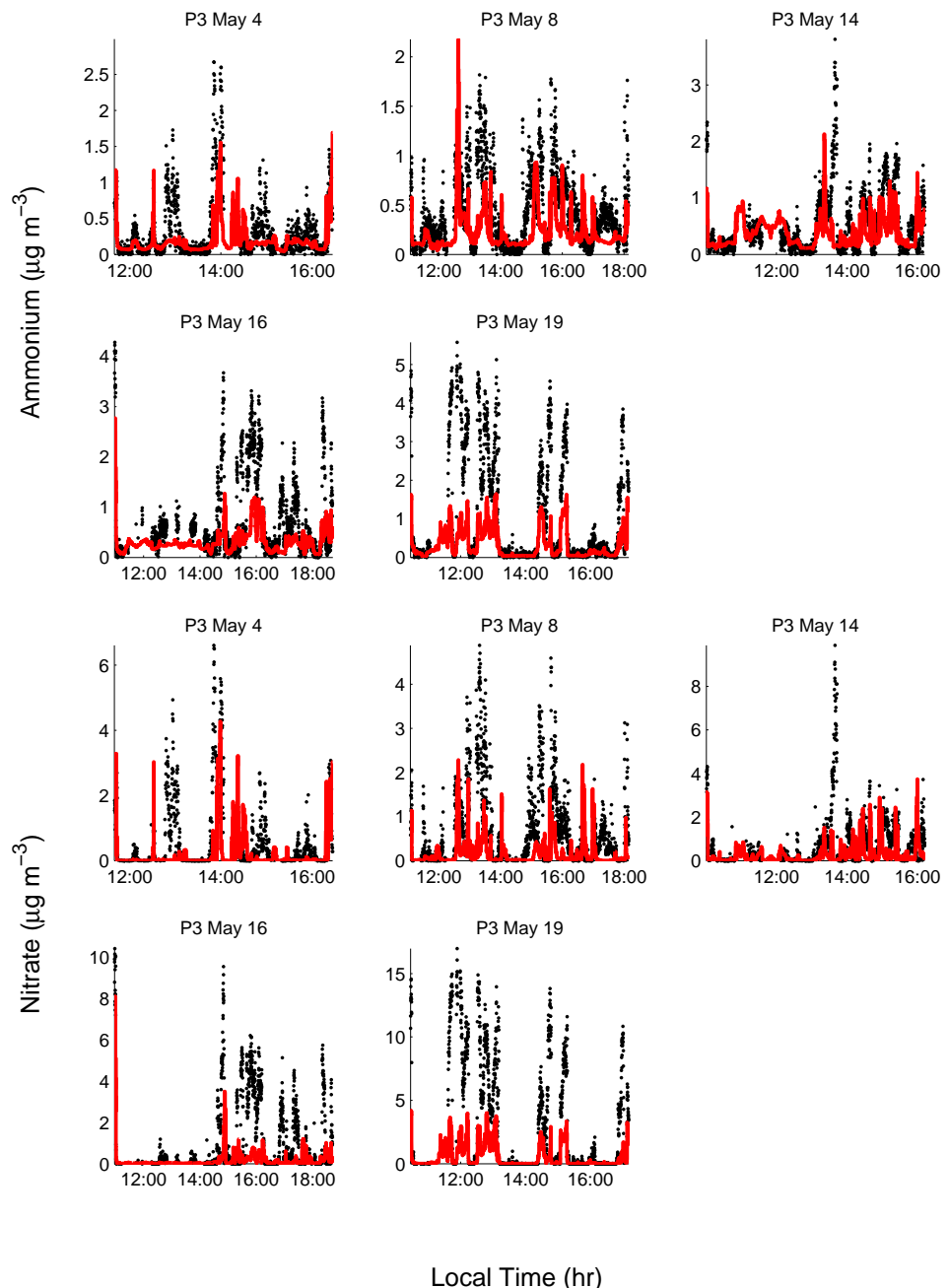


Figure 16. Measured (black) and predicted (red) particulate ammonium and nitrate concentrations for P3 flights during May 2010.

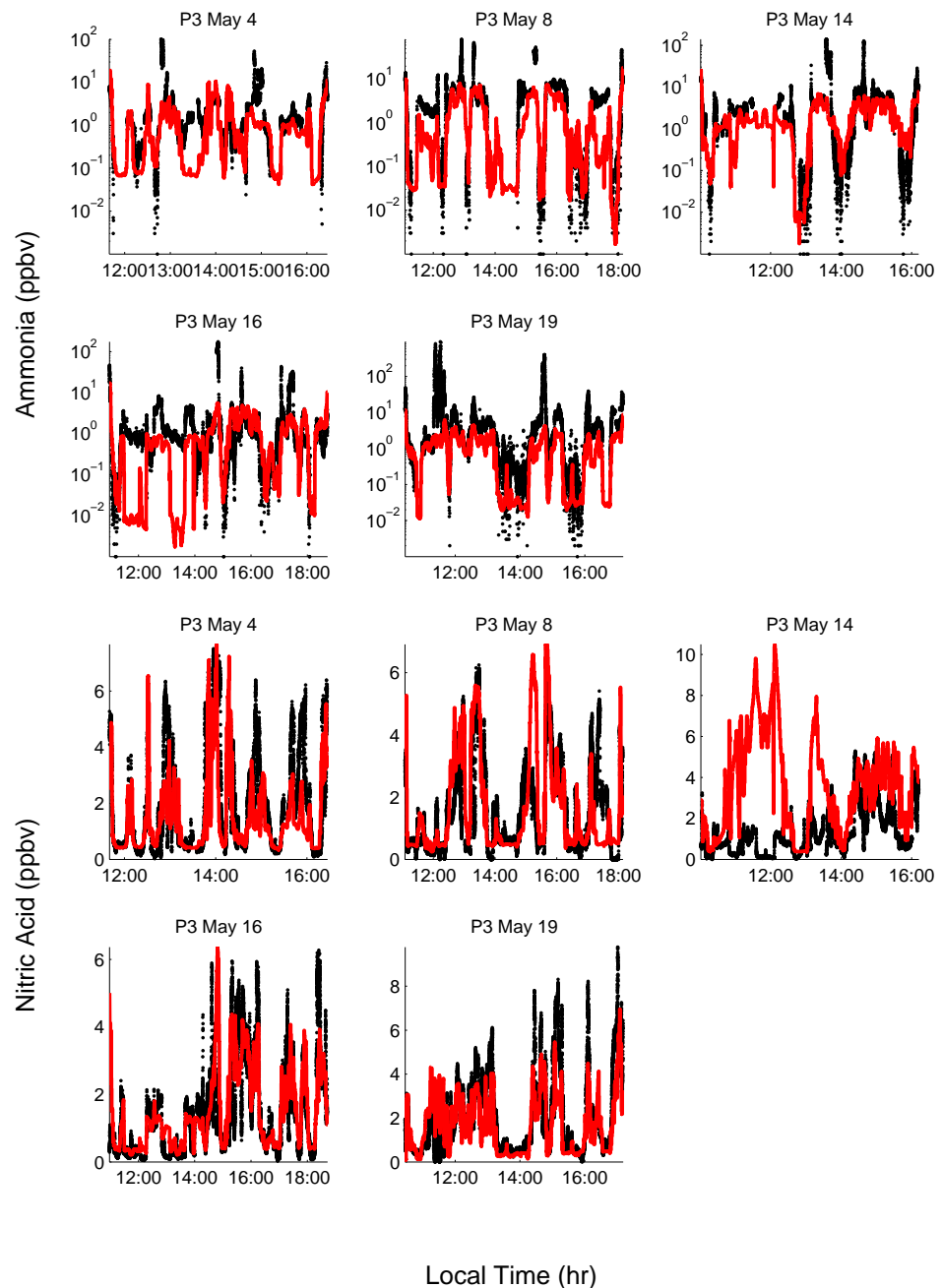


Figure 17. Measured (black) and predicted (red) ammonia and nitric acid concentrations for P3 flights during May 2010.

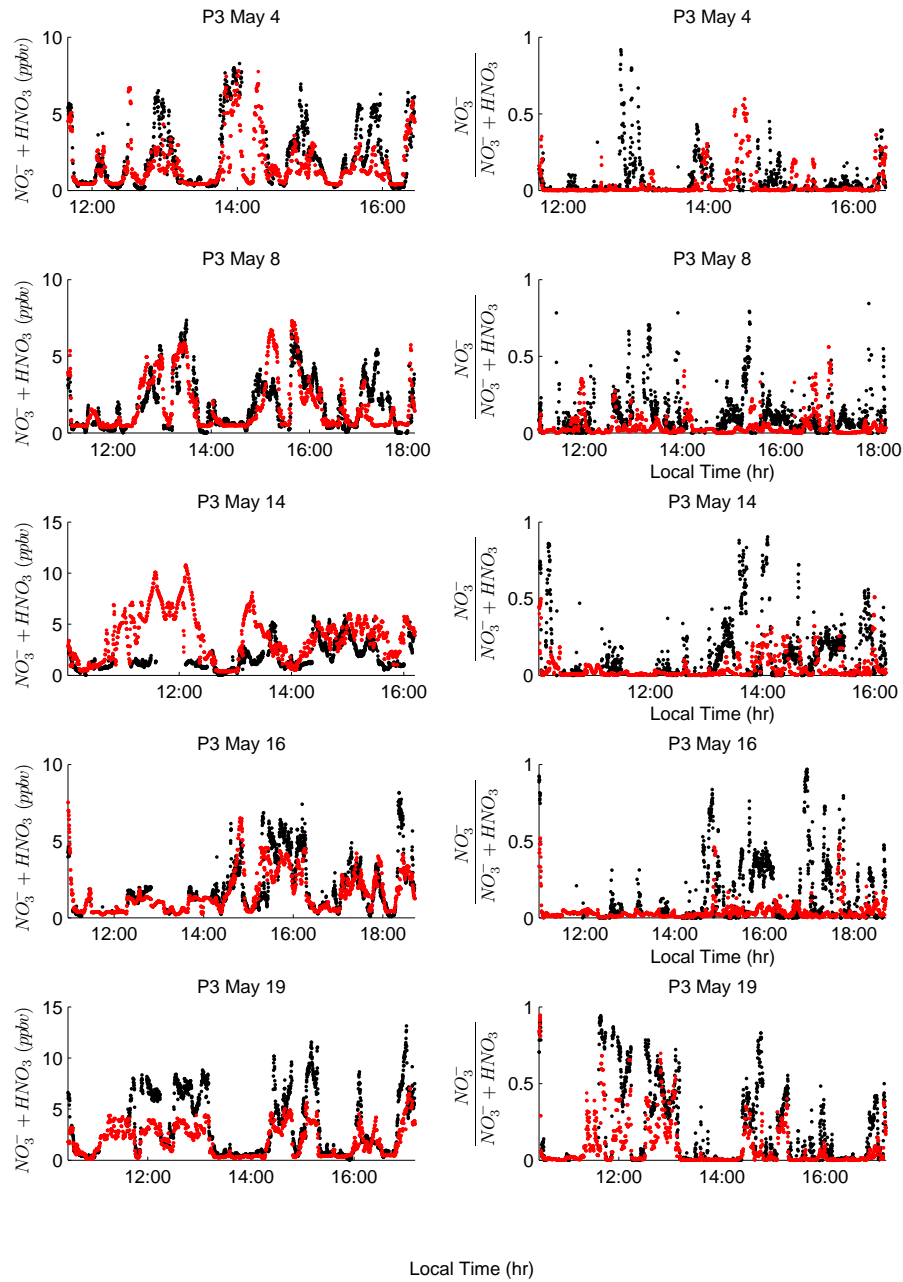


Figure 18. Measured (black) and observed (red) total nitrate ($\text{NO}_3^- + \text{HNO}_3$) mixing ratios (left column) and predicted and observed fraction of total nitrate in the particle-phase (right column) for P3 flights. Predicted nitrate concentrations are adjusted to match the transmission efficiency of the AMS based as described in the text.

**Supplement to “Inorganic and black carbon aerosols
in the Los Angeles Basin during CalNex”**

Table S1. Sulfate sources in the Aitken, accumulation, and coarse aerosol modes in CMAQ.

Aitken mode	Accumulation mode	Coarse mode
Aqueous-phase Oxidation		
	$\text{H}_2\text{O}_2 + \text{S(IV)} \rightarrow \text{S(VI)} + \text{H}_2\text{O}$	
	$\text{O}_3 + \text{S(IV)} \rightarrow \text{S(VI)} + \text{O}_2$	
	$\text{O}_2 + \text{S(IV)} \rightarrow \text{S(VI)}$	
	$\text{MHP}^a + \text{S(IV)} \rightarrow \text{S(VI)}$	
	$\text{PAA}^b + \text{S(IV)} \rightarrow \text{S(VI)}$	
Gas-phase Oxidation		
$\text{SO}_2 + \text{OH} \xrightarrow{\text{O}_2, \text{H}_2\text{O}} \text{H}_2\text{SO}_4 + \text{HO}_2$	$\text{SO}_2 + \text{OH} \xrightarrow{\text{O}_2, \text{H}_2\text{O}} \text{H}_2\text{SO}_4 + \text{HO}_2$	$\text{SO}_2 + \text{OH} \xrightarrow{\text{O}_2, \text{H}_2\text{O}} \text{H}_2\text{SO}_4 + \text{HO}_2$
Primary Emissions		
0.1% Primary Anthropogenic Sulfate	99.9% Primary Anthropogenic Sulfate	
Sulfate Sea-spray		Sulfate Sea-spray
Initial conditions (IC) and boundary conditions (BC)		
Sulfate from ICBC	Sulfate from ICBC	Sulfate from ICBC

^a MHP stands for methylhydrogenperoxide. ^b PAA stands for peroxyacetic acid.

Table S2. Statistical metrics based on measured and predicted total nitrate ($\text{NO}_3^- + \text{HNO}_3$) mixing ratios for P3 flights during May 2010.

P3, AMS Transmission						
Flight Date	N	ME [ppbv]	MB [ppbv]	NME	NMB	
Total Nitrate ($\text{HNO}_3 + \text{NO}_3^-$)						
4	17219	0.99	-0.69	0.45	-0.31	
8	25439	0.90	-0.01	0.49	0.00	
14	22258	1.93	1.61	1.07	0.89	
16	27899	0.87	-0.29	0.38	-0.13	
19	24239	1.59	-1.39	0.48	-0.42	
P3, Full Transmission						
Flight Date	N	ME [ppbv]	MB [ppbv]	NME	NMB	
Total Nitrate ($\text{HNO}_3 + \text{NO}_3^-$)						
4	17219	0.99	-0.60	0.44	-0.27	
8	25439	1.05	0.25	0.58	0.14	
14	22258	2.14	1.87	1.19	1.04	
16	27899	0.90	-0.07	0.39	-0.03	
19	24239	1.31	-1.08	0.40	-0.33	

Statistical metrics based on ammonia measurements in the “no dairy” column are calculated excluding all data points east of longitude 117.7°W.

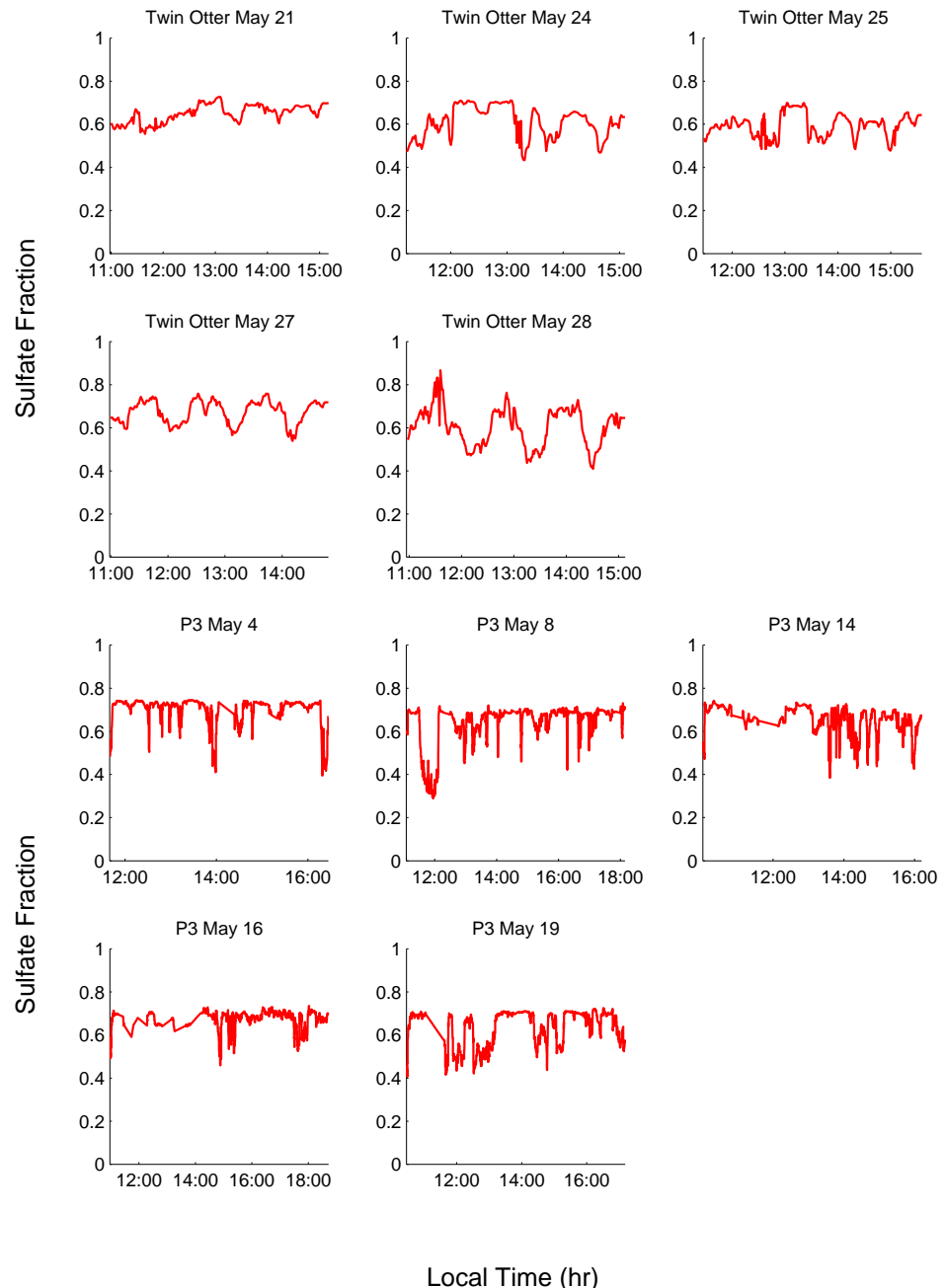


Figure S1. Fraction of total predicted sulfate along Twin Otter and P3 flight paths remaining after AMS transmission curve has been applied.

X - 44

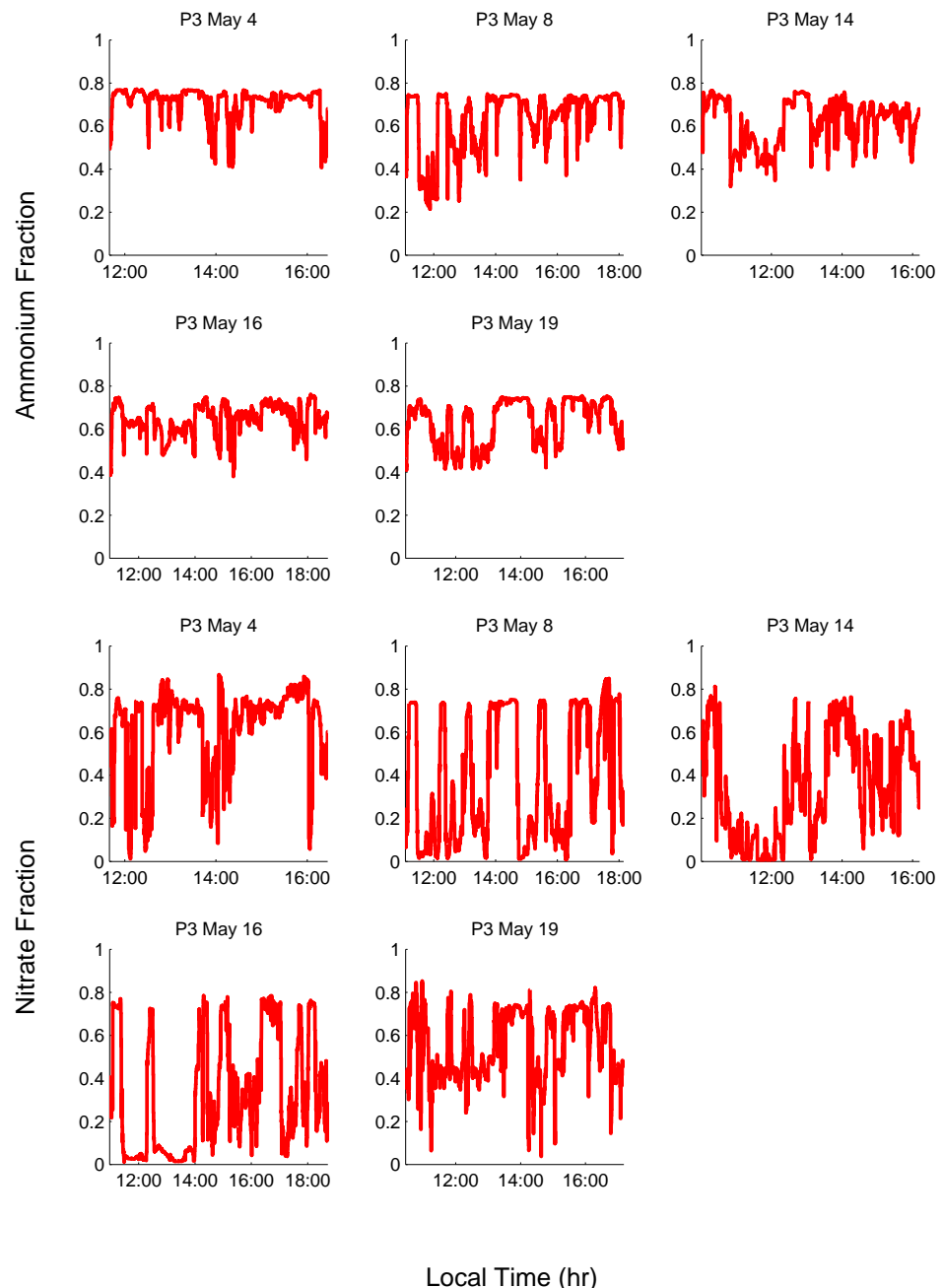


Figure S2. Fraction of total predicted ammonium and nitrate along P3 flight paths remaining after AMS transmission curve has been applied.

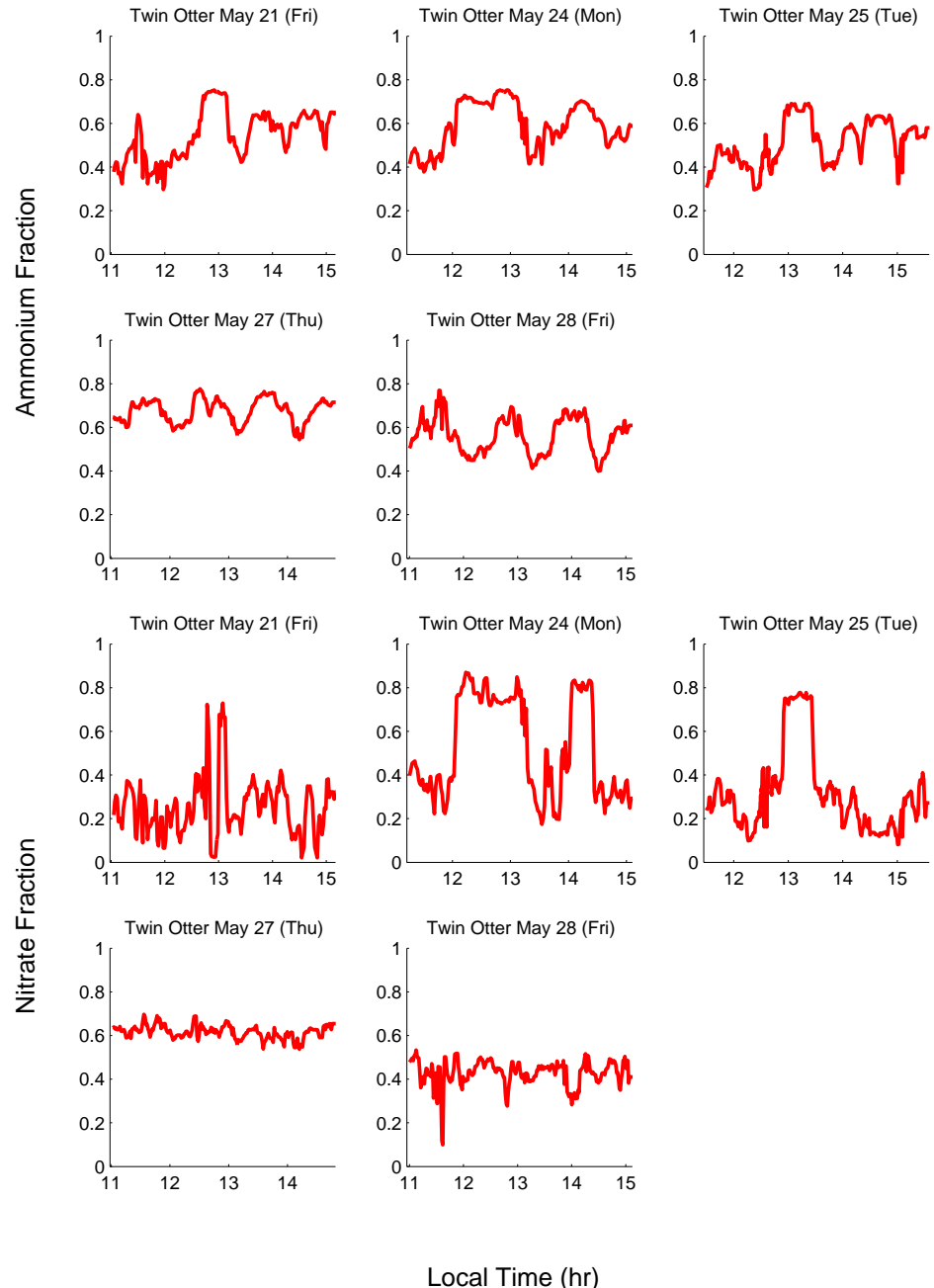


Figure S3. Fraction of total predicted ammonium and nitrate along Twin Otter flight paths remaining after AMS transmission curve has been applied.

Appendix E

Characterization and Airborne Deployment of a New Counterflow Virtual Impactor Inlet*

*Reproduced with permission from “Characterization and airborne deployment of a new counterflow virtual impactor inlet” by T. Shingler, S. Dey, A. Sorooshian, F. J. Brechtel, Z. Wang, A. Metcalf, M. Coggan, J. Mülmenstädt, L. M. Russell, H. H. Jonsson, and J. H. Seinfeld, *Atmospheric Measurement Techniques Discussions*, 5, 1515–1541, doi:10.5194/amt-5-1515-2012. Copyright 2012 by the Authors. This work is distributed under the Creative Commons Attribution 3.0 License.

Characterization and airborne deployment of a new counterflow virtual impactor inlet

T. Shingler¹, S. Dey², A. Sorooshian^{1,3}, F. J. Brechtel², Z. Wang¹, A. Metcalf⁴, M. Coggon⁴, J. Mühlstädt⁵, L. M. Russell⁵, H. H. Jonsson⁶, and J. H. Seinfeld⁴

¹Department of Chemical and Environmental Engineering, University of Arizona, P.O. Box 210011, Tucson, Arizona, 85721, USA

²Brechtel Manufacturing Inc., Hayward, California, USA

³Department of Atmospheric Sciences, University of Arizona, P.O. Box 210081, Tucson, Arizona, 85721, USA

⁴Departments of Environmental Science and Engineering and Chemical Engineering, California Institute of Technology, Pasadena, California, USA

⁵Scripps Institution of Oceanography, University of California, San Diego, La Jolla, California, USA

⁶Center for Interdisciplinary Remotely-Piloted Aircraft Studies, Naval Postgraduate School, Monterey, California, USA

Abstract. A new counterflow virtual impactor (CVI) inlet is introduced with details of its design, laboratory characterization tests, and deployment on an aircraft during the 2011 Eastern Pacific Emitted Aerosol Cloud Experiment (E-PEACE). The CVI inlet addresses three key issues in previous designs; in particular, the inlet operates with: (i) negligible organic contamination; (ii) a significant sample flow rate to downstream instruments ($\sim 15 \text{ l min}^{-1}$) that reduces the need for dilution; and (iii) a high level of accessibility to the probe interior for cleaning. Wind tunnel experiments characterized the cut size of sampled droplets and the particle size-dependent transmission efficiency in various parts of the probe. For a range of counter-flow rates and air velocities, the measured cut size was between 8.7–13.1 μm . The percentage error between cut size measurements and predictions from aerodynamic drag theory are less than 13 %. The CVI was deployed on the Center for Interdisciplinary Remotely-Piloted Aircraft Studies (CIRPAS) Twin Otter for thirty flights during E-PEACE to study aerosol–cloud–radiation interactions off the central coast of California between July and August 2011. Results are reported to assess the performance of the inlet including comparisons of particle number concentration downstream of the CVI and cloud drop number concentration measured by two independent aircraft probes. Measurements downstream the CVI are also examined from one representative case flight coordinated with shipboard-emitted smoke that was intercepted in cloud by the Twin Otter.

1 Introduction

The aerosol nuclei that are the seeds of cloud-drops and ice are a critically important component of the atmosphere as

Correspondence to: A. Sorooshian
(armin@email.arizona.edu)

they influence radiative transfer, visibility, and cloud formation. Characterization of the physical and chemical properties of these nuclei is needed to increase understanding of how aerosol particles affect clouds and, in turn, how clouds modify aerosol properties. Essential to understanding these interactions are properties including particle size distribution, chemical composition, and hygroscopicity (Twohy et al., 1989; Hudson, 1993; Hallberg et al., 1994, 1998; Ostrom et al., 2000; Sellegrí et al., 2003). Aerosol sampling from aircraft has previously relied on particle retrieval via inlets that accept all particles in the free stream, without any preferential selection for particle size. These total aerosol inlets are often unable to sufficiently decelerate the larger aerosol particles or evaporate the water residue surrounding their nuclei, typically leading to inertial deposition and droplet shatter (Huebert et al., 1990; Hudson and Frisbie, 1991; Baumgardner and Huebert, 1993; Weber et al., 1998; Hermann et al., 2001; Hegg et al., 2005). These limitations interfere with sampling a known population of aerosol in clouds, usually resulting in a mixture of interstitial aerosol particles and shattered droplets. The inlet traditionally used to sample only cloud drops is the counterflow virtual impactor (CVI), which has been discussed extensively in previous work (e.g., Ogren et al., 1985, 1987; Noone et al., 1988; Laucks and Twohy, 1998).

CVI inlets have undergone a number of design changes in the last three decades to increase their functionality and sampling efficiency. Initially, aircraft CVIs were deployed in a single fixed-tube construction, containing a large bend radius to channel the sample stream into an aircraft. Modifications to the original inlet lip structure and inner CVI geometry have led to increased collection efficiencies at lower particle diameters (Anderson et al., 1993; Schwarzenböck and Heintzenberg, 2000). Further enhancements include the addition of upstream shrouds to aid the alignment of the free stream with the inlet (Twohy, 1998). However, a number of issues still persist. For example, CVIs often are character-

ized by low sample flow rates and consequently need significant dilution flow so that a sufficient amount of air flow can be supplied to multiple instruments simultaneously. This is problematic for aircraft payloads containing multiple instruments downstream of the CVI that struggle with detection limit issues (e.g., Berg et al., 2009); for example, a particle-into-liquid sampler (PILS) typically requires approximately $12\text{--}15\text{ l min}^{-1}$ of air flow, which is a significant amount of flow when sampling downstream of a CVI (Sorooshian et al., 2006a,b; 2010). Furthermore, advanced chemical composition measurement devices, such as the Aerodyne Aerosol Mass Spectrometer (AMS) are vulnerable to contamination from compounds used to fabricate older CVI designs, including siloxane sealant (Hayden et al., 2008). Finally, accessibility to the interior of older probe designs, especially for cleaning porous sections, is challenging. A number of such issues have been addressed with the development of the CVI discussed in this work.

The goal of this work is to report on a new aircraft-mountable CVI manufactured by Brechtel Manufacturing Inc. (Model 1204, www.brechtel.com). This manuscript will provide a detailed description of the inlet design, summarize laboratory characterization results from wind tunnel experiments, and relate wind tunnel results to theoretical calculations of cut size behavior using aerodynamic drag theory. Results from a recent aircraft field campaign (2011 Eastern Pacific Emitted Aerosol Cloud Experiment, E-PEACE) are presented to summarize early results and its performance, including validation of wind tunnel results for size-dependent particle transmission efficiency and droplet cut size.

2 CVI design

The theory of CVI operation is well-documented in previous work (Ogren et al., 1985, 1987; Lin and Heintzenberg, 1995). The CVI inlet in this work operates in the same manner with a detailed description of the air streams provided below and in Fig. 1. A stream of filtered and heated air (referred to as the add-flow), provided by a compressor (Gast; P/N: 75R635) and controlled by a mass-flow controller (MFC) (Alicat Scientific; P/N: MCP-50SLPM), is forced through an annular space between the exterior housing and the inner sample-stream tubing. The inner probe tube contains a porous region, 1.02 cm in length, near the tip of the inlet. The pores allow the add-flow to enter the particle stream creating a counter-flow leaving the inlet, equivalent to the difference between the add-flow and sample-flow rates. The counter-flow stream is emitted outwards from the mouth of the inlet (diameter = 2.3 mm) and creates a stagnation plane immediately upstream of the inlet orifice (labeled 1 in Fig. 1). When sampling in cloud, small aerosol particles, lacking the inertia to penetrate the stagnation plane, are carried along the streamlines away from the orifice of the inlet. Particles capable of penetrating the exterior stagnation plane enter the ori-

fice and pass into the opposing counter-flow within the inlet. The splitting of the add-flow into the counter-flow stream and sample-flow stream creates a second stagnation plane inside the probe tip (labeled 2 in Fig. 1). Any particles decelerated to a stop before reaching the second stagnation plane return back through the inlet orifice with the counter-flow. Particles and droplets that penetrate the second stagnation plane enter the CVI sample flow. The distance created between the two stagnation planes dictates the particle cut size ($D_{p,50}$), which is defined here as the size at which 50 % of the particles are sampled by the CVI, for a specific air speed and add-flow rate.

Particles that penetrate the second stagnation plane are slowed down due to expansion of the inner tube (segment C in Fig. 1), providing additional residence time to allow water associated with particles to evaporate in the heated sample-flow stream. The sample-flow stream is directed to a 90° bend in the tubing and into the aircraft. Very large droplets ($>40\text{ }\mu\text{m}$ diameter) with a sufficiently high amount of inertia and long evaporation times cannot make the turn and impact in an extended region, referred to as the particle trap (segment E in Fig. 1). The CVI in this study was optimized for 15 l min^{-1} of sample air flow to accommodate the increased flow rate requirements to operate multiple instruments downstream of the inlet at the same time; as noted earlier, a limitation in previous designs was the large amount of dilution flow that needed to be added to the sample flow to provide enough sample flow to instruments. The sample stream flow rate is kept at a constant 15 l min^{-1} by a MFC (Alicat Scientific; P/N: MCP-50SLPM).

To address the issue of organic contamination, the inlet is constructed such that all surfaces that contact the counter-flow and sample air flow are either stainless steel or aluminum. It is further noted that the tubing in Segment B of Fig. 1 is interchangeable to allow more flexibility in optimizing for different inlet cut sizes and for cleaning purposes.

3 Laboratory characterization

CVI characterization experiments were performed using the BMI wind tunnel following methods described in Anderson et al. (1993). A dispersion of hollow glass spheres (Particle diameter, D_p , range = $2\text{--}20\text{ }\mu\text{m}$, mean diameter = $8\text{ }\mu\text{m}$, $\rho = 1.1\text{ g cm}^{-3}$, Polysciences, P/N: 19823) was introduced to the wind tunnel. A TSI Model 3321 Aerodynamic Particle Sizer (APS) obtained number-size distributions sampled by the CVI inlet. Figure 2 depicts the wind tunnel sampling configuration.

The glass sphere distribution introduced into the wind tunnel was sampled by the CVI operating in one of two modes: isokinetic sampling or CVI sampling. Total sample-flow drawn by the inlet was kept constant at 15 l min^{-1} for each sampling mode. Isokinetic sampling was performed by

drawing only 15 l min^{-1} of sample flow through the inlet orifice with no add-flow, and setting the wind tunnel velocity sufficiently low to create isokinetic sampling conditions at the CVI tip. For operation in CVI sampling mode, the add-flow is supplied and the wind tunnel is run at the full desired velocity. For the characterization experiments the tunnel was operated at two velocities: 50 m s^{-1} and 100 m s^{-1} , where the former is similar to the air speed of the aircraft during E-PEACE. The add-flow rate was varied over the $16\text{--}23 \text{ l min}^{-1}$ range to characterize a range of cut sizes. A total of 24 trials were performed for each of the following seven conditions (see also Table 1): isokinetic sampling mode and CVI sampling mode with add-flow rates of 16, 19, and 23 l min^{-1} and air speeds of 50 and 100 m s^{-1} . Resultant counter-flow rates were 1, 4, and 8 l min^{-1} , respectively.

Experimental cut size in the wind tunnel was determined by taking the ratio of the sampled CVI number-size distribution to the sampled isokinetic number-size distribution. Sampling in isokinetic mode provides a reference number-size distribution of the glass beads, to which the distribution obtained from CVI sampling mode can be compared. As described in Anderson et al. (1993), a normalization scheme where each APS size bin is divided by the sum of counts in the bins between $17\text{--}20 \mu\text{m}$ was applied prior to calculating the ratio of the measured CVI number-size distribution to reference isokinetic distribution.

Experimentally determined cut sizes are summarized in Fig. 3 and Table 1. As expected, the cut size grew with increasing add-flow rate and decreasing wind tunnel air velocity. The cut size that corresponds to the conditions in E-PEACE (air speed = 50 m s^{-1} , add-flow rate = 16 l min^{-1}) is $11 \mu\text{m}$. The overall range of cut sizes identified in the experiments for the range of flow conditions was $8.7\text{--}13.1 \mu\text{m}$. Previous work has defined cut sharpness as $\sigma = (D_{p,84}/D_{p,16})^{1/2}$, with values ranging between 1.08–1.13 for at least one other CVI design (Anderson et al., 1993). Here we define cut sharpness as $\sigma = (D_{p,69}/D_{p,31})^{1/2}$ to stay consistent with the range of transmission efficiencies obtained in the experiments. Table 1 shows that the modified cut sharpness values range from 1.15–1.22 for the 50 m s^{-1} air speed condition and 1.28–1.34 for 100 m s^{-1} .

It is useful to compare the cut sizes predicted by aerodynamic drag theory to the experimentally determined values obtained in the wind tunnel experiments, as demonstrated in previous studies (e.g., Noone et al., 1988; Anderson et al., 1993). Here we adopt most of the notation and the numerical integration technique summarized by Anderson et al. (1993), where the size-dependent impaction distance is estimated between the stagnation planes using the position-dependent counter-flow gas velocity in the counter-flow region. The numerical integration is performed assuming the particle impaction starts at a distance, L_{cur} , away from the probe tip. The change in particle velocity is calculated along the path of impaction up to the internal stagnation plane. Particles which maintain a positive velocity through the internal stagnation

plane are collected by the inlet. The theoretical cut size, $D_{p,50}$, is determined by finding the particle diameter required to have a stopping distance equal to the length of the impaction path, L_{CVI} . The distance L_{CVI} is defined in Eq. (1), where L_{min} is the fixed distance from the probe tip to the start of the porous tube and L_{por} is the length from the start of the porous tube to the internal stagnation plane:

$$L_{\text{CVI}} = L_{\text{cur}} + L_{\text{min}} + L_{\text{por}}. \quad (1)$$

Variances between predicted and measured cut sizes are accounted for by adjusting the impaction starting point, L_{cur} . Previous cut size prediction methods have defined L_{cur} as a constant ($g(r)$ or C_1) multiplied by the outer probe radius, used to account for streamline curvature of air near the orifice of the probe (Noone et al., 1988; Anderson et al., 1993). Data obtained during the wind tunnel experiments were used to predict an average C_1 value of 1.25 over the range of counter-flow rates from $1\text{--}8 \text{ l min}^{-1}$ and air speeds from $50\text{--}100 \text{ m s}^{-1}$. With this C_1 value, the error between the predicted and measured cut sizes is less than 12.6 % for the six conditions tested in Table 1.

Characterization in the wind tunnel also included evaluating particle size-dependent losses in the CVI body, mainly as a result of inertial deposition. Losses were evaluated by comparing size distributions obtained while sampling through different portions of the sampling train to the distribution of glass beads measured by the APS with no CVI tip assembly installed in the wind tunnel. Experiments were performed to isolate losses for separate segments of the wind tunnel sampling train. Particle transmission was measured through a long sampling tube labeled 3 in Fig. 2, followed by examining losses through the sample expansion section coupled to the long sampling tube (segments 2 and 3 in Fig. 2). Finally, a comparison was made to a sample from the combined segments (segments 1, 2, and 3 in Fig. 2). From this, losses in segments 1 and 2 (Fig. 2) individually were determined. It should be noted that the wind tunnel sampling configuration differs from the configuration of the inlet as installed on an aircraft. Only losses in segments 1 and 2, which correspond to segments B and C (Fig. 1), are relevant to the aircraft installation. These losses are presented in Fig. 4, showing each segment's individual contribution and the combined effect. Tubing prior to the expansion is shown to be a larger source for particle losses via turbulent deposition as compared to the expansion. At the expected cut size of $11 \mu\text{m}$ during E-PEACE the total losses amount to approximately 57 % and increase to 72 % at a particle diameter of $20 \mu\text{m}$. It is noted that the tubing prior to the expansion is interchangeable, and losses can be significantly reduced by using a shortened tube. Ongoing work is addressing these losses. However, the results in Fig. 4 are critical for interpreting the E-PEACE field data, especially for validating the cut size measurements from the wind tunnel testing.

4 Field deployment and first results

The CVI was deployed on the Center for Interdisciplinary Remotely-Piloted Aircraft Studies (CIRPAS) Twin Otter during the 2011 E-PEACE field study off the central coast of California. E-PEACE consisted of 30 research flights to study aerosol-radiation-cloud-precipitation interactions over the Eastern Pacific Ocean during the summertime when stratuscumulus cloud decks are persistent. The domain of the flights ranged between 34° N–40° N and 121.5° W–125° W. Nine of the Twin Otter flights were coordinated with the Research Vessel *Point Sur*, which generated smoke each of these days to allow the aircraft to study the effects of a known source of aerosol on cloud microphysical and macrophysical properties. A comprehensive description of this field study is forthcoming.

Six different instruments conducted measurements downstream of the CVI in stratuscumulus clouds during E-PEACE (Fig. 5). A three-way valve was used to cycle these six instruments between the CVI in cloud and a sub-isokinetic aerosol inlet out of cloud. When sampling was conducted through the CVI in cloud, the total flow required by the instruments was 4.21 min⁻¹ with the CVI sample-flow MFC controlling the remaining 10.8 l min⁻¹. When the instruments downstream of the CVI were not sampling from the CVI sample-flow stream, the MFC allowed the full 15 l min⁻¹ through the sample stream. The instruments included a condensation particle counter (CPC; TSI Model 3010) to quantify total aerosol concentration (N_a). Aerosol size distribution data were obtained by a cylindrical scanning differential mobility analyzer (DMA; TSI Model 3081) coupled to a condensation particle counter (CPC; TSI Model 3010). Aerosol particles were dried prior to entering the DMA for sizing. Aerosol absorption and scattering coefficients were measured using a three-wavelength Photoacoustic Soot Spectrometer (PASS-3; Droplet Measurement Technologies). A continuous flow thermal gradient cloud condensation nuclei counter (CCNC, Droplet Measurement Technologies Inc.; Roberts and Nenes, 2005) was used to quantify the number of particles that activated at supersaturations ranging from 0.2 % to 0.8 %. Black carbon (BC) mass measurements were obtained using a single particle soot photometer instrument (SP2; Droplet Measurement Technologies) (Schwarz et al., 2006; Metcalf et al., 2012). Measurements of inorganic mass (sulfate, nitrate, ammonium) and total non-refractory organic mass were obtained with a compact Time of Flight Aerosol Mass Spectrometer (Aerodyne C-ToF-AMS) (Drewnick et al., 2005). A comprehensive analysis of the detailed measurements of droplet residual particle properties will be addressed in a subsequent study.

Critical to the examination of field data is the quantification of the “enhancement factor” as a result of the ambient aerosol concentration being concentrated in the CVI inlet ac-

cording to the following equation:

$$EF = \frac{A_{tip}V_{plane}}{q_{sample}} \quad (2)$$

where: EF is the enhancement factor, A_{tip} is the area of the inlet tip where drops enter, V_{plane} is aircraft velocity, and q_{sample} is the volumetric flow rate of sampled air in the CVI inlet. A_{tip} is $1.67 \times 10^{-5} \text{ m}^2$, q_{sample} is 15 l min^{-1} , and the aircraft velocity was usually near 50 m s^{-1} . The latter air velocity, which was tested in the wind tunnel experiments, coincides with an EF of 3.28.

It is possible for small amounts of particles with sizes below the $D_{p,50}$ to undergo “breakthrough” by way of collisions with larger particles, or wake capture (Pekour and Cziczo, 2011). To identify whether there was any breakthrough of small particles through the CVI, the inlet was operated for small periods of time during some flights in clear air just as it would be in cloud. To ensure the aircraft was in clear air for this analysis, data were used when the cloud liquid water content (LWC), measured by a PVM-100 probe (Gerber et al., 1994), was less than 0.01 g m^{-3} . When applying an add-flow ranging between 16 – 19 l min^{-1} , the CPC concentration in clear air ($LWC = 0.002 \pm 0.009 \text{ g m}^{-3}$) was $0.08 \pm 0.09 \text{ cm}^{-3}$. The ratio of the CPC concentration downstream of the CVI relative to an identical instrument sampling simultaneously downstream of a sub-isokinetic inlet was 0.0001 ± 0.0002 , indicating that particle breakthrough and any type of small particle contamination were absent.

Prior to E-PEACE, test flights were conducted to determine the flow angle at the location of the CVI intake. The location was only a short distance forward of the port wing root. Significant angles between the oncoming air flow and the CVI inlet will increase the likelihood of droplet impaction and shatter on inlet surfaces. A Rosemount 858 flow angle probe indicated a 10° up-wash at that location during flight, and flow visualization using yarn taped to the probe’s tip verified this angle. To minimize the chance of flow separation in the sampling inlet, and possible particle losses, the CVI probe was angled into the flow and mounted on the airplane with a 10° downward tilt.

Critical to the characterization of the field performance of the CVI is the comparison of particle number concentration (N_a) measured by the CPC downstream of the CVI to in-situ measurements of cloud drop concentration (N_d). For the latter measurement, data were obtained using a Cloud and Aerosol Spectrometer (CAS; $D_p \sim 1$ – $55 \mu\text{m}$; Droplet Measurement Technologies, Inc.; Baumgardner et al., 2001) and a Cloud Droplet Probe (CDP; $D_p \sim 1$ – $51 \mu\text{m}$; Droplet Measurement Technologies, Inc.; Lance et al., 2010). CVI data are presented for the first 11 flights (8 July–23 July) since both cloud probes were operational during this time range. The comparison involved applying the EF to the CPC data and the size-dependent transmission efficiency results in Fig. 4 to the cloud probe data to assess the level of agreement between N_a and N_d . Figure 6 summarizes the com-

parison of N_a to N_d , where the latter was quantified using a variety of minimum drop sizes smaller and larger than the cut size identified from the wind tunnel experiments. It is noted that the CAS instrument has larger bin widths (i.e. bin boundaries of 9.39, 12.52, and 16.28 μm) around the vicinity of the wind tunnel CVI cut size (11 μm) relative to the CDP (i.e. bin boundaries of 10.37, 11.35, 12.4 μm). The analysis was conducted for the following conditions: (i) LWC greater than 0.05 g m^{-3} to ensure the aircraft was in cloud; (ii) aircraft speeds between $45\text{--}60 \text{ m s}^{-1}$ to allow for a meaningful comparison with the wind tunnel results at 50 m s^{-1} ; (iii) the add-flow rate was either 16 or 171 min^{-1} . The agreement between N_a and N_d is best when the CAS drop distributions were integrated above $12.52 \mu\text{m}$ ($r^2 = 0.71$) and when the CDP distributions were integrated above $10.37 \mu\text{m}$ ($r^2 = 0.84$). The slope of N_a to N_d plots were closest to unity (0.90–0.97) for these two conditions with decreasing values when integrating the cloud drop distribution above larger sizes, indicating that the CVI cut size was close to 11 μm .

One case flight is examined in greater detail to examine the temporal trends in N_a and N_d in cloud. The focus of this analysis is Research Flight 6 on 16 July 2011, which was a flight coordinated between the Twin Otter and the Research Vessel *Point Sur*. The latter was generating smoke with an on-board smoke generator, and the aircraft probed the properties of the smoke both below cloud and in cloud. The flight tracks of the Twin Otter are shown in Fig. 7 superimposed on GOES-11 visible satellite imagery to show the structure of the clouds during the period of the flight. The aircraft conducted detailed measurements of aerosol properties below the cloud deck, within the cloud at different altitudes, and above the cloud deck. Figure 8 shows a representative 20 min flight leg when the Twin Otter was sampling in cloud, during which time the aircraft sampled the ship smoke in cloud numerous times. Based on a threshold LWC value of 0.05 g m^{-3} , this particular cloud deck had a base and top of approximately 70 m and 200 m, respectively. During the flight leg shown, the aircraft ascended from a region slightly above the bases to near the middle of the cloud deck, which is reflected in the increase in droplet size (Fig. 8; bottom panel). The N_a measurement downstream of the CVI is shown to exhibit the same temporal behavior as N_d measured by the CAS and CDP, when the size distributions of the two latter cloud probes were integrated at or below the expected cut size of the CVI ($\sim 11 \mu\text{m}$). When the aircraft flew in cloud regions influenced by the ship smoke, both N_a and N_d levels are enhanced with a reduction in drop size, which is consistent with the Twomey Effect (Twomey, 1974).

There was no indication of organic contamination from the inlet during E-PEACE. AMS measurements of non-refractory organics in droplet residual particles during clean marine background conditions were typically below the AMS organic detection limit of $0.1 \mu\text{g m}^{-3}$. Increases in the AMS organic mass concentration corresponded with

enhancements in other measurements indicating signs of increasing pollution (e.g., CPC, CDP, CAS, and other aerosol/cloud instruments); therefore, E-PEACE CVI measurements indicate that organic signals are a measurement of cloud nuclei chemistry and are uninfluenced by artifacts associated with the inlet material of construction.

An example of aerosol composition measurements downstream of the CVI is shown in Fig. 9. Four representative AMS mass fraction pie charts are shown to represent the following from Flight 6: background marine aerosol below cloud; background in cloud (CVI); *Point Sur* ship smoke below cloud; and *Point Sur* ship smoke in cloud (CVI). Only sulfate and organic contributions are shown since the other non-refractory constituents (i.e., ammonium, chloride, nitrate) were below detection limits. Organics were the dominant non-refractory component of the sub-micrometer aerosol, and this is especially the case for the *Point Sur* smoke, which was nearly entirely organic ($\sim 99\%$) when sampled below cloud during this flight. The droplet residual samples examined during the time when the *Point Sur* smoke was intercepted in cloud were mainly of organic nature ($\sim 92\%$), as compared to the background cloud conditions ($\sim 67\%$).

Figure 9 also shows log-normal fits to the mean size distributions obtained from a scanning differential mobility analyzer during the same time periods as the AMS pie charts. The background aerosol below cloud, sampled from the sub-isokinetic inlet, was fit to a two lognormal mode function; the size distributions behind the CVI were fit to a single-term log-normal function. The *Point Sur* smoke crossings below cloud were sufficiently narrow that an entire DMA scan ($\sim 110 \text{ s}$) did not properly capture the size distribution of this source, and thus only one average distribution is presented. The background sub-cloud size distribution exhibits a bimodal character with a sub-100 nm mode and a larger mode indicative of cloud-processed aerosol. The droplet residual particle size distributions were unimodal with the modal diameter at approximately 200 nm, indicating that the larger of the two modes below cloud was most effective at activating into droplets. More detailed results of the physicochemical properties of droplet residual particles from the E-PEACE study will be forthcoming.

5 Conclusions

A new CVI inlet has been characterized using wind tunnel experiments and deployed on the CIRPAS Twin Otter for 30 flights during the 2011 E-PEACE field campaign. With straightforward modifications, the inlet can also be deployed at ground or mountaintop sites to sample fog and orographic clouds. With a fixed sample flow rate of 151 min^{-1} , the wind tunnel experiments explored a range of add-flow rates ($16\text{--}231 \text{ min}^{-1}$) and air velocities ($50\text{--}100 \text{ m s}^{-1}$) to obtain inlet cut sizes between $8.7\text{--}13.1 \mu\text{m}$. Calculated cut sizes

from aerodynamic drag theory agree with measured values to within 13 %. When applying size-dependent transmission efficiency results from the wind tunnel to aircraft data, there was good agreement between particle concentration (N_a) measurements downstream of the CVI and cloud drop concentrations (N_d) measured by two independent cloud probes. When integrating the drop size distributions above a diameter close to the expected 11 μm cut size (based on wind tunnel testing), slopes from N_d - N_a plots were 0.90–0.97 and correlation coefficients (r^2) were 0.71–0.84. Representative data from a case study flight show excellent temporal agreement between N_a and N_d , especially when a smoke plume from a ship was intercepted in cloud. This resulted in sudden enhancements in drop concentration and reductions in drop size. Size distribution measurements of droplet residual particles during this flight show that the modal diameter of particles activated into drops was approximately 200 nm both in and out of the smoke. Aerosol composition measurements from an AMS indicate that the majority of the sub-micrometer non-refractory mass was from organic species, with the remaining constituent being sulfate. No indication of organic contamination from the inlet itself was found. Furthermore, no evidence of particle breakthrough or small particle contamination was observed during CVI sampling during E-PEACE.

Acknowledgements. This work was funded by an ONR DURIP grant (N00014-11-1-0783), an ONR YIP award (N00014-04-1-0018), ONR grant N00014-10-1-0200, NSF grants AGS-1008848 and AGS1013423, and Sea Spray Research, Inc. The authors gratefully acknowledge the crew of both the CIRPAS Twin Otter and the Research Vessel *Point Sur*.

References

Anderson, T. L., Charlson, R. J., and Covert, D. S.: Calibration of a counterflow virtual impactor at aerodynamic diameters from 1 to 15 μm , *Aerosol Sci. Tech.*, 19, 17–329, 1993.

Baumgardner, D. and Huebert, B.: The Airborne Aerosol Inlet Workshop – meeting report, *J. Aerosol Sci.*, 24, 835–846, 1993.

Baumgardner, D., Jonsson, H., Dawson, W., O'Connor, D., and Newton, R.: The cloud, aerosol and precipitation spectrometer: a new instrument for cloud investigations, *Atmos. Res.*, 59–60, 251–264, 2001.

Berg, L. K., Berkowitz, C. M., Ogren, J. A., Hostetler, C. A., Ferrare, R. A., Dubey, M. K., Andrews, E., Coulter, R. L., Hair, J. W., Hubbe, J. M., Lee, Y. N., Mazzoleni, C., Olfert, J., and Springston, S. R.: Overview of the Cumulus Humilis Aerosol Processing Study, *B. Am. Meteorol. Soc.*, 90, 1653–1667, 2009.

Drewnick, F., Hings, S. S., DeCarlo, P., Jayne, J. T., Gonin, M., Fuhrer, K., Weimer, S., Jimenez, J. L., Demerjian, K. L., Borrmann, S., and Worsnop, D. R.: A new time-of-flight aerosol mass spectrometer (TOF-AMS) – instrument description and first field deployment, *Aerosol Sci. Tech.*, 39, 637–658, 2005.

Gerber, H., Arends, B. G., and Ackerman, A. S.: New microphysics sensor for aircraft use, *Atmos. Res.*, 31, 235–252, 1994.

Hallberg, A., Noone, K. J., Ogren, J. A., Svenningsson, I. B., Flossmann, A., Wiedensohler, A., Hansson, H. C., Heintzenberg, J., Anderson, T. L., Arends, B. G., and Maser, R.: Phase partitioning of aerosol particles in clouds at Kleiner Feldberg, *J. Atmos. Chem.*, 19, 107–127, 1994.

Hallberg, A., Noone, K. J., and Ogren, J. A.: Aerosol particles and clouds: which particles form cloud-droplets?, *Tellus B*, 50, 59–75, 1998.

Hayden, K. L., Macdonald, A. M., Gong, W., Toom-Sauntry, D., Anlauf, K. G., Leithead, A., Li, S.-M., Leitch, W. R., and Noone, K.: Cloud processing of nitrate, *J. Geophys. Res.*, 113, D18201, doi:10.1029/2007JD009732, 2008.

Hegg, D. A., Covert, D. S., Jonsson, H., and Covert, P. A.: Determination of the transmission efficiency of an aircraft aerosol inlet, *Aerosol Sci. Tech.*, 39, 966–971, 2005.

Hermann, M., Stratmann, F., Wilck, M., and Wiedensohler, A.: Sampling characteristics of an aircraft-borne aerosol inlet system, *J. Atmos. Ocean Tech.*, 18, 7–19, 2001.

Hudson, J. G.: Cloud condensation nuclei near marine cumulus, *J. Geophys. Res.*, 98, 2693–2702, 1993.

Hudson, J. G. and Frisbie, P. R.: Cloud condensation nuclei near marine stratus, *J. Geophys. Res.*, 96, 20795–20808, 1991.

Huebert, B. J., Lee, G., and Warren, W. L.: Airborne aerosol inlet passing efficiency measurement, *J. Geophys. Res.*, 95, 16369–16381, 1990.

Lance, S., Brock, C. A., Rogers, D., and Gordon, J. A.: Water droplet calibration of the Cloud Droplet Probe (CDP) and in-flight performance in liquid, ice and mixed-phase clouds during ARCPAC, *Atmos. Meas. Tech.*, 3, 1683–1706, doi:10.5194/amt-3-1683-2010, 2010.

Laucks, M. L. and Twohy, C. H.: Size-dependent collection efficiency of an airborne counterflow virtual impactor, *Aerosol Sci. Tech.*, 28, 40–61, 1998.

Lin, H. and Heintzenberg, J.: A theoretical-study of the counterflow virtual impactor, *J. Aerosol Sci.*, 26, 903–914, 1995.

Noone, K. J., Ogren, J. A., Heintzenberg, J., Charlson, R. J., and Covert, D. S.: Design and calibration of a counterflow virtual impactor for sampling of atmospheric fog and cloud-droplets, *Aerosol Sci. Tech.*, 8, 235–244, 1988.

Ogren, J. A., Heintzenberg, J., and Charlson, R. J.: In-situ sampling of clouds with a droplet to aerosol converter, *Geophys. Res. Lett.*, 12, 121–124, 1985.

Ogren, J. A., Heintzenberg, J., and Charlson, R. J.: Virtual impactor, U.S. Patent No. 4,689,052, 1987.

Ostrom, E., Noone, K. J., and Pockalny, R. A.: Cloud-droplet residual particle microphysics in marine stratocumulus clouds observed during the Monterey Area Ship Track experiment, *J. Atmos. Sci.*, 7, 2671–2683, 2000.

Pekour, M. S. and Cziczo, D. J.: Wake capture, particle breakup, and other artifacts associated with counterflow virtual impaction, *Aerosol Sci. Tech.*, 45, 758–764, 2011.

Roberts, G. C. and Nenes, A.: A continuous-flow streamwise thermal-gradient CCN chamber for atmospheric measurements, *Aerosol Sci. Tech.*, 39, 206–221, doi:10.1080/02786290913988, 2005.

Schwarz, J. P., Gao, R. S., Fahey, D. W., Thomson, D. S., Watts, L. A., Wilson, J. C., Reeves, J. M., Darbeheshti, M., Baumgardner, D. G., Kok, G. L., Chung, S. H., Schulz, M., Hendricks, J., Lauer, A., Karcher, B., Slowik, J. G., Rosenlof, K. H.,

Thompson, T. L., Langford, A. O., Loewenstein, M., and Aikin, K. C.: Single-particle measurements of midlatitude black carbon and light-scattering aerosols from the boundary layer to the lower stratosphere, *J. Geophys. Res.*, 111, D16207, doi:10.1029/2006JD007076, 2006.

Schwarzenböck, A. and Heintzenberg, J.: Cut size minimization and cloud element break-up in a ground-based CVI, *J. Aerosol Sci.*, 31, 477–489, 2000.

Sellegrí, K., Laj, P., Dupuy, R., Legrand, M., Preunkert, S., and Putaud, J. P.: Size-dependent scavenging efficiencies of multicomponent atmospheric aerosols in clouds, *J. Geophys. Res.*, 108, 4334, doi:10.1029/2002JD002749, 2003.

Sorooshian, A., Brechtel, F. J., Ma, Y. L., Weber, R. J., Corless, A., Flagan, R. C., and Seinfeld, J. H.: Modeling and characterization of a particle-into-liquid sampler (PILS), *Aerosol Sci. Tech.*, 40, 396–409, doi:10.1080/02786820600632282, 2006a.

Sorooshian, A., Varutbangkul, V., Brechtel, F. J., Ervens, B., Feingold, G., Bahreini, R., Murphy, S. M., Holloway, J. S., Atlas, E. L., Buzorius, G., Jonsson, H., Flagan, R. C., and Seinfeld, J. H.: Oxalic acid in clear and cloudy atmospheres: analysis of data from International Consortium for Atmospheric Research on Transport and Transformation 2004, *J. Geophys. Res.*, 111, D23S45, doi:10.1029/2005JD006880, 2006b.

Sorooshian, A., Murphy, S. M., Hersey, S., Bahreini, R., Jonsson, H., Flagan, R. C., and Seinfeld, J. H.: Constraining the contribution of organic acids and AMS m/z 44 to the organic aerosol budget: on the importance of meteorology, aerosol hygroscopicity, and region, *Geophys. Res. Lett.*, 37, L21807, doi:10.1029/2010GL044951, 2010.

Twohy, C. H.: Model calculations and wind tunnel testing of an isokinetic shroud for high-speed sampling, *Aerosol Sci. Tech.*, 29, 261–280, 1998.

Twohy, C. H., Clarke, A. D., Warren, S. G., Radke, L. F., and Charlson, R. J.: Light absorbing material extracted from cloud-droplets and its effect on cloud albedo, *J. Geophys. Res.*, 94, 8623–8631, 1989.

Twomey, S.: Pollution and planetary albedo, *Atmos. Environ.*, 8, 1251–1256, 1974.

Weber, R. J., Clarke, A. D., Litchy, M., Li, J., Kok, G., Schillawski, R. D., and McMurry, P. H.: Spurious aerosol measurements when sampling from aircraft in the vicinity of clouds, *J. Geophys. Res.*, 103, 28337–28346, 1998.

Table 1. Cut size behavior of the CVI inlet at different simulated air velocities and add-flow rates. Results are shown for wind tunnel experiments and theoretical calculations based on a numerical integration technique described by Anderson et al. (1993) using a C_1 value of 1.25. Values in parentheses in the “Measured” columns correspond to the cut sharpness defined as $(D_{p,69}/D_{p,31})^{1/2}$. Values in parentheses in the “Predicted” columns signify the percent error between measured and predicted values.

Add-flow (1 min^{-1})	Measured		Predicted	
	$D_{p,50}$ at 50 m s^{-1} (μm)	$D_{p,50}$ at 100 m s^{-1} (μm)	$D_{p,50}$ at 50 m s^{-1} (μm)	$D_{p,50}$ at 100 m s^{-1} (μm)
16	11.0 (1.22)	8.7 (1.34)	10.8 (1.8 %)	7.6 (12.6 %)
19	12.5 (1.20)	9.8 (1.28)	12.9 (3.2 %)	8.9 (9.2 %)
23	13.1 (1.15)	10.2 (1.30)	14.7 (12.2 %)	10.0 (2.0 %)

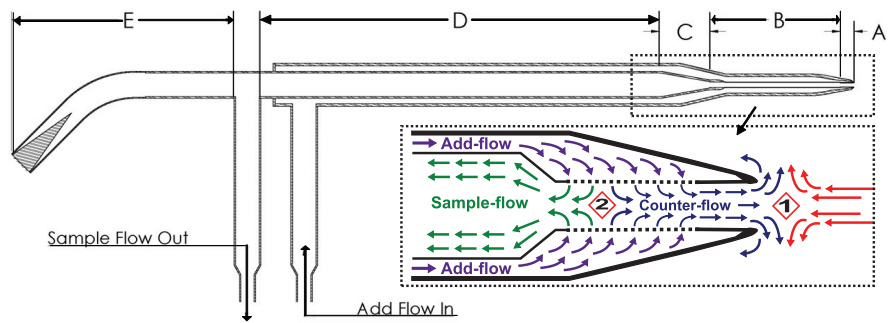


Fig. 1. Schematic depiction of the BMI CVI and flows innate to its operation. Sampled air enters the CVI through the inlet nozzle and passes through a region containing a porous tube where the heated counter-flow is introduced (A). The resulting sample flow enters an extension tube (B), before the expansion region (C). The particles then travel through additional plumbing (D) and enter the aircraft body for sample feed to instruments. Entities too large to bend into the aircraft are collected in a particle trap (E). Two stagnation planes (labeled 1 and 2) are generated between opposing flow directions. The cut size is governed by the velocity of the ambient air flow and the distance between the two stagnation planes.

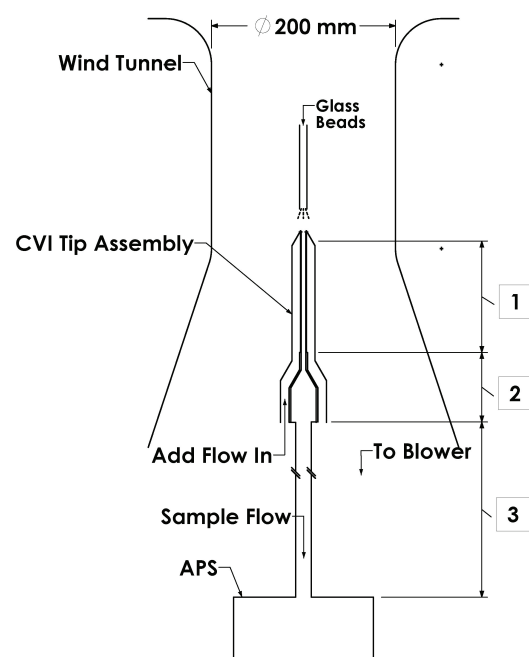


Fig. 2. Schematic of BMI wind tunnel set-up. A dispersion of glass sphere beads is introduced to the wind tunnel and the inlet operates in either isokinetic or CVI sampling mode. The ratio of the number size distributions measured by an aerodynamic particle sizer (APS) is used to determine the transmission efficiency of the inlet. These experiments followed the methods summarized by Anderson et al. (1993). The number labels are used to distinguish between different sections of the sampling train.

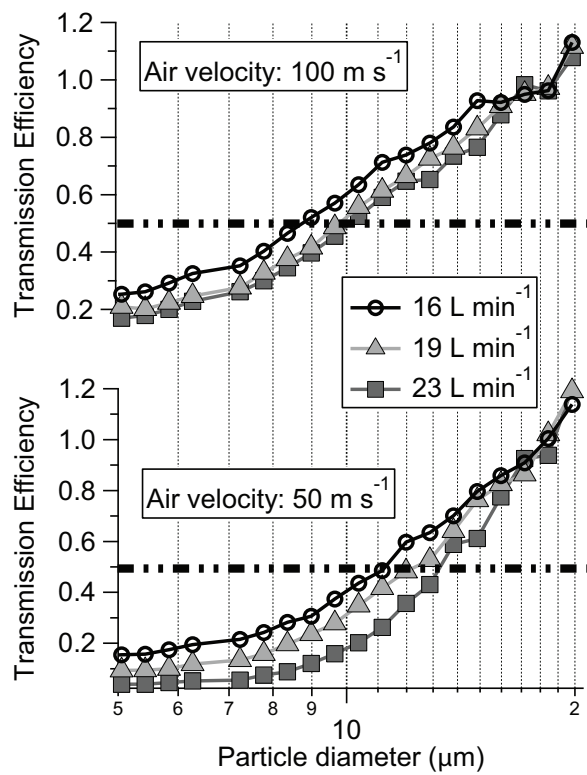


Fig. 3. Transmission efficiency of hollow glass beads at different add-flow rates based on experiments conducted with the BMI wind tunnel at different air velocity conditions (50 and 100 m s^{-1}). The dashed horizontal lines correspond to 50% transmission efficiency, which defines the inlet cut size ($D_{p,50}$).

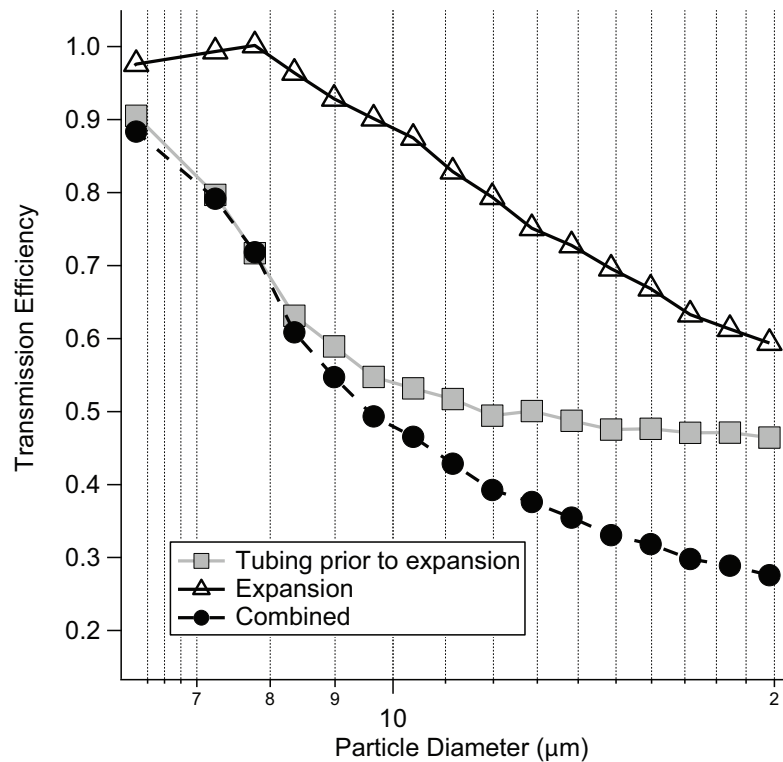


Fig. 4. Transmission efficiency for hollow glass beads in various parts of the CVI inlet based on wind tunnel experiments. “Tubing prior to expansion” refers to segment (B) in Fig. 1 and “Expansion” refers to segment (C) in Fig. 1.

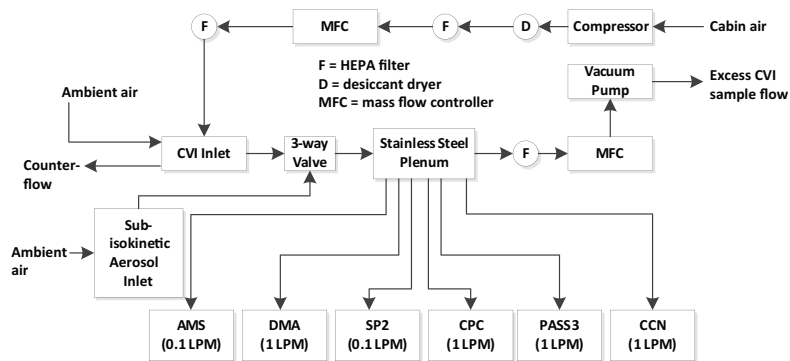


Fig. 5. Schematic of the sample air flow path through both the sub-isokinetic aerosol inlet (clear air sampling) and the CVI (in-cloud sampling) on the CIRPAS Twin Otter during the 2011 E-PEACE experiment. Six instruments characterized aerosol physicochemical properties downstream of the CVI inlet with their respective flow rates shown (total = 4.2 l min^{-1}). As the total sample flow provided was 15 l min^{-1} , the excess sample flow (10.8 l min^{-1}) was diverted out of the aircraft by a vacuum pump.

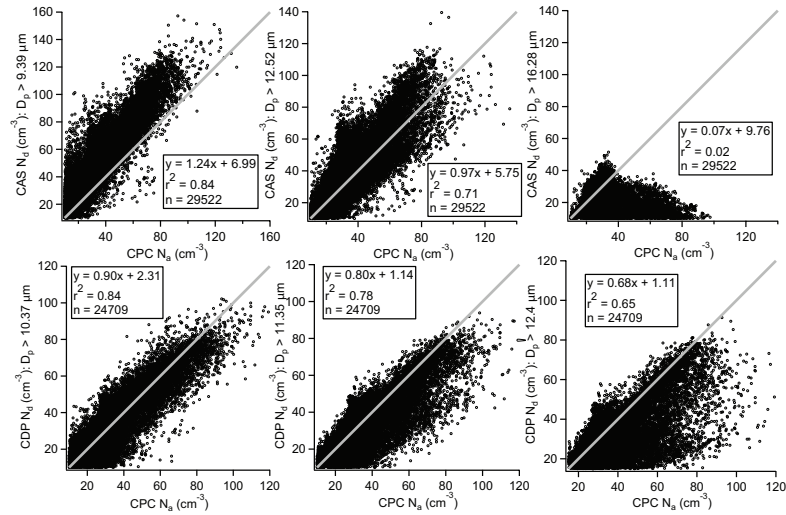


Fig. 6. Comparison of corrected total particle concentration (N_a) measured behind the CVI by a CPC and total cloud drop concentration (N_d) measured by two independent cloud probes (CDP and CAS). For both cloud probes, N_d is reported above three different minimum drop sizes around the expected cut size ($\sim 11 \mu\text{m}$) of the CVI at 50 m s^{-1} for the usual add-flow rate applied ($\sim 161 \text{ min}^{-1}$) based on wind tunnel results. Data are shown when the in-cloud liquid water content exceeded 0.05 g m^{-3} , when the aircraft speed was between $45\text{--}60 \text{ m s}^{-1}$, and when the add-flow rate was between $16\text{--}171 \text{ min}^{-1}$. The gray shaded lines signify the 1-to-1 line. The reason the slope of the top right panel is much lower than the rest is that the majority of the sampled cloud drop number concentrations were typically at lower diameters.

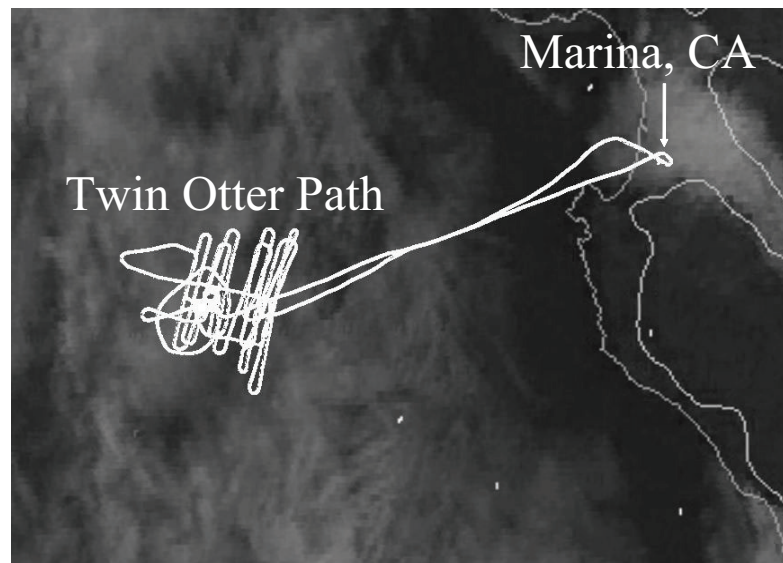


Fig. 7. GOES-11 visible satellite imagery at 18:00 UTC on 16 July 2011 with the superposition of the CIRPAS Twin Otter, which was based in Marina, California. The high density of flight track points to the far west coincides with when the aircraft was probing the smoke plume generated by the *Point Sur* ship. The corresponding time series of aircraft data is shown in Fig. 8 with aerosol size distribution and composition data shown in Fig. 9.

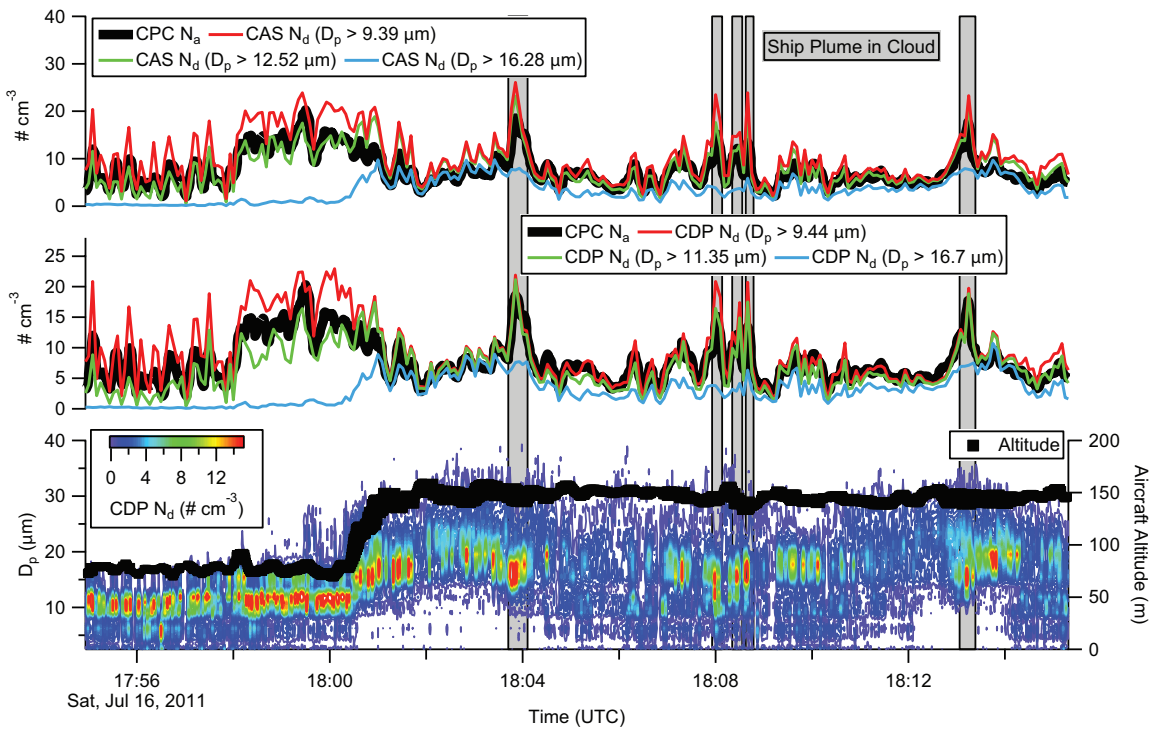


Fig. 8. Time series of aircraft data collected during Flight 6 of the 2011 E-PEACE campaign on 16 July 2011. The 20-min time segment coincides with when the Twin Otter was flying in a stratocumulus cloud deck of the coast of Monterey, California. This flight was coordinated with the Research Vessel *Point Sur*, which generated smoke that influenced the cloud in the several gray shaded regions of the time series via enhancements in drop concentration and reductions in drop size. The total particle concentration (N_a) measured behind the CVI by a CPC (with enhancement factor, ~ 3.3 , applied) is compared to total cloud drop concentration (N_d) measured by two independent probes, where N_d is integrated above three different diameters to further constrain the CVI cut size diameter. Size-dependent transmission efficiency losses from Fig. 4 are applied to the N_d data. The aircraft altitude marker size is proportional to LWC (range ~ 0.05 – 0.30 g m^{-3}).

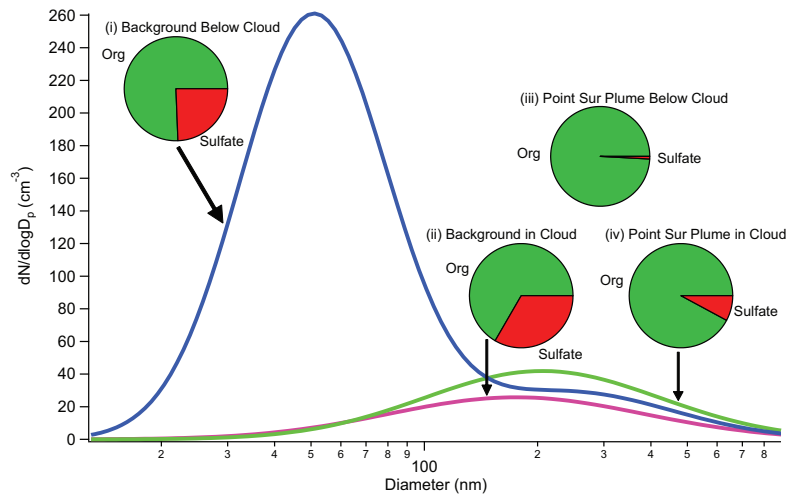


Fig. 9. DMA size distribution and AMS chemical composition measurements during Flight 6 from Figs. 7–8. The DMA data collected downstream of a sub-isokinetic inlet below cloud were fit to a two-term log-normal function while the size distributions downstream the CVI were fit to a single-term log-normal function. Only sulfate and non-refractory organics were observed above detection limits by the AMS, and their relative mass concentrations are depicted in the pie charts for four different conditions: (i)–(ii) background marine aerosol below cloud and in cloud behind the CVI; (iii)–(iv) *Point Sur* smoke below cloud and in cloud behind the CVI. DMA data are not available for the *Point Sur* smoke below cloud.

Appendix F

Eastern Pacific Emitted Aerosol Cloud Experiment (E-PEACE)*

*Submitted as “Eastern Pacific Emitted Aerosol Cloud Experiment (E-PEACE)” by L. M. Russell, A. Sorooshian, J. H. Seinfeld, B. A. Albrecht, A. Nenes, L. Ahlm, Y.-C. Chen, M. Coggon, J. S. Craven, R. C. Flagan, A. A. Frossard, H. Jonsson, E. Jung, J. J. Lin, A. R. Metcalf, R. Modini, J. Mülmenstädt, G. C. Roberts, T. Shingler, S. Song, E. Sumargo, Z. Wang, A. Wonaschütz to *Bulletin of the American Meteorological Society*. Copyright 2012 by the American Meteorological Society.

Eastern Pacific Emitted Aerosol Cloud Experiment (E-PEACE)

LYNN M. RUSSELL, * LARS AHLM, AMANDA A. FROSSARD, ROBIN MODINI,
JOHANNES MÜLMENSTÄDT, AND EDWIN SUMARGO

Scripps Institution of Oceanography, University of California, San Diego, La Jolla, CA.

ARMIN SOROOSHIAN, TAYLOR SHINGLER, ZHEN WANG, AND ANNA WONASCHÜTZ

Departments of Chemical and Environmental Engineering and of Atmospheric Sciences, University of Arizona, Tucson, AZ.

JOHN H. SEINFELD, YI-CHUN CHEN, MATTHEW COGGON, JILL S. CRAVEN,
RICHARD C. FLAGAN, AND ANDREW R. METCALF

California Institute of Technology, Pasadena, CA.

BRUCE A. ALBRECHT, EUNSIL JUNG, AND SIWON SONG

Rosenstiel School of Marine Sciences, University of Miami, Miami, FL.

ATHANASIOS NENES AND JACK J. LIN

School of Earth and Atmospheric Sciences, Georgia Institute of Technology, Atlanta, GA.

HAFLIDI JONSSON

Center Interdisciplinary Remotely-Piloted Aerosol Studies, Marina, CA.

GREG C. ROBERTS

Scripps Institution of Oceanography, University of California, San Diego, La Jolla, CA and

Centre National de la Recherche Scientifique – Groupe d'études de l'Atmosphère Météorologique, Toulouse, France.

ABSTRACT

Aerosol-cloud-radiation interactions are widely held to be the largest single source of uncertainty in climate model projections of future radiative forcing due to increasing anthropogenic emissions. The underlying causes of this uncertainty among modeled predictions of climate are the gaps in our fundamental understanding of cloud processes. There has been significant progress with both observations and models on addressing these important questions, but quantifying them correctly is nontrivial thus limiting our ability to represent them in global climate models. The Eastern Pacific Emitted Aerosol Cloud Experiment (E-PEACE) 2011 was a targeted aircraft campaign with embedded modeling studies, using the CIRPAS Twin Otter aircraft and the Research Vessel *Point Sur* in July and August 2011 off the central coast of California, with a full payload of instruments to measure particle and cloud number, mass, composition, and water uptake distributions. E-PEACE used three emitted particle sources to separate particle-induced feedbacks from dynamical variability, namely (i) shipboard smoke-generated particles with 0.1–1 μm diameters (which produced tracks measured by satellite and had drop composition characteristic of organic smoke), (ii) combustion particles from container ships with 0.05–0.2 μm diameters (which were measured in a variety of conditions with droplets containing both organic and sulfate components), and (iii) aircraft-based milled, coated salt particles with 3–5 μm diameters (which showed enhanced drizzle rates in some clouds). The aircraft observations were consistent with large eddy simulations of deeper clouds in ship tracks and aerosol-cloud parcel modeling of cloud drop number and composition, providing quantitative constraints on aerosol effects on warm cloud microphysics.

1. Introduction

Gaps in our fundamental understanding of cloud processes are the central underlying cause of uncertainty in aerosol radiative forcing, even in widespread and well-defined

systems such as those for marine stratocumulus cloud formation. Atmospheric aerosol levels have increased markedly since the Industrial Revolution. We do not fully understand the extent to which this increase has affected the

cycles of radiant energy and water in the climate system. It has been well established that clouds forming in a polluted environment tend to have more numerous, smaller droplets, which may or may not lead to a cloud of higher cloud optical depth and albedo. Once cloud droplet size and number concentration are perturbed, the dynamics of both the cloud itself and the atmospheric layer in which it is embedded change in a nonlinear manner. Many important questions arise including: (1) What is the relationship between cloud microstructure and the aerosol on which the cloud forms? (2) How can the understanding of cloud responses to increased aerosol levels be represented in theories and models of the climate system? (3) Is it possible to extract observationally the cloud response to aerosols from that of the changing ambient meteorology? Our understanding, especially of warm-phase cloud microphysics, has advanced significantly in the last decade as a result of satellite observations, computational modeling, and field studies. Still, the challenge of untangling the effects of aerosol perturbations on clouds from those of meteorological variability itself and generalizing the findings from such studies to the scales that affect climate remains daunting. Aerosol properties tend to be highly variable, both spatially and temporally, in terms of size and chemical composition. While limited attempts have been made to employ particles of known size and composition in cloud perturbation studies, and thereby alleviate uncertainties associated with cloud activation, such attempts have proved difficult to implement. Here we describe a coordinated field experiment, the Eastern Pacific Emitted Aerosol Cloud Experiment (E-PEACE) campaign, in which the effects of well-defined aerosol perturbations on marine stratocumulus clouds were probed via *in situ* aircraft and satellite observations.

Key issues that have made accurately depicting aerosol effects on clouds in large-scale models include:

1. What is the overall effect of particles and the clouds that form on them on Earth's climate?
2. What is the effect of the distribution of particles by size on cloud droplet activation and cloud microphysics?
3. How does the chemical makeup of particles affect cloud response?

2. Marine Stratocumulus and Climate

Stratocumulus clouds are characterized by their large spatial extent, and organize into distinctive patterns often with rolling, linear structures. They are primarily formed over the oceans and are a semi-persistent feature in many regions adjacent to continents. The dynamical conditions that lead to their formation involve generation of convective currents below drier, stable air that prevents continued vertical development. Based on this, stratocumulus

clouds are typically classified in three categories (Klein and Hartmann 1993). The first and most common involve the formation over oceans with relatively cold sea surface temperatures with a boundary layer that is capped by a strong temperature inversion (maintained by large-scale subsidence). These systems are typically formed in regions near western continental boundaries, where trade winds blow from midlatitudes towards the intertropical convergence zone and generate ocean upwelling. The convection that maintains the stratocumulus is driven by radiative cooling at the top of the boundary layer (Lilly 1968), while precipitation and entrainment are thought to represent key forcings that control the structure and stability of the boundary layer. Another type of stratocumulus cloud is formed in winter over oceanic western boundary currents, where cold continental air flows over warm waters, and develops convection. Unlike the first category, convection is driven by strong surface fluxes (Schubert et al. 1979a,b). Finally, Arctic stratus is formed mostly in the summer and results from radiative cooling of subpolar moist air entrained into the Arctic (Curry et al. 1988).

Considerable areas of subtropical and polar oceans are extensively covered with stratocumuli (Fig. 1). In the mid-latitude oceans (40–60°N and 50–65°S) maximum cloud cover occurs during the summer months and ranges between 62–82%; minimum cloud cover occurs in the winter and ranges around 50% (Klein and Hartmann 1993). In the subtropics, cloud cover is more variable (but still considerable) ranging from 35–72% during peak months and 17–42% during minimum activity (Klein and Hartmann 1993). The shortwave cloud albedo forcing of stratocumulus is larger than their cloud greenhouse forcing, resulting in a net cooling over the regions they cover. According to the Earth Radiation Budget Experiment (ERBE; Barkstrom 1984), the longwave cloud forcing of midlatitude stratocumulus is about 40 W m^{-2} , while the shortwave forcing reaches a minimum of -150 W m^{-2} in the Pacific and -120 W m^{-2} in the Atlantic. The strong net forcing of $\sim 100 \text{ W m}^{-2}$ is a cooling effect with considerable impacts on local and global climate.

3. Response of Marine Stratocumulus (MSc) to Aerosol Perturbations

There have been several important measurement campaigns (Table 1) as well as a number of modeling studies (Table 2) aimed at characterizing the response of marine stratocumulus to aerosol perturbations. The Monterey Area Ship Track Experiment (MAST) in 1994 (Durkee et al. 2000a) was one of the first aircraft-based studies that included detailed characterization of aerosol and cloud droplet size distributions down to 20 nm and above 20 μm . This study tracked particle emissions from ships in stratocumulus cloud conditions, allowing identification of the

Ship Tracks

In 1966, Conover (1966) reported anomalous cloud lines present in visible-wavelength satellite images from Television Infrared Observational Satellites (TIROS). He noted that these lines, as much as 500 km long and up to 25 km in width, were likely due to liquid particles from the exhaust of ocean going vessels. Twomey et al. (1968) remarked that the observations by Conover were consistent with the impact of additional cloud condensation nuclei (CCN) in a very clean marine boundary layer. Subsequent studies have strengthened the connection between ship exhaust and so-called ship tracks (e.g. Scorer 1987). Observations using near-infrared wavelengths from Advanced Very High Resolution Radiometer (AVHRR) exhibit more extensive features of ship effects on clouds (Coakley Jr et al. 1987). Twomey (1991) showed that marine stratiform clouds may be particularly sensitive to additional CCN, leading to higher cloud droplet number concentration and increased cloud reflectivity (albedo).

In-situ airborne measurements of ship tracks during the First International Satellite Cloud Climatology Project (ISCCP) Regional Experiment (FIRE) in 1987 showed that droplet sizes in the ship track itself decreased significantly, accompanied by a higher liquid water content in the ship track than in the background (Radke et al. 1989). Albrecht (1989) proposed that the increase in liquid water content resulted from drizzle suppression in the ship tracks due to smaller droplet sizes and consequent retarded coalescence. Later, aircraft measurements off the Washington coast also noted the reduction of drizzle droplet numbers in the ship tracks (Ferek et al. 1998). The Monterey Area Ship Track (MAST) experiment, which took place off the California coast in June 1994 (Durkee et al. 2000b), was designed to examine a series of hypotheses focused on links between the ship-emitted aerosol, mixing of the effluent through the boundary layer, and response in cloud droplets.

Remote sensing data from advanced satellite instrumentation has been applied in a number of studies on ship tracks (e.g. Schreier et al. 2007; Segrin et al. 2007). Recent satellite studies using Moderate Resolution Imaging Spectroradiometer (MODIS) imagery (Christensen and Stephens 2011) have observed ship tracks embedded in different cloud structures. Cloud-Aerosol Lidar with Orthogonal Polarization (CALIOP) was used to determine the extent to which ship-emitted aerosols alter the microphysical and macrophysical properties of marine stratocumulus across the North Pacific Ocean and off the coasts of South America and South Africa. The results show the key changes

effects of aerosol perturbations on cloud radiative signatures (Noone et al. 2000a,b). The Second Dynamics and Chemistry of Marine Stratocumulus (DYCOMS-II) field study consisted of 9 nighttime flights west of San Diego in July 2001 for testing large-eddy simulations of nocturnal stratocumulus (Stevens et al. 2003). A linear relationship between CCN and cloud droplet number emerged (Twohy et al. 2005), together with the drizzle-induced change in cloud structure (vanZanten and Stevens 2005). A series of Cloud Aerosol Research in the Marine Atmosphere (CARMA; Hegg et al. 2009) studies helped explain the source attribution of CCN and aerosol light scattering in the northeastern Pacific marine boundary layer. The Cloud Indirect Forcing Experiment (CIFEX) showed that aerosols over the Northeastern Pacific Ocean (primarily from North American emissions) enhance the cloud drop number concentration and reduce the drop size for marine stratocumulus and cumulus clouds, resulting in satellite-measured increases in cloud brightness (Wilcox et al. 2006).

The Marine Stratus/Stratocumulus Experiment (MASE) was carried out in two phases over the eastern Pacific Ocean off the coast of Monterey, California. The first phase (MASE-I) was undertaken in July 2005 (Lu et al. 2007), and the second phase (MASE-II) was conducted in July 2007 (Lu et al. 2009), each to evaluate aerosol-cloud-drizzle relationships in regions of uniform meteorology with localized aerosol enhancements in ship tracks. The ship track regions exhibited a smaller cloud drop effective radius, higher cloud droplet number concentration, reduced drizzle drop number concentration, and higher liquid water content than the adjacent clean regions, but trends were obscured by spatial-temporal variability. Results at the individual and ensemble scales in both MASE studies are in accord with those from other field campaigns (e.g. Brenquier et al. 2000; Feingold et al. 2006; Wilcox et al. 2006; Roberts et al. 2008), in that increased cloud drop number (CDN) concentration and decreased cloud-top effective radius are associated with increased sub-cloud aerosol concentration (at fixed liquid water path, LWP). The ship track regions exhibited a smaller cloud drop spectral width and relative dispersion in MASE-I, in accord with large eddy simulations (Lu and Seinfeld 2006). More polluted clouds were observed to have a smaller cloud-base drizzle rate; however, this did not equate to a larger amount of liquid water in that column of the atmosphere (LWP) when compared with clean clouds. Dynamic adjustment of the cloud in response to drizzle, in-cloud latent heating, sub-cloud evaporative cooling, and cloud-top entrainment would need to be taken into consideration (Ackerman et al. 2004; Lu and Seinfeld 2005). A new framework of precipitation susceptibility (Feingold and Siebert 2009; Sorooshian et al. 2009a), which quantifies the change in precipitation rate in response to aerosol perturbations, was applied in MASE-II.

The VAMOS Ocean-Cloud-Atmosphere-Land Study Regional Experiment (VOCALS-REx) was conducted in the southeast Pacific off the coast of northern Chile during October and November of 2008 to make observations of poorly understood but important components of the coupled climate system of the southeast Pacific (Bretherton et al. 2010; Wood et al. 2011a,b). VOCALS investigated (i) links between aerosol, clouds, and precipitation and their impacts on stratocumulus radiative properties, (ii) physical and chemical couplings between the upper ocean and the lower atmosphere, and (iii) datasets for the evaluation and improvement of large-scale numerical models. Transition and feedbacks of mesoscale cellular convection were addressed (Wood et al. 2011a), as well as the modeling of microphysical and meteorological controls on precipitation and cloud cellular structure (Wang et al. 2010).

Of critical importance to the aerosol-cloud system is how the clouds themselves modify aerosol physicochemical properties, which consequently affects their ability to interact with radiation outside of clouds in addition to serving as CCN the next time the particles are entrained into cloud. Most particles in the marine boundary layer likely have at some point in their lifetime been inside a cloud. Simulations of typical parcel trajectories in the marine atmosphere suggest that aerosol particles can cycle in and out of clouds numerous times during their lifetime (Feingold et al. 1998). Of the limited studies that have examined cloud effects on aerosol in the northeastern Pacific region, there is evidence that clouds alter both the inorganic and organic fractions of aerosol (Crahan et al. 2004; Sorooshian et al. 2007), which can lead to different hygroscopic properties (Hegg et al. 2008; Hersey et al. 2009). These studies motivated the need for additional work to better constrain the influence of clouds on aerosol size, composition, and water-uptake properties.

4. E-PEACE

E-PEACE combined a targeted aircraft campaign off the coast of Monterey, California, in July and August 2011, with embedded ship and satellite observations (Fig. 2) and modeling studies. Atmospheric conditions in the Monterey area of the northeastern Pacific during July are ideal for formation of homogeneous layers of persistent stratocumulus clouds. The layers observed have consistent diurnal characteristics, cloud thicknesses of 100 to 300 m, and cloud top heights typically below 500 m. The susceptibility of cloud albedo to particle perturbations is well documented for the Monterey region (Coakley Jr et al. 1987, 2000; Platnick et al. 2000).

We employed the R/V *Point Sur* to measure the aerosol below cloud and as a platform for well-characterized smoke emissions to produce a uniquely identifiable cloud signature. The Center for Interdisciplinary Remotely-Piloted

Tailor Made Particles with a Battlefield Smoke Generator

Smoke emissions were generated on the stern of the R/V *Point Sur* by two U.S.-Army-issued smoke generators (Fig. 5) manufactured in approximately 1980 for use as battlefield obscurants, purchased in 2005 and refurbished. The pulse-jet engines employ standard gasoline in a fuel injector head, which is ignited by manually pumping the air pressure to 60 psi before generating a spark with a grating device. The engine is used to pump and heat paraffin-type oil so that it vaporizes (but does not ignite) at approximately 150°C (the flash point). The oil pumps were modified at sea using pressurized air to force the pistons, likely required to offset the effects of rusting over time. Maintenance was required hourly to clean the fuel injectors and adjust the fuel and oil delivery rates to optimize the fuel-to-air ratio and temperature in the engine.

The vaporized oil is then released through three nozzles into the atmosphere where it condenses as droplets that range from 200 nm to 8 μm in diameter (Fig. 3). Some oil was emitted as vapor, producing a second smaller mode of particles from oxidized organic components about 100 nm in diameter. The generators ran close to their design values, consuming approximately 5 gal gasoline and 1 barrel (55 gal) of oil every hour. Paraffin-type oil is used in similar amounts by skywriting activities, where each 3-word message takes about 1 h of flight time and consumes 1 barrel of oil. At 10,000 ft, the lifetime of oil particles is likely 7 days, two to three times longer than that of surface-emitted particles. The Library of Congress describes the use of this oil in skywriting as environmentally safe (<http://www.loc.gov/rr/scitech/mysteries/skywriting.html>).

We operated the smoke generators from 12 to 23 July from approximately dawn until noon, following a zig-zag pattern similar to that shown in Fig. 2. We were restricted to headings into the wind by a net 5 kts or more to prevent eddies generated by the ship superstructure from carrying smoke backwards into the cabins. This meant that in lower wind conditions, the smoke trail became more concentrated. In winds slower than the ship's speed (10 kts), we were able to reverse course and measure the composition and number of particles in the smoke. These particles were 97% organic components, lacking both the ~50% sulfate typically found in cargo ships burning bunker fuel and the ~5% sulfate found in the R/V *Point Surs* emissions from marine diesel (Fig. 3). This unique almost-purely organic composition provided a fingerprint for tracking the smoke in cloud, as well as a surrogate for tracking particle properties in clouds.

Aircraft Studies (CIRPAS) Twin Otter aircraft was used with a full payload of instruments (Table 3) to measure particle and cloud number, mass, and composition. E-PEACE combined: (a) controlled release of smoke from the deck of the Pt. Sur, salt aerosol from the Twin Otter, and exhaust from container ships transiting across the study region; (b) coordinated Large Eddy Simulations (LES) and Aerosol-Cloud Parcel (ACP) modeling studies constrained by observations, to test our ability to quantitatively predict the cloud dynamical response to increases in particle concentrations in the natural atmosphere; and (c) satellite analyses of marine stratocumulus to constrain the radiative properties of the natural, perturbed, and regional cloud systems.

With 12 days of ship time on the R/V *Point Sur* and 30 flights (each ~ 4.5 h long) on the CIRPAS Twin Otter (Tables 4 and 5), we could take full advantage of the persistence of stratocumulus clouds to probe the effect of particle sources on MSc properties. Since the particles would be emitted locally, their effects on clouds could be separated from those of meteorology. And in terms of number concentration and duration, the impacts of these particle emissions would be large enough to be distinguished from natural cloud variability.

As noted above, three types of particles were involved in E-PEACE: (i) combustion exhaust particles from cargo ships of opportunity, which are the emissions responsible for ship tracks (ii) shipboard smoke-generated particles, and (iii) aircraft-based milled, coated salt particles (Fig. 3). The first type (i) is the exhaust that consists of 50 to 100 nm dry-diameter particles emitted at rates of $1016\text{--}1018\text{ s}^{-1}$ from the engines of large (2000 ton) cargo ships, in this instance on trans-Pacific, Los Angeles to San Francisco, or other commercial routes. Such emissions were responsible for the first observed ship tracks (Conover 1969). At a fuel cost of about \$100,000/day, operations of such vessels dedicated solely to research are not feasible. However, real time tracking of commercial vessels (<http://www.marinetraffic.com>) was used to identify fast-moving (>30 km/hr) cargo or container ships in the region within the aircraft operating area (as illustrated in Fig. 4). The second type (ii) involves smoke particles produced at an estimated rate of $1011\text{--}1013\text{ s}^{-1}$ on the stern deck of the R/V *Point Sur* (described in sidebar), with dry diameters that ranged from 100 nm up to $1\text{ }\mu\text{m}$. The third type (iii) of particles were dispersed from the Twin Otter aircraft in cloud. An adjustable auger fed a fluidized bed that dispensed NaCl particles, which had been milled to diameters of $3\text{--}5\text{ }\mu\text{m}$ and coated to prevent particles from sticking together.

5. Cloud Albedo Effects

In situ observations provide measurements of aerosol and cloud microphysics on spatial scales relevant to individual clouds and therefore are a critical element in understanding aerosol-cloud effects. To extrapolate from individual clouds to obtain a statistically robust assessment of aerosol effects on clouds and precipitation requires corresponding satellite observations. We used visible and infrared imagery in near-real-time from GOES satellites (~ 30 min delayed at http://www.nrlmry.navy.mil/sat-bin/epac_westcoast.cgi) and higher resolution images from the A-Train constellation of satellites (Stephens et al. 2002) for post-experiment analyses (illustrated in the top right of Fig. 2). The relevant satellite-based platforms in the eastern Pacific region include Terra and Aqua, which collectively provide retrievals of aerosol parameters (e.g. aerosol index) and cloud microphysical properties (e.g. drop effective radius, cloud optical depth). The specific emphasis of this project was to isolate aerosol effects by creating tracks with unique geometry in different cloud regimes.

We used the zig-zag pattern of the R/V *Point Sur* to create a track in cloud that was easily distinguishable from natural cloud characteristics and was broader than the constant-heading tracks made by ships in transit. These characteristics allowed us to track the plume with the CIRPAS aircraft and to isolate the effects from the smoke generated on the R/V *Point Sur*. Note the satellite image on 16 July 2011 during the 1430 (local time) overpass of Aqua (Fig. 6), in which the part of cloud affected by the smoke is whiter (i.e. more reflective) than the surrounding clouds. To confirm this identification, we calculated the expected location of the smoke (given the average wind speed near the sea surface) at the time of the satellite overpass. Even without this simple calculation, the resemblance between the patterns of the ships motion and the reflected track in cloud is striking.

We also identified tracks of cargo ships in satellite images similar to historical and recent work (Coakley Jr et al. 1987; Durkee et al. 2000a; Segrin et al. 2007). At least three examples of these tracks from cargo or container ships are visible in the lower left of Fig. 6. The increase in the reflectance of the cloud tracks from cargo ships (15% increase at 545–565 nm for all tracks in the region in July and August 2011) was similar to the cloud tracks formed from smoke emitted from the R/V *Point Sur* (14% increase at 545–565 nm).

6. Particle and Droplet Number and Composition

The Twin Otter aircraft flew into the same clouds shown in the satellite image (Fig. 6) to measure both the chemical composition of and number of cloud droplets that caused the increased shortwave reflectance. Figure 7 shows the number of particles below cloud and droplets in cloud,

and the pie graphs show that these droplets were almost entirely organic components with trace amounts of sulfate. The large organic fraction in Fig. 7A is characteristic of smoke emitted from the generators on the R/V *Point Sur* (see Sidebar) and contrasts with the composition of droplets in the cloud not affected by the smoke (Fig. 7C), which are made up of three-quarters sulfate and very little organic components. Interestingly, the particles that activated to form cloud droplets were sufficiently large ($>1.1 \mu\text{m}$, see Table 6) to make activation possible even in the near absence of soluble ions (approaching the so-called Kelvin limit).

The chemical composition of the cloud droplets was measured using a specialized inlet that separates the droplets from smaller interstitial aerosol particles (i.e. the particles that did not activate into droplets). This kind of inlet is called a Counterflow Virtual Impactor (CVI) because it uses airstreams forced to flow in different directions to separate larger-momentum droplets relative to smaller particles. The isolated droplets are then evaporated and the chemical composition of the droplet residual particles is measured using a mass spectrometer and other instruments on board the aircraft (see Table 3). Note that the CVI used in E-PEACE is a new design that exhibits a well-characterized 50% cutoff diameter ($11 \mu\text{m}$) corresponding to the specific aircraft speed and CVI flow rate conditions experienced (Shingler et al. 2012).

We also measured cloud droplets in tracks produced by cargo ships (Fig. 7B) and compared them to the surrounding clouds (Fig. 7D). The droplets in clouds affected by the cargo ship emissions contained slightly less than 50% organic components, consistent with particle measurements in cargo ship emissions (Fig. 3). Roughly five times as many droplets are in the track from the cargo ship than in the cloud perturbed by the organic smoke generated on the R/V *Point Sur*, although each is about twice the background droplet number concentration for that day. Droplets in both tracks are smaller than those in the background, with the cargo ship droplets being the smallest, having the peak in the cloud droplet number (CDN) concentration near $11.8 \mu\text{m}$ compared to $18.6 \mu\text{m}$ from the smoke. But the difference in the background cloud droplet diameter is quite striking between the two days ($14.3 \mu\text{m}$ on 10 August and $26.5 \mu\text{m}$ on 16 July). This difference likely results from both the lower supersaturation (0.09%) and the lower particle concentrations (159 cm^{-3}) on 16 July (see Table 6).

Several interesting questions arise: Why did the cargo ship droplets not grow as large as those from the smoke? Was it simply because they started out smaller and did not catch up, despite the presence of soluble sulfate ions? Also, why were the background droplet concentrations so different on these two days? Was it because of their lower particle concentrations, differences in meteorology, or both?

To address these questions, we used an aerosol cloud parcel (ACP) model, which is designed for tracking the detailed microphysical interactions of particles with different chemical composition in clouds under specified thermodynamic conditions (Russell and Seinfeld 1998). Here, we used the model to track the interactions of chemically different particle populations to isolate the increases in cloud drop number concentration to specific sources such as ship tracks. For example, Russell et al. (1999) showed that droplet number is strongly dependent on the concentration and composition of submicron aerosol particles. More recently, this model was used to analyze the role of organic particles in producing drop distributions in fog (Ming and Russell 2004), making it well suited for looking at smoke particles. The model's key computational features are a two-moment method for aerosol dynamics (both number and mass are tracked separately) and an adjustable framework for incorporating chemical properties (we choose how many different particle types to include). By simulating the step-by-step process of particle activation to droplets and growth beyond that, the model lets us address important questions, such as the role of supersaturation fluctuations from turbulence (e.g. Feingold et al. 1998) and kinetic inhibitions from reduced accommodation of water vapor onto growing droplets in marine stratocumulus in this region (e.g. Ruehl et al. 2009). It is also important to acknowledge that numerous studies have been carried out to understand some of the complex interactions of other types of cloud systems, such as pyro-convective clouds (Reutter et al. 2009).

The novel aspect of the E-PEACE ACP studies is that we can constrain the starting point with the particle number, size, and composition of emitted particles, predict their activation in cloud by constraining them to a maximum supersaturation calculated from the measured CCN spectra (Table 6), then see the extent to which the prediction of the initial cloud droplet growth in the first updraft matches in-cloud observations. In Fig. 7 we see that the simulated cloud droplet distributions are quite similar to the observed cloud droplet diameters on 10 August but that smaller diameters are predicted for both the smoke and background on 16 July. The fact that the simulations of the initial droplet growth during a single updraft in cloud are smaller than the observations for both the background and the smoke suggests that the reason the cloud droplets were larger from the smoke than the cargo ship was that they had had more time for scavenging and growth in cloud and not that they had different particle composition, number, and size. The simulated cloud properties also show that our question of why the background cloud droplets on the two days are so different has several answers – it is both the larger number and larger size of aerosol particles (148 cm^{-3} in the accumulation mode) on 10 August and the higher updraft velocities needed to give supersatura-

tions of 0.19% rather than 0.09% on 16 July. It is interesting to note that the number of below cloud accumulation particles measured by the PCASP (148 cm^{-3}) is very close to droplet number (156 cm^{-3}) on 10 August, similar to a broad range of marine stratocumulus observations (Hegg et al. 2012), but not on 16 July – perhaps suggesting that the weak updrafts and 0.09% supersaturation are not frequently present.

7. Cloud Deepening by Particles

In addition to microphysical ACP modeling studies, parallel progress has been made by investigating the complexities of the convective structure of marine boundary layers using LES models constrained by observations, as summarized in Table 2. Investigations from recent LES studies have tackled numerical issues such as spatial resolution (Hill et al. 2009) and complex feedbacks between cloud droplet distributions and LWP (Ackerman et al. 2003), between relative dispersion and albedo changes (Lu and Seinfeld 2006), between vertical stratification and LWP (Sandu et al. 2009), and between drizzle and LWP (Caldwell and Bretherton 2009; Jiang et al. 2010). These basic feedbacks can be captured in some cases by simpler mixed-layer models (Wood et al. 2009). While many of these studies focus on the changes in boundary layers that occur during the course of a day, Savic-Jovicic and Stevens (2008) have also explored the nighttime marine boundary layer.

We use large eddy simulations to represent microphysics and dynamics of marine stratocumulus. A detailed bin-resolved microphysical scheme is employed in the WRF model as the LES model (Chen et al. 2011). In the bin microphysical scheme, aerosol number, cloud drop mass, and cloud drop number are computed over a size-resolved spectrum, predicting both cloud drop mass and number concentration following the moment-conserving technique (Reisin et al. 1996; Tzivion et al. 1987, 1989). The microphysical processes include aerosol activation, drop condensation/evaporation, collision-coalescence, collisional breakup, and sedimentation. The impacts of ship plume and giant sea salt injection enable us to understand how different aerosol sizes, chemical compositions, and emitted locations affect the cloud dynamics.

Measurements on the CIRPAS aircraft show that cloud depth is an important feature of clouds that is affected by particles. As an example, on 4 and 10 August we conducted spiral soundings in an area influenced by large tanker ship emissions immediately adjacent to areas of background marine air. We used a cutoff of 0.05 g m^{-3} of liquid water to identify the top and bottom of the cloud. On 4 August, the cloud region was thicker in the track from the cargo ship. However, on 10 August, almost no difference was seen in the clean and polluted areas; in fact, the cloud in the track may have actually been somewhat thinner. GOES satellite

Giant CCN Stratocumulus Cloud Seeding

The role of giant CCN (GCCN) in stimulating precipitation production in stratocumulus clouds suggested by Woodcock (1950) has been studied recently using LES and parcel models (e.g. Feingold et al. 1999; Jensen and Lee 2008). These studies indicate that GCCN introduced into non-precipitating stratocumulus clouds can promote the growth of droplets to drizzle by acting as collector drops with higher rates of collision and coalescence. Observing the effects of GCCN in real clouds is difficult. First, GCCN concentrations in nature (10^{-4} to 10^{-2} cm^{-3}) are many orders of magnitude less than CCN (10^2 cm^{-3}) and thus difficult to measure from an aircraft. Second, cause-and-effect is difficult to establish since other factors can affect and modulate drizzle production. Marine stratocumulus clouds present laboratory-like conditions for directly evaluating how GCCN can modify the cloud and studying the science of precipitation production. By introducing GCCN directly into an unbroken and well-developed cloud, the role that other factors have in modifying the clouds can be minimized and the background cloud conditions can be easily compared with the seeded cloud areas.

Techniques for artificially seeding clouds with GCCN have been developed for the deliberate enhancement of precipitation in warm cumulus clouds. One technique that has been successfully demonstrated is airborne flares that produce a wide spectrum of hygroscopic particles with a tail of larger particles that serve as GCCN (Ghate et al. 2007). But to artificially introduce GCCN without increasing the smaller CCN, we employ a technique developed by Rosenfeld et al. (2010) that uses milled salt particles (in the range of $3\text{--}5 \mu\text{m}$ diameter) that are coated to prevent sticking and clumping of the particles. In E-PEACE we injected salt powder (provided by D. Rosenfeld) from the CIRPAS Twin Otter into the cloud. To deliver these particles we designed and fabricated an apparatus that used an auger to feed the salt powder into a fluidized bed of grit maintained by air pumped into the grit chamber that then ejects the powder into the aircraft's air flow where it is dispersed. The rate of mass of salt from the aircraft is designed to produce GCCN concentrations in the environment of the order of 10^{-3} cm^{-3} . After the GCCN are dispersed into the cloud, the aircraft samples the clouds that have been seeded with *in situ* measurements and with the airborne frequency modulated continuous wave cloud radar. Since the radar has a very shallow dead zone (less than 50 m), the reflectivity from the radar returns closest to the aircraft can be compared directly with the *in situ* probe observations.

images (Fig. 4) taken during the times when the Twin Otter was present show some differences in cloud structure, which may offer clues about these different results. Further LES studies may help to explain what subtle differences in the clouds cause these differences.

8. Precipitation Effects of Giant Particles

L'Ecuyer et al. (2009) recently showed that injection of sea salt and sulfate aerosols lead to nearly opposite cloud responses. Addition of large sea salt particles enhances precipitation and leads to less vertically developed clouds. On the other hand, addition of the considerably smaller sulfate particles suppresses precipitation in clouds and results in the onset of light precipitation at higher LWP. Also, air masses from different source regions may produce different effects on clouds (Su et al. 2010), as those originating above polluted continental areas will have a different physicochemical signature than those from remote ocean regions (Hersey et al. 2009; Sorooshian et al. 2009b).

We released the third type of emitted particle, the 3–5 μm diameter milled, coated salt particles to study the effects of giant CCN (GCCN) on precipitation. Results from one of the flights (3 August) provide evidence for a strong change in droplet number and size in the clouds that were seeded with giant nuclei. In this case GCCN were released cross-wind at a constant height in unbroken cloud. The air mass seeded was then sampled downstream where significant signatures were observed by both the optical probes and the upward-facing radar mounted on the Twin Otter (Fig. 8). Strong radar returns associated with drizzle (indicated by yellow in Fig. 8C) were observed and accompanied by a substantial decrease in the cloud liquid water content in Fig. 8D. The changes were large enough to suggest that the added salt caused a 4-fold increase in the cloud base rainfall rate (from <8 to ~20 mm dy^{-1}) on an associated depletion of the cloud water due to rainout. After seeding, cloud drop number concentrations had been reduced, indicative of vigorous collision-coalescence between drops, and the drop effective radius had increased from 11 to 14 μm at cloud top. Thus, observational evidence confirms the particular chain of events that is expected after a cloud seeding event: faster onset of rain owing to broadening of the cloud drop distribution, more rain that removes more water, leaving the cloud drier. These results support the idea that giant nuclei—produced either naturally or anthropogenically—when present in a high CCN environment can initiate drizzle and impact the cloud structure.

9. Summary and Outlook

The campaign of the Eastern Pacific Emitted Aerosol Cloud Experiment (E-PEACE) was designed to take advantage of recent advances in both instruments and models used to collect detailed, quantitative observations of the

Cooling Efficiency of Cargo Ships and Smoke

Smoke emissions from smoke generators were employed in the present study, along with the incidental emissions of transoceanic cargo ships (Conover 1969; Durkee et al. 2000a). Here we consider the extent to which each of these two types of ocean-going particle emissions provides a net cooling effect (based only on fuel consumed, not emissions from ship construction).

Take into consideration a single day for both smoke and cargo ship emissions in clouds that form tracks, an average summertime lifetime of the track in the cloud of 6 hr (amortized to a 100 yr time horizon), and an average daily fuel consumption at typical transit speeds. We calculate the asymptotic CO_2 -caused temperature increase from 3K per 280 ppmv (IPCC 2007) and find 1 nK (10-9 K) from 100,000 gal bunker fuel burned by the cargo ship and 0.008 nK for the 500 gal marine diesel burned by the R/V *Point Sur*. The cargo ship typically transits five times faster than the R/V *Point Sur*, so the area covered by the track (assuming the same wind speed in the lateral direction) is taken to be five times larger, providing 2500 km^2 for the cargo ship and 500 km^2 for the smoke. We use the 15% cloud brightening measured for the smoke on 16 July (Fig. 5) for both tracks to find 2 nK cooling for the cargo ship and 0.4 nK cooling for the smoke. That gives us ratios of cooling-to-warming (i.e. a cooling efficiency) of ~2 for the cargo ship and ~50 for the smoke generator.

Although this is a very simplified calculation, we find that, if half of the open-ocean transit days of a cargo ship result in tracks that are on average 15% brighter than surrounding clouds and cover 2500 km^2 , then cargo ship transit (for consumables only) could be considered carbon neutral (in the sense of having no net warming effect) transportation. Further we find that smoke generators on board smaller ships (that require less than 2% of the fuel per transit mile) could have been providing a net cooling effect, which may be reduced by upcoming air quality regulations.

effects of particles on clouds. Using an innovative new particle emission and measurement technology, three kinds of particles were emitted and controlled each as a single variable in the highly complex, natural system governing marine stratocumulus clouds. Since the emitted particles span 100 nm to several micrometers in diameter, the E-PEACE observations cover a wide range of cloud droplet sizes and number concentrations. The outcome of these studies revealed that both incidental smoke and ship emissions are effective at modifying cloud albedo, as well as that giant salt nuclei can increase drizzle rates. The multiple particle sizes allowed us to better constrain ACP and LES models, simultaneously allowing us to place the observations in a theoretical framework suitable for modeling. When consid-

ering these results in the context of Earth's solar radiation balance and the relative amounts of cooling and warming produced by different particle emissions (see Sidebar), we suggest that the effective carbon-offsets from cloud tracks from cargo ships should be considered.

Acknowledgments.

The E-PEACE field campaign and modeling studies were funded by the National Science Foundation (AGS-1013423; AGS-1008848; AGS-1013381; AGS-1013319; ATM-0744636; AGS-0821599; ATM-0349015) and the Office of Naval Research (N00014-11-1-0783; N00014-04-1-0018; N00014-10-1-0200; N00014-08-1-0465). Sea Spray Research, Inc., provided oil for the operation of the smoke generators. The authors gratefully acknowledge the crews of the CIRPAS Twin Otter and the R/V *Point Sur* for their assistance during the field campaign, Tom Maggard who revived and tirelessly maintained the smoke generators during the cruise, David Malmberg and the crew of the R/V Sproul for their assistance in testing the smoke generators prior to the campaign, Dean Hegg for providing the cloudwater collector, and Daniel Rosenfeld for providing the powdered salt.

REFERENCES

Ackerman, A. S., O. B. Toon, D. E. Stevens, and J. A. Coakley Jr, 2003: Enhancement of cloud cover and suppression of nocturnal drizzle in stratocumulus polluted by haze. *Geophys. Res. Lett.*, **30** (7), 1381, doi: 10.1029/2002gl016634.

Ackerman, A. S., M. P. Kirkpatrick, D. E. Stevens, and O. B. Toon, 2004: The impact of humidity above stratiform clouds on indirect aerosol climate forcing. *Nature*, **432** (7020), 1014–1017, doi:10.1038/nature03174.

Albrecht, B. A., 1989: Aerosols, Cloud Microphysics, and Fractional Cloudiness. *Science*, **245** (4923), 1227–1230, doi:10.1126/science.245.4923.1227.

Barkstrom, B. R., 1984: The Earth Radiation Budget Experiment (ERBE). *Bull. Am. Meteorol. Soc.*, **65** (11), 1170–1185, doi:10.1175/1520-0477(1984)065<1170:TERBE>2.0.CO;2.

Brenguier, J.-L., H. Pawlowska, L. Schüller, R. Preusker, J. Fischer, and Y. Fouquart, 2000: Radiative Properties of Boundary Layer Clouds: Droplet Effective Radius versus Number Concentration. *J. Atmos. Sci.*, **57** (6), 803–821, doi:10.1175/1520-0469(2000)057<0803:RPOBLC>2.0.CO;2.

Bretherton, C. S., R. Wood, R. C. George, D. Leon, G. Allen, and X. Zheng, 2010: Southeast Pacific stratocumulus clouds, precipitation and boundary layer structure sampled along 20° S during VOCALS-REx. *Atmos. Chem. Phys.*, **10**, 10639–10654, doi:10.5194/acp-10-10639-2010.

Caldwell, P. and C. S. Bretherton, 2009: Response of a Subtropical Stratocumulus-Capped Mixed Layer to Climate and Aerosol Changes. *Journal of Climate*, **22** (1), 20–38, doi:10.1175/2008JCLI1967.1.

Chen, Y. C., L. Xue, Z. J. Lebo, H. Wang, R. M. Rasmussen, and J. H. Seinfeld, 2011: A comprehensive numerical study of aerosol-cloud-precipitation interactions in marine stratocumulus. *Atmos. Chem. Phys.*, **11**, 9749–9769, doi:10.5194/acp-11-9749-2011.

Christensen, M. W. and G. L. Stephens, 2011: Microphysical and macrophysical responses of marine stratocumulus polluted by underlying ships: Evidence of cloud deepening. *J. Geophys. Res.*, **116**, D03201, doi: 10.1029/2010jd014638.

Coakley Jr, J. A., R. L. Bernstein, and P. A. Durkee, 1987: Effect of Ship-Stack Effluents on Cloud Reflectivity. *Science*, **237** (4818), 1020–1022, doi:10.1126/science.237.4818.1020.

Coakley Jr, J. A., et al., 2000: The appearance and disappearance of ship tracks on large spatial scales. *J. Atmos. Sci.*, **57** (16), 2765–2778, doi:10.1175/1520-0469(2000)057<2765:taados>2.0.co;2.

Conover, J. H., 1966: Anomalous Cloud Lines. *J. Atmos. Sci.*, **23** (6), 778–785, doi:10.1175/1520-0469(1966)023<0778:acl>2.0.co;2.

Conover, J. H., 1969: New Observations of Anomalous Cloud Lines. *J. Atmos. Sci.*, **26** (5), 1153–1154, doi: 10.1175/1520-0469(1969)026<1153:nooacl>2.0.co;2.

Crahan, K. K., D. A. Hegg, D. S. Covert, H. Jonsson, J. S. Reid, D. Khelif, and B. J. Brooks, 2004: Speciation of Organic Aerosols in the Tropical Mid-Pacific and Their Relationship to Light Scattering. *J. Atmos. Sci.*, **61** (21), 2544–2558, doi:10.1175/JAS3284.1.

Curry, J. A., E. E. Ebert, and G. F. Herman, 1988: Mean and turbulence structure of the summertime Arctic cloudy boundary layer. *Quarterly Journal of the Royal Meteorological Society*, **114** (481), 715–746, doi: 10.1002/qj.49711448109.

Durkee, P. A., K. J. Noone, and R. T. Bluth, 2000a: The Monterey Area Ship Track experiment. *J. Atmos. Sci.*, **57** (16), 2523–2541, doi:10.1175/1520-0469(2000)057<2523:tmaste>2.0.co;2.

Durkee, P. A., et al., 2000b: The impact of ship-produced aerosols on the microstructure and albedo of warm marine stratocumulus clouds: A test of MAST hypotheses 1i and 1ii. *J. Atmos. Sci.*, **57** (16), 2554–2569, doi: 10.1175/1520-0469(2000)057(2554:tiospa)2.0.co;2.

Faloona, I., et al., 2005: Observations of Entrainment in Eastern Pacific Marine Stratocumulus Using Three Conserved Scalars. *J. Atmos. Sci.*, **62** (9), 3268–3285, doi: 10.1175/JAS3541.1.

Feingold, G., W. R. Cotton, S. M. Kreidenweis, and J. T. Davis, 1999: The impact of giant cloud condensation nuclei on drizzle formation in stratocumulus: Implications for cloud radiative properties. *J. Atmos. Sci.*, **56** (24), 4100–4117, doi:10.1175/1520-0469(1999)056(4100:TIOGCC)2.0.CO;2.

Feingold, G., R. Furrer, P. Pilewskie, L. A. Remer, Q. Min, and H. Jonsson, 2006: Aerosol indirect effect studies at Southern Great Plains during the May 2003 Intensive Operations Period. *J. Geophys. Res.*, **111**, D05S14, doi: 10.1029/2004jd005648.

Feingold, G., I. Koren, H. Wang, H. Xue, and W. A. Brewer, 2010: Precipitation-generated oscillations in open cellular cloud fields. *Nature*, **466** (7308), 849–852, doi:10.1038/nature09314.

Feingold, G., S. M. Kreidenweis, and Y. Zhang, 1998: Stratocumulus processing of gases and cloud condensation nuclei 1. Trajectory ensemble model. *J. Geophys. Res.*, **103** (D16), 19 527–19 542, doi:10.1029/98JD01750.

Feingold, G. and H. Siebert, 2009: Cloud-aerosol interactions from the micro to the cloud scale. *Clouds in the Perturbed Climate System*, J. Heintzenberg and R. J. Charlson, Eds., The MIT Press, Cambridge, MA, 319–338.

Ferek, R. J., D. A. Hegg, P. V. Hobbs, P. Durkee, and K. Nielsen, 1998: Measurements of ship-induced tracks in clouds off the Washington coast. *J. Geophys. Res.*, **103** (D18), 23 199–23 206, doi:10.1029/98jd02121.

Ferek, R. J., et al., 2000: Drizzle Suppression in Ship Tracks. *J. Atmos. Sci.*, **57** (16), 2707–2728, doi:10.1175/1520-0469(2000)057(2707:DSIST)2.0.CO;2.

Frick, G. M. and W. A. Hoppel, 2000: Airship measurements of ship's exhaust plumes and their effect on marine boundary layer clouds. *J. Atmos. Sci.*, **57** (16), 2625–2648, doi:10.1175/1520-0469(2000)057(2625:amasse)2.0. co;2.

Ghate, V. P., B. A. Albrecht, P. Kollias, H. H. Jonsson, and D. W. Breed, 2007: Cloud seeding as a technique for studying aerosol-cloud interactions in marine stratocumulus. *Geophys. Res. Lett.*, **34**, L14807, doi: 10.1029/2007gl029748.

Hawkins, L. N., L. M. Russell, C. H. Twohy, and J. R. Anderson, 2008: Uniform particle-droplet partitioning of 18 organic and elemental components measured in and below DYCOMS-II stratocumulus clouds. *J. Geophys. Res.*, **113**, D14201, doi:10.1029/2007jd009150.

Hegg, D. A. and P. V. Hobbs, 1986: Sulfate and nitrate chemistry in cumuliform clouds. *Atmos. Environ.*, **20** (5), 901–909, doi:10.1016/0004-6981(86)90274-x.

Hegg, D. A., D. S. Covert, and H. H. Jonsson, 2008: Measurements of size-resolved hygroscopicity in the California coastal zone. *Atmos. Chem. Phys.*, **8**, 7193–7203, doi: 10.5194/acp-8-7193-2008.

Hegg, D. A., D. S. Covert, H. H. Jonsson, and R. Woods, 2009: Differentiating natural and anthropogenic cloud condensation nuclei in the California coastal zone. *Tellus B*, **61** (4), 669–676, doi:10.1111/j.1600-0889.2009.00435.x.

Hegg, D. A., D. S. Covert, H. H. Jonsson, and R. K. Woods, 2012: A simple relationship between cloud drop number concentration and precursor aerosol concentration for the regions of Earth's large marine stratocumulus decks. *Atmos. Chem. Phys.*, **12**, 1229–1238, doi: 10.5194/acp-12-1229-2012.

Hersey, S. P., A. Sorooshian, S. M. Murphy, R. C. Flanagan, and J. H. Seinfeld, 2009: Aerosol hygroscopicity in the marine atmosphere: a closure study using high-time-resolution, multiple-RH DASH-SP and size-resolved C-ToF-AMS data. *Atmos. Chem. Phys.*, **9**, 2543–2554, doi: 10.5194/acp-9-2543-2009.

Hill, A. A., G. Feingold, and H. Jiang, 2009: The Influence of Entrainment and Mixing Assumption on Aerosol-Cloud Interactions in Marine Stratocumulus. *J. Atmos. Sci.*, **66** (5), 1450–1464, doi:10.1175/2008JAS2909.1.

Hobbs, P. V., et al., 2000: Emissions from Ships with respect to Their Effects on Clouds. *J. Atmos. Sci.*, **57** (16), 2570–2590, doi:10.1175/1520-0469(2000)057(2570:EFSWRT)2.0.CO;2.

Hsieh, W. C., A. Nenes, R. C. Flagan, J. H. Seinfeld, G. Buzorius, and H. Jonsson, 2009: Parameterization of cloud droplet size distributions: Comparison with parcel models and observations. *J. Geophys. Res.*, **114**, D11205, doi: 10.1029/2008jd011387.

IPCC, 2007: Climate Change 2007: The Physical Science Basis. Contribution of Working Group I to the Fourth Assessment Report. Tech. rep.

Jensen, J. B. and S. Lee, 2008: Giant Sea-Salt Aerosols and Warm Rain Formation in Marine Stratocumulus. *J. Atmos. Sci.*, **65** (12), 3678–3694, doi:10.1175/2008JAS2617.1.

Jiang, H., G. Feingold, and A. Sorooshian, 2010: Effect of Aerosol on the Susceptibility and Efficiency of Precipitation in Warm Trade Cumulus Clouds. *J. Atmos. Sci.*, **67** (11), 3525–3540, doi:10.1175/2010jas3484.1.

Klein, S. A. and D. L. Hartmann, 1993: The Seasonal Cycle of Low Stratiform Clouds. *Journal of Climate*, **6** (8), 1587–1606, doi:10.1175/1520-0442(1993)006<1587:tscols>2.0.co;2.

Lance, S., C. A. Brock, D. Rogers, and J. A. Gordon, 2010: Water droplet calibration of the Cloud Droplet Probe (CDP) and in-flight performance in liquid, ice and mixed-phase clouds during ARCPAC. *Atmos. Meas. Tech.*, **3**, 1683–1706, doi:10.5194/amt-3-1683-2010.

L'Ecuyer, T. S., W. Berg, J. Haynes, M. Lebsack, and T. Takemura, 2009: Global observations of aerosol impacts on precipitation occurrence in warm maritime clouds. *J. Geophys. Res.*, **114**, D09211, doi:10.1029/2008jd011273.

Lilly, D. K., 1968: Models of cloud-topped mixed layers under a strong inversion. *Quarterly Journal of the Royal Meteorological Society*, **94** (401), 292–309, doi:10.1002/qj.49709440106.

Lu, M.-L., W. C. Conant, H. H. Jonsson, V. Varutbangkul, R. C. Flagan, and J. H. Seinfeld, 2007: The Marine Stratocumulus Experiment (MASE): Aerosol-cloud relationships in marine stratocumulus. *J. Geophys. Res.*, **112**, D10209, doi:10.1029/2006jd007985.

Lu, M.-L. and J. H. Seinfeld, 2005: Study of the aerosol indirect effect by large-eddy simulation of marine stratocumulus. *J. Atmos. Sci.*, **62** (11), 3909–3932, doi:10.1175/jas3584.1.

Lu, M.-L. and J. H. Seinfeld, 2006: Effect of aerosol number concentration on cloud droplet dispersion: A large-eddy simulation study and implications for aerosol indirect forcing. *J. Geophys. Res.*, **111**, D02207, doi:10.1029/2005jd006419.

Lu, M.-L., A. Sorooshian, H. H. Jonsson, G. Feingold, R. C. Flagan, and J. H. Seinfeld, 2009: Marine stratocumulus aerosol-cloud relationships in the MASE-II experiment: Precipitation susceptibility in eastern Pacific marine stratocumulus. *J. Geophys. Res.*, **114**, D24203, doi:10.1029/2009jd012774.

Meskhidze, N., A. Nenes, W. C. Conant, and J. H. Seinfeld, 2005: Evaluation of a new cloud droplet activation parameterization with in situ data from CRYSTALFACE and CSTRIPE. *J. Geophys. Res.*, **110**, D16202, doi:10.1029/2004jd005703.

Ming, Y. and L. M. Russell, 2004: Organic aerosol effects on fog droplet spectra. *J. Geophys. Res.*, **109**, D10206, doi:10.1029/2003jd004427.

Moore, R. H. and A. Nenes, 2009: Scanning Flow CCN Analysis-A Method for Fast Measurements of CCN Spectra. *Aerosol Sci. Technol.*, **43** (12), 1192–1207, doi:10.1080/02786820903289780.

Noone, K. J., et al., 2000a: A Case Study of Ships Forming and Not Forming Tracks in Moderately Polluted Clouds. *J. Atmos. Sci.*, **57** (16), 2729–2747, doi:10.1175/1520-0469(2000)057<2729:ACSOSF>2.0.CO;2.

Noone, K. J., et al., 2000b: A Case Study of Ship Track Formation in a Polluted Marine Boundary Layer. *J. Atmos. Sci.*, **57** (16), 2748–2764, doi:10.1175/1520-0469(2000)057<2748:ACSOST>2.0.CO;2.

Petters, M. D., J. R. Snider, B. Stevens, G. Vali, I. Falloona, and L. M. Russell, 2006: Accumulation mode aerosol, pockets of open cells, and particle nucleation in the remote subtropical Pacific marine boundary layer. *J. Geophys. Res.*, **111**, D02206, doi:10.1029/2004jd005694.

Platnick, S., et al., 2000: The role of background cloud microphysics in the radiative formation of ship tracks. *J. Atmos. Sci.*, **57** (16), 2607–2624, doi:10.1175/1520-0469(2000)057<2607:trobcm>2.0.co;2.

Radke, L. F., J. A. Coakley Jr, and M. D. King, 1989: Direct and Remote Sensing Observations of the Effects of Ships on Clouds. *Science*, **246** (4934), 1146–1149, doi:10.1126/science.246.4934.1146.

Reisin, T., Z. Levin, and S. Tzivion, 1996: Rain Production in Convective Clouds As Simulated in an Axisymmetric Model with Detailed Microphysics. Part I: Description of the Model. *J. Atmos. Sci.*, **53** (3), 497–519, doi:10.1175/1520-0469(1996)053<0497:RPICCA>2.0.CO;2.

Reutter, P., et al., 2009: Aerosol- and updraft-limited regimes of cloud droplet formation: influence of particle number, size and hygroscopicity on the activation of cloud condensation nuclei (CCN). *Atmos. Chem. Phys.*, **9** (18), 7067–7080, doi:10.5194/acp-9-7067-2009.

Roberts, G. C. and A. Nenes, 2005: A continuous-flow streamwise thermal-gradient CCN chamber for atmospheric measurements. *Aerosol Sci. Technol.*, **39** (3), 206–221, doi:10.1080/027868290913988.

Roberts, G. C., M. V. Ramana, C. Corrigan, D. Kim, and V. Ramanathan, 2008: Simultaneous observations of aerosol-cloud-albedo interactions with three stacked unmanned aerial vehicles. *Proc. Natl. Acad. Sci. U.S.A.*, **105** (21), 7370–7375, doi:10.1073/pnas.0710308105.

Rosenfeld, D., D. Axisa, W. L. Woodley, and R. Lahav, 2010: A Quest for Effective Hygroscopic Cloud Seeding. *J. Appl. Meteorol. Climatol.*, **49** (7), 1548–1562, doi:10.1175/2010JAMC2307.1.

Ruehl, C. R., P. Y. Chuang, and A. Nenes, 2009: Distinct CCN activation kinetics above the marine boundary layer along the California coast. *Geophys. Res. Lett.*, **36** (15), L15814, doi:10.1029/2009gl038839.

Russell, L. M. and J. H. Seinfeld, 1998: Size- and composition-resolved externally mixed aerosol model. *Aerosol Sci. Technol.*, **28** (5), 403–416, doi:10.1080/0278629808965534.

Russell, L. M., et al., 1999: Aerosol dynamics in ship tracks. *J. Geophys. Res.*, **104** (D24), 31 077–31 095, doi:10.1029/1999jd900985.

Sandu, I., J. L. Brenguier, O. Thouron, and B. Stevens, 2009: How important is the vertical structure for the representation of aerosol impacts on the diurnal cycle of marine stratocumulus? *Atmos. Chem. Phys.*, **9**, 4039–4052, doi:10.5194/acp-9-4039-2009.

Savic-Jovicic, V. and B. Stevens, 2008: The Structure and Mesoscale Organization of Precipitating Stratocumulus. *J. Atmos. Sci.*, **65** (5), 1587–1605, doi:10.1175/2007JAS2456.1.

Schreier, M., H. Mannstein, V. Eyring, and H. Bovensmann, 2007: Global ship track distribution and radiative forcing from 1 year of AATSR data. *Geophys. Res. Lett.*, **34**, L17814, doi:10.1029/2007gl030664.

Schubert, W. H., J. S. Wakefield, E. J. Steiner, and S. K. Cox, 1979a: Marine Stratocumulus Convection. Part I: Governing Equations and Horizontally Homogeneous Solutions. *J. Atmos. Sci.*, **36** (7), 1286–1307, doi:10.1175/1520-0469(1979)036<1286:MSCPIG>2.0.CO;2.

Schubert, W. H., J. S. Wakefield, E. J. Steiner, and S. K. Cox, 1979b: Marine Stratocumulus Convection. part II: Horizontally Inhomogeneous Solutions. *J. Atmos. Sci.*, **36** (7), 1308–1324, doi:10.1175/1520-0469(1979)036<1308:MSCPIH>2.0.CO;2.

Scorer, R. S., 1987: Ship trails. *Atmos. Environ. (1967-1989)*, **21** (6), 1417–1425, doi:10.1016/0004-6981(67)90089-3.

Segrin, M. S., J. A. Coakley, and W. R. Tahnk, 2007: MODIS Observations of Ship Tracks in Summertime Stratus off the West Coast of the United States. *J. Atmos. Sci.*, **64** (12), 4330–4345, doi:10.1175/2007JAS2308.1.

Sharon, T. M., B. A. Albrecht, H. H. Jonsson, P. Minnis, M. M. Khaiyer, T. M. van Reken, J. H. Seinfeld, and R. Flagan, 2006: Aerosol and Cloud Microphysical Characteristics of Rifts and Gradients in Maritime Stratocumulus Clouds. *J. Atmos. Sci.*, **63** (3), 983–997, doi:10.1175/JAS3667.1.

Shingler, T., et al., 2012: Characterization and airborne deployment of a new counterflow virtual impactor inlet. *Atmos. Meas. Tech. Discuss.*, **5**, 1515–1541, doi:10.5194/amt-5-1515-2012.

Sorooshian, A., G. Feingold, M. D. Lebsock, H. Jiang, and G. L. Stephens, 2009a: On the precipitation susceptibility of clouds to aerosol perturbations. *Geophys. Res. Lett.*, **36**, L13803, doi:10.1029/2009gl038993.

Sorooshian, A., M.-L. Lu, F. J. Brechtel, H. Jonsson, G. Feingold, R. C. Flagan, and J. H. Seinfeld, 2007: On the Source of Organic Acid Aerosol Layers above Clouds. *Environ. Sci. Technol.*, **41** (13), 4647–4654, doi:10.1021/es0630442.

Sorooshian, A., et al., 2009b: On the link between ocean biota emissions, aerosol, and maritime clouds: Airborne, ground, and satellite measurements off the coast of California. *Global Biogeochem. Cycles*, **23**, GB4007, doi:10.1029/2009gb003464.

Stephens, G. L., et al., 2002: The CloudSat mission and the A-train: A New Dimension of Space-Based Observations of Clouds and Precipitation. *Bull. Am. Meteorol. Soc.*, **83** (12), 1771–1790, doi:10.1175/BAMS-83-12-1771.

Stevens, B., G. Vali, K. Comstock, R. Wood, M. C. Van Zanten, P. H. Austin, C. S. Bretherton, and D. H. Lenschow, 2005: Pockets of open cells and drizzle in marine stratocumulus. *Bull. Am. Meteorol. Soc.*, **86** (1), 51–57, doi:10.1175/BAMS-86-1-51.

Stevens, B., et al., 2003: Dynamics and Chemistry of Marine Stratocumulus—DYCOMS-II. *Bull. Am. Meteorol. Soc.*, **84** (5), 579–593, doi:10.1175/BAMS-84-5-579.

Su, W., N. G. Loeb, K.-M. Xu, G. L. Schuster, and Z. A. Eitzen, 2010: An estimate of aerosol indirect effect from satellite measurements with concurrent meteorological analysis. *J. Geophys. Res.*, **115**, D18219, doi:10.1029/2010jd013948.

Sullivan, A. P., R. E. Peltier, C. A. Brock, J. A. de Gouw, J. S. Holloway, C. Warneke, A. G. Wollny, and R. J.

Weber, 2006: Airborne measurements of carbonaceous aerosol soluble in water over northeastern United States: Method development and an investigation into water-soluble organic carbon sources. *J. Geophys. Res.*, **111**, D23S46, doi:10.1029/2006jd007072.

Twohy, C. H., M. D. Petters, J. R. Snider, B. Stevens, W. Tahnk, M. Wetzel, L. M. Russell, and F. Burnet, 2005: Evaluation of the aerosol indirect effect in marine stratocumulus clouds: Droplet number, size, liquid water path, and radiative impact. *J. Geophys. Res.*, **110**, D08203, doi:10.1029/2004jd005116.

Twomey, S., 1991: Aerosols, clouds and radiation. *Atmos. Environ., Part A*, **25** (11), 2435–2442, doi:10.1016/0960-1686(91)90159-5.

Twomey, S., H. B. Howell, and T. A. Wojciechowski, 1968: Comments on “Anomalous Cloud Lines”. *J. Atmos. Sci.*, **25** (2), 333–334, doi:10.1175/1520-0469(1968)025<0333:COCL>2.0.CO;2.

Tzivion, S., G. Feingold, and Z. Levin, 1987: An Efficient Numerical Solution to the Stochastic Collection Equation. *J. Atmos. Sci.*, **44** (21), 3139–3149, doi:10.1175/1520-0469(1987)044<3139:AENSTT>2.0.CO;2.

Tzivion, S., G. Feingold, and Z. Levin, 1989: The Evolution of Raindrop Spectra. Part II: Collisional Collection/Breakup and Evaporation in a Rainshaft. *J. Atmos. Sci.*, **46** (21), 3312–3328, doi:10.1175/1520-0469(1989)046<3312:TEORSP>2.0.CO;2.

vanZanten, M. C. and B. Stevens, 2005: Observations of the structure of heavily precipitating marine stratocumulus. *J. Atmos. Sci.*, **62** (12), 4327–4342, doi:10.1175/jas3611.1.

Wang, H., G. Feingold, R. Wood, and J. Kazil, 2010: Modelling microphysical and meteorological controls on precipitation and cloud cellular structures in Southeast Pacific stratocumulus. *Atmos. Chem. Phys.*, **10**, 6347–6362, doi:10.5194/acp-10-6347-2010.

Wilcox, E. M., G. Roberts, and V. Ramanathan, 2006: Influence of aerosols on the shortwave cloud radiative forcing from North Pacific oceanic clouds: Results from the Cloud Indirect Forcing Experiment (CIFEX). *Geophys. Res. Lett.*, **33**, L21804, doi:10.1029/2006gl027150.

Wood, R., T. L. Kubar, and D. L. Hartmann, 2009: Understanding the Importance of Microphysics and Macrophysics for Warm Rain in Marine Low Clouds. Part II: Heuristic Models of Rain Formation. *J. Atmos. Sci.*, **66** (10), 2973–2990, doi:10.1175/2009jas3072.1.

Wood, R., C. S. Bretherton, D. Leon, A. D. Clarke, P. Zuidema, G. Allen, and H. Coe, 2011a: An aircraft case study of the spatial transition from closed to open mesoscale cellular convection over the Southeast Pacific. *Atmos. Chem. Phys.*, **11**, 2341–2370, doi:10.5194/acp-11-2341-2011.

Wood, R., et al., 2011b: The VAMOS Ocean-Cloud-Atmosphere-Land Study Regional Experiment (VOCALS-REx): goals, platforms, and field operations. *Atmos. Chem. Phys.*, **11**, 627–654, doi:10.5194/acp-11-627-2011.

Woodcock, A. H., 1950: Condensation nuclei and precipitation. *Journal of Meteorology*, **7** (2), 161–162, doi:10.1175/1520-0469(1950)007<0161:cnap>2.0.co;2.

TABLE 1. Previous relevant publications from aerosol-cloud interaction experiments on marine stratocumulus.

Experiment	Publications	Key Findings (for aerosol-cloud interactions)*
MAST (NE Pacific)	Russell et al. (1999)	Observed changes in drop distributions and LWC profile.
	Hobbs et al. (2000)	Ship emission characterization and size distributions.
	Frick and Hoppel (2000)	Case studies of four ship emissions that produce ship tracks.
	Durkee et al. (2000b); Noone et al. (2000a,b)	Test of aerosol-induced ship track hypothesis.
	Ferek et al. (2000)	Case studies illustrating background pollution effects on albedo sensitivity.
		Drizzle and LWC changes in ship tracks relative to unperturbed clouds.
DECS (NE Pacific)	Stevens et al. (2005)	Rift POCs study; variability in cloud drizzle characteristics
	Sharon et al. (2006)	due to natural processes and emissions.
DYCOMS II (Nocturnal) (NE Pacific)	Stevens et al. (2003)	Characterization of POCs in nocturnal marine boundary layers.
	Twohy et al. (2005)	CN/CCN/CDN relationships are linear.
	Petters et al. (2006)	CCN closure for marine boundary layer particles.
	Hawkins et al. (2008)	Composition-independence of particle activation in the aged boundary layer.
	Faloona et al. (2005)	Entrainment rates and variability in the nocturnal marine boundary layer.
	vanZanten and Stevens (2005)	Drizzle in nocturnal boundary layer in intense precipitation pockets.
CIFEX	Wilcox et al. (2006)	CCN increases correlated to CDN and reflected radiation for constant LWP.
MASE-I/II (NE Pacific)	Lu et al. (2007)	Ship tracks had smaller cloud drop effective radius, higher Nc, reduced drizzle
	Lu et al. (2009)	drop number, and larger cloud LWC than adjacent clean regions, but trends
	Sorooshian et al. (2007)	were obscured by spatial-temporal variability. Aerosol above cloud tops are
	Hersey et al. (2009)	enriched with water-soluble organic species, have higher organic volume
	Sorooshian et al. (2009a,b)	fractions, and are less hygroscopic relative to sub-cloud aerosol.
CARMA	Hegg et al. (2009)	Source attribution of CCN and aerosol light scattering.
VOCALS-REx (SE Pacific)	Bretherton et al. (2010)	Offshore drizzle not explained by CCN decrease.
	Feingold et al. (2010)	Oscillations in aerosol concentrations correspond to precipitation cycles.
	Wood et al. (2011a)	POC regions had enhanced drizzle and LWC.

*LWC is liquid water content; POC is pocket of open cells; CN is condensation nuclei; CCN is cloud condensation nuclei; CDN is cloud droplet number; LWP is liquid water path. MAST is the Monterey Area Ship Track experiment; DECS is the Drizzle and Entrainment Cloud Study; DYCOMS II is the Second Dynamics and Chemistry of Marine Stratocumulus experiment; CIFEX is the Cloud Indirect Forcing Experiment; MASE is the Marine Stratus/Stratocumulus Experiment; CARMA is the Cloud Aerosol Research in the Marine Atmosphere experiment; VOCALS-REx is the VAMOS Ocean-Cloud-Atmosphere-Land Study Regional Experiment.

TABLE 2. Recent model results on MBL cloud responses to aerosol perturbations.

Model Type	Publications	Key Findings (for aerosol-cloud interactions)*
ACP using observations	Russell et al. (1999)	Feedback effects of particles on supersaturation and LWC profile.
ACP with LES trajectories	Feingold et al. (1998)	Sensitivity of cloud properties to variability in trajectories.
ACP with supersaturation or updraft distributions	Meskhidze et al. (2005)	Effectiveness of parameterization for accurate droplet activation.
LES-Nocturnal (NE Pacific)	Hsieh et al. (2009)	Importance of maximum supersaturation rather than distribution.
LES (Pacific/Atlantic)	Hill et al. (2009)	Inhomogeneous mixing less important than particles.
Ackerman et al. (2003)	Ackerman et al. (2004)	LWP is reduced as CDN increases.
LES-Diurnal (Pacific/Atlantic)	Lu and Seinfeld (2005)	Nighttime CDN increases will suppress drizzle.
LES-Nocturnal (NE Pacific)	Lu and Seinfeld (2006)	Giant CCN increase drizzle in some conditions.
LES (SE Pacific)	Savic-Jovicic and Stevens (2008)	Relative dispersion increases apparent indirect effect.
Mixed-layer	Caldwell and Bretherton (2009)	Reduction in cloud albedo associated with drizzle.
LES	Wood et al. (2009)	Diurnal cycle controls drizzle and LWP.
	Sandu et al. (2009)	Drizzle decreases cloud height and entrainment and CDN increases.
		Vertical stratification affects LWP; diurnal transition effects on LWP.

*LWC is liquid water content; LWP is liquid water path; CCN is cloud condensation nuclei; CDN is cloud droplet number. ACP is Aerosol-Cloud Parcel modeling; LES is large eddy simulation modeling.

TABLE 3. Instruments on CIRPAS Twin Otter and R/V *Point Sur*.

Instruments	R/V <i>Point Sur</i>	CIRPAS Twin Otter
Particle and Droplet Inlets	PM10	PM1 and CVI ¹
Particle Size Distributions	CPC3010 ² for diameters>10 nm Scanning DMA ⁴ Optical Particle Sizer (OPS) Aerodynamic Particle Sizer (APS)	CPC3010 ² for diameters>10 nm CPC3025 ³ for diameters>3 nm Scanning DMA ⁵ Passive Cavity Aerosol Spectrometer Probe (PCASP)
Particle Chemical Composition	High Resolution (HR) ToF-AMS ⁶ Single-Particle Soot Photometer (SP2) Fourier Transform Infrared (FTIR) Functional Group Composition X-Ray Fluorescence (XRF) Elemental Composition PILS-TOC for water-soluble organic carbon ⁸	Compact (C) ToF-AMS ⁷ Single-Particle Soot Photometer (SP2)
Particle Properties	Tandem scanning and humidified DMAs ⁹ CCN Spectrometer ¹⁰	CCN Spectrometer ¹¹ Particle Soot Absorption Photometer (PSAP) Photoacoustic Soot Spectrometer (PASS-3)
Droplet and Drizzle Distributions		Phase Doppler Interferometer (PDI) Cloud Aerosol Spectrometer (CAS) Cloud Imaging Probe (CIP) Cloud Droplet Probe (CDP) ¹² Forward Scattering Spectrometer Probe (FSSP) Cloud Imaging Spectrometer (CIP-2D) Gerber Light Diffraction (PVM-100)
Droplet Residual Properties (by CVI)		CPC3010 ² for diameters>10 nm CPC3025 ³ for diameters>3 nm Scanning DMA ⁵ CCN Spectrometer ¹¹ Compact (C) ToF-AMS Single-Particle Soot Photometer (SP2) Photoacoustic Soot Spectrometer (PASS-3)
Cloudwater Composition		Slotted cloud water collector ¹³
Meteorological Variables	Temperature Relative humidity Pressure Wind speed and direction Altitude and GPS location	Temperature Relative humidity Pressure Wind speed and direction Altitude and GPS location
Cloud Structure	Ceilometer (cloud base height)	Upward-facing Doppler Radar ¹⁴
Seawater Properties	Sea surface temperature Chlorophyll-A	
Particle Generators	Oil smoke generator	Giant salt dispenser

¹Counterflow Virtual Impactor (Shingler et al. 2012)²Condensation Particle Counter (CPC) Model 3010 (TSI, Inc.)³Condensation Particle Counter (CPC) Model 3025 (TSI, Inc.)⁴Scanning Differential Mobility Analyzer (Brechtel Manufacturing, Inc.)⁵Scanning Differential Mobility Analyzer Models 3081 and 3010 (TSI, Inc.)⁶High Resolution Time-of-Flight Aerosol Mass Spectrometer (Aerodyne Research, Inc.)⁷Compact Time-of-Flight Aerosol Mass Spectrometer (Aerodyne Research, Inc.)⁸Particle-into-liquid sampler (Brechtel Manufacturing, Inc.) coupled to a total organic carbon analyzer (Sievers Model 800) (Sullivan et al. 2006)⁹Scanning and humidified scanning Differential Mobility Analyzers (Brechtel Manufacturing, Inc.)¹⁰Cloud Condensation Nuclei (CCN) Spectrometer (miniaturized from the design of Roberts and Nenes 2005)¹¹Cloud Condensation Nuclei (CCN) Spectrometer (Moore and Nenes 2009)¹²Cloud Droplet Probe (Droplet Measurement Technology, Lance et al. 2010)¹³Modified Mohen design (based on Hegg and Hobbs 1986)¹⁴94 GHz frequency-modulated continuous wave cloud radar

TABLE 4. Summary of CIRPAS Twin Otter flights during E-PEACE 2011.

Flight	Date	Description of clouds and particle sources sampled	Cloud level	LWC ¹
1	8 July	Thin cloud layer; salt seeding.	257–362	0.15
2	9 July	Thick, wet cloud layer; drizzling; salt seeding.	283–570	0.28
3	13 July	Broken clouds; smoke sampling. ²	–	–
4	14 July	High, thick cloud layer; smoke sampling.	651–934	0.17
5	15 July	Two broken cloud layers; cargo ships (<i>Ice Blizzard</i>); smoke sampling.	266, 550–794	0.14
6	16 July	Two broken cloud layers; smoke sampling.	142, 550–774	0.12
7	17 July	No clouds; cargo ships (<i>Hanjin Montevideo</i>); smoke sampling.	–	0.19
8	19 July	Thick, wet cloud layer, no drizzle; cargo ships (<i>Cap Preston</i>); smoke sampling.	258–533	0.21
9	21 July	Thick cloud layer, drizzling; cargo ship; smoke sampling.	212–533	0.27
10	22 July	Thick cloud layer, intermittent drizzling; smoke sampling.	235–551	0.30
11	23 July	Thick cloud layer; smoke sampling; cargo ships (<i>Pos Yantian</i>).	308–630	0.28
12	24 July	Mostly clear air, high clouds; cargo ships (<i>Ken Ryu</i>).	492–779	0.17
13	26 July	Thick cloud layer; cargo ships (<i>SCF Samotlor</i> , <i>Vinalines Galaxy</i> , <i>Gluecksburg</i>); salt seeding.	253–560	0.27
14	27 July	Low, thick cloud layer; cargo ship (<i>Mol Earnest</i>).	131–441	0.24
15	28 July	Thin cloud layer; cargo ship (<i>Hanjin Hamburg</i> , <i>Ever Develop</i> , <i>Cap Preston</i>).	267–413	0.16
16	29 July	High, wet clouds, no drizzle; cargo ship (<i>MSC Fabienne</i>); salt seeding.	265–534	0.32
17	1 August	Thin, high cloud layer; cargo ship (<i>Astro Phoenix</i>).	641–784	0.15
18	2 August	Thick, wet cloud layer, drizzling; cargo ships (<i>Riga</i> , <i>Australia Express</i>); salt seeding.	310–613	0.32
19	3 August	Thick cloud layer, some drizzle; cargo ships (<i>Xin Ya Zhou</i>); salt seeding.	309–628	0.26
20	4 August	Cumulus-like broken clouds, drizzling; cargo ships (<i>YM Cypress</i>).	294–633	0.17
21	5 August	Low cloud layer, intermittent drizzle; cargo ships (<i>Nelvana</i>).	169–501	0.27
22	8 August	Thin cloud layer.	281–448	0.22
23	9 August	Thin cloud layer.	324–485	0.21
24	10 August	Low clouds, intermittent drizzle; cargo ships (<i>Tian Shang He</i>); salt seeding.	286–553	0.29
25	11 August	Two broken cloud layers; cargo ships (<i>NYK Artemis</i>).	216, 440–600	0.19
26	12 August	Thick cloud layer; shipping lane; polluted layer above clouds.	278–578	0.24
27a,b,c	15 August	No clouds; north/south survey.	–	–
28a,b,c	16 August	Low cloud layer; north/south changes in cloud amount.	136–379	0.13
29a,b	17 August	Low cloud layer; north/south survey.	156–366	0.21
30a,b	18 August	Low cloud layer; north/south survey.	142–352	0.23

¹Liquid water content (LWC) in g kg^{-1} , calculated as a flight average for all $\text{LWC} > 0.1 \text{ g kg}^{-1}$.²Some data streams were corrupted on Flight 3, so it is not shown in Fig. 6.

TABLE 5. Summary of R/V *Point Sur* cruise during E-PEACE 2011.

Date	Description of clouds and smoke generation operations.	Cloud bases ¹	SST ²	Surface wind ³
12 July	Multiple cloud layers; testing smoke generators.	70, 160, 430	12.8	8 @ 270°
13 July	Multiple cloud layers, light winds; intermittent smoke generation.	100, 190, 360	13.1	5–20 @ 270°
14 July	High clouds; smoke generation (6 hr).	420, 660	13.9	15–20 @ 310°
15 July	Broken low and high clouds; smoke generation (6 hr).	250, 570	14.7	15 @ 330°
16 July	Multiple cloud layers; smoke generation (6 hr); plume sampling.	70, 160*, 310	13.7	<5 @ 330°
17 July	Multiple broken cloud layers; smoke generation (5 hr); plume sampling.	50, 150, 810, 930	14.6	5–10 @ 330°
18 July	Multiple broken cloud layers; smoke generation (1 hr); plume sampling.	60, 160	15.7	8–10 @ 250°
19 July	Scattered low and high clouds; smoke generation (6 hr).	50, 140, 340	14.6	15–20 @ 340°
20 July	Scattered clouds; smoke generation (1 hr).	280*	14.5	15–20 @ 330°
21 July	Low, uniform clouds; smoke generation (5 hr).	210*	14.1	15–20 @ 330°
22 July	Low, uniform clouds; smoke generation (5 hr).	250*, 340	13.9	18–22 @ 330°
23 July	Low, uniform clouds; smoke generation (6 hr).	290, 420	14.4	4–8 @ 300°

¹Altitudes [masl] of bases of cloud layers detected by ceilometer measured on R/V *Point Sur*.

²Sea surface temperatures [°C] measured on R/V *Point Sur*.

³Wind speed [kts] and direction measured on R/V *Point Sur*.

*Clouds in which ship tracks were observed in the region.

TABLE 6. Particle and droplet characteristics for below and in-cloud measurements shown in Fig. 7.

Date of measurement		16 July Background	16 July Generator Smoke	10 August Background	10 August Cargo Ship
Description of particles					
Cloud Base Height	[m]	145	145	338	338
Cloud Top Height	[m]	370	370	670	670
Simulated Updraft Velocity ⁴	[m s ⁻¹]	0.15	0.15	0.20	0.20
Calculated Maximum Supersaturation ³ (CCN)	%	0.09	0.09	0.19	0.25
Simulated Maximum Supersaturation (ACP)	%	0.10	0.09	0.19	0.28
Below Cloud Particles (CPC)	[cm ⁻³]	159	1786	361	1938
Below Cloud Accumulation Particles (PCASP)	[cm ⁻³]	46	659	148	644
In Cloud Accumulation Particles (PCASP)	[cm ⁻³]	3	188	49	214
Calculated Activation Diameter ¹	[μm]	0.13	1.1	0.06	0.09
Simulated Activation Diameter	[μm]	0.16	0.94	0.08	0.12
In Cloud Droplet Number (CAS, CDP)	[cm ⁻³]	25	49	156	277
Simulated Cloud Droplet Number (ACP)	[cm ⁻³]	69	108	235	389
In Cloud Droplet Diameter ² (CAS, CDP)	[μm]	26.5	18.6	14.3	11.8
Simulated Cloud Droplet Diameter ² (ACP)	[μm]	11.6	10.3	15.0	11.6

¹The activation diameter is calculated as the size of the smallest particle needed to activate to produce the measured CDN, assuming all larger particles activated.

²Cloud droplet diameters are reported at the peak concentration of the droplet mode.

³The supersaturation is calculated from the CCN spectrum as the supersaturation at which the measured CDN is equal to the CCN.

⁴The updraft velocity was calculated as the fixed parcel rise speed that produced the calculated maximum supersaturation in cloud.

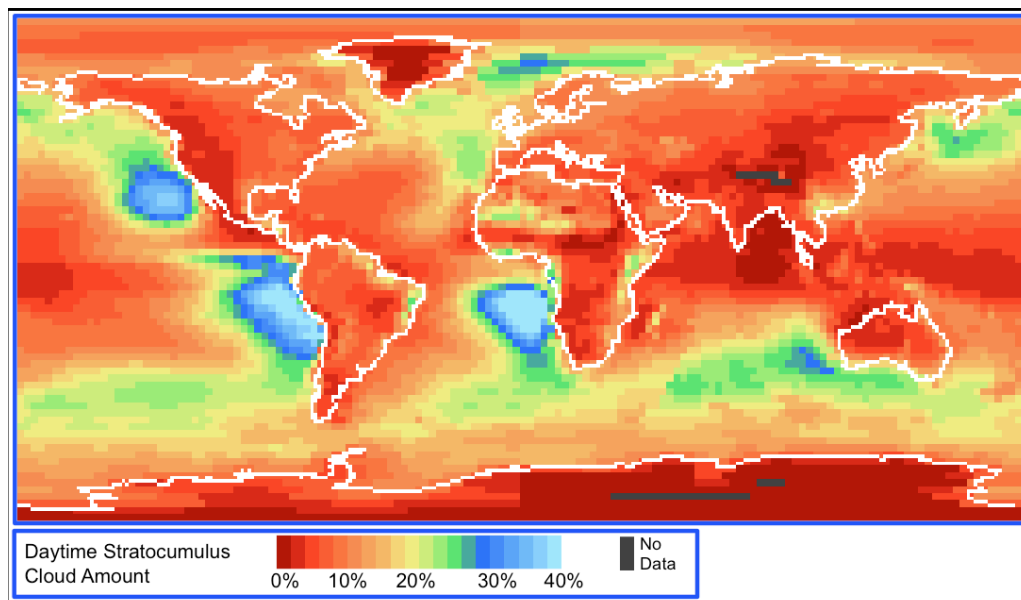


FIG. 1. Daytime annual average stratocumulus cloud amount (%) over the 1983–2009 period. Data obtained from ISCCP D2 monthly means (<http://isccp.giss.nasa.gov/products/browsed2.html>).

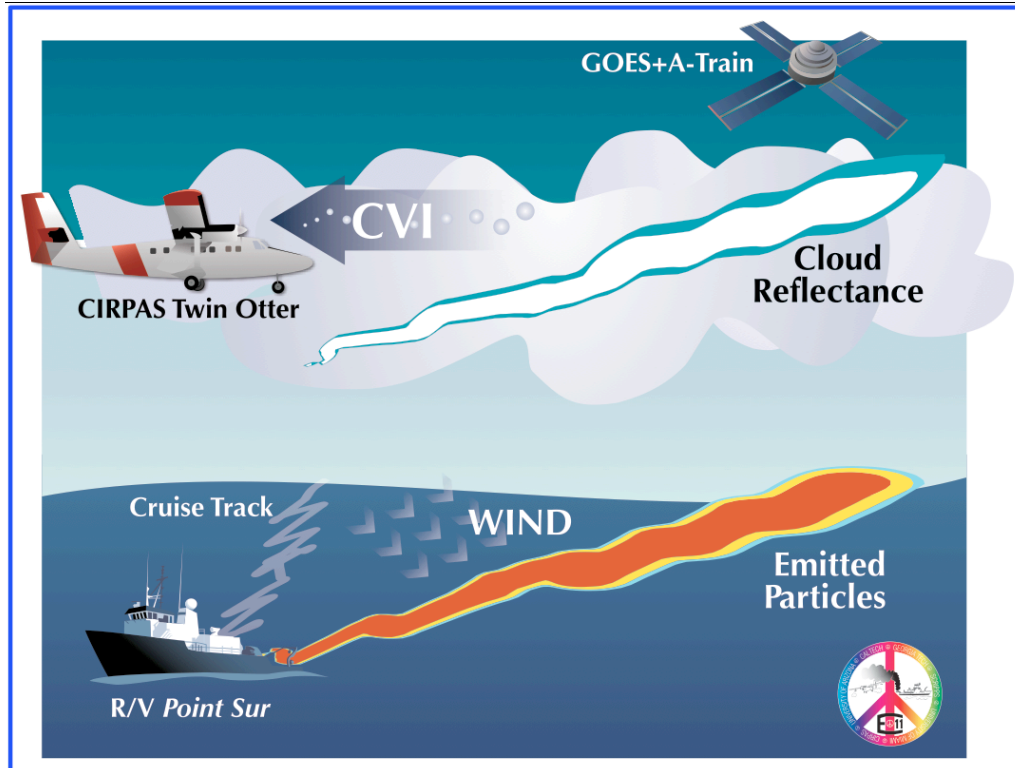


FIG. 2. Illustration of E-PEACE design and observations of emitted particles in marine stratocumulus in July and August of 2011 west of central California. The diagram shows the three platforms used in making observations of particle and cloud chemical and physical properties, namely the R/V *Point Sur*, the CIRPAS Twin Otter, and the A-Train and GOES satellites. The design included using smoke generated on board the R/V *Point Sur* that was measured after emission by the CIRPAS Twin Otter in clouds. The satellite was used to measure the changes in reflectance of sunlight due to the effects of the emitted particles on the clouds. The counterflow virtual impactor (CVI) was used as an inlet for evaporating droplets as they were brought into the aircraft, allowing sampling of droplet chemical composition.

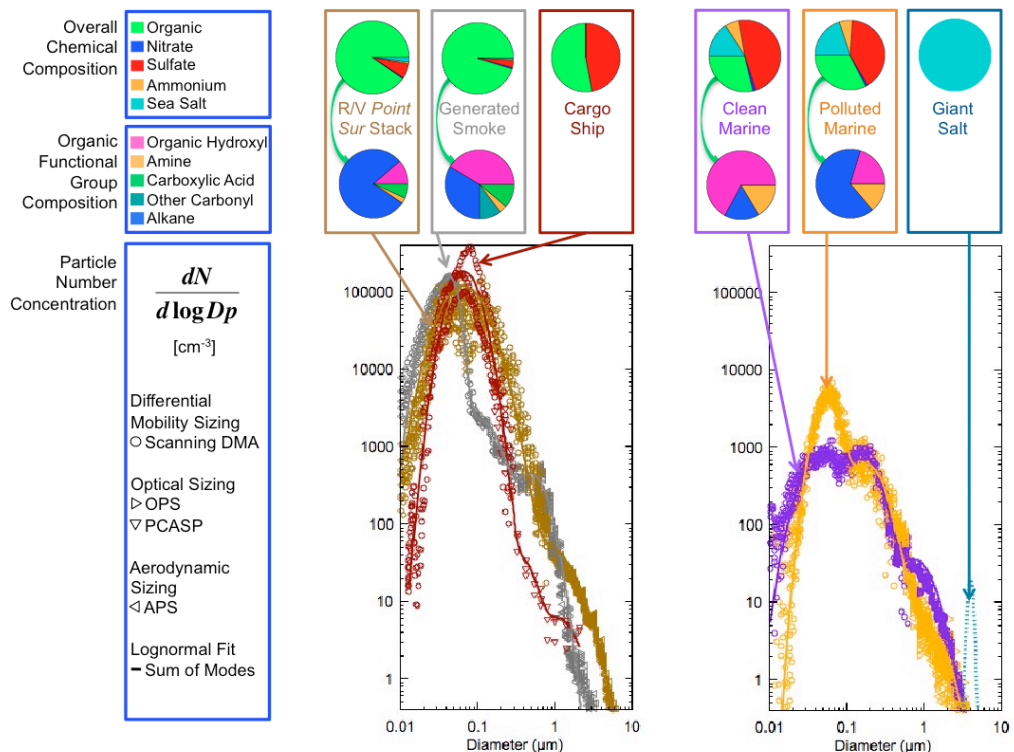


FIG. 3. Distribution by size of the number and submicron composition of particles emitted for E-PEACE, with comparison to both clean and polluted marine background particles measured during the experiment. Composition illustrates the overall composition, based on AMS and XRF, and the organic functional group composition, based on FTIR. Organic functional group composition was not available for the giant salt (since there was none) and the cargo ship (since sufficient sampling time was not available). The concentration of giant salt has been scaled by 104 so that the particle size can be shown on the same graph. Measurements collected on the R/V *Point Sur* ($0.01 \mu\text{m} < \text{Scanning DMA} < 0.9 \mu\text{m}$, $0.4 \mu\text{m} < \text{OPS} < 10 \mu\text{m}$, $0.5 \mu\text{m} < \text{APS} < 15 \mu\text{m}$) included the smoke generator (17 July 1210–1225), the R/V *Point Surs* stack emissions (22 July 2000–2200), and background aerosol for clean (20 July 1100–1135) and polluted (19 July 0220–0400) marine conditions. Measurements of cargo ship emissions ($0.01 \mu\text{m} < \text{Scanning DMA} < 0.9 \mu\text{m}$, $0.1 \mu\text{m} < \text{PCASP} < 2 \mu\text{m}$) were collected on the Twin Otter (10 August 1200–1315).

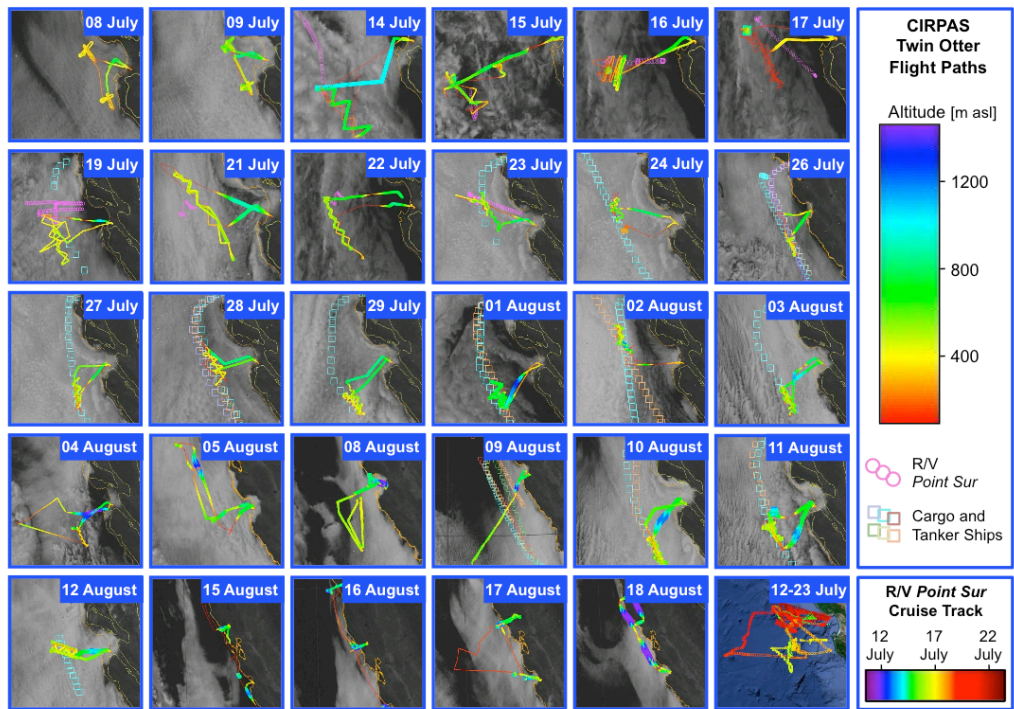


FIG. 4. Summary of the CIRPAS Twin Otter research flight paths and the R/V *Point Sur* cruise track. The first 29 panels show the CIRPAS Twin Otter flight path, colored by altitude above sea level (asl), overlaid on a GOES satellite image of the cloud cover from that day. The tracks of the R/V *Point Sur* as well as cargo and tanker ships that were targeted for sampling that day are also shown. The last panel shows the 12-day cruise track of the R/V *Point Sur*, colored by date, overlaid on a Google Earth image of the topography.

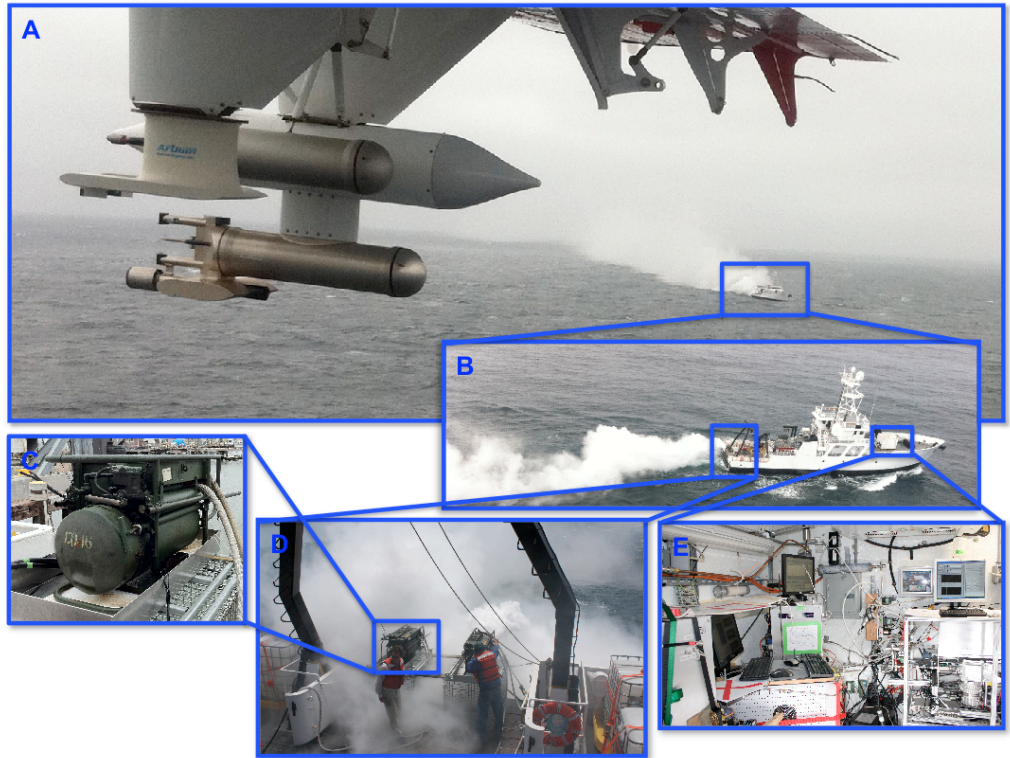


FIG. 5. Photographs of the R/V *Point Sur* from the CIRPAS Twin Otter, showing (A) the persistence of the plume of smoke from the ship in the atmosphere and some of the aircraft instruments for measuring particles and clouds, the production of smoke (B) and the operation of the smoke generators (D) on the stern of the R/V *Point Sur*, (C) one of the two smoke generators used for producing smoke, and (E) the aerosol instrumentation on the bow of the R/V *Point Sur*.

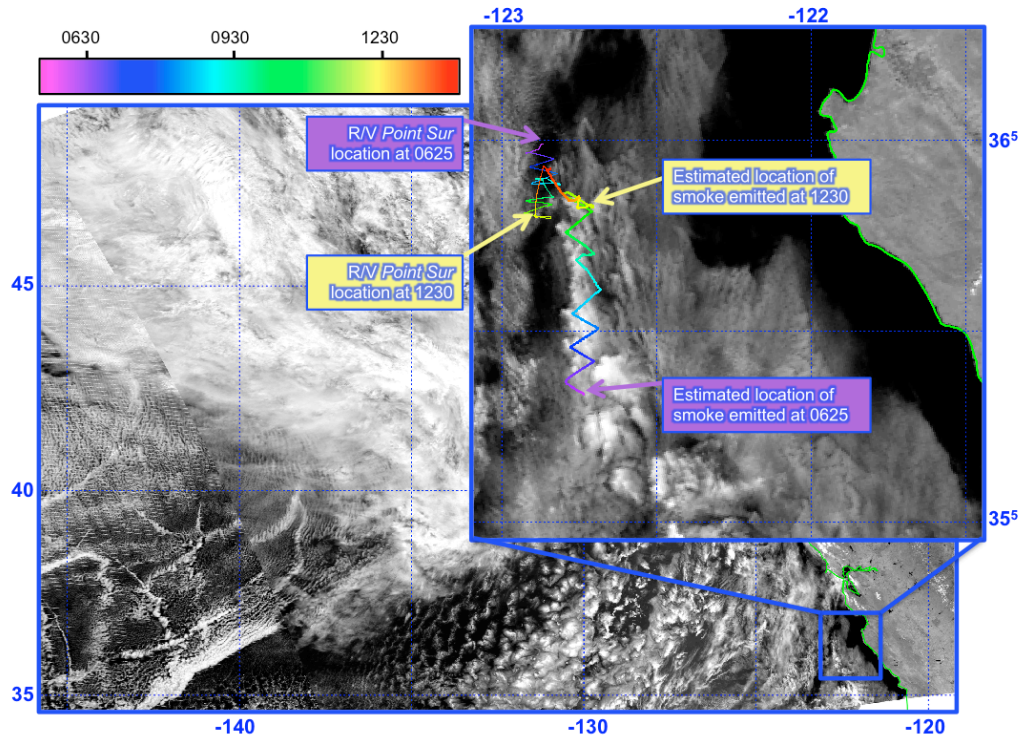


FIG. 6. Cloud tracks from cargo ships and the smoke produced on the R/V *Point Sur*. The larger image shows a composite of Aqua and Terra MODIS satellite images in the $2.2\text{ }\mu\text{m}$ channel. The Terra overpass (southwestern section of the composite image) occurred at 1250 and the Aqua overpass occurred at 1430 (local time) on 16 July 2011. The smaller image at the top right shows an enlargement of the smoke track from the region indicated. The colored lines indicate the time at which the R/V *Point Sur* was at the location indicated by the color bar (thin line) and the estimated location of particles emitted at the time of the color bar (thick line) at the time of the satellite overpass (1430). The location of emitted particles was estimated using the time between the emission and the satellite overpass, scaled by the average wind speed and direction in the boundary layer.

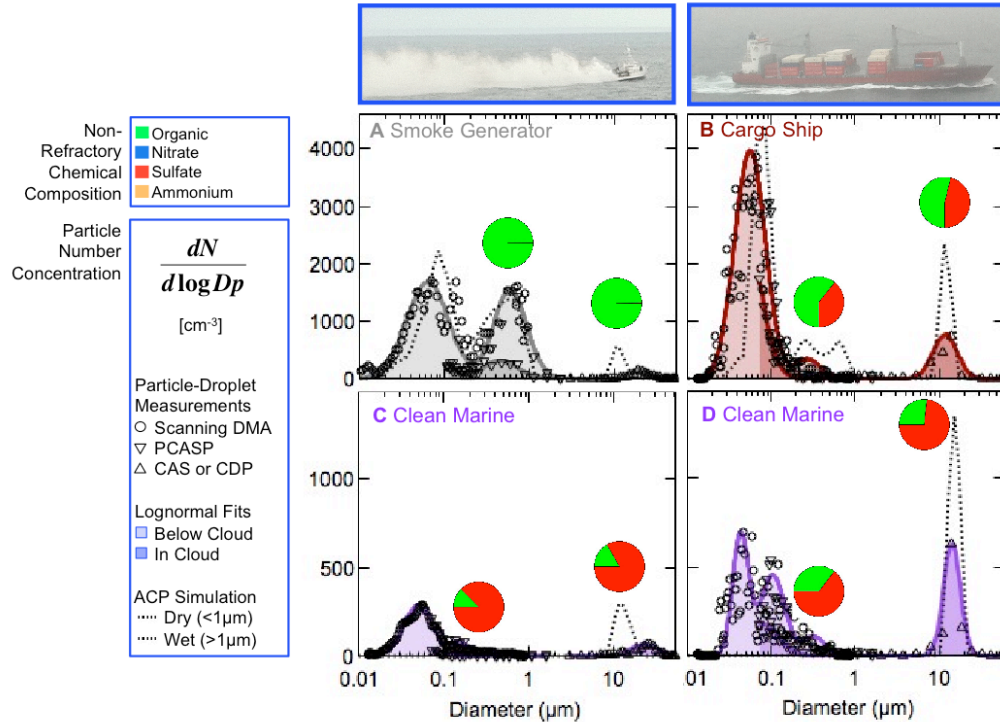


FIG. 7. Examples of particle and droplet number distributions and composition, from measurements below (light shading) and in (dark shading) cloud, for the smoke generator on the R/V *Point Sur* on 16 July (in panel A) and for the stack emissions of a cargo ship on 10 August (in panel B). Panels C and D show the background particle and droplet concentrations for 16 July and 10 August, respectively. The size distributions are plotted at the measured relative humidity, wet for supermicron droplets in cloud ($3 \mu\text{m} < \text{CDP} < 50 \mu\text{m}$ for 16 July; $1 \mu\text{m} < \text{CAS} < 50 \mu\text{m}$ for 10 August) and dried for submicron particles in (interstitial) and below cloud ($0.1 \mu\text{m} < \text{PCASP} < 2 \mu\text{m}$, $0.01 \mu\text{m} < \text{Scanning DMA} < 0.9 \mu\text{m}$). The pies show composition of the droplets in cloud measured by AMS for submicron particles below cloud (left) and for the residuals of cloud droplets (right) that are left after drying in a counterflow virtual impactor ($11 \mu\text{m} < \text{CVI}$). The measurements were collected on the CIRPAS Twin Otter on 10 August for the cargo ship (1651–1831) and 16 July for the smoke generators (1704–1801). The simulations show the drop distribution in cloud predicted by the ACP model (Russell and Seinfeld 1998) initialized by the below cloud size distribution and composition, using the supersaturation inferred from equating the measured cloud drop number with the measured cloud condensation nuclei.

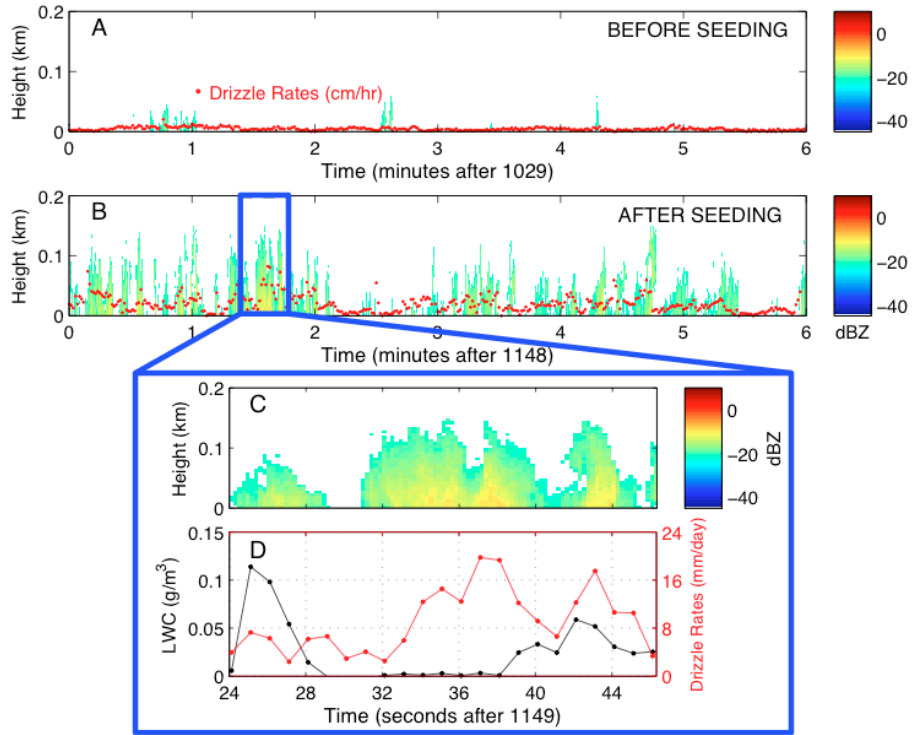


FIG. 8. The radar reflectivity (in dBZ, reflectivity Z is proportional to the sixth power of droplet diameter) shows precipitation above the flight level from an upward facing 94 GHz cloud radar mounted on top of the CIRPAS Twin Otter in a) an area of cloud sampled before seeding (flight level 340 m) and b) same air mass sampled after the seeding (flight level 310 m). The drizzle rates (cm hr^{-1}) in a) and b) were estimated from the flight-level CIP probe. The outlined box in panel b indicates where a detailed analysis was made for c) the radar reflectivity and d) precipitation rate (from CIP) in mm dy^{-1} and the cloud liquid water content (from PVM-100) in g m^{-3} .

Appendix G

Ship Impacts on the Marine Atmosphere: Insights into the Contribution of Shipping Emissions to the Properties of Marine Aerosol and Clouds*

*Submitted as “Ship Impacts on the Marine Atmosphere: Insights into the Contribution of Shipping Emissions to the Properties of Marine Aerosol and Clouds” by M. M. Coggon, A. Sorooshian, A. R. Metcalf, A. A. Frossard, Z. Wang, J. Lin, J. S. Craven, H. Jonsson, A. Nenes, L. M. Russell, R. C. Flagan, and J. H. Seinfeld to *Atmospheric Chemistry and Physics*. Copyright 2012 by the Authors.

Ship Impacts on the Marine Atmosphere: Insights into the Contribution of Shipping Emissions to the Properties of Marine Aerosol and Clouds

Matthew M. Coggon¹, Armin Sorooshian^{2,3}, Zhen Wang², Andrew R. Metcalf⁴, Amanda A. Frossard⁵, Jack J. Lin⁶, Jill S. Craven¹, Athanasios Nenes^{6,7}, Haffidi H. Jonsson⁸, Lynn M. Russell⁵, Richard C. Flagan^{1,4}, and John H. Seinfeld^{1,4}

¹Department of Chemical Engineering, California Institute of Technology, Pasadena, CA, USA

²Department of Chemical and Environmental Engineering, University of Arizona, Tucson, AZ, USA

³Department of Atmospheric Sciences, University of Arizona, Tucson, AZ, USA

⁴Department of Environmental Science and Engineering, California Institute of Technology, Pasadena, CA, USA

⁵SCRIPPS Institution of Oceanography, University of California, San Diego, CA, USA

⁶School of Earth and Atmospheric Sciences, Georgia Institute of Technology, Atlanta, GA, USA

⁷School of Chemical and Biomolecular Engineering, Georgia Institute of Technology, Atlanta, GA, USA

⁸Naval Postgraduate School, Monterey, CA, USA

Abstract. We report properties of marine aerosol and clouds measured in the shipping lanes between Monterey Bay and San Francisco off the coast of central California. Using a suite of aerosol instrumentation onboard the CIRPAS Twin Otter aircraft, these measurements represent a unique set of data contrasting the properties of clean and ship-impacted marine air masses in dry aerosol and cloud droplet residuals. Average mass and number concentrations of below-cloud aerosol of $2 \mu\text{g m}^{-3}$ and 510 cm^{-3} are consistent with previous studies performed off the coast of California. Enhancement of vanadium and cloud droplet number concentration observed concurrently with a decrease in cloud water pH suggests that periods of high aerosol loading are primarily linked to increased ship influence. Mass spectra from a compact time-of-flight Aerodyne aerosol mass spectrometer reveal an enhancement in the fraction of organic at m/z 42 (f_{42}) and 99 (f_{99}) in ship-impacted clouds. These ions are well correlated to each other ($R^2 > 0.64$) both in and out of cloud and dominate organic mass during periods of enhanced sulfate. High-resolution mass spectral analysis of these masses from ship measurements suggests that the ions responsible for this variation were oxidized, possibly due to cloud processing. We propose that the organic fractions of these ions be used as a metric for determining the extent to which ships impact the marine atmosphere where ($f_{42} > 0.15$; $f_{99} > 0.04$) would imply heavy influence from shipping emissions, ($0.05 < f_{42} < 0.15$; $0.01 < f_{99} < 0.04$) would imply moderate, but persistent, influences from ships, and ($f_{42} < 0.05$; $f_{99} < 0.01$) would imply clean, non-ship-influenced air.

1 Introduction

Ship exhaust is estimated to account for 14 and 16% of global NO_x and SO_x emissions, respectively (Corbett and Fischbeck, 1997). Models show that ship emissions also contribute 1.67 Tg yr^{-1} to global particulate matter, which is nearly equivalent to current estimates of particulate matter emitted by all on-road vehicles (Eyring et al., 2005; Yan et al., 2011). Because many shipping lanes are located along coastal regions where marine stratocumuli persist, ship emissions have the potential to directly affect cloud microphysics. Studies of cargo ship exhaust / cloud interactions have shown distinct cloud responses to these perturbations (e.g., Coakley et al., 1987; Ackerman et al., 1995; Frick and Hoppel, 2000; Durkee et al., 2000; Hudson et al., 2000; Noone et al., 2000; Lu et al., 2009; Christensen and Stephens, 2011). Satellite imagery shows that ship tracks can exist hours after initial emission (Coakley et al., 1987; Durkee et al., 2000; Christensen and Stephens, 2011) and therefore have the potential to exert a significant effect on local radiative fluxes.

Ship emissions mix with marine aerosol and subsequently with cloud droplets, however the extent of this effect is not well established. Marine aerosol is a complex mixture of natural and anthropogenic sources, and thus the signature from shipping emissions is difficult to detect. Natural marine aerosol comprises particles resulting from sea-spray (e.g., NaCl , KCl , organics), marine biological activity (e.g., dimethylsulfide and subsequent oxidation products), and those from continental origins (e.g., dust, secondary products from biogenic oxidation). Anthropogenic sources include ship emissions, continental pollution, and biomass burning. Sea-salt typically dominates the super micrometer aerosol ($D_p > 1 \mu\text{m}$), whereas organics, sulfate, and ammonium from natural and anthropogenic sources constitute a large portion of mass in the submicrometer regime ($D_p \leq 1 \mu\text{m}$) (Cunningham and Zoller, 1981; McInnes et al., 1996).

With its location along busy shipping lanes and near heav-

Correspondence to: John H. Seinfeld
(seinfeld@caltech.edu)

ily populated areas and the persistent cloud coverage during the summer months, the California coastal zone is an especially advantageous region to evaluate the anthropogenic contribution to marine aerosol and cloud condensation nuclei (CCN). Table 1 summarizes studies conducted in the vicinity of the California coastal zone on marine aerosol and cloud droplets. Important studies by Hegg et al. (2008, 2009, 2010) have utilized source apportionment models to attribute size-resolved hygroscopicity, light scattering coefficient, and CCN activity of marine aerosol to natural and anthropogenic sources. They estimated that 50% of the measured CCN concentrations and 57% of the light-scattering coefficient of marine aerosol in the California coastal region originated from anthropogenic sources. Though anthropogenic signatures contribute significantly to measured aerosol properties, the extent to which ship emissions contribute to this signal remains uncertain.

Few studies along the California coast have investigated marine aerosol and cloud properties simultaneously (Table 1). In this study, we utilize state-of-the-art aerosol measurements to build upon the knowledge of marine aerosol and cloud properties, with special attention to the contribution from ship emissions.

2 Methodology

2.1 Field Mission Description

From July – August 2011, the Eastern Pacific Emitted Aerosol Cloud Experiment 2011 (E-PEACE) was operated out of the Center for Interdisciplinary Remotely-Piloted Aircraft Studies (CIRPAS) in Marina, CA (Russell et al., 2012). The purpose of the field mission was to study the effect of ship emissions, sea-salt and organic aerosol on Eastern Pacific marine stratocumulus commonly found off the coast of central California. Thirty flights were conducted by the CIRPAS Twin Otter aircraft to probe the emissions of cargo and tanker ships and their effects on marine stratocumulus. The focus of this study is a set of measurements made during twenty-six flights conducted in a sampling region between San Francisco and Monterey Bay (Fig. 1). Four additional flights were performed outside of this sampling region and are analyzed in Section 4.1 to compare aerosol properties during cloudy and clear conditions, however a more extensive analysis of these flights will be forthcoming. In addition to sampling direct ship emissions, measurements of aerosol and cloud properties were made below, within, and above cloud during each flight. Simultaneous measurements of marine aerosol properties were conducted onboard the R/V *Point Sur*. Averaged measurements made outside direct ship fumigation were taken to reflect the variation of marine aerosol and cloud properties over the course of the campaign.

2.2 Aerosol and Cloud Droplet Measurement Methodology

Cloud and aerosol properties were measured by ship and aircraft using a suite of aerosol instruments (Table 2). A detailed description of the instrumentation used in this study can be found in the Appendix. Cloud droplet residuals were measured downstream of a counterflow virtual impactor (CVI) inlet with a cut size of 11 μm (Shingler et al., 2012).

In the following discussion, we report cloud residual mass concentrations measured behind the CVI inlet. Despite the improved CVI design that can accommodate high sample flow and thus reduce the need for large counterflow and dilution (Shingler et al., 2012), uncertainties remain in total mass and number concentrations that are common among all CVI inlets. Primarily, the transmission efficiency (TE) of the CVI is a function of several parameters, including aircraft speed, sample-flow dilution, and particle diameter. In addition, the instrument is characterized by a cut size that restricts the smallest particle that can be sampled; thus, the cloud residual mass concentrations reported in this study (Table 3) are less than the total cloud residual mass. The variation of mass between flights, however, suggests a qualitative difference between periods of low and high mass concentrations.

An altitude-dependent, zig-zag aircraft sampling pattern was utilized to measure unperturbed and perturbed air masses. Upon locating a ship, the Twin Otter sampled below, within and above cloud in close proximity to the ship's plume. While in cloud, measurements were made behind the CVI, thus sampling only cloud droplet residuals. Measurements made out of cloud were sampled through the main sub-isokinetic inlet.

3 Aerosol and Cloud Droplet Properties

In the following discussion, we use terminology such as "background" and "perturbed" to define aerosol conditions of the marine atmosphere. We acknowledge, however, that the assignment of these terms is not without ambiguity. A solely background signal in the remote marine atmosphere is a condition that occurs only when natural marine processes contribute to the aerosol. Without anthropogenic or continental influences, one might presume that a true baseline marine signal exists. However, even in a total absence of anthropogenic influence, such a signal is likely not unique and constant throughout the remote marine atmosphere. Varying wind speeds that generate sea spray, or biological production of dimethyl sulfide (DMS), which leads to homogeneously nucleated particles, can affect the local "background" signal. Even in the absence of non-marine sources, the natural background marine aerosol is dynamic.

Rather than relying on a definition of "background" aerosol, we choose to distinguish between "clean" and "per-

turbed” conditions based on the extent to which the marine atmosphere is impacted by shipping emissions. We define “perturbed” air masses as being pockets of the local marine atmosphere that have been directly impacted by local ship emissions. This would comprise relatively small spatial regions in which the aerosol number concentration has increased, the aerosol number size distribution has shifted in mean diameter, and the aerosol composition has changed relative to the surrounding region. The atmosphere unperturbed by ship emissions, which we take to be synonymous with the term “clean,” can be broken into a spectrum of conditions with varying degrees of non-ship related influences. Here, we are interested in comparing properties of the marine aerosol during periods of high aerosol mass loading owing to ship emissions (defined here as “perturbed”) with properties in adjacent air masses not directly impacted by ship emissions (defined here as “clean”). The nature of the marine aerosol can be consistently categorized using data from the aerosol mass spectrometer (AMS), which transmits particles with vacuum diameters ranging between 60 - 600 nm with 100% transmission efficiency. Initially we will rely on bulk AMS mass concentrations as the basis on which to identify and define “clean” and “perturbed” conditions, but subsequently, we will derive conditions that more concretely define air masses directly impacted by shipping emissions.

Table 3 reports average aerosol properties for each flight compared to measurements reported by other studies conducted in the Eastern Pacific. We note that observations from this study agree broadly with previous findings. Notably, aerosol mass measured by the AMS agrees well with that measured by filter sampling reported in McInnes et al. (1996). Mass loadings from this study reflect submicrometer, non-refractory aerosol, whereas loadings reported by McInnes et al. (1996) reflect total submicrometer mass. The close agreement suggests that the mass measured in the submicrometer regime is dominated by non-sea salt components. This is consistent with McInnes et al. (1997) who show that 87-96% of the total number concentration of submicrometer particles in the remote marine atmosphere are non-sea salt.

We can use the results from Table 3 to identify flights that were clean and perturbed during the E-PEACE campaign. Figure 2 shows the mass contributions of bulk AMS species to dry marine aerosol and cloud droplet residuals over the course of the study. As is also shown in Table 3, submicrometer aerosol mass concentrations strongly varied between flights. In the beginning of the study, a continual period of low aerosol loading was observed between July 15 - 19 (RF 5 - 8). These measurements were among the lowest aerosol mass concentrations observed during E-PEACE. In the present study, these were likely to have been the least influenced by shipping emissions and are therefore defined as “clean.”

Of particular interest are flights with elevated sulfate concentrations. Sulfate in the marine atmosphere is primarily attributed to DMS, continental pollution, and shipping ex-

haust. Flights conducted between July 27 - August 2 (RF 14 - 18) exhibited enhancements in total aerosol mass concentrations that were nearly double the amount observed during clean conditions. These flights also had some of the highest concentrations of sulfate in both below-cloud aerosol and residual cloud droplets. Though there were other flights in which the total aerosol mass concentration was high, the period during RF 14 - 18 represents nearly a week of uninterrupted enhancements in aerosol mass. Thus, we focus our attention to these flights and define them as “perturbed.”

3.1 Cloud-Processed Aerosol

Figure 3 shows typical marine aerosol number size distributions as measured by the scanning mobility particle sizer (SMPS). In general, marine aerosol exhibits two modes at approximately 60 and 200 nm, respectively. The peak at 200 nm, which is the cloud residue mode commonly observed in regions with marine stratocumulus (Hoppel et al., 1986, 1994; Frick and Hoppel, 2000), implies that the aerosol has undergone cloud processing.

During perturbed flights, the total aerosol volume concentration is approximately twice as large as that for clean flights. For example, the aerosol volume concentration for flights 16, 26 (perturbed) and 8, 20 (clean) are $2.24, 2.74 \mu\text{m}^3 \text{ cm}^{-3}$ and $1.47, 0.47 \mu\text{m}^3 \text{ cm}^{-3}$, respectively. Representative size distributions of fresh ship exhaust from three ships (Fig. 3, bottom panel) exhibit a primary mode between 56 - 73 nm, which falls in the range of non cloud-processed aerosol. It is possible that ship emissions enhanced the number concentration of small mode aerosol during perturbed flights.

Cloud processing was also observed to affect aerosol composition (Fig. 4), which is consistent with previous studies. Cloud scavenging and subsequent reaction of gaseous sulfur species lead to the accumulation of sulfate (Faloona (2009) and references therein). Under conditions of low acidity, some studies have shown that organics can also be formed from aqueous-phase processing. For example, Sorooshian et al. (2007a,b), showed that the ratio of oxalate:sulfate increases in cloud droplets with higher liquid water content (LWC). After the droplet evaporates, the low volatility organics formed by aqueous-phase chemistry remain in particle residuals (Sorooshian et al. (2007a) and references therein). Figure 4 shows the average out-of-cloud organic:sulfate ratio as a function of altitude. As observed by Sorooshian et al. (2007a), the ratio of organic:sulfate increases with altitude, a finding that is also coincident with an average increase in LWC. It is likely that aqueous-phase chemistry and subsequent droplet evaporation played a significant role controlling aerosol composition in the present study, which is consistent with the observation of a cloud-processed mode in the aerosol size distribution data (Fig. 3).

3.2 Cloud Water Chemistry

Figure 5 summarizes the trends in major cloud water ion and metal concentrations. These data are presented similarly to those reported by Straub et al. (2007) and Benedict et al. (2012), such that the present values can be easily compared. In this study, Na, Ca, Mg and K are measured by ICP-MS and are therefore representative of total metal content. Species such as Cl^- , SO_4^{2-} , and NO_3^- are measured by IC and are therefore representative of soluble ions. In the present study, we assume that Na, Ca, Mg, and K originate from soluble seawater species. Furthermore, to calculate concentrations in units of normality (μN), we assume that when present in the aqueous phase, these metals exist in their most stable valence state. If we assume that sodium concentrations reported in this study are representative of soluble sodium with +1 valence, then E-PEACE concentrations (0.7 - 3,900 μN) are consistent with those observed by Straub et al. (2007) (36 - 2,784 μN). Of all the common seawater species, Cl^- , Mg, and K exhibit a ratio with respect to Na that is consistent with the global average ratio found in seawater. Calcium is observed at a ratio slightly higher than typical seawater. Similar enhancements in calcium have been observed previously (e.g. Straub et al., 2007; Benedict et al., 2012) and may be the result of dissolved crustal minerals. The strong linear correlation with sodium, however, implies that the variation in calcium was primarily influenced by sea spray.

Of particular interest is the variation of seawater species between flights. Markers in Fig. 5 colored by blue and red indicate flights performed during clean (RF 5 - 8) and perturbed (RF 14 - 18) conditions, respectively. In general, the concentration of seawater species in marine cloud water is invariant during clean and perturbed flights. These species also appear to be present at lower concentrations during these flights than compared to all other flights performed during E-PEACE. It is reasonable, therefore, to neglect the mass contribution from seawater to the variation of sulfate observed in Table 3 and Fig. 2, given that clean and perturbed flights show little variation in sea-related species.

Sulfate and nitrate in the present study do not exhibit a strong linear relationship with sodium. These species are also enhanced during perturbed conditions (Fig. 5). In Section 3.4, we show that metals associated with shipping emissions (such as vanadium) are also enhanced during perturbed conditions and that their variation is coincident with higher concentrations of sulfate in dry marine aerosol. It is possible that enhanced sulfate and nitrate in cloud water samples originated from ship-impacted air masses.

3.3 CCN Measurements of Background Marine Aerosol

CCN measurements of marine aerosol are summarized in Fig. 6. In the top panel, CCN activation spectra are compared for perturbed (red, RF 15) and clean (blue, RF 20) flights. In

general, the fraction of activated particles at a given supersaturation is enhanced under perturbed conditions. For example, at 0.7% supersaturation, 90% of the particles measured during RF 15 activate in the CCN instrument. In contrast, only 60% of the particles activate in the instrument during RF 20. If we fit a sigmoidal curve of the form $\text{CCN/CN} = a_0 / (1 + (x/a_1)^{-a_2})$ (where a_0 , a_1 and a_2 are fitted parameters) and take the inflection point to reflect the aerosol population ensemble critical supersaturation (Moore et al., 2011), we find that the critical supersaturation is lower for particles measured during RF 15 than those measured during RF 20 (0.23% vs 0.27%).

The bottom panel in Fig. 6 shows the fraction of activated particles at 0.15, 0.3, 0.5 and 0.7% supersaturation for all dry aerosol measurements. Markers are colored by sulfate loading to illustrate the extent to which shipping emissions may have influenced the measurement. In general, a higher fraction of activated particles is coincident with elevated concentrations of sulfate. This is consistent with the averaged spectrum in Fig. 6 (top) which shows that more particles activated during perturbed flight RF 15 compared to clean flight RF 20. From Fig. 3, we see that the aerosol measured during RF 20 exhibited two modes that, when normalized by total aerosol number, have similar peak shape to aerosol measured during a perturbed flight (e.g., RF 16). The only observable difference in normalized number size distributions is that the small mode from RF 20 peaks at a smaller diameter (40 nm) than RF 16 (60 nm). While this may partially explain the increased fraction of CCN during perturbed conditions, the enhancement of activated particles may also result from elevated concentrations of sulfate (as shown in Fig. 6).

Enhanced CCN concentrations in the presence of anthropogenic pollution events has been previously observed in the Eastern Pacific (Hegg et al., 2009, 2010; Langley et al., 2010). Langley et al. (2010) found that anthropogenic pollution acted as condensation sites for sulfur species, resulting in an increase in CCN number concentrations. Hegg et al. (2010) deduced that 67% of the CCN off the coast of California are anthropogenic in origin. The CCN concentrations reported in the present study are consistent with those results (see Table 3 comparison), suggesting that anthropogenic sources are major contributors to the CCN properties reported in Fig. 6. In Section 3.4, we show that sulfate measured during periods of elevated aerosol mass can be primarily linked to shipping emissions; thus, shipping emissions may have exerted a strong control on CCN properties during this study.

3.4 Relationship between Marine Aerosol and Cloud Droplet Properties

In this study, sulfate is a major constituent of submicrometer marine aerosol (Fig. 2). Sulfate affects cloud water chemistry and cloud droplet number concentrations by low-

ering cloud water pH (via SO_2 oxidation) and increasing CCN concentrations (eg. ship emissions, homogeneous nucleation of H_2SO_4 or MSA) (Hegg and Hobbs, 1986; Hoppe et al., 1994; Straub et al., 2007; Hegg et al., 2010; Langley et al., 2010). Sources of sulfate in the marine atmosphere include ship emissions, DMS, and continental pollution. Here, we relate sulfate measured below cloud to properties of cloud water chemistry and present evidence that elevated sulfate measured during perturbed flights was largely influenced by ship emissions. In the present discussion, we only compare trace metals such as iron and vanadium due to their links to shipping. Subsequent work will provide a more complete overview of cloud water chemistry during the E-PEACE campaign.

Figure 7 compares below-cloud sulfate with various cloud properties. Iron and vanadium were measured in cloud water samples using ICP-MS, while hydronium concentrations were calculated from cloud water pH. All data are presented in air equivalent units, which represents the mass of a species per unit volume of air (see Appendix for details). We observe that sulfate in below-cloud aerosol correlates well with pH (not shown) and cloud droplet number concentration ($R^2 = -0.57$ and 0.64, respectively). This is consistent with observations of enhanced cloud water acidification and CCN in the presence of sulfate (e.g., Hoppe et al., 1994; Straub et al., 2007; Langley et al., 2010). Perturbed flights exhibit greater acidification in cloud water samples and higher concentration of cloud droplets, vanadium, and iron as compared to clean flights. Of all the flights, the highest concentration of sulfate below cloud occurred during RF 15, which also exhibited the greatest amount of acidification, highest concentration of vanadium, highest concentration of cloud droplets, and second highest concentration of iron in cloud water samples. This enhancement is clearly seen in Table 3, where perturbed flights 14 - 18 exhibit 5-10 times higher concentrations of iron and vanadium than clean flights.

The hypothesis in the present study is that cloud water acidification results from the oxidation of SO_2 originating from ship emissions. The correlation with below-cloud sulfate suggests that enhanced sulfur emissions led to an decrease in pH. Even more suggestive of ship-influenced acidification is the correlation of cloud water vanadium with cloud water acidity ($R^2 = 0.8$, Fig. 8). Studies have shown that shipping emissions are the predominant source of vanadium in the marine atmosphere (Agrawal et al., 2008; Sholkovitz et al., 2009; Furutani et al., 2011). The strong correlation between vanadium and acidity and the enhancement of both during perturbed conditions implies that in the present study, shipping emissions largely contributed to cloud water acidification.

The variation in iron concentrations with below-cloud sulfate (Fig. 7) could result from a number of sources. While iron is often attributed to continental dust, recent studies suggest that iron also has significant sources from ship emissions. Using single particle mass spectrometry, Furu-

tani et al. (2011) found that iron-containing aerosol from Asian outflows could be subdivided into several major iron-containing categories, one of which is iron associated with vanadium. Iron-containing aerosols constituted nearly 40% of the total number of particles in the ship-associated vanadium category. While it is possible that shipping emissions enhanced iron concentrations during perturbed flights, it appears that elevated iron concentrations in the present study were largely due to continental dust. Figure 8 (bottom) shows the relationship between iron and manganese in cloud water samples. The strong correlation ($R^2 = 0.9$) suggests that the two are linked to a common source.

Manganese is primarily attributed to crustal minerals (Statham and Chester, 1988; Guieu et al., 1994; Ohta et al., 2006; Duvall et al., 2008). Iron and manganese concentrations were not strongly correlated to cloud water sulfate ($R^2 = 0.27$ and 0.29 for iron and manganese, respectively); therefore, the elevation of iron and manganese in cloud water during perturbed flights is likely indicative of air transported from continental sources. The contribution of below-cloud sulfate from continental sources is difficult to quantify given that iron and manganese are related to the transport of dust and are not directly linked to anthropogenic sources. We note, however, that iron and manganese are not strongly correlated with cloud water acidification (not shown, $R^2 = 0.36$) which we hypothesize resulted from SO_2 oxidation. Furthermore, we show in Section 3.5 that perturbed flights were largely affected by air masses that were transported through major shipping lanes and not by air masses that were transported directly over land. Though we cannot rule out continental sources as contributors to below-cloud sulfate, we presume that shipping emissions exerted a stronger impact on properties of marine aerosol over continental sources given that metals associated with shipping emissions, such as vanadium, are strongly correlated to other properties of cloud water chemistry such as acidification.

DMS as a major source of sulfate during perturbed flights can be ruled out in the measurements here based on the small variation of methanesulfonic acid (MSA, DMS oxidation product). Appendix Fig. A1 shows the variation of cloud water MSA and sulfate as measured by ion chromatography. The amount of MSA in cloud water was no different during perturbed flights when compared to clean or intermediate flights. We infer from these results and those from Fig. 7 and 8 that the primary source of below-cloud sulfate during perturbed flights originated from ship exhaust.

3.5 Back-Trajectory Comparisons

As discussed in Section 3.4, the variation of manganese and iron in cloud water samples is likely indicative of crustal minerals transported from continental sources. Based on these results, we presume that the enhancement in sulfate during perturbed flights was at least partly due to changes in meteorology. These inferences are supported by the 72 h (NOAA

HYSPPLIT) back-trajectories corresponding to cloud water samples collected during clean and perturbed flights (Fig. 9).

During clean flights, air was primarily transported across the remote ocean, which may explain the observation of low mass loadings in sulfate, organics, iron, and manganese (Table 3, Fig. 2). During flights in which there is strong evidence of anthropogenic influence, air was primarily transported along the coast and through some of the most heavily transited shipping lanes. This is consistent with the observation of enhanced vanadium (shipping influences), iron, and manganese (continental influence) in cloud water samples during perturbed flights (Fig. 7 and 8). We infer from Fig. 9 that changes in meteorology likely influenced the variation in aerosol and cloud properties and that the enhancement of sulfate below cloud during perturbed conditions is partly due to the transport of air masses through shipping lanes.

4 Ship Impacts on Marine Aerosol and Clouds

4.1 Organic Aerosol Mass Spectra

In the following discussion, we compare organic aerosol spectra during clean and perturbed flights to investigate possible influences of ship emissions on the composition of cloud droplet residuals and dry, below-cloud marine aerosol (Fig. 10). Flight 9 (RF 9) was used as a basis for clean conditions, despite exhibiting slightly higher sulfate than most other flights categorized as clean, because in this flight, distinct ship tracks were observed next to unperturbed cloud. As shown in the column of spectra to the right of the dotted line in Fig. 10, comparison of perturbed and unperturbed organic spectra of cloud droplet residuals provides a reference to how the organic composition of cloud particles changes in the presence of ship emissions. These spectra can be compared to those from flight 15 (RF 15), which was found to have the highest concentrations of vanadium and sulfate within cloud and was the most likely to have been influenced by ship exhaust.

The top and middle rows in Fig. 10 are normalized organic mass spectra of cloud droplet residuals and dry, below-cloud aerosol, respectively. In general, aerosol and cloud residuals are highly oxidized, exhibiting strong signals at m/z 44 (CO_2^+). These spectra are consistent with marine aerosol measured by Murphy et al. (2009) and cloud droplet residuals measured by Lee et al. (2012). Ulbrich et al. (2009) classified aerosol with similar mass spectra observed in Pittsburgh, PA as low volatility, highly oxidized secondary organic aerosol (LV-OOA).

Many studies have shown that primary organic aerosol from ship and diesel exhaust exhibit reduced ions consistent with hydrocarbon-like organic aerosol (HOA) (e.g., Canagaratna et al., 2004; Murphy et al., 2009). The prominent HOA peaks in fresh ship exhaust (m/z 55, 57, 69, 71, etc.) constitute less than 2% of the mass in dry aerosol during per-

turbed flights. Murphy et al. (2009) attributed similar observations to dilution processes by comparing AMS measurements of fresh ship emissions to the organic spectrum of exhaust aged for 60 min. The authors showed that the organic fraction evolved to resemble the surrounding low volatility, unperturbed aerosol - the fraction of m/z 44 increased, while prominent HOA masses decreased. The authors note that this aging process could be explained primarily by dilution with unperturbed aerosol, however accumulation of low volatility organics may have also increased the fraction of oxidized mass.

The lack of prominent HOA masses in aged ship exhaust precludes the use of these peaks as tracers for ship emissions. Figure 10, however, provides evidence for a distinctive mass spectrum of ship emissions in perturbed cloud residuals. During RF 9, little difference existed between the organic signatures of cloud residuals and below-cloud aerosol (Fig. 10, bottom). In contrast, during RF 15, cloud residuals exhibited 8 and 3% enhancements in masses at m/z 42 and 99 over dry, below-cloud aerosol. This enhancement in m/z 42 and 99 is also observed between the mass spectra of perturbed and unperturbed clouds (Fig. 10, third column), suggesting that m/z 42 and 99 may be linked to cloud-processed ship emissions.

The source of m/z 42 and 99 can be further investigated when considering the time series trend of m/z 99 across multiple flights. Figure 11 illustrates the variation of m/z 99, LWC, and bulk AMS traces for 1) RF 9 - moderately clean, cloudy 2) RF 16 - perturbed, cloudy 3) RF 27 - moderately clean, no clouds and 4) RF 28 - moderately clean, clouds. Flights RF 27 and RF 28 were additional experiments that were conducted outside the sampling area shown in Fig. 1. These flights were performed along the coastline starting in Monterey Bay and ending near the California/Oregon border. Figure 12 shows the flight paths of RF 27 and RF 28 in relationship to the sampling area shown in Fig. 1. Back-trajectories of samples measured in the middle of each flight show that air was transported from the same direction on both days.

Inspection of Fig. 11 reveals multiple trends consistent with the inferences drawn from Fig. 10. First, we note that the time series of m/z 99 varies with bulk AMS traces and is most prominent when measuring ship tracks and perturbed air masses. The time series of m/z 99 shows an enhancement in mass when ship tracks are detected (marked, Fig. 11), which is not observed in nearby unperturbed clouds. Also, we see that m/z 99 is highly variable both in and out of cloud and is coincident with variations of sulfate during a perturbed flight (RF 16). From these results, we infer that the source of m/z 99 is shipping exhaust.

The trends in Fig. 11 also imply that m/z 99 is linked to cloud processing. Among the flights presented, RF 27 was the only one performed under clear meteorological conditions. This is evident by the negligible LWC during vertical soundings. In addition, the cloud-processed mode in the

aerosol size distribution (Fig. 11, top row) peaks at a lower diameter (77 nm) during clear conditions than during cloudy conditions (180 - 250 nm), implying that cloud processing contributed less mass to below-cloud aerosol during RF 27 than other flights. The time series of m/z 99 during RF 27 shows little variation over the course of the flight. If we contrast this to RF 28, which was performed during a cloudy day and along a similar flight path (as illustrated in Fig. 12), we see that the variation of m/z 99 is enhanced in and out of cloud. This evidence, along with the variation of m/z 99 in ship-impacted air masses, leads us to conclude that the variation of m/z 99 likely results from cloud processing of ship emissions.

4.2 Application of m/z 42 and 99 in Evaluating Ship-Impacted Airspace

Given the unit mass resolution of the C-ToF AMS, a number of masses could be responsible for the signals observed at m/z 42 and 99. The species $C_2H_2O^+$, $C_3H_6^+$, $C_2H_4N^+$ and $CHOCl_2^+$ are the non-isotopic ions present at m/z 42 while $C_8H_3^+$, $C_6H_{11}O^+$, $C_5H_7O_2^+$ and $C_7H_{15}^+$ are the non-isotopic ions present at m/z 99. Thus, the variation of m/z 42 and 99 in ship-impacted clouds could result from the fragmentation of aqueous-phase oxidation products ($C_2H_2O^+$, $C_5H_7O_2^+$, and $C_6H_{11}O^+$), alkane species ($C_7H_{15}^+$) or unsaturated carbon chains ($C_3H_6^+$, $C_8H_3^+$). High-resolution AMS measurements of marine aerosol performed onboard the R/V *Point Sur* suggests that the enhancements in masses at m/z 42 and 99 result from the increase in signal from $C_2H_2O^+$ and $C_5H_7O_2^+$ (see Section 4.3). This supports the presumption that the enhancement of m/z 42 and 99 in perturbed air masses result from aqueous-phase oxidation of ship emissions.

Given the large fraction of m/z 42 and 99 in perturbed air relative to clean air, we can use these masses to indicate the degree to which shipping emissions affect marine aerosol. Figure 13 shows the relationship between the fractions of m/z 42 and 99 in the present study. Markers are colored by sulfate mass concentrations to illustrate the extent to which ships may have impacted each measurement. These plots show that the fraction of m/z 42 in the organic spectra strongly correlates with the fraction of m/z 99, with $R^2 = 0.72$ and 0.67 for measurements of cloud droplet residuals and dry aerosol, respectively. Also, higher fractions of m/z 42 and 99 are coincident with higher loadings of sulfate. Appendix Fig. A2 shows the Pearson R correlation spectrum relating the fraction of m/z 42 and 99 with sulfate loading (top) and the fraction of all other organic masses (middle, bottom). Of all the masses in the organic spectrum, m/z 42 and 99 correlate most strongly with sulfate ($R = 0.58$ and 0.53 , respectively). Similarly, these two ions appear to correlate only with each other and not with typical aerosol tracers (e.g., m/z 57 for HOA spectra and m/z 44 for OOA). The relationship between m/z 42 and 99 appears to be unique and strongly linked to ship emissions.

If we take the fraction of m/z 42 and m/z 99 to reflect the degree of cloud-processed ship emissions (as suggested by Fig. 10 and 11) and that ship emissions are coincident with elevated sulfate concentrations (as suggested by Fig. 7 and the observation of high sulfate during the heaviest ship-influenced flights), then we see that Fig. 13 illustrates the extent to which ship emissions influence marine aerosol. Therefore, we propose a metric by which one can evaluate the extent of ship-impacted air masses in the presence of clouds. Measurements of the organic fractions of m/z 42 (f_{42}) and 99 (f_{99}) scattering about the red markers in Fig. 13 ($f_{42} > 0.15$; $f_{99} > 0.04$) would imply heavy influence from shipping emissions. Measurements of m/z 42 and 99 scattering about the green markers ($0.05 < f_{42} < 0.15$; $0.01 < f_{99} < 0.04$) would imply moderate, but persistent, ship influences. Finally, measurements of m/z 42 and 99 scattering about the blue markers ($f_{42} < 0.05$; $f_{99} < 0.01$) would imply clean, non-ship-influenced air. If we apply these metrics to the data in the present study, this would imply that 72% of the measurements made behind the CVI and 12% of measurements of dry aerosol were at least moderately impacted by ship emissions.

4.3 High Resolution AMS Analysis of Ions at m/z 42 and 99

Additional aerosol properties were measured below cloud onboard the R/V *Point Sur* from July 13-23. The R/V *Point Sur* was primarily deployed to generate controlled ship tracks for aerosol/cloud interaction studies (Russell et al., 2012); however, the high-resolution AMS onboard the R/V *Point Sur* continuously sampled marine aerosol. As shown in Table 3 and Fig. 2, the first half of the cruise (July 14-19) was coincident with the cleanest period of the study, whereas the latter half of the cruise (July 20-23) corresponded to periods of elevated sulfate. Investigating the variation of ions at m/z 42 and 99 during the latter half of the cruise is likely to provide information relevant to ship-impacted air masses.

Table 4 summarizes the fraction of the non-isotopic ions at m/z 42 and 99 during the R/V *Point Sur* cruise. Over the entire cruise (top), ions $C_2H_2O^+$ (m/z 42) and $C_5H_7O_2^+$ (m/z 99) constitute the majority ($> 50\%$) of the mass at their respective m/z. The contribution of these ions to the total signal increased during the latter half of the cruise. The fraction of other ions either decreased or increased little ($< 3\%$) during the period of elevated sulfate (bottom), implying that ions at m/z 42 and 99 other than $C_2H_2O^+$ and $C_5H_7O_2^+$ are not strongly associated with ship emissions.

Based on Table 4, we presume that $C_2H_2O^+$ and $C_5H_7O_2^+$ are the major ions responsible for the variation in m/z 42 and 99 observed in Fig. 9. Even though the alkane ion at m/z 99 ($C_7H_{15}^+$) constituted approximately 20% of the signal, this ion can be ruled out as a major contributor to the variation in m/z 99 because other major HOA-type ions (m/z 55, 57, 69, 71, etc.) were not observed to vary significantly with m/z 42 or 99 (see Appendix Fig. A2). $C_3H_6^+$ was also

variable and constituted a significant fraction of the signal at m/z 42. Though the contribution of this ion decreased when averaged during the perturbed period, $C_3H_6^+$ is an unsaturated, reduced ion of the series $C_nH_{2n}^+$, which is likely alkene in nature (McLafferty, 1980), that could have originated from an HOA or aged organic source.

Appendix Fig. A3 shows the variation in the organic fraction of $C_2H_2O^+$ and $C_3H_6^+$ at m/z 42 versus the organic fraction of $C_5H_7O_2^+$ at m/z 99. Over the entire cruise, $C_2H_2O^+$ is better correlated with $C_5H_7O_2^+$ than with the reduced ion ($R^2 = 0.49$ versus $R^2 = -0.09$, respectively). The two oxidized ions also exhibit a positive correlation that is consistent with the variation of m/z 42 and m/z 99 observed in Fig. 13. Appendix Fig. A3 also shows the time series trends of each ion at m/z 42 and 99 during the clean and perturbed periods. During the clean period, there is little variation in the ions at their respective masses. In contrast, during the periods of increased sulfate, the variations at m/z 42 and 99 are enhanced and are mostly attributable to $C_2H_2O^+$ and $C_5H_7O_2^+$. In conjunction with Table 5, Fig. A3 suggests that the variations in m/z 42 and 99 observed in C-ToF AMS measurements result from the enhancement of the oxidized ions $C_2H_2O^+$ and $C_5H_7O_2^+$, respectively.

5 Conclusions

A major finding of the present work is the identification of aerosol mass spectral peaks at m/z 42 and 99 as markers of cloud-processed ship emissions. The co-variation of m/z 42 and 99 in dry marine aerosol is unique and likely due to the evaporation of ship impacted cloud particles. One can use the fractions of m/z 42 and m/z 99 as a proxy for determining the extent of ship influences on cloud and aerosol properties in the marine environment. Measurements of the organic fractions of m/z 42 (f_{42}) and 99 (f_{99}) falling within the range $f_{42} > 0.15$; $f_{99} > 0.04$ would imply heavy influence from shipping emissions. Measurements of m/z 42 and 99 in the range $0.05 < f_{42} < 0.15$; $0.01 < f_{99} < 0.04$ would imply moderate, but persistent influences from ships. Finally, measurements of m/z 42 and 99 in the range $f_{42} < 0.05$; $f_{99} < 0.01$ would imply clean, non-ship-influenced air. These proxies apply under the condition in which clouds have been impacted by ship emissions. The results from this study also suggest that shipping exhaust is a major contributor to marine aerosol in regions of heavy shipping. If we apply the proposed conditions for moderate shipping influences, we find that 72% of the measurements illustrated in Fig. 13 are (at least) moderately perturbed cloud particles, while 12% of the measurements are moderately perturbed evaporated cloud droplets. The marine atmosphere off the coast of central California is likely seldom free from shipping influences and exhibits a persistent shipping signature on marine particles in the re-

gion defined between latitude 35.5 - 37.5°N and longitude 122 - 123.25°W.

Acknowledgements. This work was funded by ONR grants N00014-11-1-0783, N00014-10-1-0200, and N00014-10-1-0811, and NSF grant AGS-1008848. We acknowledge Dean Hegg for providing the cloud water collector.

Appendix A Additional Instrument Information

A1 Physical Properties of Aerosol and Cloud Droplets

Cloud and aerosol properties were measured onboard the Twin Otter using a suite of wing-mounted probes and cabin-based size classifiers. Aerosol size and number concentrations were measured outside the aircraft using a passive cavity aerosol spectrometer probe (PCASP) (Particle Measuring Systems, Boulder, CO). Simultaneous measurements were performed behind the main aerosol inlet/CVI using a custom-built scanning mobility particle sizer (SMPS) consisting of a differential mobility analyzer (DMA, model 3081, TSI) coupled to a condensation particle counter (CPC 3010, TSI, Shoreview, MN). PCASP and SMPS were calibrated using polystyrene latex spheres.

Cloud droplet distributions were measured using a cloud, aerosol and precipitation spectrometer (CAS) (Droplet Measurement Technologies, Boulder, CO) and was calibrated using glass beads. Cloud droplet number concentrations presented in this study reflect integrated CAS distributions for particles with diameters 2 - 50 μm .

Cloud condensation nuclei (CCN) number concentrations were measured using a streamwise thermal-graident cloud condensation nuclei counter (CCNC, Droplet Measurement Technologies) (Lance et al., 2006; Roberts and Nenes, 2005). A flow orifice and active control system was used to maintain instrument pressure at 700 mb independent of ambient pressure. The instrument was mostly run in scanning flow CCN analysis (SCFA) mode (Moore and Nenes, 2009). SFCA produced CCN spectra over the range 0.15 - 0.85% supersaturation every forty seconds. During zig-zag ship intercepts, CCNC operation was switched to conventional operation, maintaining a constant flow rate and constant 0.15% supersaturation.

A2 Composition Measurements by Aerosol Mass Spectrometry

A compact time-of-flight (CToF) aerosol mass spectrometer (AMS, Aerodyne Research Inc., Billerica, MA) was used onboard the Twin Otter to measure bulk aerosol chemistry. A high-resolution time-of-flight AMS (HR-ToF-AMS) was used onboard the R/V *Point Sur* to characterize detailed aerosol chemistry. The AMS has been described elsewhere and only a brief description is given here (Jayne et al., 2000;

Allan et al., 2004; Drewnick et al., 2005). The AMS measures the ensemble average mass spectra and chemically resolved size distribution of non-refractory particle phase organic and inorganic species. Spectra were analyzed in IGOR Pro (WaveMetrics, Inc., Lake Oswego, Oregon, USA) using the SQUIRREL v 1.51H and PIKA v 1.10H modules. Gas phase interferences were corrected using the fragmentation table developed by Allan et al. (2004) and Aiken et al. (2008).

Onboard the Twin Otter, MS mode was run for 8 s per saved run. A pressure-controlled inlet was used to maintain a flow rate of $1.4 \text{ cm}^{-3}/\text{s}$ to the AMS vacuum chamber. Prior to each flight, the AMS ionization efficiency (the ratio of the number of molecules ionized to the total number of molecules that enter the instrument) was calibrated using dried 350 nm NH_4NO_3 particles. Detection limits were taken to be twice the standard deviation of organic, sulfate, nitrate, ammonium and total mass measured during the filter period.

Composition dependent collection efficiencies (CE) were calculated based on the method by Middlebrook et al. (2012). Figure A4 compares aerosol mass concentrations measured by AMS to calculated aerosol mass concentrations from SMPS data before (left) and after (right) applying the CE correction factor. Volume concentrations measured by the SMPS were calculated by integrating SMPS data from 60 - 1000 nm. Volume concentrations were then converted to mass concentrations assuming a density of 1.6 g cm^{-3} , which is representative of a mixture of 60% sulfuric acid ($\rho = 1.84 \text{ g cm}^{-3}$) and 40% organics ($\rho = 1.2 \text{ g cm}^{-3}$) (Phinney et al., 2006). Before applying the CE correction, AMS and SMPS data scatter below the 1:1 line with a slope of 0.45. After applying the CE correction, AMS and SMPS data scatter close to the 1:1 line with a slope of 0.85. The bias towards higher aerosol mass concentrations calculated from SMPS data may result from a number of unknowns including overestimation of aerosol density, uncertainty of particle losses in the SMPS instrument and uncertainty in the amount of non-refractory material present in the aerosol. In general, however, the good agreement warrants use of the method developed by Middlebrook et al. (2012) in estimating the CE correction factor.

A3 Cloud Water Chemistry

Cloud water samples were collected using a modified Mohen slotted cloudwater collector (Hegg and Hobbs, 1986). Samples were collected at various altitudes and stored at 4°C until chemical analysis could be performed. Trace metals were measured using inductively coupled plasma mass spectrometry (ICP-MS) and major ions were measured using ion chromatography (IC).

To compare cloud water chemistry measured by off-line analysis to below-cloud aerosol loading measured by AMS, cloud water sample concentrations (ppb) were converted to

air equivalent concentrations ($\mu\text{g m}^{-3}$) as prescribed by (Straub et al., 2007). To achieve this conversion, the ion concentrations measured by ICP-MS and IC were multiplied by the average LWC recorded during sample collection. Measurements reported in air equivalent units reflect the total amount of material present per volume of air.

References

Ackerman, A. S., Toon, O. B., and Hobbs, P. V.: Numerical modeling of ship tracks produced by injections of cloud condensation nuclei into marine stratiform clouds, *J. Geophys. Res.*, 100, 7121–7133, 1995.

Agrawal, H., Malloy, Q. G. J., Welch, W. A., Wayne Miller, J., and Cocker III, D. R.: In-use gaseous and particulate matter emissions from a modern ocean going container vessel, *Atmos. Environ.*, 42, 5504–5510, 2008.

Aiken, A. C., DeCarlo, P. F., Kroll, J. H., Worsnop, D. R., Huffman, J. A., Docherty, K. S., Ulbrich, I. M., Mohr, C., Kimmel, J. R., Sueper, D., Sun, Y., Zhang, Q., Trimborn, A., Northway, M., Ziemann, P. J., Canagaratna, M. R., Onasch, T. B., Alfarra, M. R., Prevot, A. S. H., Dommen, J., Duplissy, J., Metzger, A., Baltensperger, U., and Jimenez, J. L.: O/C and OM/OC Ratios of Primary, Secondary, and Ambient Organic Aerosols with High-Resolution Time-of-Flight Aerosol Mass Spectrometry, *Environ. Sci. Technol.*, 42, 4478–4485, 2008.

Allan, J., Delia, A., Coe, H., Bower, K., Alfarra, M., Jimenez, J., Middlebrook, A., Drewnick, F., Onasch, T., and Canagaratna, M.: A generalised method for the extraction of chemically resolved mass spectra from Aerodyne aerosol mass spectrometer data, *J. Aerosol Sci.*, 35, 909–922, 2004.

Benedict, K. B., Lee, T., and Collett Jr., J. L.: Cloud water composition over the southeastern Pacific Ocean during the VOCALS regional experiment, *Atmos. Environ.*, 46, 104–114, 2012.

Canagaratna, M. R., Jayne, J. T., Gherter, D. A., Herndon, S., Shi, Q., Jimenez, J. L., Silva, P. J., Williams, P., Lanni, T., Drewnick, F., Demerjian, K. L., Kolb, C. E., and Worsnop, D. R.: Chase Studies of Particulate Emissions from in-use New York City Vehicles, *Aerosol Sci. Technol.*, 38, 555–573, 2004.

Christensen, M. W. and Stephens, G. L.: Microphysical and macrophysical responses of marine stratocumulus polluted by underlying ships: Evidence of cloud deepening, *J. Geophys. Res.*, 116, D03201, 2011.

Coakley, J., Bernstein, R., and Durkee, P.: Effect of Ship-Stack Effluents on Cloud Reflectivity, *Science*, 237, 1020–1022, 1987.

Corbett, J. J. and Fischbeck, P.: Emissions from ships, *Science*, 278, 823–824, 1997.

Cunningham, W. C. and Zoller, W. H.: The chemical composition of remote aerosols, *J. Aerosol Sci.*, 12, 367–384, 1981.

Drewnick, F., Hings, S., DeCarlo, P., Jayne, J., Gonin, M., Fuhrer, K., Weimer, S., Jimenez, J., Demerjian, K., Borrmann, S., and Worsnop, D.: A New Time-of-Flight Aerosol Mass Spectrometer (TOF-AMS)—Instrument Description and First Field Deployment, *Aerosol Sci. Technol.*, 39, 637–658, 2005.

Durkee, P. A., Noone, K. J., and Bluth, R. T.: The Monterey Area Ship Track Experiment, *J. Atmos. Sci.*, 57, 2523–2541, 2000.

Duvall, R. M., Majestic, B. J., Shafer, M. M., Chuang, P. Y., Simeoneit, B. R. T., and Schauer, J. J.: The water-soluble fraction of

carbon, sulfur, and crustal elements in Asian aerosols and Asian soils, *Atmos. Environ.*, 42, 5872–5884, 2008.

Eyring, V., Kohler, H., van Aardenne, J., and Lauer, A.: Emissions from international shipping: 1. The last 50 years, *J. Geophys. Res.*, 110, D17 305, 2005.

Faloona, I.: Sulfur processing in the marine atmospheric boundary layer: A review and critical assessment of modeling uncertainties, *Atmos. Environ.*, 43, 2841–2854, 2009.

Frick, G. and Hoppel, W.: Airship Measurements of Ship's Exhaust Plumes and Their Effect on Marine Boundary Layer Clouds, *J. Atmos. Sci.*, 57, 2625–2648, 2000.

Furutani, H., Jung, J., Miura, K., Takami, A., Kato, S., Kajii, Y., and Uematsu, M.: Single-particle chemical characterization and source apportionment of iron-containing atmospheric aerosols in Asian outflow, *J. Geophys. Res.*, 116, D18 204, 2011.

Guieu, C., Duce, R., and Arimoto, R.: Dissolved input of manganese to the ocean: Aerosol source, *J. Geophys. Res.*, 99, 18 789–18 800, 1994.

Hegg, D., Covert, D., and Jonsson, H.: Measurements of size-resolved hygroscopicity in the California coastal zone, *Atmos. Chem. Phys.*, 8, 7193–7203, 2008.

Hegg, D., Covert, D., Jonsson, H., and WOODS, R.: Differentiating natural and anthropogenic cloud condensation nuclei in the California coastal zone, *Tellus B*, 61, 669–676, 2009.

Hegg, D., Covert, D., Jonsson, H., and Woods, R.: The contribution of anthropogenic aerosols to aerosol light-scattering and CCN activity in the California coastal zone, *Atmos. Chem. Phys.*, 10, 7341–7351, 2010.

Hegg, D. A. and Hobbs, P. V.: Sulfate and nitrate chemistry in cumuliform clouds, *Atmos. Environ.*, 20, 901–909, 1986.

Hegg, D. A., Covert, D. S., Rood, M. J., and Hobbs, P. V.: Measurements of aerosol optical properties in marine air, *J. Geophys. Res.*, 101, 12 893–12 903, 1996.

Hersey, S., Sorooshian, A., Murphy, S. M., Flagan, R., and Seinfeld, J. H.: Aerosol hygroscopicity in the marine atmosphere: a closure study using high-time-resolution, multiple-RH DASH-SP and size-resolved C-ToF-AMS data, *Atmos. Chem. Phys.*, 9, 2543–2554, 2009.

Hoppel, W., Frick, G., and Larson, R.: Effect of Nonprecipitating Clouds on the Aerosol Size Distribution in the Marine Boundary Layer, *Geophys. Res. Lett.*, 13, 125–128, 1986.

Hoppel, W., Frick, G., and Fitzgerald, J.: Marine boundary layer measurements of new particle formation and the effects non-precipitating clouds have on aerosol size distribution, *J. Geophys. Res.*, 99, 14 443–14 459, 1994.

Hudson, J. G., Garrett, T. J., Hobbs, P. V., Strader, S. R., Xie, Y., and Yum, S. S.: Cloud Condensation Nuclei and Ship Tracks, *J. Atmos. Sci.*, 57, 2696–2706, 2000.

Jayne, J. T., Leard, D. C., Zhang, X., Davidovits, P., Smith, K. A., Kolb, C. E., and Worsnop, D. R.: Development of an Aerosol Mass Spectrometer for Size and Composition Analysis of Sub-micron Particles, *Aerosol Sci. Technol.*, 33, 49–70, 2000.

Lance, S., Nenes, A., Medina, J., and Smith, J. N.: Mapping the Operation of the DMT Continuous Flow CCN Counter, *Aerosol Sci. Technol.*, 40, 242–254, 2006.

Langley, L., Leaitch, W., Lohmann, U., Shantz, N., and Worsnop, D.: Contributions from DMS and ship emissions to CCN observed over the summertime North Pacific, *Atmos. Chem. Phys.*, 10, 1287–1314, 2010.

Lee, A., Hayden, K., Herckes, P., Leaitch, W., Liggio, J., Macdonald, A., and Abbatt, J.: Characterization of aerosol and cloud water at a mountain site during WACS 2010: secondary organic aerosol through oxidative cloud processing, *Atmos. Chem. Phys.*, 12, 6019–6047, 2012.

Lu, M.-L., Sorooshian, A., Jonsson, H. H., Feingold, G., Flagan, R. C., and Seinfeld, J. H.: Marine stratocumulus aerosol-cloud relationships in the MASE-II experiment: Precipitation susceptibility in eastern Pacific marine stratocumulus, *J. Geophys. Res.*, 114, D24 203, 2009.

McInnes, L., Quinn, P., Covert, D., and Anderson, T.: Gravimetric analysis, ionic composition, and associated water mass of the marine aerosol, *Atmos. Environ.*, 30, 869–884, 1996.

McInnes, L., Covert, D., and Baker, B.: The number of sea-salt, sulfate, and carbonaceous particles in the marine atmosphere, *Tellus*, 49, 300–313, 1997.

McLafferty, F.: Interpretation of Mass Spectra., University Science Books, third edn., 1980.

Middlebrook, A. M., Bahreini, R., Jimenez, J. L., and Canagaratna, M. R.: Evaluation of Composition-Dependent Collection Efficiencies for the Aerodyne Aerosol Mass Spectrometer using Field Data, *Aerosol Sci. Technol.*, 46, 258–271, 2012.

Moore, R. H. and Nenes, A.: Scanning Flow CCN Analysis—A Method for Fast Measurements of CCN Spectra, *Aerosol Sci. Technol.*, 43, 1192–1207, 2009.

Moore, R. H., Bahreini, R., Brock, C. A., Froyd, K. D., Cozic, J., Holloway, J. S., Middlebrook, A. M., Murphy, D. M., and Nenes, A.: Hygroscopicity and composition of Alaskan Arctic CCN during April 2008, *Atmos. Chem. Phys.*, 11, 11 807–11 825, 2011.

Moore, R. H., Cerully, K., Bahreini, R., Brock, C. A., Middlebrook, A. M., and Nenes, A.: Hygroscopicity and composition of California CCN during summer 2010, *J. Geophys. Res.*, 117, D00V12, 2012.

Murphy, S. M., Agrawal, H., Sorooshian, A., Padró, L. T., Gates, H., Hersey, S., Welch, W. A., Jung, H., Miller, J. W., Cocker III, D. R., Nenes, A., Jonsson, H. H., Flagan, R. C., and Seinfeld, J. H.: Comprehensive Simultaneous Shipboard and Airborne Characterization of Exhaust from a Modern Container Ship at Sea, *Environ. Sci. Technol.*, 43, 4626–4640, 2009.

Noone, K., Ostrom, E., Ferek, R., Garrett, T., Hobbs, P., Johnson, D., Taylor, J., Russell, L., Flagan, R., Seinfeld, J. H., O'Dowd, C., Smith, M., Durkee, P., Nielsen, K., Hudson, J., Pockalny, R., De Bock, L., Van Grieken, R., Gasparovic, R., and Brooks, I.: A Case Study of Ships Forming and Not Forming Tracks in Moderately Polluted Clouds, *American Meterological Society*, 57, 2729–2747, 2000.

Ohta, A., Tsuno, H., Kagi, H., Kanai, Y., Nomura, M., Zhang, R., and Terashima, S.: Chemical compositions and XANES speciations of Fe, Mn and Zn from aerosols collected in China and Japan during dust events, *Geochem. J.*, 40, 363–376, 2006.

Phinney, L., Richard Leaitch, W., Lohmann, U., Boudries, H., Worsnop, D. R., Jayne, J. T., Toom-Sauntry, D., Wadleigh, M., Sharma, S., and Shantz, N.: Characterization of the aerosol over the sub-arctic north east Pacific Ocean, *Deep Sea Research Part II: Topical Studies in Oceanography*, 53, 2410–2433, 2006.

Roberts, G. C. and Nenes, A.: A Continuous-Flow Streamwise Thermal-Gradient CCN Chamber for Atmospheric Measurements, *Aerosol Sci. Technol.*, 39, 206–221, 2005.

Russell, L. M., Sorooshian, A., Seinfeld, J. H., Albrecht, B. A.,

Nenes, A., Ahlm, L., Chen, Y.-C., Coggon, M. M., Craven, J. S., Flagan, R. C., Frossard, A. A., Jonsson, H., Jung, E., Lin, J. J., Metcalf, A. R., Modini, R., Mulmenstadt, J., Roberts, G. C., Shingler, T., Song, S., Wang, Z., and Wonaschutz, A.: Eastern Pacific Emitted Aerosol Cloud Experiment (E-PEACE), *Bull. Am. Meteorol. Soc.*, p. submitted, 2012.

Shingler, T., Dey, S., Sorooshian, A., Brechtel, F. J., Wang, Z., Metcalf, A. R., Coggon, M., Mulmenstadt, J., Russell, L. M., Jonsson, H. H., and Seinfeld, J. H.: Characterization and Airborne Deployment of a New Counterflow Virtual Impactor, *Atmos. Meas. Tech.*, 5, 1515–1541, 2012.

Sholkovitz, E. R., Sedwick, P. N., and Church, T. M.: Influence of anthropogenic combustion emissions on the deposition of soluble aerosol iron to the ocean: Empirical estimates for island sites in the North Atlantic, *Geochimica et Cosmochimica Acta*, 73, 3981–4003, 2009.

Sorooshian, A., Lu, M.-L., Brechtel, F. J., Jonsson, H., Feingold, G., Flagan, R. C., and Seinfeld, J. H.: On the Source of Organic Acid Aerosol Layers above Clouds, *Environ. Sci. Technol.*, 41, 4647–4654, 2007a.

Sorooshian, A., Ng, N. L., Chan, A. W. H., Feingold, G., Flagan, R. C., and Seinfeld, J. H.: Particulate organic acids and overall water-soluble aerosol composition measurements from the 2006 Gulf of Mexico Atmospheric Composition and Climate Study (GoMACCS), *J. Geophys. Res.*, 112, D13201, 2007b.

Sorooshian, A., Padró, L. T., Nenes, A., Feingold, G., McComiskey, A., Hersey, S. P., Gates, H., Jonsson, H. H., Miller, S. D., Stephens, G. L., Flagan, R. C., and Seinfeld, J. H.: On the link between ocean biota emissions, aerosol, and maritime clouds: Airborne, ground, and satellite measurements off the coast of California, *Global Biogeochem. Cycles*, 23, 2009.

Statham, P. and Chester, R.: Dissolution of manganese from marine atmospheric particulates into seawater and rainwater, *Geochim. Cosmochim. Acta*, 52, 2433–2437, 1988.

Straub, D. J., Lee, T., and Collett Jr., J. L.: Chemical composition of marine stratocumulus clouds over the eastern Pacific Ocean, *J. Geophys. Res.*, 112, 2007.

Ulbrich, I., Canagaratna, M., Zhang, Q., Worsnop, D., and Jimenez, J. L.: Interpretation of organic components from Positive Matrix Factorization of aerosol mass spectrometric data, *Atmos. Chem. Phys.*, 9, 2891–28918, 2009.

Yan, F., Winijkul, E., Jung, S., Bond, T. C., and Streets, D. G.: Global emission projections of particulate matter (PM): I. Exhaust emissions from on-road vehicles, *Atmos. Environ.*, 45, 4830–4844, 2011.

Table 1. Previous studies on the properties of marine aerosol over the northeastern Pacific Ocean. Footnotes define instrument abbreviations

Author	Research Location	Instruments	Aircraft/Ship/Ground	Sources Sampled	CCN Properties	Hygroscopicity	Size Properties	Chemical Properties	Species Analyzed	Summary
Hegg et al. (1996)	Pacific Coast	nephelometer PCASP, SMPS, DNH	Aircraft	Dry Aerosol	—	yes	—	—	—	Authors report the optical and hygroscopic properties of marine aerosol in the vicinity of the California coast. The hygroscopic growth factor was shown to be 1.7 while the ratio of backscatter to total scattering was found to be 0.3. This study investigated the composition of sub-micron marine aerosol. Gravimetric measurements showed that a significant amount of mass (0-7%) was unaccounted for in filter measurements. Water uptake on the filter samples made up 29% of the mass and the remaining mass was likely to be organic in nature.
McLennan et al. (1996)	E. Pacific	Filter Sampling and off-line analytical chemistry	Ground, Ship	Dry Aerosol	—	—	—	yes	sea salt, ions, sulfate, ammonium, water	
Phinney et al. (2008)	N.E. Pacific	SMPS, PCASP, MOUDI, AMS, GC	Ship	Dry Aerosol	—	yes	—	yes	MSA, sulfate, organics, nitrate, ammonium, sea salt	
Straub et al. (2007)	California Coast	Cloud-particle collector inlet and off-line analytical chemistry, FSASP, PCASP, PAM (LWC)	Aircraft	Cloud Particles	—	—	—	yes	TOC, inorganic ions, sulfate, nitrate, chloride, BC, organic, nitrate, sulfate, nitrate, chloride, ammonium, water, organic, particle, formamide, hydroperoxide, oxalate, sulfate	
Soroshian et al. (2007a)	California Coast	PILS, LWC, CVI	Aircraft	Cloud Particles	—	—	—	yes	oxalate, sulfate, organic, inorganics, BC, sulfate, lead	
Hegg et al. (2008)	California Coast	Filter Sampling and off-line analytical chemistry, AMS, Light-scattering humidity, PSAP	Aircraft	Dry Aerosol	—	yes	—	yes	oxalate, sulfate, organic, inorganics, BC, sulfate, lead	
Hegg et al. (2009)	California Coast	Filter Sampling and off-line analytical chemistry, AMS, PSAP, CCN, PCASP	Aircraft	Dry Aerosol	yes	—	yes	yes	DEA, MSA	
Hegg et al. (2009)	California Coast	AMS, DASH-SP	Aircraft	Dry Aerosol	—	yes	—	—	organics, inorganics, BC, sulfate, lead	
Soroshian et al. (2009)	California Coast	PILS, LWC, FSASP, SMPS, CCN, DASH-SP	Aircraft, ground, satellite	Aerosol, Clouds	yes	yes	yes	yes	MSA, SO_2 , organics	
Hegg et al. (2010)	California Coast	Filter Sampling and off-line analytical chemistry, AMS, PSAP, CCN, PCASP	Aircraft	Dry Aerosol	yes	yes	yes	yes	organic, nitrate, sulfate, ammonium	
Langley et al. (2010)	N.E. Pacific	AMS, SMPS, CCN, gas phase SO ₂	Ship	Dry Aerosol	yes	—	yes	yes	MSA, SO_2 , organics	
Moore et al. (2012)	N.E. Pacific	AMS, SMPS, CCN	Aircraft	Dry Aerosol	yes	yes	yes	yes	MSA, SO_2 , organics	
PCASP - Passive Cavity Aerosol Sizing Probe SMPS - Scanning Mobility Particle Sizer AMS - Aerosol Mass Spectrometer DNH - dual nephelometer hydrometer MOUDI - Micro-Orifice Uniform-Deposit Impactor PILS-IC - Particle Into Liquid Sampler - Ion Chromatography										
PSAP - Particle Soot Absorption Photometer CCN - Cloud Condensation Nuclei DASH-SP - Differential Aerosol Sizing and Hydrosopic Spectrometer Probe PILS-IC - Particle Into Liquid Sampler - Ion Chromatography										

Table 2. Instruments onboard the Twin Otter aircraft and R/V *Point Sur*.

Parameter	Instrument	Time Resolution	Detection Limit	Size Range	Twin Otter	Point Sur
Particle Number Concentration	Condensation Particle Counter (TSI CPC 3010)	1s	< 50,000 cm ⁻³	D _p = 10 nm	✓	✓
Aerosol Size Distribution	Scanning Mobility Particle Sizer (SMPS)	110s	N/A	10–700 nm	✓	✓
Aerosol Size Distribution	Passive Cavity Aerosol Spectrometer Probe (PCASP)	1s	N/A	0.1–2.6 μ m	✓	
Aerosol Size Distribution	Optical Particle Sizer (OPS)	2 min	N/A	0.3–9 μ m	✓	
Aerosol Size Distribution	Aerodynamic Particle Sizer (APS)	2 min	N/A	0.5–20 μ m	✓	
Cloud Droplet Residuals	Counterflow Virtual Impactor (CVI)	N/A	N/A	> 11 μ m	✓	
Bulk Cloud Water Composition	Modified Mohn Slotted Cloud Water Collector	N/A	N/A	N/A	✓	
Cloud Droplet Size Distribution	Cloud Droplet Probe (CDP)	1s	N/A	2.4–50 μ m	✓	
Cloud and Aerosol Size Distribution	Cloud and Aerosol Spectrometer Probe (CAS)	1s	N/A	0.65–55 μ m	✓	
Cloud Droplet Liquid Water Content	Light Diffraction (Gerber PVM-100 probe)	1s	N/A	5–50 μ m	✓	
Aerosol Soluble Organics	Particle-Into-Liquid Sampler (PLS)	6 min	0.1 μ g m ⁻³	1 μ m	✓	
Aerosol Bulk Composition	High Resolution Time-of-Flight Aerosol Mass Spectrometer (HR-ToF-AMS)	2 min	≤ 1 μ g m ⁻³	60–600 nm	✓	
Aerosol Bulk Composition	Compact Time-of-Flight Aerosol Mass Spectrometer (C-ToF-AMS)	8–12 s	≤ 1 μ g m ⁻³	60–600 nm	✓	
Cloud Condensation Nuclei (CCN) Number Concentration	Continuous Flow Streamwise Thermal Gradient CCN chamber	1–20s	< 20,000 cm ⁻³	s.s. 0.2–0.7 %	✓	
Hygroscopicity	Humidified Tandem Differential Mobility Analyzer (HTDMA)	1s	N/A	10–700 nm	✓	
Soot Absorption	Single Particle Soot Photometer (SP2)	1s	N/A	80–600 nm	✓	✓
Soot Absorption	Photo-acoustic Soot Spectrometer (PASS-3)	1s	10 Mm ⁻¹	< 1 μ m	✓	

Table 3. Summary of average aerosol and cloud properties over the course of the E-PEACE campaign. Bottom table summarizes key aerosol properties from previous studies of marine aerosol and cloud droplets off the coast of central California. Values in brackets represent standard deviations of the average. Values in parenthesis list the range of measurements. Values below detection limit (DL) are noted.

Research Flight (RF)	Date	Below Cloud Background Aerosol Measurements						Background Cloud Measurements ^a						Air Equivalent Cloud Water Chemistry					
		Total Mass ^b ($\mu\text{g m}^{-3}$)	Organic ^b ($\mu\text{g m}^{-3}$)	Sulfate ^b ($\mu\text{g m}^{-3}$)	CPC ^b (cm^{-3})	CCN(0.15%) ^b (cm^{-3})	CCN(0.3%) ^b (cm^{-3})	Total Mass ^b ($\mu\text{g m}^{-3}$)	Organic ^b ($\mu\text{g m}^{-3}$)	Sulfate ^b ($\mu\text{g m}^{-3}$)	pH	Na (10^{-3}) ($\mu\text{g m}^{-3}$)	Mn (10^{-3}) ($\mu\text{g m}^{-3}$)	V (10^{-3}) ($\mu\text{g m}^{-3}$)	IMC ^b (g m^{-3})				
1	8-Jul	9.32	0.50	0.51	282	—	238	1.37	0.76	0.84	235	4.02	57.182	5.141	4.72	2.12	0.09		
2	9-Jul	1.04	0.60	0.45	908	—	131	1.68	0.84	0.69	93	4.23	16.056	2.663	2.12	1.29	0.16		
4	14-Jul	0.86	0.75	0.20	364	—	78	0.92	0.49	0.20	23	4.32	<(DL)	<(DL)	1.29	0.11			
5	15-Jul	0.90	0.58	0.31	329	—	131	1.68	0.84	0.69	93	4.63	6.88	0.19	0.31	0.01			
6	16-Jul	0.77	0.72	0.18	341	—	1.06	0.67	0.22	0.22	27	4.50	127	<(DL)	2.02	0.11			
7 ^c	17-Jul	0.88	0.44	0.40	323	—	1.24	0.68	0.54	145	4.21	—	—	—	—	—			
8	19-Jul	1.83	0.70	0.78	578	217	—	1.08	0.63	0.39	127	5.16	17.662	4.88	3.11	4.25	0.19		
9	21-Jul	1.80	0.49	1.02	376	213	—	1.81	0.79	0.78	116	4.67	15.212	7.58	1.08	1.50	0.23		
10	22-Jul	1.80	0.86	1.56	976	300	400	1.84	0.88	0.81	169	4.30	13.889	17.61	1.55	2.46	0.25		
11	23-Jul	2.83	1.57	1.76	300	355	1.90	0.87	0.85	170	3.99	15.85	5.82	3.28	0.18	0.18			
12	24-Jul	0.92	0.92	0.92	226	—	1.16	0.56	0.32	87	4.95	11.702	5.13	1.36	3.12	0.10			
13	26-Jul	0.60	0.34	0.23	75	—	1.16	1.53	0.64	0.80	199	3.96	14.045	4.857	2.29	16.78	0.23		
14 ^d	27-Jul	0.81	0.81	0.55	207	—	2.21	0.98	2.50	327	2.50	20.772	86.38	4.89	43.08	0.12			
15	28-Jul	0.74	0.66	0.66	314	406	—	2.14	0.89	1.13	252	3.84	16.463	17.47	19.99	0.28			
16	29-Jul	2.62	0.70	0.70	96	304	304	1.10	0.62	1.10	212	3.77	9.78	47.07	2.71	7.35	0.10		
17	1-Aug	2.22	0.58	1.44	400	78	352	1.34	0.80	0.80	269	4.07	22.77	27.67	1.98	8.62	0.21		
18	2-Aug	2.55	0.89	1.47	567	184	335	1.11	0.60	0.38	120	4.80	11.406	4.45	3.63	0.19	—		
19	3-Aug	1.41	0.57	0.57	167	173	—	—	—	—	—	—	—	—	—	—	—		
20 ^e	4-Aug	0.52	0.55	0.29	44	83	—	—	—	—	—	—	—	—	—	—	—		
21	5-Aug	0.66	1.17	0.66	1.17	254	1.15	0.57	0.48	163	4.65	8.76	19.96	1.69	1.05	0.19			
22	8-Aug	0.75	1.01	2.24	757	328	353	0.52	1.30	1.30	323	3.66	42.794	1.31	4.17	0.11			
23	9-Aug	1.59	1.59	1.59	428	28	294	1.79	0.75	0.80	226	4.06	34.543	1.01	1.24	0.11			
24	10-Aug	1.57	0.88	0.88	79	296	49	0.99	0.65	0.44	150	4.54	20.015	3.142	1.76	7.64	0.25		
25	11-Aug	1.18	0.53	0.46	252	157	91	0.86	0.58	0.21	41	5.07	1.538	0.59	3.97	0.13			
26	12-Aug	1.49	1.24	1.94	670	—	459	1.80	0.71	0.97	257	3.90	22.109	17.24	1.07	3.26	0.14		
Min		0.77	0.44	0.18	221	28	78	0.86	0.49	0.20	23	2.92	127	0.19	0.07	0.31	0.01		
Max		4.74	1.24	3.14	976	528	459	4.98	2.21	2.50	327	5.16	87.182	17.47	43.08	0.28	—		
Author/Mission		Total Mass ^b ($\mu\text{g m}^{-3}$)	Organic ^b ($\mu\text{g m}^{-3}$)	Sulfate ^b ($\mu\text{g m}^{-3}$)	CPC ^b (cm^{-3})	CCN(0.15%) ^b (cm^{-3})	CCN(0.3%) ^b (cm^{-3})	Total Mass ^b ($\mu\text{g m}^{-3}$)	Organic ^b ($\mu\text{g m}^{-3}$)	Sulfate ^b ($\mu\text{g m}^{-3}$)	pH	Na (10^{-3}) ($\mu\text{g m}^{-3}$)	Mn (10^{-3}) ($\mu\text{g m}^{-3}$)	V (10^{-3}) ($\mu\text{g m}^{-3}$)	IMC ^b (g m^{-3})				
E-PEACE Average		1.98	0.73	0.73	1.07	510	148	1.67	0.78	0.75	171	4.48	13.227	23	5.4	0.16	—		
Hegg et al. (2010) ^c	Jul-Aug, 2011	[1.07]	[0.19]	[0.76]	[225]	[120]	[91]	[0.85]	[0.54]	[0.50]	[86]	[0.72]	[15.531]	[37]	[4.1]	[0.07]	—		
CARMA II	Jul, 2004	3.12	—	1.34	—	—	—	—	—	—	—	—	—	—	—	—	—		
CARMA IV	Aug, 2007	16.3	—	1.04	197.6	104	—	75.1150	—	—	—	—	—	—	—	—	—		
Sorooshian et al. (2009)	Jul, 2007	—	—	0.78	307	—	73	—	—	—	104	—	—	—	—	—	0.15		
MASE II	McInnes et al. (1996) ^f	April - Jun, 1994	2.21	—	—	—	—	—	—	—	[56]	—	—	—	—	—	[0.07]		
Stauber et al. (2007)	Jul, 2001	[1.16]	—	—	—	—	—	—	—	—	174	3.264.82	[39000 - 133,900]	71	2.3	—	0.33		
DYCOMS-II	—	—	—	—	—	—	—	—	—	—	[79]	—	—	—	—	—	[0.17]		

^a Measurement from AMS
^b Averaged cloud probe data during cloud water sampling period
^c No clouds (7/17), few cloud measurements by probes (8/4)
^d AMS Failure - limited measurements available below cloud (7/27)
^e Filter samples for aerosol > 2.7 μm in diameter
^f Filter samples for aerosol < 1 μm in diameter

^g Organics, sulfate and total mass concentrations measured behind the CVI

are a fraction of the total loading and may reflect absolute mass concentrations. See text for details.

Table 4. Fraction of each ion at m/z 42 and m/z 99 over the entire *R/V Point Sur* cruise (top) and during periods of high sulfate loading (bottom). Values in parenthesis are the variance in the measurement.

M/z 42			M/z 99		
Average Over Entire Cruise			Average Over Entire Cruise		
Ion	Fraction of Total Organic Signal	Fraction of Signal at m/z 42	Ion	Fraction of Total Organic Signal	Fraction of Signal at m/z 99
$\text{C}_2\text{H}_2\text{O}^+$	0.014 (5.1E-5)	0.57 (0.030)	$\text{C}_5\text{H}_7\text{O}_2^+$	4.22E-4 (1.26E-7)	0.51 (0.044)
C_3H_6^+	0.008 (2.43E-5)	0.33 (0.037)	$\text{C}_7\text{H}_{15}^+$	2.42E-4 (5.48E-8)	0.21 (0.036)
$\text{C}_2\text{H}_4\text{N}^+$	0.002 (2.36E-6)	0.08 (0.005)	$\text{C}_6\text{H}_{11}\text{O}^+$	1.84E-4 (2.40E-8)	0.19 (0.020)
CHOCl_2^+	4.01E-4 (1.26E-7)	0.02 (0.0004)	C_8H_3^+	7.81E-5 (9.21E-9)	0.09 (0.008)
Average During Period of Elevated Sulfate (July 19 - 23)					
Ion	Fraction of Total Organic Signal	Fraction of Signal at m/z 42	Ion	Fraction of Total Organic Signal	Fraction of Signal at m/z 99
$\text{C}_2\text{H}_2\text{O}^+$	0.020 (5.07E-5)	0.72 (0.013)	$\text{C}_5\text{H}_7\text{O}_2^+$	6.72E-4 (1.25E-7)	0.58 (0.030)
C_3H_6^+	0.004 (8.27E-6)	0.15 (0.009)	$\text{C}_7\text{H}_{15}^+$	2.23E-4 (5.11E-8)	0.15 (0.023)
$\text{C}_2\text{H}_4\text{N}^+$	0.003 (2.51E-6)	0.11 (0.006)	$\text{C}_6\text{H}_{11}\text{O}^+$	2.23E-4 (2.78E-8)	0.18 (0.013)
CHOCl_2^+	2.92E-4 (1.21E-7)	0.01 (0.0004)	C_8H_3^+	1.08E-4 (1.17E-8)	0.10 (0.007)

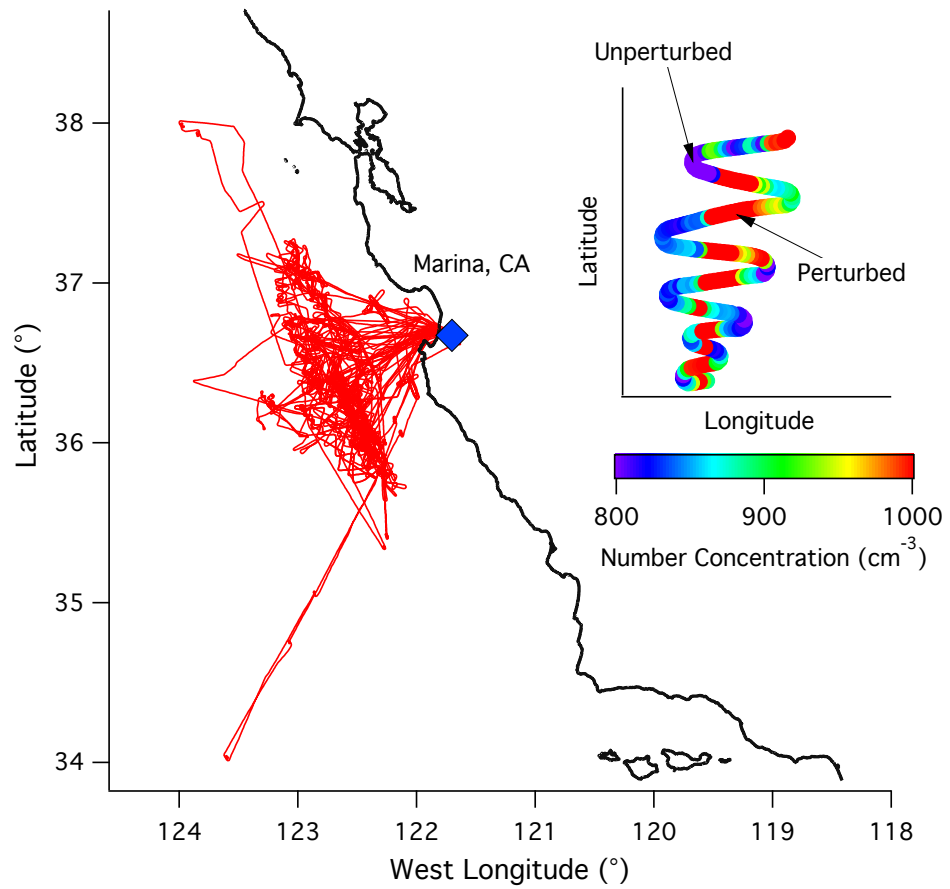


Fig. 1. Twin Otter flight paths for RF 1-26 during the E-PEACE mission. Inset shows a typical sampling pattern when encountering a ship exhaust plume. The color bar indicates the total aerosol number concentration as measured by the Twin Otter CPC.

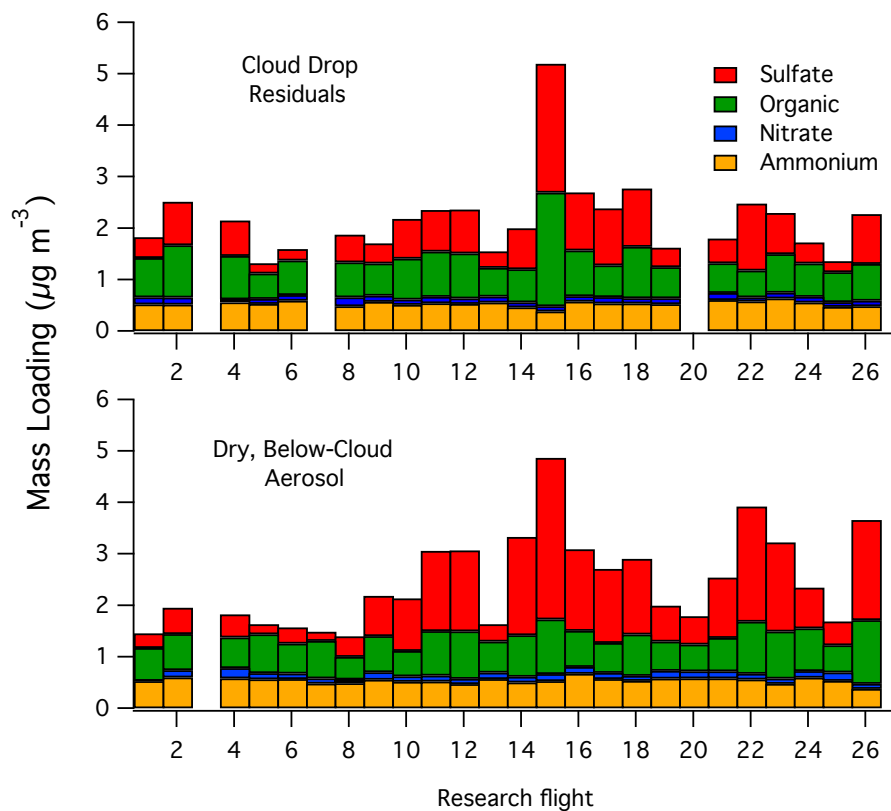


Fig. 2. Bulk AMS species measured in cloud drop residuals (top panel) and dry, below-cloud aerosol (bottom panel) over the course of the study. Only organic and sulfate vary significantly each day (variance of organic = 0.04, sulfate = 0.6 in below-cloud aerosol). Ammonium and nitrate exhibit variances that are at most 0.5% of the variance of sulfate.

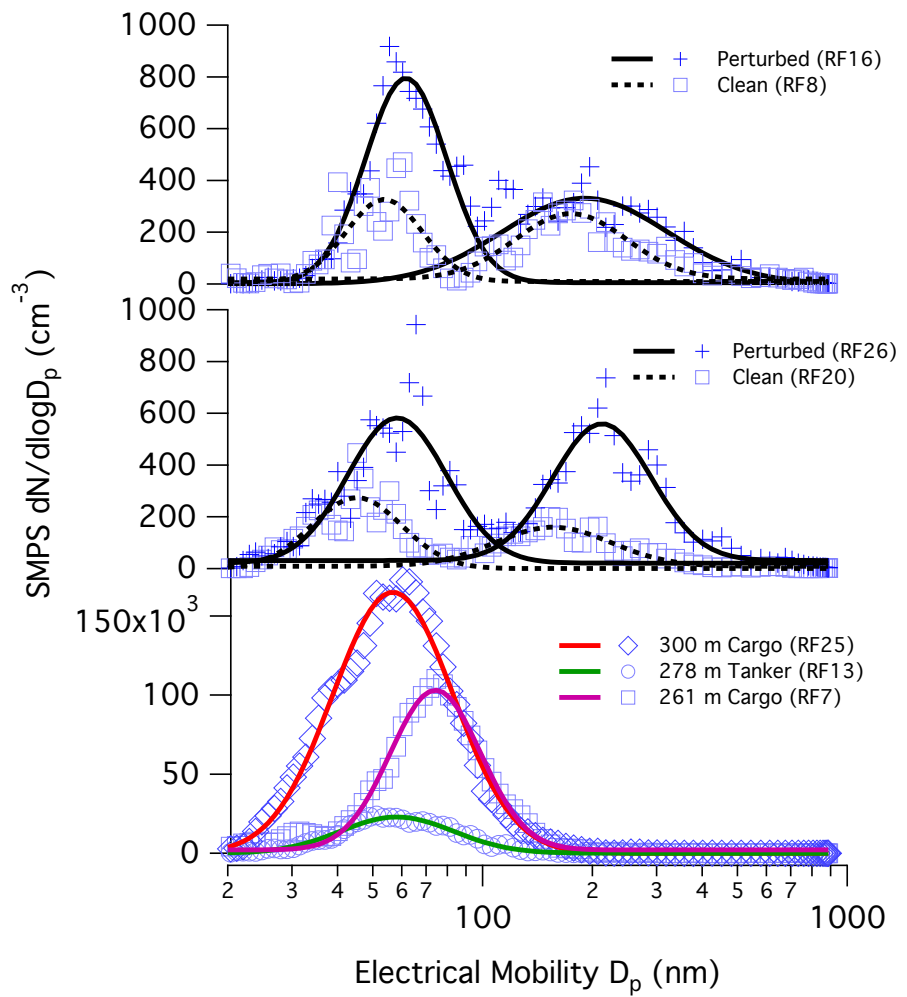


Fig. 3. Marine aerosol number size distributions of below-cloud aerosol measured during clean and perturbed flights (top and middle panels). Aerosol size distributions for the exhaust of three ships (bottom panel). Lines are log-normal fits.

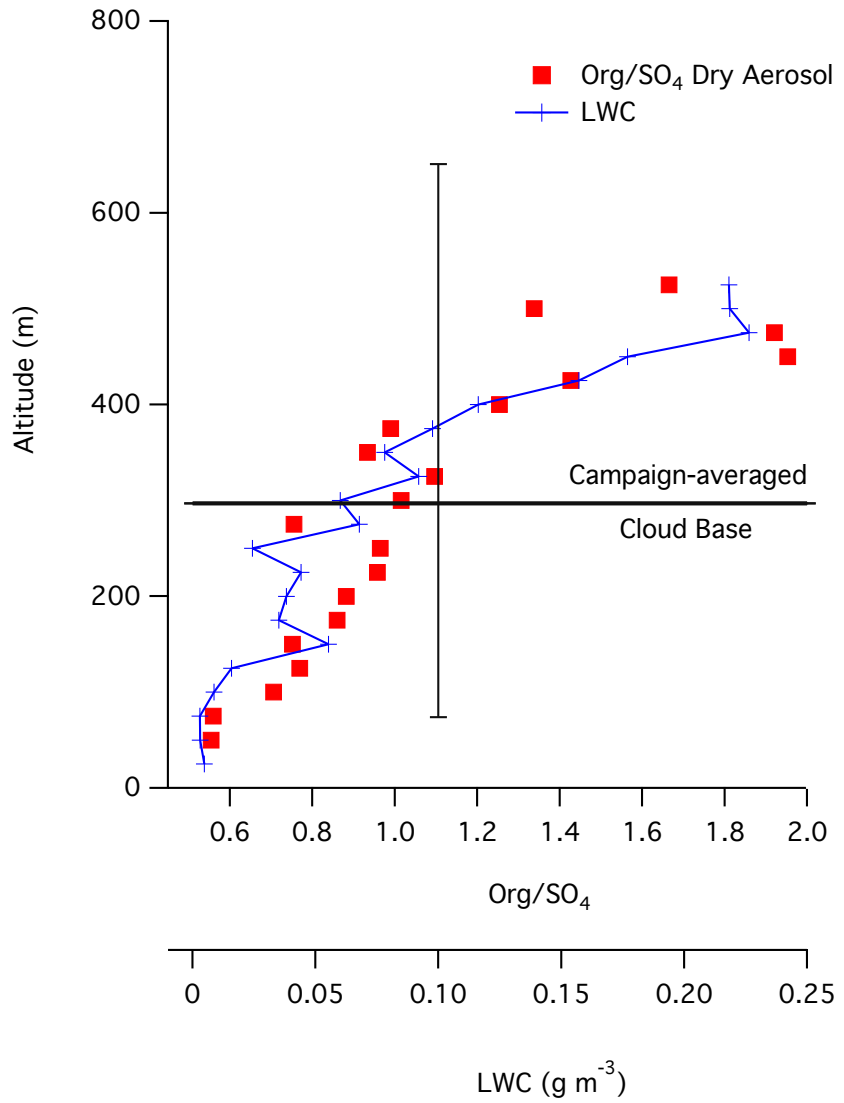


Fig. 4. Average organic:sulfate mass ratio of dry, unperturbed marine aerosol sampled in cloud-free air as a function of altitude. For clarity, standard deviations bars are omitted, however we note that variation increased with altitude. Average LWC is presented to illustrate the study-averaged, below-cloud top liquid water profile and show that cloud processing was prevalent at all altitudes. The campaign-average cloud base is shown with bars depicting the range of cloud bases and tops observed during the campaign. Cloud base altitudes were measured during aircraft soundings.

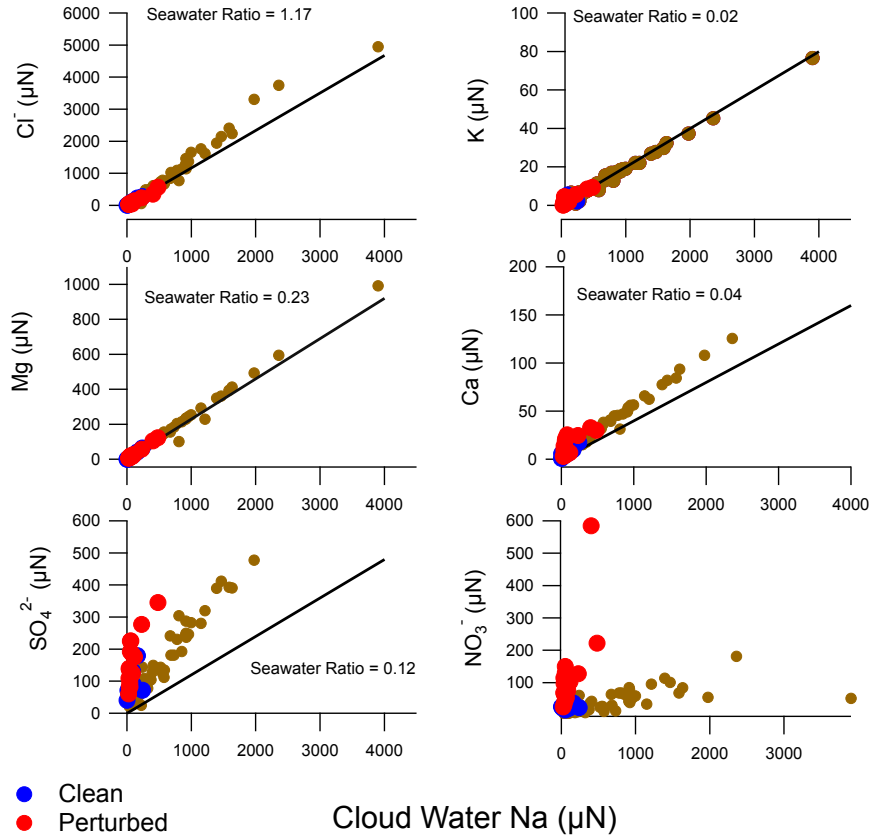


Fig. 5. Summary of major seawater species measured in marine cloud water. Data are presented analogously to those reported by Straub et al. (2007) and Benedict et al. (2012). In the present study, we assume that seawater species measured by ICP-MS (e.g. Na, K, Mg, Ca) reflect aqueous phase ions. The solid lines indicate the ion ratio typically observed in seawater. Each point represents a single cloud water measurement. Clean flights (RF 5 - 8) are colored in blue while perturbed flights (RF 14 - 18) are colored in red. The remainder of the flights are shown as brown circles.

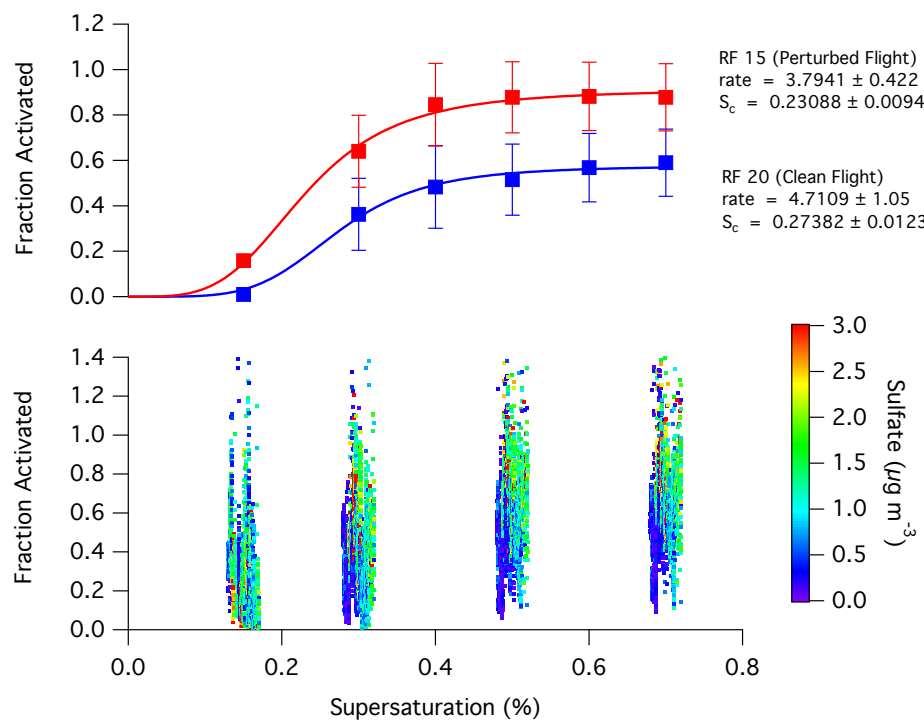


Fig. 6. CCN spectra showing the activation of particles at various supersaturations. The top panel is CCN data from a perturbed flight (red markers, RF 15) and clean flight (blue markers, RF 20) fitted to a sigmoidal curve of the form $\text{CCN/CN} = a_0 / (1 + (x/a_1)^{-a_2})$ where a_0 , a_1 and a_2 are fitted parameters. The error bars represent the measurement standard deviation. The bottom panel shows all CCN measurements made over the course of the campaign at 0.15, 0.3, 0.5 and 0.7% supersaturation.

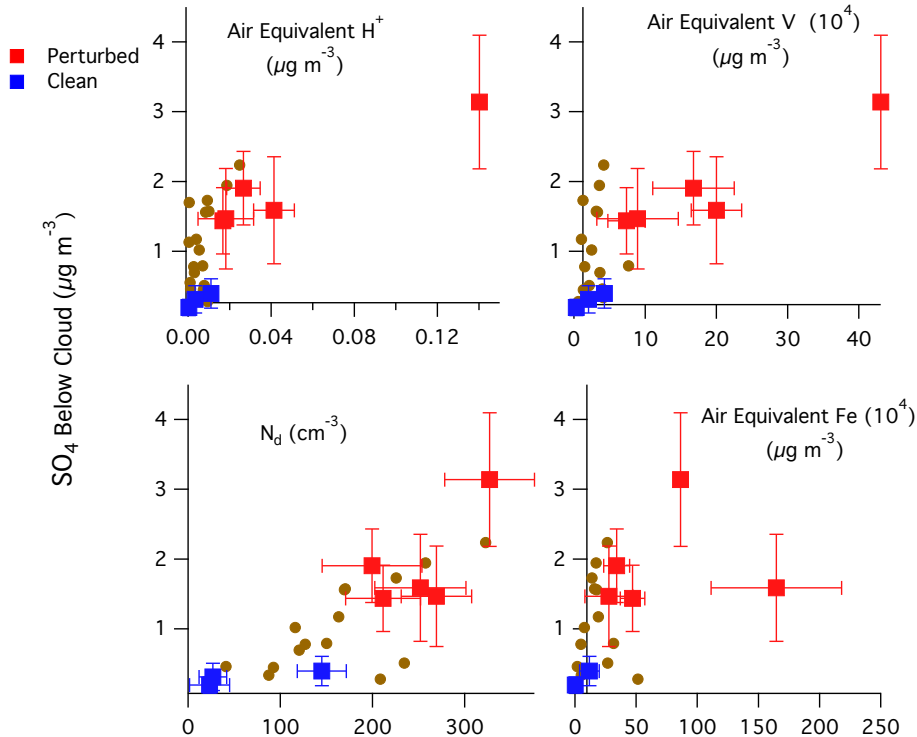


Fig. 7. Trends in below cloud sulfate vs. air equivalent H^+ , cloud droplet number concentration (N_d), air equivalent V and air equivalent Fe. Iron and vanadium were measured in cloud water samples using ICP-MS. Hydronium concentrations were calculated based on cloud water sample pH. Air equivalent units are calculated as the product of the concentration of a species in a bulk cloud water sample and the average liquid water content measured during the cloud water collection period. Each point represents a single flight. Clean flights (RF 5 - 8) are colored blue while perturbed flights (RF 14 - 18) are colored red. Error bars show the standard deviation of each measurement. The remainder of the flights are shown as brown circles.

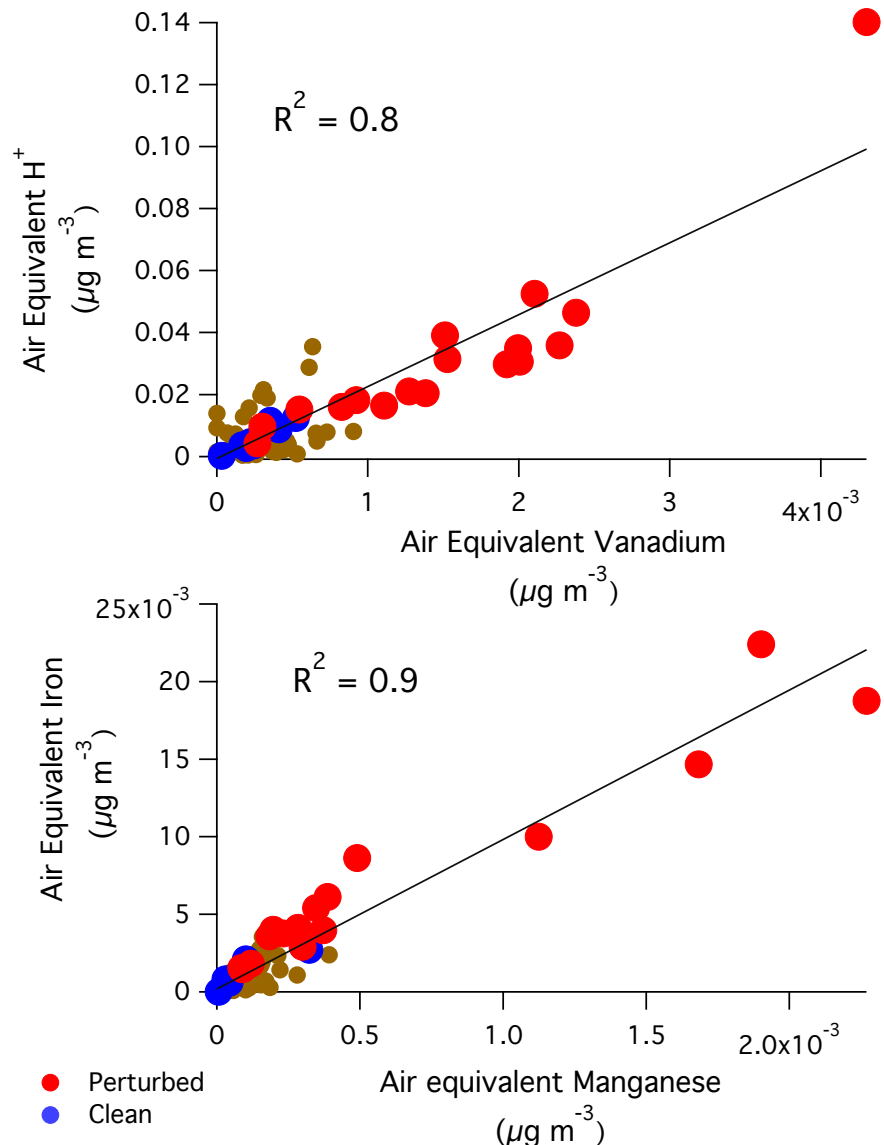


Fig. 8. Top - variation in air equivalent vanadium with respect to air equivalent hydronium concentrations for cloud water samples. Hydrogen concentrations were calculated based on cloud water sample pH. Bottom - trend in manganese and iron concentrations in cloud water for measurements made during clean (blue) and perturbed (red) days, respectively.

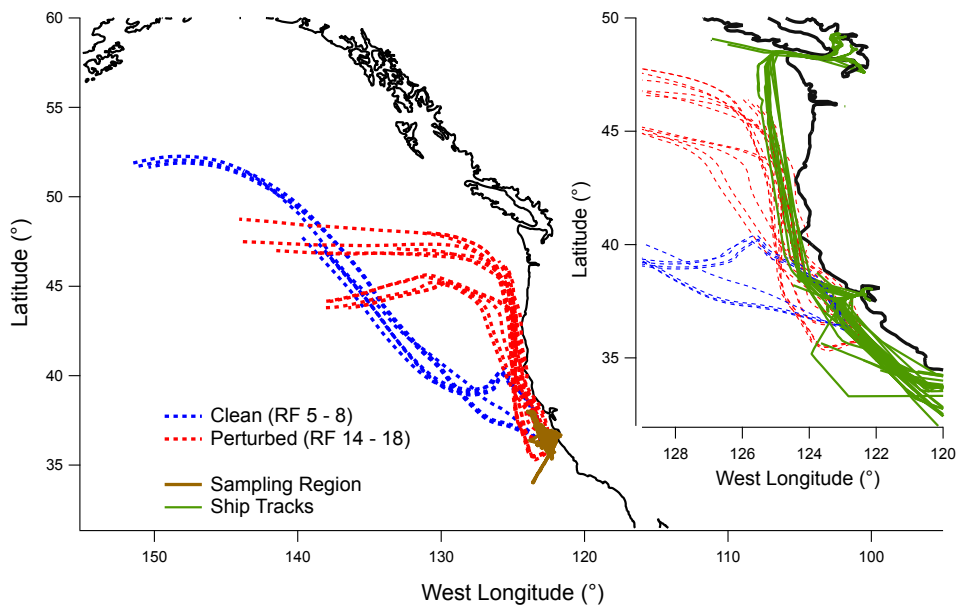


Fig. 9. Back-trajectories (72 hr) of cloud water samples collected during clean (blue) and perturbed (red) flights. Back-trajectories were calculated using the NOAA HYSPLIT model (available at: <http://www.arl.noaa.gov/ready/hysplit4.html>). Simulations were initialized with trajectories ending at the time, location and altitude of cloud water sampling. Inset shows a closer perspective of the California coast. The green traces are the ship tracks of 15 cargo and tanker ships probed during the campaign and illustrate the general location of the shipping lanes north of Long Beach, CA.

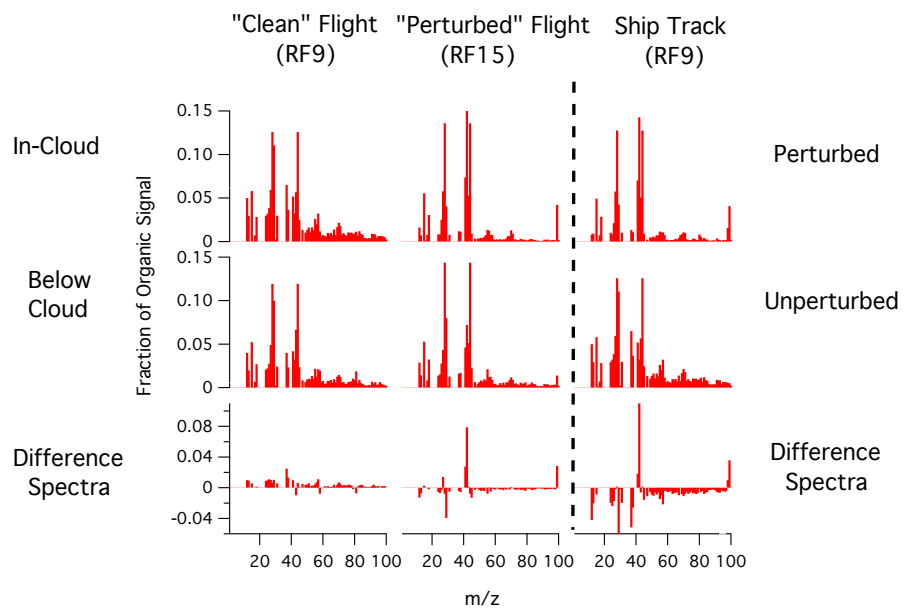


Fig. 10. Aerosol mass spectra comparing the organic signature of aerosol below and within cloud for a clean flight (RF 9) and perturbed flight (RF 15). To the right of the dotted line is a comparison of a ship track in cloud observed during RF 9 to the unperturbed, in-cloud background organics. The bottom row illustrates normalized difference spectra, which are the differences in the normalized (m/z mass / total mass) mass spectra of measurements presented in the top and middle rows. Positive values indicate a relative enhancement in masses observed in the top row spectra whereas negative values indicate a relative enhancement in masses observed in the middle row spectra.

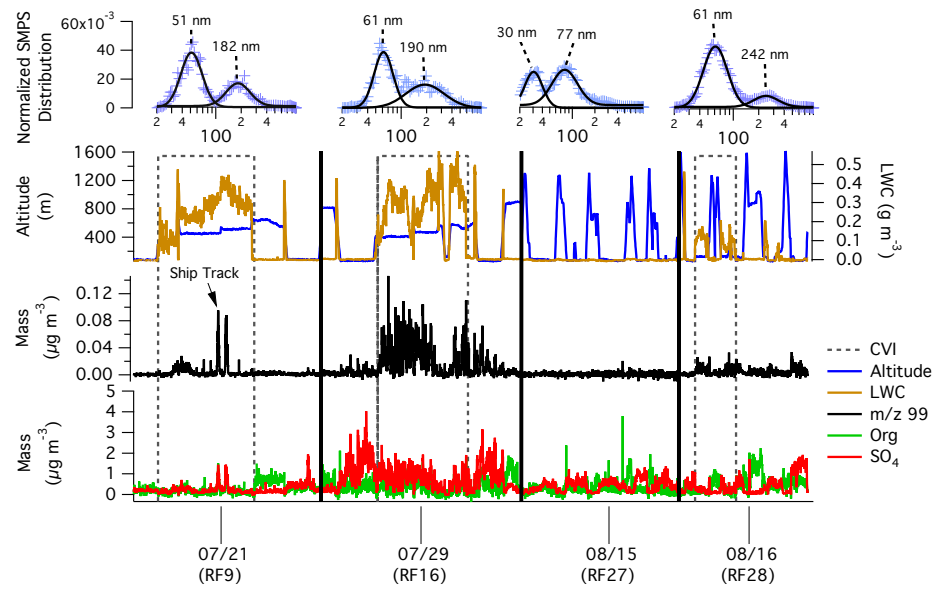


Fig. 11. Time series of organic, sulfate, organic m/z 99, LWC and altitude for research flights RF 9 (moderately clean, clouds), RF 16 (perturbed, clouds), and two additional flights that were performed outside the sampling region defined in Fig. 1, RF 27 (moderately clean, no clouds) and RF 28 (moderately clean, clouds). The top row of normalized aerosol number distributions ($dN/d\log D_p$ / (integrated loading)) show the distribution of marine aerosol below cloud for each flight. The dotted boxes show periods when samples were collected through the CVI inlet.

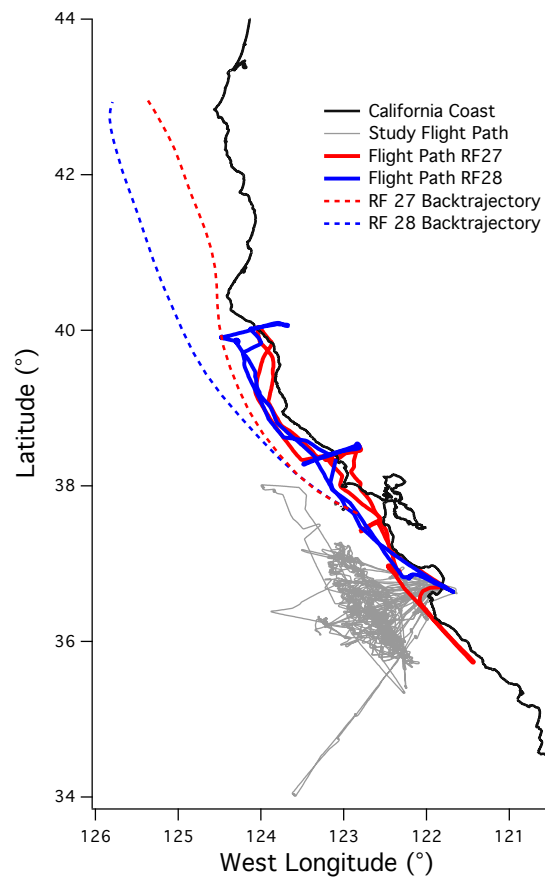


Fig. 12. Path of additional flights RF 27 (red) and RF 28 (blue) compared to the path of all other flights in the present study (grey, dotted line). Dotted lines are back-trajectories (24 hr) for air masses measured during the middle of each flight. RF 27 and RF 28 were coastal gradient flights conducted on clear (RF 27) and cloudy (RF 28) days.

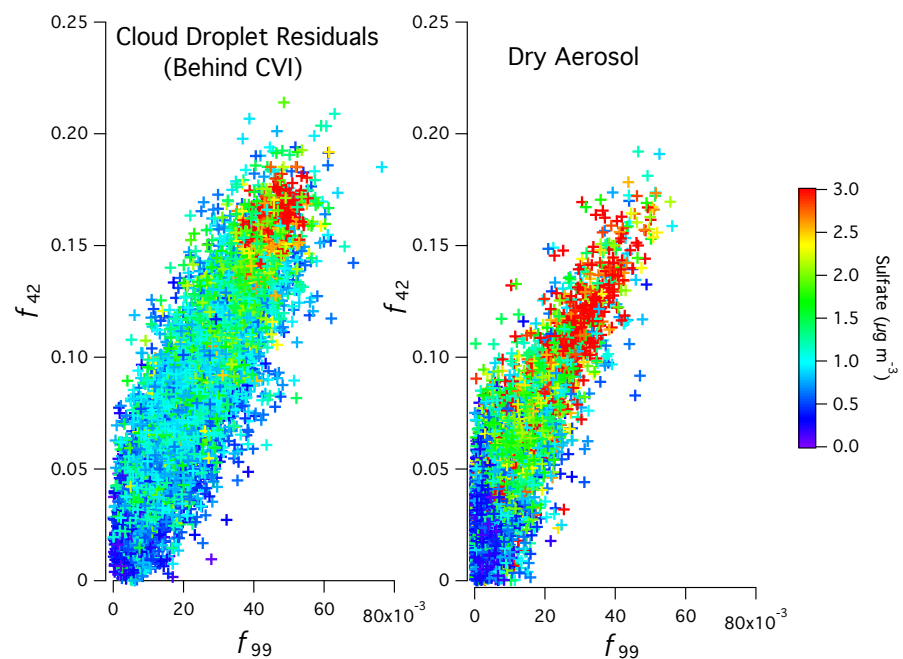


Fig. 13. Variation of the organic fraction of m/z 42 and m/z 99 (f_{42} , f_{99}) in the organic spectra of cloud water droplet residuals and dry aerosol. Markers are colored by sulfate loading to illustrate the potential impact of ships on each measurement.

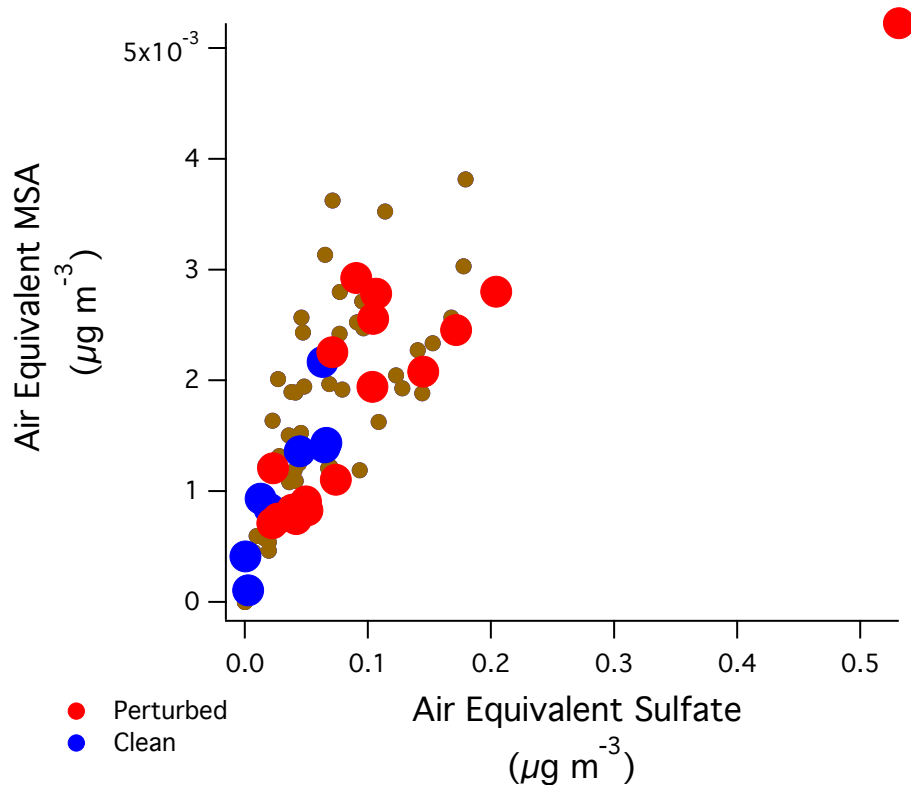


Fig. A1. Variation of air equivalent MSA and sulfate in cloud water droplets. Red markers represent measurements made during perturbed flights (RF 14 - 18), blue markers represent measurements made during clean flights (RF 5 - 8). Brown markers are all other measurements.

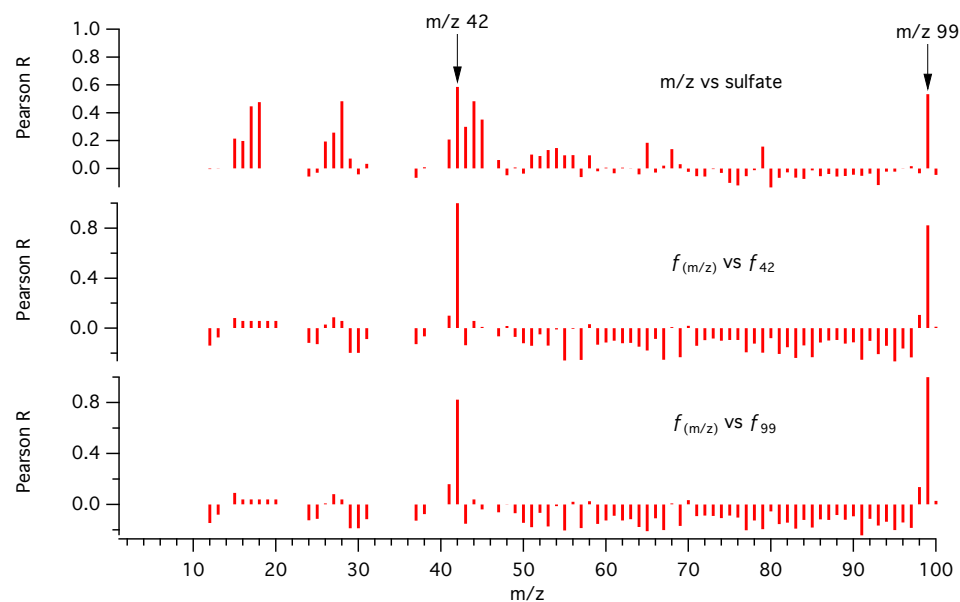


Fig. A2. Pearson R spectrum showing the variation of m/z concentrations vs. the concentration of sulfate (top), the variation of the fraction of m/z 42 (f_{42}) against the fraction of all other organic masses (middle), and the variation of the fraction of m/z 99 (f_{99}) against the fraction of all other organic masses (bottom). These correlations were calculated for measurements made outside of cloud.

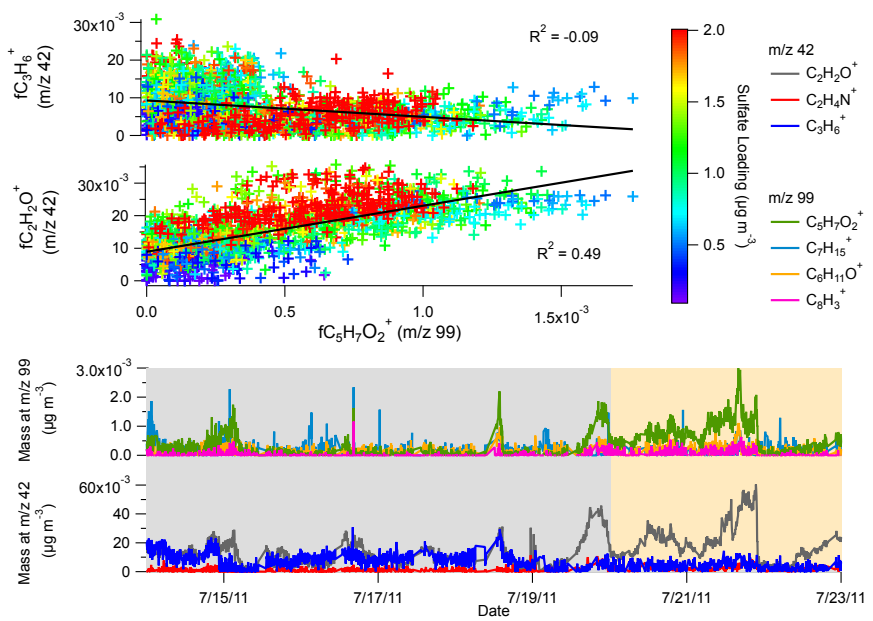


Fig. A3. Top - variation of $\text{C}_2\text{H}_2\text{O}^+$ and C_3H_6^+ at m/z 42 with $\text{C}_5\text{H}_7\text{O}_2^+$ at m/z 99. Markers are colored by sulfate loading. Bottom - time series trend showing the variation of the ions at m/z 42 and 99. Region shaded grey corresponds to the clean period of the cruise, region shaded light brown corresponds to the perturbed period of cruise.

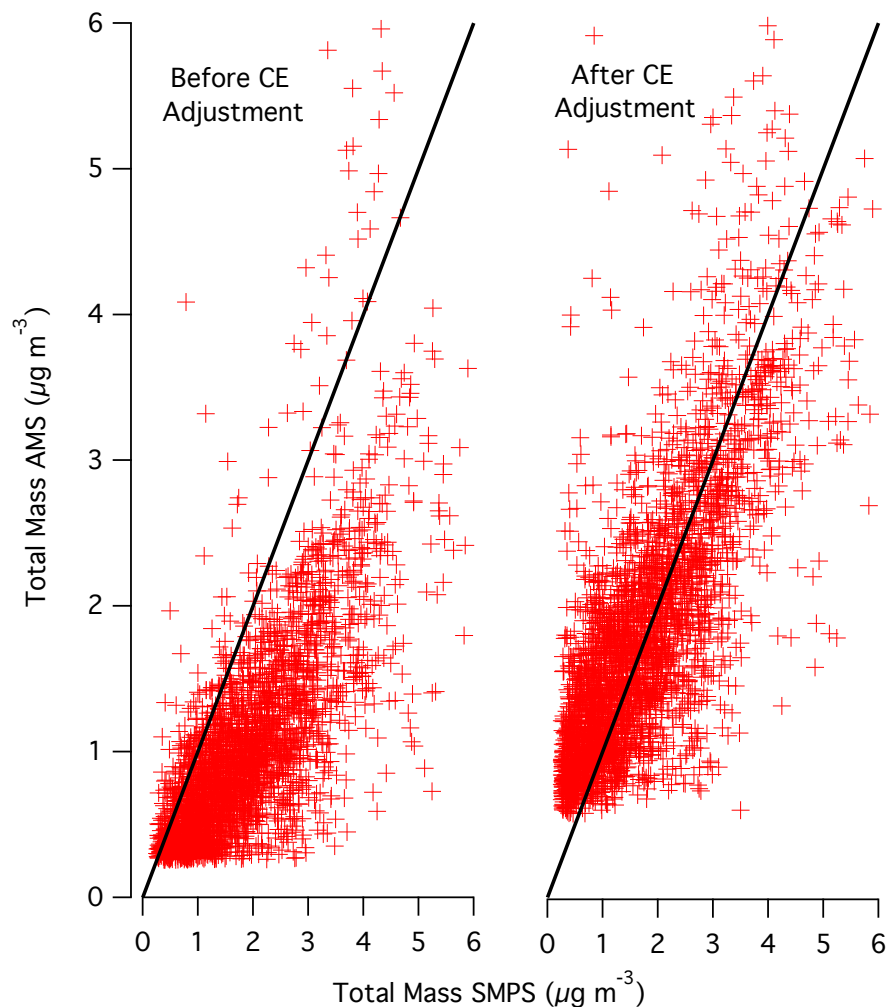


Fig. A4. Comparison of collection efficiency (CE) corrected AMS mass measurements to calculated total mass measured by SMPS. The plot on the left is the trend before CE correction (slope = 0.45), the plot on the right is the trend after CE correction (slope = 0.85). Volume concentration measured by SMPS was converted to mass concentration assuming a density of 1.6 g cm^{-3} , which is representative of a mixture of 60% sulfuric acid ($\rho = 1.84 \text{ g cm}^{-3}$) and 40% organics ($\rho = 1.2 \text{ g cm}^{-3}$) (Phinney et al. 2006).